Terminal Rare-Earth-Metal Imides and Phosphinidenes

Dissertation

der Mathematisch-Naturwissenschaftlichen Fakultät
der Eberhard Karls Universität Tübingen
zur Erlangung des Grades eines
Doktors der Naturwissenschaften
(Dr. rer. nat.)

vorgelegt von
M. Sc. Theresa E. Rieser
aus Tübingen

Tübingen
2024

Gedruckt mit Genehmigung der Mathematisch-Naturwissenschaftlichen Fakultät der Eberhard Karls Universität Tübingen.

Tag der mündlichen Qualifikation:	23.07.2024
Dekan:	Prof. Dr. Thilo Stehle
1. Berichterstatter:	Prof. Dr. Reiner Anwander
2. Berichterstatterin:	Prof. Dr. Doris Kunz

Terminal Rare-Earth-Metal Imides and Phosphinidenes

Theresa E. Rieser

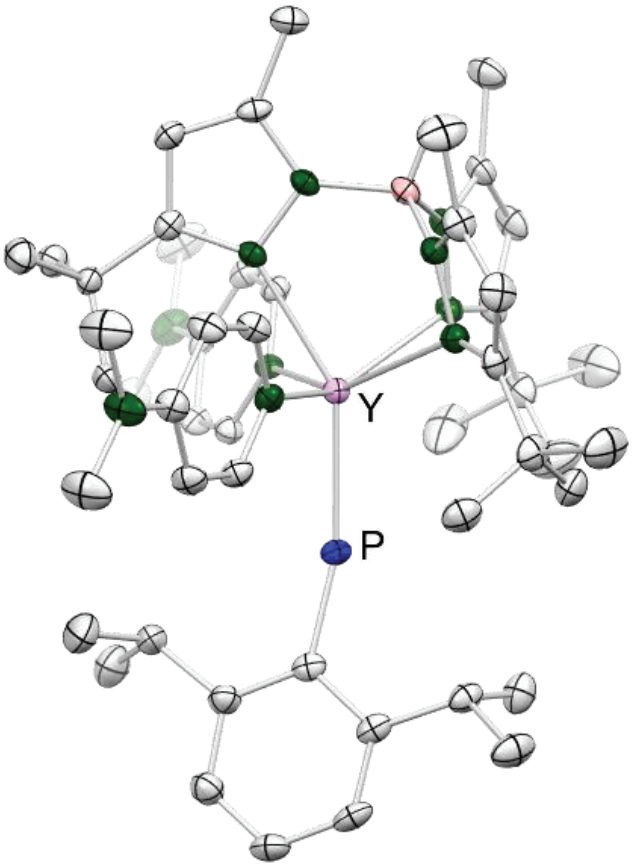

Preface

The following PhD thesis consists of a survey on the synthesis and reactivity of rare-earth-metal imide and phosphinidene complexes, a summary of the main results, and original scientific papers. The work has been carried out at the Institut für Anorganische Chemie of the Eberhard Karls Universität Tübingen, Germany, over the period from March 2019 to March 2023 under the supervision of Prof. Dr. Reiner Anwander.

Parts of this thesis have been presented at international and national conferences as poster contributions.

Acknowledgements

First of all, I would like to thank my supervisor Prof. Dr. Reiner Anwander. Thank you for the great opportunity to work in your high standard synthesis laboratory, providing me with this interesting research topic, as well as for your helpful advice in any scientific problem. I would like to thank you that you enabled me a great room for my personal and professional development by giving me the chance to attend international as well as national conferences, and by making the research internship with Prof. Dr. Warren Piers in Calgary, Canada, possible.

Special thanks go to Dr. Cäcilia Maichle-Mössmer for all help regarding crystal structure determinations and helpful discussions, to Dr. Klaus Eichele and Kristina Heß for maintaining the high standard equipment, as well as their help in all aspects regarding NMR spectroscopy. Additionally, I'd like to thank Wolfgang Bock and Mohammad Ghani for performing elemental analyses.

I further thank Tobias Wolf and especially Elke Niquet for their maintaining the laboratory equipment and their friendly and always helpful nature. Many thanks to Nadja Wettering for her IT support. Additionally, I want to thank the staff of the metal, electronics and glass workshops for manufacturing and repairing lab equipment.

I want to emphasize very special thanks to Sabine Ehrlich for the persistent and great work she is doing in the background as well as in the foreground. Thank you for helping me with any administrative issue but thank you most notably for the long and sometimes very philosophical talks we had together and for sharing the greatest hobby on earth with me.

I also would like to thank my current and former coworkers of the Anwander group. Especially Dr. Christoph O. Hollfelder, Dr. Tassilo Berger, Dr. Lorenz Bock, Dr. Dennis A. Buschmann, Dr. Markus Katzenmayer, Felix Kracht, Jakob P. Lebon, Eric C. Moinet and Dr. Georgios Spiridopoulos for being who you are, for all the moments we shared, for discovering Aventurien together, for your friendship and for your support all these years. Further thanks go to Jannik Barth, Dr. Uwe Bayer, Dr. Lars Hirneise, Dr. Yucang Liang, Dr. Alexandros Mortis, Jonas Riedmaier, Dr. Dorothea Schädle, Dr. Christoph Stuhl, Dr. Simon Trzmiel, Jitpisut Poolwang, Dr. Benjamin Wolf, Yali Yang, and Gernot Zug for the warm and friendly work environment you provided in the lab.

In diesem Rahmen möchte ich mich bei meiner lieben Familie und bei allen meinen Freunden bedanken. Danke an meine Eltern, die mich mit Liebe großgezogen haben, die ausnahmslos immer für mich da sind und die alles tun, dass ich meinen Weg gehen kann. Danke an meinen Bruder und seine junge Familie, für die Unterstützung in schwierigen Lebenslagen, für wunderschöne Momente und die ganze gemeinsame Zeit, die wir miteinander verbringen.

Für unvergessliche Momente, für Liebe und Geborgenheit, für Geschwindigkeit und Entschleunigung, für Deine Schulter in Zeiten, in denen ich nicht alleine stehen konnte, für alles was Du mir gegeben hast, möchte ich Dir danken, mein Hendrik.

Contents

Abbreviations

Ar	Aryl	E	main group elements (C, N, P, O, S)
9-BBN	9-Borabicyclo[3.3.1]nonane	EA	Elemental Analysis
*t*Bu	*tert*-Butyl	*e.g.*	*exempli gratia*
COSY	Correlated Spectroscopy	EN	electronegativity
Cp	Cyclopentadienyl	*et al.*	*et alii* or *et aliae*
Cp^{tBu}	$C_5Me_3(tBu)_2$	Et	Ethyl
Cp^*	C_5Me_5	HMBC	Heteronuclear Multiple Bond Correlation
Cp^{Si}	$C_5H_4SiMe_3$	HMDS	Hexamethyldisilazane
DEPT	Distortionless Enhancement by Polarization Transfer	HOMO	Highest Occupied Molecular Orbital
DFT	Density Functional Theory	HSAB	Hard and Soft Acids and Bases
DMAP	*N*,*N*-Dimethylaminopydridine	IR	Infrared
DME	Dimethoxyethane	LA	Lewis Acid
do	Donor	LB	Lewis Base
DRIFT	Diffuse Reflectance Infrared Fourier Transform	Ln	Rare-earth metals (Sc, Y, La – Lu)
Dipp	2,6-Di*iso*propylphenyl	L	Ligand

LUMO	Lowest Occupied Molecular Orbital	Tp^{Me}	Tris(3,5-dimethyl-pyrazolyl) borato
Me	Methyl	$Tp^{tBu,Me}$	Tris(3-*tert*-butyl-5-methyl-pyrazolyl) borato
Mes	Mesityl	Tp^{Ph}	Tris(3,5-diphenyl-pyrazolyl) borato
NBO	Natural Bond Orbital	UV-Vis	Ultraviolet–Visible
Ph	Phenyl	VT	Variable temperature
PNP	pincer-type ligand	X	halogens (F, Cl, Br, I)
*i*Pr	*iso*-Propyl		
ppm	parts per million		
Pz	Pyrazolyl		
R	rest		
r.t.	ambient temperature		
THF	Tetrahydrofuran		
TMEDA	Tetramethylethylenediamine		
tol	toluene		

Summary

As transition metals can contribute to the stabilization of organometallic complexes via covalent orbital interactions of the *d* metal orbitals and the *p* ligand orbitals, this approach turns out to be unfeasible for rare-earth metals (Ln = Sc, Y, La – Lu). Mainly ionic interactions with donor ligands and very hard, electropositive metal centers mean that rare-earth metals tend to undergo rapid ligand exchange and oligomerization if this is not prevented by the appropriate choice of the ligands and their steric and electronic properties.

Only a few terminal and multiply bonded rare-earth metal complexes for elements with completely empty 4*f* orbitals are described in the literature (Ln = Sc(III), Y(III), Ce(IV), Lu(III)). There are no examples for lanthanides with only partially filled 4*f* shells.

As a result, this work first addressed the question of whether terminal rare-earth metal imides can be isolated with suitable precursors such as methylidenes of the form [Tp$^{t\mathrm{Bu,Me}}$LnCH$_2$(μ_2 MeMMe$_2$)$_2$] (M = Al, Ga). It was successfully shown that a transformation of [Ln=CH$_2$] to [Ln=NR] groups is possible. These newly generated terminal neodymium and samarium imide complexes [Tp$^{t\mathrm{Bu,Me}}$Ln(NC$_6$H$_3$*i*Pr$_2$-2,6)(thf)$_2$] are characterized by very short Ln–N$_{imido}$ distances and nearly linear Ln–N$_{imido}$–C$_{ipso}$ angles.

In the second part of this work, the synthesis of terminal imides with smaller lanthanides like dysprosium and holmium was turned to. Here, too, the synthesis was successful, but a bis(alkylic) precursor [Tp$^{t\mathrm{Bu,Me}}$LnMe(μ_2-MeGaMe$_3$)] had to be used. The nucleophilic behavior of the terminal imido group could be demonstrated in reactivity studies.

Inspired by these results, it was even possible to go one step further. The [NR]$^{2-}$ fragment is characterized by its hard Lewis basicity and therefore preferentially forms ionic interactions with hard rare-earth metals. The question arose whether terminal rare-earth metal compounds could also be isolated with a softer donor, such as a doubly negatively charged phosphorus atom. Indeed, by exploiting sterical demanding donor ligands, it was possible to isolate the terminal yttrium phosphinidene [Tp$^{t\mathrm{Bu,Me}}$Y(PC$_6$H$_3$*i*Pr$_2$-2,6)(dmap)$_2$] with the shortest known Y–P intramolecular distance.

Zusammenfassung

Können Übergangsmetalle noch zusätzlich über kovalente Orbitalwechselwirkungen der *d* Metallorbitale und der *p* Ligandenorbitale zur Stabilisierung von Organometallkomplexen beitragen, gestaltet sich dieser Ansatz für seltene Erden (Ln = Sc, Y, La – Lu) als schwierig. Hauptsächlich ionische Wechselwirkungen mit Donorliganden und sehr harte, elektropositive Metallzentren führen dazu, dass Seltenerdmetalle zu schnellem Ligandenaustausch und Oligomerisierungen neigen, wenn man dies nicht über eine geeignete Wahl der Liganden und ihren sterischen, sowie elektronischen Eigenschaften unterbindet.

In der Literatur sind nur wenige terminale und mehrfach gebundene Seltenerdmetallkomplexe für Elemente mit gänzlich leeren 4*f* Orbitalen beschrieben (Ln = Sc(III), Y(III), Ce(IV), Lu(III)). So gibt es für Lanthanoide mit nur teilweise gefüllter 4*f* Schale noch keine Beispiele.

In dieser Arbeit wurde sich in Folge dessen zunächste der Fragestellung gewidmet, ob mit geeigneten Vorstufen, wie Methylidenen, der Form $[Tp^{tBu,Me}LnCH_2(\mu_2\text{-}MeMMe_2)_2]$ (M = Al, Ga), terminale Seltenerdmetallimide isoliert werden können. Es konnte erfolgreich gezeigt werden, dass eine Transformation von $[Ln{=}CH_2]$ zu [Ln=NR] Gruppen möglich ist. Diese neu generierten terminalen Neodym- und Samariumimidkomplexe $[Tp^{tBu,Me}Ln(NC_6H_3iPr_2\text{-}2,6)(thf)_2]$ zeichnen sich durch sehr kurze $Ln–N_{imido}$ Abstände und nahezu lineare $Ln–N_{imido}–C_{ipso}$ Winkel aus.

Im zweiten Teil dieser Arbeit, wurde sich der Synthese von terminalen Imiden mit kleineren Lanthanoiden, wie Dysprosium und Holmium zugewandt. Auch hier war die Synthese erfolgreich, dabei musste aber auf eine bis(alkylische) Vorstufe $[Tp^{tBu,Me}LnMe(\mu_2\text{-}MeGaMe_3)]$ zurückgegriffen werden. In Reaktivitätsstudien konnte das nukleophile Verhalten der terminalen Imidogruppe nachgewiesen werde.

Das $[NR]^{2–}$ Fragment zeichnet sich durch seine harte Lewis Basizität aus und bildet daher bevozugt ionische Wechselwirkungen mit harten Seltenerdmetallen aus. Es stellte sich daher die Frage, ob mit einem weicherer Donor, wie einem zweifach negativ geladenen Phosphoratom es ebenfalls möglich ist terminale Seltenerdmetallverbindungen zu isolieren. Tatsächlich konnte unter Ausnutzung von sterisch anspruchsvollen Donorliganden, ein terminales Yttriumphosphiniden $[Tp^{tBu,Me}Y(PC_6H_3iPr_2\text{-}2,6)(dmap)_2]$ isoliert werden.

Publications

Publications incorporated into this thesis:

Paper I Open Shell Early Lanthanide Terminal Imides
T. E. Rieser, R. Thim-Spöring, D. Schädle, P. Sirsch, R. Litlabø, K. W. Törnroos, C. Maichle-Mössmer, R. Anwander
J. Am. Chem. Soc. **2022**, *144*, 9, 4102 – 4113
https://doi.org/10.1021/jacs.1c13142

Paper II A Terminal Yttrium Phosphinidene
T. E. Rieser, P. Wetzel, C. Maichle-Mössmer, P. Sirsch, R. Anwander
J. Am. Chem. Soc. **2023**, *145*, 32, 17720 – 17733
https://doi.org/10.1021/jacs.3c04335

Paper III Terminal Dysprosium and Holmium Organoimides
T. E. Rieser, D. Schädle, C. Maichle-Mössmer, R. Anwander
Chem. Sci., **2024**
https://doi.org/10.1039/D3SC06584G

Poster presentations

Poster I Terminal Rare-Earth-Metal Imides
T. E. Rieser, C. Maichle-Mössmer, R. Anwander
XXX. Tage der Seltenen Erden, Montpellier, France, *September 22-24*, **2021**.

Poster II Formation and Reactivity of Terminal Rare-Earth-Metal Imides
T. E. Rieser, C. Maichle-Mössmer, R. Anwander
Canadian Chemistry Conference and Exhibition CSC CCCE, Calgary, Canada, *June 13-17*, **2022**.

Personal Contribution

Paper I:

All reactions and analyses described were planned and conducted by myself (except [Tp^{tBu,Me}Ln{(μ_3-CH$_2$)[(μ_2-Me)MMe$_2$]$_2$}] (Ln = Ce, Nd; M = Al, Ga) and [Tp^{tBu,Me}Ce(NC$_6$H$_3$*i*Pr$_2$-2,6)(thf)$_2$]). Analyses include one-dimensional (^{1}H, ^{11}B{^{1}H}) NMR spectroscopic methods and DRIFT. Manuscript writing was also done by me. The synthesis and characterization of [Tp^{tBu,Me}Ce(NC$_6$H$_3$*i*Pr$_2$-2,6)(thf)$_2$]) and [Tp^{tBu,Me}Ln{(μ_3-CH$_2$)[(μ_2-Me)MMe$_2$]$_2$}] (Ln = Ce, Nd; M = Al, Ga) were done by Dr. Renita Thim and Dr. Dorothea Schädle.

Elemental analyses were performed by Wolfgang Bock. The structural analyses by single crystal X-ray diffraction were performed by Dr. Cäcilia Maichle-Mössmer.

Paper II:

All reactions and analyses described were planned and conducted by myself (except of the NMR scale experiments [Tp^{tBu,Me}Y(μ_2-PC$_6$H$_3$*i*Pr$_2$-2,6)(μ_2-MeAlMe$_2$)] + CO$_2$ and benzophenone, [Tp^{tBu,Me}LuMe(HPC$_6$H$_3$*i*Pr$_2$-2,6) and [Tp^{tBu,Me}LuMe(HPC$_6$H$_3$*i*Pr$_2$-2,6)(dmap)] which were conducted by Philipp Wetzel). Analyses include one-dimensional (^{1}H, ^{13}C{^{1}H}) NMR spectroscopic methods and DRIFT. Manuscript writing was also done by me.

Elemental analyses were performed by Wolfgang Bock and Mohammad Ghani. The structural analyses by single crystal X-ray diffraction were performed by Dr. Cäcilia Maichle-Mössmer. DFT analysis were conducted by Dr. Peter Sirsch.

Paper III:

All reactions and analyses described were planned and conducted by myself (except Ho(Ga(CH$_3$)$_4$)$_3$ and Dy(Ga(CH$_3$)$_4$)$_3$). Analyses include one-dimensional (^{1}H, ^{13}C{^{1}H}) NMR spectroscopic methods and DRIFT. Manuscript writing was also done by me. The synthesis and characterization of Ho(Ga(CH$_3$)$_4$)$_3$ and Dy(Ga(CH$_3$)$_4$)$_3$were done by Dr. Dorothea Schädle.

Elemental analyses were performed by Wolfgang Bock and Mohammad Ghani. The structural analyses by single crystal X-ray diffraction were performed by Dr. Cäcilia Maichle-Mössmer.

Objective of this Thesis

The main emphasis of this thesis is to synthesize and investigate the reactivity of terminal rare-earth-metal complexes with multiple bonded ligands such as imides and phosphinidenes.

Chapter A gives an overview of recent efforts in main group to rare-earth-metal coordination chemistry. Hereby, the concentration will be set on multiple bonding situations with nitrogen and phosphorous atoms and their nucleophilic reaction behavior towards unsaturated substrates.

Chapter B contains a summary of the main results of this thesis and is divided in to two parts:

- Terminal Rare-Earth-Metal Imide Complexes
- Terminal Rare-Earth-Metal Phosphinidene Complexes

In **Chapter C** unpublished results, which are not part of a publication or manuscript, are presented. This contains terminal rare-earth-metal methyl complexes and cerium imido chemistry.

Chapter E is a compilation of publications.

A

Terminal Multiple Bonded Rare-Earth Metal Complexes

1 Introduction

The quest for terminally, multiply bonded rare-earth metals (Ln = Sc, Y, La – Lu) to main group elements has witnessed a tremendous momentum in the past decade. Fundamental understanding of highly polarized, non-directional ionic interactions of rare-earth metals with main group elements and their unique reactivity patterns are considered a key issue in organic and inorganic synthesis and catalysis. Most notably, the transitionmetal metathesis catalyst of the Grubbs[2]/Schrock[3] system culminated in the noble prize in 2005[4], as well as Tebbe methylation.[5] The Ln–$E_{terminal}$ moiety is known to activate small molecules in multiple bond metathesis reactions of olefines, alkynes, imines, aldehydes, carbodiimides[6-8], and insertion reactions.[9-11] Moreover, it is used as building block in metalorganic synthesis, such as cycloadditions (metallacycle formation) of alkynes, alkenes and unsaturated substrates,[9, 12] as well as for C–H bond activations.[13] Being understood best, the Ln–N_{imido} fragment could be a relevant intermediate in N_2 fixation, as well. The high oxophilicity of the hard rare-earth cations renders them suitable activators of carbonyl groups such as C=O bonds in carbon dioxide. Considering the vast impacts of carbon dioxide in modern societies, this is a major challenge in present chemistry.

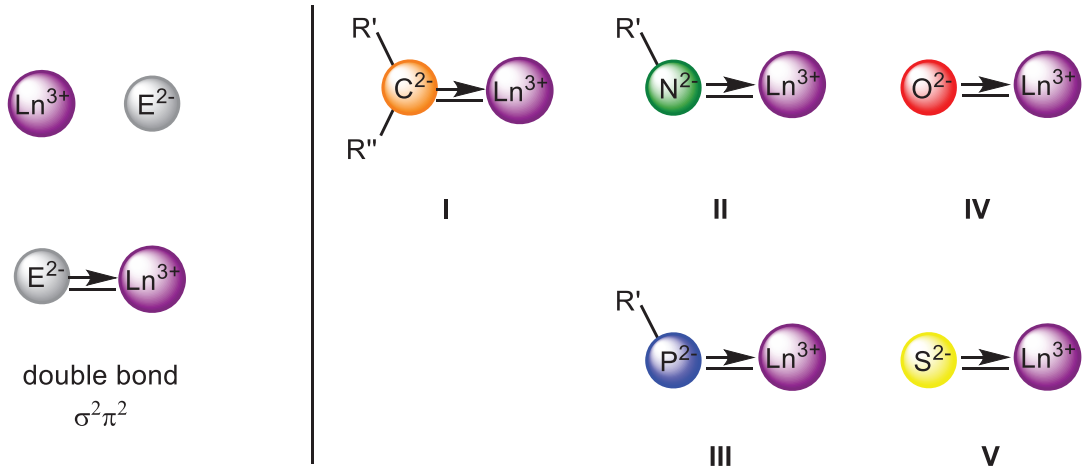

Figure A1. The non-directional ionic interactions in main group/rare-earth-metal complexes are commonly described with a double bond formalism (left). However, this does not reflect the bonding situation in these complexes. Selected bond patterns of eligible main group elements with double negative charge coordinating to relatively hard, trivalent rare-earth metal ions (right).

Other than covalent bond interactions in transition metals, rare-earth metals instead engage mainly in non-directional ionic interactions, caused by the low radial extension of the 4*f* orbitals and the shielding of the 4*f* electrons by exterior orbitals. This leads to complexes that are prone

to rapid ligand exchange/redistribution (Schlenk equilibria), oligomerizations and aggregations. Therefore, the double-bond formalism commonly used does not reflect the nature of the bonding but will be employed in the following.

Almost exclusively steric (kinetic stabilization)[14] and electrostatic factors must be considered to avoid aggregation, bridging and oligomerization,[7, 15-18] that is caused by the highly polarized/basic ligands $[E]^{2-}$, the size of the rare-earth metal ions and their electropositivity. Hence, monomeric neutral complexes can be routinely achieved in the presence of strong Lewis acids (LA) such as boranes $[BR_3]$,[7, 19] alanes $[AlR_3]$[1, 20] and their higher homologues gallanes $[GaR_3]$ to form Lewis acid capped complexes in form of $[Ln(\mu\text{-}NR)(LA)]$,[20, 21] to provide steric saturation, dispense of electron density, and prevent consecutive reactions. Since the early 90's of the last century the imido $[NR]^{2-}$ ligand is regarded to be the best choice to stabilize rare-earth metal complexes with terminally bonded main group elements.[22] Compared to the oxo $[O]^{2-}$ ligand, the substituent on the imido nitrogen offers possibilities to fine-tune the steric and acidic properties. Compared to the methylidene $[CR_2]^{2-}$ ligand, dianionic nitrogen is less soft and more favored to coordinate to hard rare-earth metals. Again, judicious selection of the ancillary ligand plays a pivotal role to kinetically stabilize terminal $Ln–N_{imido}$ functionalities as C–H bond activation of the ligand scaffold or solvent molecules occur without sufficient shielding.[15, 23] On the other hand, the highly reactive configurations of those challenging double bonded fragments will lead to striking reactivity patterns.

However, synthesis protocols suitable for transition metals and actinides are mostly not applicable for rare-earth metals due to their beforehand discussed inimitably properties. The insufficient overlap of the rare-earth metal 5*d* orbitals and the ligands *p* orbitals renders electronically frustrated moieties that deficiently lower the ligands π-basicity and the resulting nucleophilic reaction behavior demands for adjusted techniques and synthesis routes.

This short survey over the research efforts done in terminal rare-earth metal and main group element chemistry among the last three decades is parted into two sections. In Chapter 2 the focus is on the achievements in rare-earth-metal imide chemistry and the utilization of newly developed synthesis pathways, whereas Chapter 3 emphasizes the growing field of the recently emerging rare-earth metal phosphinidene chemistry.

2 Rare-Earth-Metal Nitrogen Compounds

2.1 Introduction

In organo-transition[24-37] and -actinide[38-44] metal chemistry both terminal and stabilized imide complexes are well-known. However, examples for rare-earth-metal imide species are scarce and terminal rare-earth-metal imide complexes are limited to few examples. In fact, most of the reported terminal rare-earth-metal imide complexes are bearing a scandium metal center,[9, 12, 45-47] as not only the imido functionalities with sufficiently bulky moieties provide adequate steric protection and electrostatic stabilization, but the small ionic radius of scandium can impede oligomerizations or the complexation by additional Lewis acids by diminishing the amount of ligands attached to the metal center.

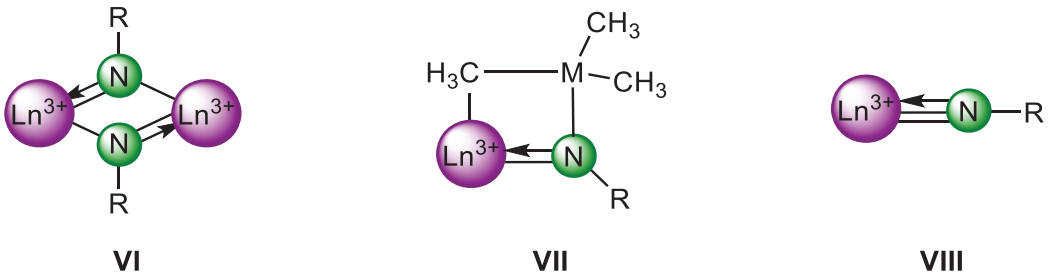

Figure A2. Possible bonding motifs for rare-earth-metal imide complexes: Oligomers with bridging imido nitrogens (**VI**), Lewis acid stabilized, bimetallic complexes (**VII**), and terminal rare-earth-metal imides (**VIII**).

The high electropositivity, and thus resulting high Lewis acidity, and the low radial extension of the 4*f* valence orbitals force rare-earth metals to develop mainly ionic interactions. This results often in oligomerizations (Figure A2, **VI**),[15, 48] more stable bi- or multinuclear arrangements with bridging moieties (Figure A2, **VI**),[11, 22, 49-54] stabilization with additional Lewis acids (Figure A2, **VII**),[55] like sodium/lithium[56] instead of terminal species (Figure A2, **VIII**). Hence, multiple bonds to main group elements are challenging.[15, 17, 48, 57-60] Aside from that, the high charge density of hard, monodentate $[E]^{n-}$ (E = O, N, P) ligands promote cluster formation. Once established, rare-earth metal imides can activate C–H bonds in solvents, assemble as more stable bimetallic μ_2-bridging complexes or multimetallic clusters.[47-48] To find remedy for these obstacles, the ligand design is of vital interest, since sterically demanding and electron rich ancillary ligands can provide sufficient shielding and affect the polarization of Ln–N_{imido} interactions. On the other hand, the highly reactive Ln–N_{imido} bond gives the opportunity

to investigate new reactivities such as group transfer and bond activation applications[15, 48, 61-62], as well as fundamental insights into non-directional ionic interactions.

2.2 Rare-Earth-Metal Imide Complexes

The following section is divided in three chapters, according to the discussed bond motifs, starting with dimeric, bridging rare-earth metal imides.

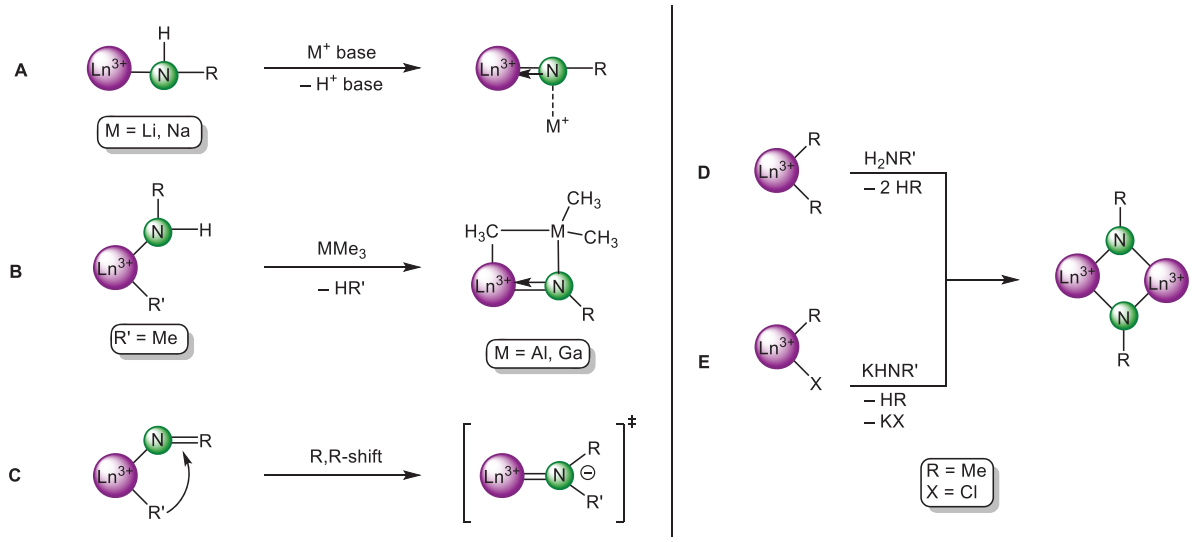

Scheme A1. Synthesis pathways to isolate rare-earth-metal imide complexes mainly based on deprotonation reactions, in dependence of the used precursors.

Treatment of the anilido ytterbium complex $[(Ar^{iPr}NH)_2Yb(\mu_2\text{-}NHAr^{iPr})_2Na(thf)]$ with a strong, external base such as *n*-butyllithium leads to deprotonation of the [NH]-moiety. The resulting mixed imido/amido ytterbium "ate"-complex $[(2,6\text{-}iPr_2C_6H_3N)(2,6\text{-}iPr_2C_6H_3NH)Yb(\mu_2\text{-}NC_6H_3iPr_2\text{-}2,6)]_2[\{Li_2(thf)\}\{Na(thf)\}]_2$ is coordinated by additional lithium and potassium cations. Addition of two equivalents of *n*-butyllithium leads to continuing deprotonation and the formation of trivalent, dimeric complex $[(2,6\text{-}iPr_2C_6H_3N)_2Yb(\mu_2\text{-}NC_6H_3iPr_2\text{-}2,6)]_2[\{Li_2(thf)\}\{Na(thf)\}]_2$ (**1**) (Scheme A1, **A**; Figure A3), which bears two bridging imido functionalities between the ytterbium centers and four imido units capped by alkali metal cations. The Yb–N_{imido} distances of the outer imido functionalities have an average value of 2.122 Å.[56] Deprotonation of a dimeric anilido samarium complex is as well successful by adding excess Lewis acid, such as trimethylaluminium, to form $[(\mu_2\text{-}NAr^{iPr})Sm(\mu_2\text{-}HNAr^{iPr})(\mu_2\text{-}Me)AlMe_2]_2$ (Scheme A1, **B**; Figure A3, **2**). A significant interaction between the *ipso* carbon of the bridging imido moiety and the samarium centers causes the asymmetry of the Sm_2N_2 core (Sm–N: 2.152(8) – 2.271(7) Å). [55] In 2003 Teuben et al. pursued a completely other approach to achieve rare-earth-metal imide complexes by reacting a scandium 2,3-dimethyl-1,3-butadienyl species reacting with benzonitrile to form the dimeric scandium imide complex

$[\{C_5H_4(CH_2)_2NMe_2\}Sc\{\mu_2\text{-}NC(Ph)C_6H_{10}\}]_2$ (Figure A3, **3**). The postulated reaction mechanism is described as a nitrile insertion into one of the Sc–CH_2 bonds of the butadienyl ligand. Hereupon, the second carbon of the other Sc–CH_2 bond attacks nucleophilically the carbon atom of the former nitrile group and precedes to a five-membered ring closure. The unsaturated imido species readily dimerizes (Scheme A1, **C**; Figure A3, **3**), due to its reactivity and the missing steric protection.[51]

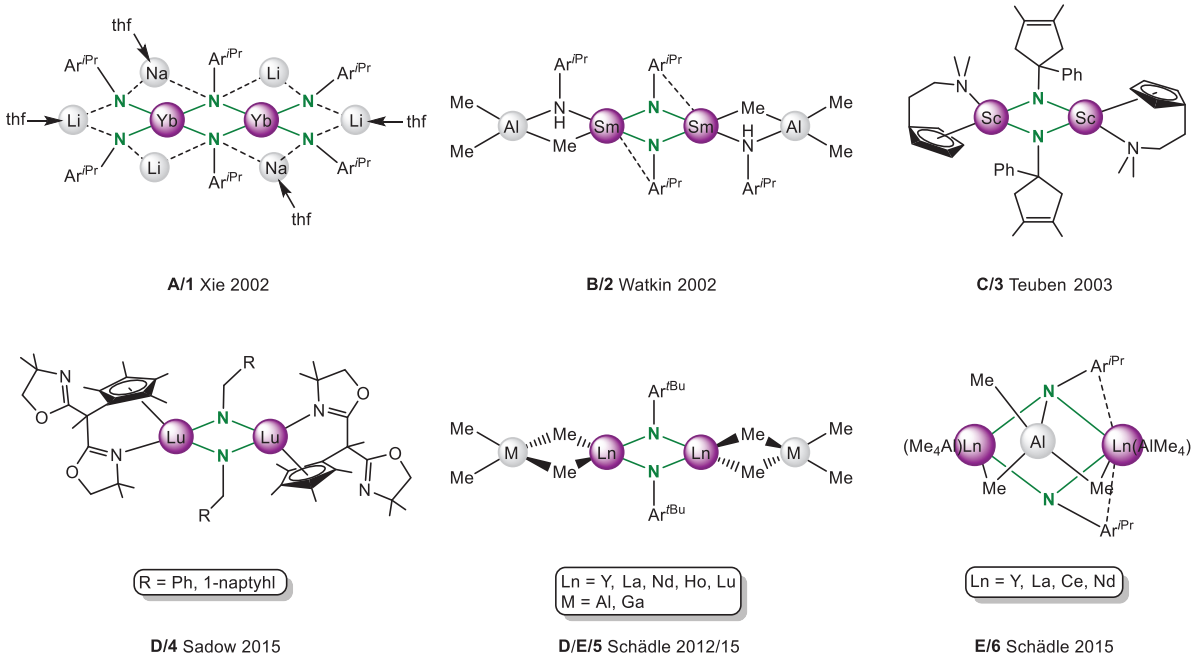

Figure A3. Exemplary dimeric, imido-bridged rare-earth-metal complexes obtained via the synthesis pathways (**A** – **E**) depicted in Scheme A1.

Double deprotonation and concerted elimination of smaller molecules is a further possibility to obtain rare-earth-metal imide complexes (Scheme A1, **D**). Indeed, this reaction pattern is one of the mainly used pathways to successfully synthesize imide complexes with rare-earth metals. The reaction of a monomeric lutetium precursor complex, bearing two benzyl functionalities with primary benzylamine [H_2NCH_2Ph] leads to the formation of a dimeric, imido-bridged lutetium complex $[\{Bo^MCp^{tet}\}LuNCH_2R]_2$ (R = Ph, 1-naphthyl; Bo^MCp^{tet} = tetramethylcyclopentadienyl–bis(4,4-dimethyl-2-oxazoline)) (Scheme A1, **D**; Figure A3, **4**) with Lu–N_{imido} interatomic distances of 2.116(4) Å and 2.163(4) Å.[63] This kind of substitution reactions in which alkyl groups are displaced by amido ligands is well-known *e.g.*, as initial step in rare-earth-metal promoted hydroamination reactions of alkenes and alkynes.[64-65] Methane elimination or salt metathesis/protonolysis tandem reactions with the corresponding aniline derivatives lead to the heterobimetallic, homoleptic complexes

$[Ln(MMe_4)(\mu_2\text{-}NC_6H_3tBu_3\text{-}2,4,6)]_2$ (Ln = Y, La, Nd, Ho, Lu; M = Al, Ga) (Scheme A1, **D**/**E**; Figure A3, **5**). Again, an asymmetric Ln_2N_2 core is assigned to interactions with *ipso*/*ortho* carbon atoms of the aryl group in the imido functionality. Short Ln–N_{imido} distances (Ln = Y: 2.1089(9)/2.2909(9) Å; Ln = La 2.224(5)/2.414(5) Å; Ln = Nd 2.155(3)/2.330(3) Å; Ln = Ho: M = Ga: 2.107(1)/2.283(1) Å, M = Al: 2.102(3)/2.288(3) Å; Ln = Lu 2.071(1)/2.249(1) Å) and the intriguing fact, that these synthesis protocols fit to a vast range of different sized rare-earth metals are major discoveries.[54, 66] Via salt metathesis/protonolysis tandem reaction a dimeric, bridging rare-earth-metal imide with a supporting Lewis acid (trimethylaluminium) for larger lanthanides (Ln = La, Ce, Nd) gave complex $[Ln_2(\mu_2\text{-}NC_6H_3iPr_2\text{-}2,6)(\mu_3\text{-}NC_6H_3iPr_2\text{-}2,6)[(\mu_2\text{-}Me)_2AlMe](AlMe_4)_2]$ (Scheme A1, **F**; Figure A3, **6**). The highly fluxional alkylaluminat groups (proven by NMR studies) are easily exchanged by other donor molecules such as DMAP ([$AlMe_3$]-unit) or cyclopentadienyl derivatives ([$AlMe_4$]-units), but not by application of vacuum (Ln–N_{imido}: Ln = La: 2.454(2)/2.342(2) Å; Ln = Ce: 2.465(3)/2.172(3) Å; Ln = Nd 2.400(3)/2.309(3) Å).[67]

The second section will concentrate on bridging, multinuclear rare-earth-metal imide complexes, starting with the very first rare-earth-metal imide complex, that was synthesized in 1991 by Bochkarev and Schumann (Figure A4, **IX**).

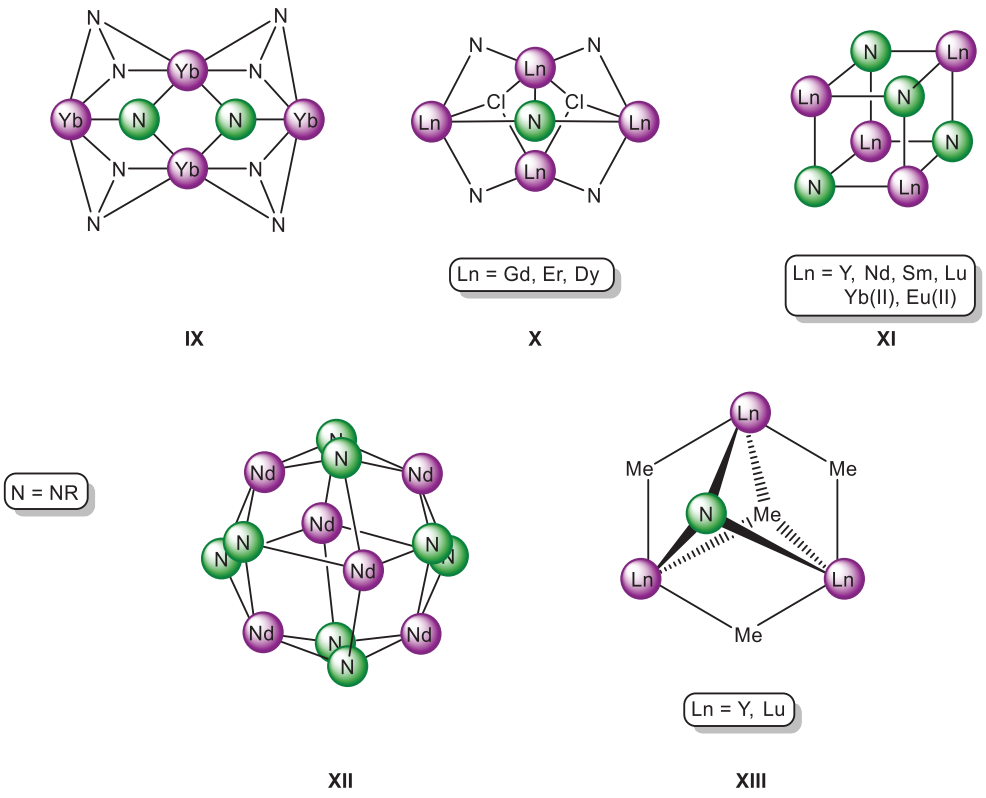

Figure A4. Bridging and multinuclear core structures of rare-earth-metal(III) imide complexes.

In Figure A4 the different multinuclear bond motifs of rare-earth-metal imide complexes are depicted. Bond motif **IX** is a tetranuclear and trivalent ytterbium complex that was isolated while the attempt to generate stable intermediates that were considered to evolve in the process of nitrogen fixation at that time. Ytterbium(II) is known to reduce atmospheric nitrogen from N_2 to N^{3-} in presence of alkali metal naphthalides.[22] Bond motif **X** is exemplary for tetranuclear and trivalent rare-earth metal imido complexes (Figure A4). This structure was gained for the lanthanides gadolinium, erbium and dysprosium and is the first example for a central μ_4-imido core in an organolanthanide complex. The butterfly-like arrangement of the four metal centers is connected by four doubly bridging μ_2-$NHSiMe_2$ units, and two triply bridging μ_3-Cl atoms. The average Ln–N_{imido} distances are 2.450 Å for gadolinium, 2.406 Å for erbium and 2.418 Å for dysprosium, respectively.[49-50] Moreover, cubane-like structural motif **XI** are the most known multinuclear rare-earth-metal imide structures. Both smaller and larger rare-earth metals can adopt this structure with adequately supporting ligands either by the reductive cleavage of benzonitrile[68], and azobenzene[53] or with the imido-transfer reagent [PhNMg(thf)].[69] The resulting cubane-like complexes (Figure A4) are nucleophilic, showing a wide reactivity spectrum toward unsaturated substrates and can engage in α-hydrogen-transfer reactions.[11] The Ln_4N_4 cubane core **XI** consists of four μ_3-imido bridges and four rare-earth-metal centers for both smaller and larger lanthanides (Ln–N_{imido}: Ln = Lu: 2.192(4) – 2.322(4) Å; Ln = Nd 2.335(6) – 2.478(7) Å; Ln = Sm 2.238(3) – 2.459(3) Å),[53, 68-69] as well as for the divalent lanthanides ytterbium (2.352(4) – 2.430(5) Å) and europium (2.473(4) – 2.519(5) Å).[70] Unique example of multinuclear rare-earth-metal imide complexes is bond motif **XII**. It is the only known hexanuclear cluster of rare-earth-metal imides bearing a $Nd_6(\mu_3\text{-}NR)_8^{2-}$ core. The octahedral cluster contains eight μ_3-bridging imido ligands and six neodymium metal centers.[69] Trinuclear rare-earth-metal imide complexes $[L_3Ln_3(\mu_2\text{-}Me)_3(\mu_3\text{-}Me)(\mu_2\text{-}NR)]$ (Ln = Y, Lu; L = $[PhC(NC_6H_3iPr_2\text{-}2,6)_2]^-$; R = Ph, 2,6-$Me_2C_6H_3$, *p*-$ClC_6H_4$, *p*-$MeOC_6H_4$, $Me_2CHCH_2CH_2$) were synthesized by methane elimination of corresponding rare-earth-metal methylidene complexes and primary aniline/amine derivatives for the smaller rare-earth metals yttrium and lutetium (Figure A4, core **XIII**). Those are also the first examples of trivalent rare-earth metal promoted cleavages of the azobenzene N=N double bond. The imido-bridging groups are side-on chelating and connect three LLn fragments (Figure A4, core **XIII**; R = Ph; ø Lu–N: 2.252 Å, ø Y–N: 2.308(3) Å).[10]

In the last section Lewis acid stabilized and alkali metal capped rare-earth-metal imide complexes are discussed.

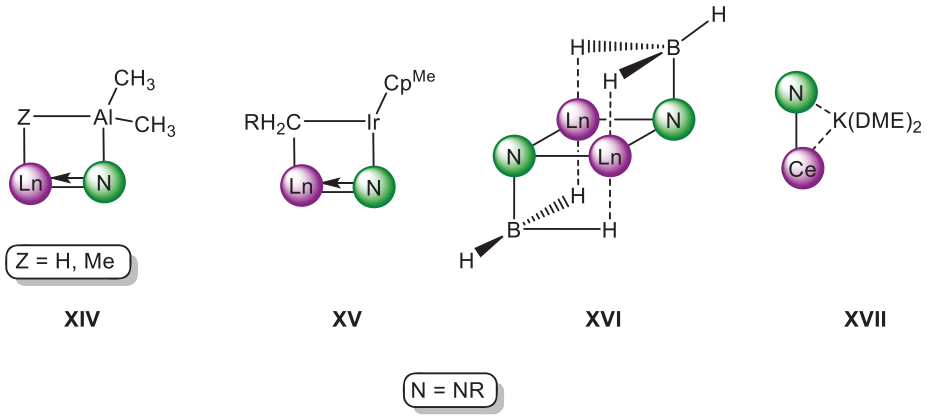

Figure A5. Lewis acid stabilized (**XIV** – **XVI**) and alkali-metal capped (**XVII**) rare-earth-metal imido bond motifs.

Imido functionalities can be stabilized by adjusting various parameters. One of these parameters is the application of Lewis acids, such as [AlR_3] (Figure A5, **XIV**), [IrR_2] (Figure A5, **XV**), [BR_3] (Figure A5, **XVI**), capping alkali metal cations (Figure A5, **XVII**). Most known Lewis acid stabilized imido complexes are trimethylaluminum-stabilized compounds (Figure A5, **XIV**). Compounds **XIV** are monomeric or multinuclear rare-earth-metal complexes and form via μ_2-/μ_3-bridging imido nitrogens heteroleptic, bimetallic complexes such as the neodymium imide complex [{$Me_2Al(\mu_2\text{-}Me_2)$}$_2$Nd($\mu_3$-NPh)($\mu_2$-Me)AlMe]$_2$.[71] The Nd–$N_{imido}$ distances are relatively long for bridging imido ligands (2.401(5) Å), which is accounted by the additional electron shift to the aluminum atom.[71] In reported divalent lanthanide imide complexes [$(thf)_xLn(\mu_2\text{-}NR)(AlMe_3)]_2$ (Ln = Sm, Eu, Yb; R = $C_6H_3iPr_2$-2,6, $SiPh_3$), the stabilization is achieved by trimethylaluminium as well. Interestingly, the dimeric ytterbium compound crystallized at ambient temperature whereas, being crystallized at –35 °C the monomeric ytterbium imide complex [$(thf)_4Yb((\mu_2\text{-}NR)(AlMe_3)]$ evolved.[21] Monomeric trimethylaluminum-stabilized rare-earth-metal imide complexes need the support of bulky ancillary ligands. A commonly used ligand that provides kinetic stabilization is the hydrotris(pyrazolyl)borato ligand ($Tp^{tBu,Me}$). Schädle et al. were able to synthesize a series of monomeric Lewis acid stabilized rare-earth-metal imide complexes, which are stabilized by trimethylaluminum or dimethylaluminum-hydride (Scheme A1, **B**; Figure A5, **XIV**).[1, 72] With primary aniline and amine derivatives and the suitable metal precursors with the bulky ligand attached complexes of the type [$Tp^{tBu,Me}Ln(\mu_2\text{-}NR)(\mu_2\text{-}ZAlMe_2)$] (Ln = Y: R = adamantyl, *t*Bu, $C_6H_3Me_2$-2,6, Z = H, Me; Ln = Lu: R = $C_6H_3Me_2$-2,6, Z = H; Ln = Ho: R = adamantyl, *t*Bu, Z = Me) were synthesized. Noteworthy, the elimination of the Lewis acid by applying vacuum or donor solvent molecules such as DMAP or THF was unsuccessful. This may have its reason

in the unfluxional behavior of the methyl groups of the trimethylaluminum, due to a strong interaction between the [μ_2-MeAlMe$_2$] unit, the rare-earth metal ion, and the imido nitrogen, which is reversed in the precursor compounds.[1, 62, 72] But not only bulky ancillary complexes can lead to the successful isolation of imide complexes as the next example demonstrates. The protonolysis of homoleptic, bimetallic [Ln(AlMe$_4$)$_3$] (Ln = La, Ce) with two equivalents of primary aniline [H$_2$NAr$^{i\text{Pr}}$] generated diimido complexes with additional donor solvent molecules (THF), which are linked in bidentate fashion by a [AlMe$_2$]-moiety ([(thf)$_4$Ln(μ_2-NC$_6$H$_3$*i*Pr$_2$-2,6)$_2$(AlMe$_2$)]).[73] Other possible Lewis acids, that stabilize imido functionalities are revealed iridium-capped complexes (Figure A5, **XV**)[74] or [BH$_3$] (Figure A5, **XVI**).[75] Alkali-metal capped examples are reported for cerium(IV) imides (Figure A5, **XVII**).[76]

2.2.1 Terminal Rare-Earth-Metal Imide Complexes

Terminal rare-earth-metal imide chemistry is dominated by scandium, holding a plethora of literature known examples for terminal imide complexes. Indeed, the small scandium(III) ion bears several advantages for the synthesis of highly reactive imide complexes, since the dianionic nitrogen bond needs shielding to avoid degradation.

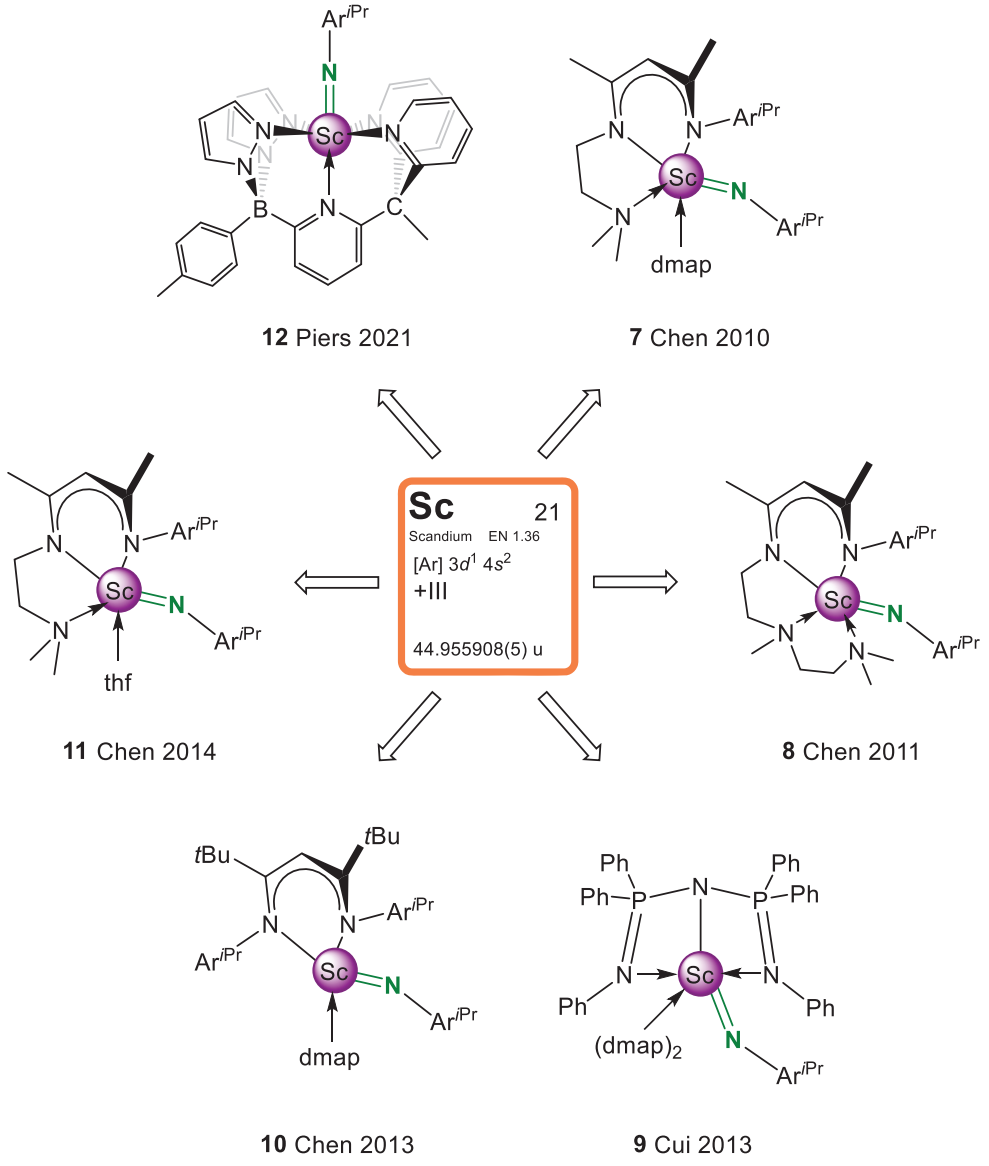

Figure A6. Known scandium complexes with terminal imido functionalities since the first successful isolation of [LSc(NAr^{iPr})(dmap)] (**7**) (L = $N_2C_3HAr^{iPr}$-1-Me_2-2,4-($EtNMe_2$)-5) by Chen et al. in 2010.

Chen et al. isolated the first terminal rare-earth-metal imide complex in 2010.[77] The addition of a *β*-diketiminato-based tridentate ligand which provides steric/electrostatic shielding to $ScCl_3(thf)_3$ and methyllithium, gave the dimethyl precursor [$LScMe_2$]

(L = $N_2C_3HAr^{iPr}$-1-Me_2-2,4-(EtNMe_2)-5) *in situ*. The resultant dimethyl complex decomposes rapidly, whereas it is immediately reacted with 2,6-di*iso*propylaniline affording a mixed amido/methyl scandium complex. After addition of DMAP the quick coordination of the Lewis base to the scandium-metal center of the mixed amido/methyl precursor was indicated by slow evolution of methane and directed the formation of the terminal scandium imide complex [LSc(NAr^{iPr})(dmap)] (**7**) (L = $N_2C_3HAr^{iPr}$-1-Me_2-2,4-(EtNMe_2)-5). In contrast, attempted methane elimination only upon heating of the precursor had no effect. Crystallographic investigations revealed a Sc–N_{imido} interatomic distance of 1.881(5) Å and an almost linear Sc–N_{imido}–C_{ipso} angle of 169.6(5)°. Furthermore, Chen et al. isolated different variants of terminal scandium imide complexes either without additional neutral donor ligands (**8**),[77] which was achieved by using a ligand with higher steric pressure, or bearing a modified ligand system (**10**),[7] or different donor solvents (THF, **11**),[12] (Figure A6).

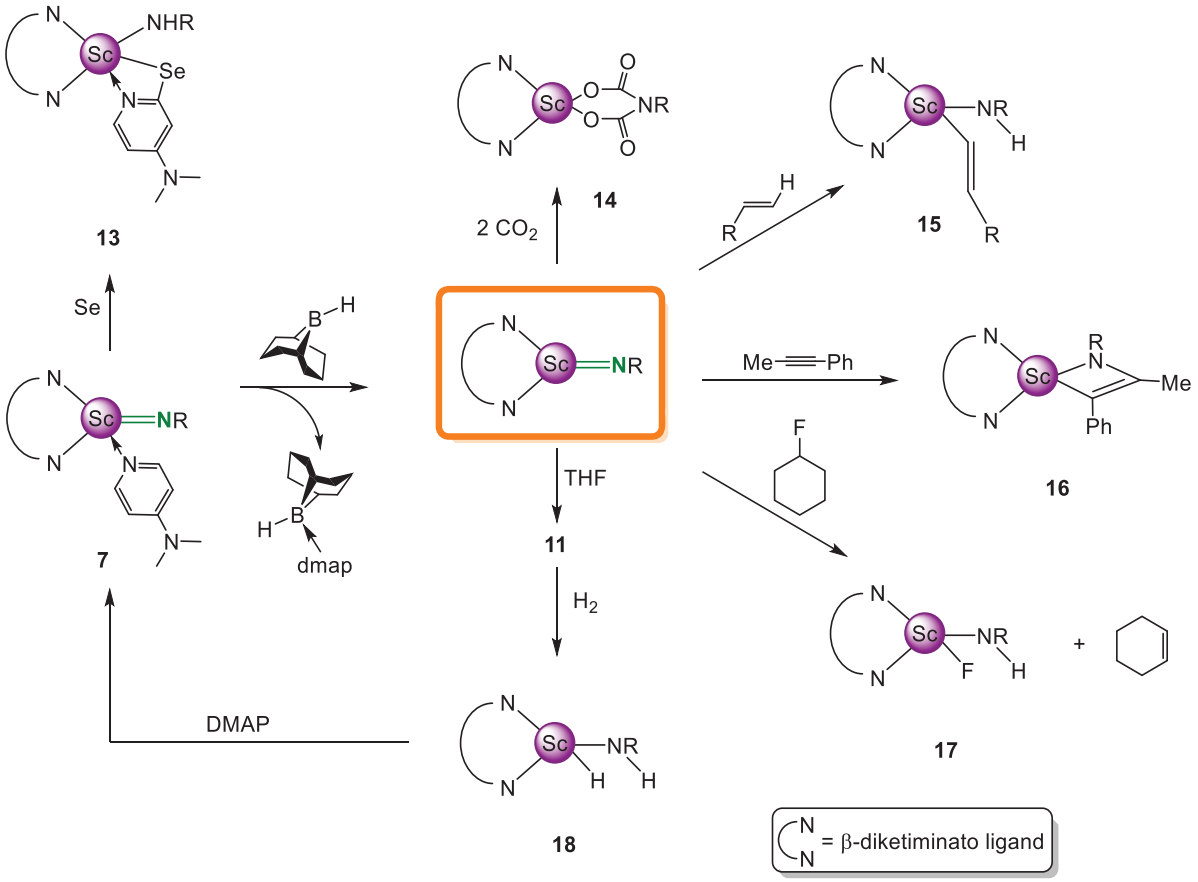

Scheme A2. Novel reactivity patterns of complex **7** after activation with the Lewis acid 9-BBN and subsequent elimination of DMAP.

The novel Sc–N_{imido} moiety promises a manifold of new reactivities which were under investigation for the past decade. The most intriguing reactivity pattern is the selenation of the

scandium metal of complex **7** (Scheme A2). Reaction with elemental selenium afforded a scandium anilido selenolate (Scheme A2, **13**) [77] with a selenolated sp_2 carbon in *ortho*-position of the DMAP ligand. Until today this is the first and only Sc–Se bond (2.7654(11) Å) reported. A proposed reaction mechanism assumes that the formation proceeds via [2+1]-cycloaddition of the selenium atom across the Sc–N_{imido} bond via a Sc–N–Se three membered ring. The transient ring arrangement and the fact that $[N–Se]^{2–}$-units are not very stable leads to N–Se bond cleavage, H_{ortho} transfer and finally to compound **13** (Scheme A2).[77] Upon addition of a Lewis acid, like 9-borabicyclo[3.3.1]nonane, complex **7** gets activated by separation of the Lewis-acid base adduct [DMAP·9-BBN] and the unsupported Sc–N_{imido} species is *in situ* generated. Different unsaturated substrates, such as carbon dioxide (Scheme A2, **14**), terminal alkenes (Scheme A2, **15**), or internal alkynes (Scheme A2, **16**) lead to insertion, [2+2]-cycloaddition, and C–H bond activation. The cycloaddition is highly regioselective as only the *anti*- Markovnikov product is observed. Also, the alkene activation only shows the *trans* isomer, which is accounted for by the steric strain around the metal center. Noteworthy, the reaction with fluoro-substituted benzenes or alkenes gave scandium-anilido fluorides at ambient temperature (Scheme A2, **17**). The reaction rate depends on the acidity of the fluorinated hydrocarbon. Before the strong C–F bond is cleaved, a C–H bond activation in *ortho* position proceeds and the former C–F bond dissociates.[12] Treatment of the THF adduct [LSc(NAr^{iPr})(thf)] (**11**) (L = $N_2C_3HAr^{iPr}$-1-Me_2-2,4-($EtNMe_2$)-5) with dihydrogen resulted in a terminal mixed hydrido/amido complex [LScH($HNAr^{iPr}$)] (**18**) (Scheme A2). The 1,2-addition of dihydrogen is reversible and complex **18** can eliminate H_2 upon addition of DMAP to regenerate the Sc–N_{imido} bond.[78] Finally, the unsupported terminal scandium imide **8** revealed similar reactivity patterns as complex **7**. Reaction with propylenoxide gave a ring-opening and addition to the scandium metal center with reprotonation of the imido nitrogen.[7]

One of the other literature known terminal scandium imido species is a complex with a bis(phenylated)phosphazene, a pincer-like ancillary ligand (Figure A6, **9**). Instead of using methyl as a leaving group, a silylalkyl moiety was utilized and after intermolecular deprotonation of the anilido ligand, the terminal scandium imide complex [(PNP)Sc(NAr^{iPr})$(dmap)_2$] (PNP = $N(PPh_2{=}NPh)_2$) evolved. However, the same synthesis protocol did not apply for the larger rare-earth metals yttrium and lutetium. Also, the thermal elimination of HMDS by intramolecular proton abstraction of [(PNP)Sc($HNAr^{iPr}$)(CH_2SiMe_3)] did not yield the desired compound [(PNP)Sc(NAr^{iPr})]. The Sc–N_{imido} bond in [(PNP)Sc(NAr^{iPr})$(dmap)_2$] is one of the shortest known (1.853(3) Å) and the Sc–N_{imido}–C_{ipso} angle close to linear (168.8(3)°).[46]

In recent approaches the Piers group found a monoanionic, pentadentate ligand as suitable scaffold for the crucial stabilization of terminal imido functionalities (Figure A6, **12**). Due to a higher basicity of the negatively charged antetype of the dianionic imido ligand, the required stabilization for the highly reactive scandium imido species is not provided. With the monoanionic ligand and a scandium metal center, 2,6-di*iso*propylaniline was used to form the terminal anilido complex [(BPz_2Py_3)Sc(NAr^{iPr})] (BPz_2Py_3 = (tolBPz_2)Py($CMePy_2$)). The first alkane elimination is described to be quite rapid, though the second deprotonation with a Brønsted base took several days at ambient temperature. Labeling experiments with ^{15}N heteronucleus showed in the ^{15}N NMR spectrum a sharp signal at 291.8 ppm, which is assigned to the imido nitrogen. X-ray analysis revealed a Sc–N_{imido} distance of 1.877(3) Å and an almost linear Sc–N_{imido}–C_{ipso} angle of 173.1(3)° in scandium complex [(BPz_2Py_3)Sc(NAr^{iPr})] (**12**).[79] These data fit well to the previously reported terminal scandium imide complexes.[6,12,45,46,62,77,80] Wiberg bond index analysis of the complex [(BPz_2Py_3)Sc(NAr^{iPr})] yielded 1.298 for the Sc–N_{imido} bond and both HOMO and HOMO–1 orbitals show clearly π bonding between scandium and the nitrogen atom. The imido nitrogen bears a significant negative charge density and is therefore highly basic, but nevertheless, the complex is thermally stable. Comparable to Chen's terminal scandium imide **7**, it reacts readily with two equivalents of carbon dioxide via insertion into the Sc–N_{imido} bond.[79]

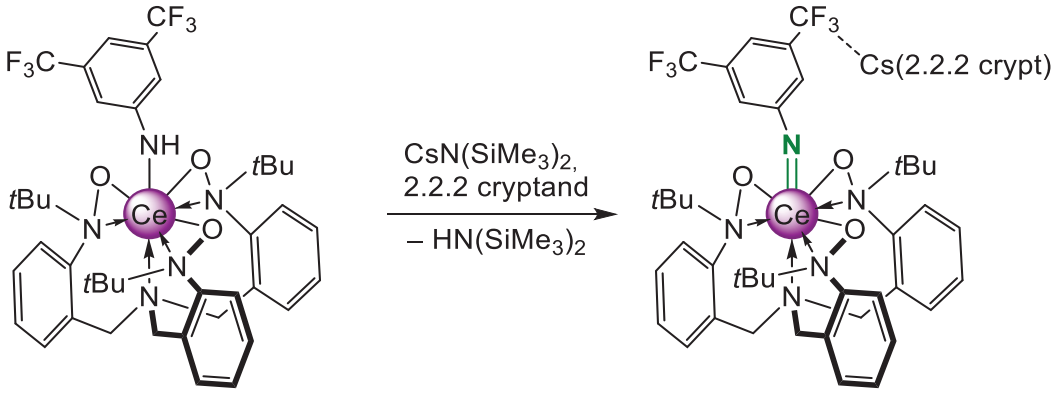

19

Scheme A3. Deprotonation of a cerium(IV) amide precursor with alkali-metal silylamides and 2.2.2-cryptand afforded terminal cerium(IV)-imide "ate"-complex **19** with an encapsulated caesium counter ion.

The Schelter group used the bulky heptadentate tris(hydroxylaminato) ligand $[TriNOx]^{3-}$ (Scheme A3, **19**) with three nitroxide functionalities. A tetravalent rare-earth metal, such as cerium(IV), is assumed to be more beneficial due to the electrostatic stabilization of the more electropositive, tetravalent metal core. This enables the lowering of 5*d* orbital energies and

improves the overlap with 2*p* ligand orbitals of the nitrogen. Furthermore, the aniline [$H_2NC_6H_3(CF_3)_2$-3,5] has electron withdrawing substituents (CF_3) lowering the electron density at the nitrogen atom. These two parameters facilitate the isolation of a series of alkali-metal capped cerium(IV) imide complexes.[6, 76] Moreover, larger and softer alkali metals seem to interact weaker with the Ce–N_{imido} core which is conversely strengthened. An one-pot reaction of the amide precursor compound [(TriNOx)Ce($HNC_6H_3(CF_3)_2$-3,5)], [$CsN(SiMe_3)_2$] and 2.2.2-cryptand formed the terminal cerium-imide "ate" complex **19**. The crystal structure of this thermally unstable compound revealed a weak interaction of the encapsulated counterion Cs^+ with a fluorine atom of one of the CF_3 moieties. Being the first tetravalent, terminal cerium imide complex, **19** (Scheme A3) has the shortest reported Ce–N_{imido} intermolecular distance (2.077(3) Å) and a Ce–N_{imido}–C_{ipso} angle of 157.3(3)°.[6, 76]

A precursor similar to Chen´s imide chemistry is exploited for the synthesis of terminal yttrium and lutetium imide complexes when using methane elimination as an entropic driving force (Scheme A4). The reaction of mixed methyl/anilido yttrium and lutetium complexes with a strong Lewis base (DMAP) leads to a geometrical rearrangement of the anilido moiety and the methyl group getting into spatial proximity and enhancing the possibility of methane release. Beforehand the Lewis base induced elimination, the synthesis of the precursor complex is interesting. Again, a bulky ancillary, monoanionic ligand ($Tp^{tBu,Me}$) is used to sterically and electrostatically shield the trivalent rare-earth-metal centers. The [$Tp^{tBu,Me}$] ligand revealed useful properties to isolate terminal imide complexes of early *d*-block transition metals and proved to have the same striking impact in rare-earth-metal imide chemistry.[62]

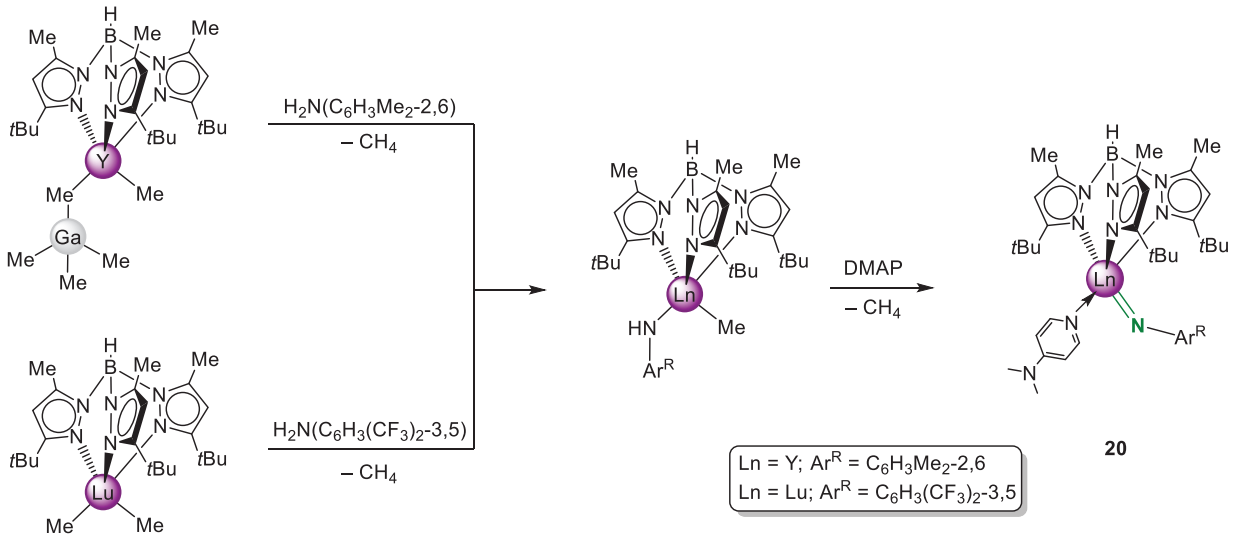

Scheme A4. Synthesis of terminal yttrium and lutetium imide complexes **20** via mixed methyl/amido precursors and addition of a strong Lewis base (DMAP).

The anilido ligand must fulfill different requirements according to acidity (aromatic anilines versus aliphatic anilines), steric demand (substituents in 2,6-position favored over other positions), and the inductive effects of the substituents, to form terminal imido species for each the yttrium and the lutetium variant. As the terminal yttrium imido complex readily forms with a less acidic aniline [$H_2NC_6H_3Me_2$-2,6], the same aniline was not successful for the formation of a terminal lutetium imido. In this case a far more Brønsted acidic aniline was necessary, as well as the shift of the substituent from positions 2 and 6 to positions 3 and 5, hence the [NH]-moiety gets accessible. Successful synthesis of the terminal lutetium imide complex **20^{Lu}** is accomplished with the less sterically shielded and higher Brønsted acidic aniline [$H_2NC_6H_3(CF_3)_2$-3,5]. Noteworthy, terminal imide complexes do not form after addition of DMAP if aliphatic amido complexes are used. Another obstacle is the selection of the bimetallic precursor. Reaction of the suitable aniline with [Tp^{tBu,Me}LnMe(μ_2-MeAlMe$_3$)] (Ln = Y, Lu) leads to the Lewis acid stabilized imide [Tp^{tBu,Me}Ln(NAr^R)AlMe$_3$)] (Ln = Y, R = 2,6-Me$_2$; Ln = Lu, R = 3,5-(CF$_3$)$_2$). Yet, the same reaction with the congener [Tp^{tBu,Me}YMe(μ_2-MeGaMe$_3$)] resulted in a mixed methyl-anilido complex (Scheme A4). For the lutetium analogue, [Tp^{tBu,Me}LuMe$_2$] is used, as it is more stable than the highly reactive [Tp^{tBu,Me}YMe$_2$], but yielded the same mixed methyl/anilido precursor. Apparently, trimethylgallium is much weaker coordinated to the [Ln–Me]-unit than its homologue AlMe$_3$, although both [(μ_2-Me)MMe$_3$]$^-$-units at the metal center were proven to be highly fluxional. The decreasing basicity of [(μ_2-Me)GaMe$_3$]$^-$ compared to [(μ_2-Me)AlMe$_3$]$^-$ is not potent enough to double deprotonate the aniline. Crystallographic investigation of complexes **20** showed short Ln–N$_{imido}$ distances (Ln = Y: 2.024(4) Å, Ln = Lu: 1.993(5) Å) and almost linear Ln–N$_{imido}$–C$_{ipso}$ angles (Ln = Y: 173.6(4)°, Ln = Lu: 175.8(5)°).

Table A1. Selected intermolecular distances and angles of terminal Ln–N$_{imido}$ compounds **7** – **12**, **19**, and **20**.

No.	Formula	Ln–N$_{imido}$ [Å]	Ln–N$_{imido}$–C$_{ipso}$ [°]	Ref.
7	[L^{1}Sc(NAr^{iPr})(dmap)]	1.881(5)	169.6(5)	45
8	[L^{2}Sc(NAr^{iPr})]	1.8591(18)	167.90(17)	77
9	[(PNP)Sc(NAr^{iPr})(dmap)$_2$]	1.853(3)	168.8(3)	46
10	[L^{3}Sc(NAr^{iPr})(dmap)]	–	–	80
11	[L^{1}Sc(NAr^{iPr})(thf)]	1.852(4)	168.6(3)	12
12	[(BPz$_2$Py$_3$)Sc(NAr^{iPr})]	1.877(3)	173.1(3)	79
19	[(TriNOx)CeNAr^{CF}][Cs(2.2.2-cryptand)	2.077(3)	157.3(3)	6

20^{Y}	[Tp^{tBu,Me}Y(NAr^{Me})(dmap)]	2.024(4)	173.6(4)	62
20^{Lu}	[Tp^{tBu,Me}Lu(NAr^{CF})(dmap)]	1.993(5)	175.8(5)	62

L^1 = $N_2C_3HAr^{iPr}$-1-Me_2-2,4-(EtNMe_2)-5)
L^2 = $N_2C_3HAr^{iPr}$-1-Me_2-2,4-[(EtNMe)(EtNMe_2)]-5)
L^3 = $N_2C_3HAr^{iPr}_2$-1,5-tBu_2-2,4
PNP = N(PPh_2=NPh)$_2$
BPz_2Py_3 = (tolBPz_2)Py($CMePy_2$)

2.2.2 Computational Studies on Rare-Earth-Metal Imide Complexes

Before computational calculation methods heralded a paradigm change in the chemical research, it was widely accepted that Ln–$E_{terminal}$ interactions (Ln = Sc, Y, Ln; E = $[NR]^{2-}$, $[O]^{2-}$, $[CR_2]^{2-}$, $[PR]^{2-}$) are predominantly of ionic nature and highly polarized with an effective nuclear charge of +3 at the metal center.[81]

One of the first theoretical studies about lanthanide imide complexes were conducted by Gordon et al. in 2004. They examined interactions between Sm–N_{imido} bonds using the dimeric samarium imido complex $[(\mu_2\text{-}Ar^{iPr}N)Sm(\mu_2\text{-}NHAr^{iPr})(\mu_2\text{-}Me)AlMe_2]_2$ (**I**)[55] for a closer insight into the stabilization of rare-earth-metal imide species.

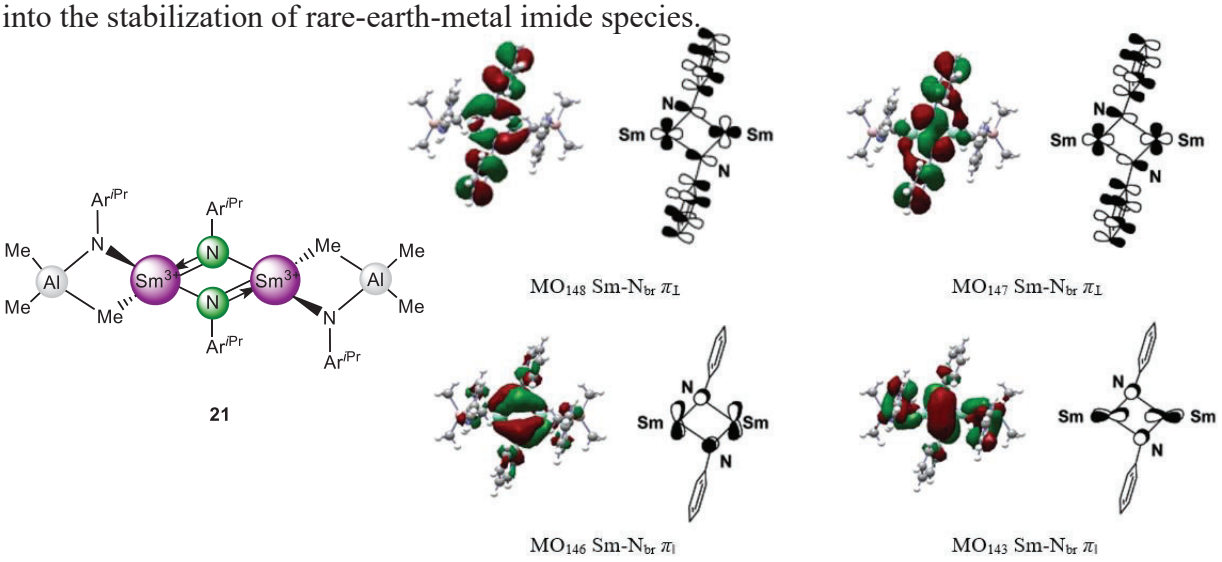

Figure A7. Dimeric scandium imide complex **21** (left) by Gordon et al. Computational investigations gave closer insight into samarium to main group element interactions. Presentation of highest occupied molecular orbitals (HOMO) for the complex model from DFT calculations (right).[55]

As 4*f* orbitals are contracted and their radial extensions are minor compared to 5*d*, 6*s* and 6*p* orbitals, they play a subordinated role in chemical bonding.[82] This fact allowed to utilize effective core potentials which minimize the role of 4*f* electrons and accentuate the role of the other valence orbitals. By employing the B3LYP functional on a simplified model complex (replacement of di*iso*propylaryl moieties by phenyl rings) valuable information about the stabilization effects on the Sm_2N_2 core were gained. To analyze the role of the 5*d* orbitals of the samarium ion, 5*d* basis functions were either included or excluded. It showed that by excluding these basis functions, the Sm–N_{imido} distance is extended by 0.09 Å and the Sm–N_{amido} distance is extended by 0.11 Å, which implies an existing role of the 5*d* orbitals in the stabilization of imido/amido interactions. Furthermore, Mulliken analysis show an overall 5*d* population of 1.28 electrons per metal center, donated by the nitrogen ligand. The analysis of the frontier

orbitals of the bridging imido ligands revealed an interaction of orbitals with corresponding symmetry of the samarium ions. In this case, each samarium center contributes partially (5 – 8%) with the 5*d* orbital to the bond interaction. In conclusion, the HOMO's are ligand based, but the samarium 5*d* orbitals contribute to a notable amount.[48, 55]

These calculations prove that although being highly electropositive, not only steric and electrostatic interactions contribute to the bonding in rare-earth metal/main group complexes but also agostic interactions show the participation of metal *d* orbitals. Nevertheless, the ionic contribution is predominant.

In the year 2010, as Chen and coworkers reported on the first terminal scandium imide complex DFT calculations (B3LYP/6-311G*/Lan12DZ)[45] supported the study of Gordon et al.[55] Calculated Wiberg bond orders yielded for Sc–N_{imido} 1.32 in [LSc(NAr$^{i\text{Pr}}$)(dmap)] (**7**) (L = $N_2C_3HAr^{i\text{Pr}}$-1-Me_2-2,4-($EtNMe_2$)-5) which is significantly larger than 0.66 for the Sc–N_{amido} bond in [LScMe(HNAr$^{i\text{Pr}}$)]. Hence, the interaction between the imido nitrogen and scandium is stronger than for a scandium amido interaction. NBO charges showed electron donation from the nitrogen ligand to the scandium metal and molecule orbital analyses display two *p* orbitals of the imido nitrogen forming two π bonds, which interact with two symmetrical suitable 3*d* orbitals of the scandium. In this particular case, the imido ligand acts as a $2\sigma4\pi$ electron donor.

Cerium(IV) imido interactions were calculated by Schelter et al. (B3LYP/6-31G*) in 2016 and 2017. The cerium(IV) imido and anilido interactions show an increasing contribution of 4*f* and 5*d* orbital fractions, which result in the shortening of the Ce–N_{imido} bond compared to a Ce–N_{amido} bond.[76] For alkali-metal capped cerium imide complexes the major contribution to the bond interaction comes from the nitrogen ligand. Nevertheless, cerium contributes to σ-type bonds (10 – 14%) and to π-bonds (17 – 20%), depending on the capping alkali metal. Notably, the major contribution derives from the 5*d* orbitals, but by increasing the negative charge from amido ligands to charge separated imido anions the contribution of the 4*f* orbitals increases from 27% to 34% in the overall cerium orbital contribution.[6]

Computational methods give a deeper insight into highly polarized bond interactions between rare-earth metals and main group elements, as these bond interactions are predominantly ionic but show metal *d* orbital contributions. Calculations for cerium even revealed a small contribution of 4*f* orbitals to the bond stabilization depending on the negative charge of the ligand.

3 Rare-Earth-Metal Phosphorus Compounds

3.1 Introduction

Although in the past decade great progress in the field of rare-earth-metal phosphorus complexes has been attained[83-88], establishing new Ln–P interactions has remained a challenging task. Indeed, there is a lack of studies on terminal rare-earth-metal phosphinidene complexes as well as on mono- and dianionic phosphorus rare-earth-metal complexes[87-92], most of them being organophosphino compounds with neutral donating ligands. Nevertheless, the heavier main group representative phosphorus is valued as an element that can imitate others of the group 15 and is common especially in transition-metal catalysis.[93-95]

The high reactivity of complexes bearing phosphorus ligands, and the resulting difficulties in the syntheses of such compounds, may have its origin in the mismatch of the orbital levels of soft Lewis bases and hard Lewis acids described by Pearson's HSAB principle.[96] Being a soft donor ligand, phosphorus matches the relatively hard rare-earth metal ions poorly, and consequently, an interaction is unfavorable. This mismatch leads to many obstacles, as oligomerization[97-100] and complexation by harder Lewis acids[101] are often and for phosphinidene complexes exclusively observed.[8, 85-86, 88, 101-102,103]

Marks et al. underlined that Ln–P bond interactions are less favorable, by determining absolute Sm–E (E = main group elements) bond disruption enthalpies. A series of Cp^{Me}Sm–R ($Cp^{Me} = C_5Me_5$) complexes gave the following order [kcal/mol]: H 54.3, $CH(SiMe_3)_2$ 47.0, NMe_2 48.2, O*t*Bu 82.4, Cl 97.1, Br 83.6, I 69.4, S*n*Pr 73.4, PEt_2 32.6. In this study, the phosphorus ligand showed the weakest bonding interaction.[104]

In Chapter 3.2 to 3.4, four different classes of phosphorus ligands regarding the formal charge at the phosphorus are discussed. The main focus is set on neutral (**XIX**), and monoanionic (**XX**) rare-earth metal complexes as well as complexes with a formal negative charge higher than –1 (**XXI**, Figure A8).

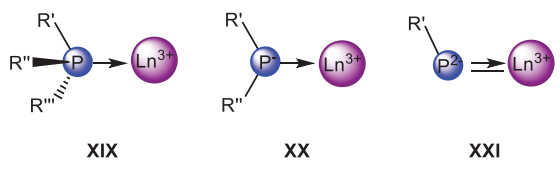

Figure A8. Different classes of phosphorus ligands according to formal charge. Neutral organophosphines [R_3P] (**XIX**), monoanionic organophosphidos $[R_2P]^-$ (**XX**), and dianionic organophosphinidenes $[RP]^{2-}$ (**XXI**).

3.2 Phosphorus Complexes with Neutral P-Ligands

This chapter gives a short survey on neutral phosphorus coordination chemistry with rare-earth metals. Since neutral, organiophosphorus moieties are essentially used as integral componnts or functional groups of ancillary ligands, rare-earth-metal compounds with monoanionic and dianionic ligands are discussed in Chapter 3.3 and 3.4.

The first neutral phosphine rare-earth-metal compound appeared 1969[105] and was structurally characterized in 1988.[106-107] Hydrogenation of the scandium alkyl complex [{$Me_2Si(C_5Me_4)_2$}ScCH($SiMe_3$)$_2$] in the presence of trimethylphosphine afforded a monomeric scandium hydride **22** with a neutral, ternary phosphine donor. Although being weakly bonded to the scandium center, the [PMe_3] coordination circumvents oligomerization or decomposition reactions by steric shielding.

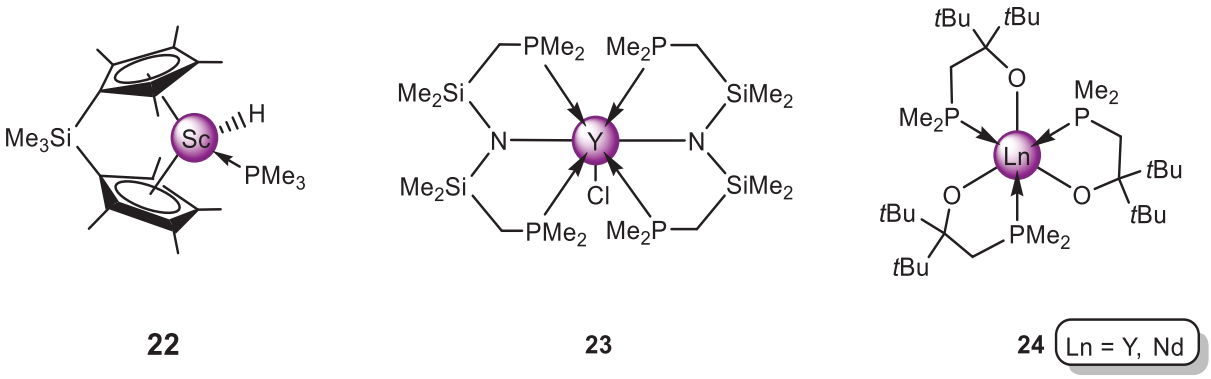

22 **23** **24** Ln = Y, Nd

Figure A9. Coordination of neutral phosphine moieties to group 3 metals. A [PMe_3]-stabilized scandium hydride complex (**22**), a yttrium pincer complex (**23**), and a rare-earth-metal monomeric alkoxide complex (**24**) stabilized by intramolecular phosphide donors.

In 1988 the yttrium complex [{$N(SiMe_2CH_2PMe_2)_2$}$_2$YCl] (**23**, Figure A9) coordinated by a neutral, NPP-pincer-type amido ligand with phosphine side arms was published by Fryzuk and coworkers.[108] Whereas Lappert et al. synthesized homoleptic yttrium and neodymium complexes [Ln($OtBu_2CH_2PMe_2$)$_3$] (**24**, Figure A9; Ln = Y, Nd) with bidentate phosphino-alkoxy ligands, with average Y–P distances of 3.045 Å.[109]

Especially, pincer-type ligands like displayed by complex **23** are suitable to stabilize and saturate the larger coordination sphere of rare-earth metals.[1, 46, 62, 110] The negatively charged amido-nitrogen atom has additional stabilization effects, since interactions between the soft phosphorus atom and rare-earth metals are relatively weak and easy to cleave.[104] However, the

advantage of the relatively large size of phosphorus atoms can be exploited, as for trialkyl phosphines such as [PMe_3], which offer these adjuvant effects which are broadly used to stabilize low-coordinate complexes by blocking the coordination sites.[111]

3.3 Phosphorus Complexes with Monoanionic P-Ligands

Since rare-earth-metal amide complexes are widely used for the synthesis of terminal imide complexes, the higher phosphorus homologues appear to be the preferred choice as potential starting materials of corresponding terminal phosphinidenes. As mixed methyl/amido/phosphido rare-earth metal compounds contain the expedient leaving group methane, intramolecular elimination reactions can trigger the isolation of terminal imido/phosphinidene complexes. However, suitable rare-earth-metal phosphide complexes bearing $[HPR]^-$ units have remained elusive.

3.3.1 Rare-Earth-Metal Phosphide Complexes

In 1986, Schumann et al. isolated "ate" phosphide complex $[Cp_2Lu(PPh_2)_2Li(thf)_2]$ (**25**, Figure A10), which was obtained via methane elimination by reacting the dimethyl lutetium complex $[Cp_2LuMe_2Li(thf)_2]$ with two equivalents of diphenylphosphine. The reaction did not work with either sterically demanding $[HPtBu_2]$ or less demanding primary phosphine $[HPMe_2]$. The Lu–$P_{phosphido}$ interatomic distances in complex **25** are 2.782(1) Å and 2.813(2) Å.[99]

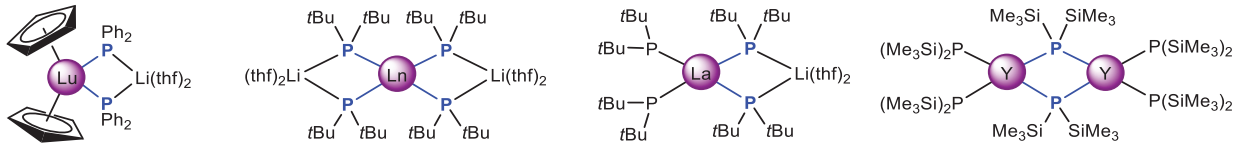

25 **26** Ln = Yb, Eu, Sm **27** **28**

Figure A10. Crystallographically characterized rare-earth metal complexes with monoanionic phosphido ligands, stabilized by additional lithium counter cations (**25** – **27**) or in bridging mode (**28**).

Subsequently, other "ate" complexes were published in the 1990's. The group of Rabe synthesized the first homoleptic rare-earth-metal phosphide compounds via salt metathesis and concomitant reduction of trivalent ytterbium, europium, and samarium to obtain isostructural, divalent complexes $[Ln\{(PtBu_2)_2Li(thf)_2\}_2]$ (**26**, Figure A10), whereas in contrast, the same reaction with lanthanum leads to $[(tBu_2P)_2La(\mu_2\text{-}PtBu_2)_2Li(thf)_2]$ (**27**, Figure A10).[98, 112-113]

Protonolysis of $[Y\{CH(SiMe_3)_2\}_3]$ with $[HP(SiMe_3)_2]$ afforded homoleptic yttrium phosphido complex $[\{(Me_3Si)_2P\}_2Y(\mu_2\text{-}P(SiMe_3)_2\}]_2$ (**28**, Figure A10) with terminal and bridging phosphido ligands. Complex **28** feature Y–$P_{phosphido}$ interatomic distances of 2.677 Å and 2.848 Å, respectively.[114]

3.3.2 Terminal Rare-Earth-Metal Phosphide Complexes

Due to the higher polarization of terminally bonded phosphido moieties compared to bridging P-ligands, interesting reactivity patterns are expected for these compounds. However, examples for exclusively terminal rare-earth-metal phosphide complexes are still rare. High reactivity and the tendency to oligomerize or react in intramolecular fashion are major obstacles which prevent the isolation of terminally bonded compounds and are vital to be considered.

In the early nineties of the last century, the first terminal rare-earth-metal phosphide complex was isolated und structurally characterized. Before that, it was impossible to handle these highly moisture and air sensitive compounds. Smith et al. utilized a secondary phosphine (diphenylphosphane) and reacted it with [{(Me$_3$Si)$_2$N}$_3$La(OPPh$_3$)] in the presence of additional triphenylphosphine oxide to afford [{(Me$_3$Si)$_2$N}$_2$(Ph$_3$PO)$_2$La(PPh$_2$)] (**29**, Scheme A5). The crystal structure is rather ruled by steric factors than by the need of maximizing the interaction with the phosphorus lone pair.[115]

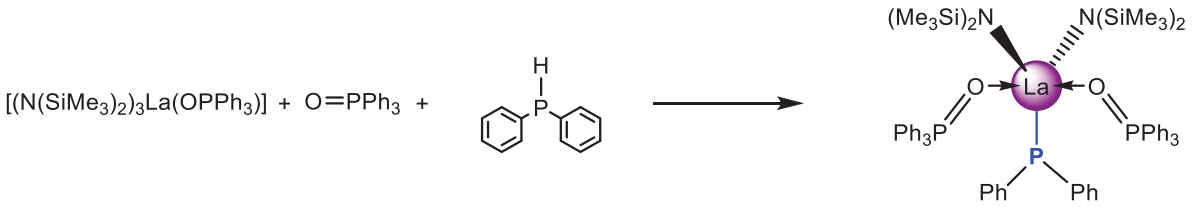

29

Scheme A5. First isolated and characterized lanthanum complex **29** with a terminally bonded phosphido ligand (La–P$_{phosphido}$ 3.165(6) Å).

Requirements to form thermally stable and isolable terminal [R$_2$P]$^-$ units are driven by steric and electrostatic constraints. These hindrances were solved by Rabe et al. for divalent terminal rare-earth-metal phosphide complexes. Divalent samarium and ytterbium iodides SmI$_2$(thf)$_2$/YbnI$_2$(thf)$_2$ react via salt metathesis with potassium diphenylphosphide [KPPh$_2$] to octahedrally coordinated, donor solvent stabilized bis(phosphido) complexes [(R$_2$P)Ln(thf)$_4$] (**30**, Figure A11; Ln = Sm, R = Ph, Mes; Ln = Yb, R = Ph).

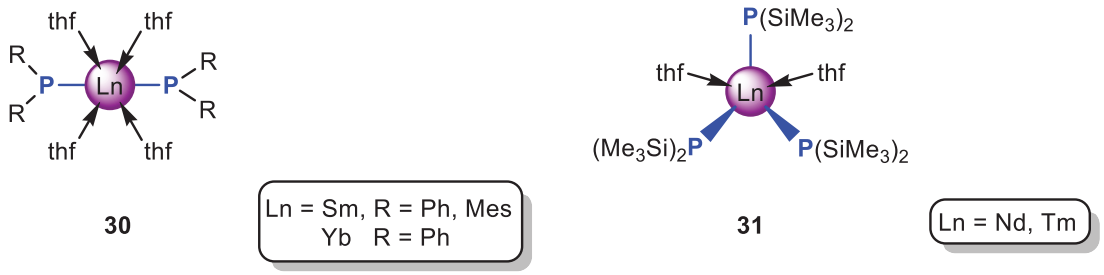

Figure A11. Examples for thermally stable and terminally bonded phosphide complexes.

Complex **30** shows comparable Ln–$P_{phosphido}$ interatomic distances (Ln = Sm, R = Ph: 3.139(3) Å, R = Mes: 3.034(2) Å; Ln = Yb, R = Ph: 2.991(2) Å), since minor differences are accounted for by different ionic radii of the metal centers. Especially the Sm–$P_{phosphido}$ distance is similar to the previously reported La–$P_{phosphido}$ distance in complex **29**. The divalent samarium complexes $\mathbf{30^{Sm}}$ (R = Ph, Mes) with variable phosphorus substituents exhibit Sm–P distance differing by ~0.1 Å, which is mainly caused by the unequal steric demand of the mesityl ring compared to the phenyl ring.[116-118]

The first terminal neodymium and thulium triphosphido complexes were synthesized in 1995. Interestingly, the rare-earth metals are representatives of both larger and smaller lanthanides, but nevertheless, the reaction protocol applies well for both of them. Reaction of the THF adduct of the triiodides of neodymium and thulium [$LnI_3(thf)_x$] (Ln = Nd, Tm) with potassium tris(trimethyl)silylphosphide gave pentagonal coordinated complexes [$\{(Me_3Si)_2P\}_3Ln(thf)_2$] (**31**, Figure A11); Ln = Nd, Tm), with two additional donor solvent molecules. Compared to the Nd–N_{amido} distance in [$Nd\{N(SiMe_3)_2\}_3$] (2.29(2) Å), the average Nd–$P_{phosphido}$ distance (2.80(4) Å)[119] in **31** are longer than expected. Reasons here might be the additional steric pressure of the THF molecules and the larger radius of the phosphorus atom as well as the different coordination numbers (CN = 5 versus CN = 3).[120-121]

Complexes **32** – **35** (Figure A12) exploit diphenylphosphine [$HPPh_2$], which can sufficiently saturate the coordination sphere around the rare-earth-metal centers. Electron donating ancillary ligands are modified *N*-heterocyclic carbenes (NHC) or cyclopentadienyls (C_5R_5), which prevent aggregation or intramolecular, as well as intermolecular activations. These ligands can be easily adapted to the different sizes of both trivalent and divalent rare-earth-metal centers.

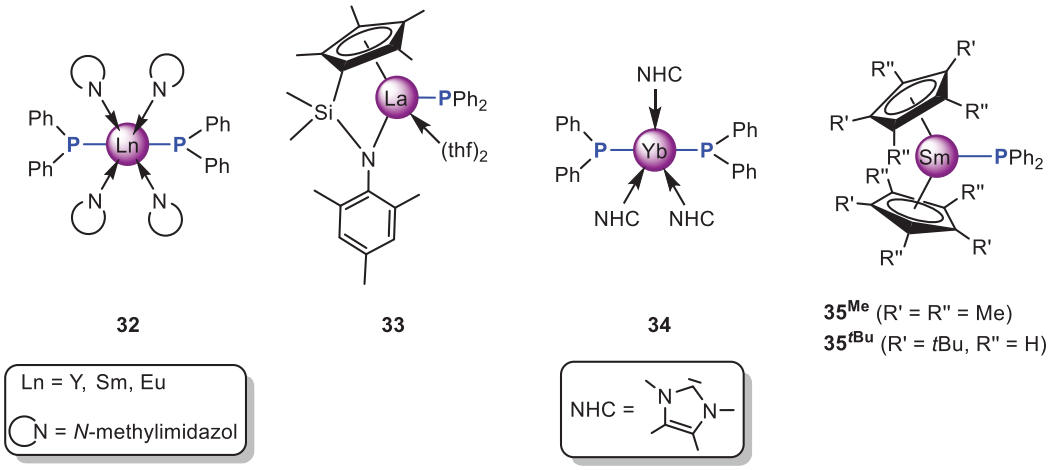

Figure A12. Terminal rare-earth-metal phosphide complexes with secondary phosphide ligands.

Complex **34** is able to hydrophosphinate sytrene. Nevertheless, Cui et al. discovered that the amide starting material [Yb{N(SiMe$_3$)$_2$}$_2$(NHC)$_3$] used *in situ* with diphenylphosphine is more reactive than [Yb(NPh$_2$)$_2$(NHC)$_3$] (**34**, Figure A12) itself. Addition of diphenylphosphine seems to generate a lowcoordinate ytterbium complex, which assumably has a higher reactivity due to an open reaction site at the metal center.[83]

In complex **35^{Me}** the phosphido ligand is nucleophilic enough to activate THF via ring opening if the ancillary cyclopentadienyl ligands are not sterically adequate.[122] For comparison, in transient complex [Cp$^{Me}_2$Sm(PPH$_2$)(thf)] (**35^{Me}**, Figure A12) an additional THF molecule is assumed to coordinate to the samarium center and promotes the ring opening reaction of the donor molecule to polymer [Cp$^{Me}_2$Sm(μ_2-O(CH$_2$)$_4$PPh$_2$)]$_\infty$, whereas complex [Cp$^{tBu}_2$Sm(PPH$_2$)] (**35^{tBu}**) is isolable since the coordination sphere is saturated and no additional donor molecule can coordinate to the metal center.[122]

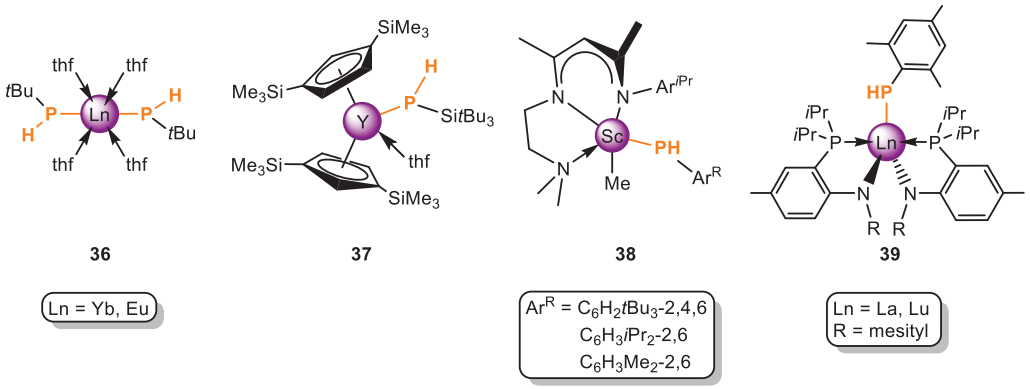

Figure A13. Rare-earth metal phosphido complexes with terminally bonded [HPR]$^-$ units.

The most interesting terminal rare-earth-metal phosphides are those bearing a $[HPR]^-$ unit. Assumable, the acidic proton at the phosphorus atom can be eliminated via smart choice of a sufficient leaving group or external base induced deprotonation. Unfortunately, in literature only four different types of complexes are known, which bear a $[HPR]^-$ unit. However, deprotonation of these complexes were unsuccessful so far (Figure A13).[113, 114, 45, 92, 123]

The first lanthanide compounds with $[HPR]^-$ units were the divalent complexes $[Ln(HPAr^{tBu})_2(thf)_4]$ (**36**, Figure A13; Ln = Yb, Eu). The synthesis was carried out via salt metathesis of $K[HPAr^{tBu}]$ and $[YbI_2(thf)_2]$ or $[EuI_2(thf)_2]$, respectively. Crystallographic investigations revealed quite long Ln–$P_{phosphido}$ interatomic distances ($Ln = Yb^{2+}$: 3.025(2) Å; $Ln = Eu^{2+}$: 3.143(3) Å) with the two phosphido units in *trans* position. $^{31}P\{^1H\}$ NMR spectroscopic studies revealed a signal at –90.1 ppm ($^1J_{YbP}$ = 650 Hz, $^1J_{PH}$ = 179 Hz).[113] To isolate a monomeric structure with a $[HPR]^-$ unit, Westerhausen utilized the sterical demanding cyclopentadienyl ligand Cp^{Si} ($Cp^{Si} = C_5H_3(SiMe_3)_2$-1,4). The acidic, primary potassium salt of $[H_2P(Sit Bu_3)]$ and $[(C_5H_3(SiMe_3)_2\text{-}1,4)_2YCl]$ were reacted in THF to afford complex $[(C_5H_3(SiMe_3)_2\text{-}1,4)_2Y(HPSit Bu_3)(thf)]$ (**37**, Figure A13). Although the removal of the solvent leads to immediate decomposition of the complex, it was possible to gain NMR spectroscopic data and to solve the crystal structure. Hence, the ^{31}P NMR spectrum shows a doublet of doublet at –181.1 ppm ($^1J_{YP}$ = 144 Hz, $^1J_{PH}$ = 201 Hz), representing the coupling of both the yttrium nucleus and the proton with the phosphorus nucleus. Moreover, the crystal structure revealed a relatively long interatomic Y–$P_{phosphido}$ distance of 2.770(1) Å and due to intramolecular constraints the Y–$P_{phosphido}$–Si angle (152.18(6)°) is broadened. This example is also the first heteroleptic yttrium phosphide known so far.[114] The most promising precursor for the synthesis of terminal phosphinidenes via internal deprotonation was published in 2015 by Chen and coworkers. Complexes $[L^1ScMe(HPAr^R)]$ ($L^1 = N_2C_3HAr^{iPr}$-1-Me_2-2,4-(EtN*i*Pr_2)-5, R = Me, *i*Pr, *t*Bu) (**38**, Figure A13) are coordinated by a terminal methyl group, a sufficient leaving group to undergo a intramolecular deprotonation and methane elimination reaction, which is a tremendous driving force. In complex $[L^1ScMe(HPAr^{iPr})]$ (**38^{iPr}**) the intramolecular Sc–$P_{phosphido}$ distance is 2.653(1) Å. Interestingly, the Sc–$P_{phosphido}$–C_{ipso} angle is more acute (109.29(9)°), which indicates no strong interaction between the lone pair of the phosphorus atom and the 3*d* orbitals of scandium. This is a significant difference compared to $[L^1ScMe(HNAr^R)]$ ($L^1 = N_2C_3HAr^{iPr}$-1-Me_2-2,4-(EtN*i*Pr_2)-5, R = *i*Pr) with an amido functionality. In this complex the Sc–N_{amido}–C_{ipso} angle is 153.7(3)°, which implicates a strong interaction between the lone pair of nitrogen and the scandium metal center.[45] Attempts to convert the methyl/phosphido scandium complex $[L^1ScMe(HPAr^R)]$ (**38**) into a terminal

phosphinidene complex either afforded bridging phosphinidene complexes or with triphenylphosphinoxide the release of phosphine [H_2PAr^R] and addition of the oxide to afford [$L^1Ln(Ph)\{CH_2P(O)Ph_2\}$].[92]

Very recently, reports of terminal lanthanum and lutetium phosphido complexes **39** were published by. Again, the salt metathesis of a primary phosphine, and the starting material [$(NC_6H_3(PiPr_2)$-2-Me-4)$_2$LnX] (Ln = La, Lu; X = Cl, I), afforded complexes [$(NC_6H_3(PiPr_2)$-2-Me-4)$_2$Ln($HPAr^{Mes}$)] (**39**, Figure A13). Both complexes revealed long Ln–$P_{phosphido}$ distances (Ln = La: 3.053(1) Å; Ln = Lu: 2.735(1) Å) with P–H vibration bands at 2294 cm^{-1} (Ln = La) and 2306 cm^{-1} (Ln = Lu).[123]

3.4 Phosphorus Complexes with Dianionic P-Ligands – Synthesis and Reactivity

3.4.1 Synthesis of Rare-Earth-Metal Phosphinidene Complexes

While the high reactivity of well-defined terminal rare-earth metal and main group element interactions is mainly proved for terminal imide complexes with $[NR]^{2-}$ units,[7, 9, 45, 77] terminal phosphinidene compounds are highly desirable for catalytic industrial processes, but conversely, this high reactivity renders such compounds as hard to synthesize. These challenges might have their origin in the weak interaction between a soft, dianionic phosphorus ligand with a cationic rare-earth metal center, which is a hard Lewis acids. In catalytic transformations and group transfer[94-95, 124-127] reactions, like carboamination, hydrophosphination of alkynes and dehydrocoupling of phosphines,[128-129] phosphinidenes are a desirable moiety.

Nevertheless, in the past 15 years of tremendous research efforts, these complexes have remained elusive and only few examples of rare-eart-metal complexes bearing a dianionic phosphorus ligand are known, mainly as polymeric (bridging) or as rare-earth-metal phosphinidene "ate" complexes. Hereby, the term phosphandiides is more accurate.[85, 88, 91, 101, 103, 130] Their large ionic radii makes it hard to provide enough steric shielding to stabilize terminal phosphinidenes. As they are the phosphorus analogues imide complexes, two different synthesis pathways are known. Preparation is carried out either by salt metathesis or intramolecular deprotonation reactions.

Being the first reported phosphinidene complex, $[(PNP^{iPr})Lu(\mu_2\text{-}PAr^{Mes})]_2$ (**40**, Scheme A6; $PNP^{iPr} = N(C_6H_3iPr_2\text{-}2\text{-}Me\text{-}4)_2$) was synthesized by protonolysis of pincer complex $[(PNP^{iPr})Lu(CH_2SiMe_3)_2]$ with primary phosphine $[H_2PAr^{Me}]$. The reaction afforded a dimeric complex with two bridging phosphinidene units (**40**, Scheme A6).[103] Only the reaction of $[(PNP^{iPr})Lu(CH_2SiMe_3)_2]$ with a primary phosphine gave the desired results, whereas the reaction of a more bulkier precursor, such as $[(PNP^{Ph})Lu(CH_2SiMe_3)_2]$ did not react in the expected way. Strikingly, complex $[(PNP^{iPr})Lu(\mu_2\text{-}PAr^{Mes})]_2$ (**40**, $Ar^{Mes} = C_6H_2Me_3\text{-}2,4,6$) has an asymmetric Lu_2P_2-core with two shorter (2.6031(16)/2.5973(15) Å) and two longer Lu–$P_{phosphinidene}$ interactions (2.6724(14)/2.6527(16) Å). Until today these are the shortest known Lu–P bond distances. The mesityl rings are in plain with the Lu_2P_2 core, which prohibits interactions between the *iso*-propyl groups on the PNP^{iPr} ligand and the *ortho*-CH_3 groups on

the mesityl rings. Another interesting aspect of this compound is the sum of the angles around the phosphinidene phosphorus.

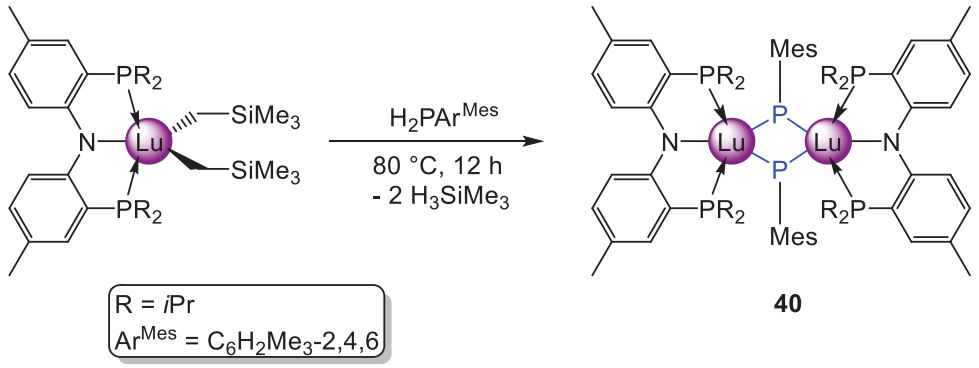

Scheme A6. Synthesis of the first rare-earth-metal phosphinidene by Kiplinger et al. in 2008. The phosphorus ligands form a bridging unit between the two lutetium nuclei of the dimeric complex.[103]

With a difference of 2.4° both sums are close to 360° ($P^1_{phosphinidene}$: 358.9°, $P^2_{phosphinidene}$: 356.5°) and hence allow for π-donation of the phosphorus lone pair to the lutetium metal core. As lutetium has a completely filled 4*f* orbital and therefore is diamagnetic, $^{31}P\{^1H\}$ NMR studies were conducted. These indicate a quintet at 186.8 ppm coupled to a triplet at 18.1 ppm with a $^2J_{PP}$ coupling constant of 14.6 Hz.

In the same year the group among Chen reported on the only known early lanthanide phosphinidene (**41**, Scheme A7).

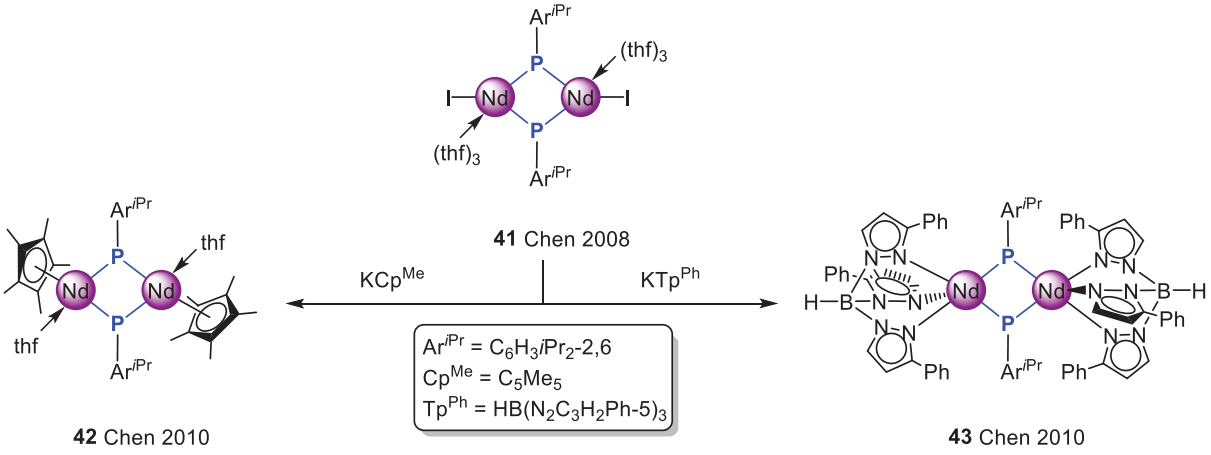

Scheme A7. First early rare-earth-metal phosphinidene complex $[(thf)_3NdI(\mu_2\text{-}PAr^{iPr})]_2$ (**41**) by Chen et al. in 2008. Introducing bulky ancillary ligands via salt metathesis with KCp^{Me} or KTp^{Ph} replaced partly the donor solvent and the iodido but retained the dimeric complexes **42** and **43**.

Via salt metathesis and dehalosilylation, the reaction of $[NdI_3(thf)_{3.5}]$ with two equivalents of the potassium salt $K[P(SiMe_3)(C_6H_3iPr_2\text{-}2,6)]$ afforded the dimeric neodymium phoshinidene $[NdI(\mu_2\text{-}PAr^{iPr})(thf)_3]_2$ (**41**, Scheme A7).[130] The crystal structure of **41** shows the same core features as $[(PNP^{iPr})Lu(\mu_2\text{-}PMes)]_2$ (**40**), bearing a nearly planar Nd_2P_2 core with slightly differing interatomic Nd–$P_{phosphinidene}$ distances (2.7314(15)/2.7769(16) Å). This structure impressively evidenced that neither a strong π-donating ancillary ligand nor highly sterically demanding ligands are needed to isolate phosphinidene complexes, even for the large lanthanides. On the other hand, the formation of terminal rare-earth metal multiple bonded complexes request for those properties.[130] It was found that the replacement of the donor solvent THF and the remaining iodido ligand was feasible by simply adding sterically demanding ancillary ligands via salt metathesis with KCp^{Me} ($Cp^{Me} = C_6(CH_3)_5$) and KTp^{Ph} (= $K[HB(N_2C_3H_2Ph\text{-}5)_3]$). The Nd–$P_{phosphinidene}$ interatomic distances for complex **42** show no significant change (2.7456(11)/2.7827(10) Å) as well as for complex **43** (2.7808(16)/2.7911(15) Å). However, a trend of increasing Nd–$P_{phosphinidene}$ interatomic distance is noted, which might be due to the higher sterical demand, as well as the additional π-donation of electron density of the cyclopentadienyl Cp^{Me} and the bulky scorpionate ligand Tp^{Ph}. Noteworthy, the Tp^{Ph} ligand undergoes a 1,2-borotropic shift at one of the phenyl substituent to avoid steric constraints.[85, 130] Unfortunately, even with those sterically demanding ligands, it was not possible to get hold of a terminal rare-earth-metal phosphinidene complex.

After these initial findings, other phosphinidene complexes were reported in literature (Figure A14). Among these examples are mostly scandium phosphinidene complexes, as the relatively small size of the scandium ion allows an easy shielding and saturation of the coordination sphere. Moreover, its 3*d* orbital energies and electronegativity are considered more favorable to engage in multiple bonding than the heavier group 3 congeners and the lanthanides.

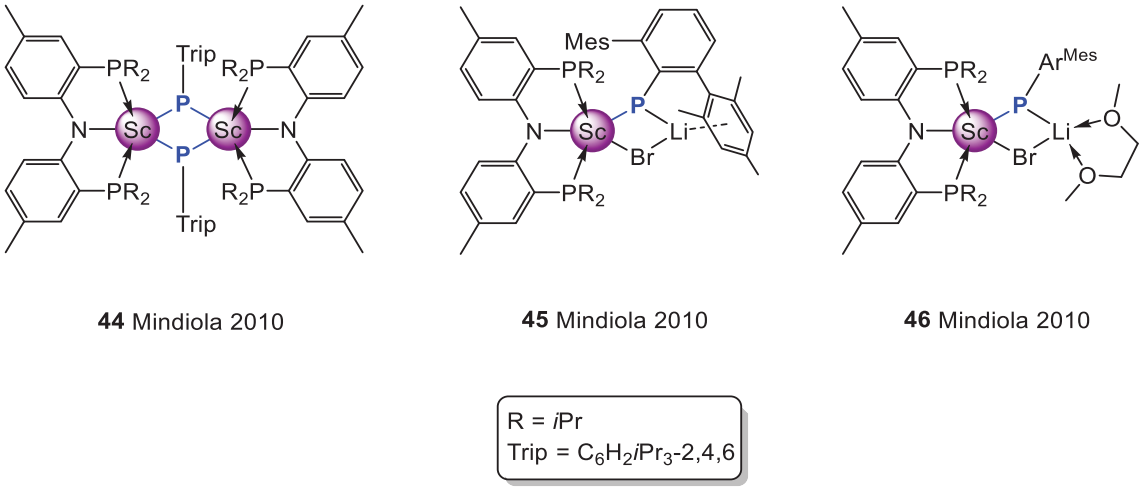

44 Mindiola 2010 **45** Mindiola 2010 **46** Mindiola 2010

Figure A14. Dimeric complex **44**, and monomeric scandium phosphinidene complexes **45** and **46**.

In 2010, Mindiola et al. presented scandium phosphinidene complexes in both neutral form and as "ate" complexes (**44** – **46**, Figure A14). Their approach utilized a similar precursor of scandium, as Kiplinger et al. did for the lutetium phosphinidene complex. [(PNP^{iPr})ScClBr] was reacted with [Li(HPAr^{Trip})] (Ar^{Trip} = $C_6H_2iPr_3$-2,4,6) and via intramolecular elimination of methane and lithium bromide the neutral complex [(PNP^{iPr})Sc(μ_2-PAr^{Trip})]$_2$ (**44**) emerged. ^{31}P NMR spectroscopic investigations revealed a highly deshielded phosphinidene resonance of 227.4 ppm, which is even more downfield shifted than in [(PNP^{iPr})Lu(μ_2-PAr^{Mes})]$_2$ (186.8 ppm). X-ray diffraction studies showed an analog complex as Kiplinger's lutetium phosphinidene with a similar dimeric structure. The intriguing difference is the high symmetry of the Sc_2P_2 core (the sum around the core is 359.92 °) and only slightly deviating Sc–$P_{phosphinidene}$ distances (2.5527(10) Å/2.5446(8) Å). Again here, the high symmetry and the planarity of the four-membered ring allow the lone pair of the phosphorus atoms to delocalize in the core. This was also shown in DFT calculations, which revealed strong interactions between the phosphorus lone pair and the empty 3*d* orbitals of scandium. However, the antibonding HOMO-1 has the same energy level as the bonding HOMO, which implies a highly polarized bond dominated by the phosphinidene phosphorus 3*p* orbital.

The next attempt to achieve a terminal scandium phosphinidene complex exploited a more hindered secondary phosphide. In this case, the same reaction with [Li(HPAr^{Mes})] instead of [Li(HPAr^{Trip})], afforded after elimination of one equivalent methane the mononuclear "ate" complex [(PNP^{iPr})Sc(μ_2-P(dmp)(μ_2-Br)Li] (**45**). This "ate" complex is the first mononuclear rare-earth metal phosphinidene complex and has the shortest known Sc–$P_{phosphinidene}$ distance (2.338(2) Å) with an almost linear Sc–$P_{phosphinidene}$–C_{ipso} angle (162.4(2)°). The remaining

lithium cation interacts weakly with one of the mesityl substituents of the terphenyl group. Although the interaction is considered to be weak (Li–C_{arene} 2.411–2.539 Å), it was not possible to remove the lithium as LiBr, shown in the ^{7}Li NMR spectrum (doublet at –0.20 ppm, $^{1}J_{LiP}$ = 34 Hz). The decomplexation of the Li–C_{arene} interaction was the result of the addition of 1,2-dimethoxyethane (DME) to afford [(PNP^{iPr})Sc(μ_2-P(dmp))(μ_2-Br)Li(dme)] (**46**, Figure A14). Another "ate" analogue [(PNP^{iPr})Sc(μ_2-P(dmp))(μ_2-Br)Li(dme)] has formed with an encapsulated lithium cation. Strikingly the resonance of the phosphorus phosphinidene atom in the ^{31}P NMR spectrum is shifted from 9.8 ppm (Complex **45**) to 56.1 ppm and the Sc–$P_{phosphinidene}$ distance is slightly elongated (2.3732(18) Å), with an Sc–$P_{phosphinidene}$–C_{ipso} angle of 155.2(2)°. Both complexes **45** and **46** have much shorter Sc–$P_{phosphinidene}$ distances than the dimeric scandium phosphinidene complex **44**.[101]

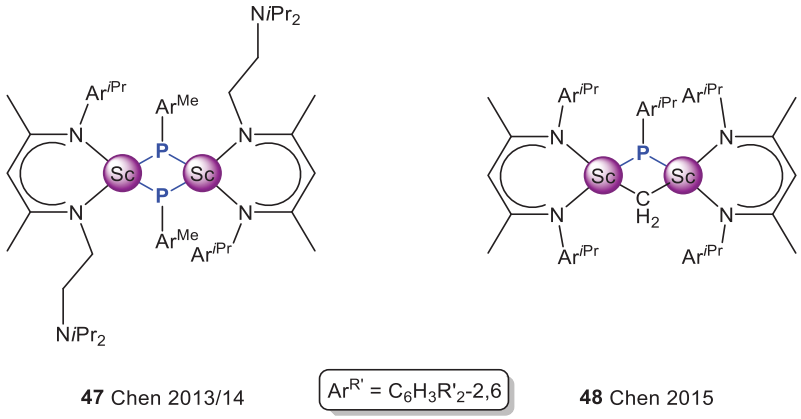

47 Chen 2013/14 $Ar^{R'} = C_6H_3R'_2$-2,6 **48** Chen 2015

Figure A15. Homoleptic, bridging scandium-phosphinidene complex **47** and heteroleptic, bridging mixed scandium methylidene/phosphinidene complex **48** by Chen et al.

In 2013 and 2014, Chen and coworkers successfully reported on another phosphinidene complex (**47**, Figure A15). Their approach utilized a 1,3-diketiminato ligand system which is well-known to support terminal rare-earth-metal multiple interactions.[45] In this case, Chen et al. reacted the mixed scandium methyl/chloride precursor [L^{1}ScMeCl] (L^{1} = $N_2C_3HAr^{iPr}$-1-Me_2-2,4-(EtN*i*Pr_2)-5)) with K[$HPAr^{Me}$]. Initially, a transient scandium methyl/phosphido emerged, proven by NMR spectroscopic monitoring. After methane evolved at room temperature, the reaction yielded the bridged scandium-phosphinidene complex [L^{1}Sc(μ_2-PAr^{Me})]$_2$ (**47**) with Sc–$P_{phosphinidene}$ bond interactions in a similar range (2.522(1)/2.528(1) Å, 2.517(1)/2.524(1) Å) as for **44**. Interestingly, the amino side arm of the ligand is not attached to the scandium due to steric constraints and the metal center in **47** is thereby four-coordinate compared to the previously reported rare-earth metal bridged phosphinidene complexes (CN 5).[101, 103, 130] Despite its steric demand and the small size of

scandium, only bridging phosphinidene complexes were accomplished, even by addition of a strong Lewis base such as DMAP. Another approach conducted by the Chen group in 2015, targeted a phosphinidene according to a methane elimination protocol. By heating a mixed phosphido/methyl complex [L^2ScMe(HPAr^{iPr})] (L^2 = $N_2C_3HAr^{iPr}_2$-1,5-Me_2-2,4) to 60 °C methane emerged, but the desired terminal scandium phosphinidene complex stayed elusive and the resulting product which accrued was instead a dimeric, mixed phosphinidene/methylidene scandium complex [L^2Sc(μ_2-CH_2)(μ_2-PAr^{iPr})]$_2$ (**48**; Sc–$P_{phosphinidene}$: 2.495(1)/2.508(1) Å). Mentionable is the byproduct of the reaction, since bis(phosphido) scandium complex is formed.[88] In studies regarding terminal rare-earth-metal imide complexes the predisposition of forming bis(amido) complexes instead of terminal imides is common as well.

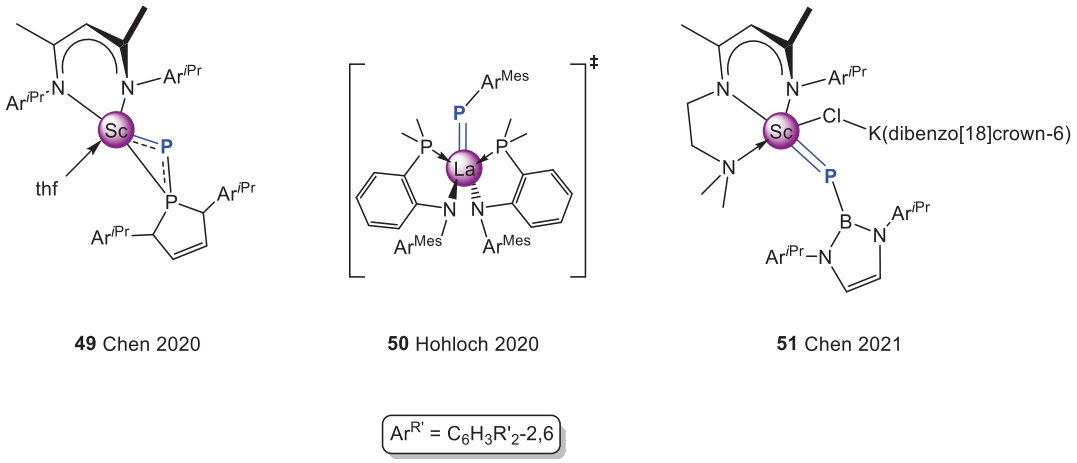

49 Chen 2020 **50** Hohloch 2020 **51** Chen 2021

Figure A16. Recent progress in the isolation of mononuclear phosphinidene rare-earth-metal complexes by the groups of Chen and Hohloch in 2020 and 2021.

Recently, some significant approaches in isolating terminal rare-earth-metal phosphinidenes were published by the groups of Chen and Hohloch. A mixed scandium phosphinophosphinidene complex [L^2Sc-P-P($N_2Ar^{iPr}_2$-2,5-C_2H_4)(thf)] (**49**, L^2 = $N_2C_3HAr^{iPr}_2$-1,5-Me_2-2,4) by Chen et al. was synthesized via salt metathesis of [L^2ScMeCl] with K[HP-P($N_2Ar^{iPr}_2$-2,5-C_2H_4)],[86] which is stable in THF but readily decomposes after evaporation of the solvent. Therefore, it obtained *in situ* with a mixed methyl/chloride scandium precursor and the targeted compound **49** is isolated in good yield (54%). The $^{31}P\{^1H\}$ NMR spectrum shows a doublet signal at 402.3 ppm with a significantly enlarged coupling constant ($^1J_{PP}$ = 501 Hz) which indicates a short P–P bond and the delocalization of the negative charge among the phosphino/phosphinidene tandem. The Sc–$P_{phosphinidene}$ distances (2.448(1) Å) is shorter compared to dimeric scandium phosphinidene

complexes [(PNP$^{i\text{Pr}}$)Sc(μ_2-PTrip)]$_2$ (**44**, Table A2)[101], [L^{1}Sc(μ_2-PAr$^{\text{Me}}$)]$_2$ (**47**, Table A2; L^1 = N$_2$C$_3$HAr$^{i\text{Pr}}$-1-Me$_2$-2,4-(EtN*i*Pr$_2$)-5))[8] and [L^{2}Sc(μ_2-CH$_2$)(μ_2-PAr$^{i\text{Pr}}$)]$_2$ (**48**, Table A2; L^2 = N$_2$C$_3$HAr$^{i\text{Pr}}_2$-1,5-Me$_2$-2,4)[88], but longer than the terminal Sc–P$_{phosphinidene}$ distances of monomeric complexes. In comparison, the Sc–P$_{phosphido}$ distance in complex **49** is much longer (2.718(1) Å). Further DFT calculations revealed that interactions between scandium and the phosphorus atom are bonding interactions as calculations of the HOMO disclose a donor-acceptor interaction between the lone pair of the phosphino phosphorus and the empty scandium *d* orbitals.[86]

Using a bidentate [(C$_6$H$_3$(P*i*Pr$_2$)-2-Me-4)-N-(C$_6$H$_2$Me$_3$-2,4,6)] (PN) ligand the group of Hohloch got deeper insight into the transient lanthanum phosphinidene complex **50** (Figure A16), though they were not able to isolate and characterize it. Attempts to isolate the terminal compound remained unsuccessful, as indicated by ^{31}P NMR studies which included no resonance referring to a dianionic phosphorus. Instead, they could evidence a doublet of a doublet at –87.4 ppm ($^1J_{PH}$ = 181.6 Hz) indicating a P–H coupling. However, labeling studies with deuterated DN(SiMe$_3$)$_2$ indicated the existence of the transient terminal lanthanum phosphinidene complex **50**.[87]

The most recent effort of the Chen group in 2021, is an anionic terminal scandium boronylphosphinidene complex **51** (Figure A16). Using their well-established precursor and ligand system [L^{1}ScMeCl] (L^1 = N$_2$C$_3$HAr$^{i\text{Pr}}$-1-Me$_2$-2,4-(EtN*i*Pr$_2$)-5)) and a boronyl phosphine gave initially, dimeric complex [L^{1}Sc=P(B(N$_2$Ar$^{i\text{Pr}}_2$-2,5-C$_2$H$_2$)Cl] K[dibenzo[18]crown-6] (**51**, L^1 = N$_2$C$_3$HAr$^{i\text{Pr}}$-1-Me$_2$-2,4-(EtN*i*Pr$_2$)-5)). The crystal structure revealed two four-membered Sc–P–Cl–K units, in which the potassium cation interacts both with the di*iso*propylphenyl-ring of the ancillary ligand and the phosphinidene phosphorus. After treatment with dibenzo-18-crown-6, the interaction between the potassium cation and the phosphinidene phosphorus is abandoned and an anionic, terminal scandium boronylphosphinidene evolves. Although, this is the first reported terminal scandium phosphinidene complex, the Sc–P$_{phosphinidene}$ interatomic distance of 2.381(1) Å is longer than it is for the Sc–P$_{phosphinidene}$ interaction in Minidola´s [(PNP$^{i\text{Pr}}$)Sc(μ_2-PAr$^{\text{Mes}}$(μ_2-Br)Li] (2.338(2) Å) (**45**, Table A2).[101] This might have its reason in the negatively charged complex as the additional chloride withdraws electron density and shifts the bond polarization which could weaken the Sc–P$_{phosphinidene}$ interaction.[91]

These few examples prove in principle feasibility of terminal rare-earth-metal phosphinidenes. The intramolecular distances between the rare-earth-metal centers and the phosphorus ligand

are among the shortest known in literature (Table A2). Nevertheless, a neutral, terminal rare-earth-metal phosphinidene complex is still elusive depsite decades of research.

Table A2. Selected intermolecular distances and ^{31}P NMR shifts of the Ln–P$_{phosphinidene}$ compounds **40** – **49**, and **51**.

No.	Formula	Ln–P distance [Å]	^{31}P [ppm]	Ref.
40	$[(PNP^{iPr})Lu(\mu_2\text{-}PAr^{Mes})]_2$	2.6031(16)/2.5973(15)	186.8	103
		2.6724(14)/2.6527(16)		
41	$[(thf)_3NdI(\mu_2\text{-}PAr^{iPr})]_2$	2.7314(15)/2.7769(16)	–	130
42	$[Cp^{Me}(thf)NdI(\mu_2\text{-}PAr^{iPr})]_2$	2.7456(11)/2.7827(10)	–	85
43	$[Tp^{Ph}NdI(\mu_2\text{-}PAr^{iPr})]_2$	2.7808(16)/2.7911(15)	–	85
44	$[(PNP^{iPr})Sc(\mu_2\text{-}PTrip)]_2$	2.5527(10)/2.5446(8)	227.4	101
45	$[(PNP^{iPr})Sc(\mu_2\text{-}PAr^{Mes}(\mu_2\text{-}Br)Li]$	2.338(2)	9.8[a]	101
46	$[(PNP^{iPr})Sc(\mu_2\text{-}PAr^{Mes})(\mu_2\text{-}Br)Li(dme)]$	2.3732(18)	56.1	101
47	$[L^1Sc(\mu_2\text{-}PAr^{Me})]_2$	2.522(1)/2.528(1)	–	8
		2.517(1)/2.54(1)		
48	$[L^2Sc(\mu_2\text{-}CH_2)(\mu_2\text{-}PAr^{iPr})]_2$	2.495(1)/2.508(1)	–	88
49	$[L^2Sc\text{-}P\text{-}P(N_2Ar^{iPr}_2\text{-}2,5\text{-}C_2H_4)(thf)]$	2.448(1)	402.3	86
51	$[L^1Sc{=}P(B(N_2Ar^{iPr}_2\text{-}2,5\text{-}C_2H_2)Cl]$ K[dibenzo[18]crown-6]	2.381(1)	19.6[b]	91

$L^1 = N_2C_3HAr^{iPr}\text{-}1\text{-}Me_2\text{-}2,4\text{-}(EtNiPr_2)\text{-}5)$
$L^2 = N_2C_3HAr^{iPr}_2\text{-}1,5\text{-}Me_2\text{-}2,4$
$PN = [(C_6H_3(PiPr_2)\text{-}2\text{-}Me\text{-}4)\text{-}N\text{-}(C_6H_2Me_3\text{-}2,4,6)]$
[a] = at 0 °C
[b] = at –30 °C

3.4.2 Reactivity of Rare-Earth-Metal Phosphinidene Complexes

Owing to the high electron density at the phosphinidene phosphorus in rare-earth metal complexes, these compounds show predominantly phospha-Wittig reaction behavior. Indeed, the negatively charged phosphorus ion reacts as a nucleophile towards unsaturated substrates, such as aldehydes, alkynes, and carbonylic compounds. Mostly, phosphaalkenes and rare-earth-metal oxide species are formed, though the latter were not isolated yet. In some cases, the reactants are inserted into the complex via addition and isolable intermediates can be obtained.

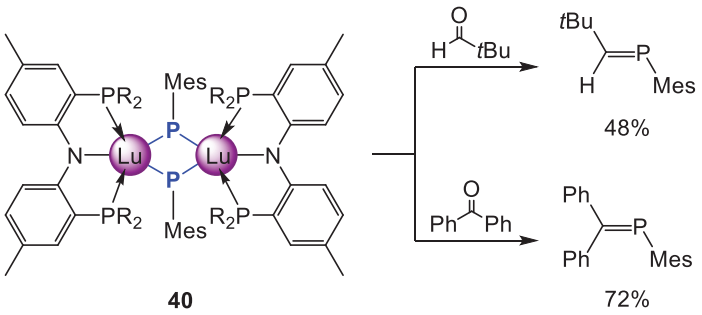

Scheme A8. Reactivity of [(PNP^{iPr})LuPMes]$_2$ (**40**) toward aldehydes and benzophenone.

Kiplinger et al. conducted several reactivity studies, which prove that the dimeric phosphinidene **40** reacts like a nucleophilic phosphinidene system, as it engages in phospha-Wittig transformations with aldehydes and ketones to phosphaalkenes (Scheme A8). The release of the phosphaalkenes, indicate the formation of an uncharacterized oxo-species of lutetium. Nevertheless, the monomerization of the dimeric compound **40** to a terminal lutetium phosphinidene or even the isolation of the oxo complex remained unsuccessful.[103]

The reactivity of Mindiola's scandium phosphinidene complexes were also studied. Whereas the dimeric scandium phosphinidene complex **44** only reacts very sluggishly with ketones – the cause might be the sterically shielded position of the dianionic phosphorus – complex **45** proves again the nucleophilic behavior of the phosphinidene scandium complex, as it shows clear phospha-Wittig performance (Scheme A9, top). Phosphaalkenes are readily formed, but a "Sc–O" complex cannot be isolated as well. Also, intermetallic group transfer reactions as shown for the zirconocene and the titanocene dichloride are feasible (Scheme A9, bottom). A significant reaction with phosphines was not observed.[101]

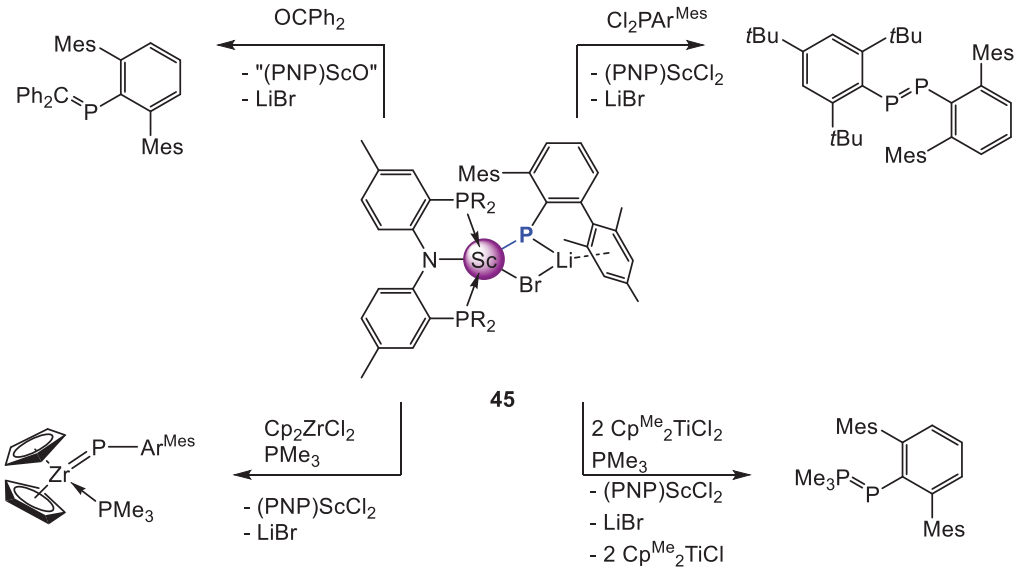

Scheme A9. The monomeric scandium phosphinidene **45** reacts nucleophilic with unsaturated substrates. It shows furthermore group transfer behavior and coupling properties.

Although, the previously mentioned scandium phosphinidene complex **44** was described to react very indolently with ketones, Chen et al. observed a different reaction behavior for the dimeric scandium phosphinidene **47** and the dimeric, heteroleptic scandium methylidene/phosphinidene **48**, since they react with a plethora of different unsaturated, organic substrates (Scheme A10).

The addition of pinacolone to **47** is fast with nearly complete conversion into a dimeric scandium pinacolate **52** (Scheme A10). This example indicates that the B–O bond is cleaved rather than the B–H bond of the pinacolborane. This is since the bond dissociation energy is much higher for a B(H)–O bond (890 kJ/mol) compared to B(O)–H (416 kJ/mol), but can be attributed to the strong oxophilicity of the scandium(III) ion. The [BH] unit of the complex connects both the former phosphinidene phosphorus which donate their lone pair into the empty borane 2*p* orbital to mitigate the electron deficiency. A similar reaction behavior was observed for catecholborane.[102]

Regarding the mixed methylidene/phosphinidene scandium complex **48** (Scheme A10), insertion reactivity is observed. Due to the oxophilicity of scandium, CO_2 is readily inserted and with two equivalents of carbon dioxide the scandium phosphinidene dicarboxylate **53** forms. Interestingly, the insertion takes place at the Sc–CH_2–Sc bond and not at the phosphorus atom. The higher homologue CS_2 with its bigger sulfur atoms inserts readily into the scandium phosphinidene moieties of dimeric complex **47**. It is to be mentioned, that complex **56** is the

first reported ethen-1,1-dithiolate rare-earth-metal derivative (Scheme A10). All insertion reactions occur at the methylidene unit and not at the phosphinidene fragment, hence the methylidene is less shielded and offers an easy access for electrophilic attacks. Even though, the phosphinidene phosphorus might be more nucleophilic, but is in return more shielded with the additional aryl group.[88]

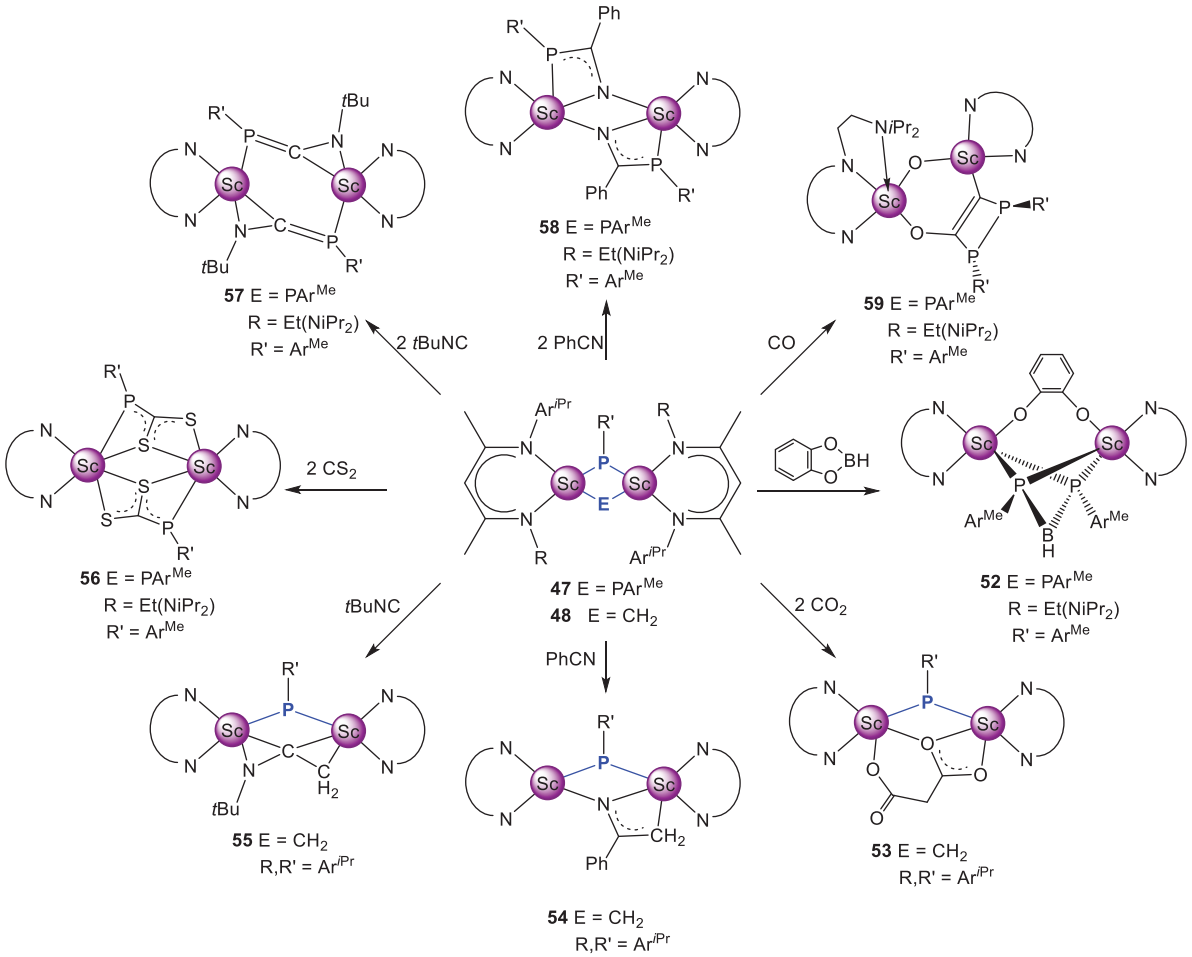

Scheme A10. Selected reactivity examples for scandium phosphinidene **47** and heteroleptic scandium methylidenen/phosphinidene complexes **48**.[8, 88, 102]

Moving on to the dimeric scandium phosphinidene complex **47**, similar reaction patterns are observed. Most interestingly, the reaction with CO leads to dimeric oxo-bridged scandium complex **53** (Scheme A10). The bonding environment around both scandium centers are no longer uniform, but show different coordination modes, as one scandium coordinates to two oxygen atoms, whereas the other scandium coordinates only to one oxygen and one carbon atom. DFT calculations indicate that the reaction starts with the insertion of one CO molecule into one of the four available Sc–$P_{phosphinidene}$ bonds. Subsequently a second CO molecule is inserted into a Sc–$P_{phosphinidene}$ bond which is located either *cis* or *trans* to the preceding CO

insertion. Only the *cis* position enables the following C–C coupling, hence the second CO will insert *cis* to the first insertion. This leads to a weakening of the C–O bond which enables the carbon atom to coordinate to the second carbon atom. After this, subsequent isomerization of the C–C coupling takes place. The C–O bond is cleaved and a Sc–O–Sc unit evolves. Finally, the P–P coupling is performed, as the remaining connection of the phosphorus to one scandium atom has a low activation barrier.[8]

Besides the expected nucleophilic reactivity of phosphinidenes toward unsaturated substrates, the reaction with differently substituted phenylalkynes is interesting.

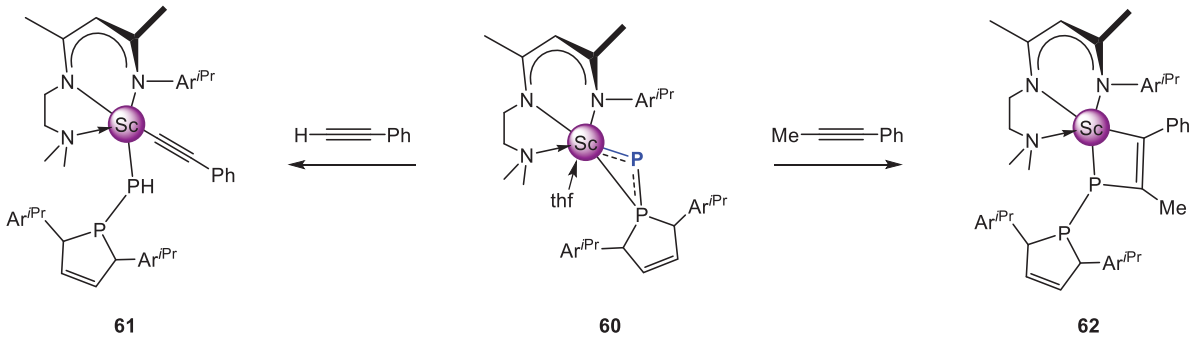

Scheme A11. Reactivity of complex **60** toward phenylacetylene and 1-phenyl-1-propyne to complexes **61** and **62**.

Phenylacetylen and phosphinophosphinidene complex **60** react under elimination of an acidic proton to mixed phosphido phenylacetylido complex **61**. On the other hand, if no proton source is offered *e.g.*, by reacting compound **60** with 1-phenyl-1-propyne a [2+2]-cycloaddition occurs and a four-membered phospha-scandium ring originates to afford **62** (Scheme A11).[86]

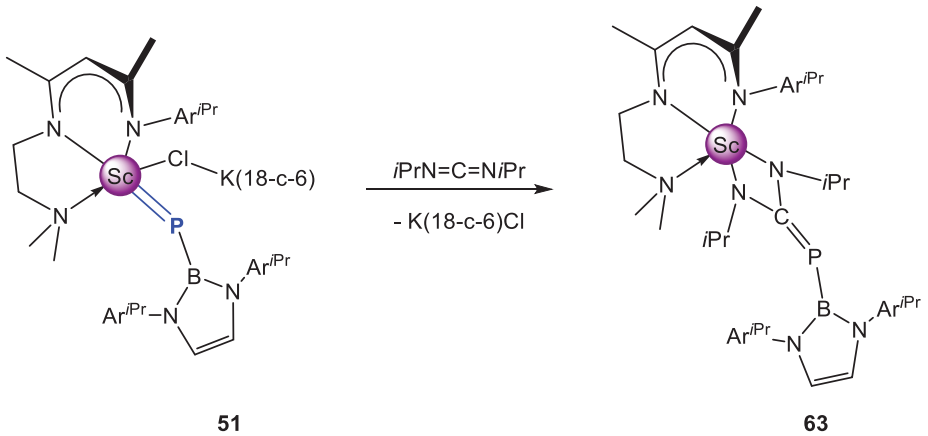

Scheme A12. Reaction of anionic, terminal scandium phosphinidene complex **51** with carbodiimides. After an initial [2+2]-cycloaddition and a [1,3]-scandium migration complex **63** forms.

Preliminary reactivity tests with the most recent efforts in rare-earth-metal phosphinidene chemistry showed that by using carbodiimides as a reagent, the same reaction behavior as known for other transition metal phosphinidene complexes toward unsaturated substrates can be observed. Complex **51** undergoes an insertion which leads to four-membered scandium metallaheterocycle **63** in rather good yields (82%). The Sc–N distances are in line with single bonds of Sc–N_{amido} compounds and of nearly the same range (2.032(3)/2.088(3) Å). Suggestions were made, that the reaction starts with an initial [2+2] cycloaddition between the Sc–$P_{phosphinidene}$ bond and the C=N bond of the carbodiimide. This intermediate undergoes step-by-step a [1,3]-scandium migration and transforms into complex **63** (Scheme A12). The reactivity toward internal alkynes, CO, and CO_2 was investigated as well, but results are still elusive.[91]

B

Summary of the Main Results

1 Rare-Earth-Metal Imide Complexes

Development of novel rare-earth metal to main group multiple bond interactions requires adjusted synthesis protocols in organorare-earth-metal chemistry. Their availability implies the identification of suitable precursors in respect to the lanthanide contraction. In this work two approaches are investigated for testing the applicability of new synthesis protocols. As many other synthesis routes emerged over time, it turned out that two procedures were the most promising – tandem salt metathesis/methane elimination reactions and double deprotonation reactions with subsequent methane elimination.[1, 6, 45, 62, 76]

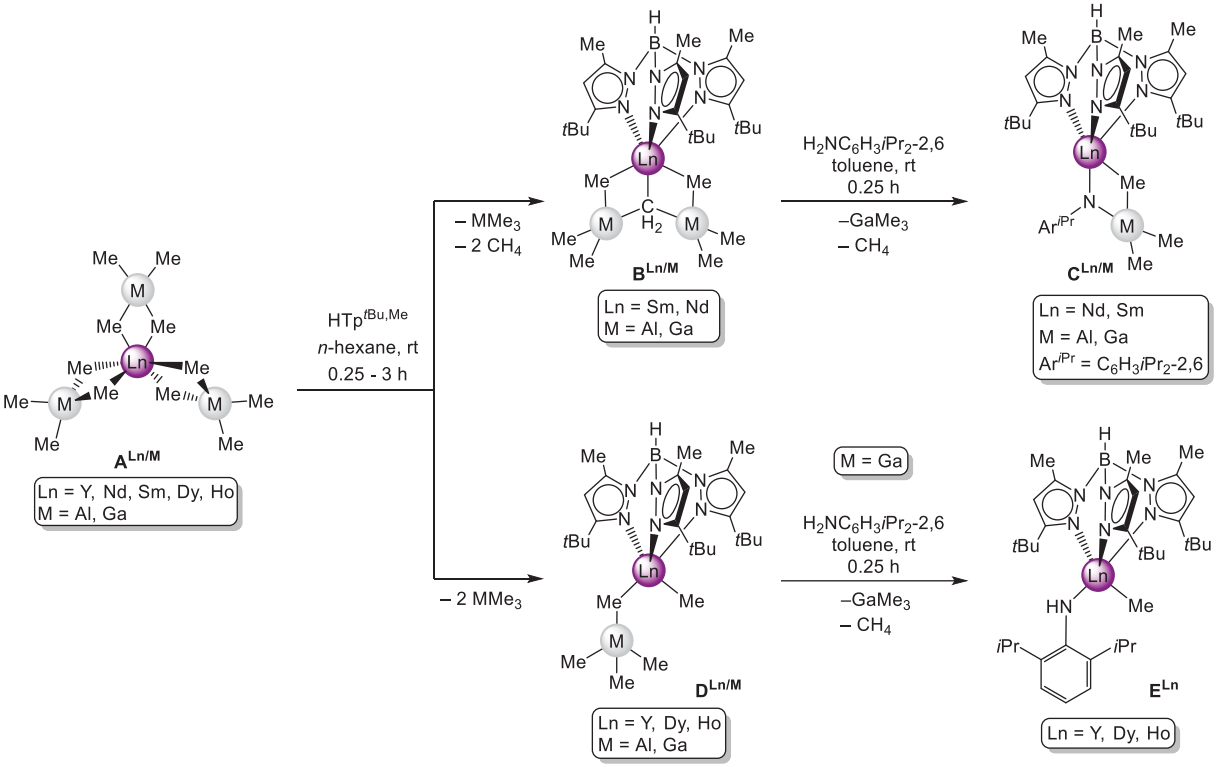

Scheme B1. Reactivity of varied rare-earth-metal tris(tetramethylaluminate or -gallate)s $\mathbf{A}^{\mathbf{Ln/M}}$ with [HTp$^{t\mathrm{Bu,Me}}$]. For early and larger lanthanides the reaction yields methylidene complexes [Tp$^{t\mathrm{Bu,Me}}$LnCH$_2$(μ_2-MeMMe$_2$)$_2$] ($\mathbf{B}^{\mathbf{Ln/M}}$) (Ln = Nd, Sm; M = Al, Ga), whereas the same reaction with smaller rare-earth metals yields [Tp$^{t\mathrm{Bu,Me}}$LnMe(μ_2-MeMMe$_3$)] ($\mathbf{D}^{\mathbf{Ln/M}}$) (Ln = Y[62], Dy, Ho; M = Al, Ga). Only the gallium derivative $\mathbf{D}^{\mathbf{Ln/Ga}}$ reacts with primary aniline [H$_2$NC$_6$H$_3$*i*Pr$_2$-2,6] to the mixed methyl/amido precursor [Tp$^{t\mathrm{Bu,Me}}$LnMe(HNC$_6$H$_3$*i*Pr$_2$-2,6)] ($\mathbf{E}^{\mathbf{Ln}}$) (Ln = Y, Dy, Ho; M = Ga). In contrast, the methylidene complexes $\mathbf{B}^{\mathbf{Ln/M}}$ form Lewis acid stabilized imide complexes $\mathbf{C}^{\mathbf{Ln/M}}$ with primary aniline under the exclusion of donor solvent.

As an ancillary ligand, the bulky scorpionate hydrotris(3-*tert*-butyl-5-methylpyrazolyl)borato ligand [HTp$^{t\mathrm{Bu,Me}}$] proved sufficient enough to saturate the coordination sphere around the trivalent rare-earth metal centers to ensure the resulting complexes are monomeric and potential

tendencies toward oligomerization are impeded. In particular, this ligand's steric nature allows the beneficial formation of a scaffold in which the metal center is enclosed, while it remains accessible on a small "reactive side" enabling modifications at the second ligand.

Interestingly, the reaction of [HTp^{tBu,Me}] with homoleptic tris(tetramethylmetallate)s (M = Al, Ga) of early and late rare-earth metals $\mathbf{A^{Ln/M}}$ shows significant differences, as only the early and larger sized lanthanides form methylidene complexes $\mathbf{B^{Ln/M}}$ (top, Scheme B1; left, Figure B1).[110] Due to the spacious coordination sphere around the metal center it is possible for additional trimethylgallium or -aluminium to coordinate. Contrariwise, the same reaction with the late and smaller rare-earth metals results in the formation of Lewis acid capped bis(alkyl) complexes $\mathbf{D^{Ln/M}}$ (bottom, Scheme B1; right, Figure B1).[54, 131] Several studies show that the cap can be removed, either liberating trimethylaluminium or trimethylgallium to yield Lewis acid free bis(alkyl) complexes of the small rare-earth metals yttrium (Chapter B2, **Paper II**), dysprosium (Chapter B2, **Paper III**), holmium and lutetium.[1]

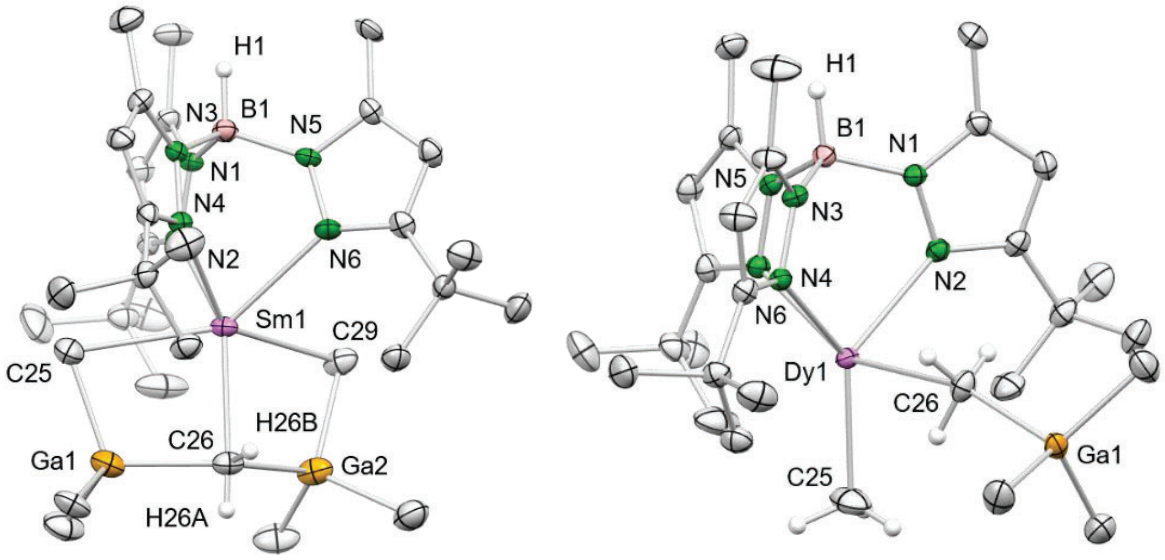

Figure B1. Crystal structures of samarium methylidene $\mathbf{B^{Sm/Ga}}$ (left, **Paper I**) and trimethylgallium-stabilized dysprosium bis(alkyl) $\mathbf{D^{Dy/Ga}}$ (right, **Paper III**).

Regarding the aforementioned synthesis approaches in organorare-earth-metal chemistry, utilizing methane elimination as driving force has distinct advantages over salt-metathesis reactions, as the volatile byproduct methane is easily removable. Instead of generated metathesis salt, the second byproducts [$AlMe_3$] and [$GaMe_3$], respectively, are volatile as well and can be eliminated under vacuum. Owing to the simple purification, the synthesis of [Tp^{tBu,Me}LnCH$_2$(μ_2-MeMMe$_2$)$_2$] ($\mathbf{B^{Ln/M}}$) (Ln = Nd, Sm; M = Al, Ga) and

[Tp^{tBu,Me}LnMe(HNC$_6$H$_3$*i*Pr$_2$-2,6)] (**E^{Ln}**) (Ln = Y, Dy, Ho; M = Ga) via methane elimination provides side product free starting materials in relatively high yields (Scheme B1).

Zhou et al. demonstrated in 2013 the addition of a primary aniline to a trinucelaric rare-earth-metal methylidene complex, resulting in a rare-earth-metal methylidene to imide transformation.[10] In this work 2,6-di*iso*propylaniline was used to test the same synthesis pathway for rare-earth-metal methylidenes (Ln = Nd, Sm) in order to achieve a [Ln=CH$_2$]→[Ln=NR] transformation for the larger lanthanides. However, the simple addition of primary aniline in non-donating solvents leads to rare-earth metal imido complexes **C$^{Ln/M}$**, which bear Lewis acid capped imido functionalities (Scheme B1, **Paper I**). Removing the additional Lewis acid by simple addition of donor molecules (*e.g.*, DMAP, THF) turns out to be unfeasible for complexes **C$^{Ln/Al}$**, as the affinity of aluminum to the negatively charged and relatively hard nitrogen (according to Pearson's HSAB concept[96, 132]) is high compared to the gallium analogues **C$^{Ln/Ga}$** (**Paper I**).

The approach to use the reactive bis(alkyl) rare-earth metal complexes **D$^{Ln/Ga}$** to isolate terminal imide complexes leads to mixed methyl/amido complexes **E^{Ln}** after addition of primary aniline [H$_2$NC$_6$H$_3$*i*Pr$_2$-2,6] and disengaging of methane (Figure B2, **Paper III**), even in donating solvents, such as THF. However, if the primary aniline is added to trimethylaluminum-stabilized bis(alkyl) rare-earth-metal complexes **D$^{Ln/Al}$** instead, [AlMe$_3$]-capped rare-earth-metal imide complexes are generated (**Paper III**).

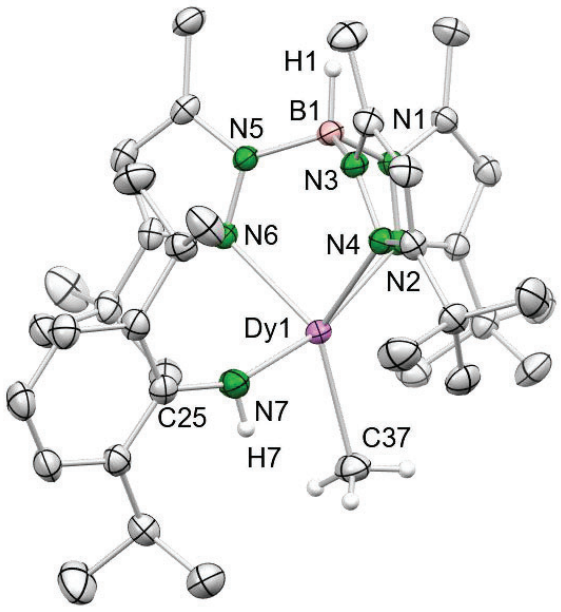

Figure B2. Crystal structure of mixed methyl/amido dysprosium complex **E^{Ln}** (**Paper III**).

Precursors $\mathbf{B}^{\mathbf{Ln/Ga}}$, $\mathbf{C}^{\mathbf{Ln/Ga}}$, and $\mathbf{E}^{\mathbf{Ln}}$ are the suitable starting materials, intended to be identified in this work, to successfully isolate terminal rare-earth-metal imide complexes. With the acidity of the primary aniline in the required range and the potential of sterical fine-tuning of the ancillary ligand, the isolation of highly reactive, yet unsupported terminal imido fragments coordinating to rare-earth metal centers is enabled.

1.1 Terminal Imide Complexes of the Early Lanthanides Neodymium and Samarium

Aiming for terminal rare-earth-metal imide complexes of the larger sized rare-earth metals, it turned out that only the trimethylgallium-stabilized methylidene complexes $\mathbf{B}^{\mathbf{Ln/Ga}}$ or the trimethylgallium-stabilized imide complexes $\mathbf{C}^{\mathbf{Ln/Ga}}$ can be successfully transformed into [Tp$^{t\mathrm{Bu,Me}}$Ln(NC$_6$H$_3$*i*Pr$_2$-2,6)(thf)$_2$] ($\mathbf{F}^{\mathbf{Ln}}$) (Ln = Nd, Sm) (Scheme B2, **Paper I**). According to Pearson's HSAB concept,[96] the [GaMe$_3$] unit of [Tp$^{t\mathrm{Bu,Me}}$LnCH$_2$(μ_2-MeGaMe$_2$)$_2$] ($\mathbf{B}^{\mathbf{Ln/Ga}}$) (Ln = Nd, Sm) and [Tp$^{t\mathrm{Bu,Me}}$Ln($\mu_2$-NC$_6H_3$*i*Pr$_2$-2,6)($\mu_2$-MeGaMe$_2$)$_2$] ($\mathbf{C}^{\mathbf{Ln/Ga}}$) (Ln = Nd, Sm) interacts weakly with both the methylidene moiety and the imido moiety, respectively. The mere addition of primary aniline leads to the elimination of one trimethylgallium molecule in $\mathbf{B}^{\mathbf{Ln/Ga}}$. If the same reaction is conducted under the influence of donor solvent THF, a volatile [GaMe$_3$(thf)] adduct is readily formed, which can be removed under vacuum (top, Scheme B2). Moreover, the addition of donor solvent to the Lewis acid stabilized imido complexes $\mathbf{C}^{\mathbf{Ln/Ga}}$ entails the elimination of [GaMe$_3$] and formation of [Tp$^{t\mathrm{Bu,Me}}$Ln(NC$_6$H$_3$*i*Pr$_2$-2,6)(thf)$_2$] ($\mathbf{F}^{\mathbf{Ln}}$) (Ln = Nd, Sm), as well (bottom, Scheme B2). It is to be noted that, the application of trimethylgallium in *n*-hexane to the terminal rare-earth metal imido complexes $\mathbf{F}^{\mathbf{Ln}}$ promotes the back reaction and leads to the addition of the Lewis acid to produce a supported imido functionality ($\mathbf{C}^{\mathbf{Ln/Ga}}$, Scheme B2).

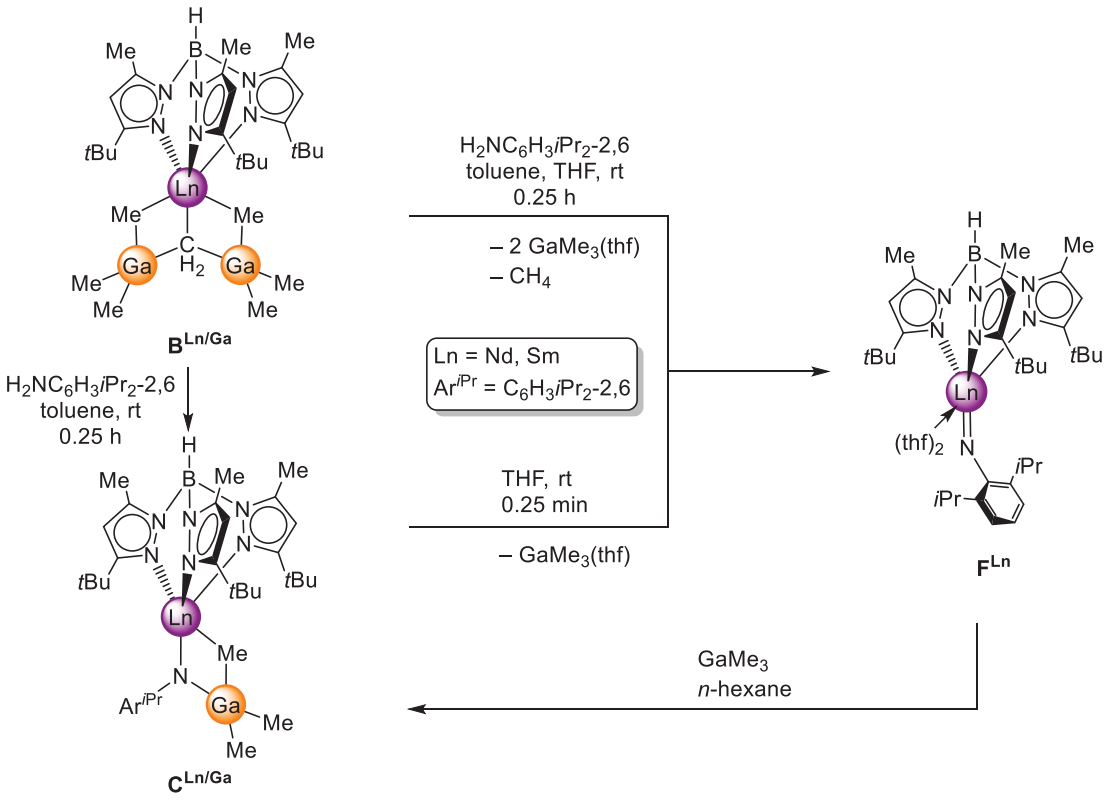

Scheme B2. Synthesis pathways to obtain [Tp^{tBu,Me}Ln(NC$_6$H$_3$*i*Pr$_2$-2,6)(thf)$_2$] (**F^{Ln}**) (Ln = Nd, Sm) via concerted double deprotonation of [H$_2$NC$_6$H$_3$*i*Pr$_2$-2,6] and complexes **B$^{Ln/Ga}$** in THF (top) or addition of donor solvent THF to complexes **C$^{Ln/Ga}$** and elimination of trimethylgallium as THF adduct (bottom). Addition of [GaMe$_3$] in *n*-hexane promotes the back reaction of complexes **F^{Ln}** to complexes **C$^{Ln/Ga}$**.

Both rare-earth metal-imido species, the Lewis acid capped (**C$^{Ln/Ga}$**) and the terminal imides (**F^{Ln}**), were crystallized and fully characterized, although conclusive interpretation of the NMR spectra is not possible, due to the paramagnetic nature of neodymium and samarium. Complexes **F^{Ln}** are the first known terminal, trivalent lanthanide imido complexes for the larger lanthanides neodymium and samarium and feature the shortest known Ln–N$_{imido}$ interatomic distances for the last mentioned (left, Figure B3; Ln = Nd: 2.076(4) Å; Ln =Sm: 2.067(5) Å; **Paper I**) and almost linear Ln–N$_{imido}$–C$_{ipso}$ angles (Ln = Nd: 169.2(4)°; Ln = Sm: 169.3(5)°; **Paper I**). By changing the crystallization process and using a more polar solvent mixture (toluene/fluorocyclohexane), one THF molecule can be abstracted which leads to a lower coordinated terminal neodymium imide complex with slightly differing interatomic distances (Nd–N$_{imido}$: 2.036(7) Å) and a more bent angle (Nd–N$_{imido}$–C$_{ipso}$: 165.8(6)°), owed to the reduction of the coordination number from 6 to 5 (**Paper I**).

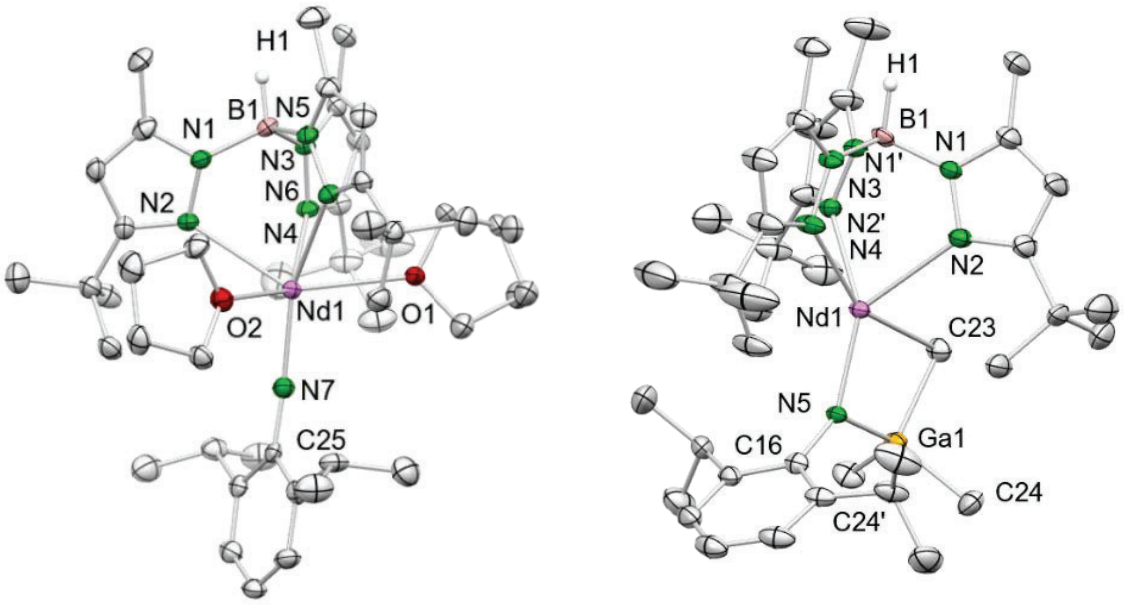

Figure B3. Crystal structures of terminal neodymium imide complex $\mathbf{F^{Nd}}$ (left, **Paper I**) and trimethylgallium-capped neodymium imide $\mathbf{C^{Nd/Ga}}$ (right, **Paper I**).

The Lewis acid stabilized imide complexes $\mathbf{C^{Ln/Ga}}$ reveal slightly longer Ln–N_{imido} interatomic distances (right, Figure B3; Ln = Nd: 2.158(3) Å; Ln = Sm: 2.158(4) Å; **Paper I**), as the additional trimethylgallium withdraws electron density from the imido nitrogen and thus weakens the Ln–N_{imido} interaction. Furthermore, the additional Lewis acid forces the aryl ring of the imido fragment to avoid steric strain and the Ln–N_{imido}–C_{ipso} angles (Ln = Nd: 141.4(3)°; Ln = Sm: 141.8(4)°; **Paper I**) get more acute. Nevertheless, the Ln–N_{imido} interatomic distances of $\mathbf{C^{Ln/Ga}}$ (Ln = Nd, Sm) are shorter than those of Ln–N_{amido} functionalities.

Conducted mechanistic studies with methylidene complex [Tp$^{t\mathrm{Bu,Me}}$NdCH$_2$(μ_2-MeGaMe$_2$)$_2$] ($\mathbf{B^{Nd/Ga}}$) revealed that reaction with 2,6-di*iso*propylaniline is initiated by the addition of the aniline derivative as amido functionality, the following release of one equivalent of trimethylgallium, owed to steric hinderances, and the intramolecular protonation of the former methylidene moiety.

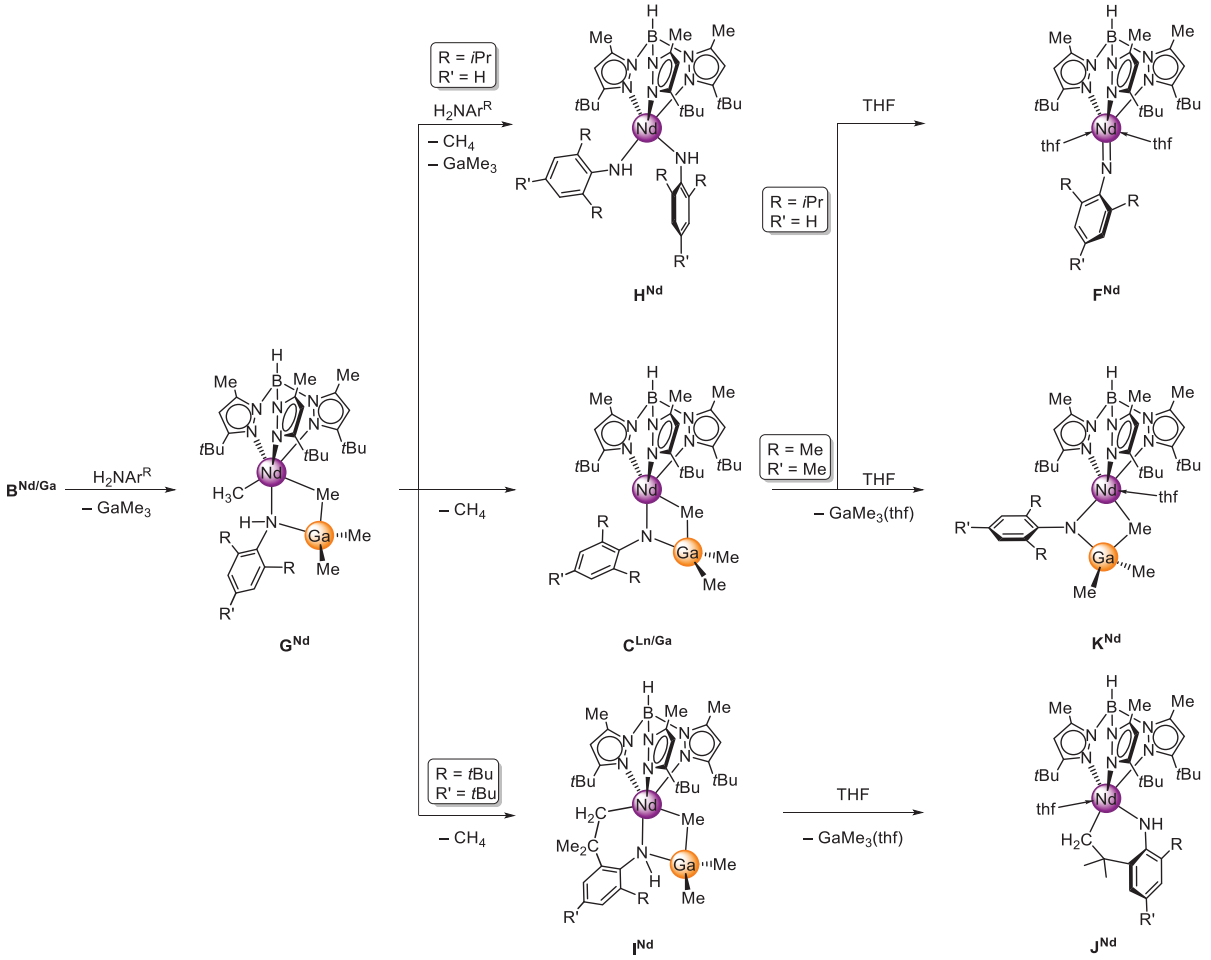

Scheme B3. Proposed mechanistic scenario for the formation of rare-earth-metal imide complexes and competitive reaction pathways involving aromatic amines (**Paper I**).

The resulting intermediate $\mathbf{G}^{\mathbf{Nd}}$ (Scheme B3, **Paper I**) discloses different reaction pathways, depending on the amount of added aniline, and the steric demand in 2 and 6 position at the aryl ring of the aniline derivative. Thereafter, [Tp$^{t\mathrm{Bu,Me}}$Nd(HNC$_6$H$_3$*i*Pr$_2$-2,6)$_2$] ($\mathbf{H}^{\mathbf{Nd}}$) forms, if the amount of aniline is greater than one equivalent. The bis(amido) complex $\mathbf{H}^{\mathbf{Nd}}$ is thermodynamically stable and successive deprotonation in order to isolate a bis(imido) species transpired to be unfeasible. Varying the steric demand of the substituents in 2 and 6 position at the aryl ring, highly demanding *tert*-butyl substituents lead to the elimination of methane and subsequent activation of one of the *tert*-butyl substituents at the aryl ring of the amido functionality. Proposed intermediate $\mathbf{I}^{\mathbf{Nd}}$ is afforded, which reacts after elimination of adduct [GaMe$_3$(thf)] and the additional coordination of the donor solvent THF, to the amido complex $\mathbf{J}^{\mathbf{Nd}}$. Whereas, sterically less demanding methyl groups in 2 and 6 position at the aryl ring were not able to eliminate the additional Lewis acid cap, even though THF is added to the metal center and complex [Tp$^{t\mathrm{Bu,Me}}$Ln(μ_2-NC$_6$H$_3$*i*Pr$_2$-2,6)(μ_2-MeGaMe$_2$)$_2$(thf)] ($\mathbf{K}^{\mathbf{Nd}}$) can be isolated. The pathway that resulted in the aforementioned elimination was an approach via an aniline

derivative with *iso*-propyl substituents in 2 and 6 position dissolved in THF leading to a complete elimination of the trimethylgallium molecules as THF adducts. Nevertheless, the aniline is small enough to prevent activation of any side arms and terminal imide complex $\mathbf{F}^{\mathbf{Nd}}$ was successfully isolated.

1.2 Terminal Imide Complexes of the Late Rare-Earth Metals Yttrium, Dysprosium, and Holmium

As rare-earth-metal methylidene complexes, which form for the larger lanthanides (Chapter B1), are not accessible for the rare-earth metals yttrium, dysprosium, and holmium, the bis(alkyl) precursors [Tp^{tBu,Me}LnMe(μ_2-MeGaMe$_3$)] (**D$^{Ln/Ga}$**) were synthesized according to a literature known procedure.[62]

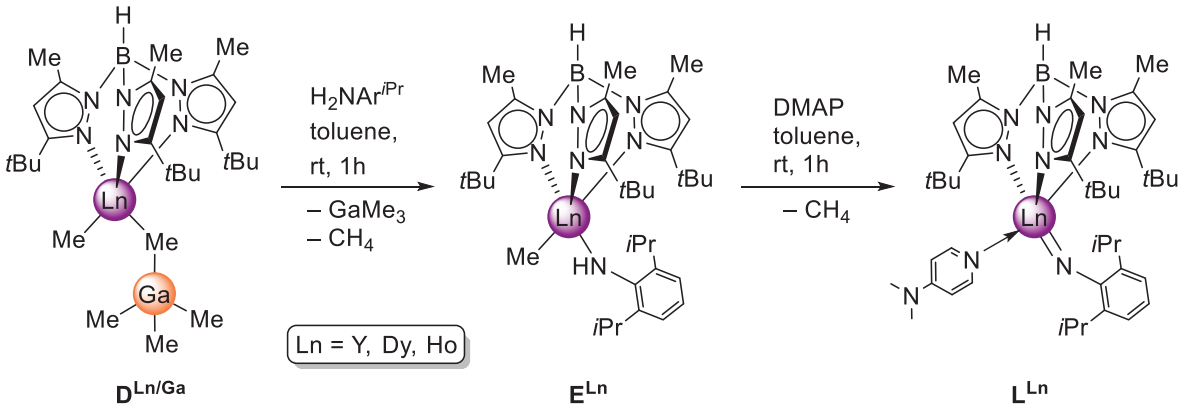

Scheme B4. Synthesis route via elimination of methane and trimethylgallium from **D$^{Ln/Ga}$** to afford mixed methyl/amido complexes [Tp^{tBu,Me}LnMe(HNC$_6$H$_3$*i*Pr$_2$-2,6)] (**E^{Ln}**). Subsequent second methane elimination after addition of DMAP leads to isolation of [Tp^{tBu,Me}Ln(NC$_6$H$_3$*i*Pr$_2$-2,6)(dmap)] (**L^{Ln}**) (Ln = Y, Dy, Ho) (**Paper III**).

The addition and deprotonation of [H$_2$NAr^{iPr}] is followed by evolution of methane and the elimination of trimethylgallium to afford [Tp^{tBu,Me}LnMe(HNAr^{iPr})] (**E^{Ln}**) (Ln = Y, Dy, Ho) (Scheme B4; **Paper III**). Once complex **E^{Ln}** is formed, applied DMAP induces the second deprotonation of the amido moiety and the terminal rare-earth-metal imide complex [Tp^{tBu,Me}Ln(NC$_6$H$_3$*i*Pr$_2$-2,6)(dmap)] (**L^{Ln}**) (Ln = Y, Dy, Ho) can be isolated. Noteworthy, the application of donor molecules weaker than DMAP, such as THF, does not lead to the desired terminal imide complexes.

Furthermore, the isolation of terminal rare-earth metal imide complexes is only possible with sufficiently acidic aniline derivatives. Conducting the same reaction with primary amines *e.g.*, 1-adamantylamine does not result in terminal imido complexes, but in the bis(amido) rare-earth metal complex [Tp^{tBu,Me}Ho(HNC$_{10}$H$_{15}$)$_2$] **X^{Ho}** (**Paper III**) instead. The same is valid for sterically less demanding aniline derivatives. If the 2 and 6 positions of the aryl ring bear methyl moieties, the four-membered metallacycle [Tp^{tBu,Me}Ln(μ_2-NC$_6$H$_3$Me$_2$-2,6)(μ_2-MeMMe$_3$)] **K^{Ln}** (Ln = Dy, Ho; M = Al, Ga) (**Paper III**) originates for both the aluminum and gallium congener.

Attempts to remove the supporting Lewis acid with the Lewis bases DMAP and THF were not successful.

Crystal structures for the complexes $\mathbf{L^{Dy}}$ and $\mathbf{L^{Ho}}$ were obtained. Their imido bond motifs are isostructural to the reported yttrium and lutetium congeners[62] with slightly differing Ln–N_{imido} interatomic distances (Ln = Dy: 2.017(3) Å; Ln = Ho: 2.012(4) Å) in the expected range caused by the different sizes of the metal ions and the different aniline derivatives. The observed angles of 166.0(2)° (Ln = Dy) and 166.7(3)° (Ln = Ho) are almost linear and depend on the steric demand of the additional neutral donor coordinated to the metal center and the substituents at the aryl ring in 2 and 6 position.

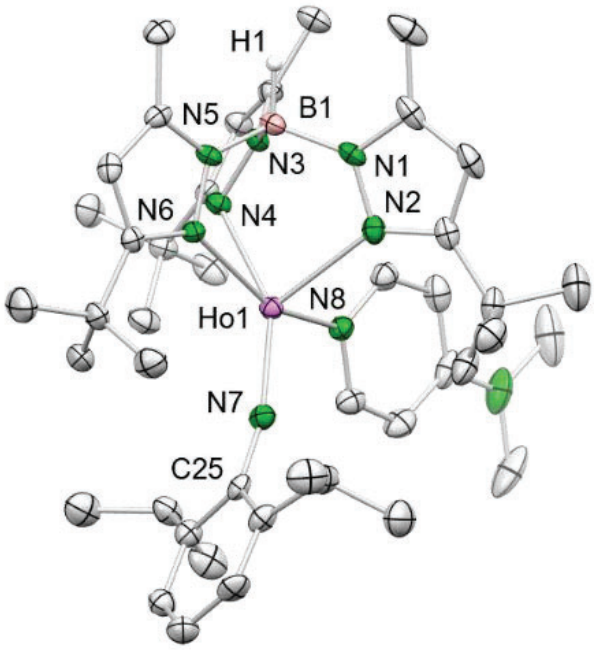

Figure B4. Crystal structure of [Tp^{tBu,Me}Ho(NC$_6$H$_3$*i*Pr$_2$-2,6)(dmap)] ($\mathbf{L^{Ho}}$) (**Paper III**).

Both complexes $\mathbf{L^{Y}}$ and $\mathbf{L^{Dy}}$ were tested for their reactivity toward different, unsaturated substrates (Scheme B5, **Paper III**). Addition of the Lewis acid 9-borabicyclo[3.3.1]nonane leads to the abstraction of DMAP, forming the Lewis acid/base adduct [9-BBN·DMAP].[9, 133] If the reaction is conducted in THF, one molecule of THF coordinates to the metal center ($\mathbf{M^{Dy}}$, Scheme B5; **Paper III**). The change of the Dy–N_{imido}–C_{ipso} angle (165.3(3)°) compared to complex $\mathbf{L^{Dy}}$ is marginal, since the coordination number does not change (CN: 5). However, the Dy–N_{imido} interatomic distance (2.004(4) Å) is shortened due to the weaker neutral donor THF attached to the metal center.

Besides the ability to exchange the additional neutral donor from DMAP to THF, 9-BBN in excess activates one of the *tert*-butyl groups of the ancillary [Tp^{tBu,Me}] ligand forming a seven-membered ring and protonation of the imido nitrogen (**N^{Dy}**, Scheme B5; **Paper III**). The crystal structure of **N^{Dy}** reveals a bent amido functionality (Dy–N$_{amido}$: 2.237(3) Å; Dy–N$_{amido}$–C$_{ipso}$: 143.4(2)°) and a μ_2-hydrid bridge between the boron and the dysprosium metal (Dy–H$_{hydrido}$: 2.17(3) Å).

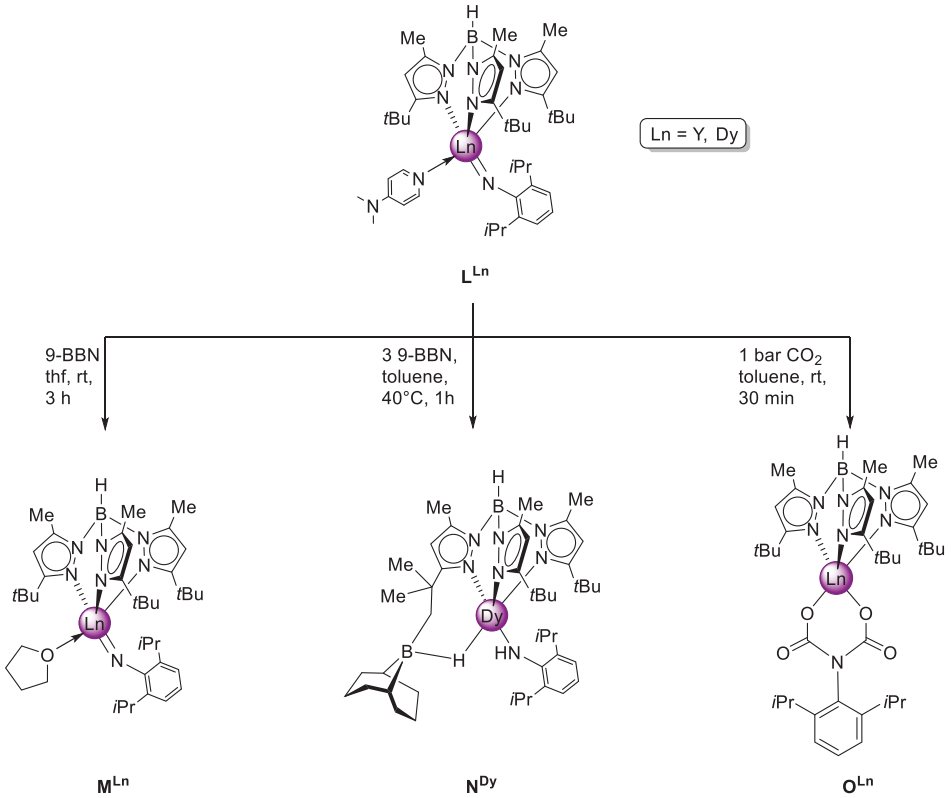

Scheme B5. Reactivity studies of complex **L$^{Y/Dy}$**. Addition of Lewis acid 9-BBN in 1:1 ratio afforded [Tp^{tBu,Me}Dy(NC$_6$H$_3$*i*Pr$_2$-2,6)(thf)] **M^{Dy}** and in 3:1 ratio Tp^{tBu,Me}Dy(μ_2-CH$_2$)(μ_2-HBC$_8$H$_{14}$)(HNC$_6$H$_3$*i*Pr$_2$-2,6) **N^{Dy}**. Complexes **K$^{Y/Dy}$** show nucleophilic behavior toward unsaturated carbonyls such as CO$_2$ (**O$^{Y/Dy}$**, **Paper III**).

Preliminary studies on the reactivity of terminal imide complex **L^{Dy}** towards carbon dioxide (1 bar) in toluene at ambient temperature indicate CO$_2$ insertion into the Dy–N$_{imido}$ bond forwarding the carbamate formation in product **O^{Dy}**. The DRIFT spectrum of **O^{Dy}** revealed typical carbonyl vibrations at 1701 cm^{-1} and 1641 cm^{-1} assigned to asymmetric and symmetric C=O stretching vibrations (**Paper III**).

2 Rare-Earth-Metal Phosphinidene Complexes

The successful isolation of terminal rare-earth-metal imide complexes for the lanthanides neodymium, samarium, dysprosium and holmium allowed the attempt to push this chemistry a step further. As a softer donor and the resulting tendency to form weaker interactions with rare-earth metals, phosphorus was chosen to test the limits of the approach of this study. After screening a large variety of possible precursors, bridged as well as terminal rare-earth metal phosphinidenes were obtained.

Searching for similar precursors as those which were successful in the rare-earth-metal imide chemistry the first approach was to use the known disguised bis(alkyl) complexes [Tp$^{t\mathrm{Bu,Me}}$YMe(μ_2-MeMMe$_3$)] (**P$^{\mathbf{Y/M}}$**) (M = Al, Ga) (Scheme B6; **Paper II**).

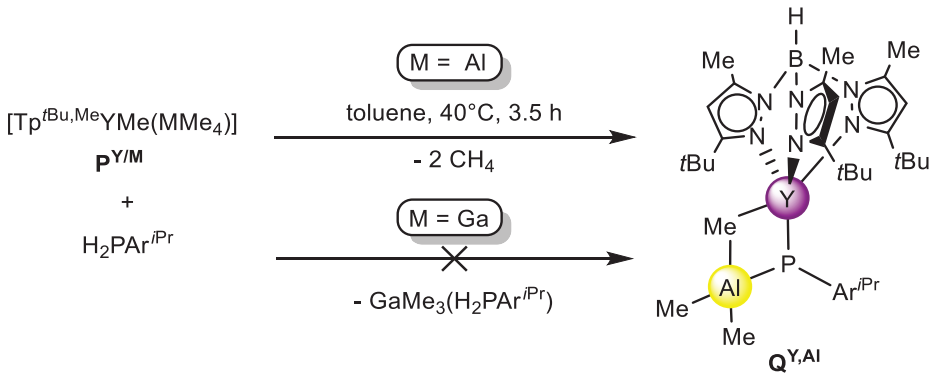

Scheme B6. Synthesis of Lewis acid-stabilized [Tp$^{t\mathrm{Bu,Me}}$Y(μ_2-PC$_6$H$_3$*i*Pr$_2$-2,6)(μ_2-MeAlMe$_2$)] (**Q$^{\mathbf{Y/Al}}$**) with primary phosphine [H$_2$PC$_6$H$_3$*i*Pr$_2$-2,6] in toluene. Only the reaction with the aluminum congener **P$^{\mathbf{Y/Al}}$** leads to a successful phosphinidene formation.

Reaction of [H$_2$PAr$^{i\mathrm{Pr}}$] with trimethylgallium stabilized complex **P$^{\mathbf{Y/Ga}}$** immediately results in the abstraction of the Lewis acid and coordination of the primary phosphine to [GaMe$_3$]. The formation of the [GaMe$_3$·H$_2$PAr$^{i\mathrm{Pr}}$] adduct is driven by the high phosphorus affinity of gallium, since both are considered as soft acid and base,[96] respectively. The same reaction with the aluminum congener **P$^{\mathbf{Y/Al}}$** instead afforded after several hours at 40 °C the trimethylaluminum-stabilized phosphinidene complex [Tp$^{t\mathrm{Bu,Me}}$Y(μ_2-PC$_6$H$_3$*i*Pr$_2$-2,6)(μ_2-MeAlMe$_2$)] (**Q$^{\mathbf{Y/Al}}$**). This four-membered ring structural motif, is comparable to the known Lewis acid-capped imide complexes [Tp$^{t\mathrm{Bu,Me}}$Ln(μ_2-NC$_6$H$_3$Me$_2$-2,6)(μ_2-MeMMe$_3$)] (Ln = Sm, Nd, Dy, Ho; M = Al, Ga) in the aforementioned Chapter B1 (**Paper I**). The Y–P$_{phosphinidene}$ interatomic distance is one of

the shortest known Ln–P distances with 2.5297(7) Å and in addition, the Y–$P_{phosphinidene}$–C_{ipso} angle (155.94(8)°) is mostly determined by the geometrical constraint around the metal center and bent by the additional Lewis acid [$AlMe_3$]. Compared to the Lewis acid-capped rare-earth-metal imide complexes (Ln = Sm, Nd, Dy, Ho; Chapter B1) the angle is even more bent, owed to the larger size of the phosphorus atom.

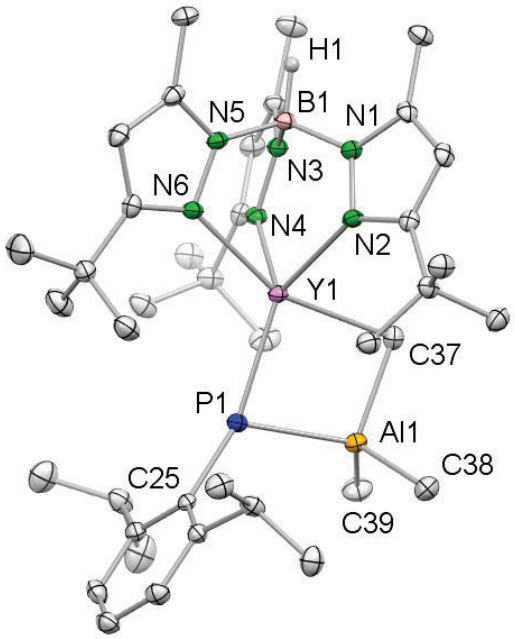

Figure B5. Crystal structure of Lewis acid-capped yttrium phosphinidene [$Tp^{tBu,Me}Y(\mu_2\text{-}PC_6H_3iPr_2\text{-}2,6)(\mu_2\text{-}MeAlMe_2)$] (**$Q^{Y/Al}$**) (**Paper II**).

By virtue of yttrium´s electronic configuration and therefore, its resulting diamagnetic characteristics, NMR spectroscopic experiments were conducted to further investigate the behavior of phosphinidene functionalities. The ^{1}H NMR spectrum of complex **$Q^{Y/Al}$** revealed highly fluxional behavior of the methyl groups of the additional Lewis acid, which is embodied by a single signal at –0.12 ppm. The ^{89}Y NMR spectrum shows a singlet at 504 ppm, implying one yttrium species. Though, the most interesting NMR spectroscopic data is revealed by the coupled and decoupled phosphorus NMR spectroscopic investigations. Both the $^{31}P\{^{1}H\}$ NMR spectrum's and the ^{31}P NMR spectrum's microstructure disclose a doublet at –53.5 ppm ($^{1}J_{YP}$ = 213 Hz). This clearly evidences the presence of a phosphinidene fragment, as no P–H coupling is observed (Figure B6). However, the separation of the additional Lewis acid by applying donor molecules such as DMAP or THF did not render the desired terminal phosphinidene complex.

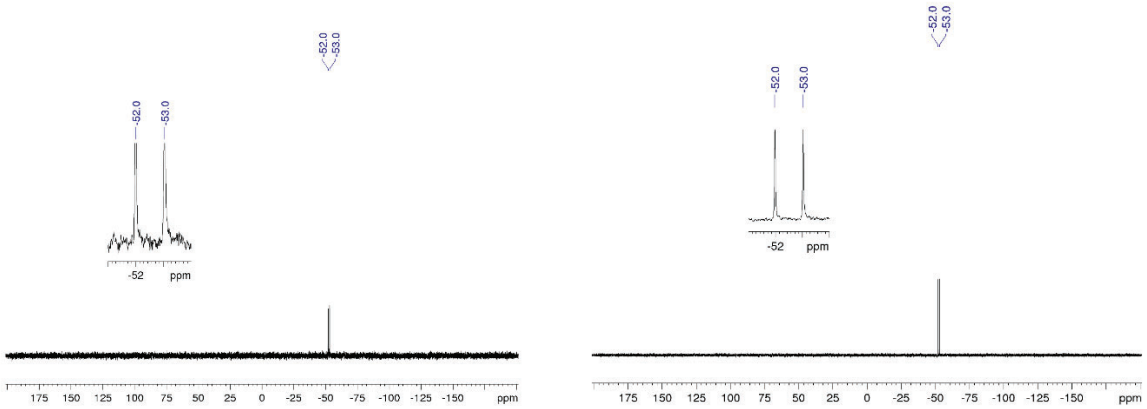

Figure B6. $^{31}P\{^{1}H\}$ NMR spectrum (202 MHz) (left) and ^{31}P NMR spectrum (202 MHz) (right) of [Tp^{tBu,Me}YMe(PC$_6$H$_3$*i*Pr$_2$-2,6)(μ_2-MeAlMe$_2$)] **3-Y^{Al}** in C$_6$D$_6$ at 26 °C. (**Q$^{Y/Al}$**) (**Paper II**).

Regarding the disruption of the trimethylgallium-stabilized bis(alkyl) complex **P$^{Y/Ga}$** into a Lewis acid/base adduct upon addition of primary phosphine, and subsequent formation of the undisguised bis(methyl) complex [Tp^{tBu,Me}YMe$_2$] (**R^{Y}**), the unmasked bis(alkyl) complexes [Tp^{tBu,Me}LnMe$_2$] (**R^{Ln}**; Ln = Y, Dy, Ho) were tested as precursors. Following the same synthesis pathway for the isolation of terminal lanthanide imide complexes for the smaller lanthanides dysprosium and holmium, the approach to isolate mixed methyl/phosphido complexes (**S^{Ln}**) was targeted (Scheme B7; **Paper II**).

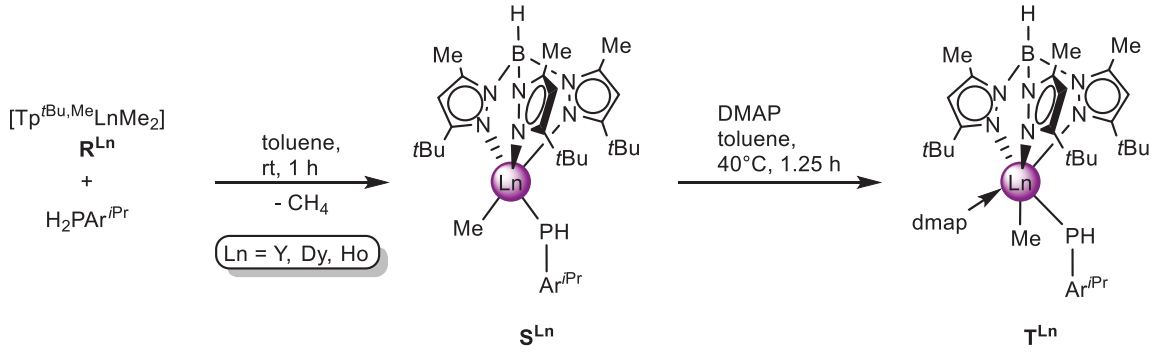

Scheme B7. Multistage synthesis pathway of mixed methyl/phosphido complexes [Tp^{tBu,Me}LnMe(HPC$_6$H$_3$*i*Pr$_2$-2,6)] (**S^{Ln}**) from bis(alkyl) complexes [Tp^{tBu,Me}LnMe$_2$)] (**R^{Ln}**) with primary phosphine [H$_2$PC$_6$H$_3$*i*Pr$_2$-2,6] and addition of DMAP to afford Lewis acid-stabilized mixed methyl/phosphido complexes [Tp^{tBu,Me}LnMe(HPC$_6$H$_3$*i*Pr$_2$-2,6)(dmap)] (**T^{Ln}**) (Ln = Y, Dy, Ho; **Paper II**).

Step one was conducted in toluene at ambient temperature and affords the desired mixed methyl/phosphido complexes [Tp$^{t\mathrm{Bu,Me}}$LnMe(HPC$_6$H$_3$*i*Pr$_2$-2,6)] (**S$^{\mathrm{Ln}}$**) (Ln = Y, Dy, Ho). These complexes are rare examples for phosphido compounds with trivalent rare-earth metals bearing a [HPR]$^-$ moiety, as only one other comparable complex is described in literature.[97] For the lanthanides dysprosium and holmium this structural motif is the first known example for terminally coordinated phosphido functionalities.

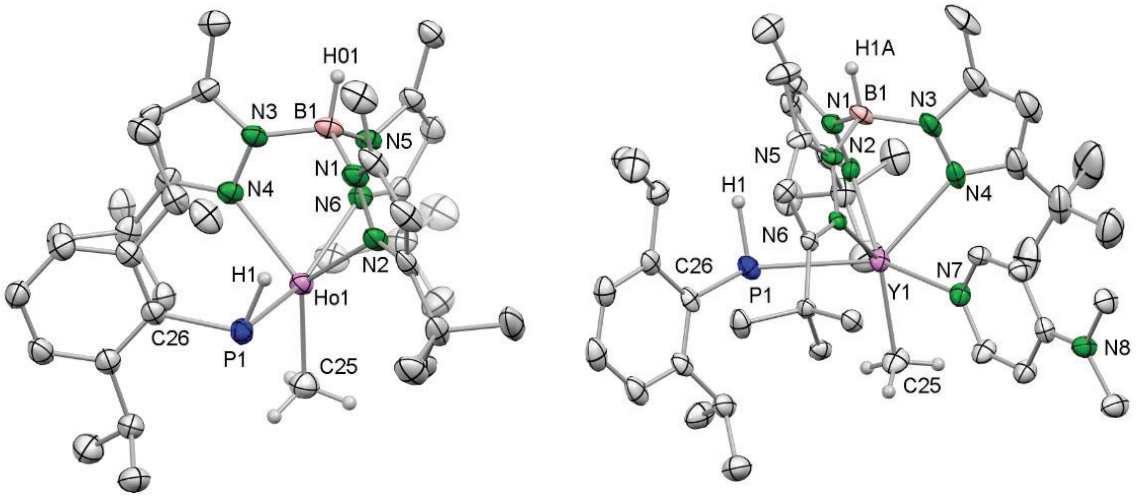

Figure B7. Crystal structure of [Tp$^{t\mathrm{Bu,Me}}$HoMe(HPC$_6$H$_3$*i*Pr$_2$-2,6)] (**S$^{\mathrm{Ho}}$**) (left) and [Tp$^{t\mathrm{Bu,Me}}$YMe(HPC$_6$H$_3$*i*Pr$_2$-2,6)(dmap)] (**T$^{\mathrm{Y}}$**) (right) (**Paper II**).

The crystal structures of the complexes **S$^{\mathrm{Ln}}$** (Ln = Y, Ho) reveal a longer Ln–P$_{phosphido}$ interatomic distance (Ln = Y: 2.8653(14) Å; Ln = Ho: 2.8516(12) Å; left, Figure B6; **Paper II**) than for the initially mentioned trimethylaluminium stabilized yttrium phosphinidene complex **Q$^{\mathrm{Y/Al}}$**, as the phosphido moiety is less negatively charged and the interaction is rather weak. Regarding the proton coupled and the proton decoupled phosphorus NMR spectra the difference is significant. In the ^{31}P{^{1}H} NMR spectrum a doublet at –118.2 ppm ($^1J_{\mathrm{YP}}$ = 63 Hz) indicates the coupling of the phosphorus to the NMR active yttrium nucleus. This coupling is also shown in the ^{31}P NMR spectrum. Additionally, the proton coupled phosphorus NMR spectrum reveals a doublet of a doublet indicating an additional P–H coupling ($^1J_{\mathrm{HP}}$ = 203 Hz) for the phosphido functionality. A down field shifted singlet at 847 ppm in the ^{89}Y NMR spectrum of [Tp$^{t\mathrm{Bu,Me}}$YMe(HPC$_6$H$_3$*i*Pr$_2$-2,6)] (**S$^{\mathrm{Y}}$**) compared to the singlet of [Tp$^{t\mathrm{Bu,Me}}$Y(μ_2-PC$_6$H$_3$*i*Pr$_2$-2,6)(μ_2-MeAlMe$_2$)] (**Q$^{\mathrm{Y/Al}}$**) at 504 ppm, indicates less electron density at the yttrium nucleus of the uncapped, mixed methyl/phosphido complex **S$^{\mathrm{Y}}$** in comparison to the trimethyl capped yttrium phosphinidene complex **Q$^{\mathrm{Y/Al}}$**.

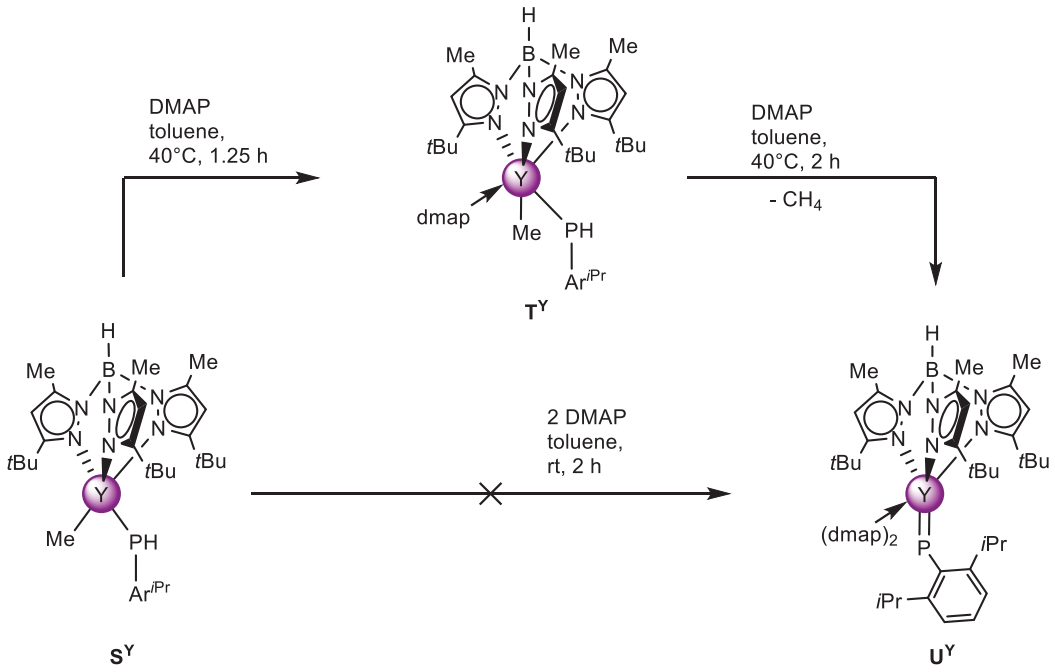

Scheme B8. Synthesis pathway of [Tp^{tBu,Me}Y(PC$_6$H$_3$*i*Pr$_2$-2,6)(dmap)$_2$] (**U^Y**) via DMAP-stabilized mixed methyl/phosphido complex **T^Y**. The direct synthesis of the terminal yttrium phosphinidene complex **U^Y** with the donor molecule free yttrium phosphido complex **S^Y** is not feasible (**Paper II**).

The consequent next step was the addition of a Lewis base. Attempts with THF and DMAP were unsuccessful, as the addition of one equivalent of DMAP only leads to the mere coordination of one donor molecule to the yttrium metal center (Scheme B7/B8, **Paper II**). Nevertheless, [Tp^{tBu,Me}LnMe(HPC$_6$H$_3$*i*Pr$_2$-2,6)(dmap)] (**T^{Ln}**) has some insightful properties shown in the crystal structure (right, Figure B6). The geometrical arrangement in the solid-state structure hints toward a spatial gap between the proton of the [HPR]$^-$ unit and the methyl group which were targeted to evolve as methane. Even in solution these two reactive fragments seem not to get into proximity, although DMAP raise the steric constraint. Furthermore, the interatomic distance of Y–P$_{phosphido}$ (2.9514(17) Å) is slightly affected of the additional coordination of DMAP, as well as the Y–P$_{phosphido}$–C$_{ipso}$ angle (121.54(19)°), which is expected due to the donor abilities and the additional steric demand of the DMAP ligand.

Investigating, if the addition of a second equivalent of DMAP could afford a methane elimination by forcing the reactive sides of the ligands into proximity, one more equivalent of DMAP was added to complex **T^Y** and the mixture was stirred for two hours at 40 °C. Methane elimination was indicated by gas evolution and the desired terminal yttrium phosphinidene complex [Tp^{tBu,Me}Y(PC$_6$H$_3$*i*Pr$_2$-2,6)(dmap)$_2$] (**U^Y**) (Figure B7; **Paper II**) was isolated. Despite of its small size, the trivalent yttrium ion is still capable of coordinating another equivalent of

DMAP. Presumably, this second addition leads to the approach of the methyl group and the proton at the phosphido fragment and finally methane is separated.

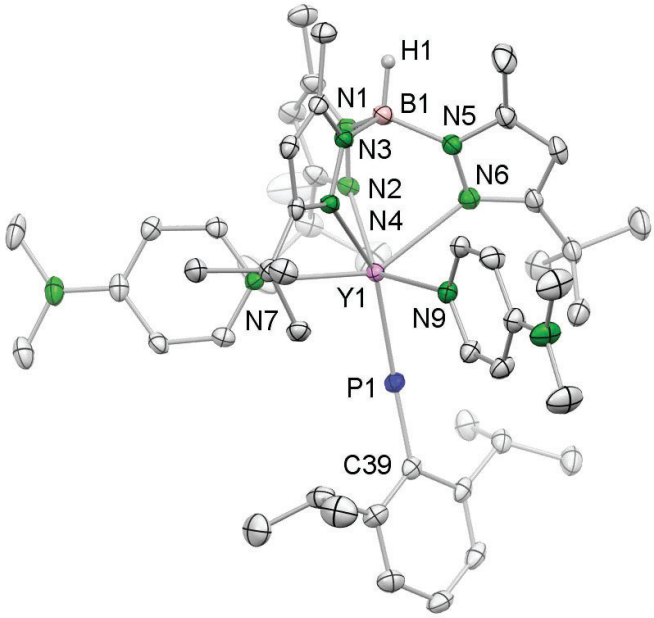

Figure B9. Crystal structure of [Tp^{tBu,Me}Y(PC$_6$H$_3$*i*Pr$_2$-2,6)(dmap)$_2$] (**U^{Y}**) (**Paper II**).

[Tp^{tBu,Me}Y(PC$_6$H$_3$*i*Pr$_2$-2,6)(dmap)$_2$] (**U^{Y}**) is the first literature known example of a terminally bonded phosphinidene fragment to a rare-earth-metal center. As expected, the Y–P$_{phosphinidene}$ interatomic distance (2.4856(7) Å) is the shortest known rare-earth-metal-phosphorus distance and the angle of Y–P$_{phosphinidene}$–C$_{ipso}$ (163.44(9)°) is almost linear, due to the steric pronamed saturation of the coordination sphere of the trivalent yttrium ion (CN: 6). ^{31}P NMR spectroscopical investigations revealed a doublet at –5.5 ppm with a coupling constant of 282 Hz, indicating only a Y–P$_{phosphinidene}$ bond interaction. This increasing coupling constant compared to complex **Q$^{Y/Al}$** underlines the rising double bond character (increasing *s* orbital ratio) of the terminal phosphinidene functionality. Furthermore, DFT calculations underline the increasing multiple bond character of the terminal phosphinidene functionality as it shows one σ- and two π-type Y–P interactions. Nevertheless, these are still highly ionic. Compared to [Tp^{tBu,Me}Y(NC$_6$H$_3$*i*Pr$_2$-2,6)(dmap)], DFT calculations reveal a much lower covalency.

Noteworthy, the reaction does not occure if two equivalents of DMAP are added directly to the unsupported yttrium phosphido complex **S^{Y}** (Scheme B8, **Paper II**).

C

Unpublished Results

1 Terminal Rare-Earth-Metal Methyl "Ate" Complexes

Introduction

Mononuclear rare-earth-metal complexes bearing basic ligands such as terminal or bridging methyl fragments, are promising starting materials for metathesis or activation reactions, as the elimination of volatile methane is a tremendous driving force.[1, 6, 45, 62, 76]

Results and Discussion

The reaction of homoleptic samarium tris(tetramethylgallate) $\mathbf{V}^{\mathbf{Sm}}$ with [HTp$^{t\mathrm{Bu,Me}}$] in *n*-hexane and THF afforded after 15 minutes stirring at ambient temperature [Tp$^{t\mathrm{Bu,Me}}$SmMe(thf)$_2$][GaMe$_4$] ($\mathbf{X}^{\mathbf{Sm}}$, Scheme C1) instead of the intended methylidene complex [Tp$^{t\mathrm{Bu,Me}}$SmCH$_2$(μ_2-MeGaMe$_2$)$_2$] (**Paper I**). Moreover, treatment of trimethylgallium masked bis(alkyl) complexes [Tp$^{t\mathrm{Bu,Me}}$LnMe(μ_2-MeGaMe$_3$)] ($\mathbf{W}^{\mathbf{Ln}}$; Ln = Y, Dy, Ho) with THF leads to the separation of the ion pair and the same terminal, unmasked monomethyl "ate" complexes [Tp$^{t\mathrm{Bu,Me}}$LnMe(thf)$_2$][GaMe$_4$] ($\mathbf{X}^{\mathbf{Ln}}$; Ln = Y, Dy, Ho) are formed (Scheme C1). Recrystallization in toluene afforded colorless crystals, which were suitable for XRD analyses.

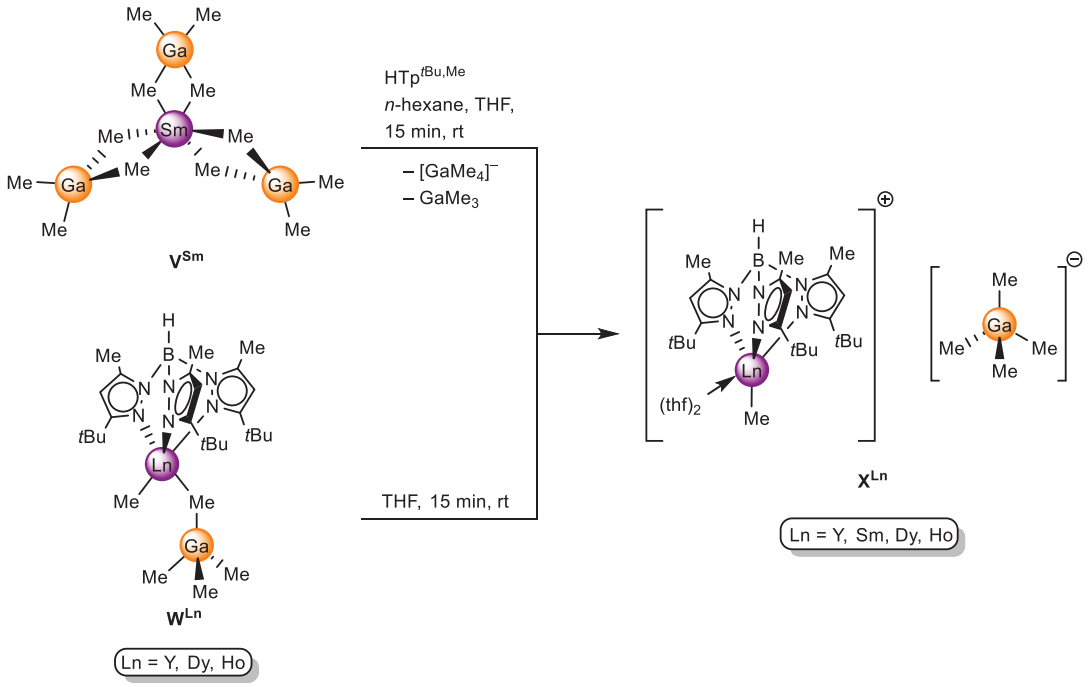

Scheme C1. Synthesis of [Tp$^{t\mathrm{Bu,Me}}$LnMe(thf)$_2$][GaMe$_4$] ($\mathbf{X}^{\mathbf{Ln}}$, Ln = Sm, Y, Dy, Ho) via [Sm(GaMe$_4$)$_3$] ($\mathbf{V}^{\mathbf{Sm}}$) and [HTp$^{t\mathrm{Bu,Me}}$] to afford complex $\mathbf{X}^{\mathbf{Sm}}$, and via addition of THF to [Tp$^{t\mathrm{Bu,Me}}$LnMe(μ_2-MeGaMe$_3$)] ($\mathbf{W}^{\mathbf{Ln}}$, Ln = Y, Dy, Ho) to afford complexes $\mathbf{X}^{\mathbf{Ln}}$ (Ln = Y, Dy, Ho).

However, the quality for complexes $\mathbf{X}^{\mathbf{Y}}$, $\mathbf{X}^{\mathbf{Sm}}$, and $\mathbf{X}^{\mathbf{Ho}}$ was too poor to obtain more than connectivity images, though, better quality was gained for the crystals of complex $\mathbf{X}^{\mathbf{Dy}}$ (Figure C1).

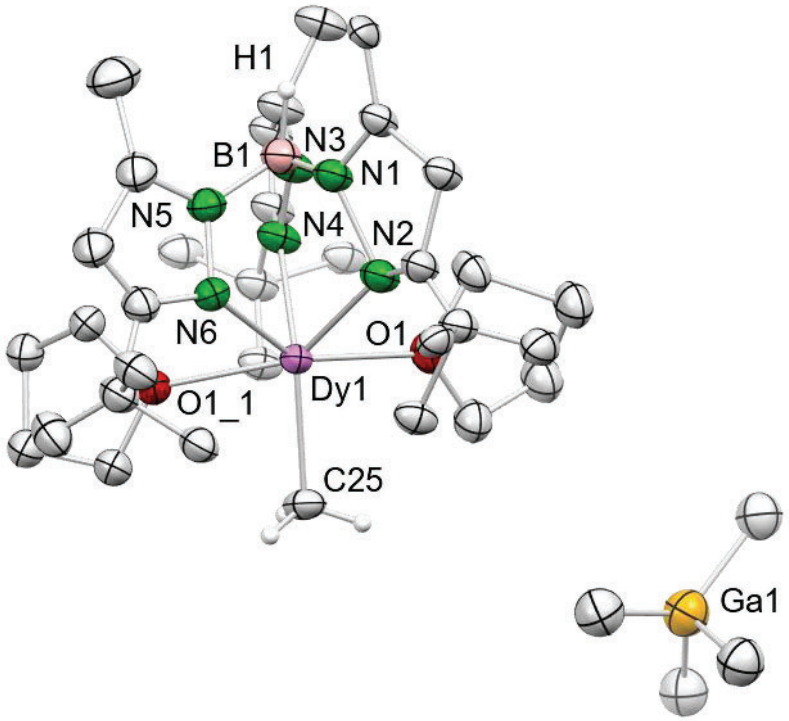

Figure C1. Crystal structure of $[Tp^{tBu,Me}DyMe(thf)_2][GaMe_4]$ ($\mathbf{X}^{\mathbf{Dy}}$).

The $[Tp^{tBu,Me}]$ ligand is attached to the six-coordinated dysprosium center in the usual κ^3 fashion (*N*, *N'*, *N''*) with Dy–N_{pz} distances of 2.38(3) – 2.492(13) Å bearing one longer and two shorter distances. Furthermore, the terminal methyl moiety has an interatomic distance of 2.398(10) Å to the dysprosium, being in the same range or matching the unmasked methyl unit of complex $\mathbf{W}^{\mathbf{Dy}}$ (Dy–$C_{terminal}$: 2.389(3) Å). On the other hand, the interatomic distance of the $[GaMe_3]$-masked methyl moiety in complex $\mathbf{W}^{\mathbf{Dy}}$ (Dy–$C_{bridging}$: 2.736(2) Å) is significantly extended by 0.3 Å compared to the unmasked methyl unit. Being a single positively charged "ate" complex $\mathbf{X}^{\mathbf{Dy}}$, the tetramethylgallate acts as the counter anion and is completely separated from the metal center. Two THF molecules as stronger donors compared to the $[GaMe_4]^-$ unit sufficiently saturate the coordination sphere of the metal center in complexes $\mathbf{X}^{\mathbf{Ln}}$ and the separated ion pair is generated. Interestingly, these separated ion pairs form not only for the smaller rare-earth metals yttrium, dysprosium and holmium, but also for the larger lanthanide samarium.

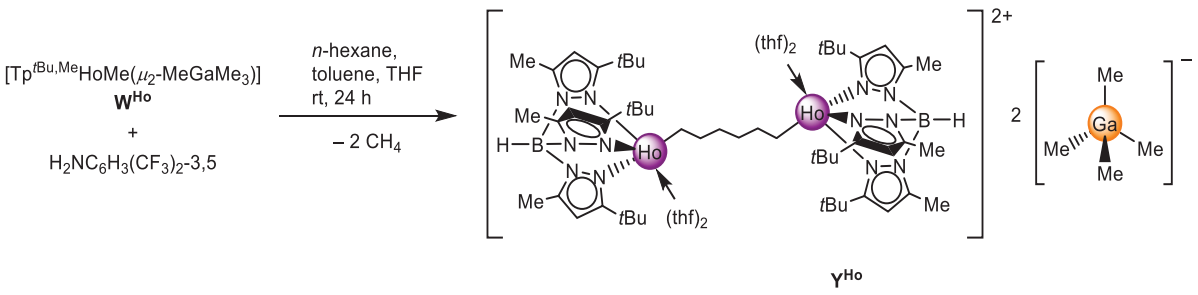

Scheme C2. Activation of *n*-hexane with [Tp^{tBu,Me}HoMe(μ_2-MeGaMe$_3$)] (**W^{Ho}**) and [$H_2NC_6H_3(CF_3)_2$-3,5] in a mixture of toluene, *n*-hexane and THF afforded [{Tp^{tBu,Me}Ho(thf)$_2$}$_2$C$_6$H$_{12}$][GaMe$_4$]$_2$ (**Y^{Ho}**).

Treatment of the masked bis(alkyl) complex **W^{Ho}** with the more acidic aniline [$H_2NC_6H_3(CF_3)_2$-3,5] leads to the activation of *n*-hexane (Scheme C2), instead of the desired mixed methyl/amido complex [Tp^{tBu,Me}HoMe(HNC$_6$H$_3$*i*Pr$_2$-2,6)], which readily forms for the aniline derivative [$H_2NC_6H_3$*i*Pr$_2$-2,6] (**Paper III**). After stirring at ambient temperature overnight and crystallization at –35 °C single crystals suitable for XRD analysis were obtained. Unfortunately, the poor quality of the single crystals provided only a connectivity image for complex **Y^{Ho}** (Figure C2).

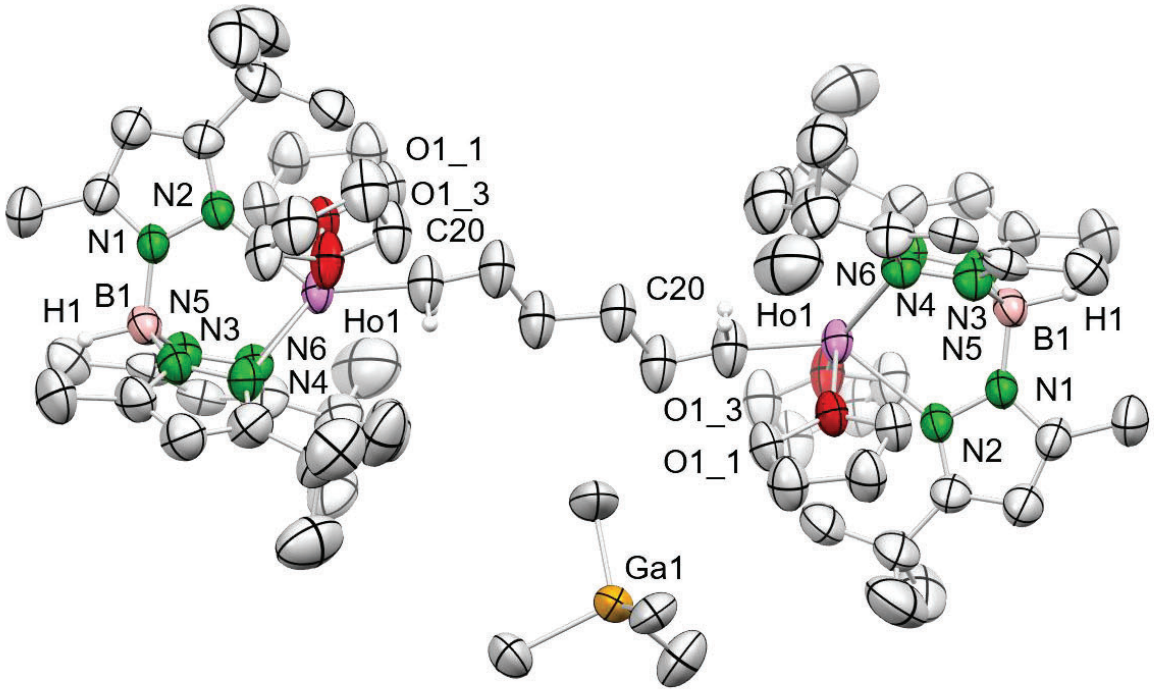

Figure C2. Connectivity image of [{Tp^{tBu,Me}Ho(thf)$_2$}$_2$C$_6$H$_{12}$][GaMe$_4$]$_2$ (**Y^{Ho}**).

Therefore, no statements about the interatomic distances and angles of **Y^{Ho}** can be made. Nevertheless, the crystals revealed the dimeric structure of [{Tp^{tBu,Me}Ho(thf)$_2$}$_2$C$_6$H$_{12}$][GaMe$_4$]$_2$ (**Y^{Ho}**), which consists of two THF-supported

$[Tp^{tBu,Me}Ho]^{2+}$ fragments connected end-on via an activated *n*-hexane bridge. The terminal methyl groups of the solvent molecule were deprotonated under methane elimination. As the complex is a double positively charged "ate" complex, two tetramethylgallates serve as counter anions.

It is possible that the beforehand discussed complex $\mathbf{X^{Ho}}$ is an intermediate in the formation of complex $\mathbf{Y^{Ho}}$ via activation of *n*-hexane. The separation of the counterion $[GaMe_4]^-$ opens the coordination site in $\mathbf{X^{Ho}}$ and the terminal methyl, a strong base, is exposed, which probably promoted the deprotonation of the terminal $[CH_3]$-units of *n*-hexane. However, it was not possible to reproduce $\mathbf{Y^{Ho}}$ to get closer insights into the reaction mechanism.

Experimental

General Considerations. All manipulations were performed under rigorous exclusion of air and moisture, using standard Schlenk, high-vacuum, and glovebox techniques (MB Braun MB200B; < 0.1 ppm O_2, < 0.1 ppm H_2O, argon atmosphere). The solvents *n*-hexane, toluene, and tetrahydrofuran (THF) were purified using Grubbs columns (MBraun SPS, solvent purification system). Tetrahydrofuran was stored over freshly activated molecular sieves (3 Å). All solvents and reagents were stored inside a glovebox. [HTp$^{t\mathrm{Bu,Me}}$] and [KTp$^{t\mathrm{Bu,Me}}$] (Tp$^{t\mathrm{Bu,Me}}$ = hydrotris(3-*tert*-butyl-5-methylpyrazol)borato) were synthesized by a modification of the published procedure of [HTp$^{t\mathrm{Bu,Ph}}$],[1] [Sm(GaMe$_4$)$_3$], and [Tp$^{t\mathrm{Bu,Me}}$LnMe(GaMe$_4$)] (Ln = Y, Dy, Ho) were synthesized according to literature procedures.[2,3,62] Elemental analyses were performed on an *Elementar Vario Micro Cube*.

[Tp$^{t\mathrm{Bu,Me}}$SmMe(thf)$_2$][GaMe$_4$] (X$^{\mathrm{Sm}}$). To a solution of [Sm(GaMe$_3$)] (174 mg, 0.322 mmol) in *n*-hexane a solution of [HTp$^{t\mathrm{Bu,Me}}$] (137 mg, 0.322 mmol) in *n*-hexane and THF was added and stirred for 15 minutes at ambient temperature. The forming red precipitate was extricated of the solvent via vacuum and washed with *n*-hexane (3x2 mL). Red single crystals suitable for XRD analysis formed at –35 °C from a toluene solution (171 mg, 0.198 mmol, 61%).

General procedure for the synthesis of [Tp$^{t\mathrm{Bu,Me}}$LnMe(thf)$_2$][GaMe$_4$] (X$^{\mathrm{Ln}}$; Ln = Y, Dy, Ho). To a solution of [Tp$^{t\mathrm{Bu,Me}}$LnMe(μ_2-MeGaMe$_3$] in toluene (3 mL), 1 mL of THF was added. The mixture was stirred 15 minutes at ambient temperature. Afterwards the solvent was evaporated, and the remaining powder was washed with *n*-hexane (3x2 mL).

[Tp$^{t\mathrm{Bu,Me}}$YMe(thf)$_2$][GaMe$_4$] (X$^{\mathrm{Y}}$). Following the procedure described above, [Tp$^{t\mathrm{Bu,Me}}$YMe(μ_2-MeGaMe$_3$] (154 mg, 235 mmol) and THF yielded **X$^{\mathrm{Y}}$** as a white precipitate (154 mg, 193 mmol, 82%). Colorless single crystals suitable for XRD analysis formed at –35 °C from a toluene solution. $^{1\mathrm{H}}$ NMR (500 MHz, toluene-d_8): δ 5.62 (s, 3H, pz-*H*), 4.66 (br, 1H, B*H*), 3.45 (m, 8H, THF-CH_2), 2.06 (s, 9H, pz-CH_3), 1.49 (s, 27H, pz-C(CH_3)$_3$), 1.33 (m, 8H, THF-CH_2), –0.15 (s, 15H, Y-CH_3; Ga(CH_3)$_4$) ppm. ^{11}B{^{1}H} NMR (160 MHz, toluene-d8): δ –8.3 ppm. Elemental analysis (%) calculated for $BN_6C_{37}H_{71}YO_2Ga$ (800.40 g/mol): C 55.45, H 8.93, N 10.49; found: C 57.59, H 8.73, N 9.63.

[Tp$^{t\mathrm{Bu,Me}}$DyMe(thf)$_2$][GaMe$_4$] (X$^{\mathrm{Dy}}$). Following the procedure described above, [Tp$^{t\mathrm{Bu,Me}}$DyMe(μ_2-MeGaMe$_3$] (114.5 mg, 0,157 mmol) and THF yielded **X$^{\mathrm{Dy}}$** as a white precipitate (68.8 mg, 0.0786 mmol, 50%). Colorless single crystals suitable for XRD analysis formed at –35 °C from a toluene solution. Elemental analysis (%) calculated for $BN_6C_{37}H_{71}DyO_2Ga$ (875.05 g/mol): C 50.79, H 8.18, N 9.60; found: C 50.68, H 7.73, N 9.76.

[Tp$^{t\mathrm{Bu,Me}}$HoMe(thf)$_2$][GaMe$_4$] (X$^{\mathrm{Ho}}$). Following the procedure described above, [Tp$^{t\mathrm{Bu,Me}}$HoMe(μ_2-MeGaMe$_3$] (20 mg, 0.0273 mmol) and THF yielded **X$^{\mathrm{Ho}}$** as a white precipitate (5.21 mg, 0.00594 mmol, 22%). Colorless single crystals suitable for XRD analysis formed at –35 °C from a toluene solution. Elemental analysis (%) calculated for $BN_6C_{37}H_{71}HoO_2Ga$ (877.48 g/mol): C 50.65, H 8.16, N 9.58; found: C 50.69, H 8.17, N 9.45.

[{Tp^{tBu,Me}Ho(thf)$_2$}$_2$C$_6$H$_{12}$][GaMe$_4$]$_2$ (Y^{Ho}). A solution of [Tp^{tBu,Me}HoMe(μ_2-MeGaMe$_3$] (26 mg, 0.0355 mmol) in toluene was added to a solution of [H$_2$NC$_6$H$_3$(CF$_3$)$_2$-3,5] (7.31 mg, 0.0319 mmol) in THF and stirred for 5 minutes at ambient temperature. The mixture turned yellow and gas evolved immediately. Single crystals suitable for XRD analysis formed at –35 °C from a toluene/THF solution.

Table C1. Crystallographic data for compound $\mathbf{X^{Dy}}$.

	$\mathbf{X^{Dy}}$
formula	$C_{37}H_{71}GaBN_6DyO_2$
M_r [g mol^{-1}]	875.02
color	colorless
crystal dimensions [mm^3]	0.174 x 0.158 x 0.077
cryst syst	monoclinic
space group	$P2_1/n$
***a* [Å]**	13.7546(10)
***b* [Å]**	16.7107(13)
***c* [Å]**	25.541(2)
***α* [°]**	90
***β* [°]**	122.6070(10)
***γ* [°]**	90
***V* [Å^3]**	4945.3(7)
Z	4
***T* [K]**	100(2)
ρ_{calcd} [g cm^{-3}]	1.175
***μ* [mm^{-1}]**	2.075
F (000)	1812
θ range [°]	1.480/28.238
unique reflns	38765
observed reflns (I>2σ)	12117
R1/*w*R2 (I>2σ)[a]	0.0936/0.1880
R1/*w*R2 (all data)[a]	0.01441/0.2105
GOF[a]	1.046

[a] $R1 = \Sigma(||F_0|-|F_c||)/\Sigma|F_0|$, $F_0 > 4\sigma(F_0)$. $wR2 = \{\Sigma[w(F_0^2-F_c^2)^2/\Sigma[w(F_0^2)^2]\}^{4/5}$.

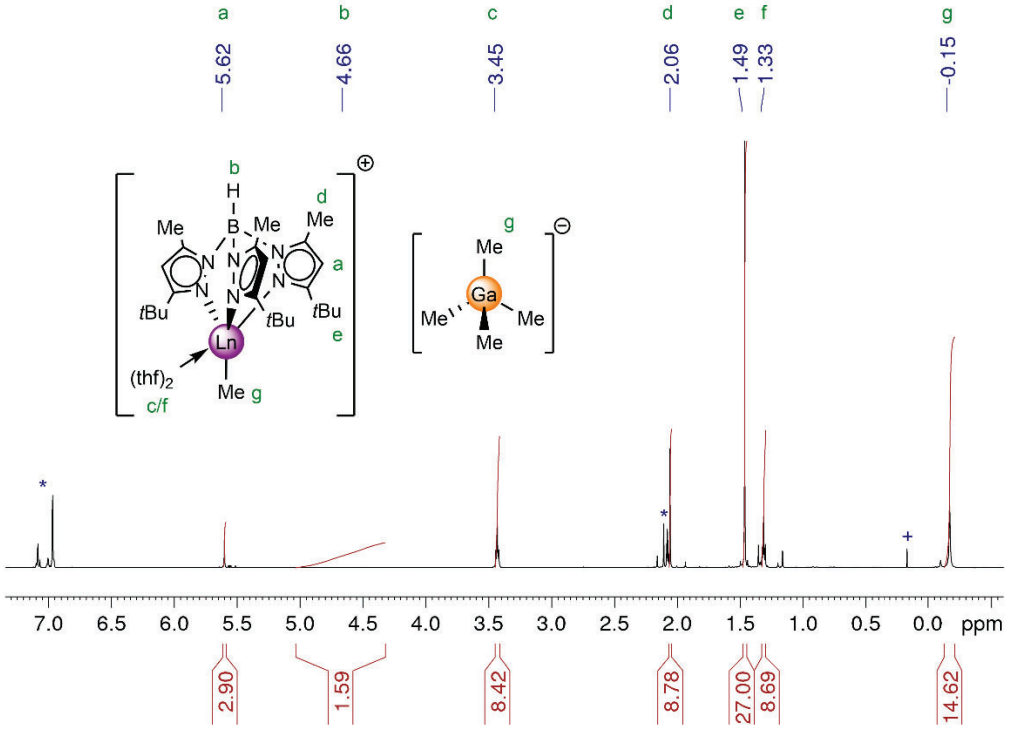

Figure C4. ^{1}H NMR spectrum (500 MHz) of compound [Tp^{tBu,Me}YMe(thf)$_2$][GaMe$_4$] (**X^{Y}**) in toluene-d_8 at 26 °C (+ methane).

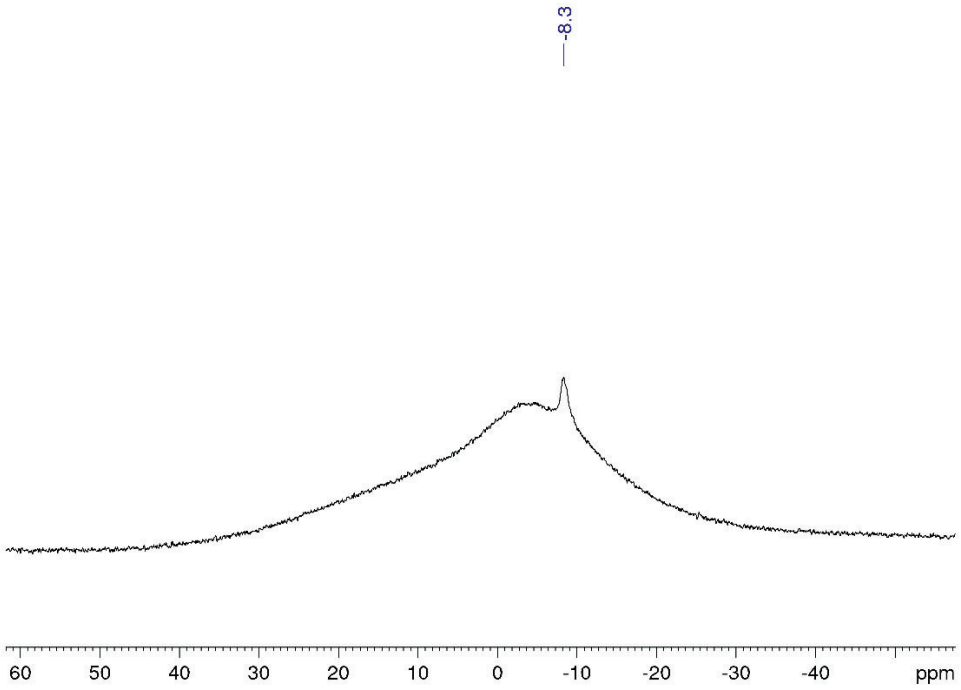

Figure C5. ^{11}B{^{1}H} NMR spectrum (160 MHz) of compound [Tp^{tBu,Me}YMe(thf)$_2$][GaMe$_4$] (**X^{Y}**) in toluene-d_8 at 26 °C.

D

Bibliography

1. D. Schädle; C. Maichle-Mössmer; C. Schädle; R. Anwander, *Chem. Eur. J.* **2015,** *21* (2), 662-670.

2. R. H. Grubbs, *Angew. Chem., Int. Ed.* **2006,** *45* (23), 3760-3765.

3. Schrock, R. R., *Angew. Chem., Int. Ed.* **2006,** *45* (23), 3748-3759.

4. Chauvin, Y., *Angew. Chem., Int. Ed.* **2006,** *45* (23), 3740-3747.

5. Tebbe, F.; Parshall, G.; Reddy, G. *J. Am. Chem. Soc.* **1978,** *100* (11), 3611-3613.

6. Solola, L. A.; Zabula, A. V.; Dorfner, W. L.; Manor, B. C.; Carroll, P. J.; Schelter, E. J., *J. Am. Chem. Soc.* **2017,** *139* (6), 2435-2442.

7. Lu, E.; Chu, J.; Chen, Y., *Acc. Chem. Res.* **2018,** *51* (2), 557-566.

8. Lv, Y.; Kefalidis, C. E.; Zhou, J.; Maron, L.; Leng, X.; Chen, Y., *J. Am. Chem. Soc.* **2013,** *135* (39), 14784-14796.

9. Chu, J.; Lu, E.; Liu, Z.; Chen, Y.; Leng, X.; Song, H., *Angew. Chem., Int. Ed.* **2011,** *50* (33), 7677-7680.

10. Hong, J.; Zhang, L.; Wang, K.; Zhang, Y.; Weng, L.; Zhou, X., *Chem. Eur. J.* **2013,** *19* (24), 7865-7873.

11. Cui, D.; Nishiura, M.; Hou, Z., *Angew. Chem., Int. Ed.* **2005,** *44* (6), 959-962.

12. Chu, J.; Han, X.; Kefalidis, C. E.; Zhou, J.; Maron, L.; Leng, X.; Chen, Y., *J. Am. Chem. Soc.* **2014,** *136* (31), 10894-10897.

13. Chu, J.; Zhou, Q.; Li, Y.; Leng, X.; Chen, Y., *Sci. China Chem.* **2014,** *57* (8), 1098-1105.

14. Mukherjee, D.; Okuda, J., *Chem. Commun.* **2018,** *54* (22), 2701-2714.

15. Summerscales, O. T.; Gordon, J. C., *RSC Adv.* **2013,** *3* (19), 6682-6692.

16. Zi, G., *Sci. China Chem.* **2014,** *57* (8), 1064-1072.

17. Kratsch, J.; Roesky, P. W., *Angew. Chem., Int. Ed.* **2014,** *53* (2), 376-383.

18. Zhu, Q.; Zhu, J.; Zhu, C., *Tetrahedron Lett.* **2018,** *59* (6), 514-520.

19. Rad'kov, V.; Dorcet, V.; Carpentier, J.-F.; Trifonov, A.; Kirillov, E., *Organometallics* **2013,** *32* (5), 1517-1527.

20. Schädle, D.; Schädle, C.; Schneider, D.; Maichle-Mössmer, C. c.; Anwander, R., *Organometallics* **2015,** *34* (20), 4994-5008.

21. Wolf, B. M.; Stuhl, C.; Maichle-Mössmer, C.; Anwander, R., *Chem. Eur. J.* **2018,** *24* (59), 15921-15929.

22. Trifonov, A. A.; Bochkarev, M. N.; Schumann, H.; Loebel, J., *Angew. Chem., Int. Ed. in English* **1991,** *30* (9), 1149-1151.

23. ZhiXiao, L.; YaoFeng, C., *Sci. Sin. Chim.* **2011,** *41* (2), 304-313.

24. Rocklage, S. M.; Schrock, R. R., T *J. Am. Chem. Soc.* **1980,** *102* (26), 7808-7809.

25. Rocklage, S. M.; Schrock, R. R., *J. Am. Chem. Soc.* **1982,** *104* (11), 3077-3081.

26. Mayer, J. M.; Curtis, C. J.; Bercaw, J. E., *J. Am. Chem. Soc.* **1983,** *105* (9), 2651-2660.

27. Jones, T. C.; Nielson, A. J.; Rickard, C. E. F., *Chem. Commun.* **1984,** (4), 205-206.

28. Cummins, C. C.; Baxter, S. M.; Wolczanski, P. T., *J. Am. Chem. Soc.* **1988,** *110* (26), 8731-8733.

29. Walsh, P. J.; Hollander, F. J.; Bergman, R. G., *J. Am. Chem. Soc.* **1988,** *110* (26), 8729-8731.

30. Hill, J. E.; Profilet, R. D.; Fanwick, P. E.; Rothwell, I. P., *Angew. Chem., Int. Ed. in English* **1990,** *29* (6), 664-665.

31. Roesky, H. W.; Voelker, H.; Witt, M.; Noltemeyer, M., *Angew. Chem., Int. Ed. in English* **1990,** *29* (6), 669-670.

32. Walsh, P. J.; Hollander, F. J.; Bergman, R. G., *Organometallics* **1993,** *12* (9), 3705-3723.

33. Bennett, J. L.; Wolczanski, P. T., *J. Am. Chem. Soc.* **1994,** *116* (5), 2179-2180.

34. Dunn, S. C.; Batsanov, A. S.; Mountford, P., *Chem. Commun.* **1994,** (17), 2007-2008.

35. Polse, J. L.; Andersen, R. A.; Bergman, R. G., *J. Am. Chem. Soc.* **1998,** *120* (51), 13405-13414.

36. Fletcher, J. S.; Male, N. A. H.; Wilson, P. J.; Rees, L. H.; Mountford, P.; Schröder, M., *Dalton Trans.* **2000,** (22), 4130-4137.

37. Basuli, F.; Bailey, B. C.; Huffman, J. C.; Mindiola, D. J., *Chem. Commun.* **2003,** (13), 1554-1555.

38. Brennan, J. G.; Andersen, R. A., *J. Am. Chem. Soc.* **1985,** *107* (2), 514-516.

39. Arney, D. S. J.; Burns, C. J., *J. Am. Chem. Soc.* **1995,** *117* (37), 9448-9460.

40. Brown, D. R.; Denning, R. G., *Inorg. Chem.* **1996,** *35* (21), 6158-6163.

41. Straub, T.; Frank, W.; Reiss, G. J.; Eisen, M. S., *Dalton Trans.* **1996,** (12), 2541-2546.

42. Kiplinger, J. L.; Morris, D. E.; Scott, B. L.; Burns, C. J., *Chem. Commun.* **2002,** (1), 30-31.

43. Castro-Rodríguez, I.; Nakai, H.; Meyer, K., *Angew. Chem., Int. Ed.* **2006,** *45* (15), 2389-2392.

44. Hayton, T. W.; Boncella, J. M.; Scott, B. L.; Palmer, P. D.; Batista, E. R.; Hay, P. J., *Science* **2005,** *310* (5756), 1941-1943.

45. Lu, E.; Li, Y.; Chen, Y., *Chem. Commun.* **2010,** *46* (25), 4469-4471.

46. Rong, W.; Cheng, J.; Mou, Z.; Xie, H.; Cui, D., *Organometallics* **2013,** *32* (19), 5523-5529.

47. Scott, J.; Basuli, F.; Fout, A. R.; Huffman, J. C.; Mindiola, D. J., *Angew. Chem., Int. Ed.* **2008,** *47* (44), 8502-8505.

48. Giesbrecht, G. R.; Gordon, J. C., *Dalton Trans.* **2004,** (16), 2387-2393.

49. Wang, S.; Yang, Q.; Mak, T. C. W.; Xie, Z., *Organometallics* **1999,** *18* (26), 5511-5517.

50. Xie, Z.; Wang, S.; Yang, Q.; Mak, T. C. W., *Organometallics* **1999,** *18* (9), 1578-1579.

51. Beetstra, D. J.; Meetsma, A.; Hessen, B.; Teuben, J. H., *Organometallics* **2003,** *22* (22), 4372-4374.

52. Avent, A. G.; Hitchcock, P. B.; Khvostov, A. V.; Lappert, M. F.; Protchenko, A. V., *Dalton Trans.* **2004,** (15), 2272-2280.

53. Pan, C.-L.; Chen, W.; Song, S.; Zhang, H.; Li, X., *Inorg. Chem.* **2009,** *48* (14), 6344-6346.

54. Schädle, D.; Schädle, C.; Törnroos, K. W.; Anwander, R., *Organometallics* **2012,** *31* (14), 5101-5107.

55. Gordon, J. C.; Giesbrecht, G. R.; Clark, D. L.; Hay, P. J.; Keogh, D. W.; Poli, R.; Scott, B. L.; Watkin, J. G., *Organometallics* **2002,** *21* (22), 4726-4734.

56. Chan, H.-S.; Li, H.-W.; Xie, Z., *Chem. Commun.* **2002,** (6), 652-653.

57. Liddle, S. T.; Mills, D. P.; Wooles, A. J., *Chem. Soc. Rev.* **2011,** *40* (5), 2164-2176.

58. Scott, J.; Mindiola, D. J., *Dalton Trans.* **2009,** (40), 8463-8472.

59. Zimmermann, M.; Anwander, R., *Chem. Rev.* **2010,** *110* (10), 6194-6259.

60. Mindiola, D. J.; Scott, J., *Nat. Chem.* **2011,** *3* (1), 15-17.

61. Schädle, D.; Anwander, R., *Chem. Soc. Rev.* **2019,** *48* (24), 5752-5805.

62. Schädle, D.; Meermann-Zimmermann, M.; Schädle, C.; Maichle-Mössmer, C.; Anwander, R., *Eur. J. Inorg. Chem.***2015,** *2015* (8), 1334-1339.

63. Lampland, N. L.; Zhu, J.; Hovey, M.; Jana, B.; Ellern, A.; Sadow, A. D., *Inorg. Chem.* **2015,** *54* (14), 6938-6946.

64. Waterman, R., *Organometallics* **2013,** *32* (24), 7249-7263.

65. Thompson, M. E.; Baxter, S. M.; Bulls, A. R.; Burger, B. J.; Nolan, M. C.; Santarsiero, B. D.; Schaefer, W. P.; Bercaw, J. E., *J. Am. Chem. Soc.* **1987,** *109* (1), 203-219.

66. Schädle, D.; Maichle-Mössmer, C.; Törnroos, K. W.; Anwander, R., *Inorg.* **2015,** *3* (4), 500-510.

67. Schädle, D.; Schädle, C.; Schneider, D.; Maichle-Mössmer, C.; Anwander, R., V*Organometallics* **2015,** *34* (20), 4994-5008.

68. Cui, D.; Tardif, O.; Hou, Z., *J. Am. Chem. Soc.* **2004,** *126* (5), 1312-1313.

69. Berthet, J.-C.; Thuéry, P.; Ephritikhine, M., *Eur. J. Inorg. Chem.***2008,** *2008* (35), 5455-5459.

70. Wolf, B. M.; Stuhl, C.; Anwander, R., *Chem. Commun.* **2018,** *54* (64), 8826-8829.

71. Evans, W. J.; Ansari, M. A.; Ziller, J. W.; Khan, S. I., *Inorg. Chem.* **1996,** *35* (19), 5435-5444.

72. Schädle, C.; Schädle, D.; Eichele, K.; Anwander, R., *Angew. Chem., Int. Ed.* **2013,** *52* (50), 13238-13242.

73. Thim, R.; Schädle, D.; Maichle-Mössmer, C.; Anwander, R., *Chem. Eur. J.* **2019,** *25* (2), 507-511.

74. Shima, T.; Yanagi, T.; Hou, Z., *New J. Chem.* **2015,** *39* (10), 7608-7616.

75. Li, J.; Gao, D.; Hu, H.; Cui, C., *New J. Chem.* **2015,** *39* (10), 7567-7570.

76. Solola, L. A.; Zabula, A. V.; Dorfner, W. L.; Manor, B. C.; Carroll, P. J.; Schelter, E. J., *J. Am. Chem. Soc.* **2016,** *138* (22), 6928-6931.

77. Lu, E.; Chu, J.; Chen, Y.; Borzov, M. V.; Li, G., *Chem. Commun.* **2011,** *47* (2), 743-745.

78. Han, X.; Xiang, L.; Lamsfus, C. A.; Mao, W.; Lu, E.; Maron, L.; Leng, X.; Chen, Y., *Chem. Eur. J.* **2017,** *23* (59), 14728-14732.

79. Patrick, E. A.; Yang, Y.; Piers, W. E.; Maron, L.; Gelfand, B. S., *Chem. Commun.* **2021,** *57* (69), 8640-8643.

80. Chu, T.; Piers, W. E.; Dutton, J. L.; Parvez, M., *Organometallics* **2013,** *32* (5), 1159-1165.

81. Raymond, K. N.; Eigenbrot, C. W., *Acc. Chem. Res.* **1980,** *13* (8), 276-283.

82. Maron, L.; Eisenstein, O., *J. Phys. Chem.* **2000,** *104* (30), 7140-7143.

83. Yuan, J.; Hu, H.; Cui, C., *Chem. Eur. J.* **2016,** *22* (16), 5778-5785.

84. Zabula, A. V.; Qiao, Y.; Kosanovich, A. J.; Cheisson, T.; Manor, B. C.; Carroll, P. J.; Ozerov, O. V.; Schelter, E. J., Structure, *Chem. Eur. J.* **2017,** *23* (71), 17923-17934.

85. Cui, P.; Chen, Y.; Borzov, M. V., *Dalton Trans.* **2010,** *39* (29), 6886-6890.

86. Feng, B.; Xiang, L.; McCabe, K. N.; Maron, L.; Leng, X.; Chen, Y., *Nat. Commun.* **2020,** *11* (1), 2916.

87. Watt, F. A.; McCabe, K. N.; Schoch, R.; Maron, L.; Hohloch, S., *Chem. Commun.* **2020,** *56* (98), 15410-15413.

88. Zhou, J.; Li, T.; Maron, L.; Leng, X.; Chen, Y., *Organometallics* **2015,** *34* (2), 470-476.

89. Li, T.; Kaercher, S.; Roesky, P. W., *Chem. Soc. Rev.* **2014,** *43* (1), 42-57.

90. Nief, F., *Coord. Chem. Rev.* **1998,** *178-180*, 13-81.

91. Feng, B.; Xiang, L.; Carpentier, A.; Maron, L.; Leng, X.; Chen, Y., *J. Am. Chem. Soc.* **2021,** *143* (7), 2705-2709.

92. Lv, Y.; Zhou, J.; Leng, X.; Chen, Y., *New J. Chem.* **2015,** *39* (10), 7582-7588.

93. Lammertsma, K., Phosphinidenes. In *New Aspects in Phosphorus Chemistry III*, Majoral, J.-P., Ed. Springer Berlin Heidelberg: Berlin, Heidelberg, 2003; pp 95-119.

94. Lammertsma, K.; Vlaar, Mark J. M., *Eur. J. Inorg. Chem.* **2002,** *2002* (7), 1127-1138.

95. Cowley, A. H.; Barron, A. R., *Acc. Chem. Res.* **1988,** *21* (2), 81-87.

96. Pearson, R. G., *Inorganica Chim. Acta* **1995,** *240* (1), 93-98.

97. Krieck, S.; Görls, H.; Westerhausen, M., *Inorg. Chem.* **2009,** *12* (5), 409-411.

98. Rabe, G. W.; Riede, J.; Schier, A., *Inorg. Chem.* **1996,** *35* (1), 40-45.

99. Schumann, H.; Palamidis, E.; Schmid, G.; Boese, R., *Angew. Chem., Int. Ed. in English* **1986,** *25* (8), 718-719.

100. Tardif, O.; Nishiura, M.; Hou, Z., *Tetrahedron Lett.* **2003,** *59* (52), 10525-10539.

101. Wicker, B. F.; Scott, J.; Andino, J. G.; Gao, X.; Park, H.; Pink, M.; Mindiola, D. J., *J. Am. Chem. Soc.* **2010,** *132* (11), 3691-3693.

102. Wang, W.; Lv, Y.; Gou, X.; Leng, X.; Chen, Y., *Chin. J. Chem.* **2014,** *32* (8), 752-756.

103. Masuda, J. D.; Jantunen, K. C.; Ozerov, O. V.; Noonan, K. J. T.; Gates, D. P.; Scott, B. L.; Kiplinger, J. L., *J. Am. Chem. Soc.* **2008,** *130* (8), 2408-2409.

104. Nolan, S. P.; Stern, D.; Marks, T. J., *J. Am. Chem. Soc.* **1989,** *111* (20), 7844-7853.

105. Greenwood, N. N.; Tranter, R. L., *J. Chem. Soc.* **1969,** (0), 2878-2883.

106. E. E. Bunel, V. S., J.E. Bercaw, 1988.

107. P. J. Shapiro, W. P. S., J. E. Bercaw, 1988.

108. Fryzuk, M. D.; Haddad, T. S., *J. Am. Chem. Soc.* **1988,** *110* (24), 8263-8265.

109. Hitchcock, P. B.; Lappert, M. F.; MacKinnon, I. A., *Chem. Commun.* **1988,** (23), 1557-1558.

110. Litlabø, R.; Zimmermann, M.; Saliu, K.; Takats, J.; Törnroos, K. W.; Anwander, R., A *Angew. Chem., Int. Ed.* **2008,** *47* (49), 9560-9564.

111. Shapiro, P. J.; Schaefer, W. P.; Labinger, J. A.; Bercaw, J. E.; Cotter, W. D., *J. Am. Chem. Soc.* **1994,** *116* (11), 4623-4640.

112. Rabe, G. W.; Riede, J.; Schier, A., *Inorg. Chem.* **1996,** *35* (9), 2680-2681.

113. Rabe, G. W.; Guzei, I. A.; Rheingold, A. L., *Inorg. Chem.* **1997,** *36* (22), 4914-4915.

114. Westerhausen, M.; Schneiderbauer, S.; Hartmann, M.; Warchhold, M.; Nöth, H., *Z. anorg. allg. Chem.* **2002,** *628* (2), 330-332.

115. Aspinall, H. C.; Moore, S. R.; Smith, A. K., *Dalton Trans.* **1992,** (1), 153-156.

116. Rabe, G. W.; Riede, J.; Schier, A., *Main Group Chem.* **1996,** *1*, 273-277.

117. Rabe, G. W.; Yap, G. P. A.; Rheingold, A. L., *Inorg. Chem.* **1995,** *34* (18), 4521-4522.

118. Nief, F.; Ricard, L., *J. Organomet. Chem.* **1997,** *529* (1), 357-360.

119. Andersen, R. A.; Templeton, D. H.; Zalkin, A., *Inorg. Chem.* **1978,** *17* (8), 2317-2319.

120. Rabe, G. W.; Ziller, J. W., *Inorg. Chem.* **1995,** *34* (21), 5378-5379.

121. Rabe, G. W.; Riede, J.; Schier, A., *Chem. Commun.* **1995,** (5), 577-578.

122. Pushkarevsky, N. A.; Ilyin, I. Y.; Petrov, P. A.; Samsonenko, D. G.; Ryzhikov, M. R.; Roesky, P. W.; Konchenko, S. N., *Organometallics* **2017,** *36* (7), 1287-1295.

123. Watt, F. A.; Krishna, A.; Golovanov, G.; Ott, H.; Schoch, R.; Wölper, C.; Neuba, A. G.; Hohloch, S., *Inorg. Chem.* **2020,** *59* (5), 2719-2732.

124. Mathey, F., Phospha-Organic Chemistry: Panorama and Perspectives. *Angew. Chem., Int. Ed.* **2003,** *42* (14), 1578-1604.

125. Shah, S.; Protasiewicz, J. D., *Coord. Chem. Rev.* **2000,** *210* (1), 181-201.

126. Stephan, D. W., *Angew. Chem., Int. Ed.* **2000,** *39* (2), 314-329.

127. Cummins, C. C.; Schrock, R. R.; Davis, W. M., *Angew. Chem., Int. Ed.* **1993,** *32* (5), 756-759.

128. Zhao, G.; Basuli, F.; Kilgore, U. J.; Fan, H.; Aneetha, H.; Huffman, J. C.; Wu, G.; Mindiola, D. J., *J. Am. Chem. Soc.* **2006,** *128* (41), 13575-13585.

129. Masuda, J. D.; Hoskin, A. J.; Graham, T. W.; Beddie, C.; Fermin, M. C.; Etkin, N.; Stephan, D. W., *Chem. Eur. J.* **2006,** *12* (34), 8696-8707.

130. Cui, P.; Chen, Y.; Xu, X.; Sun, J., *Chem. Commun.* **2008,** (43), 5547-5549.

131. Zimmermann, M.; Litlabø, R.; Törnroos, K. W.; Anwander, R., *Organometallics* **2009,** *28* (23), 6646-6649.

132. Pearson, R. G., *J. Am. Chem. Soc.* **1963,** *85* (22), 3533-3539.

133. Chu, J.; Wang, C.; Xiang, L.; Leng, X.; Chen, Y., *Organometallics* **2017,** *36* (23), 4620-4625.

E

Publications

Paper I

Open-Shell Early Lanthanide Terminal Imides

https://doi.org/10.1021/jacs.1c13142
reprinted with permission from
J. Am. Chem. Soc. **2022**, *144*, 9, 4102 – 4113

JACS
JOURNAL OF THE AMERICAN CHEMICAL SOCIETY

pubs.acs.org/JACS

Article

Open-Shell Early Lanthanide Terminal Imides

Theresa E. Rieser, Renita Thim-Spöring, Dorothea Schädle, Peter Sirsch, Rannveig Litlabø, Karl W. Törnroos, Cäcilia Maichle-Mössmer, and Reiner Anwander*

Cite This: J. Am. Chem. Soc. 2022, 144, 4102−4113

Read Online

ABSTRACT: Group 3- and 4f-element organometallic chemistry and reactivity are decisively driven by the rare-earth-metal/lanthanide (Ln) ion size and associated electronegativity/ionicity/Lewis acidity criteria. For these reasons, the synthesis of terminal "unsupported" imides [Ln═NR] of the smaller, closed-shell Sc(III), Lu(III), Y(III), and increasingly covalent Ce(IV) has involved distinct reaction protocols while derivatives of the "early" large Ln(III) have remained elusive. Herein, we report such terminal imides of open-shell lanthanide cations Ce(III), Nd(III), and Sm(III) according to a new reaction protocol. Lewis-acid-stabilized methylidene complexes [$Tp^{tBu,Me}$Ln(μ_3-CH_2){(μ_2-Me)-MMe_2}$_2$] (Ln = Ce, Nd, Sm; M = Al, Ga) react with 2,6-diisopropylaniline (H_2NAr^{iPr}) via methane elimination. The formation of arylimide complexes is governed by the Ln(III) size, the Lewis acidity of the group 13 metal alkyl, steric factors, the presence of a donor solvent, and the sterics and acidity (pK_a) of the aromatic amine. Crucially, terminal arylimides [$Tp^{tBu,Me}$Ln(═NAr^{iPr})(THF)$_2$] (Ln = Ce, Nd, Sm) are formed only for M = Ga, and for M = Al, the Lewis-acid-stabilized imides [$Tp^{tBu,Me}$Ln(NAr^{iPr})($AlMe_3$)] (Ln = Ce, Nd, Sm) are persistent. In stark contrast, the [$GaMe_3$]-stabilized imide [$Tp^{tBu,Me}$Ln(NAr^{iPr})($GaMe_3$)] (Ln = Nd, Sm) is reversibly formed in noncoordinating solvents.

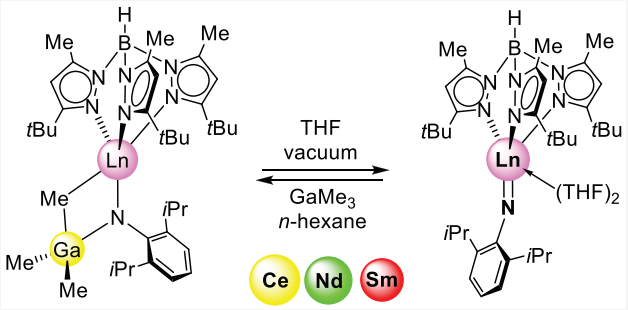

INTRODUCTION

The last two decades have witnessed ever-increasing interest in rare-earth-metal (Ln) complexes featuring multiply bonded (organo)imido ligands.[1−5] Contrary to d-transition metal and 5f-element chemistry,[5−12] the feasibility of terminal "unsupported" (organo)imides [Ln═NR] has posed a major challenge.[1−5] Predominantly ionic bonding situations in rare-earth-metal complexes direct multiply charged, hard monodentate ligands such as $[CR_2]^{2-}$[13,14] and $[NR]^{2-}$ in bridging positions.[15,16] On the other hand, kinetic stabilization (via sterically demanding imido ligands) necessitates advanced synthesis protocols.[17] The linking element of most applied syntheses is the use of highly reactive rare-earth-metal alkyl precursors in order to ensure the complete deprotonation of comparatively Brønsted acid aromatic amines and silylamines.[5] Alternatively, the ultimate deprotonation of a [Ln−NHR] moiety can be achieved by an external base (e.g., LiR, $LiNR_2$). Both strategies are prone to metal-capping or bridging imido functionalities.[18−22]

The currently available terminal rare-earth-metal imides are limited to closed-shell (d^0, f^0, f^{14}) derivatives exclusively.[22−28] In 2010, Chen and co-workers isolated the first terminal scandium imide complex [MeC(NAr)CHC(Me)(N(CH_2)$_2$-NMe_2)Sc(═NAr^{iPr})(DMAP)] (NAr^{iPr}═$NC_6H_3iPr_2$-2,6) by the reaction of the respective β-diketiminato-based tridentate-ligand-supported scandium dimethyl compound with 2,6-diisopropylaniline and *N*,*N*-dimethyl-4-aminopyridine (DMAP).[23] The X-ray structure analysis, DFT calculations, and intrinsic imido reactivity provided clear and conclusive evidence for the existence of a multiply bonded [Sc═NR] moiety.[3] In the meantime, several terminal organoimides of the smallest and least electropositive rare-earth element scandium have been structurally authenticated (six-coordinate Sc^{3+}: effective ionic radius = 0.745 Å).[23−26,28,29] We could access terminal imides of yttrium (d^0, six-coordinate Y^{3+}: 0.900 Å)[29] and lutetium (f^{14}, six-coordinate Lu^{3+}: 0.861 Å)[29] by exploiting the presence of the bulky hydrotris(3-*tert*-butyl-5-methylpyrazolyl)borato ligand ($Tp^{tBu,Me}$).[27] The applied synthesis protocol involving [$Tp^{tBu,Me}$LnMe_2] as the precursor, however, is limited to the smaller rare-earth metals.[27] Schelter and co-workers isolated the first terminal cerium(IV) imide complex stabilized by a multidentate trianionic ligand (d^0f^0, six-coordinate Ce^{4+}: 0.87 Å).[22,29] On the basis of DFT calculations, such anionic ceric imides were assigned a relatively high contribution of covalent bonding compared to trivalent lanthanides.[21,22] Terminal imides of the larger lanthanides with partially filled f orbitals have, to the best of

Received: December 14, 2021
Published: February 25, 2022

https://doi.org/10.1021/jacs.1c13142
J. Am. Chem. Soc. 2022, 144, 4102−4113

our knowledge, hitherto remained elusive. Herein, we report the Lewis-base-promoted synthesis of terminal imides $[Tp^{tBu,Me}Ln(=NAr^{iPr})(THF)_2]$ (Ln = Ce, Nd, Sm) from trimethylgallium-stabilized rare-earth-metal methylidene precursors (Ln = Ce, Nd, Sm). The successful methylidene protonolysis depends on steric factors and the acidity (pK_a) of the aromatic amine that is used.

RESULTS AND DISCUSSION

Ln(III) Alkylidene Precursors. Drawing on the approach with the highly sterically demanding $Tp^{tBu,Me}$ ancillary ligand, we aimed at further investigating its suitability to stabilize terminal imides of larger Ln(III) centers.[27] Having in mind the ready accessibility of the Lewis-acid-stabilized rare-earth-metal methylidene complex $[Tp^{tBu,Me}La(\mu_3\text{-}CH_2)\{(\mu_2\text{-}Me)\text{-}AlMe_2\}_2]$[30] and the nonavailability of $[Tp^{tBu,Me}LnMe_2]$ for the larger Ln(III), we envisaged a $[Ln{=}CH_2(MMe_3)_2] \rightarrow [Ln{=}NR(Do)_x]$ (M = Al, Ga; Do = donor molecule such as THF) instead of a $[Ln(CH_3)_2] \rightarrow [Ln{=}NR]$ transformation. The feasibility of such a methylidene-based protonolysis under mild conditions was previously demonstrated by Zhou and coworkers using a methylidene-capped trinuclear cluster.[31] Owing to the high nitrogen affinity of aluminum and the likely formation of Lewis-acid-stabilized entities $[Ln{=}NR\text{-}(AlMe_3)]$,[27] we assessed the availability of the respective gallium derivatives. Along these lines, the Ln(III) methylidene complexes $[Tp^{tBu,Me}Ln(\mu_3\text{-}CH_2)\{(\mu_2\text{-}Me)AlMe_2\}_2]$ (**1-Ln**, Ln = Ce, Nd) and $[Tp^{tBu,Me}Ln(\mu_3\text{-}CH_2)\{(\mu_2\text{-}Me)GaMe_2\}_2]$ (**2-Ln**, Ln = La, Ce, Nd, Sm) could be obtained by reacting homoleptic tris(tetramethylgallato) and the tris(tetramethylaluminato) complexes of cerium, neodymium, and samarium with $HTp^{tBu,Me}$ or $KTp^{tBu,Me}$ (Scheme 1).

Scheme 1. Synthesis of Ln(III) Methylidene Precursors $[Tp^{tBu,Me}Ln(\mu_3\text{-}CH_2)\{(\mu_2\text{-}Me)MMe_2\}_2]$ (M = Al (1-Ln), Ga (2-Ln)) via Methane Elimination[a]

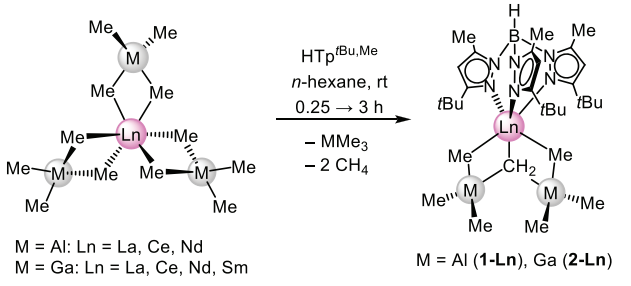

[a]The synthesis of **1-Ce** was conducted with $KTp^{tBu,Me}$ instead of $HTp^{tBu,Me}$, involving $KAlMe_4$ precipitation. (For further information, see the Supporting Information.)

The trimethylgallium-stabilized methylidene complexes **2-Ce** (Supporting Information, Figure S3), **2-Nd**, and **2-Sm** (Figure 1) as well as the trimethylaluminum congeners **1-Ce** and **1-Nd** (Figures S1/S2) are isostructural to the $\{LaAl_2\}$ derivative reported in 2008.[30] Comparing the Ln−C distances of the different lanthanide-methylidene moieties, the lanthanum complex (La−CH_2: 2.519(2) Å)[30] revealed a slightly longer Ln−CH_2 distance than in complexes **1-Ce** (Ce1−C28: 2.484(3) Å), **2-Ce** (Ce1−C25: 2.492(2) Å), **1-Nd** (Nd1−C25: 2.461(2) Å), **2-Nd** (Nd1−C1: 2.450(2) Å), and **2-Sm** (Sm1−C26: 2.414(5) Å). These minor differences are accounted for by the ionic radii of the lanthanide cations

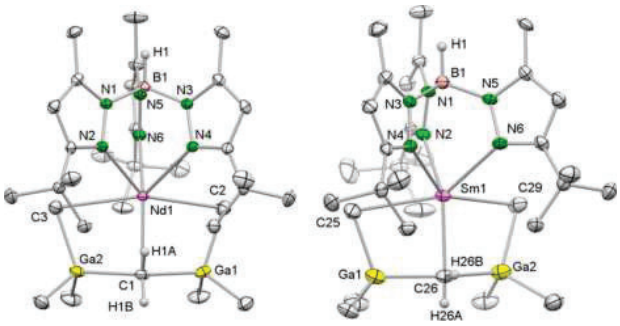

Figure 1. Crystal structures of **2-Nd** (left) and **2-Sm** (right). All atoms are represented by atomic displacement ellipsoids set at 50% probability. Solvent molecules, hydrogen atoms except for those of B−H and CH_2, and the disorder in one of the *tert*-butyl groups are omitted for clarity. Selected interatomic distances (Å) for **2-Nd**: Nd1−C3 2.831(2), Nd1−C1 2.4502(19), and Nd1−C2 2.793(2). Selected interatomic distances (Å) for **2-Sm**: Sm1−C25 2.754(6), Sm1−C26 2.414(5), and Sm1−C29 2.795(5) (Supporting Information).

and are in the expected range.[29] The shorter Nd−CH_2 distance in the case of the trimethylgallium adduct is striking, indicating stronger rare-earth-metal methylidene bonding tantamount to that of the envisaged weaker group 13 Lewis acid stabilization.

As shown in previous NMR studies, the aluminum methyl moieties of the lanthanum congener $[Tp^{tBu,Me}La(\mu_3\text{-}CH_2)\{(\mu_2\text{-}Me)AlMe_2\}_2]$ are highly fluxional,[30] which is also assumed for the paramagnetic cerium, neodymium, and samarium methylidene complexes **2-Ln**. Also, the enhanced mobility of the alkylgallate versus alkylaluminate moieties in solution coupled with a more facile/favorable displacement of the group 13 alkyl[32] should apply to the complexes under study.

$[Ln{=}CH_2(GaMe_3)_2] \rightarrow [Ln{=}NR(THF)_2]$ Transformation. The aromatic amine $[H_2NC_6H_3iPr_2\text{-}2,6]$ (H_2NAr^{iPr}) was previously found to be a convenient imide precursor.[5] Its acidity is suitable for double deprotonation, thus promoting methane elimination from methylidene species as an entropic driving force. In addition, the isopropyl substituents provide favorable steric shielding. Accordingly, methane elimination from compounds **1-Ln** and **2-Ln** was achieved by treatment with 0.9 equiv of H_2NAr^{iPr} under the strict exclusion of donor solvents to afford imide complexes $[Tp^{tBu,Me}Ln(NAr^{iPr})\text{-}(AlMe_3)]$ (**3-Ln**, Ln = Ce, Nd) and $[Tp^{tBu,Me}Ln(NAr^{iPr})\text{-}(GaMe_3)]$ (**4-Ln**, Ln = Nd, Sm) (Scheme 2).

Complexes **3-Ln** and **4-Ln** add to the library of group 13 Lewis-acid-stabilized imide species such as Mindiola's scandium imide complex $[(PNP)Sc(\mu_2\text{-}NAr^{iPr})(\mu_2\text{-}Me)AlMe_2]$ $[PNP{=}N(2\text{-}P\text{-}(CHMe_2)_2\text{-}4\text{-}methylphenyl)_2]$[33] or examples from our laboratory including $[Ln_2(\mu_2\text{-}NAr^{iPr})\{(\mu_3\text{-}NAr^{iPr})\text{-}(\mu_2\text{-}Me)_2AlMe\}(AlMe_4)_2]$ (Ln = Y, La, Ce, Nd)[34] and $[Tp^{tBu,Me}Ln(\mu_2\text{-}NR)(\mu_2\text{-}Me)AlMe_2]$ (Ln = Y, R = *t*Bu, Ad, 2,6-$(CH_3)_2C_6H_3$; Ln = Ho, R = *t*Bu, Ad).[27,35] Other bimetallic imides derived from amine deprotonation comprise Xie's mixed amido-imido-ytterbium complex $[Yb(NAr^{iPr})_2(\mu\text{-}NAr^{iPr})Li_2Na(THF)_2]_2$[20] or Schelter's cerium(IV) imides.[21,22] Any attempt to access the putative terminal lanthanum imide from methylidene $[Tp^{tBu,Me}La(\mu_3\text{-}CH_2)\{(\mu_2\text{-}Me)GaMe_2\}_2]$ (**2-La**) failed and led consistently to $[Tp^{tBu,Me}La(HNAr^{iPr})_2]$ (**9-La**).[36] (See Supporting Information Figure S43 for the ^1H NMR spectrum.) Consequently, single deprotonation and the subsequent formation of the bis(anilido) complex is favored over double deprotonation for the largest rare-earth metals

https://doi.org/10.1021/jacs.1c13142
J. Am. Chem. Soc. 2022, 144, 4102−4113

Scheme 2. Synthesis of the Group 13 Methyl-Stabilized Ln(III) Imides [$Tp^{tBu,Me}$Ln($NC_6H_3iPr_2$-2,6)$AlMe_3$] (3-Ln) and [$Tp^{tBu,Me}$Ln($NC_6H_3iPr_2$-2,6)$GaMe_3$] (4-Ln) and the Terminal Ln(III) Imides [$Tp^{tBu,Me}$Ln($NC_6H_3iPr_2$-2,6)$(THF)_2$] (5-Ln) via Methane Elimination from the Corresponding Ln(III) Methylidene Precursors 1-Ln (M = Al) and 2-Ln (M = Ga)[a]

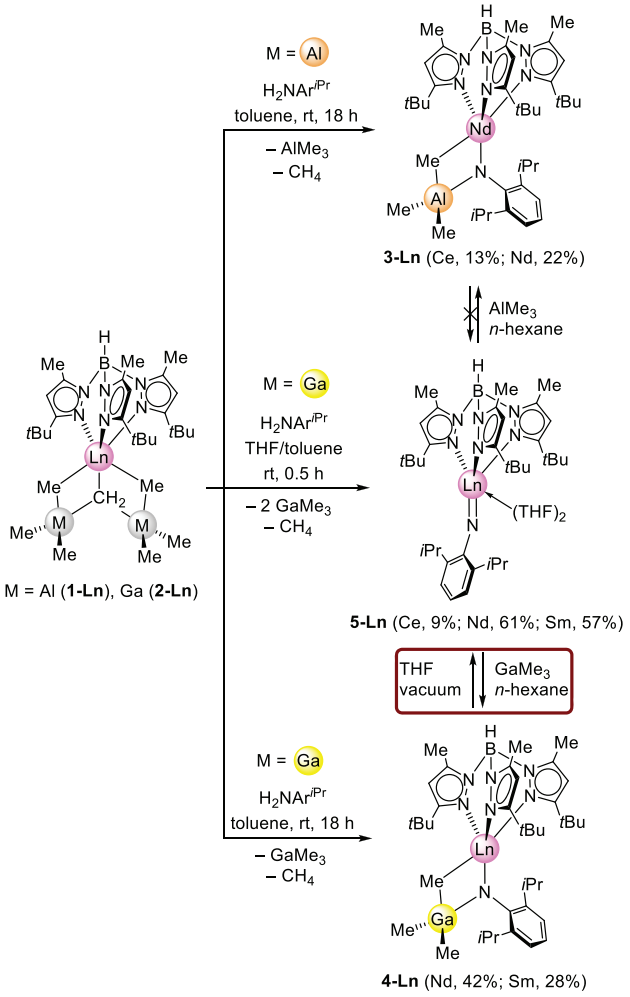

[a]The mutual transformation of **4-Ln** and **5-Ln** occurred by applying either donor addition/vacuum or Lewis acid $GaMe_3$ (Ln = Nd, Sm).

such as lanthanum even though substoichiometric amounts of H_2NAr^{iPr} were applied (vide infra).

Being insoluble in aliphatic solvents, **3-Ln** (Ln = Ce, Nd) and **4-Ln** (Ln = Nd, Sm) were crystallized from a saturated toluene/*n*-pentane solution in low to moderate yields. The X-ray diffraction (XRD) analyses revealed isotype compounds that crystallized in the orthorhombic space group *Pnma* (Figure 2). As expected, the $Tp^{tBu,Me}$ ancillary ligand is coordinated to the rare-earth-metal center center in κ^3 fashion (*N*,*N*′,*N*′′) with Ln–N(pz) distances in a narrow range (**3-Ce**: 2.566(3)–2.624(3) Å; **3-Nd**: 2.541(6)–2.591(4) Å; **4-Nd**: 2.539(4)–2.594(4) Å; and **4-Sm**: 2.514(5)–2.567(3) Å), similar to the methylidene precursors. Furthermore, the lanthanide center is coordinated by μ_2-bridging imido and methyl functionalities.

Unsurprisingly, the μ_2-bridging methyl groups show significantly elongated Al/Ga–C distances (**3-Ce**: C24–Al1

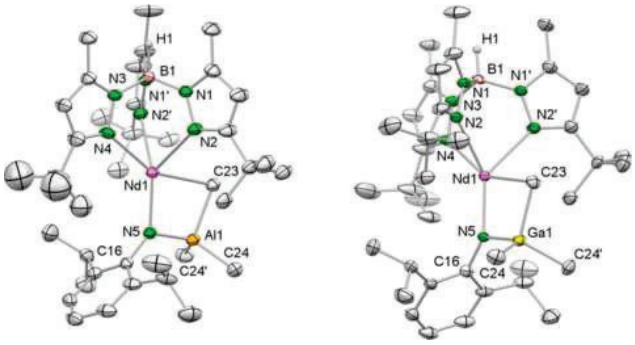

Figure 2. Crystal structures of **3-Nd** (left) and **4-Nd** (right). All atoms are represented by atomic displacement ellipsoids set at 50% probability. Solvent molecules, hydrogen atoms except for those of B–H, and the disorder in one of the *tert*-butyl groups are omitted for clarity. Selected interatomic distances (Å) and angles (deg) for **3-Nd**: Nd1–N5 2.195(5), Nd1–N5–C16 137.3(4), B1–Nd1–N5 174.5(5). Selected interatomic distances (Å) and angles (deg) for **4-Nd**: Nd1–N5 2.158(3), Nd1–N5–C16 141.4(3), and B1–Nd1–N5 172.8(1) (Supporting Information).

2.086(4) Å; **3-Nd**: C23–Al1 2.088(7) Å; **4-Nd**: C23–Ga1 2.106(5) Å; and **4-Sm**: C23–Ga1 2.098(6) Å) compared to the terminal ones (**3-Ce**: C23/23′–Al1 1.985(3) Å; **3-Nd**: C24/24′–Al1 1.990(5) Å; **4-Nd**: C24/24′–Ga1 1.999(3) Å; and **4-Sm**: C24/24′–Ga1 1.989(5) Å). The four-membered metalla-heterocyclic arrangement involving the imido ligand and the group 13 Lewis acid is markedly twisted (**3-Ce**: C24–Ce1–N5 76.27(13)°, Ce1–N5–Al1 101.17(15)°; **3-Nd**: C23–Nd1–N5 77.1(2)°, Nd1–N5–Al1 100.7(2)°; **4-Nd**: C23–Nd1–N5 79.75(13)°, Nd1–N5–Ga1 98.98(13)°; and **4-Sm**: C23–Sm1–N5 80.37(18)°, Sm1–N5–Ga1 98.07(19)°). The Ln–N(imido) distances of 2.213(3) Å (**3-Ce**), 2.195(5) Å (**3-Nd**), 2.158(3) Å (**4-Nd**), and 2.158(4) Å (**4-Sm**) are significantly shorter than the Ln–N distances in complexes with terminal or bridging anilido ligands but are in the range of similar rare-earth-metal imido bonds.[5] Once again, the shorter Nd–N(imido) distances of the trimethylgallium adducts (cf., Nd–C(methylidene) **1-Nd** versus **2-Nd**, vide supra) point to an enhanced multiple-bond character and a weaker interaction of MMe_3 across this bond. This is also supported by longer Ln–C distances in the case of the trimethylgallium adducts (**3-Ce**: 2.722(4) Å; **3-Nd**: 2.699(7) Å; **4-Nd**: 2.714(5) Å; and **4-Sm**: 2.655(6) Å). Furthermore, the Ln–N(imido)–C_{ipso} angle is bent as a result of the heterocyclic arrangement (**3-Ce**: 136.2(3)°; **3-Nd**: 137.3(4)°; **4-Nd**: 141.4(3)°; and **4-Sm**: 141.8(4)°).

The Lewis-acid-stabilized imides [$Tp^{tBu,Me}$Ln(NAr^{iPr})$AlMe_3$] (**3-Ln**) and [$Tp^{tBu,Me}$Ln(NAr^{iPr})$GaMe_3$] (**4-Ln**) gave intricate NMR spectra, but given the properties of similar Ln(III)-imide complexes, $AlMe_3$ coordination is assumed to be less fluxional than for alkylidenes **1-Ln**. Consequently, the attempted cleavage of trimethylaluminum from compounds **3-Ln** with different donor molecules such as THF, DMAP, and TMEDA (*N*,*N*′,*N*′-tetramethylethylenediamine) to produce a terminal imide proved infeasible.[27,35,37] The stabilizing group 13 Lewis acid in **3-Ln** is relatively hard according to Pearson's HSAB concept,[38] and interaction with the dianionic imido ligand is considerably stronger than the formation of the THF adduct [$AlMe_3$(THF)].

To verify our working hypothesis that trimethylgallium interacts less strongly with the Ln–N(imido) bond, we reacted

https://doi.org/10.1021/jacs.1c13142
J. Am. Chem. Soc. 2022, 144, 4102–4113

4-Ln with THF (Scheme 2).[27] Eventually, trimethylgallium could be displaced with THF as a donor molecule to afford the terminal imides $[Tp^{tBu,Me}Ln(=NAr^{iPr})(THF)_2]$ (**5-Ln**, Ln = Ce, Nd, Sm). Concomitantly, the volatile adduct $[GaMe_3(THF)]$ formed, which can be removed in vacuo. Alternatively, the terminal Ln(III) imides **5-Ln** can be accessed directly by adding a solution of H_2NAr^{iPr} in THF to a solution of **2-Ln** in toluene. Regarding the crystallized yields of **5-Ln** (**5-Ce**: 9%; **5-Nd**: 61%; and **5-Sm**: 57%), the Ln(III) ionic radii seem to play a major role given that increasing ionic radii appear to favor the single deprotonation of H_2NAr^{iPr} and the formation of bis(anilides) as shown for $[Tp^{tBu,Me}La(\mu_3\text{-}CH_2)\{(\mu_2\text{-}Me)GaMe_2\}_2]$ (**2-La**) beforehand (vide supra). The repeatedly obtained poor yield of yellow redox-sensitive **5-Ce** featuring a slightly smaller cerium(III) center can be partially explained by the formation of a red byproduct which unfortunately could not be separated and further identified (Experimental Section). Crucially, the overall marked yield losses for crystalline **5-Ln** can be attributed to several essential recrystallization/purification steps. A likely side product could be $[Me_2GaNHAr^{iPr}]_2$, which like its aluminum congener has been obtained previously by refluxing an equimolar mixture of MMe_3 with H_2NAr^{iPr} in toluene overnight.[39] Our reactions did not indicate the formation of $[Me_2GaNHAr^{iPr}]_2$ (cf., isolation of $[Tp^{tBu,Me}Nd(HNAr^{iPr})(THF)_2][(GaMe_3)_2NHAr^{iPr}]$ (**10-Nd**), vide supra).

Complexes **5-Ln** are insoluble in aliphatic solvents and poorly soluble in aromatic solvents but readily dissolve in THF. Single crystals suitable for XRD analyses were grown from saturated solutions of a THF/toluene/*n*-pentane mixture. The isotype compounds **5-Ln** crystallize in the orthorhombic space group $P2_12_12_1$. The lanthanide center in **5-Ln** is hexacoordinated to three scorpionate nitrogen atoms, the imido ligand, and two THF oxygen atoms (Figure 3).

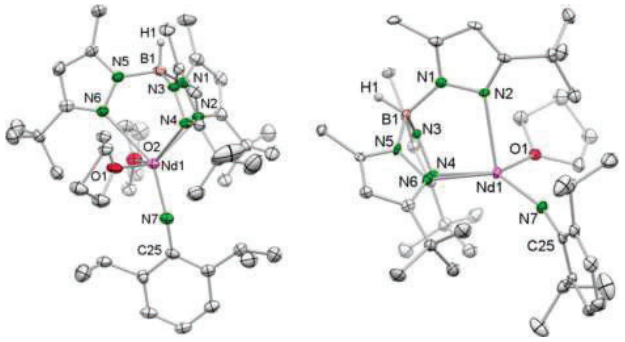

Figure 3. Crystal structures of **5-Ln**, representatively shown for **5-Nd** (left) and **6-Nd** (right). All atoms are represented by atomic displacement ellipsoids set at 50% probability. Hydrogen atoms except for those of B−H as well as the disorder in one THF molecule are omitted for clarity. Selected interatomic distances (Å) and angles (deg) for **5-Nd**: Nd1−N7 2.076(4), Nd1−N7−C25 169.2(4), and B1−Nd1−N7 162.0(2). Selected interatomic distances (Å) and angles (deg) for **6-Nd**: Nd1−N7 2.047(7), Nd1−N7−C25 163.2(6), and B1−Nd1−N7 151.62(2) (Supporting Information).

Moreover, the coordination of the $Tp^{tBu,Me}$ ligand is similar to that in compounds **3-Ln** and **4-Ln** in the routinely observed κ^3 fashion (*N*,*N*′,*N*′′) but with slightly elongated Ln−N(pz) distances in the ranges of 2.667(4) to 2.707(4) Å for **5-Ce**, 2.601(4) to 2.674(4) Å for **5-Nd**, and 2.573(5) to 2.657(6) Å for **5-Sm**, reflecting the distinct coordination number.

Compared to other Lewis-base-stabilized terminal rare-earth-metal imides, however,[27] complexes **5-Ln** feature THF as a comparatively weaker donor (cf., DMAP).[23] Note that one crystallization attempt for **5-Nd** in toluene/fluorocyclohexane yielded single crystals of five-coordinate $[Tp^{tBu,Me}Nd(NAr^{iPr})(THF)]$ (**6-Nd**, Figure 3). This suggests that the bonding of the first donor molecule to the neodymium center is weak and allows for fluxional behavior in solution. The Ln−N(imido) distances of 2.101(3) Å in **5-Ce** (six-coordinate Ce^{3+}: 1.01 Å), 2.076(4)/av. 2.041 Å in **5-Nd**/**6-Nd** (six-coordinate Nd^{3+}: 0.983 Å), and 2.067(5) Å in **5-Sm** (six-coordinate Sm^{3+}: 0.958 Å) are slightly shorter than in the tetravalent cerium ate complex $[(NO_xN)Ce(=NC_6H_3(CF_3)_2\text{-}3,5)][Cs(2.2.2\text{-}crypt)]$ (2.077(3) Å, $NO_xN=N[(CH_2C_6H_4NO(tBu))]_3$ (eight-coordinate Ce^{4+}: 0.97 Å)[22] but compare to similar other known trivalent terminal rare-earth-metal imide complexes $[Tp^{tBu,Me}Y(=NAr)(DMAP)]$ (**I**, 2.024(4) Å, $Ar=C_6H_3Me_2\text{-}2,6$)[27] and $[Tp^{tBu,Me}Lu(=NAr)(DMAP)]$ (**II**, 1.993(5) Å, $Ar=NC_6H_3(CF_3)_2\text{-}3,5$)[27] considering the differences in the ionic radii and coordination number (Table 1).

Table 1. Comparison of Selected Metrical Parameters in Trivalent Rare-Earth-Metal Imide Complexes

compound	CN	Ln=N_{imido} (Å)	Ln−N_{imido}−C_{ipso} (deg)
3-Ce	5	2.213(3)	76.27(13)
3-Nd	5	2.195(5)	137.3(4)
4-Nd	5	2.158(3)	141.4(3)
4-Sm	5	2.158(4)	141.8(4)
7-Nd	6	2.165(3)	147.6(2)
5 Ce	6	2.101(3)	171.3(3)
5-Nd	6	2.076(4)	169.2(4)
5-Sm	6	2.067(5)	169.3(5)
6-Nd[a]	5	2.047(7)/2.036(7)	163.2(6)/165.8(6)
I[27] (Ln = Y)	5	2.024(4)	173.6(4)
II[27] (Ln = Lu)	5	1.993(5)	175.8(5)
III[26] (Ln = Sc)[b]	5	1.852(4)	168.6(3)

[a]Two molecules in an asymmetric unit. [b]Shortest-known Sc=N_{imido} distance.

Naturally, the respective distances of the terminal imides of the 3d transition metal scandium are shorter, ranging from 1.852(4) to 1.881(5) Å (CN = 5 or 6). The shortest Sc−N(imido) distance of 1.852(4) Å was detected for Chen's THF adduct, five-coordinate $[MeC(NAr)CHC(Me)(N(CH_2)_2NMe_2)Sc(=NAr^{iPr})(THF)]$ (**III**, Table 1).[26] The geometry of six-coordinate complexes **5-Ln** deviates considerably from the ideal octahedral coordination. This is caused by the κ^3 coordination fashion of the ancillary ligand. The almost linear Ln−N(imido)−C_{ipso}(aryl) bond angles Ln1−N7−C25 of 171.3(3)° (**5-Ce**), 169.2(4)°/163.2(6)° (**5-Nd**/**6-Nd**), and 169.3(5)°(**5-Sm**) and the very short Ln−N(imido) distances indicate multiple bond character between the imido nitrogen and the lanthanide centers.

The coordination of the THF donor ligand is labile, enhancing the reactivity of **5-Ln**. The treatment of **5-Ln** with trimethylgallium or trimethylaluminum in aliphatic solvents led to the formation of $[Tp^{tBu,Me}Ln(NAr^{iPr})(AlMe_3)]$ (**3-Ln**) and $[Tp^{tBu,Me}Ln(NAr^{iPr})(GaMe_3)]$ (**4-Ln**), indicating reversibility for the latter reaction. The crucial difference between $[Al_2Me_6]$ and $[GaMe_3]$ is the Lewis acidity, which facilitates the isolation of **5-Ln** from **2-Ln** or **4-Ln** in donor solvents. Moreover, the

https://doi.org/10.1021/jacs.1c13142
J. Am. Chem. Soc. 2022, 144, 4102−4113

Scheme 3. Synthesis of Trimethylgallium-Stabilized Neodymium Imide 7-Nd Derived from Sterically Less Demanding 2,4,6-Trimethylaniline, CH-Bond-Activated Neodymium Amide 8-Nd with Sterically More Demanding 2,4,6-Tri-*tert*-butylaniline, and Bis(amido) Neodymium Complex 9-Nd

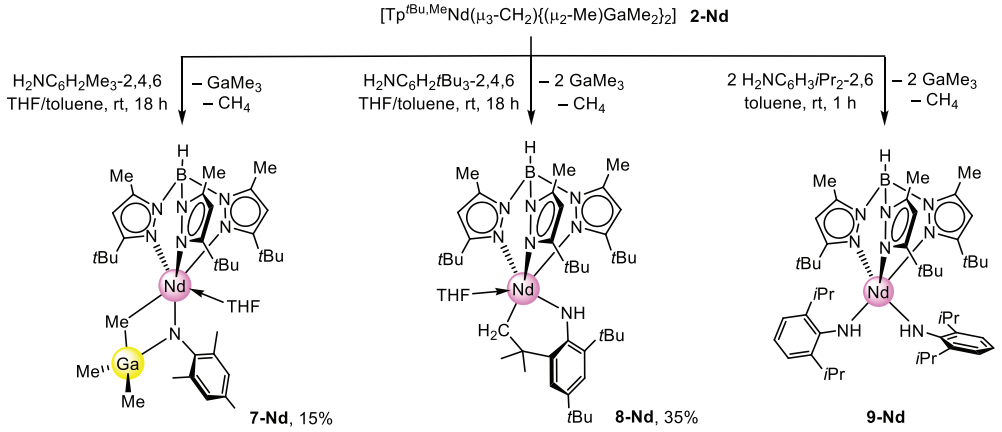

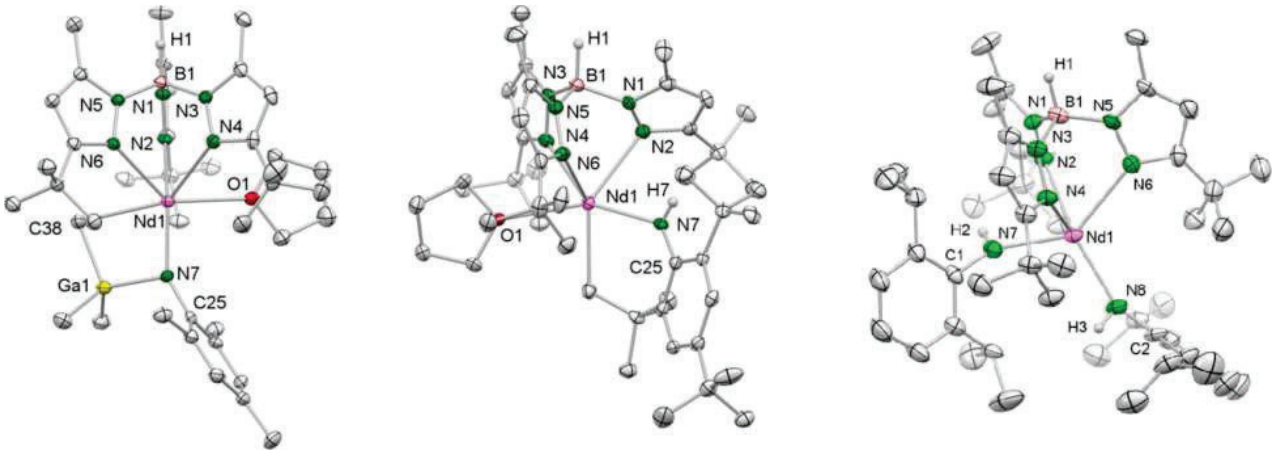

Figure 4. Crystal structures of complexes [Tp^{tBu,Me}Nd(NC$_6$H$_2$Me$_3$-2,4,6)(GaMe$_3$)(THF)] (**7-Nd**), [Tp^{tBu,Me}Nd{NH(C$_6$H$_2$*t*Bu$_2$-2,4-(CMe$_2$CH$_2$)-6)}(THF)] (**8-Nd**), and [Tp^{tBu,Me}Nd(HNAr^{iPr})$_2$] (**9-Nd**) (ellipsoids set to the 50% probability level). Hydrogen atoms except for those of B−H and N−H, the disorder in one *tert*-butyl group and one isopropyl group, and the lattice solvent (three molecules of THF) for **9-Nd** are omitted for clarity. Selected interatomic distances (Å) and angles (deg) for **7-Nd**: Nd1−N7 2.165(3), Nd1−N7−C25 147.6(2), and B1−Nd1−N7 175.74(9). Selected interatomic distances (Å) and angles (deg) for **8-Nd**: Nd1−N7 2.296(4), Nd1−N7−C25 132.2(3), and B1−Nd1−N7 107.4(1). Selected interatomic distances (Å) and angles (deg) for **9-Nd**: Nd1−N7 2.344(5), Nd1−N8 2.312(6), Nd1−N7−C1 153.8(5), and Nd1−N8−C2 144.0(5) (Supporting Information).

reaction is further driven by the formation of the volatile byproduct [GaMe$_3$(THF)].

Role of the Aromatic Amine: Investigations of the Reaction Mechanism. To further assess the role of the primary aromatic amine in the synthesis of such terminal imides, we probed the protonolysis of methylidene complex **2-Nd** with 2,4,6-trimethylaniline (mesidin) and 2,4,6-tri-*tert*-butylaniline (Scheme 3). Remarkably, by using the same protocol as in the synthesis of terminal imide **5-Nd**, the sterically less hindered mesidin afforded complex [Tp^{tBu,Me}Nd(NC$_6$H$_2$Me$_3$-2,4,6)(GaMe$_3$)(THF)] (**7-Nd**, Figure 4/left). Apparently, the unsupported imide is not accessible since the [GaMe$_3$] moiety is more strongly bound, most likely due to a better interaction with the sterically less hindered imido nitrogen. In contrast to five-coordinate [Tp^{tBu,Me}Nd(NAr^{iPr})(GaMe$_3$)] (**4-Nd**), the sterically less encumbered four-membered metalla-heterocyclic arrangement in **7-Nd** gives space for the coordination of a THF molecule. Therefore, the Nd−N(imido) distance of 2.165(3) Å in **7-Nd** is slightly longer than in **4-Nd** (2.158(3) Å). Mechanistically, THF coordination as detected in **7-Nd** represents the initiating step of the [GaMe$_3$] displacement en route to the terminal imide.

On the other hand, the 1:1 reaction of methylidene **2-Nd** with the sterically very demanding 2,4,6-tri-*tert*-butylaniline led to C−H bond activation at one of the *tert*-butyl substituents, thus following a completely different path. This comes to a halt for the metalated complex [Tp^{tBu,Me}Nd{NH(C$_6$H$_2$*t*Bu$_2$-2,4-(CMe$_2$CH$_2$)-6)}(THF)] (**8-Nd**) stage, without a second deprotonation of the amido ligand (Scheme 3, Figure 4/middle). It can be hypothesized that the six-membered heterocycle in **8-Nd** results from σ-bond metathesis of a transiently formed Nd−CH$_3$ (from first protonation) with a [C−H(*t*Bu)] moiety. Mixed methyl/amido complexes such as putative [Tp^{tBu,Me}Nd{N(H)(C$_6$H$_2$*t*Bu$_3$-2,4,6)}(CH$_3$)(THF)] are known precursors or isolable intermediates in rare-earth-metal imide chemistry.[5,35,40] Crucially, although the sterically bulky *tert*-butyl groups cotrigger [GaMe$_3$] displacement, they seem to protect the amido moiety from a second

https://doi.org/10.1021/jacs.1c13142
J. Am. Chem. Soc. 2022, 144, 4102−4113

Scheme 4. Proposed Mechanistic Scenario for the Synthesis of Rare-Earth-Metal Imide Complexes and Competitive Reaction Pathways Involving Aromatic Amines

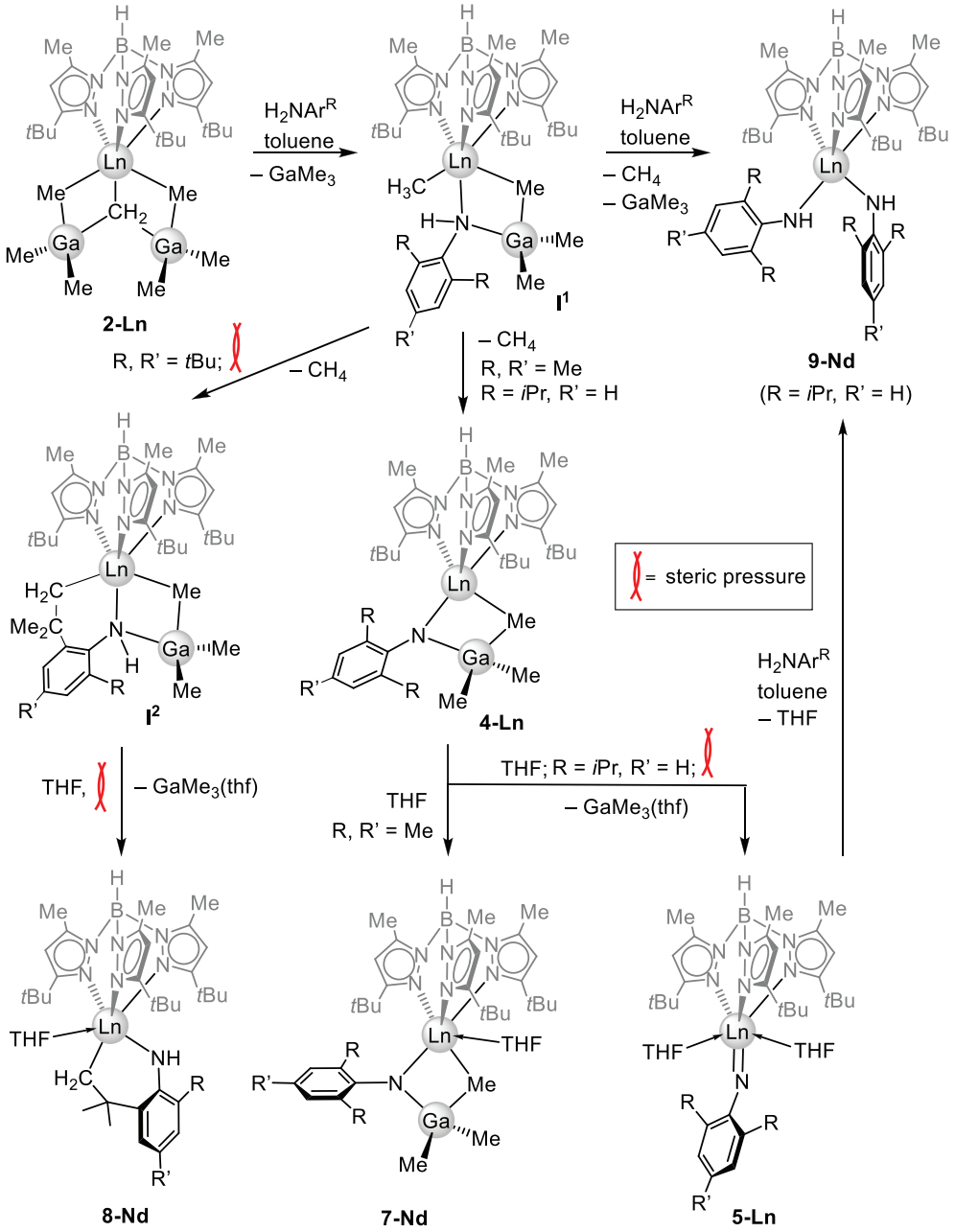

deprotonation, thus being increasingly prone to C–H bond activation. The preferred C–H bond activation of 2,4,6-tri-*tert*-butylaniline in the presence of reactive rare-earth-metal fragments has been evidenced previously.[40] The addition of the [C–H(*t*Bu)] moiety across a transiently formed Nd=NAr^{tBu} imido bond as an alternative pathway toward **8-Nd** seems unlikely on the basis of simple geometrical considerations. Although such hydrocarbyl addition reactions across the Nd=NAr^{R} imido bond have been described for substituents of the ancillary ligand,[3] the involvement of imido backbone substituents R, to the best of our knowledge, has not been observed.

Therefore, the 2,6-substitution pattern of the aromatic amine plays a pivotal role in the formation of a terminal rare-earth-metal imide. The Nd–N(amido) and Nd–C(hydrocarbyl) distances of **8-Nd** amount to 2.296(4) and 2.478(5) Å, respectively, and are therefore in the expected range.

As shown above, the somewhat substoichiometric reaction of **2-Ln** with 2,6-di-*iso*propylaniline afforded **4-Ln** or **5-Ln**. In stark contrast, the 1:2 reaction led to bis(anilido) complex [Tp^{tBu,Me}Nd(HNAr^{iPr})$_2$] (**9-Nd**) (Scheme 3, Figure 4/right). Complex **9-Nd** crystallized in the $P2_12_12_1$ orthorhombic space group and is insoluble in aliphatic solvents. In the solid state, complex **9-Nd** is five-coordinate by the pyrazolyl nitrogen atoms and the amido ligands. The Nd–N(amido) distances of 2.312 and 2.344 Å differ marginally. Nevertheless, both are in the range of similar neodymium anilide compounds.[41] The

https://doi.org/10.1021/jacs.1c13142
J. Am. Chem. Soc. 2022, 144, 4102–4113

bis(amido) formation can be rationalized on the basis that single deprotonation of the aniline is favored. Subsequent second deprotonation of the anilido ligand is impeded because the [Ln−NHAr^{R}] moiety features a proton with lower Brønsted acidity. Thus, in the presence of a second equivalent (or excess) of the amine, the formation of the bis(amido) complex prevails. Alternatively, if the Ln(III) center gets too large, then bis(amido) complex formation is already favored in the presence of substoichiometric amounts of H_2NAr^{iPr}, as shown above for **9-La**. Attempts to utilize the sterically more demanding H_2NAr^{tBu} for the larger La(III) center proved to be futile because no reaction was observed.

A similar reaction has been reported by Mindiola and coworkers showing that the protonolysis of [(PNP)Sc[(μ_3-CH$_2$){(μ_2-Me)(AlMe$_2$)}$_2$] with excess H_2NAr^{iPr} did not produce an imide complex but rather the isolable methyl/amide intermediate [(PNP)Sc(NHAr^{iPr})Me], which reacted further to produce the bis(amido) derivative [(PNP)Sc-(NHAr^{iPr})$_2$].[42] Because of the strong donation ability of the amido ligands, the application as precursors for terminal imide complexes is not feasible. In stark contrast, imido exchange reactions and intramolecular amine elimination are widespread methods of preparing titanium or uranium imide complexes, respectively.[43,44] It is worth mentioning that on one occasion the separated ion pair [Tp^{tBu,Me}Nd(HNAr^{iPr})(THF)$_2$]-[(GaMe$_3$)$_2$NHAr^{iPr}] (**10-Nd**) was isolated. (See Figure S17 for the crystal structure.) Crystals of **10-Nd** were obtained from a saturated solution of **2-Nd** and H_2NAr^{iPr} in THF/toluene at low temperature. Apparently, any released [GaMe$_3$]/[(GaMe$_3$)(THF)] in solution negatively affects the formation of terminal imides and therefore must be removed.

A plausible (not exclusive) mechanistic scenario of such Ln(III) arylimide formation sequences is sketched in Scheme 4. The initial step involves the first protonation of the methylidene moiety by the arylamine, generating mixed methyl/amide intermediate **I**^{1} upon the release of one molecule of [GaMe$_3$]. Compounds similar to **I**^{1} have been isolated and structurally characterized in the presence of cyclopentadienyl ancillary ligands.[27,40,45] A second equivalent of the amine affords a bis(amido) complex as shown for **9-Nd**. In the absence of additional amine, the reaction progress is crucially affected by the 2,6-substitution pattern of the arylamine and the size of Ln(III).

Steric pressure as exerted by the *t*Bu substituents of the amido ligand NHAr^{tBu} can trigger σ-bond metathesis with the transiently formed Ln−CH$_3$ to give intermediate **I**^{2}. Again, similar CH(*t*Bu)-bond-activated complexes involving the amido ligand NHAr^{tBu} have been structurally evidenced.[40] Because of a relatively weak interaction of [GaMe$_3$] with the sterically shielded amido nitrogen in **I**^{2}, the gallium alkyl can be easily displaced by the addition of THF to give a metallacyclic donor adduct such as that isolated for **8-Nd**.

To further investigate the formation of neodymium imide **4-Nd** and amide **8-Nd** from methylidene complex **2-Nd** via **I**^{1} and **I**^{2}, we conducted several labeling experiments with D_2NAr^{R} (R = *i*Pr, *t*Bu) at ambient temperature. A low temperature (−80 °C) was used to suppress the rapid exchange of the methyl groups in **2-Nd**, **I**^{1}, and **I**^{2}.[30] The first deuteration of the methylidene moiety by D_2NAr^{R} and concomitant amido ligand formation exhibits the rapid initiating step. Next, methane is eliminated, and in the case of an exclusive reaction of **2-Nd** with D_2NAr^{iPr}, the release of CH_2D_2 should be observed. However, at both ambient temperature and −80 °C only CH_3D could be detected because of rapidly exchanging methyl groups between [GaMe$_3$] and the methylated Nd center. It appears that this methyl group exchange cannot be suppressed at low temperatures and hence is faster than or as fast as the deuteration reaction. The formation of neodymium-bonded deuterated methyl ligands eluded identification as a result of paramagnetic broadening. For the reaction of **2-Nd** with D_2NAr^{tBu}, two different reaction pathways are conceivable: first (pathway I), one of the methyl groups of the ortho-*tert*-butyl substituents of the aromatic amido ligand in **I**^{1} could be activated by a transiently formed Nd−CH$_2$D or Nd−CH$_3$ moiety (the latter resulting from the rapid exchange of Nd−CH$_2$D with [GaMe$_3$]). Such σ-bond metathesis should generate CH_3D or preferentially CH_4 and the metallaheterocycle, while one deuterium would remain on the amido nitrogen. Second (pathway II), as previously mentioned, a transiently formed terminal Nd=N(imido) moiety (involving again initial formation of CH_2D_2 or preferentially CH_3D) could engage in the activation of one of the methyl groups of the ortho-*tert*-butyl substituents, leading to an amido nitrogen bearing a proton instead of a deuterium, and ring closure. Since the experiment at ambient temperate showed the predominant formation of CH_4 and because of the geometrical considerations stated above, reaction path I involving **I**^{1} should mainly apply. Because of otherwise inconclusive NMR experiments with paramagnetic nuclei, we decided to elucidate these reaction pathways only through the detection of gaseous component CH_4 (pathway I) or CH_3D (pathway II). Accordingly, the **2-Nd**/D_2NAr^{tBu} experiment indicated the generation of mainly undeuterated methane CH_4 (Supporting Information), thus favoring pathway I via **I**^{1} and **I**^{2} toward **8-Nd**.

In contrast, sterically less demanding substituents in the 2,6-position of the anilido ligand enable a second deprotonation of anilido ligand NHAr^{R} (R = Me, *i*Pr) via the release of methane and the formation of trimethylgallium-stabilized imide complexes (e.g., **4-Ln**). Such imide formation might be further driven by another proximal [GaMe$_3$] molecule, released during the initiating step. Finally, the interaction of a Lewis base (here THF) with the rare-earth-metal center emerges in the terminal imide upon release of the second [GaMe$_3$] molecule (**5-Ln**) or simply donor coordination to the rare-earth-metal center (**7-Nd**). Crucially, the steric pressure caused by the *i*Pr groups of the imido ligand NHAr^{iPr} seems sufficient to allow for complete [GaMe$_3$] displacement. It should be noted that the Ga−N(imido) distances in **4-Nd** and **7-Nd** are exactly the same (1.992(3) Å).

Finally, bis(amido) complex **9-Nd** could be readily generated via the equimolar reaction of imide **5-Nd** with H_2NAr^{iPr}. The reaction proceeds much more cleanly than when starting out from **2-Ln**. We consider it unlikely that bis(amido) complexes **9-Ln** of the smaller neodymium and samarium are formed in the initial reaction system by applying methylidenes **2-Ln** and slightly substoichiometric amounts of H_2NAr^{iPr}. It seems to be more likely that the imide nitrogen in rapidly formed **4-Ln** is protonated by an additional aromatic amine. This could further weaken [GaMe$_3$] coordination to the neodymium center, which would lead to bis(amido) formation in **9-Ln**. Note that terminal rare-earth-metal imide formation was not observed in the absence of any donor molecule (THF) even though the [GaMe$_3$] molecule is considered to bind weakly to the rare-earth-metal center (as

https://doi.org/10.1021/jacs.1c13142
J. Am. Chem. Soc. 2022, 144, 4102−4113

indicated by rapid methyl group exchange). The formation of bis(amido) complexes **9-Ln** (Ln = Nd, Sm) was not observed in the reactions shown in Scheme 2.

Reactivity of Terminal Imide 5-Nd toward Carbonylic Substrates. Preliminary reactivity tests were conducted with **5-Nd** and benzophenone. NMR-scale reactions showed the feasibility of a $[Nd{=}NR(THF)_2] \rightarrow [Nd{=}O]$ transformation via the generation of *N*-(diphenylmethylene)-2,6-diisopropylaniline. This points to the formation of a molecular neodymium oxide species,[22,42,46] which, however, could not be isolated and further characterized (Supporting Information).

CONCLUSIONS

The $[Ln{=}CH_2(GaMe_3)_2] \rightarrow [Ln{=}NR(THF)_2]$ transformation, utilizing methylidenes $[Tp^{tBu,Me}Ln(\mu_3\text{-}CH_2)\{(\mu_2\text{-}Me)MMe_2\}_2]$ (Ln = Ce, Nd, Sm; M = Al, Ga) and aromatic amines (H_2NAr^R), features a viable approach to synthesizing the first terminal imide complexes of the early "large" lanthanides. However, the successful applicability of such protocols appears to be like walking a tightrope. In fact, one has to draw on a fine balance among the Ln(III) size, the Lewis acidity of the group 13 metal alkyl, the presence of a donor solvent, and the sterics and acidity (pK_a) of the aromatic amine. In particular, it is the comparatively weak interaction of the soft Lewis acid $[GaMe_3]$ with the hard imido nitrogen which facilitates the formation of the unsupported terminal imides. The short Ln−N(imido) distances indicate a very strong bonding/interaction between the Ln(III) centers and the imido nitrogen. The new terminal imido complexes might engage in unprecedented intrinsic imido reactivity (changed ionicity of the Ln=NR bond due to the large Ln(III) size and apparent redox-activity of cerium and samarium), and the partially filled f orbitals might reveal new magneto-optical properties. Moreover, with $[Tp^{tBu,Me}Ln(\mu_3\text{-}CH_2)\{(\mu_2\text{-}Me)MMe_2\}_2]$ in hand, we have a potential $Ln{-}CH_2$ synthon for accessing other multiply bonded main group fragments.

EXPERIMENTAL SECTION

General Considerations. ***Caution!*** *The group 13 methyl derivatives are highly pyrophoric and react violently when exposed to air and/or moisture.* Therefore, all manipulations were performed under the rigorous exclusion of air and moisture using standard Schlenk, high-vacuum, and glovebox techniques (MB Braun MB200B; <0.1 ppm O_2, <0.1 ppm of H_2O, argon atmosphere). Solvents *n*-hexane, *n*-pentane, diethyl ether, toluene, and tetrahydrofuran (THF) were purified using Grubbs-type columns (MBraun SPS, solvent purification system). Tetrahydrofuran was stored over freshly activated molecular sieves (3 Å). 2,6-Diisopropylaniline (H_2NDipp, 97%, Sigma-Aldrich), 2,4,6-tri-*tert*-butylaniline (99%. Sigma-Aldrich), and 2,4,6-trimethylaniline (98%, Sigma-Aldrich) were dried over CaH_2 and purified by distillation. Benzophenone was purchased from Sigma-Aldrich and used as received. Deuterated 2,6-diisopropylaniline (D_2NDipp) and 2,4,6-tri-*tert*-butylaniline were obtained by stirring the protonated variants with 2 equiv of *n*-BuLi at −78 °C for several hours and subsequent quenching with D_2O and stirring overnight. C_6D_6 (99.6%, Sigma-Aldrich), [D_8]THF (99.5%, Euriso-top), and [D_8]toluene (99.6%, Sigma-Aldrich) were dried by stirring over Na/K-alloy for at least 24 h and filtered prior to use. All solvents and reagents were stored inside a glovebox. $HTp^{tBu,Me}$ and $KTp^{tBu,Me}$ ($Tp^{tBu,Me}$ = hydrotris(3-*tert*-butyl-5-methylpyrazol)borato) were synthesized by a modification of the published procedure of $HTp^{tBu,Ph}$.[47] $[Ln(AlMe_4)_3]$ and $[Ln(GaMe_4)_3]$ (Ln = Ce, Nd, Sm) were synthesized according to literature procedures.[48,49] The NMR spectra of air- and moisture-sensitive compounds were recorded by using J. Young-valved NMR tubes on a Bruker AVII+400 spectrometer (^1H: 400.13 MHz). ^1H NMR resonances are referenced to solvent residual resonances and reported in parts per million relative to tetramethylsilane (TMS). Coupling constants are given in Hertz. IR spectra were recorded on a Nicolet 6700 FTIR spectrometer with a DRIFT cell (KBr window), and the samples were prepared in a glovebox and mixed with KBr powder. Alternatively, Nujol oil was used as a carrier material. Elemental analyses were performed on an Elementar Vario Micro Cube.

*$[Tp^{tBu,Me}Ce\{(\mu_3\text{-}CH_2)[(\mu_2\text{-}Me)AlMe_2]_2\}]$ (**1-Ce**).* A suspension of $KTp^{tBu,Me}$ (626 mg, 1.35 mmol) in toluene (3 mL) was added to a solution of $[Ce(AlMe_4)_3]$ (543 mg, 1.35 mmol) in toluene (3 mL). The reaction mixture turned yellow and was stirred for 18 h at ambient temperature. The reaction mixture was dried and extracted several times with cold (−35 °C) toluene, and the extracts were dried again in vacuo to give **1-Ce** as a white powder. Yield: 280 mg, 0.39 mmol, 29%. ^1H NMR (400 MHz, C_6D_6): δ 33.53 (s, br), 10.48 (s, br), 5.91 (s, br), −3.87 (s, br), −17.33 (s, br) ppm. $^{11}B\{^1H\}$ NMR (80 MHz, C_6D_6): δ 67.0 (s, br) ppm. IR (KBr): 2965 (s), 2929 (m), 2884 (m), 2819 (w), 2764 (w, B−H), 1543 (s), 1488 (w), 1462 (m), 1427 (s), 1380 (w), 1364 (m), 1346 (s), 1320 (m), 1240 (m), 1180 (s), 1070 (s), 1063 (m), 1021 (m), 1010 (m), 984 (w), 840 (m), 799 (m), 790 (m), 769 (m), 729 (m), 728 (m), 695 (s), 690 (s), 683 (s), 656 (s), 650 (s), 582 (s), 572 (s), 519 (w), 492 (w), 471 (m), 429 (m), cm^{-1}. Elemental analysis (%) calculated for $C_{31}H_{60}Al_2BCeN_6$ (721.75 g mol^{-1}): C 51.59, H 8.38, N 11.64; found: C 51.39, H 8.20, N 11.72.

*$[Tp^{tBu,Me}Nd\{(\mu_3\text{-}CH_2)[(\mu_2\text{-}Me)AlMe_2]_2\}]$ (**1-Nd**).* To a solution of $[Nd(AlMe_4)_3]$ (200 mg, 0.493 mmol) in *n*-hexane (2 mL) a solution of $HTp^{tBu,Me}$ (209 mg, 0.493 mmol) in *n*-hexane (2 mL) was slowly added. The pale-green solution was stirred at ambient temperature for 4 h. A pale-green solid precipitated, which was filtered off and washed twice with *n*-hexane. The solid was dried under reduced pressure. Green crystals of **1-Nd** could be harvested at −35 °C in toluene. Yield: 167 mg, 0.230 mmol, 47%. ^1H NMR (500 MHz, $CDCl_3$, 26 °C): δ 33.41 (s, br), 10.80 (s, br), 6.08 (s, br), −20.25 (s, br) ppm. IR (Nujol, ν): 2583 (m, B−H), 1538 (s), 1460 (vs, Nujol), 1378 (s, Nujol), 1347 (s), 1326 (m), 1243 (w), 1174 (s), 1124 (w), 1072 (m), 1021 (w), 984 (w), 850 (w), 793 (m), 778 (m), 695 (s), 664 (m), 591 (m), 514 (w) cm^{-1}. Elemental analysis (%) calculated for $C_{31}H_{60}Al_2BN_6Nd$ (725.88 g/mol): C 51.30, H 8.33, N 11.58; found: C 51.02, H 8.11, N 11.31.

*$[Tp^{tBu,Me}Ce\{(\mu_3\text{-}CH_2)[(\mu_2\text{-}Me)GaMe_2]_2\}]$ (**2-Ce**).* A cold (−35 °C) solution of $HTp^{tBu,Me}$ (188 mg, 0.44 mmol) in toluene (3 mL) was added to a cold (−35 °C) solution of $[Ce(GaMe_4)_3]$ (235 mg, 0.44 mmol) in toluene (3 mL). The reaction mixture was stirred for 1 h at ambient temperature. A white precipitate had formed after several hours when the mixture was stored at −35 °C. The white precipitate was washed with cold *n*-hexane to yield **2-Ce** as a white powder. Yield: 284 mg, 0.35 mmol, 80%. ^1H NMR (400 MHz, C_6D_6): δ 10.88 (s, br), 6.04 (s, br), −4.62 (s, br), −17.85 (s, br) ppm. $^{11}B\{^1H\}$ NMR (80 MHz, C_6D_6): δ 64.6 (s, br) ppm. IR (KBr): 2964 (s), 2931 (m), 2861 (m), 2768 (w), 2578 (w, B−H), 1544 (s), 1489 (w), 1462 (m), 1429 (s), 1381 (w), 1363 (m), 1348 (s), 1318 (m); 1241(w), 1200 (m), 1188 (m), 1176 (s), 1071 (m), 1063 (m), 1022 (w), 1011 (w), 984 (w), 877 (w), 808 (m), 789 (m), 769 (m), 729 (m), 702 (m), 679 (m), 654 (m), 639 (m), 601 (w), 536 (m), 508 (s), 436 (m), 428 (m), 421 (m) cm^{-1}. Elemental analysis (%) calculated for $C_{31}H_{60}BCeGa_2N_6$ (807.24 g mol^{-1}): C 46.13, H 7.49, N 10.41; found: C 46.16, H 7.22, N 10.45.

*$[Tp^{tBu,Me}Nd\{(\mu_3\text{-}CH_2)[(\mu_2\text{-}Me)GaMe_2]_2\}]$ (**2-Nd**).* To a solution of $[Nd(GaMe_4)_3]$ (147 mg, 0.275 mmol) in *n*-hexane (2 mL) a solution of $HTp^{tBu,Me}$ (117 mg, 0.275 mmol) in *n*-hexane (2 mL) was added slowly. Immediate gas evolution occurred, and the blue solution turned pale blue. The solution was stirred at ambient temperature for 15 min. A pale-blue solid precipitated, which was filtered off and washed twice with *n*-hexane. The solid was dried under reduced pressure. Single crystals of **2-Nd** suitable for XRD analysis were obtained from a concentrated solution in toluene. Yield: 128 mg, 0.158 mmol, 57%. ^1H NMR (400 MHz, C_6D_6, 26 °C): δ 35.93 (s, br),

https://doi.org/10.1021/jacs.1c13142
J. Am. Chem. Soc. 2022, 144, 4102−4113

11.62 (s, br), 3.72 (s, br), −21.49 (s, br) ppm. $^{11}B\{^1H\}$ NMR (96 MHz, C_6D_6, 26 °C): δ 73.1 (s, br) ppm. DRIFT (ν): 2964 (vs), 2930 (m), 2864 (w), 2775 (w), 2543 (w, B−H), 1543 (s), 1462 (w), 1429 (s), 1362 (w), 1348 (m), 1203 (w), 1176 (s), 1069 (m), 1023 (w), 798 (m), 702(w), 646 (w), 640 (w), 512 (s), 430 (m) cm^{-1}. Elemental analysis (%) calculated for $C_{31}H_{60}BGa_2N_6Nd$ (811.36 g/mol): C 45.89, H 7.45, N 10.36; found: C 45.94, H 7.45, N 10.47.

*[Tp^{tBu,Me}Sm{(μ_3-CH$_2$)[(μ_2-Me)GaMe$_2$]$_2$}] (**2-Sm**).* Following the procedure described for **2-Nd**, $[Sm(GaMe_4)_3]$ (329 mg, 0.609 mmol) in *n*-hexane (4 mL) and a solution of HTp^{tBu,Me} (259 mg, 0.609 mmol) in *n*-hexane (5 mL) were stirred for 3 h at ambient temperature, affording **2-Sm** as an orange solid. Yield: 424 mg, 0.517 mmol, 85%. Single crystals suitable for XRD analysis formed from a mixed solution of toluene and *n*-pentane. ^1H NMR (400 MHz, C_6D_6, 26 °C): δ 5.36 (s, br), 1.87 (s, br), −4.20 (s, br), −9.35 (s, br) ppm. $^{11}B\{^1H\}$ NMR (96 MHz, C_6D_6, 26 °C): δ 6.3 (s, br) ppm. DRIFT (ν): 2965 (vs), 2862 (w), 2784 (vw), 2544 (vw, B−H), 1543 (vs), 1489 (w), 1463 (m), 1431 (vs), 1379 (vw), 1350 (m), 1325 (w), 1242 (w), 1204 (m), 1187 (s), 1120 (vw), 1069 (w), 1023 (w), 1012 (w), 981 (w), 875 (w), 856 (vw), 843 (vw), 798 (s), 790 (s), 772 (s), 729 (s), 705 (vs), 647 (s), 580 (m), 532 (vs), 513 (vs), 499 (m), 471 (w), 435 (s), 420 (vs), 414 (s) cm^{-1}. Elemental analysis (%) calculated for $C_{31}H_{60}BGa_2N_6Nd$ (817.48 g/mol): C 45.55, H 7.40, N 10.28; found: C 46.08, H 7.32, N 9.95.

*[Tp^{tBu,Me}Ce(NC$_6$H$_3$*i*Pr$_2$-2,6)(AlMe$_3$)] (**3-Ce**).* A solution of $[KHNC_6H_3iPr_2\text{-}2,6]$ (42 mg, 0.19 mmol) in toluene (3 mL) was added to a solution of **1-Ce** (140 mg, 0.19 mmol) in toluene (3 mL). The reaction mixture was stirred for 18 h at ambient temperature. Crystallization at −35 °C in THF yielded **3-Ce** as yellow crystals. Yield: 20 mg, 0.02 mmol, 13%. ^1H NMR (400 MHz, THF-d_8): δ 6.77 (s, br), 5.66 (s, br), 2.04 (s, br), 1.17 (s, br), −1.17 (s, br), −1.44 (s, br) ppm. Elemental analysis (%) calculated for $C_{39}H_{66}AlBCeN_7$ (810.91 g/mol): C 57.77, H 8.20, N 12.09; found: C 58.32, H 8.18, N 11.56.

*[Tp^{tBu,Me}Nd(NC$_6$H$_3$*i*Pr$_2$-2,6)(AlMe$_3$)] (**3-Nd**).* A solution of $[H_2NC_6H_3iPr_2\text{-}2,6]$ (29.7 mg, 0.138 mmol) in 3 mL of toluene was added to a solution of **1-Nd** (100 mg, 0.138 mmol) in 3 mL of toluene and stirred for 18 h. The solution was concentrated, and after several days at −35 °C, green single crystals of **3-Nd** suitable for XRD analysis were obtained. Crystallized yield: 25.0 mg, 0.0307 mmol, 22%. ^1H NMR (400 MHz, C_6D_6, 26 °C): δ 27.48 (s, br), 16.98 (s, br), 10.64 (s, br), 5.98 (s, br), −12.82 (s, br), −20.00 (s, br), −34.14 (s, br) ppm. $^{11}B\{^1H\}$ NMR (96 MHz, C_6D_6, 26 °C): δ 66.4 (s, br) ppm. DRIFT (ν): 2965 (m), 2931 (w), 2577 (vw, B−H), 1585 (vw), 1543 (s), 1491 (vw), 1460 (w), 1426 (s), 1380 (vw), 1346 (m), 1323 (w), 1241 (w), 1231 (w), 1184 (s), 1104 (vw), 1067 (m), 1022 (w), 1010 (w), 985 (vw), 928 (vw), 884 (vw), 858 (w), 843 (w), 801 (m), 788 (s), 769 (w), 761 (w), 697 (vs), 647 (s), 647 (s), 619 (m), 588 (m), 558 (w), 520 (vw), 495 (w), 470 (w), 439 (w), 423 (w) cm^{-1}. Elemental analysis (%) calculated for $C_{39}H_{66}AlBN_7Nd$ (815.04 g/mol): C 57.82, H 8.09, N 11.55; found: C 58.22, H 8.03, N 11.47.

*[Tp^{tBu,Me}Nd(NC$_6$H$_3$*i*Pr$_2$-2,6)(GaMe$_3$)] (**4-Nd**).* $[H_2NC_6H_3iPr_2\text{-}2,6]$ (29.5 mg, 0.166 mmol) in 3 mL of toluene was added to a solution of **2-Nd** (150 mg, 0.185 mmol) in 3 mL of toluene and stirred for 18 h. The solution was concentrated, and after several days at −35 °C, pale-green single crystals of **4-Nd** suitable for XRD analysis had formed. Yield: 67.0 mg, 0.0781 mmol, 42%. ^1H NMR (400 MHz, C_6D_6, 26 °C): δ 31.88 (s, br), 29.53 (s, br), 27.48 (s, br), 19.19 (s, br), 16.79 (s, br), 11.34 (s, br), −8.20 (s, br), −12.89 (s, br), −34.08 (s, br), −35.78 (s, br) ppm. $^{11}B\{^1H\}$ NMR (96 MHz, C_6D_6, 26 °C): δ 183.8 (s, br) ppm. DRIFT (ν): 3037 (vw), 2963 (vs), 2929 (m), 2863 (w), 2579 (vw, B−H), 1584 (vw), 1543 (vs), 1493 (vw), 1460 (w), 1428 (s), 1416 (s), 1379 (w), 1352 (s), 1342 (m), 1325 (w), 1306 (w), 1229 (m), 1241 (m), 1187 (vs), 1180 (vs), 1146 (vw), 1106 (w), 1093 (vw), 1066 (m), 1038 (vw), 1021 (w), 1010 (w), 985 (w), 931 (vw), 886 (w), 860 (vw), 846 (vw), 802 (w), 796 (m), 788 (s), 768 (s), 760 (vs), 728 (w), 693 (w), 677 (m), 647 (w), 618 (w), 602 (m), 566 (vw), 535 (w), 524 (w), 478 (w), 439 (w), 418 (m), 404 (m) cm^{-1}. Elemental analysis (%) calculated for $C_{39}H_{66}BGaN_7Nd$ (857.78 g/mol): C 54.61, H 7.76, N 11.43; found: C 54.66, H 7.50, N 11.49.

*[Tp^{tBu,Me}Sm(NC$_6$H$_3$*i*Pr$_2$-2,6)(GaMe$_3$)] (**4-Sm**).* Following the procedure described for **4-Nd**, **2-Sm** (100 mg, 0.122 mmol) in toluene (3 mL) and a solution of $[H_2NC_6H_3iPr_2\text{-}2,6]$ (21.7 mg, 0.122 mmol) in toluene (3 mL) afforded **4-Sm** as a red solid. Yield: 28 mg, 0.034 mmol, 28%. Single crystals suitable for XRD analysis formed from a mixed solution of toluene and *n*-pentane. ^1H NMR (400 MHz, C_6D_6, 26 °C): δ 12.07 (s, br), 6.62 (s, br), 4.81 (s, br), 3.96 (s, br), 2.42 (s, br), −0.78 (s, br), −2.79 (s, br), −3.26 (s, br) ppm. $^{11}B\{^1H\}$ NMR (96 MHz, C_6D_6, 26 °C): δ −0.9 (s, br) ppm. DRIFT (ν): 3037 (vw), 2964 (vs), 2927 (m), 2863 (w), 2580 (vw, B−H), 1584 (vw), 1543 (vs), 1494 (w), 1460 (m), 1418 (s), 1379 (w), 1379 (w), 1352 (m), 1325 (w), 1306 (w), 1242 (s), 1229 (m), 1188 (vs), 1179 (vs), 1146 (vw), 1106 (w), 1067 (m), 1038 (vw), 1021 (w), 1010 (w), 985 (w), 886 (w), 860 (m), 802 (w), 788 (s), 771 (s), 760 (s), 728 (w), 694 (w), 681 (w), 647 (m), 601 (w), 568 (vw), 534 (w), 522 (w), 476 (w), 438 (m), 419 (m), 407 (s) cm^{-1}. Elemental analysis (%) calculated for $C_{39}H_{66}BGaN_7Nd$ (863.90 g/mol): C 54.22, H 7.70, N 11.35; found: C 54.38, H 8.04, N 10.82.

*[Tp^{tBu,Me}Ce(NC$_6$H$_3$*i*Pr$_2$-2,6)(THF)$_2$] (**5-Ce**).* A solution of $[H_2NC_6H_3iPr_2\text{-}2,6]$ (36 mg, 0.2 mmol) in THF (3 mL) was added to a solution of **2-Ce** (136 mg, 0.16 mmol) in toluene (3 mL). The resulting solution turned from yellow to red, and was stirred for 18 h at ambient temperature. Crystallization at −35 °C in THF yielded **5-Ce** as yellow crystals and amorphous, unidentified, red side products. Yield: 13 mg, 0.01 mmol, 9%. ^1H NMR (400 MHz, THF-d_8): δ 10.13 (s, br), 4.66 (s, br), 3.48 (s, br), 1.94 (s, br), 1.41 (s, br), −0.28 (s, br), −9.39 (s, br) ppm. Elemental analysis (%) calculated for $C_{44}H_{73}BCeN_7O_2$ (883.04 g mol^{-1}): C 59.85, H 8.33, N 11.10; found: C 59.77, H 8.25, N 10.98.

*[Tp^{tBu,Me}Nd(NC$_6$H$_3$*i*Pr$_2$-2,6)(THF)$_2$] (**5-Nd**).* Compound **2-Nd** (200 mg, 0.246 mmol) was dissolved in 3 mL of toluene. A solution of $[H_2NC_6H_3iPr_2\text{-}2,6]$ (39.2 mg, 0.221 mmol) in 3 mL of THF was added slowly, and the reaction mixture was stirred for 30 min. The solution was concentrated, and after several days at −35 °C, green crystals had formed. Compound **5-Nd** was recrystallized several times. Yield: 132 mg, 0.149 mmol, 61%. ^1H NMR (400 MHz, [D$_8$]THF, 26 °C): δ 38.66 (s, br), 23.12 (s, br), 11.71 (s, br), 8.15 (s, br), −32.86 (s, br) ppm. $^{11}B\{^1H\}$ NMR (96 MHz, C_6D_6, 26 °C): δ 147.4 (s, br) ppm. DRIFT (ν): 2959 (vs), 2860 (w), 2559 (vw, B−H), 1580 (w), 1543 (vw), 1486 (m), 1460 (m), 1423 (m), 1396 (s), 1350 (m), 1317 (vs), 1203 (m), 1180 (s), 1136 (w), 1102 (vw), 1067 (s), 1030 (m), 1011 (w), 986 (w), 896 (s), 870 (w), 845 (w), 792 (m), 782 (m), 763 (w), 728 (m), 707 (vw), 669 (vw), 647 (m), 585 (vw), 513 (vw), 440 (vw) cm^{-1}. Elemental analysis (%) calculated for $C_{44}H_{73}BN_7NdO_2$ (887.17 g/mol): C 59.57, H 8.29, N 11.05; found: C 59.35, H 8.38, N 10.72.

*[Tp^{tBu,Me}Sm(NC$_6$H$_3$*i*Pr$_2$-2,6)(THF)$_2$] (**5-Sm**).* Following the procedure described for **5-Nd**, using **2-Sm** (212 mg, 0.259 mmol) in toluene (4 mL) and a solution of $[H_2NC_6H_3iPr_2\text{-}2,6]$ (46.0 mg, 0.259 mmol) in THF (4 mL) afforded **5-Sm** as a dark-red solid. The compound was recrystallized several times. Yield: 131 mg, 0.147 mmol, 57%. Single crystals suitable for XRD analysis formed from a mixed solution of THF and *n*-hexane. ^1H NMR (400 MHz, C_6D_6, 26 °C): δ 5.91 (s, br), 5.17 (s, br), 4.73 (s, br), 4.23 (s, br), 1.87 (s, br), 1.13 (s, br), −3.16 (s, br), −5.56 (s, br) ppm. $^{11}B\{^1H\}$ NMR (96 MHz, C_6D_6, 26 °C): δ 11.3 (s, br) ppm. DRIFT (ν): 2962 (vs), 2861 (w), 2561 (vw, B−H), 1580 (w), 1543 (vs), 1487 (vw), 1458 (m), 1419 (s), 1397 (s), 1350 (s), 1320 (vs), 1257 (vs), 1202 (s), 1179 (vs), 1137 (w), 1103 (vw), 1068 (vs), 1028 (m), 1012 (w), 986 (w), 897 (m), 869 (w), 846 (w), 792 (m), 784 (s), 766 (m), 729 (w), 708 (w), 669 (w), 647 (s), 600 (vw), 586 (vw), 518 (vw), 472 (vw), 441 (m), 418 (vw) cm^{-1}. Elemental analysis (%) calculated for $BN_7C_{44}H_{73}O_2Sm$ (893.29 g/mol): C 59.16, H 8.24, N 10.98; found: C 59.19, H 7.79, N 10.95.

*[Tp^{tBu,Me}Nd(NC$_6$H$_3$Me$_3$-2,4,6)(GaMe$_3$)(THF)] (**7-Nd**).* Following the procedure described for **5-Nd**, using **2-Nd** (158 mg, 0.195 mmol) in toluene (3 mL) and a solution of $[H_2NC_6H_3Me_3\text{-}2,4,6]$ (26.3 mg, 0.195 mmol) in THF (2 mL) afforded **7-Nd** as a green solid. Yield:

https://doi.org/10.1021/jacs.1c13142
J. Am. Chem. Soc. 2022, 144, 4102−4113

27.3 mg, 0.0297 mmol, 15%. Single crystals suitable for XRD analysis formed from a toluene solution. ^{1}H NMR (400 MHz, C_6D_6, 26 °C): δ 26.62 (s, br), 15.70 (s, br), 14.84 (s, br), 11.72 (s, br), −17.18 (s, br), −32.76 (s, br), −38.34 (s, br), ppm. ^{11}B{^{1}H} NMR (96 MHz, C_6D_6, 26 °C): δ −0.3 (s, br) ppm. Multiple attempts to obtain a satisfactory microanalysis failed.

*[Tp^{tBu,Me}Nd{HN(C$_6$H$_2$tBu$_2$-2,4-(CMe$_2$CH$_2$)-6}(THF)] (**8-Nd**).* Following the procedure described for **5-Nd**, using **2-Nd** (55.3 mg, 0.0681 mmol) in toluene (3 mL) and a solution of [H$_2$NC$_6$H$_3$*t*Bu$_3$-2,4,6] (17.8 mg, 0.0681 mmol) in THF (2 mL) afforded **8-Nd** as a green solid. Yield: 21.4 mg, 0.0238 mmol, 35%. Single crystals suitable for XRD analysis formed from a toluene solution. ^{1}H NMR (400 MHz, C_6D_6, 26 °C): δ 24.18 (s, br), 12.64 (s, br), 11.64 (s, br) ppm. ^{11}B{^{1}H} NMR (96 MHz, C_6D_6, 26 °C): δ −5.0 (s, br) ppm. Elemental analysis (%) calculated for $GaC_{42}H_{74}BN_7NdO$ (899.22 g/mol): C 61.44, H 8.63, N 10.90; found: C 61.18, H 8.44, N 9.25.

*[Tp^{tBu,Me}La(HNC$_6$H$_3$*i*Pr$_2$-2,6)$_2$] (**9-La**).* In a J. Young-valved tube, to a solution of [H$_2$NC$_6$H$_3$*i*Pr$_2$-2,6] (5.3 mg, 0.0299 mmol) in 0.2 mL of C_6D_6 a solution of [Tp^{tBu,Me}La{(μ_3-CH$_2$)[(μ_2-Me)GaMe$_2$]$_2$}] (24.1 mg, 0.0299 mmol) in 0.2 mL of C_6D_6 was added. ^{1}H NMR (400 MHz, C_6D_6, 26 °C): δ 7.94 (d, 4H, $^3J_{HH}$ 6.72 Hz, *m*-ArH), 6.84 (t, 2H, $^3J_{HH}$ 15.47 Hz, *p*-ArH), 5.60 (s, 3H, pz-H), 5.00 (s, 2H, NH), 3.19 (m, 4H, *i*Pr-CH), 1.94 (s, 9H, pz-CH$_3$), 1.28 (s, 27H, pz-C(CH$_3$)$_3$), 1.24 (d, 24H, $^3J_{HH}$ 6.80 Hz, *i*Pr-CH$_3$) ppm.

*[Tp^{tBu,Me}Nd(HNC$_6$H$_3$*i*Pr$_2$-2,6)$_2$] (**9-Nd**).* Method (a): To a solution of [H$_2$NC$_6$H$_3$*i*Pr$_2$-2,6] (92.9 mg, 0.524 mmol) in 3 mL of toluene a solution of **2-Nd** (170 mg, 0.201 mmol) in 3 mL of toluene was added and stirred for 1 h. The concentrated solution was stored at −35 °C, and after several days, green crystals had formed, which were analyzed by XRD as **9-Nd**. Method (b): To a solution of **5-Nd** (19.4 mg, 0.0217 mmol) in 3 mL of toluene a solution of [H$_2$NC$_6$H$_3$*i*Pr$_2$-2,6] (3.87 mg, 0.0217 mmol) in 3 mL of toluene was added. The color changed from green to blue immediately. Afterward the solvent was removed under vacuum. ^{1}H NMR (400 MHz, C_6D_6, 26 °C): δ 14.03 (s, br), 9.06 (s, br), 3.17 (s, br), 1.85 (s, br), 13.00 (s, br) ppm. Elemental analysis (%) calculated for $C_{48}H_{76}BN_8Nd$ (920.24 g/mol): C 62.65, H 8.32, N 12.18; found: C 62.71, H 8.30, N 12.13.

*[Tp^{tBu,Me}Nd(HNC$_6$H$_3$*i*Pr$_2$-2,6)$_2$][(GaMe$_3$)$_2$(HNC$_6$H$_3$*i*Pr$_2$-2,6)] (**10-Nd**).* To a solution of [H$_2$NC$_6$H$_3$*i*Pr$_2$-2,6] (39.3 mg, 0.222 mmol) in 3 mL of THF a solution of [Tp^{tBu,Me}Nd{(μ_3-CH$_2$)[(μ_2-Me)-GaMe$_2$]$_2$}] (200 mg, 0.246 mmol) in 3 mL of toluene was added and stirred for 18 h. After several days at −35 °C, a few green crystals were obtained, which were analyzed by XRD as **10-Nd**.

*[Ph$_2$C═N(C$_6$H$_3$*i*Pr$_2$-2,6)].* In a J. Young-valved tube, to a solution of [Tp^{tBu,Me}Nd(NC$_6$H$_3$*i*Pr$_2$-2,6)(THF)$_2$] (**5-Nd**) (3.8 mg, 0.00428 mmol) in 0.2 mL of C_6D_6 a solution of benzophenone (0.78 mg, 0.00428 mmol) in 0.2 mL of C_6D_6 was added. ^{1}H NMR (400 MHz, C_6D_6, 26 °C): δ 7.95 (d, 2H, $^3J_{HH}$ 6.91 Hz), 7.10−6.99 (m, 6H), 6.94−6.83 (m, 4H), 3.06 (m, 2H, *i*Pr-CH), 1.23 (d, 6H, $^3J_{HH}$ 6.77 Hz, *i*Pr-CH$_3$), 0.98 (d, 6H, $^3J_{HH}$ 6.74 Hz, *i*Pr-CH$_3$) ppm; signals are given only for imine *N*-(diphenylmethylene)-2,6-diisopropylaniline.

Labeling Studies. In a J. Young-valved tube, to a solution of **2-Nd** (R = *i*Pr: 7.2 mg, 0.00893 mmol; R = *t*Bu: 8.3 mg, 0.0102 mmol) in 0.4 mL of C_6D_6 a solution of D$_2$NAr^R (R = *i*Pr: 1.6 mg, 0.00893 mmol, 0.2 mL C_6D_6; R = *t*Bu: 2.7 mg, 0.0102 mmol, 0.2 mL [D$_8$]THF) was added at ambient temperature. Low-temperature experiments were started by adding the aromatic amine solution to a solution of **2-Nd** in [D$_8$]toluene, precooled to −80 °C.

■ ASSOCIATED CONTENT

Supporting Information

The Supporting Information is available free of charge at https://pubs.acs.org/doi/10.1021/jacs.1c13142.

Supporting figures, detailed crystallographic data, and spectroscopic data (NMR) (PDF)

Accession Codes

CCDC 2125445−2125461 contain the supplementary crystallographic data for this paper. These data can be obtained free of charge via www.ccdc.cam.ac.uk/data_request/cif, or by emailing data_request@ccdc.cam.ac.uk, or by contacting The Cambridge Crystallographic Data Centre, 12 Union Road, Cambridge CB2 1EZ, UK; fax: +44 1223 336033.

■ AUTHOR INFORMATION

Corresponding Author

Reiner Anwander − *Institut für Anorganische Chemie, Eberhard Karls Universität Tübingen, 72076 Tübingen, Germany;* orcid.org/0000-0002-1543-3787; Email: reiner.anwander@uni-tuebingen.de

Authors

Theresa E. Rieser − *Institut für Anorganische Chemie, Eberhard Karls Universität Tübingen, 72076 Tübingen, Germany*

Renita Thim-Spöring − *Institut für Anorganische Chemie, Eberhard Karls Universität Tübingen, 72076 Tübingen, Germany*

Dorothea Schädle − *Institut für Anorganische Chemie, Eberhard Karls Universität Tübingen, 72076 Tübingen, Germany*

Peter Sirsch − *Institut für Anorganische Chemie, Eberhard Karls Universität Tübingen, 72076 Tübingen, Germany*

Rannveig Litlabø − *Department of Chemistry, University of Bergen, N-5007 Bergen, Norway*

Karl W. Törnroos − *Department of Chemistry, University of Bergen, N-5007 Bergen, Norway;* orcid.org/0000-0001-6140-5915

Cäcilia Maichle-Mössmer − *Institut für Anorganische Chemie, Eberhard Karls Universität Tübingen, 72076 Tübingen, Germany;* orcid.org/0000-0001-7638-1610

Complete contact information is available at: https://pubs.acs.org/10.1021/jacs.1c13142

Notes

The authors declare no competing financial interest.

■ ACKNOWLEDGMENTS

Dedicated to Prof. Dr. Kazushi Mashima on the occasion of his 65th birthday. We gratefully acknowledge support from the German Science Foundation (grant: AN 238/15-2).

■ REFERENCES

(1) Giesbrecht, G. R.; Gordon, J. C. Lanthanide alkylidene and imido complexes. *Dalton Trans.* **2004**, 2387−2393.

(2) Summerscales, O. T.; Gordon, J. C. Complexes containing multiple bonding interactions between lanthanoid elements and main-group fragments. *RSC Advance* **2013**, *3*, 6682−6692.

(3) Lu, E.; Chu, J.; Chen, Y. Scandium Terminal Imido Chemistry. *Acc. Chem. Res.* **2018**, *51*, 557−566.

(4) Zhu, Q.; Zhu, J.; Zhu, C. Recent progress in the chemistry of lanthanide-ligand multiple bonds. *Tetrahedron Lett.* **2018**, *59*, 514−520.

(5) Schädle, D.; Anwander, R. Rare-earth metal and actinide organoimide chemistry. *Chem. Soc. Rev.* **2019**, *48*, 5752−5805.

(6) Pedersen, S. F.; Schrock, R. R. Multiple metal-carbon bonds. 27. Preparation of tungsten(VI) phenylimido alkyl and alkylidene complexes. *J. Am. Chem. Soc.* **1982**, *104*, 7483−7491.

(7) (a) Mountford, P. New titanium imido chemistry *Chem. Commun.* **1997**, 2127−2134. (b) Hazari, N.; Mountford, P. Reactions and Applications of Titanium Imido Complexes. *Acc. Chem. Res.* **2005**, *38*, 839−849.

(8) Duncan, A. P.; Bergman, R. G. Selective transformations of organic compounds by imidozirconocene complexes. *Chem. Rec.* **2002**, *2*, 431−445.
(9) (a) Mindiola, D. J. Oxidatively Induced Abstraction Reactions. A Synthetic Approach to Low-Coordinate and Reactive Early Transition Metal Complexes Containing Metal−Ligand Multiple Bonds. *Acc. Chem. Res.* **2006**, *39*, 813−821. (b) Fout, A. R.; Kilgore, U. J.; Mindiola, D. J. The Progression of Synthetic Strategies to Assemble Titanium Complexes Bearing the Terminal Imide Group. *Chem.—Eur. J.* **2007**, *13*, 9428−9440.
(10) Nomura, K.; Zhang, W. (Imido)vanadium(v)-alkyl, -alkylidene complexes exhibiting unique reactivity towards olefins and alcohols. *Chem. Sci.* **2010**, *1*, 161−173.
(11) Kawakita, K.; Parker, B. F.; Kakiuchi, Y.; Tsurugi, H.; Mashima, K.; Arnold, J.; Tonks, I. A. Reactivity of terminal imido complexes of group 4−6 metals: Stoichiometric and catalytic reactions involving cycloaddition with unsaturated organic molecules. *Coord. Chem. Rev.* **2020**, *407*, 213118.
(12) Grünwald, A.; Anjana, S. S.; Munz, D. Terminal Imido Complexes of the Groups 9−11: Electronic Structure and Developments in the Last Decade. *Eur. J. Inorg. Chem.* **2021**, *2021*, 4147−4166.
(13) For examples, see (a) Dietrich, H. M.; Törnroos, K. W.; Anwander, R. Ionic Carbenes": Synthesis, Structural Characterization, and Reactivity of Rare-Earth Metal Methylidene Complexes. *J. Am. Chem. Soc.* **2006**, *128*, 9298−9299. (b) Gerber, L. C. H.; Le Roux, E.; Törnroos, K. W.; Anwander, R. Elusive Trimethyllanthanum: Snapshots of Extensive Methyl Group Degradation in La·Al Heterobimetallic Complexes. *Chem.—Eur. J.* **2008**, *14*, 9555−9564. (c) Zhang, W.-X.; Wang, Z.; Nishiura, M.; Xi, Z.; Hou, Z. $Ln_4(CH_2)_4$ Cubane-Type Rare-Earth Methylidene Complexes Consisting of "$(C_5Me_4SiMe_3)LnCH_2$" Units (Ln = Tm, Lu). *J. Am. Chem. Soc.* **2011**, *133*, 5712−5715. (d) Li, S.; Wang, M.; Liu, B.; Li, L.; Cheng, J.; Wu, C.; Liu, D.; Liu, J.; Cui, D. Lutetium-Methanediide-Alkyl Complexes: Synthesis and Chemistry. *Chem.—Eur. J.* **2014**, *20*, 15493−15498. (e) Li, T.; Zhang, G.; Guo, J.; Wang, S.; Leng, X.; Chen, Y. Tris(pyrazolyl)methanide Complexes of Trivalent Rare-Earth Metals. *Organometallics* **2016**, *35*, 1565−1572.
(14) Kratsch, J.; Roesky, P. W. Rare-Earth-Metal Methylidene Complexes. *Angew. Chem., Int. Ed.* **2014**, *53*, 376−383.
(15) (a) Trifonov, A. A.; Bochkarev, M. N.; Schumann, H.; Loebel, J. Reduction of Azobenzene by Naphthaleneytterbium: A Tetranuclear Ytterbium(III) Complex Combining 1,2-Diphenylhydrazido(2−) and Phenylimido Ligands. *Angew. Chem., Int. Ed.* **1991**, *30*, 1149−1151. (b) Cui, D.; Tardif, O.; Hou, Z. Tetranuclear Rare Earth Metal Polyhydrido Complexes Composed of "$(C_5Me_4SiMe_3)LnH_2$" Units. Unique Reactivities toward Unsaturated C−C, C−N, and C−O Bonds. *J. Am. Chem. Soc.* **2004**, *126*, 1312−1313. (c) Berthet, J.-C.; Thuéry, P.; Ephritikhine, M. Polyimido Clusters of Neodymium and Uranium, Including a Cluster with an $M_6(\mu_3\text{-}N)_8$ Core. *Eur. J. Inorg. Chem.* **2008**, *2008*, 5455−5459.
(16) Anwander, R. Self-Assembly" in Organolanthanide Chemistry: Formation of Rings and Clusters. *Angew. Chem., Int. Ed.* **1998**, *37*, 599−602.
(17) Strongly polarized Al−N imido bonds and associated high reactivity also frustrate the isolation of terminal aluminum imides: (a) Li, J.; Li, X.; Huang, W.; Hu, H.; Zhang, J.; Cui, C. Synthesis, Structure, and Reactivity of a Monomeric Iminoalane. *Chem.—Eur. J.* **2012**, *18*, 15263−15266. (b) Anker, M. D.; Schwamm, R. J.; Coles, M. P. Synthesis and reactivity of a terminal aluminium−imide bond. *Chem. Commun.* **2020**, *56*, 2288−2291.
(18) Evans, W. J.; Ansari, M. A.; Ziller, J. W.; Khan, S. I. Utility of Arylamido Ligands in Yttrium and Lanthanide Chemistry. *Inorg. Chem.* **1996**, *35*, 5435−5444.
(19) Gordon, J. C.; Giesbrecht, G. R.; Clark, D. L.; Hay, P. J.; Keogh, D. W.; Poli, R.; Scott, B. L.; Watkin, J. G. The First Example of a μ_2-Imido Functionality Bound to a Lanthanide Metal Center: X-ray Crystal Structure and DFT Study of $[(\mu\text{-ArN})Sm(\mu\text{-NHAr})(\mu\text{-Me})AlMe_2]_2$ (Ar = 2,6-$iPr_2C_6H_3$). *Organometallics* **2002**, *21*, 4726−4734.
(20) Chan, H.-S.; Li, H.-W.; Xie, Z. Synthesis and structural characterization of imido−lanthanide complexes with a metal−nitrogen multiple bond. *Chem. Commun.* **2002**, 652−653.
(21) Solola, L. A.; Zabula, A. V.; Dorfner, W. L.; Manor, B. C.; Carroll, P. J.; Schelter, E. J. An Alkali Metal-Capped Cerium(IV) Imido Complex. *J. Am. Chem. Soc.* **2016**, *138*, 6928−6931.
(22) (a) Solola, L. A.; Zabula, A. V.; Dorfner, W. L.; Manor, B. C.; Carroll, P. J.; Schelter, E. J. Cerium(IV) Imido Complexes: Structural, Computational, and Reactivity Studies. *J. Am. Chem. Soc.* **2017**, *139*, 2435−2442. (b) Cheisson, T.; Kersey, K. D.; Mahieu, N.; McSkimming, A.; Gau, M. R.; Carroll, P. J.; Schelter, E. J. Multiple Bonding in Lanthanides and Actinides: Direct Comparison of Covalency in Thorium(IV)- and Cerium(IV)-Imido Complexes. *J. Am. Chem. Soc.* **2019**, *141*, 9185−9190.
(23) Lu, E.; Li, Y.; Chen, Y. A scandium terminal imido complex: synthesis, structure and DFT studies. *Chem. Commun.* **2010**, *46*, 4469−4471.
(24) Lu, E.; Chu, J.; Chen, Y.; Borzov, M. V.; Li, G. Scandium terminal imido complex induced C−H bond selenation and formation of an Sc−Se bond. *Chem. Commun.* **2011**, *47*, 743−745.
(25) Rong, W.; Cheng, J.; Mou, Z.; Xie, H.; Cui, D. Facile Preparation of a Scandium Terminal Imido Complex Supported by a Phosphazene Ligand. *Organometallics* **2013**, *32*, 5523−5529.
(26) Chu, J.; Han, X.; Kefalidis, C. E.; Zhou, J.; Maron, L.; Leng, X.; Chen, Y. Lewis Acid Triggered Reactivity of a Lewis Base Stabilized Scandium-Terminal Imido Complex: C−H Bond Activation, Cycloaddition, and Dehydrofluorination. *J. Am. Chem. Soc.* **2014**, *136*, 10894−10897.
(27) Schädle, D.; Meermann-Zimmermann, M.; Schädle, C.; Maichle-Mössmer, C.; Anwander, R. Rare-Earth Metal Complexes with Terminal Imido Ligands. *Eur. J. Inorg. Chem.* **2015**, *2015*, 1334−1339.
(28) Patrick, E. A.; Yang, Y.; Piers, W. E.; Maron, L.; Gelfand, B. S. A monoanionic pentadentate ligand platform for scandium−pnictogen multiple bonds. *Chem. Commun.* **2021**, *57*, 8640−8643.
(29) Shannon, R. D. Revised effective ionic radii and systematic studies of interatomic distances in halides and chalcogenides. *Acta Crystallogr., Sect. A* **1976**, *32*, 751−767.
(30) Litlabø, R.; Zimmermann, M.; Saliu, K.; Takats, J.; Törnroos, K. W.; Anwander, R. A Rare-Earth Metal Variant of the Tebbe Reagent. *Angew. Chem., Int. Ed.* **2008**, *47*, 9560−9564.
(31) Hong, J.; Zhang, L.; Wang, K.; Zhang, Y.; Weng, L.; Zhou, X. Methylidene Rare-Earth-Metal Complex Mediated Transformations of C-N, N-N and N-H Bonds: New Routes to Imido Rare-Earth-Metal Clusters. *Chem.—Eur. J.* **2013**, *19*, 7865−7873.
(32) Zimmermann, M.; Litlabø, R.; Törnroos, K. W.; Anwander, R. "Metastable" $Lu(GaMe_4)_3$ Reacts Like Masked $[LuMe_3]$: Synthesis of an Unsolvated Lanthanide Dimethyl Complex. *Organometallics* **2009**, *28*, 6646−6649.
(33) Scott, J.; Basuli, F.; Fout, A. R.; Huffman, J. C.; Mindiola, D. J. Evidence for the Existence of a Terminal Imidoscandium Compound: Intermolecular C-H Activation and Complexation Reactions with the Transient Sc-NAr Species. *Angew. Chem., Int. Ed.* **2008**, *47*, 8502−8505.
(34) Schädle, D.; Schädle, C.; Schneider, D.; Maichle-Mössmer, C.; Anwander, R. Versatile $Ln_2(\mu\text{-NR})_2$-Imide Platforms for Ligand Exchange and Isoprene Polymerization. *Organometallics* **2015**, *34*, 4994−5008.
(35) Schädle, D.; Maichle-Mössmer, C.; Schädle, C.; Anwander, R. Rare-Earth-Metal Methyl, Amide, and Imide Complexes Supported by a Superbulky Scorpionate Ligand. *Chem.—Eur. J.* **2015**, *21*, 662−670.
(36) Recent attempts to isolate a related terminal [La═PR] phosphinidene were frustrated by ancillary backbone activation: Watt, F. A.; McCabe, K. N.; Schoch, R.; Maron, L.; Hohloch, S. A transient lanthanum phosphinidene complex. *Chem. Commun.* **2020**, *56*, 15410−15413.

https://doi.org/10.1021/jacs.1c13142
J. Am. Chem. Soc. 2022, 144, 4102−4113

(37) Schädle, C.; Schädle, D.; Eichele, K.; Anwander, R. Methylaluminum-Supported Rare-Earth-Metal Dihydrides. *Angew. Chem., Int. Ed.* **2013**, *52*, 13238−13242.
(38) Pearson, R. G. Hard and Soft Acids and Bases. *J. Am. Chem. Soc.* **1963**, *85*, 3533−3539.
(39) Waggoner, K. M.; Power, P. P. Reactions of Trimethylaluminum and Trimethylgallium with Bulky Primary Amines: Structural Characterization of the Thermolysis Products. *J. Am. Chem. Soc.* **1991**, *113*, 3385−3393.
(40) Schädle, D.; Enders, M.; Schädle, C.; Maichle-Mössmer, C.; Törnroos, K. W.; Anwander, R. Reactivity of halfsandwich rare-earth metal methylaluminates toward potassium (2,4,6-tri-tert-butylphenyl)amide and 1-adamantylamine. *New J. Chem.* **2015**, *39*, 7640−7648.
(41) (a) Li, W.; Xue, M.; Xu, F.; Tu, J.; Zhang, Y.; Shen, Q. Synthesis, characterization of bridged bis(amidinate) lanthanide amides and their application as catalysts for addition of amines to nitriles for monosubstituted N-arylamidines. *Dalton Trans.* **2012**, *41*, 8252−8260. (b) Liu, C.; Qian, Q.; Nie, K.; Wang, Y.; Shen, Q.; Yuan, D.; Yao, Y. Lanthanide anilido complexes: synthesis, characterization, and use as highly efficient catalysts for hydrophosphonylation of aldehydes and unactivated ketones. *Dalton Trans.* **2014**, *43*, 8355−8362.
(42) Scott, J.; Fan, H.; Wicker, B. F.; Fout, A. R.; Baik, M.-H.; Mindiola, D. J. Lewis Acid Stabilized Methylidene and Oxoscandium Complexes. *J. Am. Chem. Soc.* **2008**, *130*, 14438−14439.
(43) Hayton, T. W.; Boncella, J. M.; Scott, B. L.; Palmer, P. D.; Batista, E. R.; Hay, P. J. Synthesis of Imido Analogs of the Uranyl Ion. *Science* **2005**, *310*, 1941−1943.
(44) Schwarz, A. D.; Nielson, A. J.; Kaltsoyannis, N.; Mountford, P. The first group 4 metal bis(imido) and tris(imido) complexes. *Chem. Sci.* **2012**, *3*, 819−824.
(45) Thim, R.; Dietrich, H. M.; Bonath, M.; Maichle-Mössmer, C.; Anwander, R. Pentamethylcyclopentadienyl-Supported Rare-Earth-Metal Benzyl, Amide, and Imide Complexes. *Organometallics* **2018**, *37*, 2769−2777.
(46) Schädle, D.; Meermann-Zimmermann, M.; Maichle-Mössmer, C.; Schädle, C.; Törnroos, K. W.; Anwander, R. Rare-earth metal methylidene complexes with $Ln_3(\mu_3\text{-}CH_2)(\mu_3\text{-}Me)(\mu_2\text{-}Me)_3$ core structure. *Dalton Trans.* **2015**, *44*, 18101−18110.
(47) Kisko, J. L.; Hascall, T.; Kimblin, C.; Parkin, G. Phenyl tris(3-*tert*-butylpyrazolyl)borato complexes of lithium and thallium, [PhTpBu]M (M = Li, Tl): a novel structure for a monomeric tris(pyrazolyl)boratothallium complex and a study of its stereochemical nonrigidity by ^{1}H and ^{205}Tl NMR spectroscopy. *J. Chem. Soc., Dalton Trans.* **1999**, 1929−1936.
(48) Zimmermann, M.; Frøystein, N. Å.; Fischbach, A.; Sirsch, P.; Dietrich, H. M.; Törnroos, K. W.; Herdtweck, E.; Anwander, R. Homoleptic Rare-Earth Metal(III) Tetramethylaluminates: Structural Chemistry, Reactivity, and Performance in Isoprene Polymerization. *Chem.—Eur. J.* **2007**, *13*, 8784−8800.
(49) Evans, W. J.; Anwander, R.; Doedens, R. J.; Ziller, J. W. The Use of Heterometallic Bridging Moieties To Generate Tractable Lanthanide Complexes of Small Ligands. *Angew. Chem., Int. Ed. Engl.* **1994**, *33*, 1641−1644.

https://doi.org/10.1021/jacs.1c13142
J. Am. Chem. Soc. 2022, 144, 4102−4113

Supporting Information

Open-Shell Early Lanthanide Terminal Imides

Theresa E. Rieser,[a] Renita Thim-Spöring,[a] Dorothea Schädle,[a] Peter Sirsch,[a] Rannveig Litlabø,[b] Karl W. Törnroos,[b] Cäcilia Maichle-Mössmer,[a] and Reiner Anwander[a,*]

[a] Institut für Anorganische Chemie, Eberhard Karls Universität Tübingen, Auf der Morgenstelle 18, 72076 Tübingen, Germany

[b] Department of Chemistry, University of Bergen, Allégaten 41, N-5007 Bergen, Norway

*E-mail for R.A.: reiner.anwander@uni-tuebingen.de.

Table of Contents

Crystallography

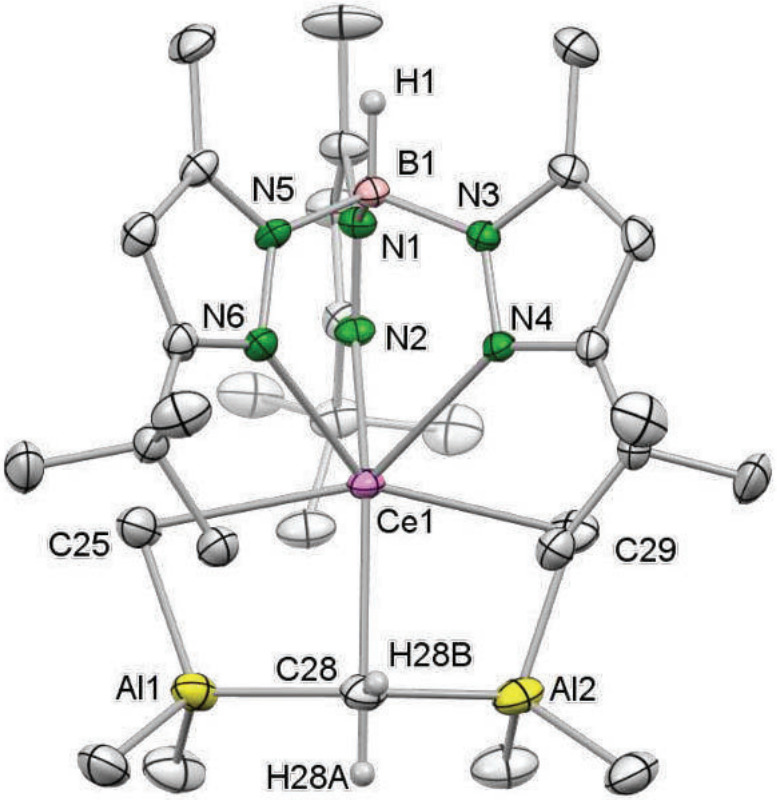

Figure S1. Crystal structure of **1-Ce**. Hydrogen atoms except for the BH and CH_2, two additional toluene molecules and the disorder in one *tert*-butyl group are omitted for clarity. Atomic displacement ellipsoids were set at 50% probability. Selected interatomic distances [Å] and angles [°]: Ce1–N2 2.553(2), Ce1–N4 2.589(2), Ce1–N6 2.572(2), Ce1–C25 2.820(4), Ce1–C28 2.484(3), Ce1–C29 2.789(4), Al1–C28 2.059(4), Al2–C28 2.066(4); N2–Ce1–N4 85.03(8), N2–Ce1–N6 85.82(7), N2–Ce1–C25 85.88(9), N2–Ce1–C28 135.19(10), N2–Ce1–C29 84.01(10), N4–Ce1–N6 67.01(8), N4–Ce1–C25 143.89(9), N4–Ce1–C28 129.89(10), N4–Ce1–C29 78.23(10), N6–Ce1–C25 77.52(10), N6–Ce1–C28 129.91(10), N6–Ce1–C29 144.47(9), C25–Ce1–C28 78.61(11), C25–Ce1–C29 135.23(12), C28–Ce1–C29 78.49(11).

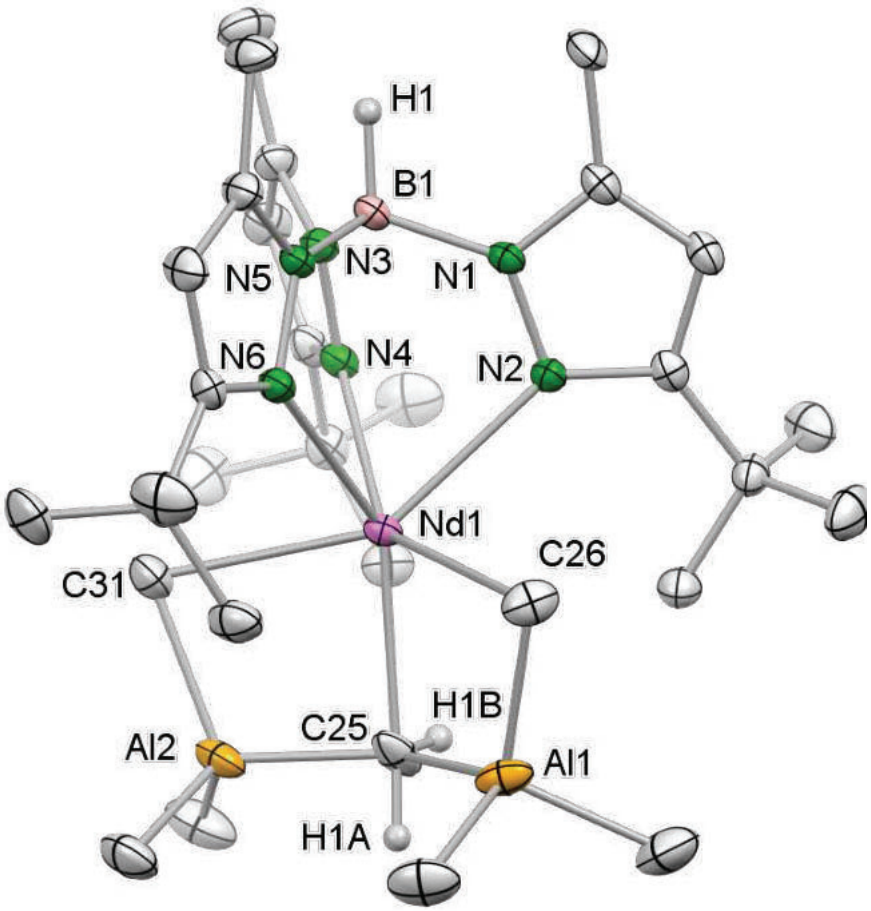

Figure S2. Crystal structure of **1-Nd**. Hydrogen atoms except for the BH and CH_2, two additional toluene molecules, the disorder in one *tert*-butyl group and one methyl group are omitted for clarity. Atomic displacement ellipsoids were set at 50% probability. Selected interatomic distances [Å] and angles [°]: Nd1–N2 2.4861(16), Nd1–N4 2.5855(16), Nd1–N6 2.5532(17), Nd1–C31 2.726(2), Nd1–C25 2.461(2), Nd1–C26 2.811(2), Al1–C25 2.038(2), Al2–C25 2.010(2); N2–Nd1–N4 68.34(5), N2–Nd1–N6 85.31(5), N2–Nd1–C31 143.15(6), N2–Nd1–C25 129.12(7), N2–Nd1–C26 77.82(7), N4–Nd1–N6 84.21(5), N4–Nd1–C31 75.57(6), N4–Nd1–C25 129.86(7), N4–Nd1–C26 145.53(6), N6–Nd1–C31 83.92(7), N6–Nd1–C25 136.12(7), N6–Nd1–C26 86.75(6), C31–Nd1–C25 80.45(7), C31–Nd1–C26 136.32(8), C25–Nd1–C26 77.28(7).

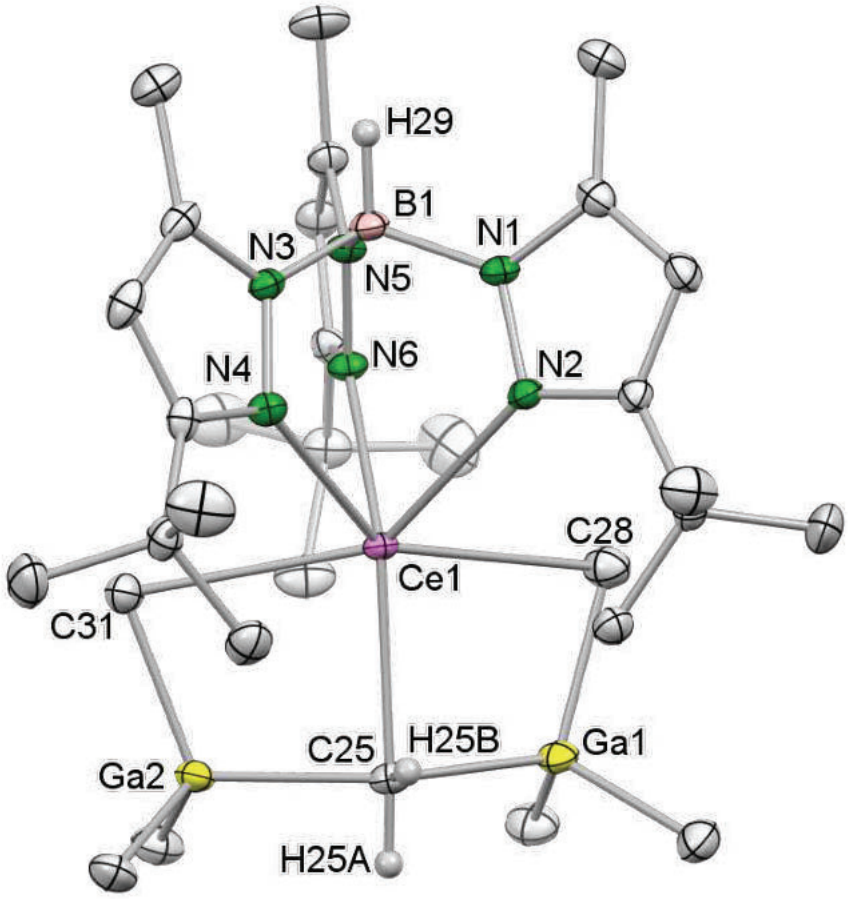

Figure S3. Crystal structure of **2-Ce**. Hydrogen atoms except for the BH and CH_2 and one additional *n*-hexane molecule are omitted for clarity. Atomic displacement ellipsoids were set at 50% probability. Selected interatomic distances [Å] and angles [°]: Ce1–N2 2.5743(18), Ce1–N4 2.5884(19), Ce1–N6 2.5477(17), Ce1–C31 2.824(2), Ce1–C25 2.492(2), Ce1–C28 2.820(3), Ga1–C25 2.116(2), Ga2–C25 2.120(2); N2–Ce1–N4 65.87(6), N2–Ce1–N6 85.03(6), N2–Ce1–C31 140.79(6), N2–Ce1–C25 129.97(7), N2–Ce1–C28 77.44(7), N4–Ce1–N6 86.46(6), N4–Ce1–C31 75.89(6), N4–Ce1–C25 129.35(7), N4–Ce1–C28 142.25(6), N6–Ce1–C31 84.27(6), N6–Ce1–C25 135.56(7), N6–Ce1–C28 81.72(7), C31–Ce1–C25 81.35(7), C31–Ce1–C28 137.52(7), C25–Ce1–C28 81.21(7).

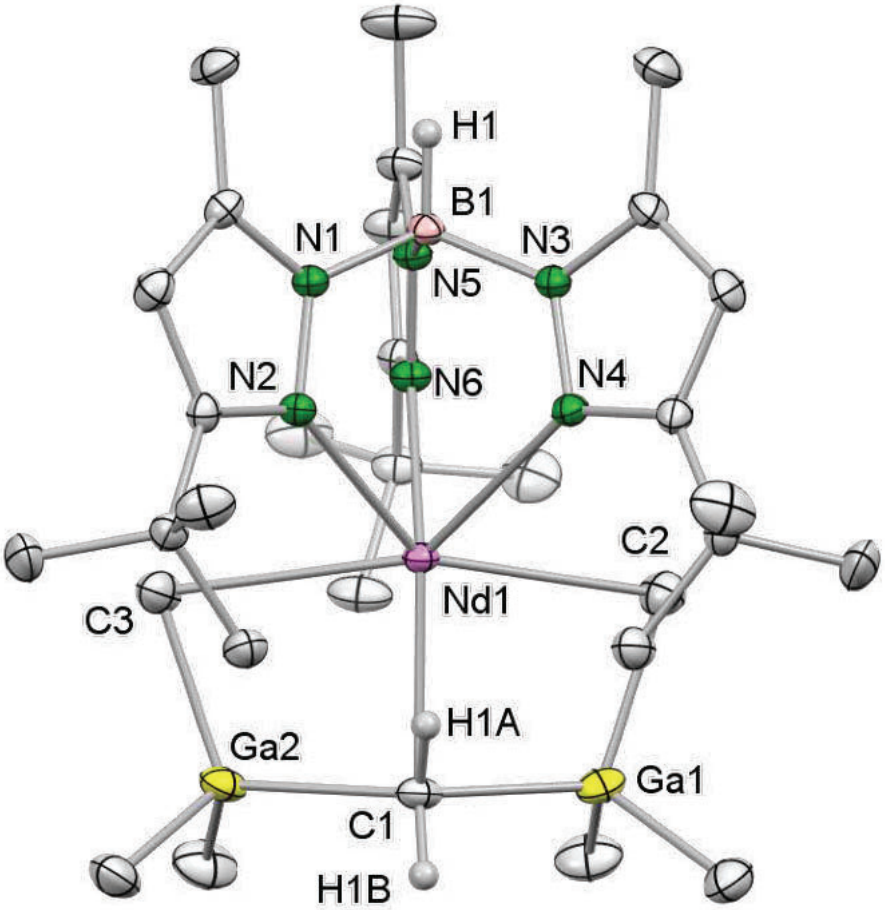

Figure S4. Crystal structure of **2-Nd**. Hydrogen atoms except for the BH and CH_2, two additional toluene molecules, and the disorder in one *tert*-butyl group are omitted for clarity. Atomic displacement ellipsoids were set at 50% probability. Selected interatomic distances [Å] and angles [°]: Nd1–N2 2.5492(16), Nd1–N4 2.5691(16), Nd1–N6 2.5287(16), Nd1–C3 2.831(2), Nd1–C1 2.4502(19), Nd1–C2 2.793(2)), Ga1–C1 2.110(2), Ga2–C1 2.115(2); N2–Sm1–N4 67.27(5), N2–Nd1–N6 86.59(5), N2–Nd1–C3 75.55(6), N2–Nd1–C1 128.58(6), N2–Nd1–C2 142.19(6), N4–Nd1–N6 85.97(5), N4–Nd1–C3 141.88(6), N4–Sm1–C1 128.42(6), N4–Nd1–C2 76.03(6), N6–Nd1–C383.66(6), N6–Nd1–C1 136.07(6), N6–Sm1–C2 81.96(6), C3–Nd1–C1 81.78(7), C3–Nd1–C2 137.89(7), C1–Nd1–C2 81.72(7).

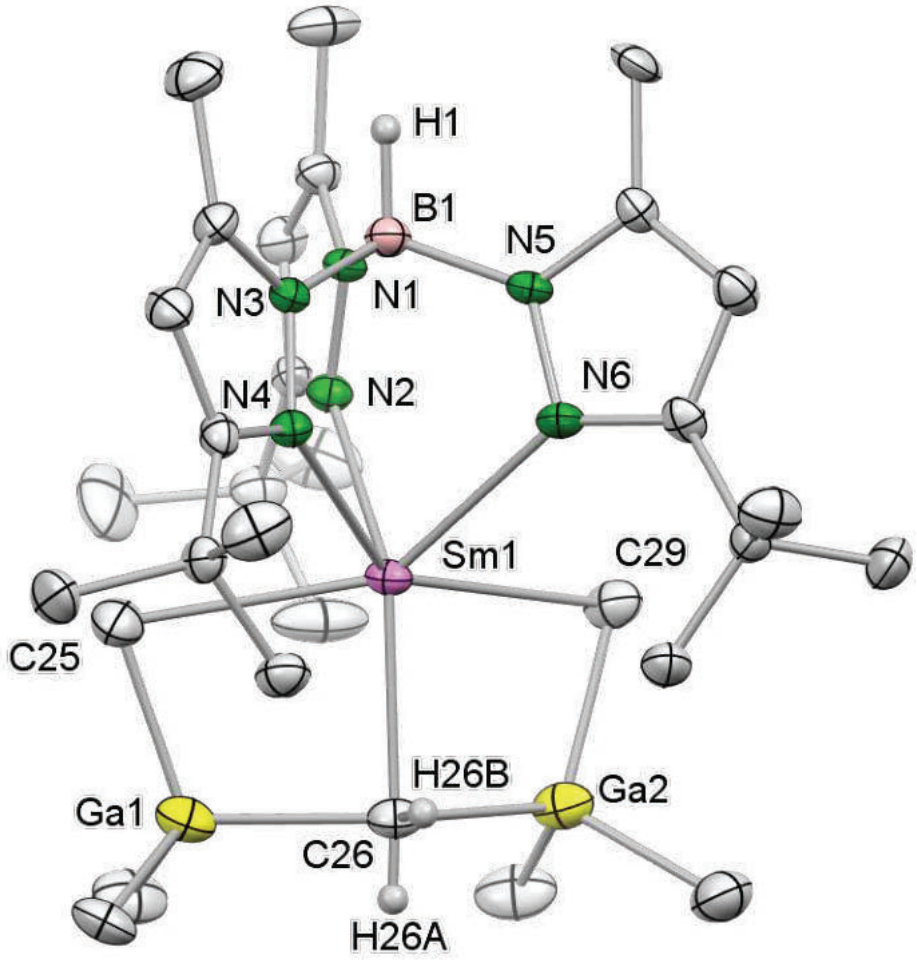

Figure S5. Crystal structure of **2-Sm**. Hydrogen atoms except for the BH and CH_2, and two additional toluene molecules are omitted for clarity. Atomic displacement ellipsoids were set at 50% probability. Selected interatomic distances [Å] and angles [°]: Sm1–N2 2.505(4), Sm1–N4 2.544(4), Sm1–N6 2.526(4) Sm1–C25 2.754(6), Sm1–C26 2.414(5), Sm1–C29 2.795(5), Ga1–C26 2.102(5), Ga2–C26 2.110(5); N2–Sm1–N4 86.05(12), N2–Sm1–N6 87.20(12), N2–Sm1–C25 81.99(15), N2–Sm1–C26 136.36(15), N2–Sm1–C 29 83.71(14), N4–Sm1–N6 67.61(12), N4–Sm1–C25 75.63(14), N4–Sm1–C26 128.00(15), N4–Sm1–C29 141.71(15), N6–Sm1–C25 142.26(14), N6–Sm1–C26 127.84(15), N6–Sm1–C29 75.11(15), C25–Sm1–C26 81.88(17), C25–Sm1–C29 138.49(18), C26–Sm1–C29 82.16(16).

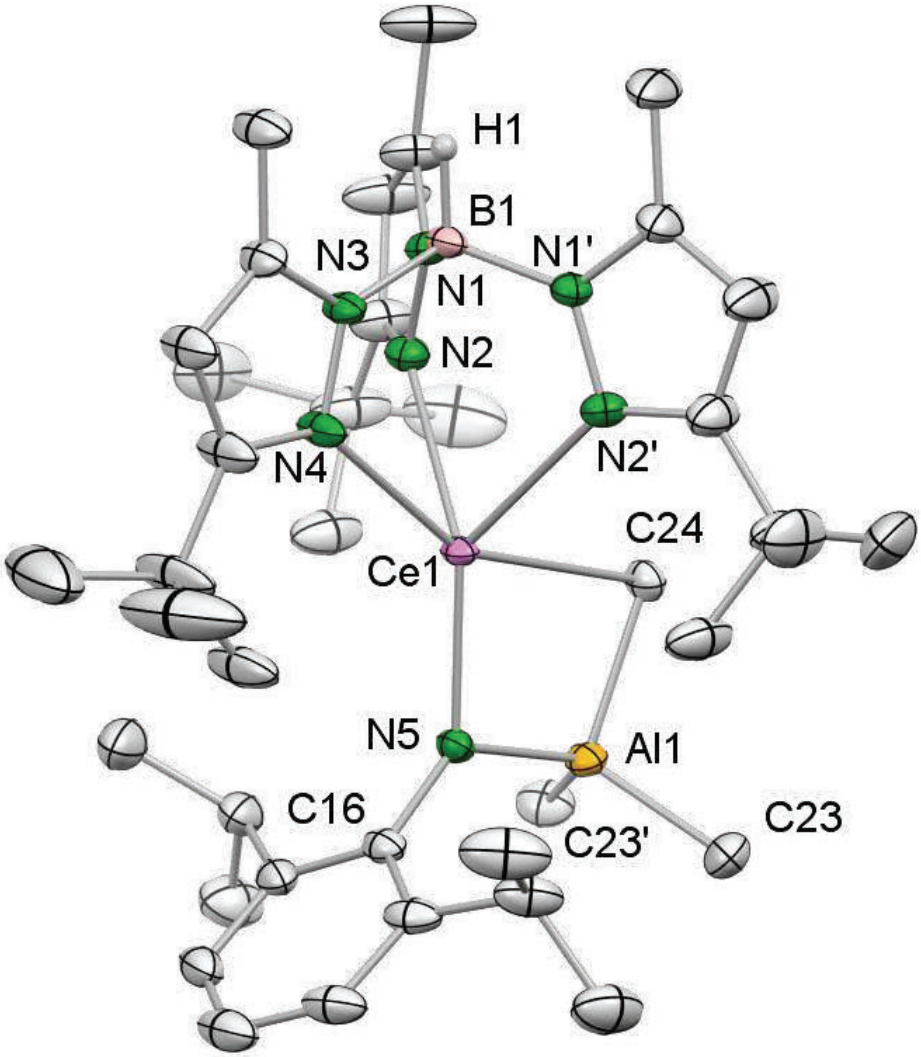

Figure S6. Crystal structure of **3-Ce**. Hydrogen atoms except for the BH, one additional toluene molecule and the disorder in one *tert*-butyl group are omitted for clarity. Atomic displacement ellipsoids were set at 50% probability. Selected interatomic distances [Å] and angles [°]: Ce1–N2 2.624(3), Ce1–N2' 2.624(3), Ce1–N4 2.566(3), Ce1–N5 2.213(3), Ce1–C24 2.722(7), Al1–N5 1.904(4); N2'–Ce1–N2 84.08(11), N2–Ce1–N4 74.55(8), N2–Ce1–N5 134.97(6), N2–Ce1–C24 86.91(9), N2'–Ce1–N4 74.55(8), N2'–Ce1–N5 134.97(6), N2'–Ce1–C24 86.91(9), N4–Ce1–N5 128.92(12), N4–Ce1–C24 154.81(12), N5–Ce1–C24 76.27(13), Ce1–N5–C16 136.2(3).

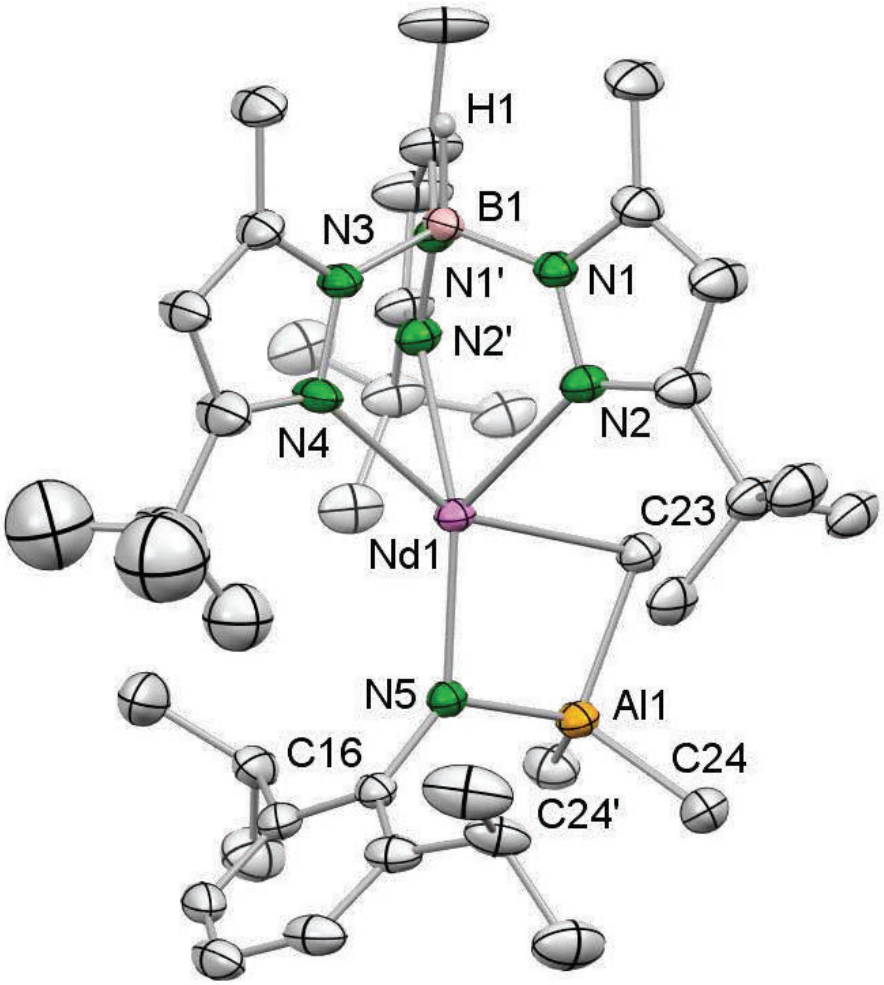

Figure S7. Crystal structure of **3-Nd**. Solvent molecules, hydrogen atoms except for those of BH as well as the disorder in one *tert*-butyl group are omitted for clarity. Atomic displacement ellipsoids were set at 50% probability. Selected interatomic distances [Å] and angles [°] (‘ = x, –y+0.5, z): Nd1–N2 2.591(4), Nd1–N4 2.541(6), Nd1–N5 2.195(5), Nd1–C23 2.699(7), Al1–N5 1.899(6); N2–Nd1–N2’ 85.36(16), N2–Nd1–N4 75.24(12), N2–Nd1–N5 134.61(9), N2–Nd1–C23 86.85(14), N2’–Nd1–C23 86.85(14), N4–Nd1–N5 127.47(19), N4–Nd1–C23 155.43(19), N5–Nd1–C23 77.1(2), Nd1–N5–C16 137.3(4).

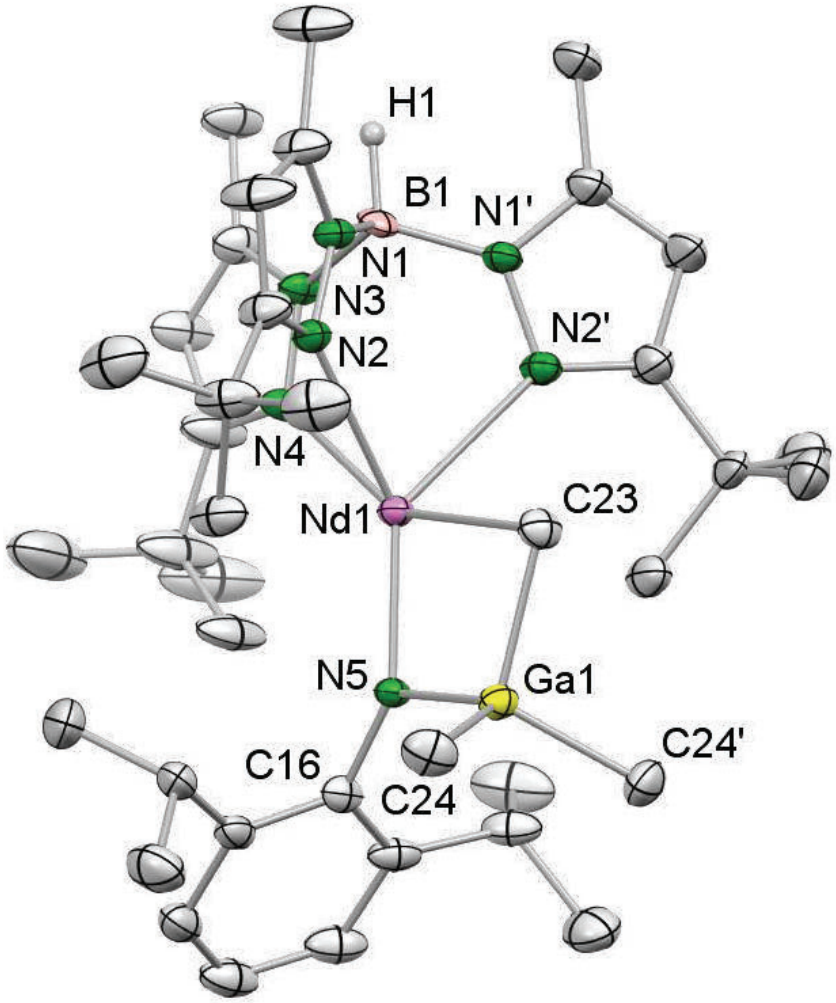

Figure S8. Crystal structure of **4-Nd**. Hydrogen atoms except for those of the BH and the disorder in all of the *tert*-butyl groups are omitted for clarity. Atomic displacement ellipsoids were set at 50% probability. Selected interatomic distances [Å] and angles [°] (‘ = x, –y+0.5, z): Nd1–N2 2.594(3), Nd1–N4 2.539(4), Nd1–N5 2.158(3), Nd1–C23 2.714(5), Ga1–N5 1.992(3); N2–Nd1–N2’ 85.02(11), N2–Nd1–N4 75.28(8), N2–Nd1–N5 135.29(6), N2–Nd1–C23 86.21(9), N2’–Nd1–N4 75.28(8), N2’–Nd1–C23 86.21(9), N4–Nd1–N5 125.56(12), N4–Nd1–C23 154.69(13), N5–Nd1–C23 79.75(13), Nd1–N5–C16 141.4(3).

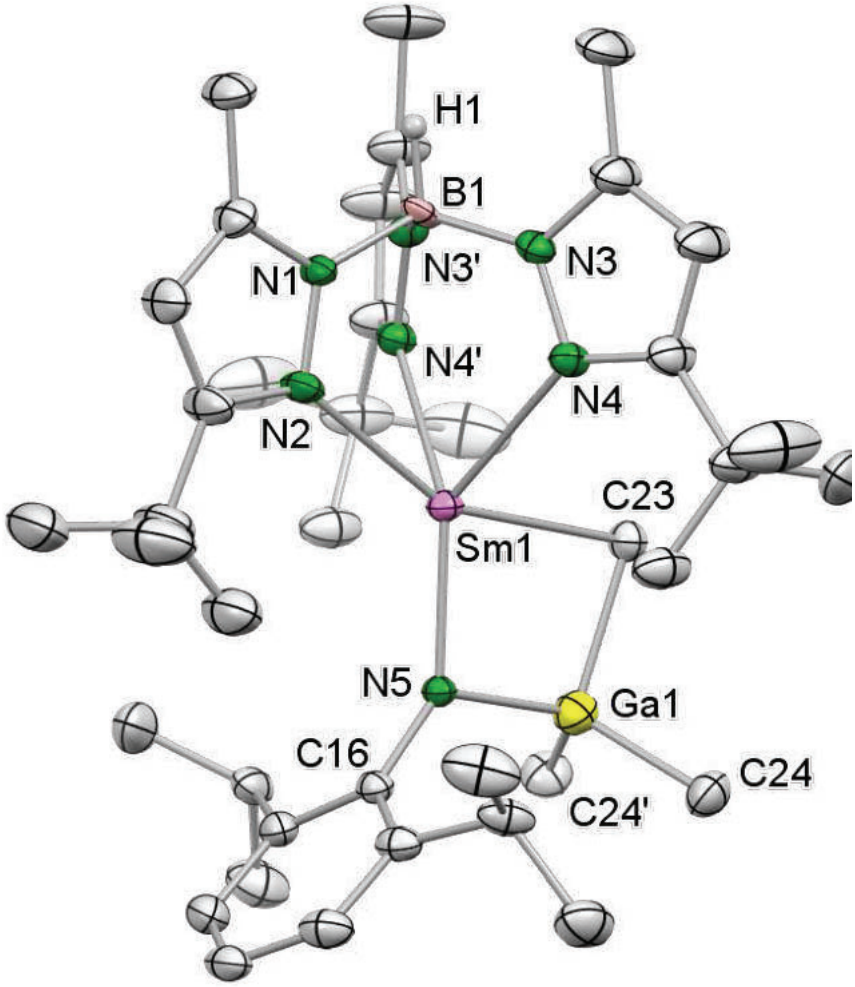

Figure S9. Crystal structure of **4-Sm**. Hydrogen atoms except for the BH, one additional toluene molecule and the disorder of one *tert*-butyl group are omitted for clarity. Atomic displacement ellipsoids were set at 50% probability. Selected interatomic distances [Å] and angles [°] (‘ = x, –y+1.5, z): Sm1–N2 2.514(5), Sm1–N4 2.567(3), Sm1–N5 2.158(4), Sm1–C23 2.655(6), Ga1–N5 1.977(5); N2–Sm1–N4 75.79(11), N2–Sm1–N5 124.07(16), N2–Sm1–C23 155.56(18), N4–Sm1–N4’ 85.69(15), N4–Sm1–N5 135.22(8), N4–Sm1–C23 86.43(13), N4’–Sm1–N5 135.22(8), N4’–Sm1–C23 86.43(13), N5–Sm1–C23 80.37(18), Sm1–N5–C16 141.8(4).

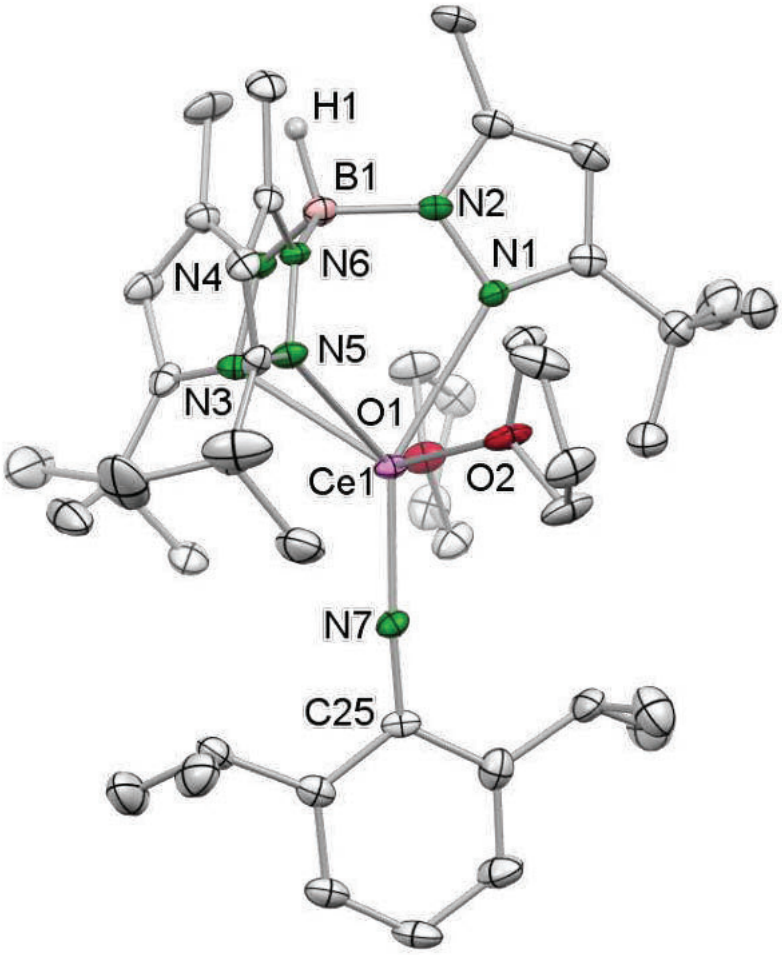

Figure S10. Crystal structure of **5-Ce**. Hydrogen atoms except for the BH and the disorder in one *tert*-butyl group and in both thf molecules are omitted for clarity. Atomic displacement ellipsoids were set at 50% probability. Selected interatomic distances [Å] and angles [°]: Ce1–N1 2.707(4), Ce1–N3 2.667(4), Ce–N5 2.673(4), Ce1–N7 2.101(3), Ce1–O1 2.599(3), Ce1–O2 2.628(3); N1–Ce1–N3 84.82(11), N1–Ce1–N5 83.20(12), N1–Ce1–N7 146.17(13), N1–Ce1–O1 74.28(11), N1–Ce1–O2 72.07(10), N3–Ce1–N5 65.83(11), N3–Ce1–N7 118.17(13), N3–Ce1–O1 73.96(10), N3–Ce1–O2 133.90(10), N5–Ce1–N7 127.66(13), N5–Ce1–O1 135.29(11), N5–Ce1–O2 72.10(11), N7–Ce1–O1 87.99(12), N7–Ce1–O2 101.94(11), O1–Ce1–O2 132.29 (11), Ce1–N7–C25 171.3(3).

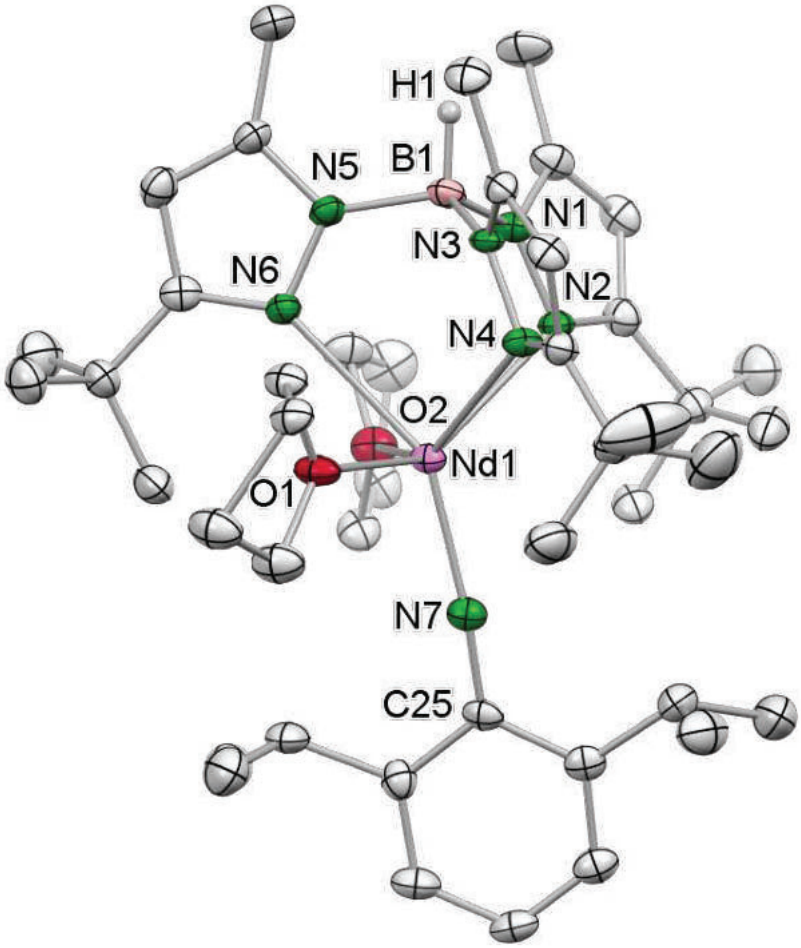

Figure S11. Crystal structure of **5-Nd**. Hydrogen atoms except for the BH, and the disorder of one of the thf molecules are omitted for clarity. Atomic displacement ellipsoids were set at 50% probability. Selected interatomic distances [Å] and angles [°]: Nd1–N2 2.625(4), Nd1–N4 2.601(4), Nd1–N6 2.674(4), Nd1–N7 2.076(4), Nd1–O1 2.594(3), Nd1–O2 2.557(4); N2–Nd1–N4 67.67(13), N2–Nd1–N6 87.09(13), N2–Nd1–N7 115.46(15), N2–Nd1–O1 137.45(12), N2–Nd1–O2 74.06(12), N4–Nd1–N6 86.55(13), N4–Nd1–N7 121.43(15), N4–Nd1–O1 74.11(13), N4–Nd1–O2 137.83(13), N6–Nd1–N7 148.51(14), N6–Nd1–O1 72.37(12), N6–Nd1–O2 74.25(13), N7–Nd1–O1 99.88(14), N7–Nd1–O2 90.44(14), O1–Nd1–O2 130.96(13), Nd1–N7–C25 169.2(4).

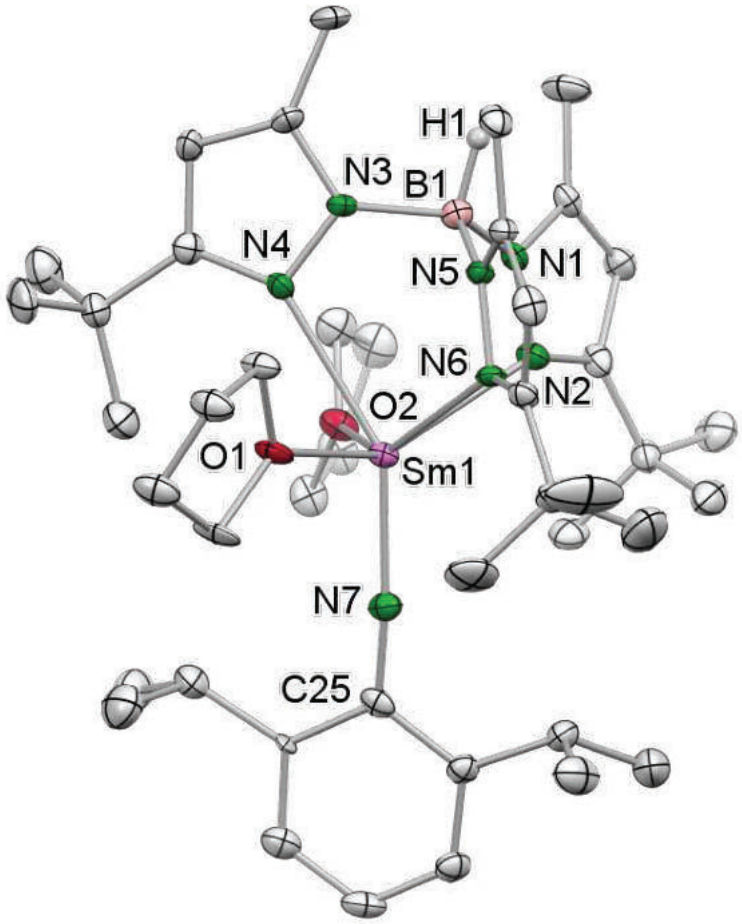

Figure S12. Crystal structure of **5-Sm**. Hydrogen atoms except for the BH, and the disorder of one of the thf molecules are omitted for clarity. Atomic displacement ellipsoids were set at 50% probability. Selected interatomic distances [Å] and angles [°]: Sm1–N2 2.607(6), Sm1–N4 2.657(6), Sm1–N6 2.573(5), Sm1–N7 2.067(5), Sm1–O1 2.560(4), Sm1–O2 2.527(5); N2–Sm1–N4 87.67(17), N2–Sm1–N6 68.53(17), N2–Sm1–N7 115.50(19), N2–Sm1–O1 138.48(15), N2–Sm1–O2 74.36(16), N4–Sm1–N6 87.03(17), N4–Sm1–N7 147.88(18), N4–Sm1–O1 72.52(16), N4–Sm1–O2 74.29(17), N6–Sm1–N7 121.17(19), N6–Sm1–O1 74.20(16), N6–Sm1–O2 138.94(17), N7–Sm1–O1 98.97(18), N7–Sm1–O2 90.20(19), O1–Sm1–O2 130.41(16), Sm1–N7–C25 169.3(5).

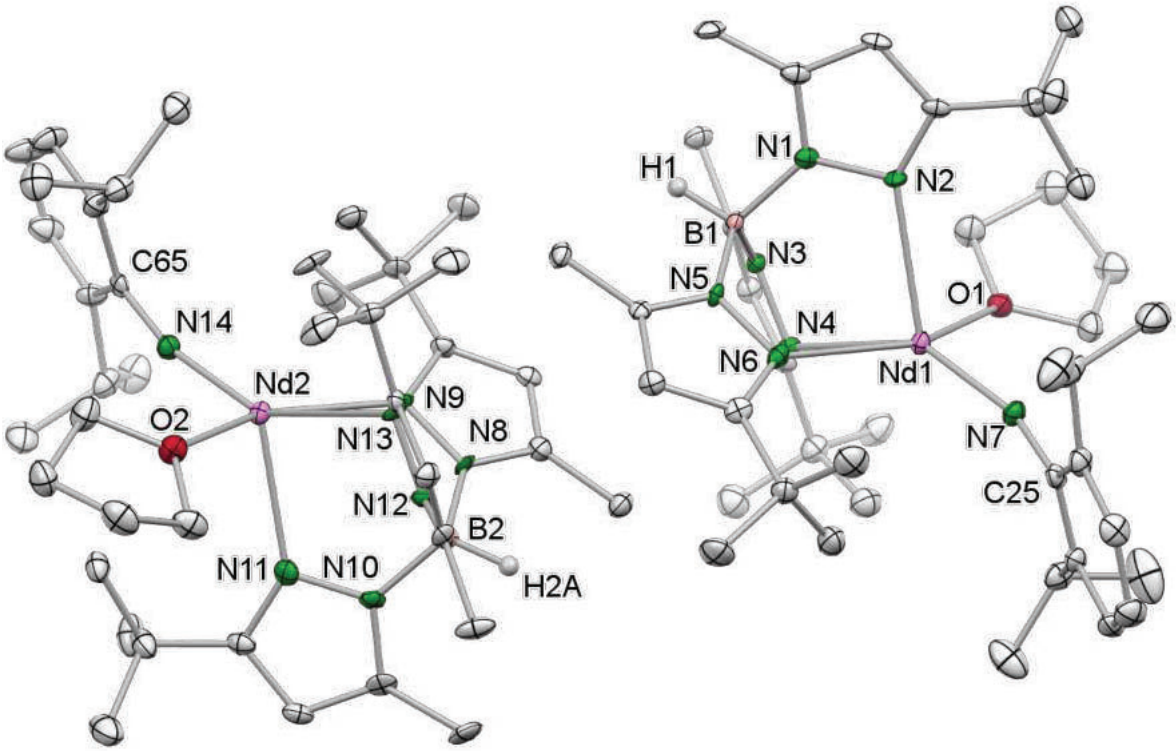

Figure S13. Crystal structure of **6-Nd**. Hydrogen atoms except for the BH, and one toluene molecule are omitted for clarity. The unit cell contains two independent molecules with different parameters. Atomic displacement ellipsoids were set at 50% probability. Selected interatomic distances [Å] and angles [°]: Nd1–N2 2.586(7), Nd1–N4 2.608(7), Nd1–N6 2.560(8), Nd1–N7 2.047(7), Nd1–O1 2.511(6), Nd2–N9 2.566(7), Nd2–N11 2.528(7), Nd2–N13 2.652(7), Nd2–N14 2.036(7), Nd2–O2 2.517(6); N2–Nd1–N4 91.5(2), N2–Nd1–N6 81.6(2), N2–Nd1–N7 121.6(3), N2–Nd1–O1 90.4(2), N4–Nd1–N6 70.8(2), N4–Nd1–N7 146.6(3), N4–Nd1–O1 80.8(2), N6–Nd1–N7 107.4(3), N6–Nd1–O1 150.1(2), N7–Nd1–O1 101.3(3), N9–Nd2–N11 79.6(2), N9–Nd2–N13 70.5(2), N9–Nd2–N14 106.5(3), N9–Nd2–O2 152.4(2), N11–Nd2–N13 90.3(2), N11–Nd2–N14 118.5(3), N11–Nd2–O2 92.2(2), N13–Nd2–N14 150.6(3), N13–Nd2–O2 83.3(2), N14–Nd2–O2 100.6(3), Nd1–N7–C25 163.2(6), Nd2–N14–C65 165.8(6).

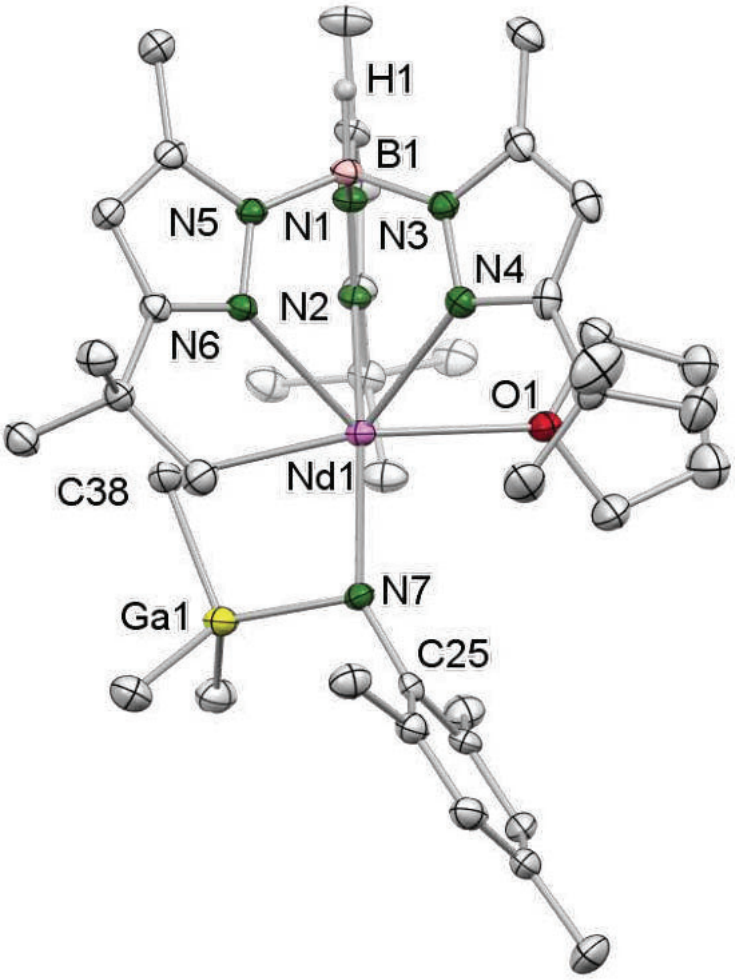

Figure S14. Crystal structure of **7-Nd**. Hydrogen atoms except for those of BH, the disorder in one thf molecule are omitted for clarity. Atomic displacement ellipsoids were set at 50% probability. Selected interatomic distances [Å]: Nd1–N2 2.594(3), Nd1–N4 2.558(3), Nd1–N6 2.666(3), Nd1–N7 2.165(3), Nd1–C38 2.836(4), Nd1–O1 2.601(2), Ga1–N7 1.992(3); N2–Nd1–N4 85.16(8), N2–Nd1–N6 84.90(8), N2–Nd1–N7 134.41(9), N2–Nd1–C38 82.03(10), N2–Nd1–O1 76.29(8), N4–Nd1–N6 67.42(8), N4–Nd1–N7 132.89(9), N4–Nd1–C38 142.99(10), N4–Nd1–O1 70.41(8), N6–Nd1–N7 128.22(9), N6–Nd1–C38 76.93(10), N6–Nd1–O1 134.90(8), N7–Nd1–C38 77.68(10), N7–Nd1–O1 92.50(9), C38–Nd1–O1 138.06(10), Nd1–N7–C25 147.6(2).

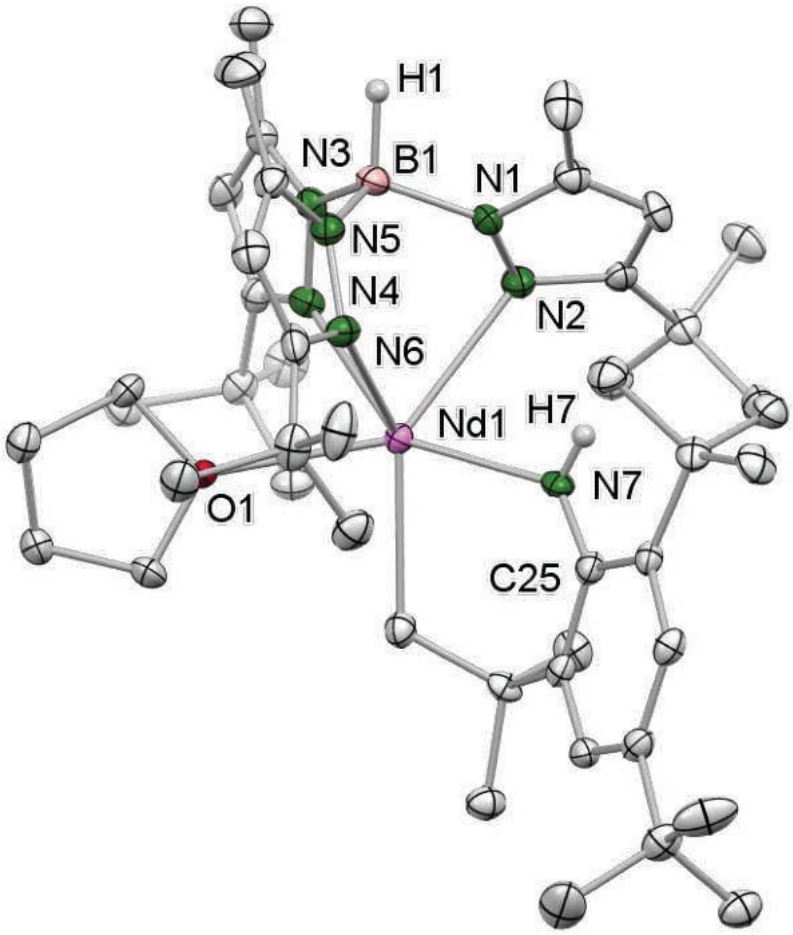

Figure S15. Crystal structure of **8-Nd**. Hydrogen atoms except for those of BH and NH, as well as lattice solvent (one molecule of toluene) are omitted for clarity. Atomic displacement ellipsoids were set at 50% probability. Selected interatomic distances [Å]: Nd1–N2 2.687(4), Nd1–N4 2.568(4), Nd1–N6 2.534(4), Nd1–N7 2.296(4), Nd1–C40 2.478(5), Nd1–O1 2.593(3); N2–Nd1–N4 64.41(13), N2–Nd1–N6 90.37(12), N2–Nd1–N7 78.53(13), N2–Nd1–C40 136.05(14), N2–Nd1–O1 136.66(10), N4–Nd1–N6 85.97(12), N4–Nd1–N7 142.91(13), N4–Nd1–C40 130.02(14), N4–Nd1–O1 74.00(12), N6–Nd1–N7 96.04(13), N6–Nd1–C40 127.71(15), N6–Nd1–O1 74.63(11), N7–Nd1–C40 76.59(14), N7–Nd1–O1 142.23(12), C40–Nd1–O1 80.77(13).

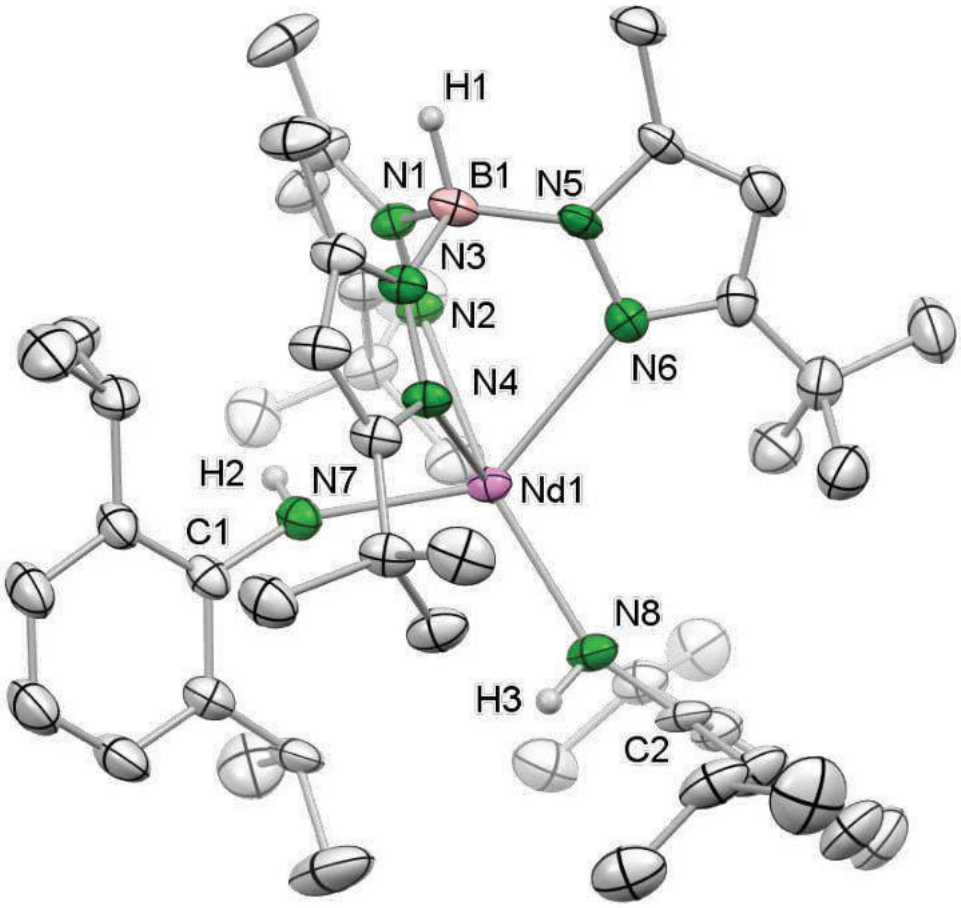

Figure S16. Crystal structure of **9-Nd**. Hydrogen atoms except for those of BH and NH, the disorder in one *tert*-butyl group and one *iso*-propyl group as well as lattice solvent (three molecules of THF) are omitted for clarity. Atomic displacement ellipsoids were set at 50% probability. Selected interatomic distances [Å]: Nd1–N2 2.532(5), Nd1–N4 2.588(6), Nd1–N6 2.558(6), Nd1–N7 2.344(5), Nd1–N8 2.312(6); N2–Nd1–N4 74.52(19), N2–Nd1–N6 88.95(18), N2–Nd1–N7 122.59(19), N2–Nd1–N8 82.6(2), N4–Nd1–N6 70.31(19), N4–Nd1–N7 108.8(2), N4–Nd1–N8 139.88(19), N6–Nd1–N7 147.70(19), N6–Nd1–N8 76.9(2), N7–Nd1–N8 111.2(2).

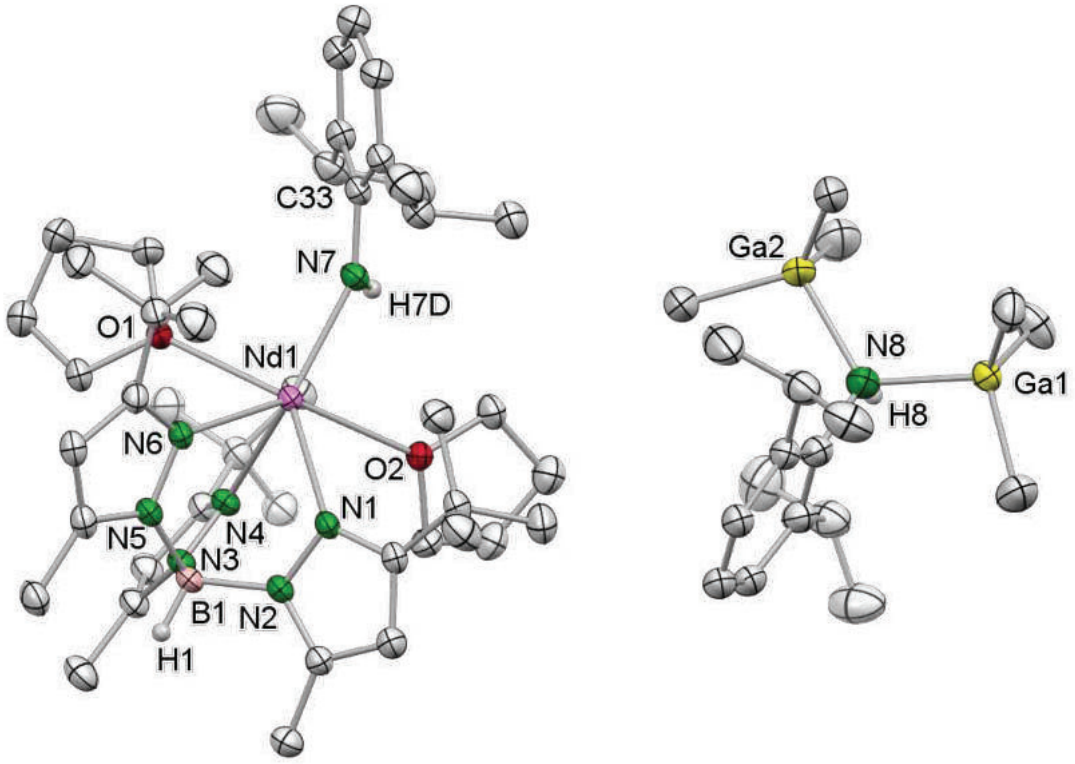

Figure S17. Crystal structure of **10-Nd**. Hydrogen atoms except for the BH, NHs and the disorder in one *tert*-butyl group and in both $GaMe_3$ molecules are omitted for clarity. Atomic displacement ellipsoids were set at 50% probability. Selected interatomic distances [Å] and angles [°]: Nd1–N1 2.593(4), Nd1–N4 2.516(4), Nd1–N6 2.502(4), Nd1–N7 2.291(4), Nd1–O1 2.542(4), Nd1–O2 2.515(3), Ga1–N8 2.123(6), Ga2–N8 2.111(5); N1–Nd1–N4 84.45(14), N1–Nd1–N6 66.98(13), N1–Nd1–N7 133.34(15), N1–Nd1–O1 136.34(12), N1–Nd1–O2 74.14(12), N4–Nd1–N6 86.80(14), N4–Nd1–N7 131.56(16), N4–Nd1–O1 72.60(13), N4–Nd1–O2 81.87(13), N6–Nd1–N7 131.13(16), N6–Nd1–O1 74.94(13), N6–Nd1–O2 140.34(12), N7–Nd1–O1 88.02(14), N7–Nd1–O2 82.18(14), O1–Nd1–O2 135.32(13), Nd1–N7–C33 148.9(4), Ga1–N8–Ga 2 118.1(3).

X-ray Crystallography and Crystal Structure Determinations. Single crystals of **1-Ce**, **1-Nd**, **2-Ce**, **2-Nd**, **2-Sm**, **3-Ce**, **3-Nd**, **4-Nd**, **4-Sm**, **5-Ce**, **5-Nd**. **5-Sm**, **6-Nd**, **7-Nd**, **8-Nd**, **9-Nd**, and **10-Nd** were grown by standard techniques from saturated solutions using a mixture of toluene and *n*-pentane (**1-Nd**, **2-Nd**, **2-Sm, 3-Nd, 4-Nd**, and **4-Sm**), a mixture of THF and *n*-hexane (**3-Ce**, **5-Ce**, **5-Nd**, **5-Sm**), a mixture of toluene and fluorocyclohexane (**6-Nd**), and toluene (**1-Ce**, **2-Ce**, **7-Nd**, **8-Nd**, **9-Nd**, and **10-Nd**). Suitable crystals for X-ray structure analyses were selected in a glovebox and coated with Parabar 10312 (previously known as Paratone N, Hampton Research) and fixed on a nylon loop/glass fiber.

X-ray data for above mentioned compounds were collected on a Bruker APEX III DUO (all remaining; instruments equipped with an IμS microfocus sealed tube and QUAZAR optics for MoK_α (λ = 0.71073 Å) and $_{CuK\alpha}$ (λ = 1.54184 Å) radiation. The data collection strategy was determined using COSMO[1] employing ω-scans (APEX III). Raw data were processed using APEX[2] and SAINT,[3] corrections for absorption effects were applied using SADABS.[4] The structures were solved by direct methods and refined against all data by full-matrix least-squares methods on F^2 using ShelXtl[5] and ShelXle.[6] All structures, except **3-Nd** and **2-Ce**, showed disorder in the solvent molecules and/or part of the ligands. Disorder models were calculated using DSR, a program for refining disordered structures in ShelXL.[7] All graphics were produced employing ORTEP-3[8] and POV-Ray.[9] Further details of the refinement and crystallographic data are listed in Table S1-S6, and in the CIF files. CCDC depositions 2125445-2125461 contain all the supplementary crystallographic data for this paper. These data can be obtained free of charge from The Cambridge Crystallographic Data Centre via www.ccdc.cam.ac.uk/structures/.

Table S1. Crystallographic data for compounds **1-Ce**, **1-Nd**, and **2-Ce**.

	1-Ce	**1-Nd**	**2-Ce**
formula	$C_{31}H_{60}Al_2BN_6Ce \cdot 2C_7H_8$	$C_{31}H_{60}Al_2BN_6Nd \cdot 2C_7H_8$	$C_{31}H_{60}Ga_2BN_6Ce \cdot C_5H_{12}$
CCDC	2125450	2125446	2125445
M_r [g mol^{-1}]	906.00	910.12	879.36
color	colorless	pale blue	colorless
crystal dimensions [mm^3]	0.194 x 0.087 x 0.054	0.360 x 0.220 x 0.170	0.130 x 0.093 x 0.092
cryst syst	monoclinic	monoclinic	triclinic
space group	*P2₁/n*	*P2₁/n*	*P-1*
a [Å]	13.189(4)	13.1347(4)	9.9300(3)
b [Å]	9.926(3)	9.9349(3)	12.0131(3)
c [Å]	37.117(11)	36.9684 (12)	18.6185(5)
α [°]	90	90	83.1060(10)
β [°]	98.686(5)	98.525(2)	81.4670(10)
γ [°]	90	90	76.8360(10)
V [Å^3]	4803(2)	4770.8(3)	2130.11(10)
Z	4	4	2
T [K]	100(2)	123(2)	100(2)
ρ_{calcd} [g cm^{-3}]	1.253	1.267	1.371
μ [mm^{-1}]	1.020	1.161	2.336
F (000)	1908	1916	910
θ range [°]	1.577/27.485	1.568/29.130	1.748/28.331
Reflns measured	99799	111500	49998
independent reflns	10991	12853	10558
R1/*w*R2 (I>2σ)[a]	0.0385/0.0733	0.0316/0.0634	0.0272/0.0536
R1/*w*R2 (all data)[a]	0.0571/0.0799	0.0397/0.0660	0.0377/0.0570
GOF[a]	1.027	1.075	1.031

[a] $R1 = \Sigma(||F_0|-|F_c||)/\Sigma|F_0|$, $F_0 > 4\sigma(F_0)$. $wR2 = \{\Sigma[w(F_0^2-F_c^2)^2/\Sigma[w(F_0^2)^2]\}^{4/5}$.

Table S2. Crystallographic data for compounds **2-Nd**, **2-Sm**, and **3-Ce**.

	2-Nd	**2-Sm**	**3-Ce**
formula	$C_{31}H_{60}Ga_2BN_6Nd \cdot 2C_7H_8$	$C_{31}H_{60}Ga_2BN_6Sm \cdot 2C_7H_8$	$C_{39}H_{66}AlBN_7Ce \cdot 2C_7H_8$
CCDC	2125452	2125449	2125447
M_r [g mol^{-1}]	995.60	1001.71	995.16
color	colorless	yellow	light yellow
crystal dimensions [mm^3]	0.277 x 0.131 x 0.100	0.139 x 0.075 x 0.060	0.156 x 0.069 x 0.062
cryst syst	monoclinic	monoclinic	orthorhombic
space group	*P2₁/n*	*P2₁/n*	*Pnma*
a [Å]	13.0505(10)	13.0415(10)	24.169(5)
b [Å]	9.9832(8)	9.9846(8)	22.599(5)
c [Å]	36.895(3)	36.943(3)	9.686(2)
α [°]	90	90	90
β [°]	98.264(4)	98.423(2)	90
γ [°]	90	90	90
V [Å^3]	4756.9(7)	4758.6(6)	5290.6(19)
Z	4	4	4
T [K]	100(2)	100(2)	100(2)
ρ_{calcd} [g cm^{-3}]	1.390	1.398	1.249
μ [mm^{-1}]	2.236	2.378	0.917
F (000)	2060	2068	2100
θ range [°]	1.595/30.585	1.114/29.130	1.911/28.419
Reflns measured	171446	78618	60922
independent reflns	14613	12824	6775
R1/*w*R2 (I>2σ)[a]	0.0292/0.0639	0.0518/0.1171	0.0403/0.0833
R1/*w*R2 (all data)[a]	0.0373/0.0668	0.0829/0.1330	0.0608/0.0918
GOF[a]	1.051	1.042	1.048

[a] $R1 = \Sigma(||F_0|-|F_c||)/\Sigma|F_0|$, $F_0 > 4\sigma(F_0)$. $wR2 = \{\Sigma[w(F_0^2-F_c^2)^2/\Sigma[w(F_0^2)^2]\}^{4/5}$.

Table S3. Crystallographic data for compounds **3-Nd**, **4-Nd**, and **4-Sm**.

	3-Nd	**4-Nd**	**4-Sm**
formula	$C_{39}H_{66}AlBN_7Nd{\cdot}2C_7H_8$	$C_{39}H_{66}GaBN_7Nd{\cdot}2C_7H_8$	$C_{39}H_{66}GaBN_7Sm{\cdot}2C_7H_8$
CCDC	2125454	2125460	2125458
M_r [g mol^{-1}]	999.28	1042.02	1048.13
color	colorless	colorless	colorless
crystal dimensions [mm^3]	0.143 x 0.072 x 0.062	0.167 x 0.119 x 0.070	0.231 x 0.092 x 0.088
cryst syst	orthorhombic	orthorhombic	orthorhombic
space group	*Pnma*	*Pnma*	*Pnma*
a [Å]	24.1232(17)	24.1805(6)	24.123(3)
b [Å]	22.6114(17)	22.6350(6)	22.643(2)
c [Å]	9.6713(7)	9.6748(3)	9.6617(10)
α [°]	90	90	90
β [°]	90	90	90
γ [°]	90	90	90
V [Å^3]	5275.3(7)	5295.3(3)	5277.3(10)
Z	4	4	4
T [K]	173(2)	100(2)	100(2)
ρ_{calcd} [g cm^{-3}]	1.258	1.307	1.319
μ [mm^{-1}]	1.041	1.519	1.653
F (000)	2108	2180	2188
θ range [°]	1.914/25.372	1.684/28.263	1.913/30.521
Reflns measured	46239	71568	46551
independent reflns	4961	6698	8226
R1/*w*R2 (I>2σ)[a]	0.0472/0.1082	0.0394/0.0930	0.0565/0.1470
R1/*w*R2 (all data)[a]	0.0702/0.1212	0.0524/0.1005	0.0831/0.1641
GOF[a]	1.019	1.036	1.047

[a] $R1 = \Sigma(||F_0|-|F_c||)/\Sigma|F_0|$, $F_0 > 4\sigma(F_0)$. $wR2 = \{\Sigma[w(F_0^2-F_c^2)^2/\Sigma[w(F_0^2)^2]\}^{4/5}$.

Table S4. Crystallographic data for compound **5-Ce**, **5-Nd**, and **5-Sm**.

	5-Ce	**5-Nd**	**5-Sm**
M	$C_{44}H_{73}BN_7CeO_2$	$C_{44}H_{73}BN_7NdO_2$	$C_{44}H_{73}BN_7NdO_2$
CCDC	2125453	2125448	2125451
M_r [g mol^{-1}]	883.02	887.17	893.25
color	Light yellow	colorless	orange
crystal dimensions [mm^3]	0.196 x 0.117 x 0.100	0.287 x 0.168 x 0.166	0.177 x 0.105 x 0.057
cryst syst	orthorhombic	orthorhombic	orthorhombic
space group	$P2_12_12_1$	$P2_12_12_1$	$P2_12_12_1$
a [Å]	10.9584(12)	11.0316(12)	11.062(2)
b [Å]	19.694(2)	19.439(2)	19.518(4)
c [Å]	21.026(2)	21.035(2)	20.993(4)
α [°]	90	90	90
β [°]	90	90	90
γ [°]	90	90	90
V [Å^3]	4537.7(9)	4510.9(9)	4532.7(15)
Z	4	4	4
T [K]	100(2)	173(2)	100(2)
ρ_{calcd} [g cm^{-3}]	1.293	1.306	1.309
μ [mm^{-1}]	1.045	1.194	1.338
F (000)	1860	1868	1876
θ range [°]	2.068/26.716	2.095/27.105	1.425/28.283
Reflns measured	66656	46259	35779
independent reflns	9600	9925	11167
R1/wR2 (I>2σ)[a]	0.0385/0.0472	0.0355/0.0754	0.0476/0.0870
R1/wR2 (all data)[a]	0.0601/0.0509	0.0409/0.0778	0.0655/0.0952
GOF[a]	1.022	1.045	0.979

[a] $R1 = \Sigma(||F_0|-|F_c||)/\Sigma|F_0|$, $F_0 > 4\sigma(F_0)$. $wR2 = \{\Sigma[w(F_0^2-F_c^2)^2/\Sigma[w(F_0^2)^2]\}^{4/5}$.

Table S5. Crystallographic data for compound **6-Nd**, **7-Nd**, and **8-Nd**.

	6-Nd	**7-Nd**	**8-Nd**
M	$C_{40}H_{65}BN_7NdO \cdot 1/2C_7H_8$	$C_{40}H_{68}BGaN_7NdO$	$C_{46}H_{77}Bn_7NdO \cdot C_7H_8$
CCDC	2125457	2125461	2125456
M_r [g mol^{-1}]	861.10	887.78	991.32
color	green	green	blue
crystal dimensions [mm^3]	0.203 x 0.191 x 0.099	0.121 x 0.116 x 0.116	0.095 x 0.076 x 0.049
cryst syst	orthorhombic	monoclinic	monoclinic
space group	*Pna*2$_1$	*P*2$_1$/*n*	*P*2$_1$/*n*
a [Å]	19.973(3)	12.6700(6)	10.762(10)
b [Å]	11.5823(15)	17.3951(8)	17.710(15)
c [Å]	37.491(5)	19.5063(9)	27.88(2)
α [°]	90	90	90
β [°]	90	93.5460(10)	94.469(10)
γ [°]	90	90	90
V [Å^3]	8673.1(19)	4290.9(3)	5297(8)
Z	8	4	4
T [K]	100(2)	100(2)	100(2)
ρ_{calcd} [g cm^{-3}]	1.319	1.374	1.243
μ [mm^{-1}]	1.238	1.862	1.022
F (000)	3616	1844	2100
θ range [°]	1.086/27.103	1.570/27.102	2.087/25.681
Reflns measured	67859	101800	66540
independent reflns	18614	9479	10044
R1/*w*R2 (I>2σ)[a]	0.0532/0.1196	0.0342/0.0695	0.0446/0.0900
R1/*w*R2 (all data)[a]	0.0587/0.1225	0.0560/0.0793	0.0790/0.1064
GOF[a]	1.125	1.045	1.018

[a] $R1 = \Sigma(||F_0|-|F_c||)/\Sigma|F_0|$, $F_0 > 4\sigma(F_0)$. $wR2 = \{\Sigma[w(F_0^2-F_c^2)^2/\Sigma[w(F_0^2)^2]\}^{4/5}$.

Table S6. Crystallographic data for compound **9-Nd**, and **10-Nd**.

	9-Nd	**10-Nd**
M	$C_{48}H_{76}BGaN_8Nd \cdot 3THF$	$C_{62}H_{110}BGa_2N_8NdO_2$
CCDC	2125455	2125459
M_r [g mol^{-1}]	1136.52	1294,06
color	colorless	colorless
crystal dimensions [mm^3]	0.301 x 0.267 x 0.234	0.202 x 0.195 x 0.084
cryst syst	orthorhombic	monoclinic
space group	$P2_12_12_1$	$P2_1/c$
a [Å]	12.6355(16)	17.973(4)
b [Å]	17.357(2)	18.705(5)
c [Å]	28.129(14)	19.775(7)
α [°]	90	90
β [°]	90	93.26(3)
γ [°]	90	90
V [Å^3]	6169.2(14)	6637(3)
Z	4	4
T [K]	173(2)	173(2)
ρ_{calcd} [g cm^{-3}]	1.224	1.295
μ [mm^{-1}]	0.889	1.622
F (000)	2420	2724
θ range [°]	1.767/28.324	2.178/26.372
Reflns measured	87231	43659
independent reflns	15293	12989
R1/*w*R2 (I>2σ)[a]	0.0487/0.1303	0.0541/0.1218
R1/*w*R2 (all data)[a]	0.0510/0.1315	0.0933/0.1443
GOF[a]	1.139	1.012

[a] $R1 = \Sigma(||F_0|-|F_c||)/\Sigma|F_0|$, $F_0 > 4\sigma(F_0)$. $wR2 = \{\Sigma[w(F_0^2-F_c^2)^2/\Sigma[w(F_0^2)^2]\}^{4/5}$.

NMR Spectroscopy

Notes on NMR spectroscopic characterizations.

Due to the paramagnetic nature of Nd(III) and Sm(III) any conclusive interpretation of the recorded NMR spectra was not possible. In general, solvent peaks are marked with an asterisk (*).

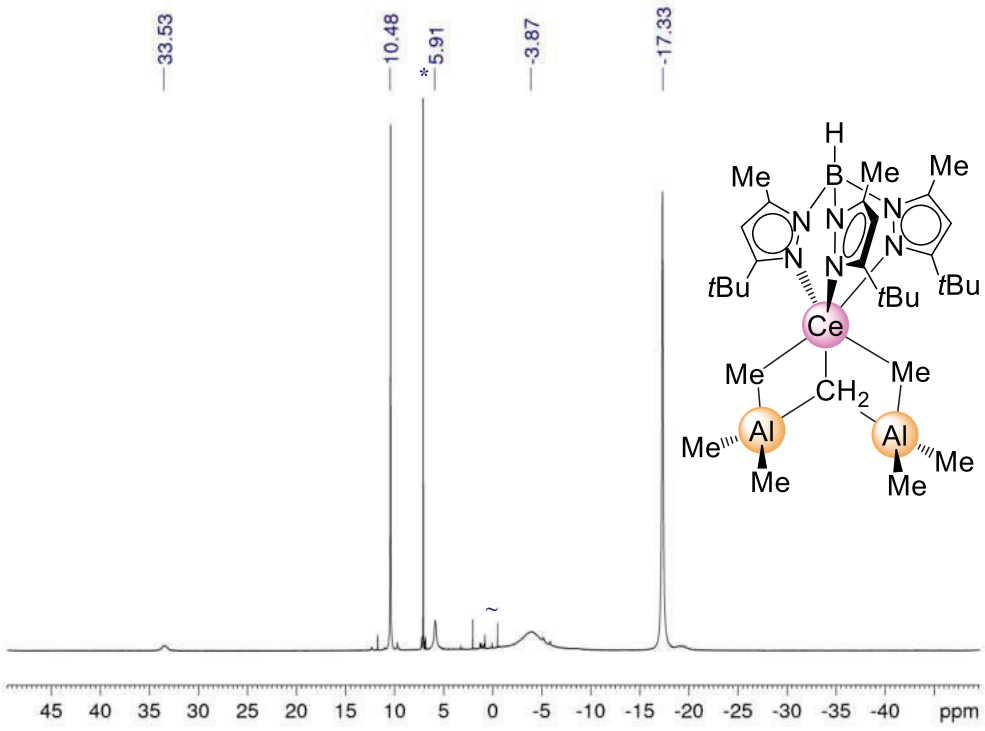

Figure S18. ^{1}H NMR spectrum (400 MHz) of compound [Tp^{tBu,Me}Ce{(μ_3-CH$_2$)[(μ_2-Me)AlMe$_2$]$_2$}] (**1-Ce**) in C_6D_6 at 26 °C. Minor impurities are marked with (~).

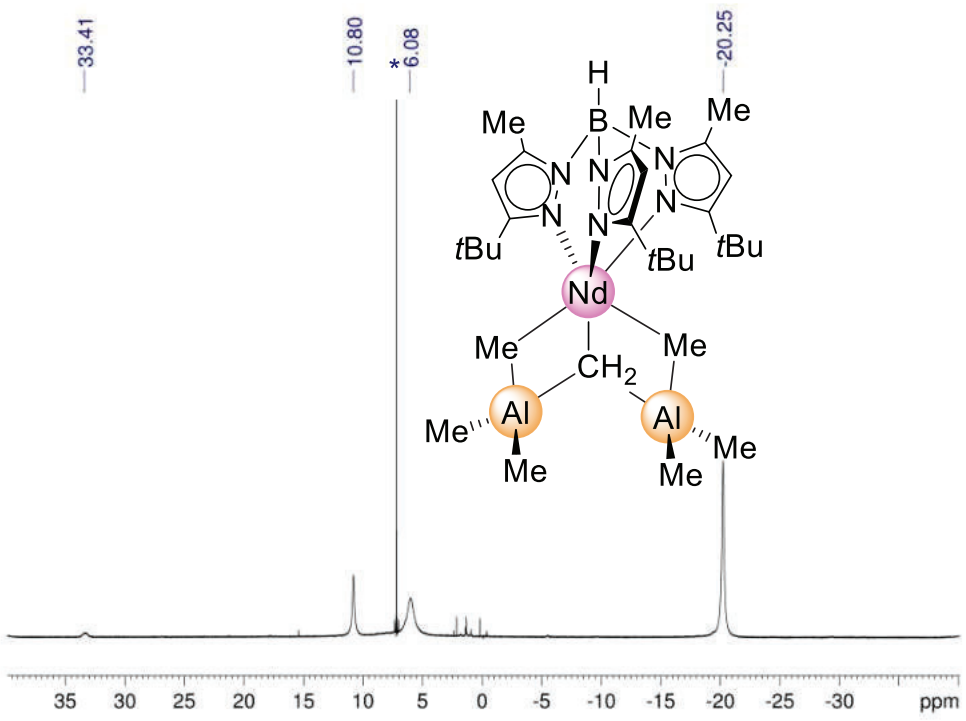

Figure S19. ^{1}H NMR spectrum (400 MHz) of compound [Tp^{tBu,Me}Nd{(μ_3-CH$_2$)[(μ_2-Me)AlMe$_2$]$_2$}] (**1-Nd**) in CDCl$_3$ at 26 °C.

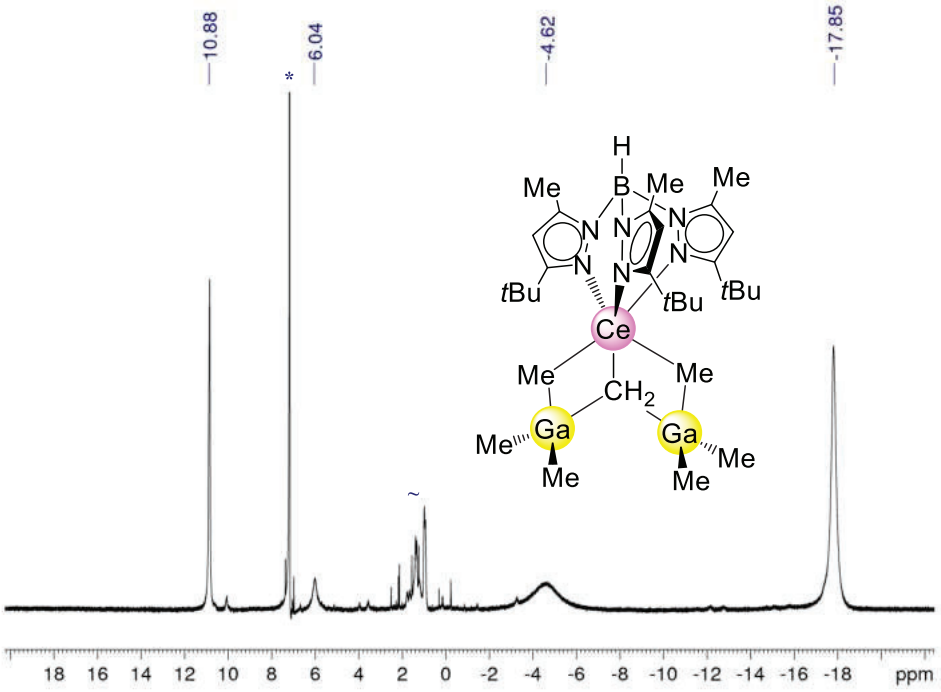

Figure S20. ^{1}H NMR spectrum (400 MHz) of compound [Tp^{tBu,Me}Ce{(μ_3-CH$_2$)[(μ_2-Me)GaMe$_2$]$_2$}] (**2-Ce**) in C$_6$D$_6$ at 26 °C. Minor impurities are marked with (~).

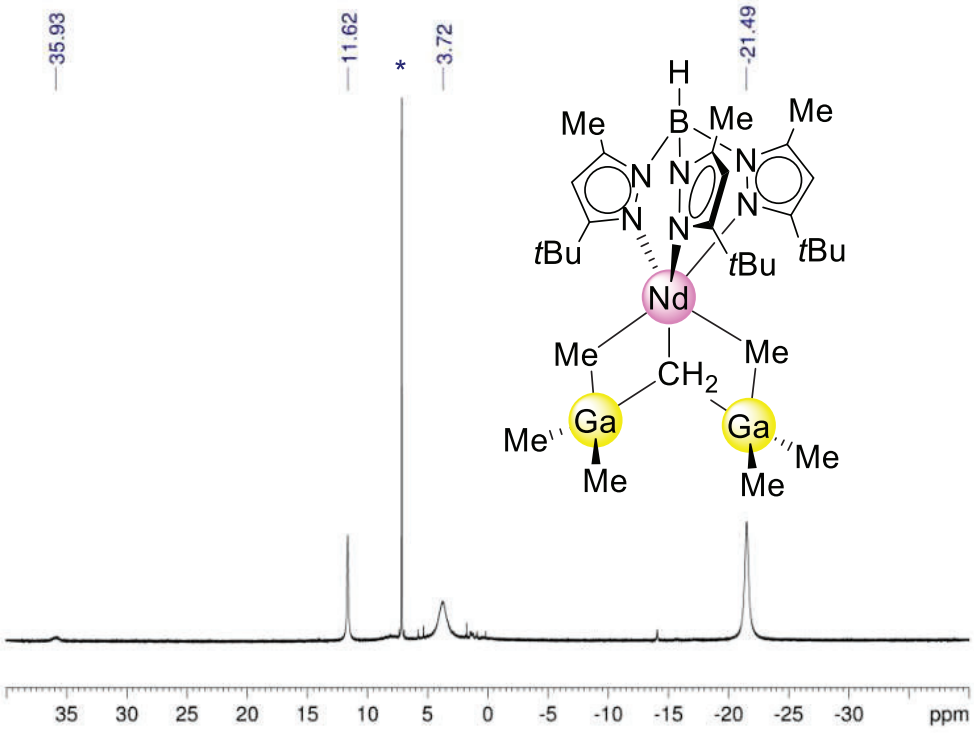

Figure S21. ^{1}H NMR spectrum (400 MHz) of compound [Tp^{tBu,Me}Nd{(μ_3-CH_2)[(μ_2-Me)$GaMe_2$]$_2$}] (**2-Nd**) in C_6D_6 at 26 °C.

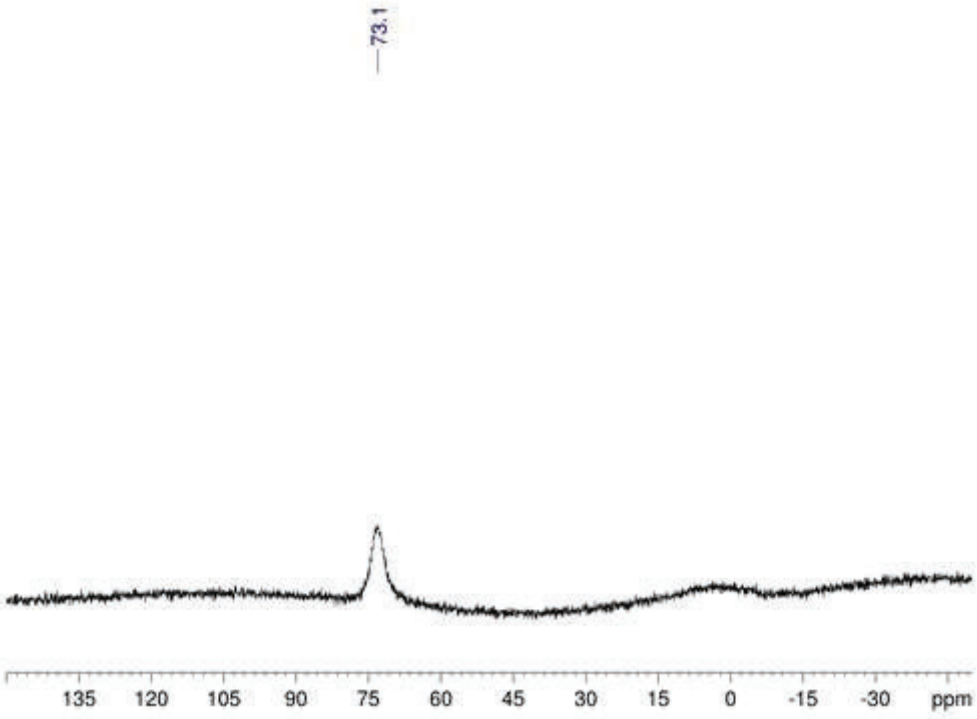

Figure S22. $^{11}B\{^{1}H\}$ NMR spectrum (96 MHz) of compound [Tp^{tBu,Me}Nd{(μ_3-CH_2)[(μ_2-Me)$GaMe_2$]$_2$}] (**2-Nd**) in C_6D_6 at 26 °C.

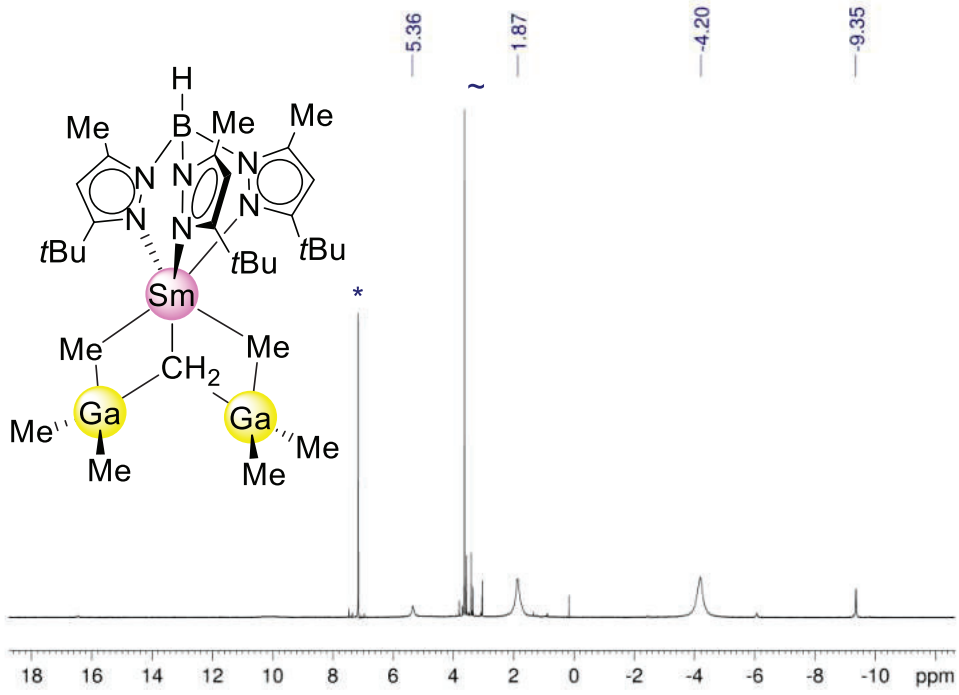

Figure S23. ^{1}H NMR spectrum (400 MHz) of compound [Tp^{tBu,Me}Sm{(μ_3-CH_2)[(μ_2-Me)$GaMe_2$]$_2$}] (**2-Sm**) in C_6D_6 at 26 °C. Minor impurities are marked with (~).

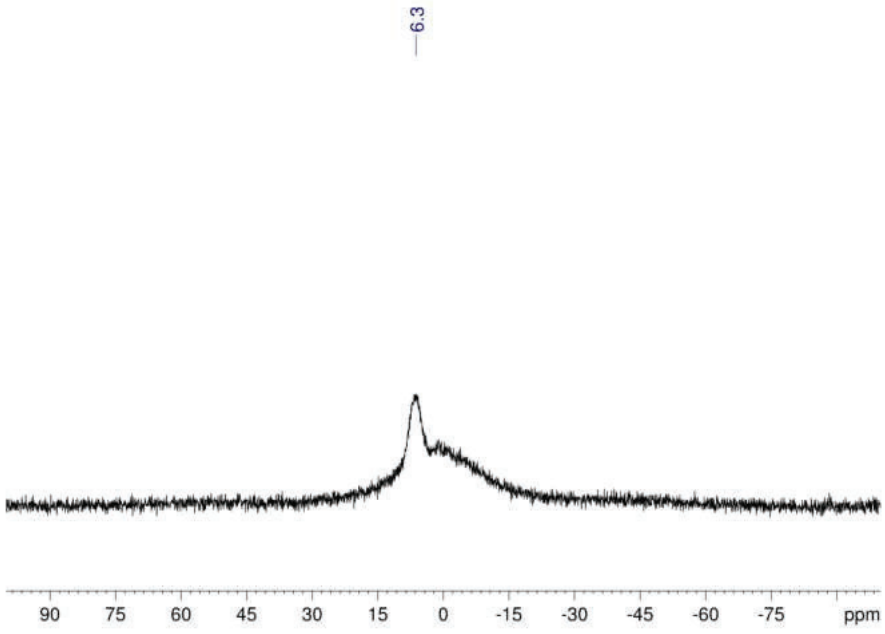

Figure S24. $^{11}B\{^{1}H\}$ NMR spectrum (96 MHz) of compound [Tp^{tBu,Me}Sm{(μ_3-CH_2)[(μ_2-Me)$GaMe_2$]$_2$}] (**2-Sm**) in C_6D_6 at 26 °C.

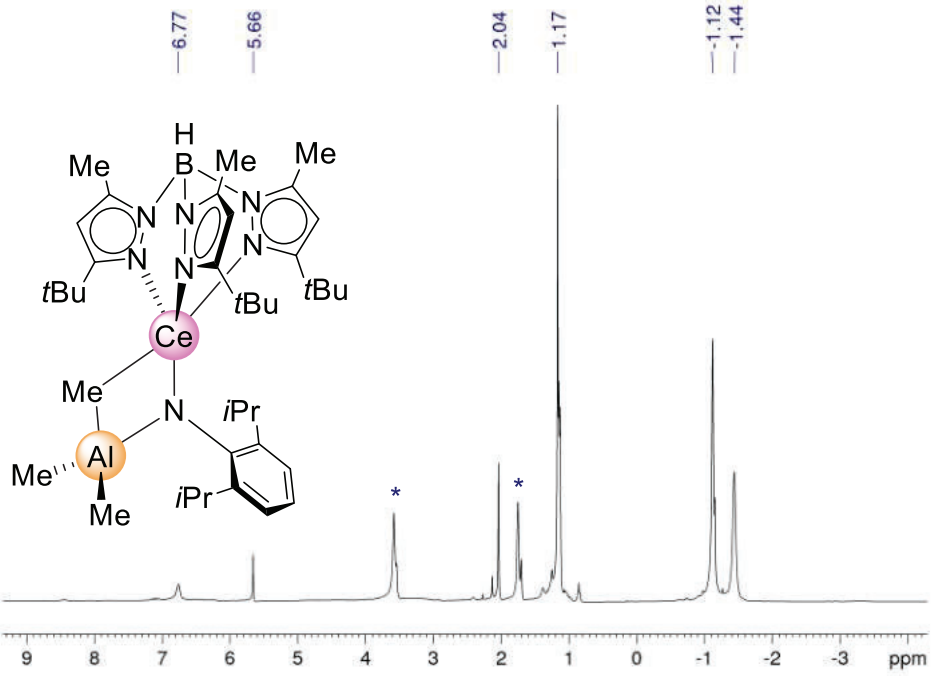

Figure S25. ^{1}H NMR spectrum (400 MHz) of compound [Tp^{tBu,Me}Ce(NC$_6$H$_3$*i*Pr$_2$-2,6)(AlMe$_3$)] (**3-Ce**) in [D$_8$]thf at 26 °C.

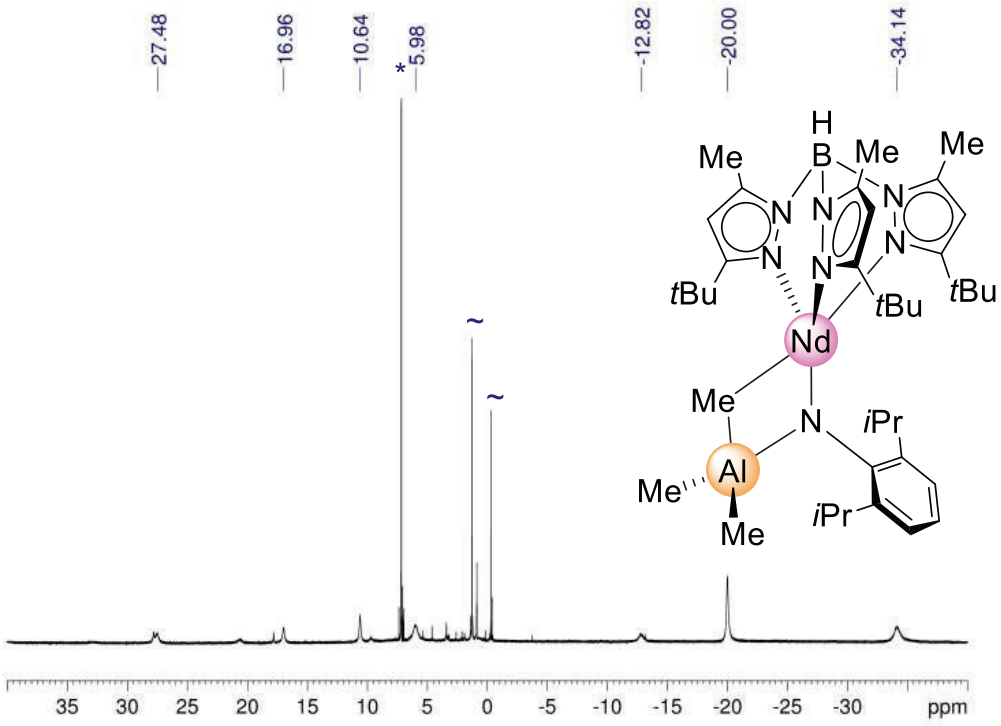

Figure S26. ^{1}H NMR spectrum (400 MHz) of compound [Tp^{tBu,Me}Nd(NC$_6$H$_3$*i*Pr$_2$-2,6)(AlMe$_3$)] (**3-Nd**) in C$_6$D$_6$ at 26 °C. Minor impurities are marked with (~).

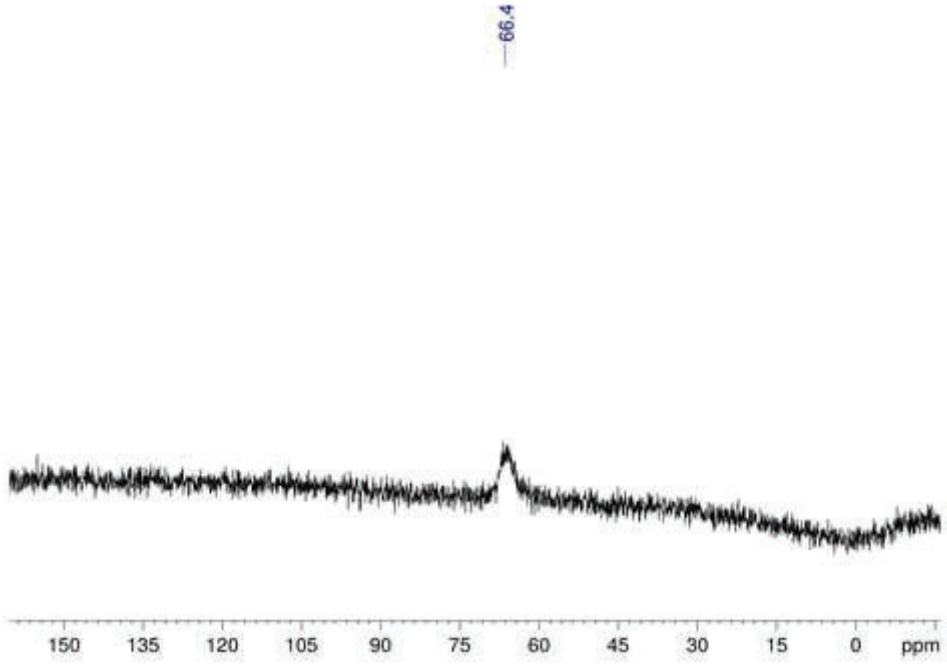

Figure S27. $^{11}B\{^{1}H\}$ NMR spectrum (96 MHz) of compound [Tp^{tBu,Me}Nd(NC$_6$H$_3$*i*Pr$_2$-2,6)(AlMe$_3$)] (**3-Nd**) in C$_6$D$_6$ at 26 °C.

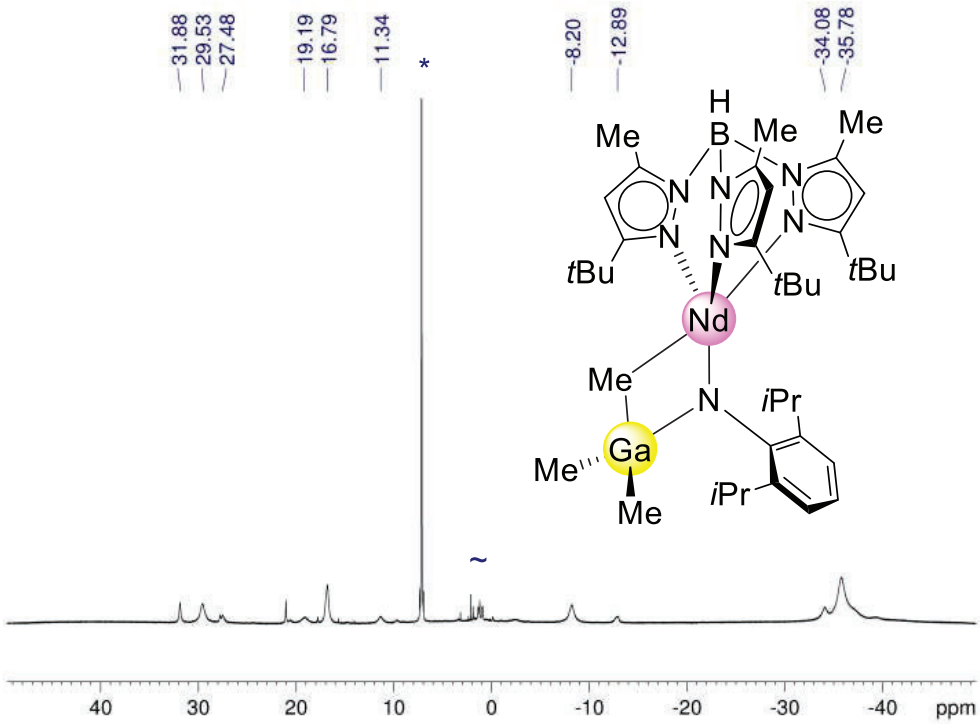

Figure S28. ^{1}H NMR spectrum (400 MHz) of compound [Tp^{tBu,Me}Nd(NC$_6$H$_3$*i*Pr$_2$-2,6)(GaMe$_3$)] (**4-Nd**) in C$_6$D$_6$ at 26 °C. Minor impurities are marked with (~).

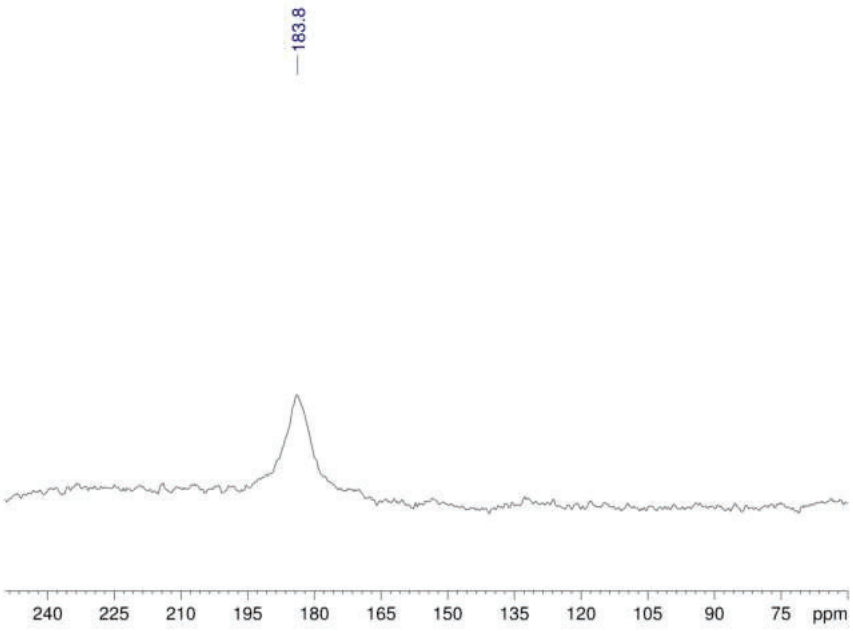

Figure S29. $^{11}B\{^{1}H\}$ NMR spectrum (96 MHz) of compound [Tp^{tBu,Me}Nd(NC$_6$H$_3$*i*Pr$_2$-2,6)(GaMe$_3$)] (**4-Nd**) in C_6D_6 at 26 °C.

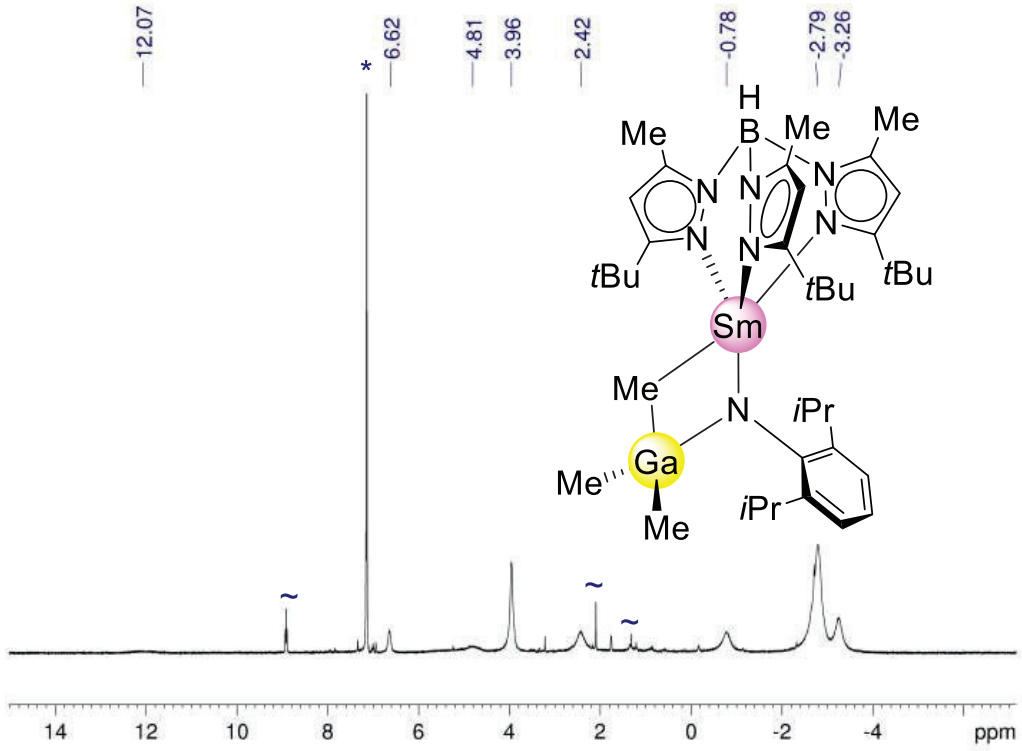

Figure S30. ^{1}H NMR spectrum (400 MHz) of compound [Tp^{tBu,Me}Sm(NC$_6$H$_3$*i*Pr$_2$-2,6)(GaMe$_3$)] (**4-Sm**) in C_6D_6 at 26 °C.

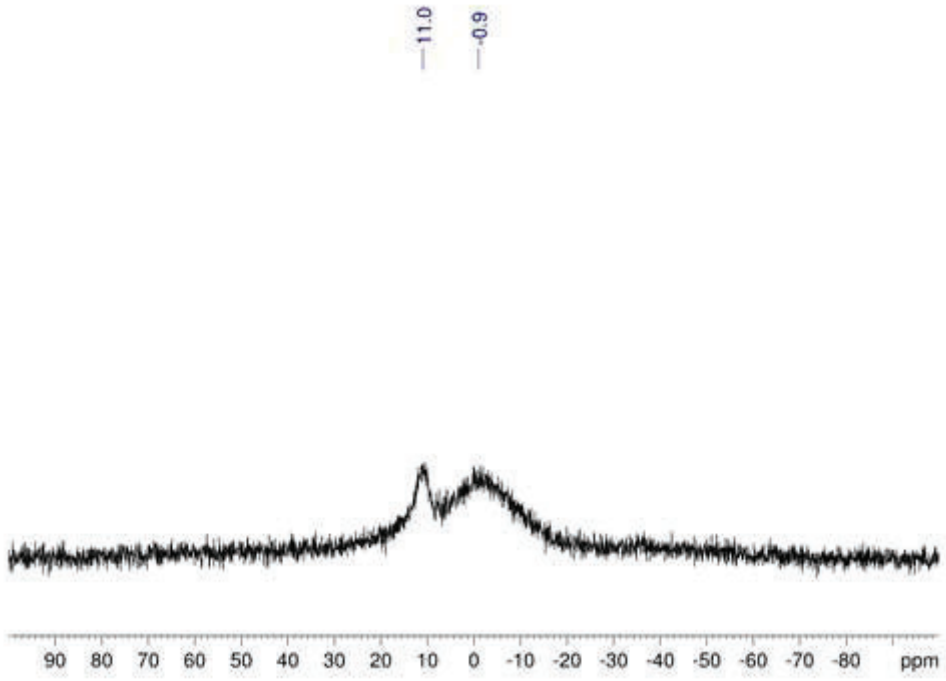

Figure S31. $^{11}B\{^{1}H\}$ NMR spectrum (96 MHz) of compound [Tp^{tBu,Me}Sm(NC$_6$H$_3$*i*Pr$_2$-2,6)(GaMe$_3$)] (**4-Sm**) in C_6D_6 at 26 °C

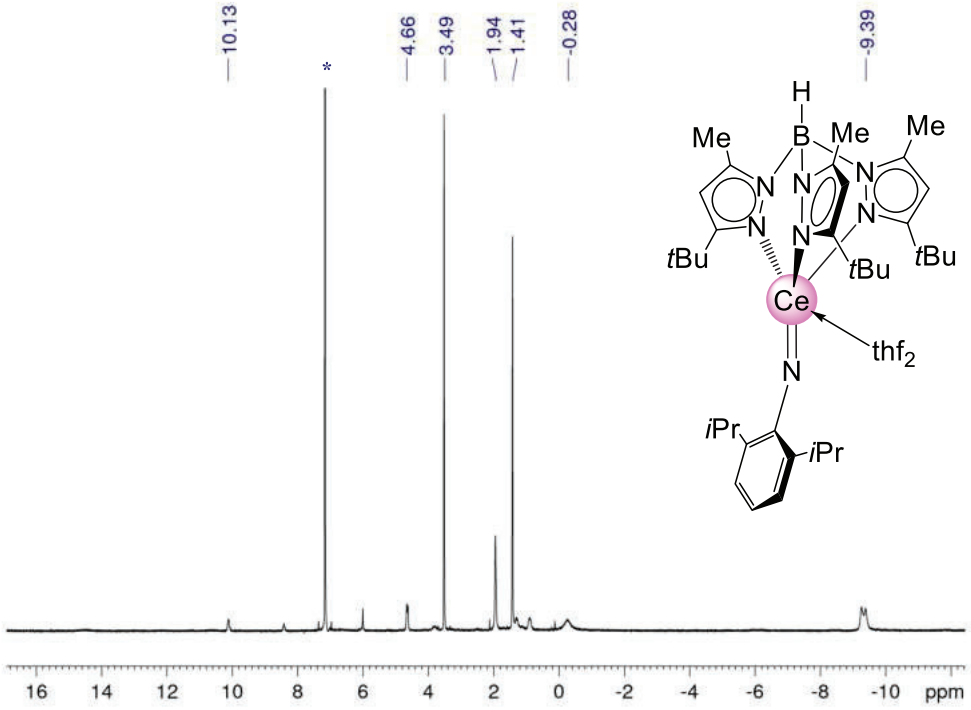

Figure S32. ^{1}H NMR spectrum (400 MHz) of compound [Tp^{tBu,Me}Nd(NC$_6$H$_3$*i*Pr$_2$-2,6)(thf)$_2$] (**5-Nd**) in C_6D_6 at 26 °C.

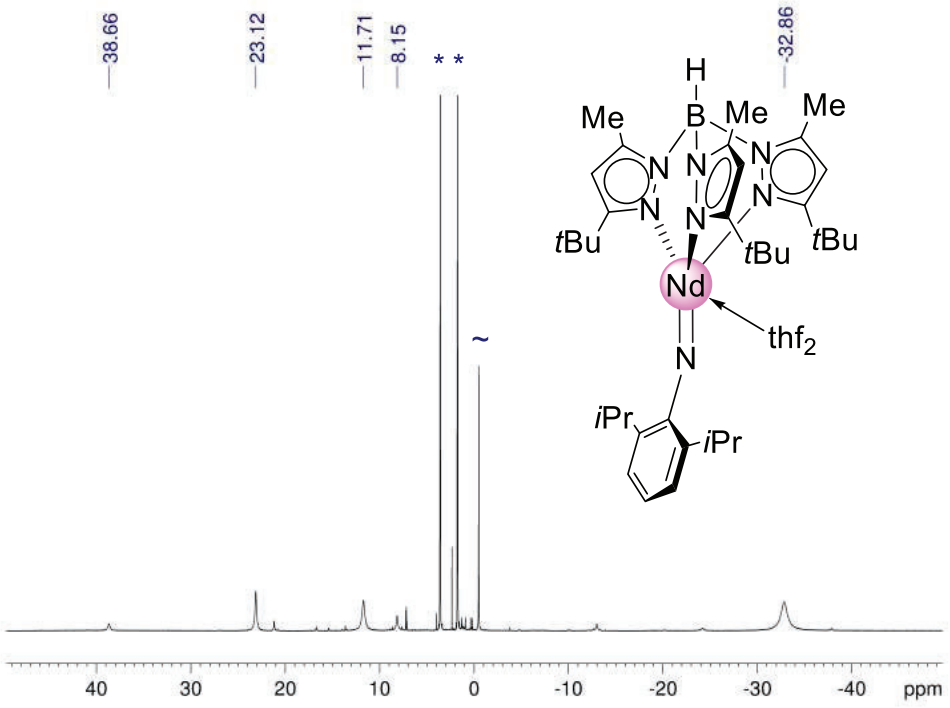

Figure S33. ^{1}H NMR spectrum (400 MHz) of compound [Tp^{tBu,Me}Nd(NC$_6$H$_3$*i*Pr$_2$-2,6)(thf)$_2$] (**5-Nd**) in [D$_8$]thf at 26 °C. Remaining GaMe$_3$ is marked with (~).

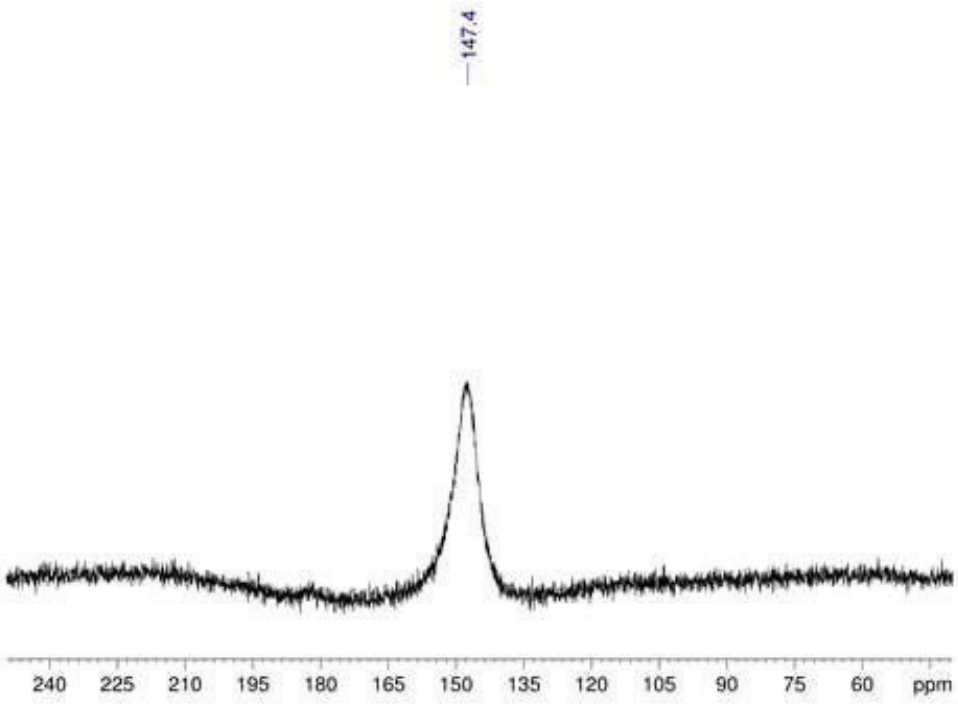

Figure S34. ^{11}B{^{1}H} NMR spectrum (96 MHz) of compound [Tp^{tBu,Me}Nd(NC$_6$H$_3$*i*Pr$_2$-2,6)(thf)$_2$] (**5-Nd**) in C$_6$D$_6$ at 26 °C.

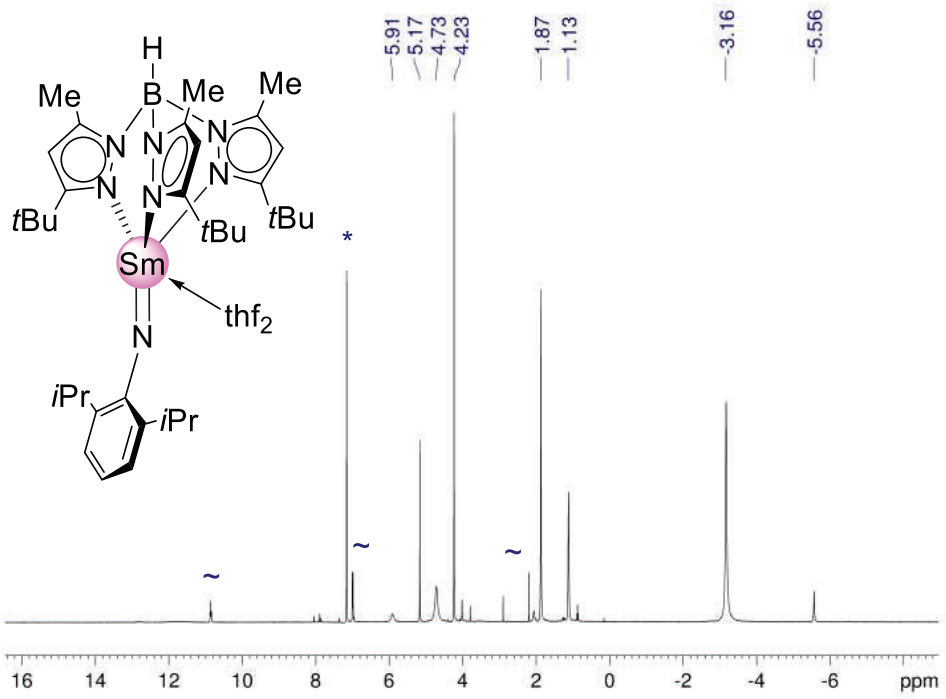

Figure S35. ^{1}H NMR spectrum (400 MHz) of compound [Tp^{tBu,Me}Sm(NC$_6$H$_3$*i*Pr$_2$-2,6)(thf)$_2$] (**5-Sm**) in C$_6$D$_6$ at 26 °C. Minor impurities are marked with (~). .

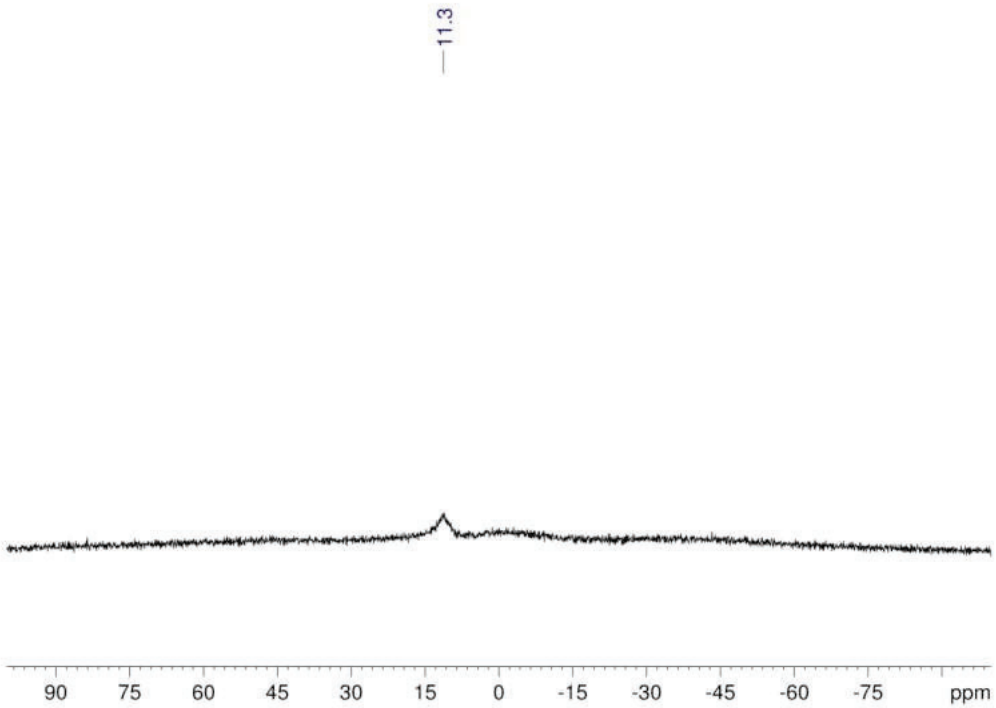

Figure S36. ^{11}B{^{1}H} NMR spectrum (96 MHz) of compound [Tp^{tBu,Me}Sm(NC$_6$H$_3$*i*Pr$_2$-2,6)(thf)$_2$] (**5-Sm**) in C$_6$D$_6$ at 26 °C.

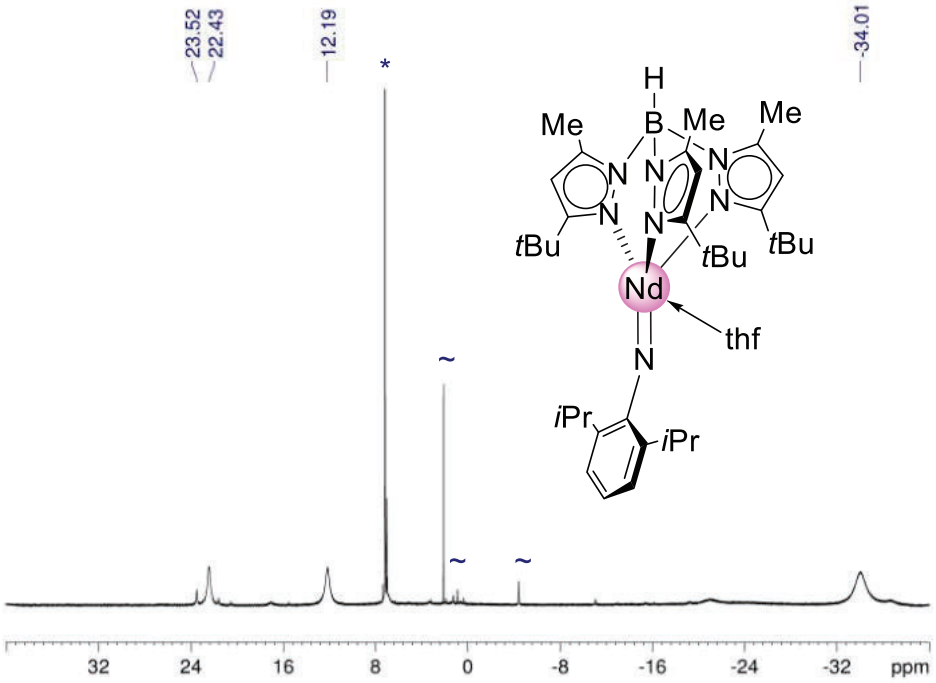

Figure S37. ^{1}H NMR spectrum (400 MHz) of compound [Tp^{tBu,Me}Nd(NC$_6$H$_3$*i*Pr$_2$-2,6)(thf)] (**6-Nd**) in C$_6$D$_6$ at 26 °C. Minor impurities are marked with (~).

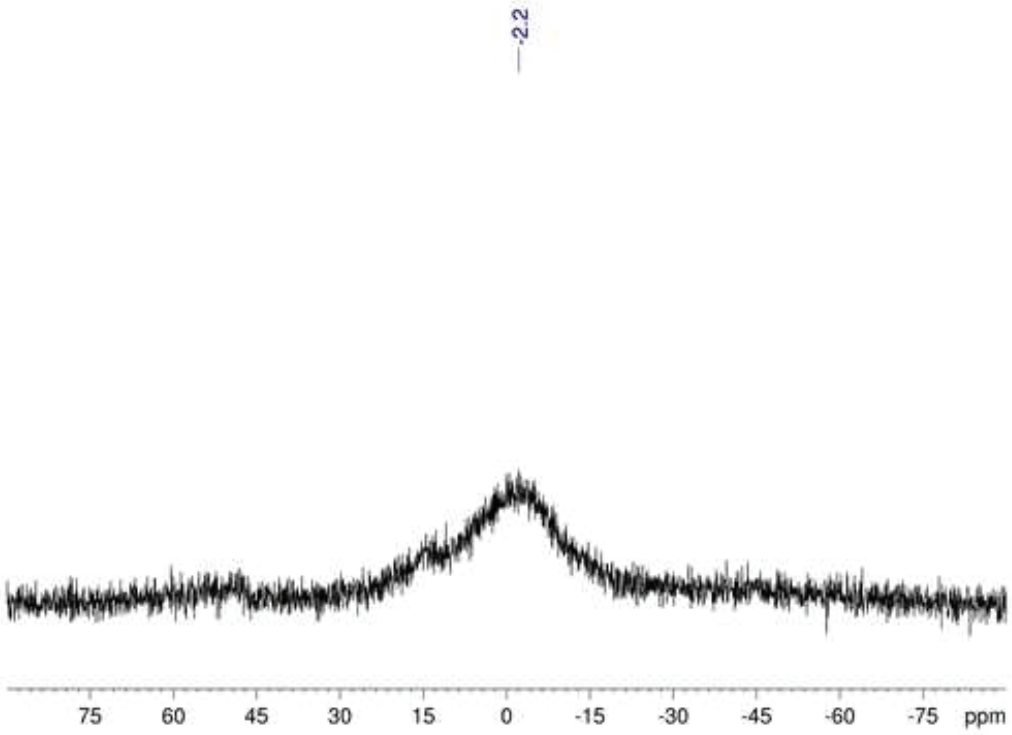

Figure S38. ^{11}B{^{1}H} NMR spectrum (96 MHz) of compound [Tp^{tBu,Me}Nd(NC$_6$H$_3$*i*Pr$_2$-2,6)(thf)] (**6-Nd**) in C$_6$D$_6$ at 26 °C.

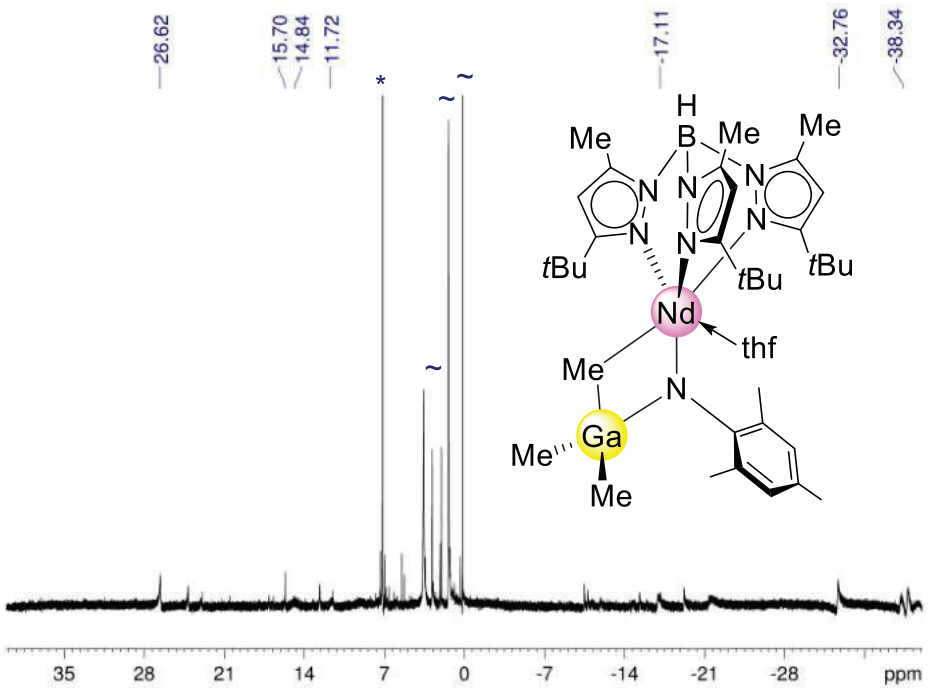

Figure S39. ^{1}H NMR spectrum (400 MHz) of compound [Tp^{tBu,Me}Nd(NC$_6$H$_2$Me$_3$-2,4,6)(GaMe$_3$)(thf)] (**7-Nd**) in C_6D_6 at 26 °C. Minor impurities are marked with (~).

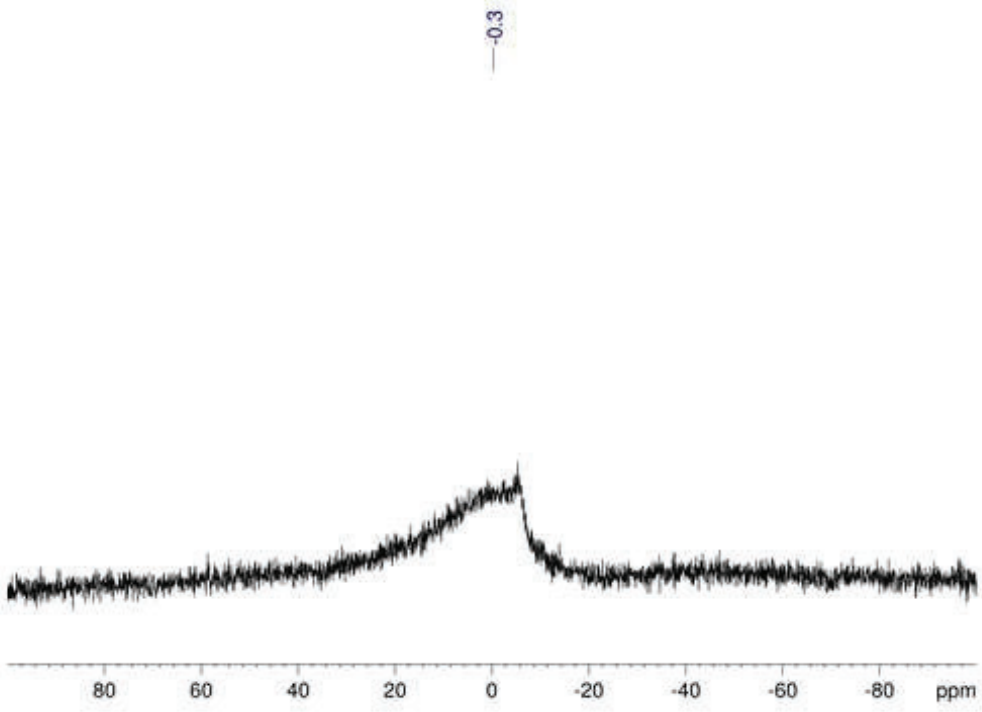

Figure S40. $^{11}B\{^{1}H\}$ NMR spectrum (96 MHz) of compound [Tp^{tBu,Me}Nd(NC$_6$H$_2$Me$_3$-2,4,6)(GaMe$_3$)(thf)] (**7-Nd**) in C_6D_6 at 26 °C

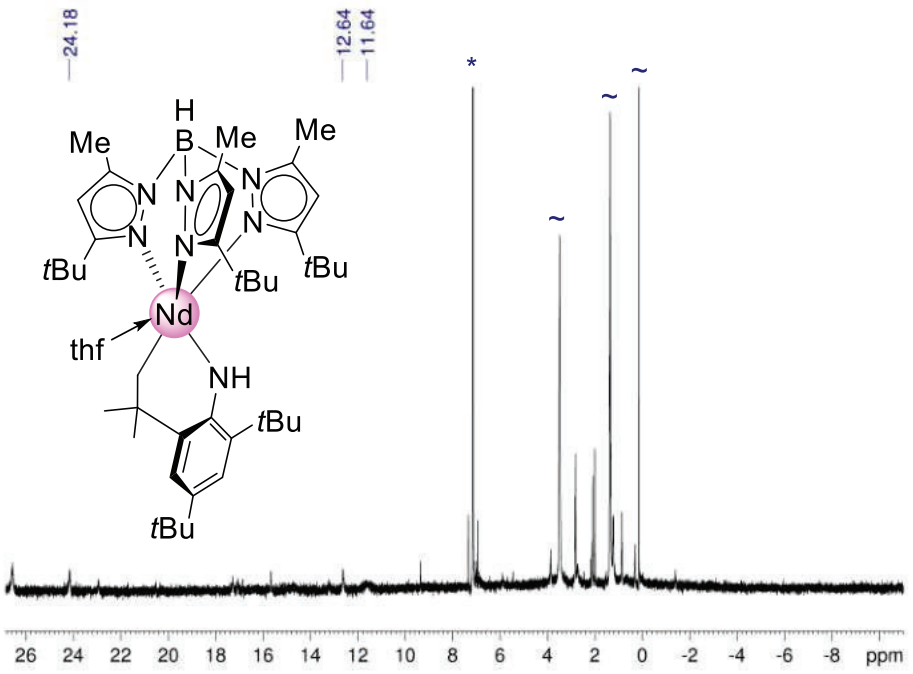

Figure S41. ^{1}H NMR spectrum (400 MHz) of compound [Tp^{tBu,Me}Nd{HN($C_6H_2tBu_2$-2,4-(CMe_2CH_2)-6}(thf)] (**8-Nd**) in C_6D_6 at 26 °C. Minor impurities are marked with (~). .

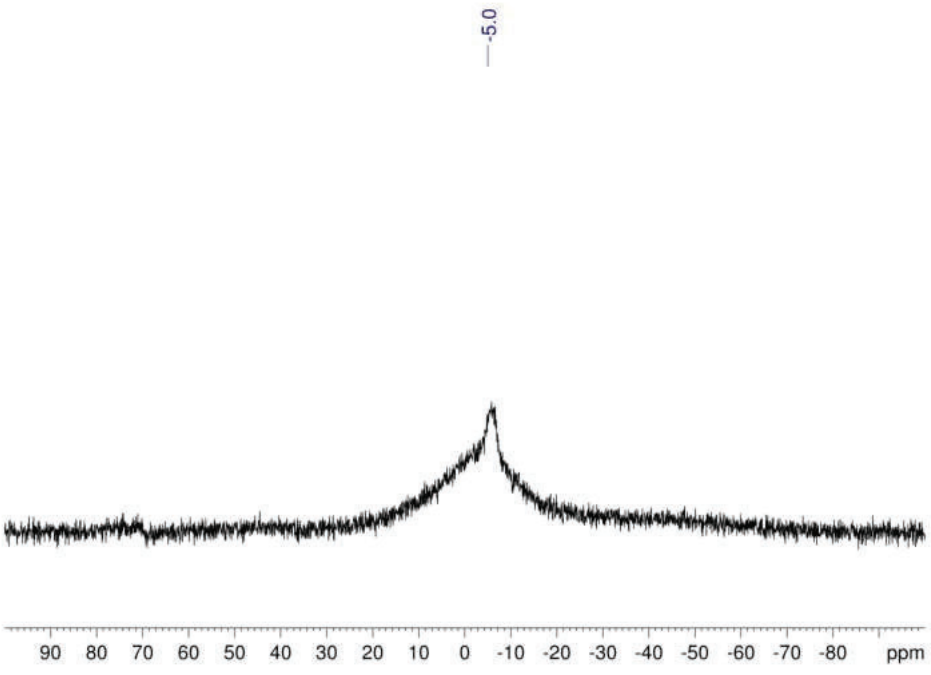

Figure S42. $^{11}B\{^{1}H\}$ NMR spectrum (96 MHz) of compound [Tp^{tBu,Me}Nd{HN($C_6H_2tBu_2$-2,4-(CMe_2CH_2)-6}(thf)] (**8-Nd**) in C_6D_6 at 26 °C.

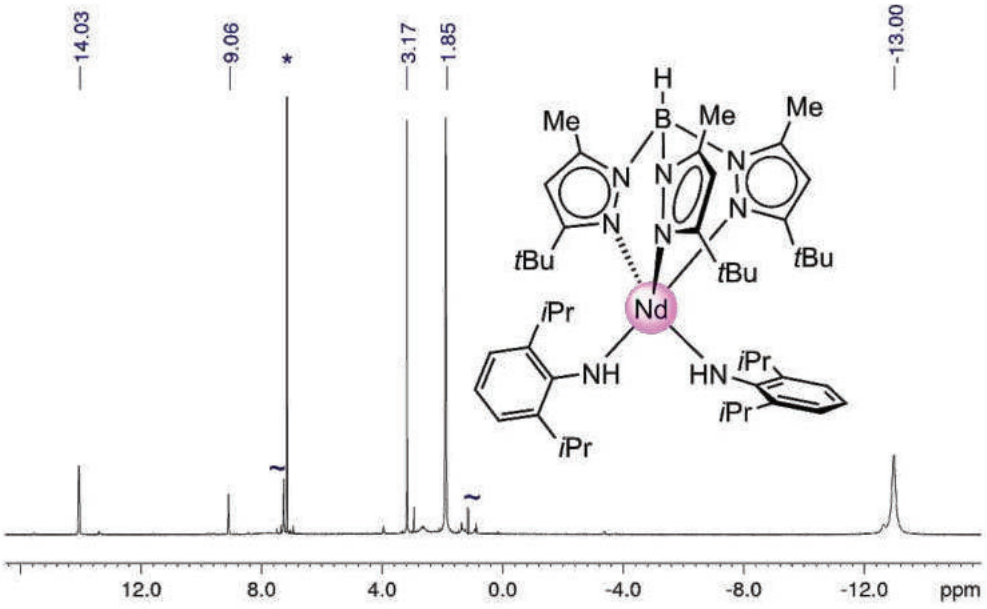

Figure S43. ^{1}H NMR spectrum (400 MHz) of compound [Tp^{tBu,Me}Nd{HN(C$_6$H$_2$*i*Pr$_2$-2,6)$_2$}] (**9-Nd**) in C$_6$D$_6$ at 26 °C. Minor impurities are marked with (~).

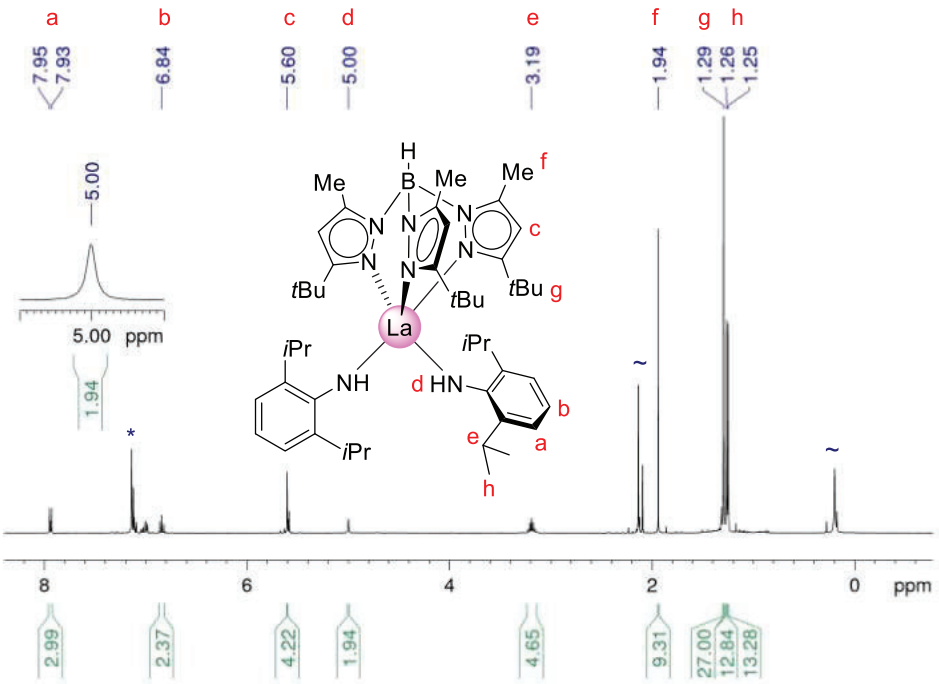

Figure S44. ^{1}H NMR spectrum (400 MHz) of compound [Tp^{tBu,Me}La{HN(C$_6$H$_2$*i*Pr$_2$-2,6)$_2$}] (**9-La**) in C$_6$D$_6$ at 26 °C. Inconclusive signals are marked with (~).

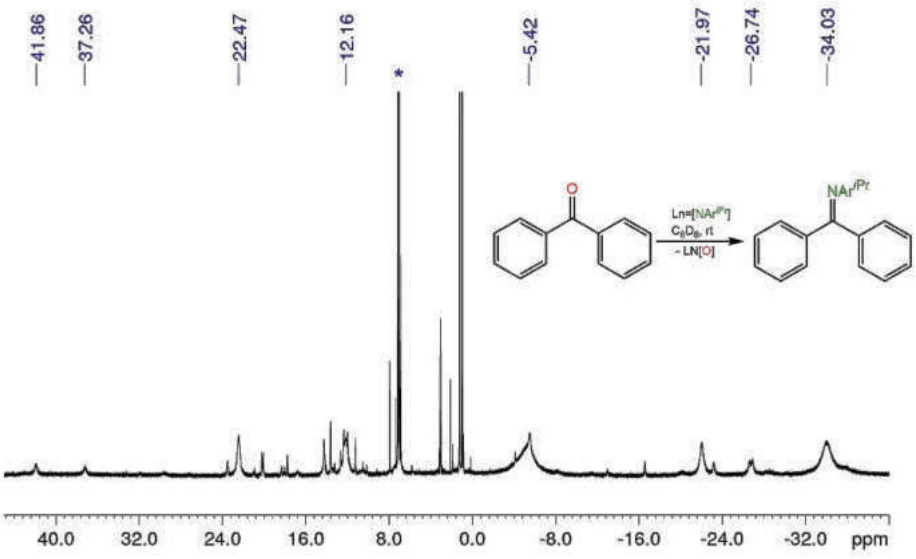

Figure S45. ^{1}H NMR spectrum (400 MHz) of NMR-scale reaction of **5-Nd** with benzophenone in C_6D_6 at 26 °C.

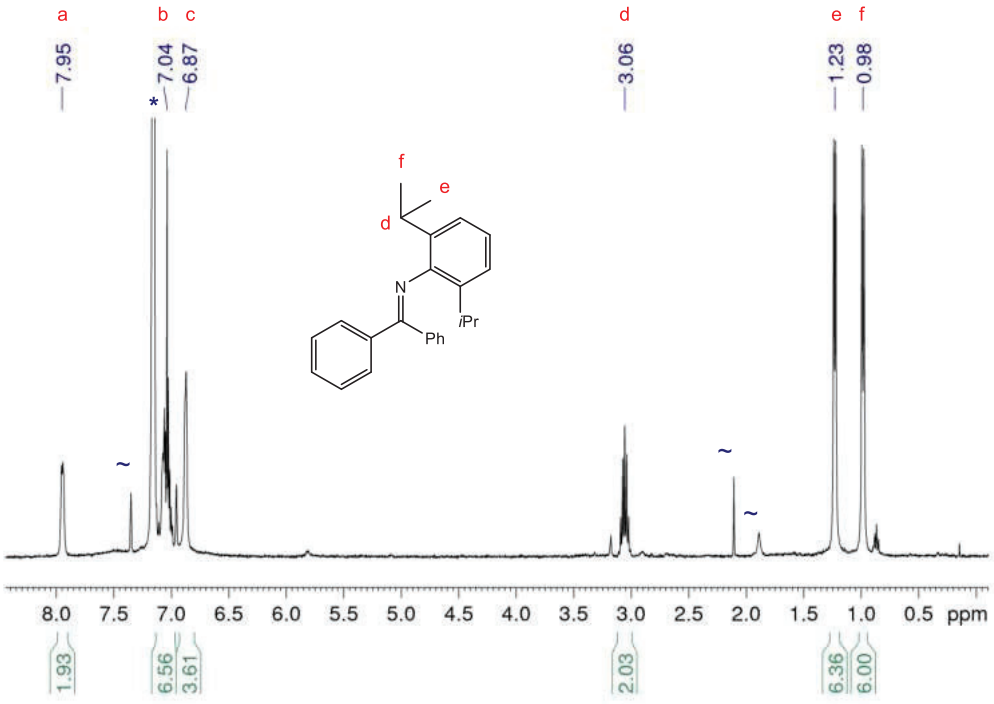

Figure S46. Close-up ^{1}H NMR spectrum (400 MHz) of imine [$Ph_2C{=}N(C_6H_2iPr_2$-2,6)] in C_6D_6 at 26 °C. Non belonging signals are marked with (~), signals a, b, and c belong to aromatic protons.

Experiments with Deuterated Substrates

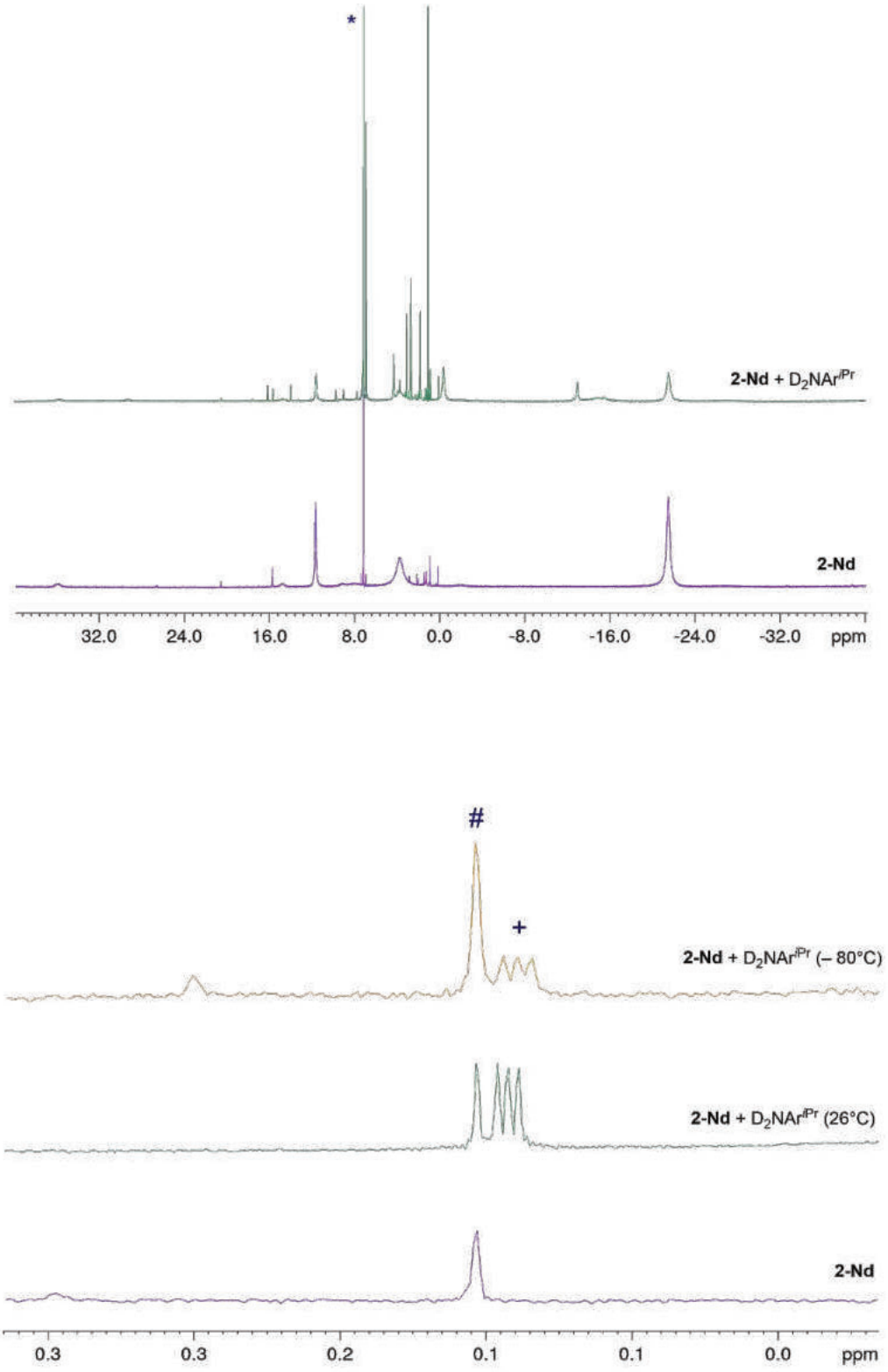

Figure S47. ^{1}H NMR spectra (400 MHz) of compound $[Tp^{tBu,Me}Nd\{(\mu_3\text{-}CH_2)[(\mu_2\text{-}Me)GaMe_2]_2\}]$ (**2-Nd**, purple) in C_6D_6 at 26 °C; reaction of **2-Nd** with D_2NAr^{iPr} in C_6D_6 at 26 °C (green) and in [D_8]toluene at – 80 °C (orange). (#) denotes CH_4 and (+) belongs to CH_3D.

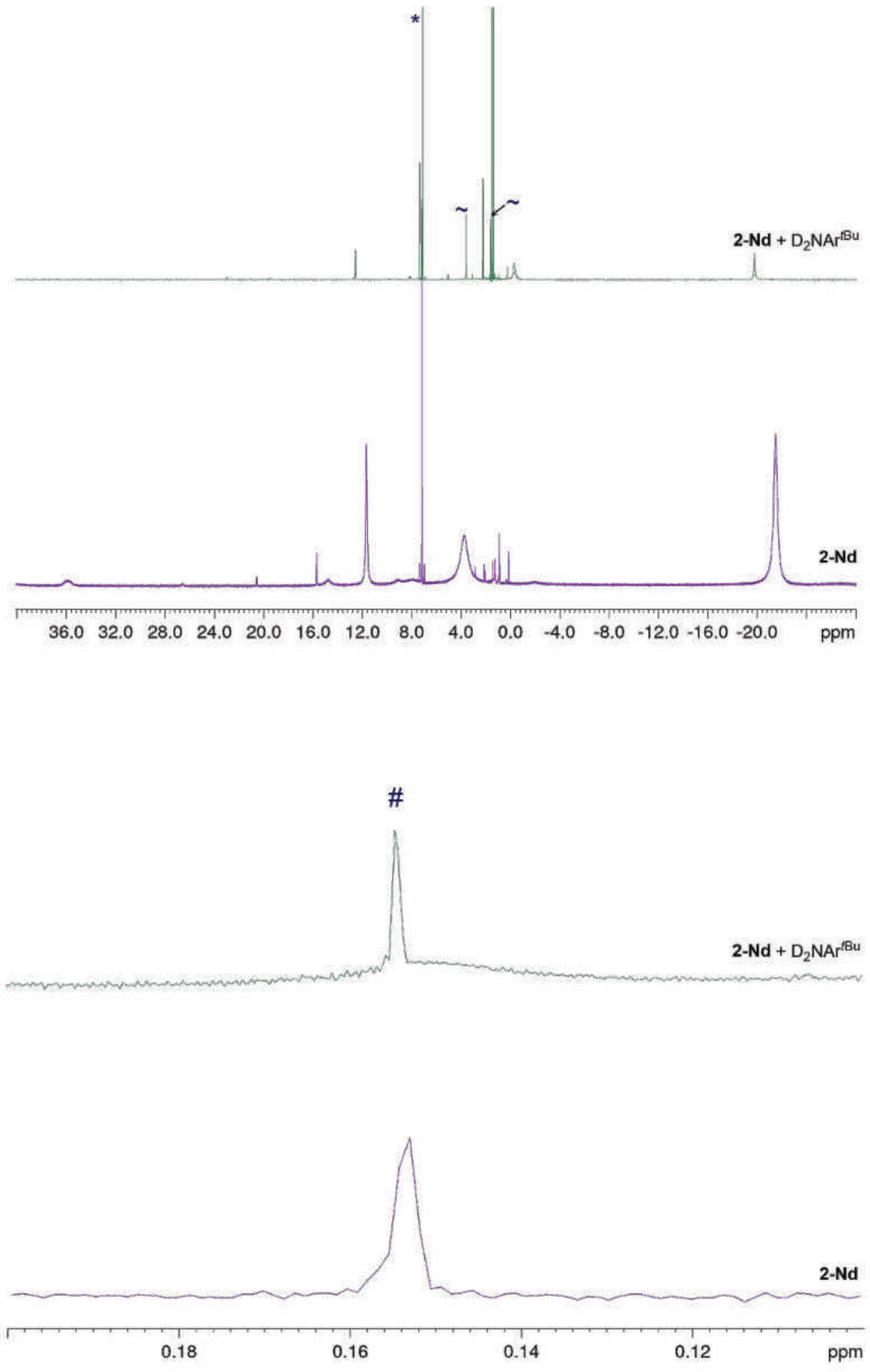

Figure S48. ^{1}H NMR spectra (400 MHz) of compound [Tp^{tBu,Me}Nd{(μ_3-CH$_2$)[(μ_2-Me)GaMe$_2$]$_2$}] (**2-Nd**, purple) in C_6D_6 at 26 °C; the reaction of **2-Nd** with D$_2$Nar^{tBu} in C_6D_6 at 26 °C (green). (#) denotes CH_4 and (~) belongs to [D_8]THF.

References

1. COSMO, v. 1.61; Bruker AXS Inc.: Madison, WI, **2012**.
2. APEX 3, V. 2017.3-0, Bruker AXS Inc., Madison, WI, **2017**.
3. SAINT, v. 8.34A; Bruker AXS Inc., Madison, WI, **2017**.
4. Krause, L.; Herbst-Irmer, R.; Sheldrick, G. M.; Stalke, D., SADABS – Comparison of silver and molybdenum microfocus X-ray sources for single-crystal structure determination. *J. Appl. Cryst.* **2015**, *48*, 3-10.
5. Sheldrick, G. M., SHELXTL – Integrated space-group and crystal-structure determination. *Acta Cryst.* **2015**, *A71*, 3–8.
6. Hübschle, C. B.; Sheldrick, G. M.; Dittrich, B., ShelXle: a Qt graphical user interface for ShelXle. *J. Appl. Cryst.* **2011**, *44*, 1281-1284.
7. Kratzert, D.; Holstein, J. J.; Krossing, I., DSR: enhanced modelling and refinement of disordered structures with SHELXL. *J. Appl. Cryst.* **2015**, *48*, 933-938.
8. Farrugia, L. J., ORTEP-3 for Windows – a version of ORTEP-III with a Graphical User Interface (GUI). *J. Appl. Cryst.* **1997**, *30*, 565-566.
9. POV-Ray v. 3.6; Persistence of Vision Pty. Ltd.: Williamstown, Victoria, Australia, **2004**. http://www.povray.org/.

Paper II

A Terminal Yttrium Phosphinidene

https://doi.org/10.1021/jacs.3c04335
reprinted with permission from
J. Am. Chem. Soc. **2023**, *145*, 32, 17720 – 17733

JACS
JOURNAL OF THE AMERICAN CHEMICAL SOCIETY
pubs.acs.org/JACS
Article

A Terminal Yttrium Phosphinidene

Theresa E. Rieser, Philipp Wetzel, Cäcilia Maichle-Mössmer, Peter Sirsch,* and Reiner Anwander*

Cite This: J. Am. Chem. Soc. 2023, 145, 17720−17733

Read Online

ACCESS | Metrics & More | Article Recommendations | Supporting Information

ABSTRACT: Terminal, nondirectional ionic "multiple" bond interactions between group 15 elements and rare-earth metals (Ln) have remained a challenging target until present. Although reports on terminal imide species have accumulated in the meantime, examples of terminal congeners with the higher homologue phosphorus are yet elusive. Herein, we present the synthesis of the first terminal yttrium organophosphinidene complex, $Tp^{tBu,Me}Y(=PC_6H_3iPr_2\text{-}2,6)(DMAP)_2$, according to a double-deprotonation sequence previously established for organoimides of the smaller rare-earth metals. Subsequent deprotonation of the primary phosphane $H_2PC_6H_3iPr_2\text{-}2,6$ (H_2PAr^{iPr}) with discrete dimethyl compound $Tp^{tBu,Me}YMe_2$ in the presence of DMAP under simultaneous methane elimination generated a terminal multiply bonded phosphorus. The primary phosphide intermediates $Tp^{tBu,Me}YMe(HPAr^{iPr})$ and $Tp^{tBu,Me}YMe(HNPAr^{iPr})(DMAP)$ are isolable species and were also obtained and fully characterized for holmium and dysprosium. The Lewis acid-stabilized yttrium phosphinidene $Tp^{tBu,Me}Y[(\mu_2\text{-}PAr^{iPr})(\mu_2\text{-}Me)AlMe_2]$ was obtained by treatment of H_2PAr^{iPr} with $Tp^{tBu,Me}YMe(AlMe_4)$ but could not be converted into a terminal phosphinidene via cleavage of trimethylaluminum. The corresponding reaction of H_2PAr^{iPr} with $Tp^{tBu,Me}YMe(GaMe_4)$ led to adduct $[GaMe_3(PH_2Ar^{iPr})]$ rather than to the formation of a yttrium phosphinidene. The yttrium−phosphorus interaction in the obtained organophosphide and phosphinidene complexes was scrutinized by $^{31}P/^{89}Y$ NMR spectroscopy and DFT calculations, unambiguously supporting the existence of multiple bonding.

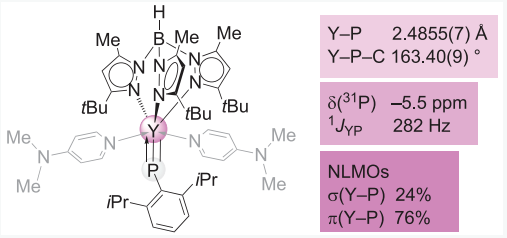

INTRODUCTION

The limited accessibility and stability of molecular compounds with unsupported rare-earth-metal (Ln)−phosphorus bonds ($Ln-PR_x$) are generally ascribed to a considerable hard/soft mismatch according to Pearson's HSAB concept.[1] On the other hand, it has been hypothesized that soft phosphorus donors might engage in enhanced covalent bonding to the rare-earth metals.[2] Naturally, the hard/soft mismatch is particularly pronounced for entities of type ($Ln^{III} \leftarrow PR_3$) with neutral terminal phosphines (Chart 1, **A**).[3] In the meantime, a significant number of Ln^{II}/Ln^{III} complexes bearing monoanionic organophosphido (phosphanido) ligands, that is $Ln-PR_2$ moieties (**B** and **C**) have been accessed,[2,4] cotriggered by their relevance for catalytic reactions like the hydrophosphination of alkenes.[5] The first structurally characterized terminal phosphines, as well as bridged and terminal unsupported phosphanides, comprise $(C_5Me_5)_2YbCl(PMe_2CH_2PMe_2)$,[6] $(C_5H_5)_2Lu(\mu\text{-}PPh_2)_2Li(TMEDA)$ (TMEDA = tetramethylethylenediamine),[7] and $La\{N(SiMe_3)_2\}_2(PPh_2)(OPPh_3)_2$.[8] Primary phosphanides have been mainly identified with $[Ln-(\mu\text{-}PHR)-Ln/M]$ bridged motifs (**B**),[5a,9] but a few [Ln−PHR] terminal variants (**C**) have also emerged.[10]

Crucially, such terminal primary phosphanides are considered as potential precursors/intermediates en route to terminal rare-earth-metal phosphinidenes (phosphinidiides) [Ln = PR] (**E**).[11−14] This synthesis approach is geared to the deprotonation protocols, which have been most successfully applied for accessing terminal rare-earth-metal imides [Ln = NR].[15,16] The latter terminal imide synthesis draws on intramolecular alkane/methane elimination from $[Ln(NHR)(CH_3)]$ entities in the presence of strong donor molecules.[16] Analogous $[Sc(PHR)(CH_3)]$ have been isolated[17] or are assumed intermediates toward terminal phosphinidenes.[11,12,14] However, the isolation of terminal scandium phosphinidenes (**E**-type) proved difficult and was hampered by the high bridging tendency of such dianionic ligands (**D**-type), ate complexation,[11] ancillary ligand activation,[14,18] and otherwise divergent reaction pathways.[17,19]

Overall, in contrast to d-transition metal chemistry,[20] only a few discrete rare-earth-metal phosphinidene complexes have been structurally identified. The prevalent structural motifs are **D**-type bridging[11,12,21−23] and metathesis-salt-coordinated Ln=P fragments.[11] In 2008, Kiplinger et al. reported the first rare-earth-metal phosphinidene complex, $[(PNP^{iPr})Lu(\mu\text{-}PMes)]_2$, by the utilization of lutetium neosilyl complex $(PNP^{iPr})Lu(CH_2SiMe_3)_2$ (PNP^{iPr} = $N(C_6H_3PiPr_2\text{-}2\text{-}Me\text{-}4)_2$) and deprotonation of the monophosphane H_2PAr^{Mes} (Ar^{Mes} = $C_6H_2Me_3\text{-}2,4,6$) (Chart 1, **I**, Table 1).[21] Applying the same

Received: April 26, 2023
Published: August 2, 2023

https://doi.org/10.1021/jacs.3c04335
J. Am. Chem. Soc. 2023, 145, 17720−17733

Chart 1. (Top) Ln−P Interactions in Organometallics[a] and (Bottom) Selected Examples of Bridging and Terminal Rare-Earth-Metal Organophosphinidene Complexes

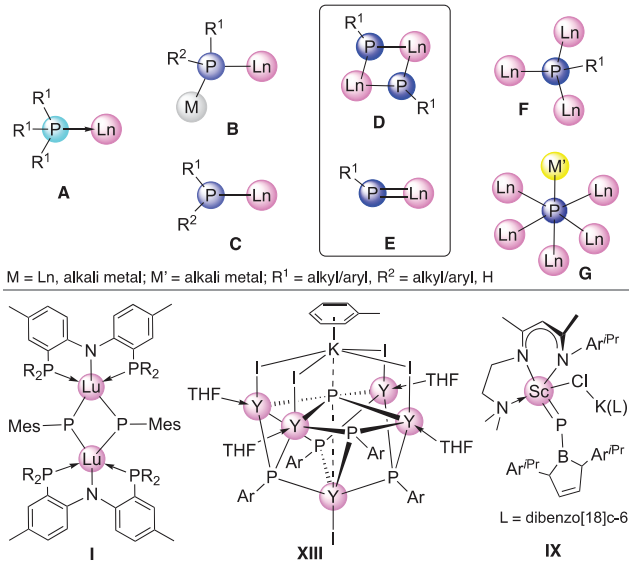

[a]Terminal organophosphine (**A**), terminal and bridging organophosphides (**B** and **C**), terminal and bridging organophosphinidenes (**D**, **E**, and **F**), and bridging parent phosphide (**G**).

pincer-PNP ligand, the Mindiola group isolated dimeric $[(PNP^{iPr})Sc(\mu\text{-PTrip})]_2$ (Trip = $C_6H_2iPr_3$-2,4,6; **II**, Table 1) and ate complexes $(PNP^{iPr})Sc(=PTrip)(LiBr)(DME)_x$ (x = 0, 1; **III** and **IV**, Table 1).[11] Chen and co-workers employed similar methane elimination protocols for the synthesis of bulky β-diketiminato ("nacnac")-supported bridged phosphinidenes $[(nacnac)Sc(\mu\text{-}PC_6H_3Me_2\text{-}2,6)]_2$ (**V**, Table 1) and $[(nacnac)Sc(\mu\text{-}PC_6H_3Me_2\text{-}2,6)(DMAP)]_2$ (DMAP = *N*,*N*-dimethyl-4-aminopyridine; **VI**, Table 1).[12] Unfortunately, such dimeric phosphinidenes could not be cleaved, and they were stabilized using Lewis bases (e.g., THF and DMAP). More recently, the same group succeeded in obtaining the first monomeric scandium and lutetium phosphinophosphinidene complexes (**VII** and **VIII^{Ln}**, Table 1),[24] and the first terminal boronylphosphinidene complex (Chart 1, **IX**, Table 1).[25] Also in 2008, the group of Chen could access the bridging neodymium phosphinidene complex $[(THF)_3NdI(\mu\text{-}PC_6H_3iPr_2\text{-}2,6)]_2$ (**X**, Table 1) from $NdI_3(THF)_{3.5}$ and 2 equiv of $K[P(C_6H_3iPr_2\text{-}2,6)(SiMe_3)]$.[22] Two years later, the only other examples of early lanthanide phosphinidene complexes, $[(C_5Me_5)Nd(\mu\text{-}PC_6H_3iPr_2\text{-}2,6)(THF)]_2$ and $[Tp^{Ph}Nd(\mu\text{-}PC_6H_3iPr_2\text{-}2,6)(THF)]_2$ (**XI** and **XII**, Table 1), have been obtained by subsequent salt metatheses.[23] Noteworthy, the reaction of preisolated organophosphide $YI_2[P(C_6H_3iPr_2\text{-}2,6)(SiMe_3)](THF)_3$ with primary phosphanide $K[PH(C_6H_3iPr_2\text{-}2,6)]$ resulted in extensive phosphido ligand degradation and formation of the phosphido/phosphinidene cluster $[Y_5I(THF)_4(\mu_3\text{-}PC_6H_3iPr_2\text{-}2,6)_4(\mu_6\text{-}P)(\mu\text{-}I)K(toluene)]$ (Chart 1, **G**-type, **XIII**, Table 1).[26]

Homometallic trinuclear phosphinidene cluster $[LLn(\mu\text{-}Me)]_3(\mu_3\text{-}Me)(\mu_3\text{-}PPh)$ (**XIV^{Ln}**, **F**-type, Ln = Y, Lu; L = bulky benzamidinato $PhC(NC_6H_4iPr_2\text{-}2,6)_2$) was obtained by Zhou, Luo, Zhang, and co-workers via protonolysis of the respective methylidene complex.[27] The heterometallic anionic clusters $[\{(C_5H_4Me)_2Ln\}_3(\mu\text{-}PMes)_3Li][Li(THF)_4]_2$ (**XV^{Ln}**, Ln = Y, Dy) were accessed via a deprotonation sequence starting from primary phosphine adduct $(C_5H_4Me)_3Ln(PH_2Mes)$.[28] Finally, in 2020, Hohloch et al. referred to a transient, terminal anionic lanthanum phosphinidene complex, $[(PN)_2La(=PMes)][K(L)]$ (PN = N(Mes)$[C_6H_3(PiPr_2)$-2-Me-4]; L = 18-c-6 or 2.2.2-crypt) verified by theoretical calculations and reactivity tests.[13] Previous studies emphasize the distinct stability and reactivity of [Ln=NR] versus [Ln=PR] moieties as revealed by strongly divergent synthesis protocols for imide and phosphinidene complexes, respec-

Table 1. Selected Metrical Parameters in Terminal and Bridging Rare-Earth-Metal Phosphinidene Complexes[a]

compound	CN	Ln−P−C_{ipso} [°]	Ln−$P_{Phosphinidene}$ [Å]	ref
$Tp^{tBu,Me}Y[(\mu_2\text{-}PC_6H_3iPr_2\text{-}2,6)(\mu_2\text{-}Me)AlMe_2]$ (**3-Y^{Al}**)[b]	5	155.94(8)	2.5297(7)	this work
$Tp^{tBu,Me}Y(=PC_6H_3iPr_2\text{-}2,6)(DMAP)_2$ (**6-Y**)	7	163.40(9)	2.4855(7)	this work
$[(PNP^{iPr})Lu(\mu_2\text{-}PAr^{Mes})]_2$ (**I**)[c]	5	118.40(13)−141.50(18)	2.5973(15)−2.6724(14)	21
$[(PNP^{iPr})Sc(\mu_2\text{-}PTrip)]_2$ (**II**)[c]	5	131.28(10)/133.87(10)	2.5446(8)−2.5527(10)	11
$(PNP^{iPr})Sc[(\mu_2\text{-}PAr^{Mes})(\mu_2\text{-}Br)Li]$ (**III**)[b]	5	162.4(2)	2.338(2)	11
$(PNP^{iPr})Sc[(\mu_2\text{-}PAr^{Mes})(\mu_2\text{-}Br)Li(DME)]$ (**IV**)[b]	5	155.2(2)	2.3732(18)	11
$[L^1Sc(\mu_2\text{-}PC_6H_3Me_2\text{-}2,6)]_2$ (**V**)[c]	4	121.15(11)−135.86(11)	2.522(1)/2.528(1)	12
$[L^1Sc(\mu_2\text{-}PC_6H_3Me_2\text{-}2,6)(DMAP)]_2$ (**VI**)[c]	4	119.79(12)/127.42(13)	2.540(1)/2.589(1)	12
$L^2Sc\text{−}P\text{−}P(N_2Ar^{iPr}_2\text{-}2,5\text{-}C_2H_4)(THF)$ (**VII**)[d]	5		2.448(1)	24
$L^3Ln\text{−}P\text{−}P(N_2Ar^{iPr}_2\text{-}2,5\text{-}C_2H_4)(THF)$ (**VIII^{Sc}/VIII^{Lu}**)[d]	6		2.484(1)/2.608(1)	24
$L^3Sc[=PB(N_2Ar^{iPr}_2\text{-}2,5\text{-}C_2H_2)](\mu_2\text{-}Cl)K(L^4)$ (**IX**)[e]	5	148.8(1)	2.381(1)	25
$[(THF)_3NdI(\mu\text{-}PC_6H_3iPr_2\text{-}2,6)]_2$ (**X**)[c]	6	127.29(17)/136.45(17)	2.7314(15)/2.7769(16)	22
$[(C_5Me_5)Nd(\mu\text{-}PC_6H_3iPr_2\text{-}2,6)(THF)]_2$ (**XI**)[c]	6	124.14(13)/128.82(14)	2.7456(11)/2.7827(10)	23
$[Tp^{Ph}Nd(\mu\text{-}PC_6H_3iPr_2\text{-}2,6)(THF)]_2$ (**XII**)[c]	6	127.67(19)/128.01(19)	2.7808(16)/2.7911(15)	23
$Y_5I(THF)_4(\mu_3\text{-}PC_6H_3iPr_2\text{-}2,6)_4(\mu_6\text{-}P)(\mu\text{-}I)K(tol)$ (**XIII**)[c]	5		2.6720(11)−2.9801(10)	26
$[L^5Y(\mu\text{-}Me)]_3(\mu_3\text{-}Me)(\mu_3\text{-}PPh)$ (**XIV^{Y}**)[c]	5		2.7142(11)−2.9432(12)	27
$[L^5Lu(\mu\text{-}Me)]_3(\mu_3\text{-}Me)(\mu_3\text{-}PPh)$ (**XIV^{Lu}**)[c]	5		2.6389(17)−2.902(2)	27
$[\{(C_5H_4Me)_2Y\}_3(\mu_3\text{-}PMes)_3Li][Li(THF)_4]_2$ (**XV^{Y}**)[c]	8		2.923(2)−2.954(2)	28
$[\{(C_5H_4Me)_2Dy\}_3(\mu_3\text{-}PMes)_3Li][Li(THF)_4]_2$ (**XV^{Dy}**)[c]	8		2.926(6)−2.951(6)	28

[a]L^1 = $N_2C_3HAr^{iPr}$-1-Me_2-2,4-$(C_2H_4NiPr_2)$-5. L^2 = $N_2C_3HAr^{iPr}_2$-1,5-Me_2-2,4. L^3 = $N_2C_3HAr^{iPr}$-1-Me_2-2,4-$(C_2H_4NMe_2)$-5. L^4 = dibenzo-18-crown-6. L^5 = $PhC(NC_6H_4iPr_2\text{-}2,6)_2$. [b]Heterometal-stabilized phosphinidene. [c]Bridging phosphinidene. [d]Phosphinophosphinidenes. [e]Boronylphosphinidene, Ln−P−B [°].

https://doi.org/10.1021/jacs.3c04335
J. Am. Chem. Soc. 2023, 145, 17720−17733

Scheme 1. Synthesis of the Group 13-Stabilized Y(III) Phosphinidene $Tp^{tBu,Me}Y(PC_6H_3iPr_2\text{-}2,6)AlMe_3$ (3-Y^{Al}), the Ln(III) Phosphides $Tp^{tBu,Me}LnMe(HPC_6H_3iPr_2\text{-}2,6)$ (4-Ln), the Lewis Base-Stabilized Phosphides $Tp^{tBu,Me}LnMe(HPC_6H_3iPr_2\text{-}2,6)(DMAP)$ (5-Ln), and the Terminal Phosphinidene $Tp^{tBu,Me}Y(=PC_6H_3iPr_2\text{-}2,6)(DMAP)_2$ (6-Y) via Deprotonation of the Primary Phosphine H_2PAr^{iPr} with the Bis(alkyl) Ln(III) Precursors 1-Ln and 2-Ln^M (Ln = Y, Dy, Ho; M = Al, Ga)

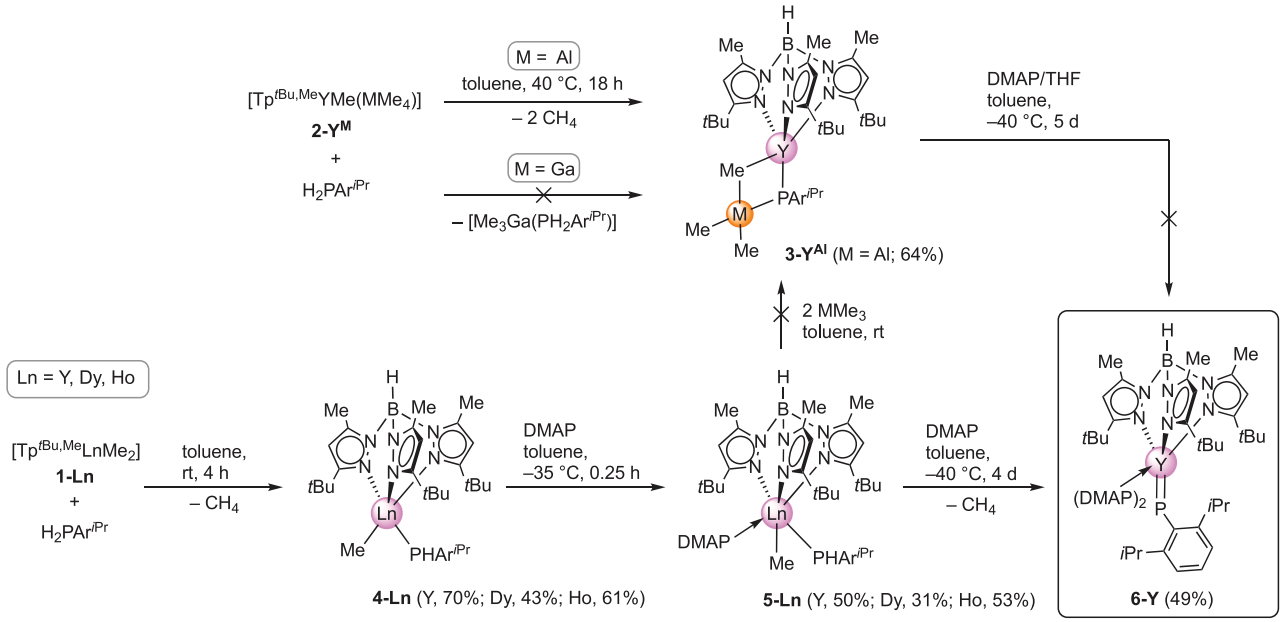

tively. The near inaccessibility of terminal rare-earth-metal phosphinidene compounds may have its origin in a thermodynamically unpreferred and therefore weak interaction between the metal and the phosphorus ligand.[29] However, the predominantly nondirectional ionic bond interactions of rare-earth-metal complexes might be gamed by kinetic stabilization via advanced synthesis protocols.

RESULTS AND DISCUSSION

Until today, terminal rare-earth-metal complexes bearing alkylidene or phosphinidene moieties have remained elusive whereas several examples of terminal rare-earth-metal imides and oxides have emerged, demonstrating the feasibility of multiple bonded ligands in the presence of a suitable ancillary ligand scaffold.[16,30−32] In this study, we present the first monomeric rare-earth-metal(III) phosphinidene complexes beyond scandium. The combined structural characterization and DFT analysis of a discrete terminal yttrium phosphinidene provide insight into the bonding characteristic of [Ln=NR] versus [Ln=PR] moieties.

The Ln(III) Bis(alkyl) Precursors. Recently, we reported on the synthesis of terminal lanthanide and group 3 imide complexes by exploiting the dimethyl lutetium complex $Tp^{tBu,Me}LuMe_2$ (**1-Lu**)[33] and the [$GaMe_3$]-capped dimethyl yttrium congener $Tp^{tBu,Me}YMe(GaMe_4)$ (**2-Y^{Ga}**), respectively.[16d] From these findings we hypothesized that the sterically demanding, monoanionic hydrotris(3-*tert*-butyl-5-methylpyrazolyl)borato ligand ($Tp^{tBu,Me}$) and the primary aromatic phosphine $H_2PC_6H_3iPr_2$-2,6 (H_2PAr^{iPr}) might provide auspicious candidates for the synthesis of mononuclear, terminal phosphinidene complexes of the smaller rare-earth metals.[16d,34] However, the attempted **2-Y^{Ga}**/H_2PAr^{iPr} reaction only revealed the high affinity of phosphorus to gallium, resulting in the abstraction of $GaMe_3$ to form compound [$Me_3Ga(PH_2Ar^{iPr})$] (Scheme 1; for further information, see the Supporting Information). This can be rationalized on the basis of Pearson's HSAB concept,[1] with the soft phosphine base being prone to interacting with the soft Lewis acid $GaMe_3$ to form a strong interaction instead of eliminating methane to induce an yttrium phosphido coordination. Such reaction behavior was also supposed for complexes $Tp^{tBu,Me}LnMe(GaMe_4)$ (**2-Ln^{Ga}**, Ln = Dy, Ho) and therefore the corresponding reactions were not pursued further (Supporting Information). Based on this reaction outcome, we included the "harder" $AlMe_3$-capped dimethyl yttrium complex $Tp^{tBu,Me}YMe(AlMe_4)$ (**2-Y^{Al}**) on the shortlist of potential precursors.[35] Moreover, the known group 13 Lewis acid-free rare-earth-metal dimethyl complexes $Tp^{tBu,Me}LnMe_2$ (**1-Ln**, Ln = Y, Ho)[34] were likewise examined as suitable precursors and their scope extended to the dysprosium derivative **1-Dy**. (Figure 1).

Compound **1-Dy** features a nonsolvated dimethyl complex of a midsized rare-earth-metal center, which is reflected in the larger Ln−C distances of 2.403(2) and 2.408(2) Å compared to the lutetium anolog (2.364(3) and 2.375(2) Å, space group *Pnma*).[33] **1-Dy** and **1-Y** are isostructural (space group *C*2/*c*) and show very similar metrics (for detailed metric data, see the Supporting Information).

Group 13-Stabilized Rare-Earth-Metal Phosphinidenes. Aiming at terminal rare-earth-metal phosphinidenes via an intermediate trimethylaluminum-stabilized phosphinidene, the previously reported $Tp^{tBu,Me}YMe[(\mu_2\text{-}Me)AlMe_3]$ (**2-Y^{Al}**)[34] was examined as precursor. Accordingly, **2-Y^{Al}** was reacted successfully with H_2PAr^{iPr} to afford trimethylaluminum-stabilized yttrium phosphinidene $Tp^{tBu,Me}Y[(\mu_2\text{-}PC_6H_3iPr\text{-}2,6)(\mu_2\text{-}Me)AlMe_2]$ (**3-Y^{Al}**) (Scheme 1). In contrast to the gallium congener **2-Y^{Ga}** (vide supra), the harder [$AlMe_4$] moiety did not primarily interact with the primary phosphane via [$Me_3AlPH_2Ar^{iPr}$] separation but enforced methane elimination and formation of a phosphinidene ligand.

https://doi.org/10.1021/jacs.3c04335
J. Am. Chem. Soc. 2023, 145, 17720−17733

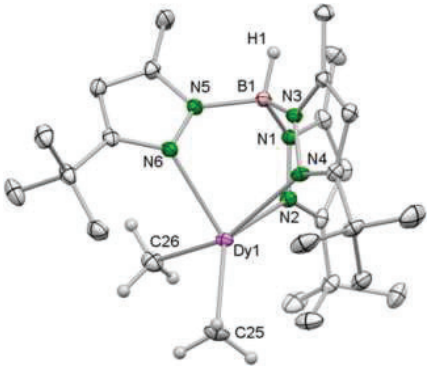

Figure 1. Crystal structure of $Tp^{tBu,Me}DyMe_2$ (**1-Dy**). All atoms are represented by atomic displacement ellipsoids set at 50% probability. Solvent molecules and hydrogen atoms except for those of B−H and Dy−CH_3 are omitted for clarity. Selected interatomic distances (Å) for **1-Dy** are as follows: Dy1−C25 2.4033(18) and Dy1−C26 2.4075(18). Select interatomic distances for **1-Y** are as follows: Y1−C25 2.424(2) and Y1−C26 2.400(2) (for more metrics, see the Supporting Information).

Complex **3-Y^{Al}** is insoluble in *n*-hexane but readily dissolves in toluene and polar solvents such as THF and diethyl ether.

Though featuring an isotypic molecular structure like the imide congeners $Tp^{tBu,Me}Ln[(\mu_2\text{-}NC_6H_3iPr_2\text{-}2,6)(\mu_2\text{-}Me)\text{-}MMe_2]$ (Ln = Ce, Nd, Sm; M = Al, Ga; orthorhombic space group *Pnma*),[30b] **3-Y^{Al}** crystallized in the triclinic space group $P\bar{1}$. The yttrium center of **3-Y^{Al}** is coordinated by μ_2-bridging phosphinidene and methyl functionalities with an elongated Al1−C37 distance (2.098(3) Å) (Figure 2). The Y−P distance

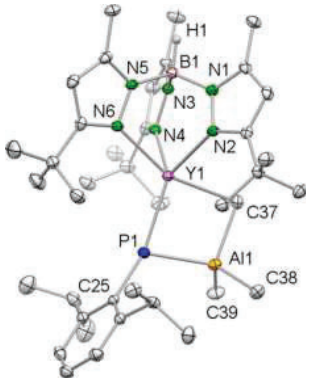

Figure 2. Crystal structure of $[AlMe_3]$-stabilized phosphinidene $[Tp^{tBu,Me}Y(\mu_2\text{-}PC_6H_3iPr_2\text{-}2,6)(\mu_2\text{-}Me)AlMe_2)]$ (**3-Y^{Al}**). All atoms are represented by atomic displacement ellipsoids set at 50% probability. Solvent molecules and hydrogen atoms except for those of B−H are omitted for clarity. Selected interatomic distances (Å) and angles (°) for **3-Y^{Al}** are as follows: Y1−P1 2.5297(7) and Y1−P1−C25 155.94(8) (for more metrics, see the Supporting Information).

of 2.5297(7) Å is significantly shorter than those for the terminal primary phosphanides $[C_5H_3(SiMe_3)_2\text{-}1,3]_2Y[P(H)\text{-}SitBu_3)](THF)$ (2.770(1) Å, **XXI**)[10b] as well as **4-Y** (2.8653(14) Å) and **5-Y** (2.9519(18)/2.9737(18) Å) described vide infra (Table 2). This is not surprising due to the increased electron density on the phosphinidene phosphorus atom, rendering a stronger ionic interaction. Despite the smaller size of scandium and lutetium, the Y−P distance of compound **3-Y^{Al}** is shorter or in the same range as those of the bridging phosphinidene complexes **I**, **II**, **V**, and **VI** shown in Table 1. Compared to the heterometallic phosphinidene complexes $(PNP^{iPr})Sc(=PTrip)(LiBr)\text{-}(DME)_x$ (x = 0,1; **III** and **IV**),[11] the Ln−P distance of **3-Y^{Al}** is longer, reflecting the larger yttrium[36] and probably also the more electron-withdrawing bromido ligand at the scandium center (compared to the methyl group at the yttrium center in **3-Y^{Al}**).

As the diamagnetic nature of the yttrium nucleus enables conclusive NMR-spectroscopic investigations, in particular the Y−P bond situation of complex **3-Y^{Al}** could be examined more closely. Full deprotonation of the phosphorus atom was revealed in the proton NMR spectrum by the absence of the doublet signal around δ = 2.2 ppm. The $AlMe_3$ methyl groups in **3-Y^{Al}** are fluxional at ambient temperature, as shown by a proton singlet at δ = −0.12 ppm. Decoalescing signals for the bridging $[\mu_2\text{−Me}]$ and the remaining methyl groups at the aluminum atom are detected at ambient temperature in the carbon NMR spectrum (δ = 6.3/−4.5 ppm; Figure 3) and via ^{1}H VT NMR spectroscopy (Figure S18). As anticipated, both proton-coupled and decoupled ^{31}P NMR spectra show only a doublet signal at δ = −52.5 ppm, indicating $^{31}P-^{89}Y$ coupling but no $^{31}P-^{1}H$ coupling.

The increasing coupling constant of $^1J_{YP}$ = 212 Hz in compound **3-Y^{Al}** compared to $^1J_{YP}$ = 63 Hz of the primary phosphanide **4-Y** (vide infra) indicates an increasing s-orbital ratio participating in the interaction between the metal center and the phosphorus atom and the higher electron density at the phosphorus atom ($[HPR]^- \rightarrow [PR]^{2-}$ transformation). For further comparison, the corresponding coupling constant in the terminal primary phosphanide $[C_5H_3(SiMe_3)_2\text{-}1,3]_2Y\text{-}[P(H)(SitBu_3)](THF)$ (**XXI**) was determined as $^1J_{YP}$ = 144 Hz.[10b]

Attempts to convert the mixed methyl/phosphido complexes **4-Y** and **5-Y** (vide infra) into Lewis acid-stabilized phosphinidene complexes such as complex **3-Y^{Al}**, via treatment with trimethylgallium or trimethylaluminum, have been unsuccessful so far. We assume the disruption of the Y−P bond and separation of monoanionic species like $[Me_3M\text{-}(PHAr^{iPr})]^-$ (M = Al, Ga; Supporting Information). Moreover, the transformation of compound **3-Y^{Al}** into a terminal phosphinidene by addition of donor molecules such as DMAP or THF was also not successful, resembling the previously reported rare-earth-metal imide chemistry.[15]

Synthesis of Mixed Methyl/Phosphido Rare-Earth-Metal Complexes. We next envisaged an approach that was successful for the synthesis of terminal rare-earth-metal imides.[16] There, the methyl group of mixed methyl/amido complexes such as $Tp^{tBu,Me}YMe(HNC_6H_3iPr_2\text{-}2,6)$ could be forced to intramolecularly deprotonate the primary amido ligand $[HNAr^R]$ in the presence of the Lewis base DMAP. As a strong Lewis base (compared to THF), DMAP donates enhanced electron density to the metal center and consequently weakens the coordination of the methyl and the phosphido ligands, widening the interatomic distances. Second, DMAP forces the elimination of methane due to steric oversaturation of the metal coordination sphere. Including both the favorably bulky $[Tp^{tBu,Me}]$ ancillary ligand and DMAP, a coordination environment is achieved that eminently shields the rare-earth-metal center from dimerization and forces the alkyl and phosphido ligand into an expedient position. With these considerations in mind, the implementation of an analogous synthesis procedure was targeted for the isolation of a terminal rare-earth-metal phosphinidene complex from the

https://doi.org/10.1021/jacs.3c04335
J. Am. Chem. Soc. 2023, 145, 17720−17733

Table 2. Selected Metrical Parameters of Late Lanthanide Primary Phosphide Complexes Including Scandium and Yttrium[a]

compound	CN	IR [Å][d,36]	Ln−P−X [°]	Ln−$P_{phosphido}$ [Å]	ref
$Tp^{tBu,Me}YMe[P(H)C_6H_3iPr_2$-2,6] (**4-Y**)	5		116.36(15)	2.8653(14)	this work
$Tp^{tBu,Me}HoMe[P(H)C_6H_3iPr_2$-2,6] (**4-Ho**)	5		116.36(14)	2.8516(12)	this work
$Tp^{tBu,Me}YMe[P(H)C_6H_3iPr_2$-2,6](DMAP) (**5-Y**)	6	0.900	121.57(19)/124.7(2)	2.952(2)/2.974(2)	this work
$Tp^{tBu,Me}HoMe[P(H)C_6H_3iPr_2$-2,6](DMAP) (**5-Ho**)	6	0.901	121.7(3)	2.9414(12)	this work
$Tp^{tBu,Me}DyMe[P(H)C_6H_3iPr_2$-2,6](DMAP) (**5-Dy**)	6	0.912	122.4(9))	2.939(16)	this work
$L^3ScMe[P(H)C_6H_3tBu_3$-2,4,6] (**XVI**)[b]	5		109.29(9)	2.653(1)	17
$Yb[P(H)(C_6H_2tBu_3$-2,4,6)$]_2(THF)_4$ (**XVII**)[b]	6	1.02[e]	121.4(1)	3.025(2)	10a
$[(C_5Bn_5)Yb\{\mu_2$-P(H)Ph$\}(THF)]_2$ (**XVIII**)[c]	6	1.02[e]		2.9174(9)/2.956(2)	9d
$[(C_5Me_5)_2Y\{\mu_2$-P(H)Ph$\}]_2$ (**XIX**)[c]	7	0.96	120.20(7)	3.021(3)	5a
$[(THF)_3YCl_2\{\mu_2$-P(H)Mes$\}]_2$ (**XX**)[c]	7	0.96	119.3(2)/119.8(2)	2.951(2)−2.970(2)	9c
$[C_5H_3(SiMe_3)_2$-1,3$]_2Y[P(H)SitBu_3](THF)$ (**XXI**)[b]	8	1.019	152.18(6)	2.770(1)	10b
$[C_5H_3(SiMe_3)_2$-1,3$]_2Y[\mu_2$-P(H)SiiPr$_3]_2Li(THF)$ (**XXII**)[c]	8	1.019	149.52(4)/149.97(5)	2.8388(9)/2.8406(9)	9b
$[C_5H_3(SiMe_3)_2$-1,3$]_2Y[\mu_2$-P(H)SiiPr$_3]_2K(C_6H_6)$ (**XXIII**)[c]	8	1.019	141.4(2)/148.4(2)	2.851(3)/2.841(3)	9b

[a]L^3 = $N_2C_3HAr^{iPr}$-1-Me_2-2,4-$(C_2H_4NMe_2)$-5. [b]Terminal phosphido complexes. [c]Bridging phosphido complexes. [d]Effective ionic radii. [e]Ytterbium(II).

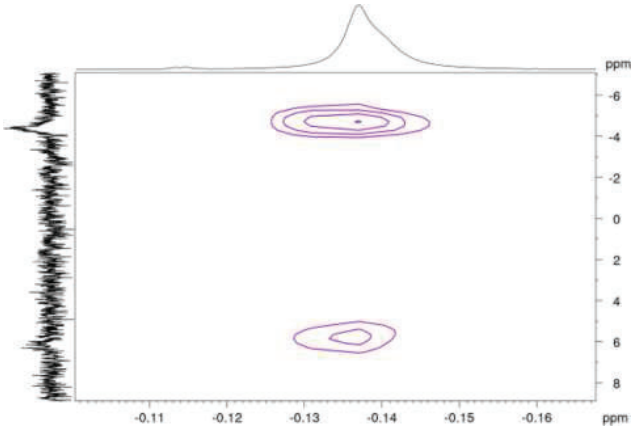

Figure 3. $^1H^{13}C$ HSQC NMR spectrum of phosphinidene complex $Tp^{tBu,Me}Y[(\mu_2$-$PC_6H_3iPr_2$-2,6$)\{(\mu_2$-Me$)AlMe_2]$ (**3-Y^{Al}**). Highly fluxional methyl moieties split into two independent signals in the carbon NMR spectrum, and both signals (δ = 6.3 and −4.5 ppm) are coupled to the singlet signal of the proton NMR spectrum (δ = −0.12 ppm).

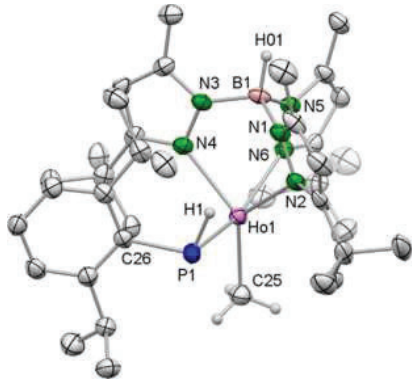

Figure 4. Crystal structure of mixed methyl/phosphido compound $Tp^{tBu,Me}HoMe(HPC_6H_3iPr_2$-2,6) (**4-Ho**). All atoms are represented by atomic displacement ellipsoids set at 50% probability. Hydrogen atoms except for those of B−H, P−H and CH_3 are omitted for clarity. Selected interatomic distances (Å) and angles (°) for **4-Ho** are as follows: Ho1−P1 2.8516(12), Ho1−C25 2.363(5), and Ho1−P1−C26 116.36(14) (for further metrics and the crystal structure of **4-Y**, see the Supporting Information).

increasingly Brønsted acidic phosphine H_2PAr^{iPr} (compared to the aniline H_2NAr^{iPr}). To exclude any side reactions caused by group 13 alkyls, we chose discrete dimethyls $Tp^{tBu,Me}LnMe_2$ (**1-Ln**, Ln = Y, Dy, Ho). Following this methane elimination protocol, the mixed methyl/phosphido complexes $Tp^{tBu,Me}LnMe(HPC_6H_3iPr_2$-2,6) (**4-Ln**, Ln = Y, Dy, Ho) could be accessed in decent yields (Scheme 1). The yttrium and holmium derivatives **4-Ln** are poorly soluble in *n*-hexane but willingly dissolve in toluene and donor solvents (e.g., THF and diethyl ether) and crystallized from toluene. Entailing the isostructural unit [Me−Y−EH] (E = N, P), both the previously reported amide analogs $[Tp^{tBu,Me}LnMe(HNC_6H_3R)]$ (Ln = Y, Lu; R = Me_2-2,6, $(CF_3)_2$-3,5)[16d] and the five-coordinate phosphides $Tp^{tBu,Me}LnMe(HPC_6H_3iPr_2$-2,6) (**4-Ln** Ln = Y, Ho) under study crystallize in the same monoclinic space group $P2_1/n$ (Figure 4 and Supporting Information).

The $[Tp^{tBu,Me}]$ ligand is coordinated to the rare-earth-metal center in a κ^3-fashion (*N*,*N*′,*N*″) with Ln−N_{pz} distances (**4-Y**, 2.341(4)−2.461(4) Å; **4-Ho**, 2.348(4)−2.467(4) Å) in the expected range.[16d,34,35] The Ln−P distances (**4-Y**, 2.8653(14) Å; **4-Ho**, 2.8516(12) Å) are markedly elongated compared to those in Rabe's five-coordinate $Tm[P(SiMe_3)_2]_3(THF)_2$ (2.709(1) and 2.701(2) Å)[37] but come close to the 2.845(2) Å value in eight-coordinate $Tp^{Me,Me}Y(C_5H_5)(PPh_2)(THF)$.[38]

Comparison of the different yttrium primary phosphanide complexes (Table 2) with the **4-Y** reported here is difficult to conduct, since the actor and spectator ligands are different in their steric demand and electronic situation. However, compared to similar primary amide complexes like $Tp^{tBu,Me}LuMe[N(H)(C_6H_3Me_2$-2,6)] (Lu−N, 2.189(2) Å; Lu−N_{amido}−C_{ipso}, 153.8(1)°),[16d] **4-Ln** show considerably lengthened Ln−$P_{phosphido}$ bonds and extremely acute Ln−$P_{phosphido}$−C_{ipso} bond angles (**4-Y**, 116.36(15)°; **4-Ho**, 116.36(14)°). For further comparison, the Y−P distance in eight-coordinate $[\{C_5H_3(SiMe_3)_2$-1,3$\}_2Y\{P(H)(SitBu_3)\}(THF)]$ (**XXI**, Table 2) is markedly shorter (2.776(1) Å) and the Ln−$P_{phosphido}$−C_{ipso} angle closer to linear (152.18(6)°).[10b] A similarly acute Ln−$P_{phosphido}$−C_{ipso} angle has been observed for complex [(nacnac)ScMe{P(H)-$C_6H_3tBu_3$-2,4,6}] (**XVI**, 109.29(9)°) and interpreted with the lack of significant interaction of the lone pair of the phosphorus atom with the empty 3d orbital of Sc(III).[17] Overall, the distinct Ln-phosphido/amido coordination might

https://doi.org/10.1021/jacs.3c04335
J. Am. Chem. Soc. 2023, 145, 17720−17733

point to a different reaction behavior when offered a donor such as DMAP.

^{1}H NMR spectroscopic investigations on **4-Y** revealed a triplet at 0.59 ppm for the methyl group attached to the yttrium center ($^2J_{YH}$ = 2.77 Hz) and a doublet for the P−H proton at 2.15 ppm ($^1J_{PH}$ = 194.47 Hz). As expected, the ^{31}P{^{1}H} and ^{31}P NMR spectra of **4-Y** show a doublet and a doublet of doublets at −118.2 ppm, respectively (Figures S22 and S23). Compared to [$C_5H_3(SiMe_3)_2$-1,3]$_2$Y[P(H)-(Si*t*Bu$_3$)](THF) (**XXI**, $\delta(^{31}P)$ = −181.1 ppm, $^1J_{PY}$ = 144 Hz),[10b] the signal is vastly shifted to lower field. Moreover, the $^1J_{PY}$ coupling constant of complex **4-Y** ($^1J_{PY}$ = 63 Hz) is much smaller than those for **XXI** and complex **3-Y^{Al}** ($^1J_{PY}$ = 213 Hz). The ^{31}P chemical shift of the phosphinidene **3-Y^{Al}** (δ = −52.5 ppm) at higher field points to a more deshielded phosphorus atom. On the other side, the ^{89}Y NMR signal of compound **4-Y** (δ = 847 ppm) is detected at lower field compared to that of **3-Y^{Al}** (δ = 504 ppm), which is indicative of a higher electron density at the yttrium center of the phosphinidene **3-Y^{Al}** but also reflects the deshielding effect of σ-bonded alkyl ligands.

As shown in several previous studies including the double deprotonation of aniline H_2NAr^{iPr}, a second deprotonation can be achieved by offering donor molecules such as DMAP to the Ln−methyl/primary amido unit.[16] However, the equimolar reaction of Tp^{tBu,Me}LnMe(HPC$_6$H$_3$*i*Pr$_2$-2,6) (**4-Ln**, Ln = Y, Dy, Ho) with DMAP did not afford the targeted terminal rare-earth-metal phosphinidene. The Lewis base was merely added to the rare-earth-metal center instead of deprotonating the increasingly Brønsted acidic primary phosphido fragment (relative to a corresponding amido derivative) (Scheme 1). The monoadducts **5-Ln** (Ln = Y, Dy, Ho) do not dissolve in nonpolar solvents such as *n*-hexane but instead in toluene and in polar solvents (THF and diethyl ether). Also, like the donor-free mixed methyl/phosphido complexes **4-Ln**, **5-Ln** crystallize in the monoclinic space group $P2_1/n$ (Figure 5) and show the $\kappa^3(N,N',N'')$ coordination of the [Tp^{tBu,Me}] ligand (Ln−N$_{pz}$ **5-Y**, 2.393(4)−2.493(5)/2.423(5)−2.499(5) Å; **5-Ho**, 2.368(8)−2.451(10) Å; **5-Dy**, 2.379(14)- 2.516(9) Å). Naturally, the six-coordinate complexes **5-Ln** exhibit significantly longer Ln−P distances than the donor free five-coordinate precursors **4-Ln**, whereas the Ln−P$_{phosphido}$−C$_{ipso}$ angles widen by only ca. 5° upon DMAP coordination (Table 2).

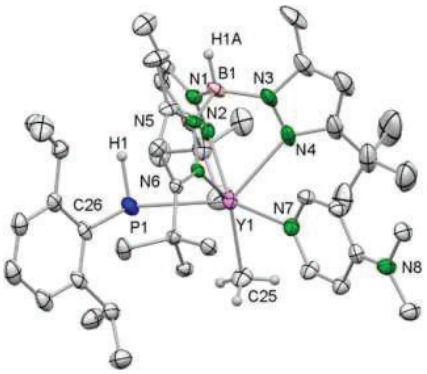

Figure 5. Crystal structure of mixed methyl/phosphido compound Tp^{tBu,Me}YMe(HPC$_6$H$_3$*i*Pr$_2$-2,6)(DMAP) (**5-Y**). All atoms are represented by atomic displacement ellipsoids set at 50% probability. Solvent molecules and hydrogen atoms except for those of B−H, P−H, and CH$_3$ are omitted for clarity. Selected interatomic distances (Å) and angles (°) for **5-Y** are as follows: Y1−P1 2.9519(17), Y1−C25 2.387(5), Y1−N7 2.560(5), and Y1−P1−C26 121.7(19) (for more metrics and isostructural **5-Ho** and **5-Dy**, see the Supporting Information).

Notably, the long Ln−P$_{phosphido}$ distances in **5-Ln** match those of bridging phosphido ligands in formally higher coordinated complexes (cf., **XX**, Table 2) and come close to those of Yb(II) primary phosphanides with equal coordination number (cf., **XVII** and **XVIII**, Table 2). For further comparison, the terminal Ln−P$_{Phosphido}$ distances in five-coordinate (PN)$_2$Ln[P(H)Mes] (PN = N(Mes)-[C$_6$H$_3$(P*i*Pr$_2$)-2-Me-4]) are 2.735(1) (Ln = Lu) and 3.053(1) Å (Ln = La).[11c]

Apparently, the steric and electronic impact of the additional DMAP ligand is not sufficient to promote the deprotonation and formation of a terminal rare-earth-metal phosphinidene. Although the phosphido ligand is more Brønsted acidic than the corresponding anilido, the steric shielding associated with a geometrical alignment of the actor ligands plays a pivotal role in a successful methane elimination. The solid-state structures of complexes **5-Y** suggest that the methyl group and the proton of the primary phosphido ligand seem mispositioned to engage in methane elimination via an intramolecular reaction pathway.

The ^{1}H/^{31}P{^{1}H}/^{31}P/^{89}Y NMR spectroscopic data collected for complex **5-Y** are in the same range as those for complex **4-Y** (Supporting Information). Regarding the ^{1}H NMR spectroscopic data, it is salient that in contrast to the available spectra of the imides Tp^{tBu,Me}Y(NC$_6$H$_3$Me$_2$-2,6)(DMAP) and Tp^{tBu,Me}Lu[NC$_6$H$_3$(CF$_3$)$_2$-3,5](DMAP),[16d] the DMAP ligand in **5-Y** is not hindered in a free rotation around its coordination axis. The ^{1}H NMR spectrum of **5-Y** shows two signals at 8.35 and 5.98 ppm for chemically equivalent aromatic protons at the 2,6- and 3,5-positions (Figure S25), whereas the DMAP signals for the two mentioned terminal rare-earth-metal imides split into four independent signals.[16d]

A Terminal Yttrium Phosphinidene. As shown above and suggested by the solid-state structures of **5-Ln**, one additional donor molecule does not sufficiently saturate the coordination sphere of the yttrium center, and the long Ln−P$_{phosphido}$ distance disfavors the proximity of the proton at the phosphorus atom to the methyl group. To better constrain the actor ligands into a geometrical arrangement where it is likely for them to form methane, we added 1 equiv of DMAP (Scheme 1). Upon methane evolution, finally, the first neutral, terminal rare-earth metal phosphinidene was achieved and could be structurally characterized (Figure 6).

Complex Tp^{tBu,Me}Ln(=PC$_6$H$_3$*i*Pr-2,6)(DMAP)$_2$ (**6-Y**) does not dissolve in *n*-hexane, but it readily dissolves in toluene and THF. Complex **6-Y** crystallized in the monoclinic space group *C*2/*c* as orange crystals. The [Tp^{tBu,Me}] ancillary ligand features an almost symmetrical $\kappa^3(N,N',N'')$ coordination (Y−N$_{pz}$ 2.472(2)−2.499(2) Å) and not the routinely observed "scorpionate" one with one longer/two shorter distances (cf., **4-Y** and **5-Y**). Noteworthy, the DMAP donor molecules exhibit slightly shorter bonds to the yttrium center (Y1−N7 2.526(2) Å, Y1−N9 2.532(2) Å) compared to precursor **5-Y**. However, the most striking feature of terminal yttrium phosphinidene complex **6-Y** is the short Y−P distance of 2.4855(7) Å, which is the shortest known for yttrium. The scandium phosphinophosphinidene complexes **VII** (2.448(1) Å) and **VIII** (2.484(1) Å) (Table 1) exhibit distances in a similar range.[24] This is remarkable, as the ion size of the trivalent scandium is the smallest among the trivalent rare-

https://doi.org/10.1021/jacs.3c04335
J. Am. Chem. Soc. 2023, 145, 17720−17733

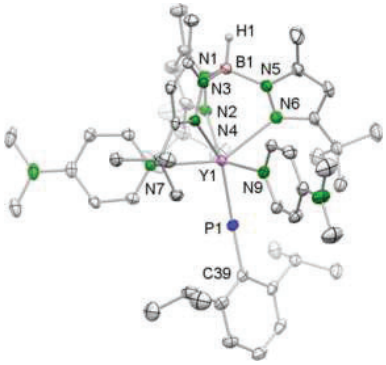

Figure 6. Crystal structure of terminal phosphinidene compound $Tp^{tBu,Me}Y(=PC_6H_3iPr_2\text{-}2,6)(DMAP)_2$ (**6-Y**). All atoms are represented by atomic displacement ellipsoids set at 50% probability. Solvent molecules, hydrogen atoms except for that of B−H are omitted for clarity. Selected interatomic distances (Å) and angles (°) for **6-Y** are as follows: Y1−P1 2.4855(7), Y1−N7 2.526(2), Y1−N9 2.532(2), and Y1−P1−C39 163.40(9) (for more metrics, see the Supporting Information).

Table 3. ^{31}P NMR Spectroscopic Details of Selected Rare-Earth-Metal Phosphinidene Complexes[a]

compound	δ [ppm]	$^1J_{YP}$ [Hz]	ref
$Tp^{tBu,Me}Y[(\mu_2\text{-}PC_6H_3iPr_2\text{-}2,6)(\mu_2\text{-}Me)AlMe_2]$ (**3-Y^{Al}**)[b]	−52.5	212	this work
$Tp^{tBu,Me}Y(=PC_6H_3iPr_2\text{-}2,6)(DMAP)_2$ (**6-Y**)	−5.5[d]	282[d]	this work
$L^3Sc[=PB(N_2Ar^{iPr}{}_2\text{-}2,5\text{-}C_2H_2)](\mu_2\text{-}Cl)K(L^4)$ (**IX**)[b]	19.62		25
$(PNP^{iPr})Sc(\mu_2\text{-}PAr^{Mes})(\mu_2\text{-}Br)Li$ (**III**)[b]	9.8		11
$(PNP^{iPr})Sc(\mu_2\text{-}PAr^{Mes})(\mu_2\text{-}Br)Li(DME)$ (**IV**)[b]	56.1		11
$[(PNP^{iPr})Lu(\mu_2\text{-}PAr^{Mes})]_2$ (**I**)[c]	186.8		21
$[(PNP^{iPr})Sc(\mu_2\text{-}PTrip)]_2$ (**II**)[c]	227.4		11
$[\{(C_5H_4Me)_2Y\}_3(\mu_3\text{-}PMes)_3Li][Li(THF)_4]_2$ (**XV^Y**)[c]	57.24		28
$[L^5Y(\mu\text{-}Me)]_3(\mu_3\text{-}Me)(\mu_3\text{-}PPh)$ (**XIV^Y**)[b]	138.79	41.28	27
$Y_5I(THF)_4(\mu_3\text{-}PC_6H_3iPr_2\text{-}2,6)_4(\mu_6\text{-}P)(\mu\text{-}I)K(tol)$ (**XIII**)[c]	154.7		26

[a] $L^3 = N_2C_3HAr^{iPr}\text{-}1\text{-}Me_2\text{-}2,4\text{-}(C_2H_4NMe_2)\text{-}5$. L^4 = dibenzo-18-crown-6. $L^5 = [PhC(NC_6H_4iPr_2\text{-}2,6)_2]$. [b] Heterometal-stabilized phosphinidene. [c] Bridging phosphinidene complexes. [d] Very weak signal due to rapid decomposition in solution.

earth metals.[36] Furthermore, the coordination number in those particular complexes is less (CN = 5) compared to that of **6-Y** (CN = 6).

Compared to the phosphanide precursors **4-Ln** and **5-Ln** (Ln = Y, Dy, Ho,) the Y−P distance in **6-Y** is about 0.5 Å shorter, as the electron density at the phosphorus atom is increased and the covalent interaction of the metal center and the phosphinidene fragment is intensified (DFT vide infra). The $Ln-P-C_{ipso}$ angle of 163.40(9)° in **6-Y** is close to the $Ln-N_{imido}-C_{ipso}$ angles of related terminal rare-earth-metal imide complexes. However, the imide complexes show more linear arrangements, as revealed by fivefold coordinated $Tp^{tBu,Me}Ln(NC_6H_3R)(DMAP)$ (Ln = Y, R = Me_2-2,6:173.6(4)°; Ln = Lu, R = $(CF_3)_2$-3,5:175.8(5)°),[16d] and sixfold coordinated early lanthanide complexes $Tp^{tBu,Me}Ln(NC_6H_3iPr_2\text{-}2,6)(THF)_2$ (Ln = Ce 171.3(3)°; Ln = Nd 169.2(4)°; Ln = Sm 169.3(5)°).[30b] Considering only steric factors, the comparatively longer $Ln=P_{phosphinidene}$ bond (versus $Ln=N_{imido}$) lessens the constraints of the bulky aryl moiety. Noteworthy, the $Sc-P-B_{ipso}$ angle of five-coordinate boronylphosphinidene $L^3Sc[=PB(N_2Ar^{iPr}{}_2\text{-}2,5\text{-}C_2H_2)](\mu_2\text{-}Cl)K(L^4)$ (**IX**, Table 1 and 3) is listed as 148.8(1)° (Table 1).[25]

The proton-decoupled ^{31}P NMR spectrum of complex **6-Y** revealed a very weak signal at −5.5 ppm, which is significantly shifted to a lower field compared to that of **3-Y^{Al}** at −52.2 ppm (Table 3). This is indicative of an increased electron density at the yttrium center in **6-Y** (DFT, vide infra) and the signal tentatively assigned to the phosphinidene phosphorus atom. Furthermore, the proton-coupled ^{31}P NMR spectrum of **6-Y** shows a doublet indicating a vast coupling constant of 282 Hz, implying an exclusive yttrium−phosphorus interaction, without proton coupling in the nearfield of the two nuclei. This maximum coupling constant detected so far for yttrium−phosphorus bonds underlines the increasing multiple bond character of the terminal phosphinidene functionality. The recently published terminal boronylphosphinidene "ate" complex $L^3Sc[=PB(N_2Ar^{iPr}{}_2\text{-}2,5\text{-}C_2H_2)](\mu_2\text{-}Cl)K(L^4)$ (**IX**, Table 3)[25] and the alkali-metal stabilized phosphinidene complex $(PNP^{iPr})Sc(\mu_2\text{-}PAr^{Mes})(\mu_2\text{-}Br)Li(DME)$ (**IV**, Table 3)[11] feature a ^{31}P NMR signal at lower field compared to the neutral, terminal phosphinidene complex **6-Y**.

The tentatively assigned $\delta(^{31}P)$ = 9.8 ppm for ate complex $(PNP^{iPr})Sc(\mu_2\text{-}PAr^{Mes})(\mu_2\text{-}Br)Li$ (**III**, Table 3)[11] comes closest to the phosphorus shift detected for **6-Y**. Bridging rare-earth-metal phosphinidene complexes reveal an even larger chemical shift to a higher field (Table 3). For further comparison, there is already a significant number of terminal actinide organophosphinidene complexes, and the respective phosphorus resonances span the range from $\delta(^{31}P)$ = 71.06 ppm for $(C_5Me_5)_2U(PC_6H_2tBu_3\text{-}2,4,6)(OPMe_3)$ to $\delta(^{31}P)$ = 177.85 ppm for $[(C_5Me_5)_2Th(PC_6H_2iPr_3\text{-}2,4,6)\{P(H)C_6H_2iPr_3\text{-}2,4,6\}][K(2,2,2\text{-crypt})]$.[39]

As complex **6-Y** is thermally quite unstable (rapid decomposition at ambient temperature as evidenced by NMR spectroscopy, Figures S37 and S38) and separation from its precursor in higher yields was unsuccessful so far, derivatization experiments of the novel terminal yttrium phosphinidene complex are still under investigation. Unfortunately, the putative open-shell derivatives **6-Ho** and **6-Dy** have remained elusive, and their synthesis and isolation might require further fine-tuning of both the $[Tp^{R,R'}]$ ancillary ligand and the phosphinidene backbone. In a similar vein, NMR-scale reactions with $Tp^{tBu,Me}LuMe_2$ (**1-Lu**)[33] corroborate the importance of the metal size for the successful application of the protocol, which led to the isolation of **6-Y**. Already the reaction of lutetium dimethyl complex **1-Lu** with phosphine H_2PAr^{iPr} proceeds very slowly, and only prolonged reaction times of 24 h gave a satisfying conversion to $Tp^{tBu,Me}LuMe(HPC_6H_3iPr_2\text{-}2,6)$ (**4-Lu**, Figures S39−42). Crucially, treatment of **4-Lu** with neither one nor two equiv of DMAP led to the formation of putative terminal phosphinidene **6-Lu** (Figure S43−49). This is substantiated by the ^{1}H and ^{31}P NMR spectra showing the preservation of both the proton resonance of the nonreacted $Lu-CH_3$ moiety and the phosphorus signal of the phosphido ligand of **4-Lu**/**5-Lu**, respectively. This distinct reaction behavior can be rationalized on the basis of a significantly smaller lutetium center and hence on steric grounds.

https://doi.org/10.1021/jacs.3c04335
J. Am. Chem. Soc. 2023, 145, 17720−17733

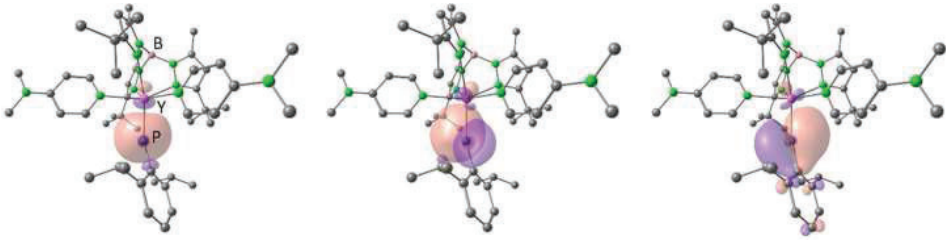

Figure 7. NLMOs representing one σ-type and two π-type Y−P bonding interactions in **6-Y**; all hydrogen atoms are omitted for clarity.

Preliminary reactivity studies have been performed on Lewis acid-stabilized yttrium phosphinidene $Tp^{tBu,Me}Y[(\mu_2\text{-}PAr^{iPr})(\mu_2\text{-}Me)AlMe_2]$ (**3-Y**). The reaction of **3-Y** with benzophenone revealed the effective formation of $Ph_2C{=}PAr^{iPr}$ (^{31}P NMR: δ 233.9 ppm, Figures S50 and 51; cf., refs 11, 21). The reaction of **3-Y** with $^{13}CO_2$ was less conclusive but indicated the formation of carbon monoxide (Figure S52).

DFT Calculations. To gain more insight into the nature of the bonding between the yttrium center and the phosphinidene ligand, we carried out DFT calculations,[40] followed by a natural bond orbital (NBO) analysis.[41] The geometry optimization (B3PW91) of **6-Y** revealed structural parameters in very good agreement with their experimental counterparts: in particular, the Y−P (2.50 Å) and P−C (1.84 Å) distances closely resembled the observed X-ray distances of 2.4855(7) and 1.816(3) Å, respectively. The calculated angle Y−P−C deviated to some extent from the experimental value (151.4° vs 163.40(9)°), which, however, might be attributed to packing effects in the densely packed crystal structure of **6-Y**. This is corroborated by a restricted geometry optimization with the angle Y−P−C fixed at 163.4°. The geometry thus obtained was less than 1 kJ/mol higher in energy than for the fully optimized system, while the Y−P and P−C bond lengths changed by less than 1%.

The NBO analysis confirmed the Y−P multiple bond character: one σ-type and two π-type interactions were derived, which were all strongly polarized toward the phosphinidene ligand. Due to the small contribution of the yttrium center to the σ-bond, the latter was described as a donor−acceptor-type interaction, in NBO terms, in which a lone pair on phosphorus delocalizes toward the yttrium center. Figure 7 depicts the three obtained natural localized molecular orbitals (NLMOs) contributing to the Y−P bonding. They represent localized, Lewis-like NBOs along with the delocalization tails of their electron pairs into adjacent orbitals. The NLMO displayed on the right thereby indicates some involvement of the aryl substituent in one of the Y−P π-interactions due to a suitable alignment of its ring plane. However, the composition of this NLMO (Table 4) points to a relatively minor contribution, as only 3.2% of its electron density can be attributed to the attached carbon atom of the aromatic ring. For all three bonding interactions, the electron density resides mainly on the phosphorus atom with values ranging from 75% to 88%, while the yttrium center contributes between 11% and 19%. The pronounced ionic nature of the Y−P interaction is confirmed by the natural atomic charges listed in Table 5, whereas a Wiberg bond index (WBI) of 1.37 for the Y−P interaction further supports the view of multiple bonding. For comparison, for the phosphide complex **5-Y**, a WBI(Y−P) of 0.55 was obtained (for details, see the Supporting Information). It is noteworthy that the σ-type bond seems markedly weaker than the two π-bonds. This is also indicated by the analysis of the extent of overlap between hybrids in the respective NLMOs; therefore, the σ-type interaction accounts for 24% of the NLMO-derived Y−P bond order in **6-Y** compared to 42% and 34%, respectively, for the two π-type interactions.

Table 4. Composition (%) of the Natural Localized Molecular Orbitals (NLMOs) Describing σ- and π-Bonding Contributions between the Rare-Earth-Metal Center and the Phosphinidene and Imido Ligand, respectively, in Complexes IX, 6-Y, and XXIV

	σ(Sc/Y−P/N)		π(Sc/Y−P/N)		π(Sc/Y−P/N−B/C)		
compound	Sc/Y	P/N	Sc/Y	P/N	Sc/Y	P/N	B/C
IX	9.9	88.6	17.0	79.2	14.7	74.4	7.5
6-Y	10.9	88.0	19.4	76.7	15.5	75.4	3.2
XXIV	6.6	92.4	12.2	83.9	9.5	76.0	7.8

To put our findings for the Y−P bonding in **6-Y** into better context, the bonding in two related complexes was analyzed using the same methodology. One was the recently published first terminal scandium boronylphosphinidene complex (**IX**), for which a strong Sc−P π-interaction was reported.[25] It features a boronyl substituent attached to phosphorus instead of the aryl group employed in **6-Y**. The other was the closely related terminal yttrium imide complex $Tp^{tBu,Me}Y[{=}NC_6H_3(CH_3)_2\text{-}2,6](DMAP)$ (**XXIV**).[16d] It utilizes aligand set very similar to **6-Y**, with the same Tp ligand, a similar aryl substituent (with two methyl groups instead of isopropyl groups), and one (instead of two) DMAP donor ligands. This allows for a highly interesting comparison of the bonding between a rare-earth-metal center and a phosphinidene and imido ligand, respectively.

For **IX**, the Sc−P bonding obtained was very similar to the one for Y−P in **6-Y**: one σ-type and two π-type Sc−P interactions were revealed, all of which displayed a slightly reduced contribution of the smaller and harder scandium center compared to yttrium in **6-Y** (see Table 4).[42] Moreover, a significant amount of electron density was delocalized toward the boronyl substituent, with the boron atom accounting for 8% in one of the two NLMOs representing the Sc−P π-interactions (see Table 4). This contributes to the higher P−B bond order (WBI) of 1.24 (see Table 5).

Interestingly, the bonding between yttrium and the imido ligand in **XXIV** exhibited the same pattern (one σ-type and two π-type interactions), as described above. The NBO analysis, however, revealed some significant differences. As can be seen in Table 4, the contribution of yttrium is clearly reduced in all three NLMOs, with values ranging between 7% and 12% compared to, e.g., 11−19% in **6-Y**. A larger ionic character of the Y−N interaction is also reflected in the higher atomic charges obtained for Y (+1.86) and N (−1.24), and

https://doi.org/10.1021/jacs.3c04335
J. Am. Chem. Soc. 2023, 145, 17720−17733

Table 5. Natural Atomic Charges and Wiberg Bond Indices (WBIs) of the Key Atoms in the Rare-Earth-Metal Phosphinidene/Imido Moieties in Complexes IX, 6-Y, and XXIV

	natural atomic charge			WBI	
compound	Sc/Y	P/N	B/C	Sc/Y–P/N	P/N–B/C
IX	+1.35 (Sc)	−0.95 (P)	+0.59 (B)	1.26 (Sc–P)	1.24 (P–B)
6-Y	+1.40 (Y)	−0.60 (P)	−0.27 (C)	1.37 (Y–P)	1.05 (P–C)
XXIV	+1.86 (Y)	−1.24 (N)	+0.19 (C)	0.91 (Y–N)	1.25 (N–C)

accordingly the Y–N bond index is considerably lower (0.91 vs 1.37 for Y–P in **6-Y**). On the other hand, due to the better orbital overlap, the N–C interaction is strengthened (WBI of 1.25), as more electron density from one of the two Y–N π-interactions is now delocalized toward the aryl substituent (see Table 5).

CONCLUSION

Terminal rare-earth-metal organophosphinidene complexes are isolable. Complexes like $Tp^{tBu,Me}Y(=PC_6H_3iPr_2\text{-}2,6)(DMAP)_2$ with multiple Ln–P bonds can be accessed via a donor-supported consecutive deprotonation of primary phosphine $H_2PC_6H_3iPr_2$-2,6 (H_2PAr^{iPr}) employing $Tp^{tBu,Me}YMe_2$. The synergistic interplay of the bulky monoanionic hydrotris(3-*tert*-butyl-5-methylpyrazolyl)borato ligand ($Tp^{tBu,Me}$), Ln(III) size, methyl superbasicity, and amount of additional Lewis base DMAP plays a pivotal role for the effective formation of $Tp^{tBu,Me}Y(=PAr^{iPr})(DMAP)_2$. The primary phosphide intermediates $Tp^{tBu,Me}YMe(HPAr^{iPr})$ and $Tp^{tBu,Me}YMe(HNPAr^{iPr})(DMAP)$ are also isolable species. Proper selection of the bis(alkyl) rare-earth-metal complexes is crucial for terminal phosphinidene formation and for excluding side reactions. Thus, Lewis acid-stabilized yttrium phosphinidene $Tp^{tBu,Me}Y[(\mu_2\text{-}PAr^{iPr})(\mu_2\text{-}Me)AlMe_2]$ was obtained from $Tp^{tBu,Me}YMe(AlMe_4)$ whereas the reaction of H_2PAr^{iPr} with $Tp^{tBu,Me}YMe(GaMe_4)$ led to immediate abstraction of $GaMe_3$, hampering the formation of putative metallacycle derivative $Tp^{tBu,Me}Y[(\mu_2\text{-}PAr^{iPr})(\mu_2\text{-}Me)GaMe_2]$. It is striking that the synthesis of terminal phosphinidene $Tp^{tBu,Me}Y(=PC_6H_3iPr_2\text{-}2,6)(DMAP)_2$ adopts a similar procotol as that recently established for the respective terminal organoimides. However, the sterically more flexible phosphido ligand takes a second equivalent of the Lewis base DMAP to engage in the ultimate second deprotonation. The shortest molecular Y–P distance of 2.4855(7) Å and a maximum $^1J_{YP}$ coupling constant of 282 Hz detected so far underline the multiple bond character of the terminal phosphinidene functionality, which is also confirmed by DFT calculations. They revealed one σ- and two π-type Y–P interactions, all of which are of a highly ionic nature. Calculations on the related imide complex $Tp^{tBu,Me}Y[=NC_6H_3(CH_3)_2\text{-}2,6](DMAP)$ resulted in the same bonding pattern but pointed to a considerably lower covalent character for the bonding of yttrium to the imido ligand. Finally, the elaborate synthesis and low stability of compound $Tp^{tBu,Me}Y(=PC_6H_3iPr_2\text{-}2,6)(DMAP)_2$ are in sharp contrast to the behaviors of d-transition metal and 5f-element terminal organophosphinidene complexes, which can draw on the stabilizing effect of extensive orbital interactions.

EXPERIMENTAL SECTION

General Considerations. ***Caution!*** The group 13 and rare-earth-metal methyl derivatives are highly pyrophoric and react violently when exposed to air and/or moisture. Therefore, all manipulations were performed under rigorous exclusion of air and moisture, using standard Schlenk, high-vacuum, and glovebox techniques (MB Braun MB200B; <0.1 ppm of O_2, <0.1 ppm of H_2O, and argon atmosphere). The solvents *n*-hexane, *n*-pentane, diethyl ether, toluene, and tetrahydrofuran (THF) were purified using Grubbs-type columns (MBraun SPS, solvent purification system). Tetrahydrofuran was stored over freshly activated molecular sieves (3 Å). C_6D_6 (99.6%, Sigma-Aldrich) was dried by stirring it over Na/K-alloy for at least 24 h and filtered prior to use. Benzophenone and $^{13}CO_2$ were purchased from Sigma-Aldrich and used as received. All solvents and reagents were stored inside a glovebox. 2,6-Diisopropylphenylphosphan (H_2PAr^{iPr}) was synthesized according to a slightly modified literature procedure.[43] $HTp^{tBu,Me}$ was synthesized by a modification of procedure published for $HTp^{tBu,Ph}$.[44] $Ln(AlMe_4)_3$, $[LnMe_3]_n$, $Ln(GaMe_4)_3$, $Tp^{tBu,Me}LuMe_2$ (**1-Lu**), $Tp^{tBu,Me}LnMe(GaMe_4)$ (**2-Ln^{Ga}**, Ln = Y, Ho), and $Tp^{tBu,Me}LnMe(AlMe_4)$ (**2-Ln^{Al}**, Ln = Y, Dy, Ho) were synthesized according to literature procedures.[16d,33,35,45−47] The NMR spectra of air- and moisture-sensitive compounds were recorded by using J. Young-valved NMR tubes on a Bruker AVII+400 spectrometer (^{1}H, 400.13 MHz; ^{31}P, 121 MHz) and on a Bruker AVII +500 spectrometer (^{1}H, 500.13 MHz; ^{13}C, 125.76 MHz; ^{11}B, 160.46 MHz; ^{31}P, 202.46 MHz; ^{89}Y, 25.51 MHz). ^{1}H NMR resonances are referenced to solvent residual resonances and reported in parts per million relative to tetramethylsilane (TMS). Coupling constants are given in Hertz. IR spectra were recorded on a NICOLET 6700 FTIR spectrometer with a DRIFT cell (KBr window); the samples were prepared in a glovebox and mixed with KBr powder. Alternatively, Nujol oil was used as a carrier material. Elemental analyses were performed on an Elementar Vario Micro Cube.

[Tp^{tBu,Me}YMe$_2$] (1-Y). According to a modified literature procedure,[33] to a suspension of $Tp^{tBu,Me}YMe(GaMe_4)$ (**2-Y^{Ga}**, 300 mg, 0.456 mmol) in *n*-hexane (5 mL) was added *N*,*N*,*N*′,*N*′-tetramethylethyl-1,2-diamine (53.0 mg, 0.456 mmol) in *n*-hexane (3 mL). The reaction mixture was stirred for 1 h at ambient temperature, washed three times with cold *n*-hexane (−35 °C), and dried in vacuo to give **1-Y** as a white powder. Colorless crystals of **1-Y** could be harvested at −35 °C in toluene. Yield: 182 mg, 0.336 mmol, 74%. ^{1}H NMR (400 MHz, C_6D_6): δ 5.63 (s, 3H, pz-*H*) 2.06 (s, 9H, pz-CH_3), 1.50 (s, 27H, pz-C(CH_3)$_3$), −0.08 (d, 6H, $^2J_{YH}$ 1.98 Hz, Y(CH_3)) ppm. Elemental analysis (%) calcd for $C_{26}H_{46}BYN_6$ (542.41 g/mol): C 57.57, H 8.55, N 15.49. Found: C 57.35, H 8.39, N 15.54.

[Tp^{tBu,Me}DyMe$_2$] (1-Dy). Following the procedure described for **1-Y**, to a solution of $Tp^{tBu,Me}DyMe(GaMe_4)$ (**2-Dy^{Ga}**, 758 mg, 1.04 mmol) in *n*-hexane (6 mL) was added *N*,*N*,*N*′,*N*′-tetramethylethyl-1,2-diamine (121 mg, 1.04 mmol) in *n*-hexane (2 mL), and the mixture was stirred for 1 h at ambient temperature. Colorless crystals of **1-Dy** could be harvested at −35 °C in toluene. Yield: 361 mg, 0.586 mmol, 56%. Elemental analysis (%) calcd for $C_{26}H_{46}BDyN_6$ (616.01 g/mol): C 50.70, H 7.53, N 13.64. Found: C 49.84, H 7.18, N 13.58.

[Tp^{tBu,Me}HoMe$_2$] (1-Ho). Following the procedure described for **1-Y**, to a solution of $Tp^{tBu,Me}HoMe(GaMe_4)$ (504 mg, 0.687 mmol) in *n*-hexane (5 mL) was added *N*,*N*,*N*′,*N*′-tetramethylethyl-1,2-diamine (79.9 mg, 0.687 mmol) in *n*-hexane (3 mL), and the mixture was stirred for 1 h at ambient temperature. Yield: 360 mg, 0.582 mmol, 85%. Elemental analysis (%) calcd for $C_{26}H_{46}BHoN_6$ (618.44 g/mol): C 50.50, H 7.50, N 13.59. Found: C 49.86, H 7.28, N 13.62.

[Tp^{tBu,Me}DyMe(GaMe$_4$)] (2-Dy^{Ga}). To a solution of $Dy(GaMe_4)_3$ (198 mg, 0.359 mmol) in *n*-pentane (3 mL) was slowly added a solution of an equimolar amount of $HTp^{tBu,Me}$ (152 mg, 0.359 mmol) in *n*-pentane (3 mL). The mixture was stirred for 15 min. After the

https://doi.org/10.1021/jacs.3c04335
J. Am. Chem. Soc. 2023, 145, 17720−17733

formation of a yellow precipitate, the solution was decanted, and the remaining powder was washed with *n*-pentane (3 × 5 mL). Single crystals suitable for XRD analysis formed from a toluene solution. Yield: 221 mg, 0.302 mmol, 84%. Elemental analysis (%) calcd for $BN_6C_{29}H_{55}GaDy$ (730.83 g/mol): C 47.66, H 7.59, N 11.50; found: C 47.87, H 7.53, N 11.34.

[Tp^{tBu,Me}Y(PC$_6$H$_3$*i*Pr-2,6)(AlMe$_3$)] (3-Y^{Al}). To a solution of Tp^{tBu,Me}YMe(AlMe$_4$) (**2-Y^{Al}**, 175 mg, 0.285 mmol) in toluene (4 mL) was added a solution of $H_2PC_6H_3$*i*Pr-2,6 (55.3 mg, 0.285 mmol) in toluene (2 mL), and the mixture stirred overnight at 40 °C. The solvent was removed under vacuum, and the remaining yellow residue was washed with *n*-hexane (5 × 4 mL). Yellow crystals of **3-Y^{Al}** could be harvested at −35 °C in toluene. Yield: 142 mg, 0.182 mmol, 64%. ^{1}H NMR (500 MHz, C_6D_6, 26 °C): δ 7.31−7.24 (m, 3H, *p*/*m*-Ar*H*), 5.60 (s, 3H, pz-*H*), 4.93 (m, 2H, *i*Pr-C*H*), 1.91 (s, 9H, pz-CH_3), 1.57 (s, 27H, pz-C(CH_3)$_3$), 1.54 (d, 12H, $^3J_{HH}$ 6.95 Hz, *i*Pr-CH_3), −0.12 (s, 9H, Al(CH_3)$_3$) ppm. ^{13}C{^{1}H} NMR (126 MHz, C_6D_6, 26 °C): δ 167.1 (5-pz-*C*), 153.7 (*o*-Ar*C*), 148.3 (3-pz-*C*), 143.3 (*i*-Ar*C*), 126.2 (*p*-Ar*C*), 122.8 (*m*-Ar*C*), 104.8 (4-pz-*C*), 33.7 (ArCH(CH$_2$)$_2$), 32.6 (pz-C(CH$_3$)$_3$), 31.9 (pz-C(CH$_3$)$_3$), 25.1 (ArCH(CH$_2$)$_2$), 13.0 (pz-CH$_3$), 6.3 (Y(μ-CH$_3$)), −4.5 (Al(CH$_3$)$_2$) ppm. ^{11}B{^{1}H} NMR (160 MHz, C_6D_6, 26 °C): δ −8.1 ppm. ^{31}P{^{1}H} NMR (202 MHz, C_6D_6, 26 °C): δ −52.5 (d, $^1J_{PY}$ 213 Hz) ppm. ^{31}P NMR (202 MHz, C_6D_6, 26 °C): δ −52.5 (d, $^1J_{PY}$ 212 Hz) ppm. ^{89}Y NMR (from ^{1}H−^{89}Y HSQC, 25 MHz, C_6D_6, 26 °C): δ 504 ppm. IR (nujol, $\tilde{\nu}$): 2973 (nujol), 2868 (m), 2826 (m), 2754 (w), 1807 (w), 1725 (w), 1691 (m), 1584 (s), 1481 (nujol), 1362 (nujol), 1282 (w), 1201 (m), 1091 (s), 1041 (m), 1017 (m), 952 (m), 888 (m), 816 (m), 776 (s), 731 (s), 676 (s) cm^{-1}. Elemental analysis (%) calcd for $C_{39}H_{66}AlBYPN_6$ (776.67 g/mol): C 60.31, H 8.57, N 10.82. Found: C 59.35, H 8.48, N 10.53.

[Tp^{tBu,Me}YMe(HPC$_6$H$_3$*i*Pr-2,6)] (4-Y). To a solution of Tp^{tBu,Me}YMe$_2$ (**1-Y**, 338 mg, 0.623 mmol) in toluene (5 mL) was added a solution of $H_2PC_6H_3$*i*Pr-2,6 (121 mg, 0.623 mmol) in toluene (3 mL), and the mixture was stirred for 4 h at ambient temperature. Yellow crystals of **4-Y** could be harvested at −35 °C in toluene. Yield: 314 mg, 0.436 mmol, 70%. ^{1}H NMR (500 MHz, C_6D_6, 26 °C): δ 7.06 (t, 1H, $^3J_{HH}$ 3.68 Hz, *p*-Ar*H*), 7.04 (d, 2H, $^3J_{HH}$ 1.60 Hz, *m*-Ar*H*), 5.57 (s, 3H, pz-*H*), 4.67 (d, 1H, B*H*), 3.32 (m, 2H, *i*Pr-C*H*), 2.15 (d, 1H, $^1J_{PH}$ 194.47 Hz, P*H*), 2.10 (s, 9H, pz-CH_3), 1.39 (s, 27H, pz-C(CH_3)$_3$), 1.29 (d, 12H, $^3J_{HH}$ 6.78 Hz, *i*Pr-CH_3), 0.57 (t, 3H, $^1J_{YH}$ 2.77 Hz, Y(CH_3)) ppm. ^{13}C{^{1}H} NMR (126 MHz, C_6D_6, 26 °C): δ 165.4 (5-pz-*C*), 147.5 (*o*-Ar*C*), 145.9 (3-pz-*C*), 145.6 (*i*-Ar*C*), 122.3 (*p*-Ar*C*), 121.8 (*m*-Ar*C*), 103.7 (4-pz-*C*), 33.0 (pz-C(CH$_3$)$_3$), 32.6 (ArCH(CH$_2$)$_2$), 31.5 (pz-C(CH$_3$)$_3$), 30.5 (Y(CH$_3$)), 23.8 (ArCH-(CH$_2$)$_2$), 13.1 (pz-CH$_3$) ppm. ^{11}B{^{1}H} NMR (160 MHz, C_6D_6, 26 °C): δ −8.2 ppm. ^{31}P{^{1}H} NMR (202 MHz, C_6D_6, 26 °C): δ −118.2 (d, $^1J_{PY}$ = 63 Hz) ppm. ^{31}P NMR (202 MHz, C_6D_6, 26 °C): δ −118.2 (dd, $^1J_{PY}$ = 62/63 Hz; $^1J_{PH}$ = 203 Hz) ppm. ^{89}Y NMR (from ^{1}H−^{89}Y HSQC, 25 MHz, C_6D_6, 26 °C): δ 847 ppm. IR (nujol, $\tilde{\nu}$): 2957 (vs), 2924 (nujol), 2856 (vs), 2464 (vw, B−H), 2359 (vw, P−H), 1587 (vw), 1567 (w), 1482 (w), 1462 (nujol), 1364 (nujol), 1288 (w), 1255 (vw), 1197 (w), 1162 (w), 1138 (vw), 1106 (w), 1091 (w), 1045 (vw), 995 (vw), 973 (vw), 803 (w), 776 (w), 744 vw), 689 (vw), 652 (vw), 627 (vw), 580 (vw), 535 (w), 506 (w), 487 (w), 450 (w), 417 (w), 403 (w) cm^{-1}. Elemental analysis (%) calcd for $C_{37}H_{61}BYPN_6$ (720.63 g/mol): C 61.67, H 8.53, N 11.66. Found: C 61.98, H 8.47, N 11.64.

[Tp^{tBu,Me}DyMe(HPC$_6$H$_3$*i*Pr-2,6)] (4-Dy). Following the procedure described for **4-Y**, to Tp^{tBu,Me}DyMe$_2$ (**1-Dy**, 124 mg, 0.201 mmol) in toluene (4 mL) was added a solution of $H_2PC_6H_3$*i*Pr-2,6 (39.1 mg, 0.201 mmol) in toluene (2 mL), and the mixture was stirred for 4 h at ambient temperature. Yield: 68.3 mg, 0.0860 mmol, 43%. Elemental analysis (%) calcd for $C_{37}H_{61}BDyPN_6$ (794.22 g/mol): C 55.96, H 7.74, N 10.58. Found: C 53.48, H 7.77, N 12.65. Although the microanalytical data are still outside the range viewed as establishing analytical purity, they are provided to illustrate the best values obtained to date.

[Tp^{tBu,Me}HoMe(HPC$_6$H$_3$*i*Pr-2,6)] (4-Ho). Following the procedure described for **4-Y**, to Tp^{tBu,Me}HoMe$_2$ (**1-Ho**, 93.0 mg, 0.150 mmol) in toluene (5 mL), a solution of $H_2PC_6H_3$*i*Pr-2,6 (29.2 mg, 0.150 mmol) in toluene (2 mL) was added, and the mixture was stirred for 4 h at ambient temperature. Yellow crystals of **4-Ho** could be harvested at −35 °C in toluene. Yield: 73.3 mg, 0.0920 mmol, 61%. Elemental analysis (%) calcd for $C_{37}H_{61}BHoPN_6$ (796.65 g/mol): C 55.78, H 7.72, N 10.55. Found: C 54.27, H 7.94, N 11.94. Although the microanalytical data are still outside the range viewed as establishing analytical purity, they are provided to illustrate the best values obtained to date.

[Tp^{tBu,Me}YMe(HPC$_6$H$_3$*i*Pr-2,6)(DMAP)] (5-Y). To a solution of Tp^{tBu,Me}YMe(HPC$_6$H$_3$*i*Pr-2,6) (**4-Y**, 88.5 mg, 0.123 mmol) in toluene (3 mL) was added a solution of DMAP (15.0 mg, 0.123 mmol) in toluene (2 mL) at −35 °C, and the mixture was stirred for 0.5 h at ambient temperature. The solvent was removed under vacuum, and the remaining yellow residue was washed with *n*-hexane (5 × 4 mL). Yellow crystals of **5-Y** could be harvested at −35 °C in toluene. Yield: 51.8 mg, 0.0615 mmol, 50%. ^{1}H NMR (500 MHz, C_6D_6, 26 °C): δ 8.35 (s, 2H, 2-py-*H*), 7.07−7.01 (m, 3H, *p*/*m*-Ar*H*), 5.98 (s, 2H, 3-py-*H*), 5.60(s, 3H, pz-*H*), 3.35 (m, 2H, *i*Pr-C*H*), 2.17 (d, 1H, $^1J_{PH}$ 195.19 Hz, P*H*), 2.13 (s, 9H, pz-CH_3/s, 6H, N(CH_3)$_2$), 1.39 (s, 27H, pz-C(CH_3)$_3$), 1.30 (d, 12H, $^3J_{HH}$ 6.79 Hz, *i*Pr-CH_3), 0.59 (t, 3H, $^1J_{YH}$ 3.01 Hz, Y(CH_3)) ppm. ^{13}C{^{1}H} NMR (126 MHz, C_6D_6, 26 °C): δ 165.3 (5-pz-*C*), 154.1 (*i*-Ar*C*), 150.7 (4-py-*C*), 147.7 (3-pz-*C*), 147.0 (2-py-*C*), 128.4 (*m*-Ar*C*), 121.8 (*o*-Ar*C*), 106.3 (*p*-Ar*C*), 103.8 (3-py-*C*), 102.0 (4-pz-*C*), 38.0 (N(CH$_3$)$_2$), 31.9 (ArCH(CH$_2$)$_2$), 31.4 (pz-C(CH$_3$)$_3$), 24.0 (pz-C(CH$_3$)$_3$), 23.1 (ArCH(CH$_2$)$_2$), 14.4 (pz-CH$_3$) ppm (signals for Y(CH$_3$) could not be detected). ^{11}B{^{1}H} NMR (160 MHz, C_6D_6, 26 °C): δ −8.1 ppm. ^{31}P{^{1}H} NMR (202 MHz, C_6D_6, 26 °C): δ −117.8 (d, $^1J_{PY}$ = 61 Hz) ppm. ^{31}P NMR (202 MHz, C_6D_6, 26 °C): δ −117.8 (dd, $^1J_{PY}$ = 62/60 Hz; $^1J_{PH}$ = 191 Hz) ppm. ^{89}Y NMR (from ^{1}H−^{89}Y HSQC, 25 MHz, C_6D_6, 26 °C): δ 843 ppm. IR (nujol, $\tilde{\nu}$): 2951 (w), 2924 (nujol), 2907 (s), 2852 (m), 2548 (vw, B−H), 2345 (vw, P−H), 1578 (vw), 1541 (vw), 1458 (nujol), 1392 (nujol), 993 (vw), 810 (vw), 733 (vw), 667 (vw), 589 (vw), 557 (vw), 492 (w), 467 (w), 456 (m), 430 (m) cm^{-1}. Elemental analysis (%) calcd for $C_{44}H_{71}BYPN_8$ (842.80 g/mol): C 62.71, H 8.49, N 13.30. Found: C 63.65, H 9.27, N 12.82.

[Tp^{tBu,Me}DyMe(HPC$_6$H$_3$*i*Pr-2,6)(DMAP)] (5-Dy). Following the procedure described for **5-Y**, to Tp^{tBu,Me}DyMe(HPC$_6$H$_3$*i*Pr-2,6) (**4-Dy**, 85.3 mg, 0.0931 mmol) in toluene (3 mL) was added a solution of DMAP (11.4 mg, 0.0931 mmol) in toluene (2 mL). Yellow crystals of **5-Dy** could be harvested at −35 °C in toluene. Crystallized yield: 26.0 mg, 0.0284 mmol, 31%. Elemental analysis (%) calculated for $C_{44}H_{71}BDyPN_8$ (916.39 g/mol): C 57.67, H 7.81, N 12.23. Found: C 58.54, H 7.53, N 11.98.

[Tp^{tBu,Me}HoMe(HPC$_6$H$_3$*i*Pr-2,6)(DMAP)] (5-Ho). Following the procedure described for **5-Y**, to Tp^{tBu,Me}HoMe(HPC$_6$H$_3$*i*Pr-2,6) (**4-Ho**, 100 mg, 0.126 mmol) in toluene (3 mL) was added a solution of DMAP (15.3 mg, 0.126 mmol) in toluene (2 mL). Red crystals of **5-Ho** could be harvested at −35 °C in toluene. Yield: 50.0 mg, 0.0663 mmol, 53%. Elemental analysis (%) calcd for $C_{44}H_{71}BHoPN_8{\cdot}C_7H_8$ (1010.96 g/mol): C 62.71, H 8.49, N 13.30. Found: C 60.59, H 7.88, N 11.08. Although the microanalytical data are still outside the range viewed as establishing analytical purity, they are provided to illustrate the best values obtained to date.

[Tp^{tBu,Me}Y(=PC$_6$H$_3$*i*Pr-2,6)(DMAP)$_2$] (6-Y). To a solution of Tp^{tBu,Me}YMe(HPC$_6$H$_3$*i*Pr-2,6) (**4-Y**, 98.3 mg, 0.136 mmol) in toluene (3 mL) was added a solution of DMAP (33.3 mg, 0.273 mmol) in toluene (2 mL), and the mixture was stirred for 4 d at −40 °C. Orange crystals of **6-Y** could be harvested at −35 °C in toluene. Yield: 63.5 mg, 0.0669 mmol, 49%. ^{1}H NMR (400 MHz, C_6D_6, 26 °C): δ 8.34 (s, 4H, 2-py-*H*), 7.06−7.01 (m, 3H, *p*/*m*-Ar*H*), 6.06 (s, 4H, 3-py-*H*), 5.75 (s, 3H, pz-*H*), 3.13 (m, 2H, *i*Pr-C*H*), 2.49 (s, 6H, N(CH_3)$_2$), 2.26 (s, 9H, pz-CH_3), 1.38 (s, 27H, pz-C(CH_3)$_3$), 1.21 (d, 12H, $^3J_{HH}$ 6.99 Hz, *i*Pr-CH_3) ppm. ^{31}P{^{1}H} NMR (121 MHz, C_6D_6, 26 °C): δ −5.5 (d, $^1J_{PY}$ = 282 Hz) ppm. ^{31}P NMR (121 MHz, C_6D_6, 26 °C): δ −5.5 (d, $^1J_{PY}$ 282 Hz) ppm. ^{89}Y NMR (from ^{1}H−^{89}Y HSQC, 25 MHz, C_6D_6, 26 °C): δ 563 ppm. Elemental analysis (%) calcd for $C_{50}H_{77}BYPN_{10}$ (948.93 g/mol): C 63.29, H 8.18, N 14.76. Found: C 63.94, H 8.01, N 13.94.

https://doi.org/10.1021/jacs.3c04335
J. Am. Chem. Soc. 2023, 145, 17720−17733

NMR-Scale Reactivity Studies. *[Tp^{tBu,Me}LuMe(HPC$_6$H$_3$iPr-2,6)] (**4-Lu**).* To a solution of Tp^{tBu,Me}LuMe$_2$ (**1-Lu** 97.0 mg, 0.154 mmol) in toluene (2 mL) was added a solution of H$_2$PC$_6$H$_3$*i*Pr-2,6 (30.0 mg, 0.154 mmol) in toluene (2 mL), and the mixture was stirred for 24 h at ambient temperature. The successful formation of Tp^{tBu,Me}LuMe(HPC$_6$H$_3$*i*Pr-2,6)] was proven by NMR spectroscopy. ^{1}H NMR (400 MHz, C$_6$D$_6$, 26 °C): δ 7.06 (d, 2H, $^3J_{HH}$ 1.40 Hz, *m*-ArH), 7.01 (dd, 1H, $^3J_{HH}$ 6.60 Hz, *p*-ArH), 5.60 (s, 3H, pz-*H*), 4.66 (b, 1H, B*H*), 3.30 (m, 2H, *i*Pr-C*H*), 2.08 (s, 9H, pz-CH_3), 1.97 (d, 1H, $^1J_{PH}$ 196.31 Hz, P*H*), 1.40 (s, 27H, pz-C(CH_3)$_3$), 1.29 (d, 12H, $^3J_{HH}$ 6.72 Hz, *i*Pr-CH_3), 0.62 (d, 3H, $^1J_{YH}$ 1.39 Hz, Y(CH_3)) ppm. ^{11}B{^{1}H} NMR (128 MHz, C$_6$D$_6$, 26 °C): δ −8.32 ppm. ^{31}P{^{1}H}NMR (162 MHz, C$_6$D$_6$, 26 °C): δ −118.06 ppm. ^{13}C{^{1}H} NMR (100 MHz, C$_6$D$_6$, 26 °C): δ 199.1, 181.7, 166.5, 148.4, 122.9, 121.9, 104.6, 33.4, 33.3, 32.9, 31.6, 24.3, 13.4 ppm.

*Reaction of **4-Lu** with 1 equiv of DMAP.* A J. Young NMR tube was charged with a solution of Tp^{tBu,Me}LuMe(HPC$_6$H$_3$*i*Pr-2,6) (**4-Lu**, 8.47 mg, 0.01 mmol) in C$_6$D$_6$ (0.4 mL). To the solution was added DMAP (1.28 mg, 0.01 mmol) in C$_6$D$_6$ (0.2 mL) at −35 °C. The tube was allowed to warm to ambient temperature and agitated. ^{1}H and ^{31}P{^{1}H} NMR spectra did not indicate the generation of a terminal phosphinidene.

*Reaction of **4-Lu** with 2 equiv of DMAP.* The aforementioned NMR tube was transferred to a vial and dried under vacuum, and DMAP (1.28 mg, 0.01 mmol) in toluene (0.6 mL) was added at −35 °C. The solution was stirred at −35 °C for 3 days, after which the solvent was evaporated under vacuum. ^{1}H NMR and ^{31}P{^{1}H} NMR spectra did not indicate the generation of a terminal phosphinidene.

*Reaction of **3-Y^{Al}** with O=CPh$_2$.* A J. Young NMR tube was charged with a solution of Tp^{tBu,Me}Y(PC$_6$H$_3$*i*Pr-2,6)(AlMe$_3$) (**3-Y^{Al}**, 46.4 mg, 0.04 mmol) in C$_6$D$_6$ (0.4 mL). To the solution was added benzophenone (8.02 mg, 0.04 mmol) as a solution in C$_6$D$_6$ (0.2 mL), and the tube was agitated. The ^{31}P{^{1}H} NMR spectrum confirmed the formation of Ar^{iPr}P=CPh$_2$. ^{31}P{^{1}H} NMR (162 MHz, C$_6$D$_6$, 26 °C): δ 233.91 ppm.

*Reaction of **3-Y^{Al}** with ^{13}CO$_2$.* A J. Young NMR tube was charged with a solution of Tp^{tBu,Me}Y(PC$_6$H$_3$*i*Pr-2,6)(AlMe$_3$) (**3-Y^{Al}**, 12.34 mg, 0.01 mmol) in C$_6$D$_6$ (0.4 mL). The tube was gassed with 1 bar ^{13}CO$_2$. ^{13}C{^{1}H} NMR spectra confirmed the generation of CO. ^{13}C{^{1}H} NMR (126 MHz, C$_6$D$_6$, 26 °C): 184.1 (s, CO) ppm.

Computational Details. DFT calculations were carried out with the Gaussian 16 program package[40] using the B3PW91 hybrid functional.[48] For Sc, Y, K, and Cl, Stuttgart/Dresden effective core potentials were employed in combination with the optimized valence basis sets as implemented in Gaussian 16.[49] For all other atoms, the 6-31G(d,p) basis set was used.[50] Starting with the molecular structures, as determined by X-ray crystallography, the geometries were optimized without imposing any symmetry constraints, and the structures obtained were confirmed as true minima by calculating analytical frequencies. No dispersion correction was employed, as the geometry optimizations either failed or led to bonding parameters that deviated significantly from the X-ray geometries. The NBO analyzes were carried out using NBO 6.0.[41] All NBO and structural plots were generated using Chemcraft.[51]

■ ASSOCIATED CONTENT

Supporting Information

The Supporting Information is available free of charge at https://pubs.acs.org/doi/10.1021/jacs.3c04335.

Supporting figures, detailed crystallographic and computational data, and spectroscopic data (PDF)

Accession Codes

CCDC 2256661−2256670 contain the supplementary crystallographic data for this paper. These data can be obtained free of charge via www.ccdc.cam.ac.uk/data_request/cif, or by emailing data_request@ccdc.cam.ac.uk, or by contacting The Cambridge Crystallographic Data Centre, 12 Union Road, Cambridge CB2 1EZ, UK; fax: +44 1223 336033.

■ AUTHOR INFORMATION

Corresponding Authors

Reiner Anwander − *Institut für Anorganische Chemie, Eberhard Karls Universität Tübingen, 72076 Tübingen, Germany*; orcid.org/0000-0002-1543-3787; Email: reiner.anwander@uni-tuebingen.de

Peter Sirsch − *Institut für Anorganische Chemie, Eberhard Karls Universität Tübingen, 72076 Tübingen, Germany*; Email: peter.sirsch@uni-tuebingen.de

Authors

Theresa E. Rieser − *Institut für Anorganische Chemie, Eberhard Karls Universität Tübingen, 72076 Tübingen, Germany*

Philipp Wetzel − *Institut für Anorganische Chemie, Eberhard Karls Universität Tübingen, 72076 Tübingen, Germany*

Cäcilia Maichle-Mössmer − *Institut für Anorganische Chemie, Eberhard Karls Universität Tübingen, 72076 Tübingen, Germany*; orcid.org/0000-0001-7638-1610

Complete contact information is available at: https://pubs.acs.org/10.1021/jacs.3c04335

Notes

The authors declare no competing financial interest.

■ ACKNOWLEDGMENTS

We acknowledge support by the State of Baden-Württemberg through bwHPC and the German Research Foundation (DFG) through Grant INST 40/575-1 FUGG (JUSTUS 2 cluster).

■ REFERENCES

(1) Pearson, R. G. Hard and Soft Acids and Bases. *J. Am. Chem. Soc.* **1963**, *85*, 3533−3539.

(2) For examples, see: (a) Raymond, K. N.; Eigenbrot, C. W., Jr Structural Criteria for the Mode of Bonding of Organoactinides and -lanthanides and Related Compounds. *Acc. Chem. Res.* **1980**, *13*, 276−283. (b) Rabe, G. W.; Yap, G. P. A.; Rheingold, A. L. Divalent Lanthanide Chemistry: Three Synthetic Routes to Samarium(II) and Ytterbium(II) Bis(phosphido) Species Including the Structural Characterization of Yb[PPh$_2$]$_2$(thf)$_4$ and Sm[PPh$_2$]$_2$(N-MeIm)$_4$. *Inorg. Chem.* **1995**, *34*, 4521−4522. (c) Berardini, M.; Emge, T. J.; Brennan, J. G. Lanthanide−Group 12 metal Chalkogenolates: A Versatile Class of Compounds. *Inorg. Chem.* **1995**, *34*, 5327−5334. (d) Rabe, G. W.; Yap, G. P. A.; Rheingold, A. L. Lanthanide Phosphido Complexes: A Comparison of the Divalent Homoleptic Species Ln[(μ-P*t*Bu$_2$)$_2$Li(thf)]$_2$ (Ln = Yb, Eu, Sm) Including the Structural Characterization and a Europium-151 Mössbauer Spectrum of Eu[(μ-P*t*Bu$_2$)$_2$Li(thf)]$_2$. *Inorg. Chem.* **1997**, *36*, 3212−3215. (e) Nief, F.; Ricard, L. New examples of lanthanide(II) phosphides and arsenides with planar coordination at the heteroatom: Crystal structures of [(Mesityl)$_2$P]$_2$Sm(THF)$_4$ and of [(Mesityl)$_2$As]$_2$Sm(THF)$_4$. *J. Organomet. Chem.* **1997**, *529*, 357−360. (f) Rabe, G. W.; Riede, J.; Schier, A. Synthesis, X-ray Crystal Structure Determination, and NMR Spectroscopic Investigation of Two Homoleptic Four-Coordinate Lanthanide Complexes: Trivalent (tBu$_2$P)$_2$La[(μ-P*t*Bu$_2$)$_2$Li(thf)] and Divalent Yb[(μ-P*t*Bu$_2$)$_2$Li(thf)]$_2$. *Inorg. Chem.* **1996**, *35*, 40−45.

(3) Fryzuk, M. D.; Haddad, T. S.; Berg, D. J. Complexes of Groups 3, 4, The Lanthanides And The Actinides Containing Neutral Phosphorus Donor Ligands. *Coord. Chem. Rev.* **1990**, *99*, 137−212.

(4) For reviews, see: (a) Nief, F. Complexes containing bonds between group 3, lanthanide or actinide metals and non-first-row main group elements (excluding halogens. *Coord. Chem. Rev.* **1998**, *178*−*180*, 13−81. (b) Li, T.; Kaercher, S.; Roesky, P. W. Synthesis, structure and reactivity of rare-earth metal complexes containing anionic phosphorus ligands. *Chem. Soc. Rev.* **2014**, *43*, 42−57.

(5) For examples comprising structural data on Ln-phosphide catalysts, see: (a) Douglass, M. R.; Stern, C. L.; Marks, T. J. Intramolecular Hydrophosphination/Cyclization of Phosphinoalkenes and Phosphinoalkynes Catalyzed by Organolanthanides: Scope, Selectivity, and Mechanism. *J. Am. Chem. Soc.* **2001**, *123*, 10221−10238. (b) Zhang, W.-X.; Nishiura, M.; Mashiko, T.; Hou, Z. Half-Sandwich *o*-*N*,*N*-Dimethylaminobenzyl Complexes over the Full Size Range of Group 3 and Lanthanide metals. Synthesis, Structural Charcterization, and Catalysis of Phosphine P−H bond Addition to Carbodiimides. *Chem. Eur. J.* **2008**, *14*, 2167−2179. (c) Yuan, J.; Hu, H.; Cui, C. N-Heterocyclic Carbene−Ytterbium Amide as a Recyclable Homogeneous Precatalyst for Hydrophosphination of Alkenes and Alkynes. *Chem. Eur. J.* **2016**, *22*, 5778−5785.

(6) Tilley, T. D.; Andersen, R. A.; Zalkin, A. Tertiary Phosphine complexes of the f-Block Metals. Preparation of Pentamethylcyclopentadienyl-Tertiary Phosphine Complexes of Ytterbium(II), Ytterbium(III) and Europium(II). Crystal Structure of Yb(Me_5C_5)$_2$Cl($Me_2PCH_2PMe_2$). *Inorg. Chem.* **1983**, *22*, 856−859.

(7) Schumann, H.; Palamidis, E.; Schmid, G.; Boese, R. [($Cp_2Lu\{\mu$-$PPh_2\}_2$Li(tmeda)] · 1/2 $C_6H_5CH_3$, the First Organolanthanoid-Phosphane Compound to be Characterized by X-Ray Structure Analysis. *Angew. Chem., Int. Ed. Engl.* **1986**, *25*, 718−719.

(8) Aspinall, H. C.; Moore, S. R.; Smith, A. K. Synthesis and crystal structure of a lanthanum complex with a diphenylphosphide ligand. *J. Chem. Soc., Dalton Trans.* **1992**, 153−156.

(9) (a) Hou, Z.; Zhang, Y.; Tezuka, H.; Xie, P.; Tardif, O.; Koizumi, T.; Yamazaki, H.; Wakatsuki, Y. C_5Me_5/ER-Ligate Samarium(II) Complexes with the Neutral "C_5Me_4M" Ligand (ER = OAr, SAr, NRR', or PHAr; M = K or Na): A Unique Catalytic System for Polymerization and Block-Copolymerization of Styrene and Ethylene. *J. Am. Chem. Soc.* **2000**, *122*, 10533−10543. (b) Westerhausen, M.; Schneiderbauer, S.; Makropoulos, N.; Warchhold, M.; Nöth, H.; Piotrowski, H.; Karaghiosoff, K. Synthesis and Structures of Lithium and Potassium Complexes of Phosphanyl-Substituted Bis[1,3-bis(trimethylsilyl)cyclopentadienyl]yttriates. *Organometallics* **2002**, *21*, 4335−4341. (c) Krieck, S.; Görls, H.; Westerhausen, M. Synthesis and crystal structure of dinuclear [($thf)_3YCl_2\{\mu$-P(H)C_6H_2-2,4,6-$Me_3\}]_2$ with seven-coordinate yttrium atoms. *Inorg. Chem. Commun.* **2009**, *12*, 409−411. (d) Selikhov, A. N.; Mahrova, T. V.; Cherkasov, A. V.; Fukin, G. K.; Kirillov, E.; Lamsfus, C. A.; Maron, L.; Trifonov, A. A. Yb(II) Triple-Decker Complex with the μ-Bridging Naphthalene Cianion [Cp^{Bn5}Yb(DME)]$_2$(μ-η^4:η^4-$C_{10}H_8$). Oxidative Substitution of $[C_{10}H_8]^{2-}$ by 1,4-Diphenylbuta-1,3-diene and P_4 and Protonolysis of Yb−$C_{10}H_8$ Bond by $PhPH_2$. *Organometallics* **2016**, *35*, 2401−2409.

(10) (a) Rabe, G. W.; Guzei, I. A.; Rheingold, A. L. Synthesis and X-ray Crystal Structure Determination of the First Lanthanide Complexes Containing Primary Phosphide Ligands: Ln[P(H)-Mes*]$_2$($thf)_4$ (Ln = Yb, Eu). *Inorg. Chem.* **1997**, *36*, 4914−4915. (b) Westerhausen, M.; Schneiderbauer, S.; Hartmann, M.; Warchhold, M.; Nöth, H. Synthese und Strukturen von Yttrium-tris[bis(trimethylsilyl)phosphanid] und 1, 1', 3, 3'-Tetrakis-(trimethylsilyl)yttrocen-tri(tert-butyl)silylphosphanid. *Z. Anorg. Allg. Chem.* **2002**, *628*, 330−332. (c) Watt, F. A.; Krishna, A.; Golovanov, G.; Ott, H.; Schoch, R.; Wölper, C.; Neuba, A. G.; Hohloch, S. Monoanionic Anilidophosphine Ligand in Lanthanide Chemistry: Scope, Reactivity, and Electrochemistry. *Inorg. Chem.* **2020**, *59*, 2719−2732.

(11) Wicker, B. F.; Scott, J.; Andino, J. G.; Gao, X.; Park, H.; Pink, M.; Mindiola, D. J. Phosphinidene Complexes of Scandium: Powerful PAr Group-Transfer Vehicles to Organic and Inorganic Substrates. *J. Am. Chem. Soc.* **2010**, *132*, 3691−3693.

(12) Lv, Y.; Kefalidis, C. E.; Zhou, J.; Maron, L.; Leng, X.; Chen, Y. Versatile Reactivity of a Four-Coordinate Scandium Phosphinidene Complex: Reduction, Addition, and CO Activation Reactions. *J. Am. Chem. Soc.* **2013**, *135*, 14784−14796.

(13) Watt, F. A.; McCabe, K. N.; Schoch, R.; Maron, L.; Hohloch, S. A transient lanthanum phosphinidene complex. *Chem. Commun.* **2020**, *56*, 15410−15413.

(14) Patrick, E. A.; Yang, Y.; Piers, W. E.; Maron, L.; Gelfand, B. S. A monoanionic pentadentate ligand platform for scandium−pnictogen multiple bonds. *Chem. Commun.* **2021**, *57*, 8640−8643.

(15) For reviews, see: (a) Giesbrecht, G. R.; Gordon, J. C. Lanthanide alkylidene and imido complexes. *Dalton Trans.* **2004**, 2387−2393. (b) Summerscales, O. T.; Gordon, J. C. Complexes containing multiple bonding interactions between lanthanoid elements and main-group fragments. *RSC Advance* **2013**, *3*, 6682−6692. (c) Lu, E.; Chu, J.; Chen, Y. Scandium Terminal Imido Chemistry. *Acc. Chem. Res.* **2018**, *51*, 557−566. (d) Zhu, Q.; Zhu, J.; Zhu, C. Recent progress in the chemistry of lanthanide-ligand multiple bonds. *Tetrahedron Lett.* **2018**, *59*, 514−520. (e) Schädle, D.; Anwander, R. Rare-earth metal and actinide organoimide chemistry. *Chem. Soc. Rev.* **2019**, *48*, 5752−5805.

(16) (a) Lu, E.; Li, Y.; Chen, Y. A scandium terminal imido complex: synthesis, structure and DFT studies. *Chem. Commun.* **2010**, *46*, 4469−4471. (b) Lu, E.; Chu, J.; Chen, Y.; Borzov, M. V.; Li, G. Scandium terminal imido complex induced C−H bond selenation and formation of an Sc−Se bond. *Chem. Commun.* **2011**, *47*, 743−745. (c) Rong, W.; Cheng, J.; Mou, Z.; Xie, H.; Cui, D. Facile Preparation of a Scandium Terminal Imido Complex Supported by a Phosphazene Ligand. *Organometallics* **2013**, *32*, 5523−5529. (d) Schädle, D.; Meermann-Zimmermann, M.; Schädle, C.; Maichle-Mössmer, C.; Anwander, R. Rare-Earth Metal Complexes with Terminal Imido Ligands. *Eur. J. Inorg. Chem.* **2015**, *2015*, 1334−1339.

(17) Lv, Y.; Zhou, J.; Leng, X.; Chen, Y. Substitution reaction of triphenylphosphine oxide with rare-earth metal phosphido methyl complexes. *New J. Chem.* **2015**, *39*, 7582−7588.

(18) Zhou, J.; Xiang, L.; Guo, J.; Leng, X.; Chen, Y. Formation and Reactivity of a C-P-N-Sc Four-Membered Ring: H_2, O_2, CO, Phenylsilane, and Pinacolborane Activation. *Chem. Eur. J.* **2017**, *23*, 5424−5428.

(19) Zhou, J.; Li, T.; Maron, L.; Leng, X.; Chen, Y. A Scandium Complex Bearing Both Methylidene and Phosphinidene Ligands: Synthesis, Structure, and Reactivity. *Organometallics* **2015**, *34*, 470−476.

(20) For reviews, see: (a) Huttner, G.; Knoll, K. RP-Bridged Metal Carbonyl Clusters: Synthesis, Properties, and Reactions. *Angew. Chem., Int. Ed. Engl.* **1987**, *26*, 743−760. (b) Cowley, A. H.; Barron, A. R. The Quest for Terminal Phosphinidene Complexes. *Acc. Chem. Res.* **1988**, *21*, 81−87. (c) Stephan, D. W. Zirconium − Phosphorus Chemsitry: Strategies in Syntheses, Reactivity, Catalysis, and Utility. *Angew. Chem., Int. Ed.* **2000**, *39*, 314−329. (d) Mathey, F. Phospha-Organic Chemistry:Panorama and Perspectives. *Angew. Chem., Int. Ed.* **2003**, *42*, 1578−1604. (e) Greenberg, S.; Stephan, D. W. Stoichiometric and catalytic activation of P−H and P−P bonds. *Chem. Soc. Rev.* **2008**, *37*, 1482−1489. (f) Waterman, R. Metal-phosphido and -phosphinidene complexes in P−E bond-forming reactions. *Dalton Trans.* **2009**, 18−26. (g) Aktas, H.; Slootweg, J. C.; Lammertsma, K. Nucleophilic Phosphinidene Complexes: Access and Applicability. *Angew. Chem., Int. Ed.* **2010**, *49*, 2102−2113.

(21) Masuda, J. D.; Jantunen, K. C.; Ozerov, O. V.; Noonan, K. J. T.; Gates, D. P.; Scott, B. L.; Kiplinger, J. L. A Lanthanide Phosphinidene Complex: Synthesis, Structure, and Phospha-Wittig Reactivity. *J. Am. Chem. Soc.* **2008**, *130*, 2408−2409.

(22) Cui, P.; Chen, Y.; Xu, X.; Sun, J. An unprecedented lanthanide phosphinidene halide: synthesis, structure and reactivity. *Chem. Commun.* **2008**, 5547−5549.

(23) Cui, P.; Chen, Y.; Borzov, M. V. Neodymium(III) phosphinidene complexes supported by pentamethylcyclopentadienyl and hydridotris(pyrazolyl)borate ligands. *Dalton Trans.* **2010**, *39*, 6886−6890.

(24) (a) Feng, B.; Xiang, L.; McCabe, K. N.; Maron, L.; Leng, X.; Chen, Y. Synthesis and versatile reactivity of scandium phosphino-

https://doi.org/10.1021/jacs.3c04335
J. Am. Chem. Soc. 2023, 145, 17720−17733

phosphinidene complexes. *Nat. Commun.* **2020**, *11*, 2916. (b) Feng, B.; Zhang, H.-Y.; Qin, H.; Peng, Q.; Leng, X.; Chen, Y. Hydrogenation of Alkenes Catalyzed by Rare-Earth Metal Phosphinophosphinidene Complexes: 1,2-Addition/Elimination Versus σ-Bond Metathesis Mechanism. *CCS Chem.* **2022**, *4*, 3309−3318.
(25) Feng, B.; Xiang, L.; Carpentier, A.; Maron, L.; Leng, X.; Chen, Y. Scandium-Terminal Boronylphosphinidene Complex. *J. Am. Chem. Soc.* **2021**, *143*, 2705−2709.
(26) Lv, Y.; Xu, X.; Chen, Y.; Leng, X.; Borzov, M. V. Well-Defined Soluble P^{3-}-Containing Rare-Earth-Metal Compounds. *Angew. Chem., Int. Ed.* **2011**, *50*, 11227−11229.
(27) Wang, K.; Luo, G.; Hong, J.; Zhou, X.; Weng, L.; Luo, Y.; Zhang, L. Homometallic Rare-Earth Metal Phosphinidene Clusters: Synthesis and Reactivity. *Angew. Chem., Int. Ed.* **2014**, *53*, 1053−1056.
(28) Pugh, T.; Tuna, F.; Ungur, L.; Collison, D.; McInnes, E. J. L.; Chibotaru, L. F.; Layfield, R. A. Influencing the properties of dysprosium single-molecule magnets with phosphorus donor ligands. *Nat. Commun.* **2015**, *6*, 7492.
(29) Nolan, S. P.; Stern, D.; Marks, T. J. Organo-f-element thermochemistry. Absolute metal-ligand bond disruption enthalpies in bis(pentamethylcyclopentadienyl)samarium hydrocarbyl, hydride, dialkylamide, alkoxide, halide, thiolate, and phosphide complexes. Implications for organolanthanide bonding and reactivity. *J. Am. Chem. Soc.* **1989**, *111*, 7844−7853.
(30) (a) Chu, J.; Han, X.; Kefalidis, C. E.; Zhou, J.; Maron, L.; Leng, X.; Chen, Y. Lewis Acid Triggered Reactivity of a Lewis Base Stabilized Scandium-Terminal Imido Complex: C−H Bond Activation, Cycloaddition, and Dehydrofluorination. *J. Am. Chem. Soc.* **2014**, *136*, 10894−10897. (b) Rieser, T. E.; Thim-Spöring, R.; Schädle, D.; Sirsch, P.; Litlabø, R.; Törnroos, K. W.; Maichle-Mössmer, C.; Anwander, R. Open-Shell Early Lanthanide Terminal Imides. *J. Am. Chem. Soc.* **2022**, *144*, 4102−4113.
(31) (a) Solola, L. A.; Zabula, A. V.; Dorfner, W. L.; Manor, B. C.; Carroll, P. J.; Schelter, E. J. Cerium(IV) Imido Complexes: Structural, Computational, and Reactivity Studies. *J. Am. Chem. Soc.* **2017**, *139*, 2435−2442. (b) Cheisson, T.; Kersey, K. D.; Mahieu, N.; McSkimming, A.; Gau, M. R.; Carroll, P. J.; Schelter, E. J. Multiple Bonding in Lanthanides and Actinides: Direct Comparison of Covalency in Thorium(IV)- and Cerium(IV)-Imido Complexes. *J. Am. Chem. Soc.* **2019**, *141*, 9185−9190.
(32) (a) So, Y.-M.; Wang, G.-C.; Li, Y.; Sung, H. H.-Y.; Williams, I. D.; Lin, Z.; Leung, W.-H. A Tetravalent Cerium Complex Containing a Ce = O Bond. *Ange. Chem. Int. Ed.* **2014**, *53*, 1626−1629. (b) Damon, P. L.; Wu, G.; Kaltsoyannis, N.; Hayton, T. W. Formation of a Ce(IV) Oxo Complex via Inner Sphere Nitrate Reduction. *J. Am. Chem. Soc.* **2016**, *138*, 12743−12746. (c) Assefa, M. K.; Wu, G.; Hayton, T. W. Synthesis of a terminal Ce(IV) oxo complex by photolysis of a Ce(III) nitrate complex. *Chem. Sci.* **2017**, *8*, 7873−7878.
(33) Zimmermann, M.; Litlabø, R.; Törnroos, K. W.; Anwander, R. Metastable" $Lu(GaMe_4)_3$ Reacts Like Masked $[LuMe_3]$: Synthesis of an Unsolvated Lanthanide Dimethyl Complex. *Organometallics* **2009**, *28*, 6646−6649.
(34) Schädle, D.; Maichle-Mössmer, C.; Schädle, C.; Anwander, R. Rare-Earth-Metal Methyl, Amide, and Imide Complexes Supported by a Superbulky Scorpionate Ligand. *Chem. Eur. J.* **2015**, *21*, 662−670.
(35) Litlabø, R.; Zimmermann, M.; Saliu, K.; Takats, J.; Törnroos, K. W.; Anwander, R. A Rare-Earth Metal Variant of the Tebbe Reagent. *Angew. Chem., Int. Ed.* **2008**, *47*, 9560−9564.
(36) Shannon, R. D. Revised effective ionic radii and systematic studies of interatomic distances in halides and chalcogenides. *Acta Crystallogr., Sect. A* **1976**, *32*, 751−767.
(37) Rabe, G. W.; Riede, J.; Schier, A. Synthesis and structural characterization of the first lanthanide tris(phosphido) complex: $Tm[P(SiMe_3)_2]_3(thf)_2$. *J. Chem. Soc., Chem. Commun.* **1995**, 577−578.
(38) Yi, W.; Zhang, J.; Hong, L.; Chen, Z.; Zhou, X. Insertion of Isocyanate into the Ln−P σ-Bond of Organolanthanide Phosphides. *Organometallics* **2011**, *30*, 5809−5814.
(39) For terminal actinide organophosphinidenes, see: (a) Arney, D. S.; Schnabel, R. S.; Scott, B. C.; Burns, C. J. Preparation of Actinide Phosphinidene Complexes: Steric Control of Reactivity. *J. Am. Chem. Soc.* **1996**, *118*, 6780−6781. (b) Vilanova, S. P.; Alayoglu, P.; Heidarian, M.; Huang, P.; Walensky, J. R. Metal−LigandMultiple Bonding in Thorium Phosphorus and Thorium Arsenic Complexes. *Chem. Eur. J.* **2017**, *23*, 16748−16752. (c) Zhang, C.; Hou, G.; Zi, G.; Ding, W.; Walter, M. D. A Base-Free Terminal Actinide Phosphinidene Metallocene: Synthesis, Structure, Reactivity, and Computational Studies. *J. Am. Chem. Soc.* **2018**, *140*, 14511−14225. (d) Wang, D.; Ding, W.; Hou, G.; Zi, G.; Walter, M. D. Experimental and Computational Studies on a Base-Free Terminal Uranium Phosphinidene Metallocene. *Chem. Eur. J.* **2020**, *26*, 16888−16899. (e) Wang, D.; Hou, G.; Zi, G.; Walter, M. D. Influence of the Lewis base Ph_3PO on the Reactivity of the Uranium Phosphinidene (η^5-$C_5Me_5)_2U(=P\text{-}2,4,6\text{-}^iPr_3C_6H_2)(OPPh_3)$. *Organometallics* **2021**, *40*, 383−396. (f) Wang, D.; Wang, S.; Li, T.; Heng, Y.; Hou, G.; Zi, G.; Walter, M. D. Reactivity studies involving a Lewis base supported terminal uranium phosphinidene metallocene (η^5-1,3-$(Me_3C)_2C_5H_3)_2U(=P\text{-}2,4,6\text{-}^iPr_3C_6H_2)(OPMe_3)$. *Dalton Trans.* **2021**, *50*, 8349−8363.
(40) Frisch, M. J.; Trucks, G. W.; Schlegel, H. B.; Scuseria, G. E.; Robb, M. A.; Cheeseman, J. R.; Scalmani, G.; Barone, V.; Petersson, G. A.; Nakatsuji, H.; Li, X.; Caricato, M.; Marenich, A. V.; Bloino, J.; Janesko, B. G.; Gomperts, R.; Mennucci, B.; Hratchian, H. P.; Ortiz, J. V.; Izmaylov, A. F.; Sonnenberg, J. L.; Williams-Young, D.; Ding, F.; Lipparini, F.; Egidi, F.; Goings, J.; Peng, B.; Petrone, A.; Henderson, T.; Ranasinghe, D.; Zakrzewski, V. G.; Gao, J.; Rega, N.; Zheng, G.; Liang, W.; Hada, M.; Ehara, M.; Toyota, K.; Fukuda, R.; Hasegawa, J.; Ishida, M.; Nakajima, T.; Honda, Y.; Kitao, O.; Nakai, H.; Vreven, T.; Throssell, K.; Montgomery, J. A., Jr; Peralta, J. E.; Ogliaro, F.; Bearpark, M. J.; Heyd, J. J.; Brothers, E. N.; Kudin, K. N.; Staroverov, V. N.; Keith, T. A.; Kobayashi, R.; Normand, J.; Raghavachari, K.; Rendell, A. P.; Burant, J. C.; Iyengar, S. S.; Tomasi, J.; Cossi, M.; Millam, J. M.; Klene, M.; Adamo, C.; Cammi, R.; Ochterski, J. W.; Martin, R. L.; Morokuma, K.; Farkas, O.; Foresman, J. B.; Fox, D. J.*Gaussian 16*, rev. C.01; Gaussian, Inc.: Wallingford, CT, 2016.
(41) Glendening, E. D.; Badenhoop, J. K.; Reed, A. E.; Carpenter, J. E.; Bohmann, J. A.; Morales, C. M.; Landis, C. R.; Weinhold, F. *NBO 6.0*; Theoretical Chemistry Institute, University of Wisconsin: Madison, WI, 2013.
(42) Since the NLMO compositions were not reported in (ref 25), and also for better comparison, we reoptimized the DFT geometry of **IX**, followed by NBO analysis, using the same methodology as for **6-Y**.
(43) Kölle, P.; Linti, G.; Nöth, H.; Wood, G. L.; Narula, C. K.; Paine, R. T. Contributions to the chemistry of boron, 188. Synthesis and Structures of New 1,3,2,4-Diphosphadiboretanes. *Chem. Ber.* **1988**, *121*, 871−879.
(44) Kisko, J. L.; Hascall, T.; Kimblin, C.; Parkin, G. Phenyl tris(3-tert-butylpyrazolyl)borato complexes of lithium and thallium, [PhTpBu]M (M = Li, Tl): a novel structure for a monomeric tris(pyrazolyl)boratothallium complex and a study of its stereochemical nonrigidity by ^1H and ^{205}Tl NMR spectroscopy. *J. Chem. Soc., Dalton Trans.* **1999**, 1929−1936.
(45) Zimmermann, M.; Frøystein, N. Å.; Fischbach, A.; Sirsch, P.; Dietrich, H. M.; Törnroos, K. W.; Herdtweck, E.; Anwander, R. Homoleptic Rare-Earth Metal(III) Tetramethylaluminates: Structural Chemistry, Reactivity, and Performance in Isoprene Polymerization. *Chem. Eur. J.* **2007**, *13*, 8784−8800.
(46) Dietrich, H. M.; Raudaschl-Sieber, G.; Anwander, R. Trimethylyttrium and Trimethyllutetium. *Angew. Chem., Int. Ed.* **2005**, *44*, 5303−5306.
(47) Dietrich, H. M.; Meermann, C.; Törnroos, K. W.; Anwander, R. Sounding out the Reactivity of Trimethylyttrium. *Organometallics* **2006**, *25*, 4316−4321.
(48) (a) Becke, A. D. Density-funtional thermochemistry. III. The role of exact exchange. *J. Chem. Phys.* **1993**, *98*, 5648−5652. (b) Burke, K.; Perdew, J. P.; Yang, Y. Derivation of a Generalized Gradient Approximation: The PW91 Density Functional. In *Electronic*

https://doi.org/10.1021/jacs.3c04335
J. Am. Chem. Soc. 2023, 145, 17720−17733

Density Functional Theory: Recent Progress and New Directions; Dobson, J. F., Vignale, G., Das, M. P., Eds.; Plenum: New York, NY, 1998; p 81.
(49) (a) Dolg, M.; Wedig, U.; Stoll, H.; Preuss, H. Energy-adjusted ab initio pseudopotentials for the first row transition elements. *J. Chem. Phys.* **1987**, *86*, 866−872. (b) Andrae, D.; Haeussermann, U.; Dolg, M.; Stoll, H.; Preuss, H. Energy-adjusted ab initio pseudopotentials for the second and third row transition elements. *Theor. Chim. Acta* **1990**, *77*, 123−141. (c) Leininger, T.; Nicklass, A.; Küchle, W.; Stoll, H.; Dolg, M.; Bergner, A. The accuracy of the pseudopotential approximation: non-frozen-core effects for spectroscopic constants of alkali fluorides XF (X = K, Rb, Cs). *Chem. Phys. Lett.* **1996**, *255*, 274−280. (d) Bergner, A.; Dolg, M.; Küchle, W.; Stoll, H.; Preuss, H. Ab initio energy-adjusted pseudopotentials for elements of groups 13−17. *Mol. Phys.* **1993**, *80*, 1431−1441.
(50) (a) Ditchfield, R.; Hehre, W. J.; Pople, J. A. Self-consistent molecular-orbital methods. IX. An extended Gaussian-type basis for molecular-orbital studies of organic molecules. *J. Chem. Phys.* **1971**, *54*, 724−728. (b) Dill, J. D.; Pople, J. A. Self-consistent molecular orbital methods. XV. Extended Gaussian-type basis sets for lithium, beryllium, and boron. *J. Chem. Phys.* **1975**, *62*, 2921−2923. (c) Francl, M. M.; Pietro, W. J.; Hehre, W. J.; Binkley, J. S.; Gordon, M. S.; DeFrees, D. J.; Pople, J. A. Self-consistent molecular orbital methods. XXIII. A polarization-type basis set for second-row elements. *J. Chem. Phys.* **1982**, *77*, 3654−3665.
(51) *Chemcraft - graphical software for visualization of quantum chemistry computations*, ver. 1.8, build 5236. http://www.chemcraftprog.com (accessed 2023-03−31).

https://doi.org/10.1021/jacs.3c04335
J. Am. Chem. Soc. 2023, 145, 17720−17733

Supporting Information

A Terminal Yttrium Phosphinidene

Theresa E. Rieser,[a] Philipp Wetzel,[a] Cäcilia Maichle-Mössmer,[a] Peter Sirsch,[a,*] and Reiner Anwander[a,*]

[a] Institut für Anorganische Chemie, Eberhard Karls Universität Tübingen, Auf der Morgenstelle 18, 72076 Tübingen, Germany

*E-mail for R. A.: reiner.anwander@uni-tuebingen.de

Table of Contents

Crystallography

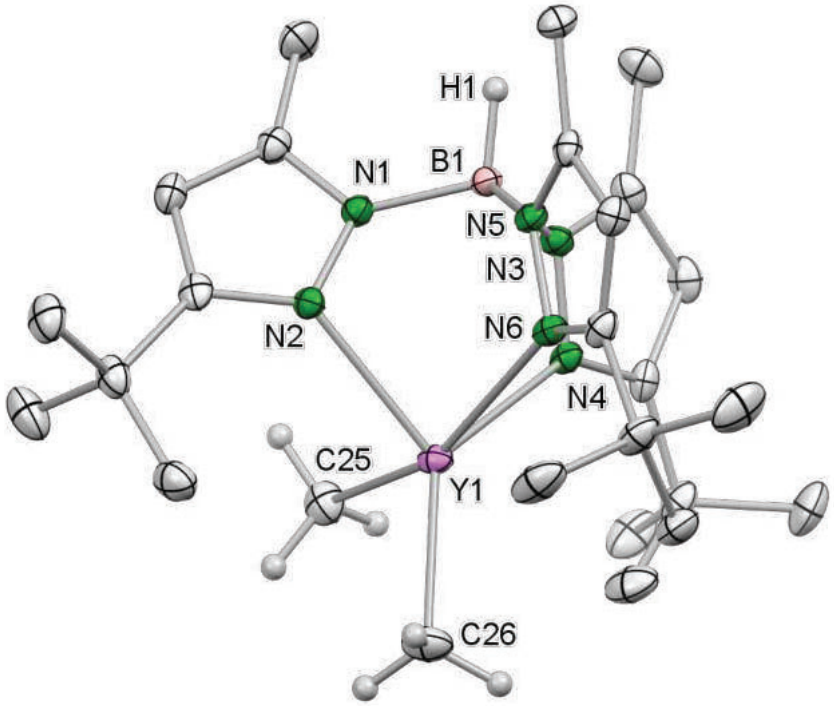

Figure S1. Crystal structure of **1-Y**. Hydrogen atoms except for the BH and two CH_3, and one additional toluene molecule are omitted for clarity. Atomic displacement ellipsoids were set at 50% probability. Selected interatomic distances [Å] and angles [°]: Y1–N2 2.3908(18), Y1–N4 2.3989(17), Y1–N6 2.5280(18), Y1–C25 2.424(2), Y1–C26 2.400(2); N2–Y1–N4 95.50(6), N2–Y1–N6 77.61(6), N2–Y1–C25 86.74(8), N2–Y1–C26 127.77(8), N4–Y1–N6 72.71(6), N4–Y1–C25 88.61(7), N4–Y1–C26 136.40(8), N6–Y1–C25 154.09(7), N6–Y1–C26 108.07(8), C25–Y1–C26 97.84(9).

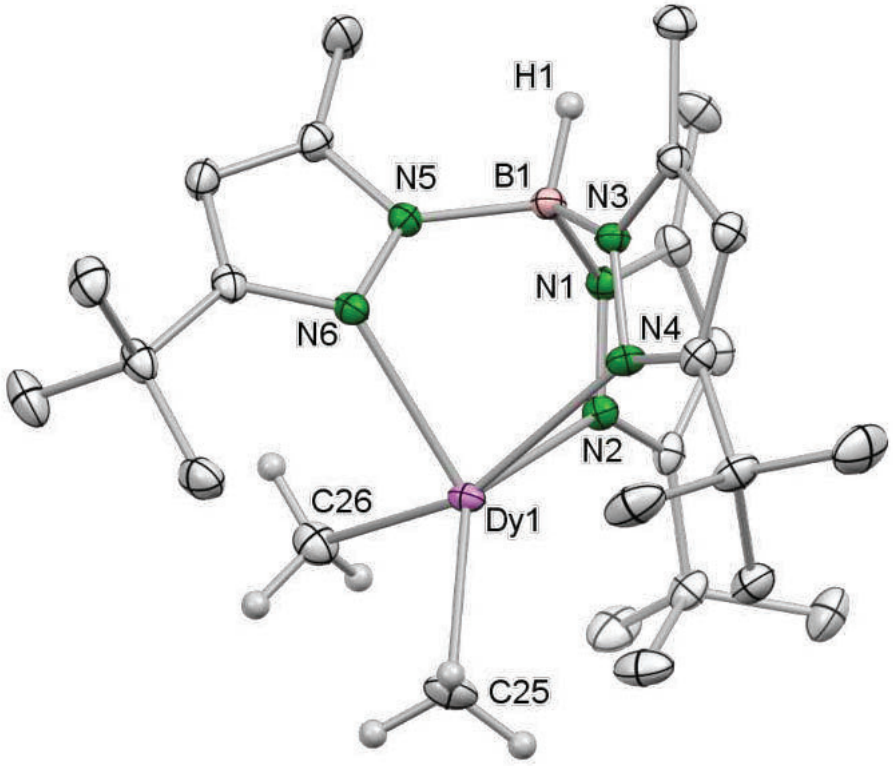

Figure S2. Crystal structure of **1-Dy**. Hydrogen atoms except for the BH and two CH_3, and one additional toluene molecule are omitted for clarity. Atomic displacement ellipsoids were set at 50% probability. Selected interatomic distances [Å] and angles [°]: Dy1–N2 2.4053(13), Dy1–N4 2.5235(14), Dy1–N6 2.3993(13), Dy1–C25 2.4033(18), Dy1–C26 2.4075(18); N2–Dy1–N4 72.71(4), N2–Dy1–N6 95.56(4), N2–Dy1–C25 136.33(5), N2–Dy1–C26 88.34(5), N4–Dy1–N6 77.45(4), N4–Dy1–C25 108.91(6), N4–Dy1–C26 153.59(5), N6–Dy1–C25 127.89(5), N6–Dy1–C26 86.53(5), C25–Dy1–C26 97.50(7).

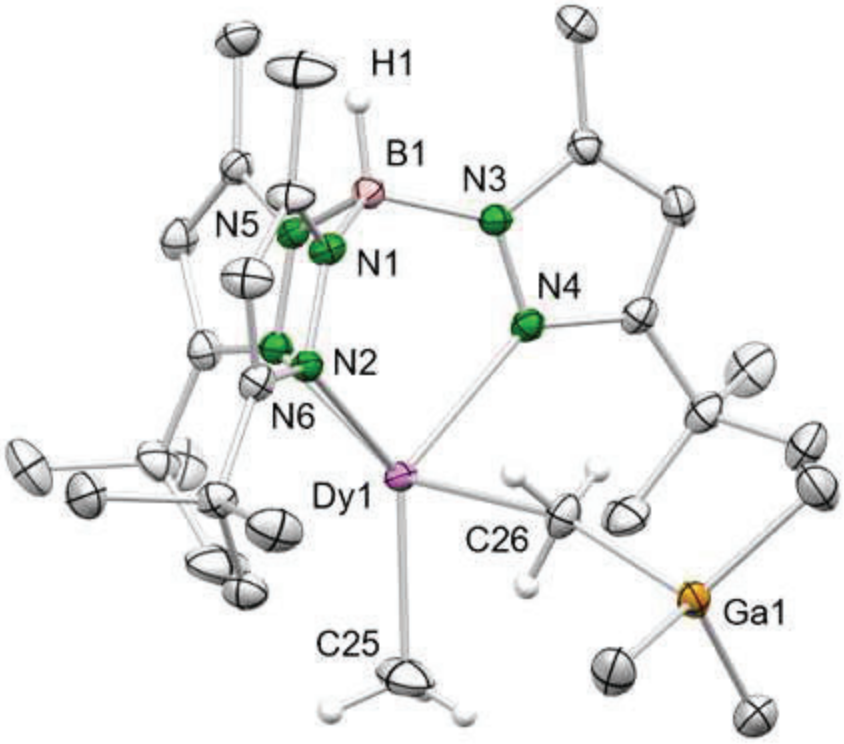

Figure S3. Crystal structure of **2-Dy^{Ga}**. Hydrogen atoms except for the B–H and H–C25/26, and the disorder of one *tert*-butyl group are omitted for clarity. Atomic displacement ellipsoids were set at 50% probability. Selected bond lengths [Å] and angles [°]: Dy1–N2 2.4320(17), Dy1–N4 2.3823(17), Dy1–N6 2.3725(16), Dy1–C25 2.391(2), Dy1–C26 2.738(2); N2–Dy1–N4 77.60(6), N2–Dy1–N6 75.49(5), N2–Dy1–C25 121.12(8), N2–Dy1–C26 151.29(7), N4–Dy1–N6 93.77(5), N4–Dy1–C25 131.35(8), N4–Dy1–C26 82.62(7), N6–Dy1–C25 132.85(8), N6–Dy1–C26 85.36(6), C25–Dy1–C26 87.58(9), Dy1–C26–Ga1 159.27(12).

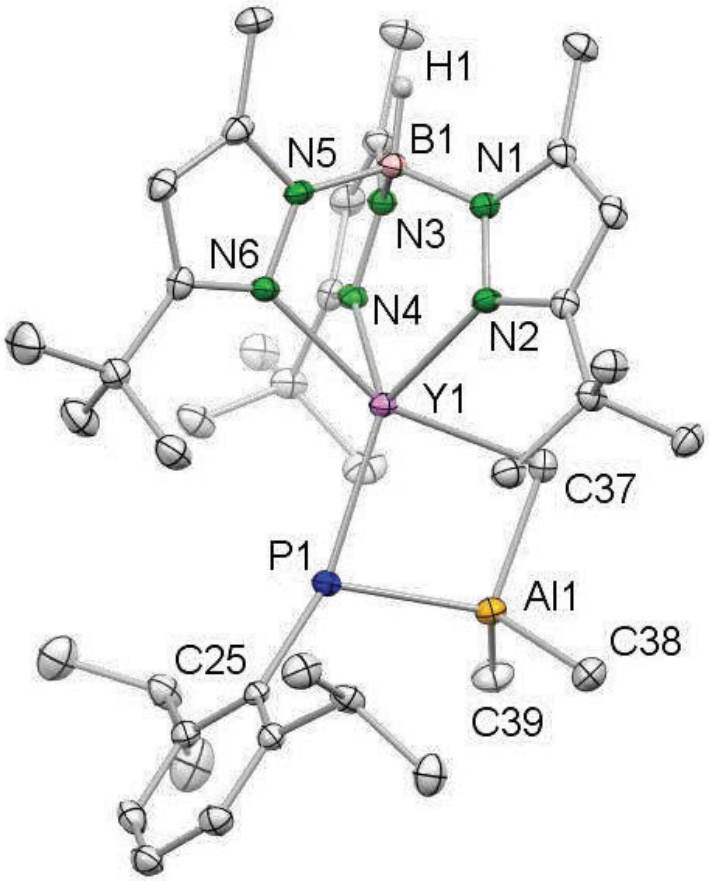

Figure S4. Crystal structure of **3-Y^{Al}**. Hydrogen atoms except for the BH, and three additional toluene molecules are omitted for clarity. Atomic displacement ellipsoids were set at 50% probability. Selected interatomic distances [Å] and angles [°]: Y1–N2 2.372(2), Y1–N4 2.375(2), Y1–N6 2.416(2), Y1–P1 2.5297(7), Y1–C37 2.585(3), Al1–P1 2.3939(10); N2–Y1–N4 99.03(7), N2–Y1–N6 78.47(7), N2–Y1–P1 140.05(5), N2–Y1–C37 86.52(8), N4–Y1–N6 77.25(7), N4–Y1–P1 120.12(5), N4–Y1–C37 89.71(8), N6–Y1–P1 115.61(5), N6–Y1–C37 158.17(8), P1–Y1–C37 86.04(6), Y1–P1–C25 155.94(8).

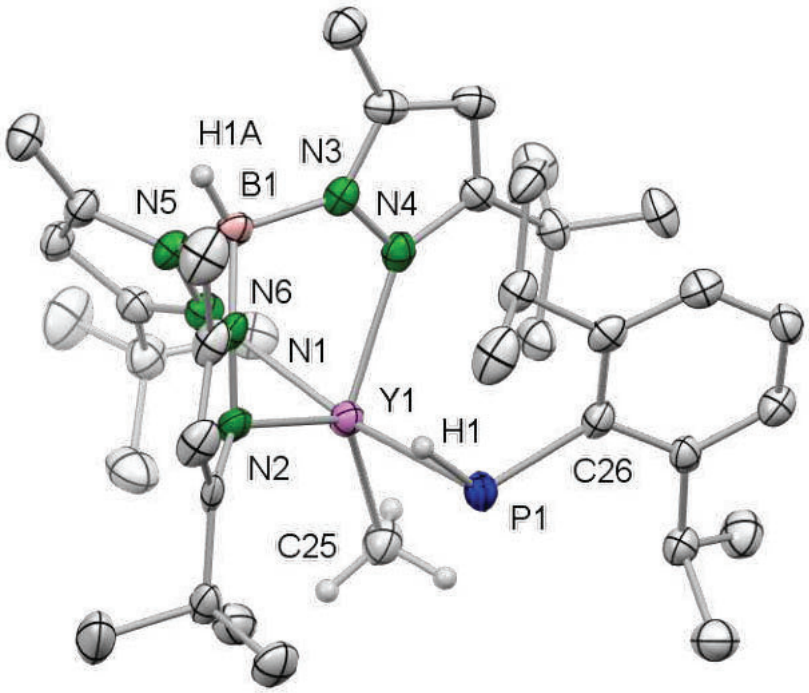

Figure S5. Crystal structure of **4-Y**. Hydrogen atoms except for the BH, PH and CH_3 are omitted for clarity. Atomic displacement ellipsoids were set at 50% probability. Selected interatomic distances [Å] and angles [°]: Y1–N2 2.356(4), Y1–N4 2.341(4), Y1–N6 2.461(4), Y1–C25 2.380(5), Y1–P1 2.8653(14); N2–Y1–N4 96.56(14), N2–Y1–N6 76.21(13), N2–Y1–C25 129.98(17), N2–Y1–P1 80.52(10), N4–Y1–N6 73.71(13), N4–Y1–C25 133.37(16), N4–Y1–P1 92.13(9), N6–Y1–C25 110.56(16), N6–Y1–P1 150.95(10), C25–Y1–P1 97.67(13), Y1–P1–C26 116.36(15).

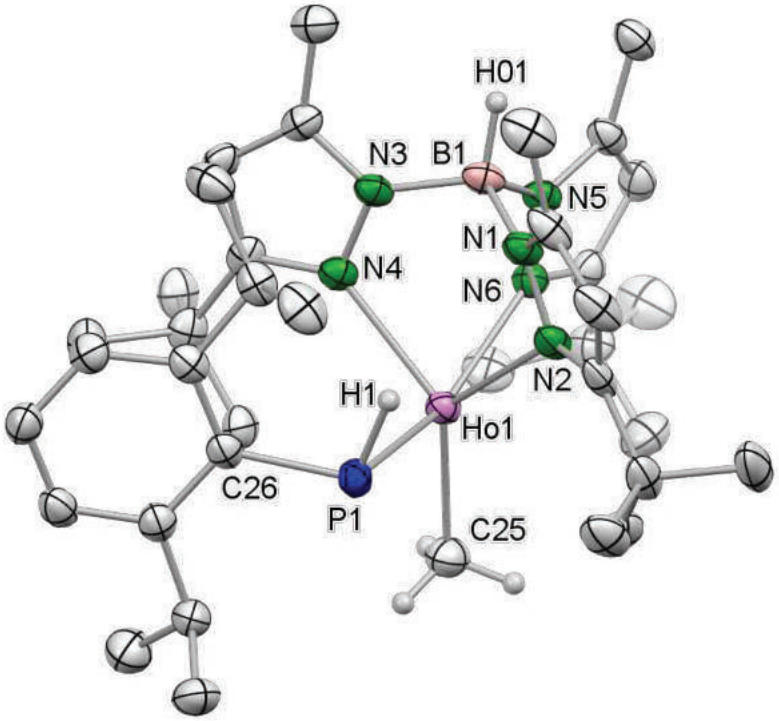

Figure S6. Crystal structure of **4-Ho**. Hydrogen atoms except for the BH, PH and CH_3 are omitted for clarity. Atomic displacement ellipsoids were set at 50% probability. Selected interatomic distances [Å] and angles [°]: Ho1–N2 2.362(4), Ho1–N4 2.348(4), Ho1–N6 2.467(4), Ho1–C25 2.363(5), Ho1–P1 2.8516(12); N2–Ho1–N4 96.79(12), N2–Ho1–N6 75.88(12), N2–Ho1–C25 130.27(15), N2–Ho1–P1 80.69(9), N4–Ho1–N6 73.56(12), N4–Ho1–C25 132.86(15), N4–Ho1–P1 92.28(9), N6–Ho1–C25 111.07(16), N6–Ho1–P1 150.73(9), C25–Ho1–P1 97.42(13), Ho1–P1–C26 116.36(14).

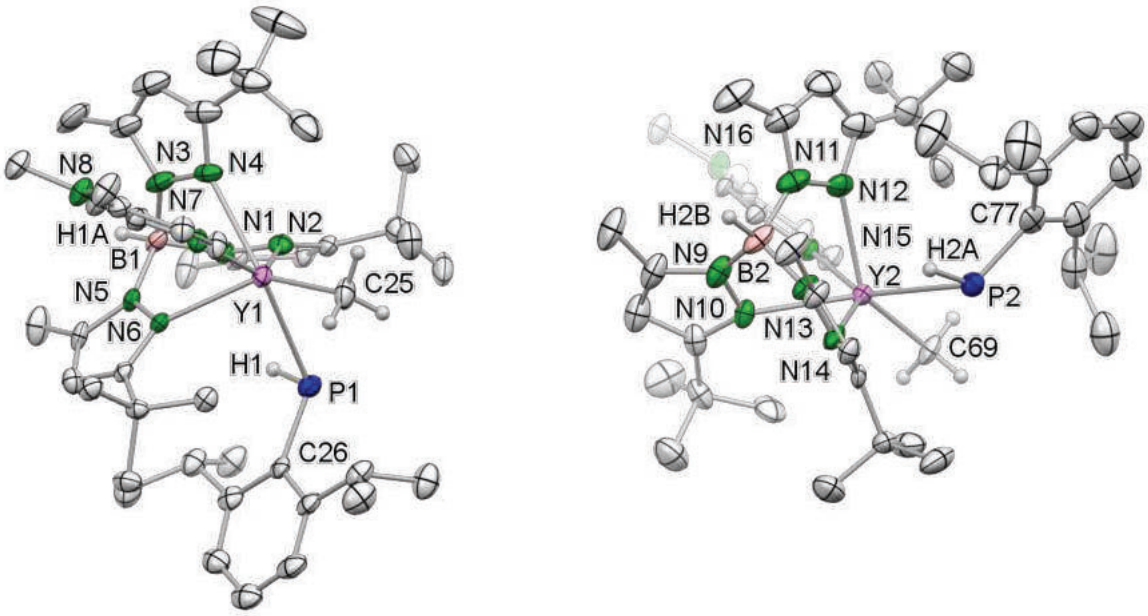

Figure S7. Crystal structure of **5-Y**. Hydrogen atoms except for the BH, PH and CH_3, and two toluene molecules are omitted for clarity. The unit cell contains two independent molecules with different parameters. Atomic displacement ellipsoids were set at 50% probability. Selected interatomic distances [Å] and angles [°]: Y1–N2 2.458(5), Y1–N4 2.493(5), Y1–N6 2.393(4), Y1–N7 2.560(5), Y1–P1 2.9519(18), Y1–C25 2.387(6), Y2–N10 2.499(5), Y2–N12 2.424(5), Y2–N14 2.453(5), Y2–N15 2.549(5), Y2–P2 2.9737(18), Y2–C69 2.406(5); N2–Y1–N4 67.77(16), N2–Y1–N6 94.29(16), N2–Y1–N7 140.36(16), N2–Y1–P1 69.57(11), N2–Y1–C25 124.31(19), N4–Y1–N6 84.62(16), N4–Y1–N7 72.83(16), N4–Y1–P1 134.48(13), N4–Y1–C25 128.1(2), N6–Y1–N7 78.21(15), N6–Y1–P1 83.41(11), N6–Y1–C25 135.13(19), N7–Y1–P1 145.40(12), N7–Y1–C25 83.50(19), P1–Y1–C25 89.39(15), Y1–P1–C26 121.57(19), N10–Y2–N12 86.35(17), N10–Y2–N14 67.79(16), N10–Y2–N15 73.28(15), N10–Y2–P2 135.48(12), N10–Y2–C69 124.05(18), N12–Y2–N14 92.76(17), N12–Y2–N15 78.31(16), N12–Y2–P2 84.69(12), N12–Y2–C69 138.1(2), N14–Y2–N15 140.53(16), N14–Y2–P2 69.21(12), N14–Y2–C69 123.69(19), N15–Y2–P2 145.65(11), N15–Y2–C69 83.72(18), P2–Y2–C69 89.58(15), Y2–P2–C77 124.8(2).

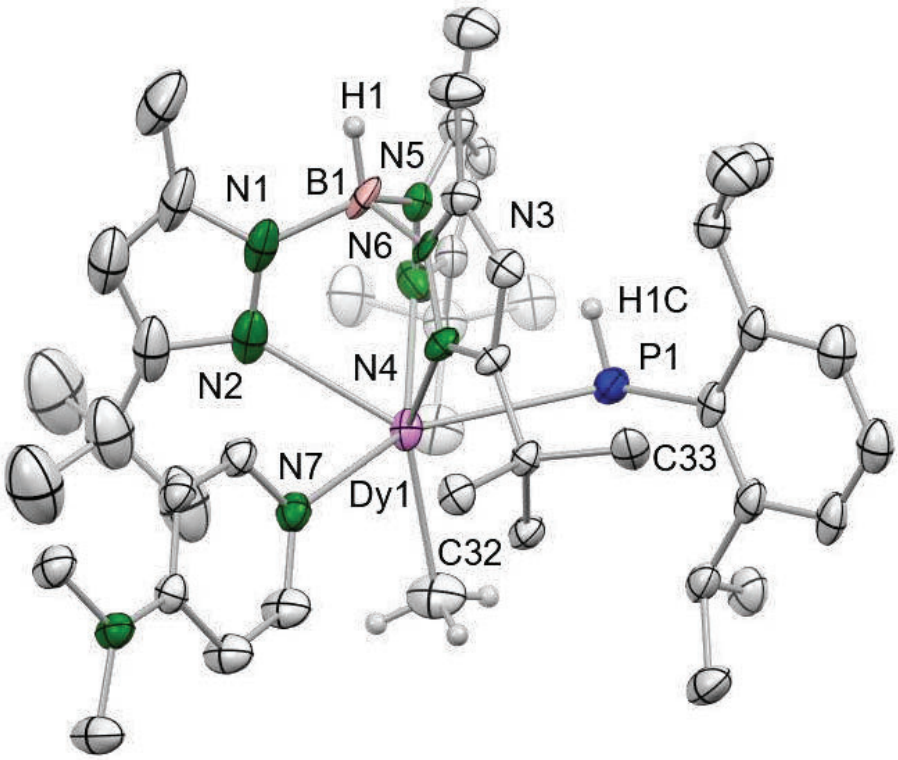

Figure S8. Crystal structure of **5-Dy**. Hydrogen atoms except for the BH, PH and CH_3, and one toluene molecule, and the disorder of the whole molecule are omitted for clarity. Atomic displacement ellipsoids were set at 50% probability. Selected interatomic distances [Å] and angles [°]: Dy1–N2 2.487(19), Dy–N4 2.379(14), Dy1–N6 2.516(9), Dy1–N7 2.569(8), Dy1–P1 2.939(16), Dy1–C32 2.407(11); N2–Dy1–N4 85.5(5), N2–Dy1–N6 68.5(5), N2–Dy1–N7 72.4(5), N2–Dy1–P1 136.1(5), N2–Dy1–C32 128.7(6), N4–Dy1–N6 95.6(4), N4–Dy1–N7 76.6(4), N4–Dy1–P1 84.4(5), N4–Dy1–C32 132.5(4), N6–Dy1–N7 140.7(3), N6–Dy1–P1 70.1(3), N6–Dy1–C32 125.2(3), N7–Dy1–P1 144.5(3), N7–Dy1–C32 83.6(3), P1–Dy1–C32 87.7(4), Dy1–P1–C33 122.4(9).

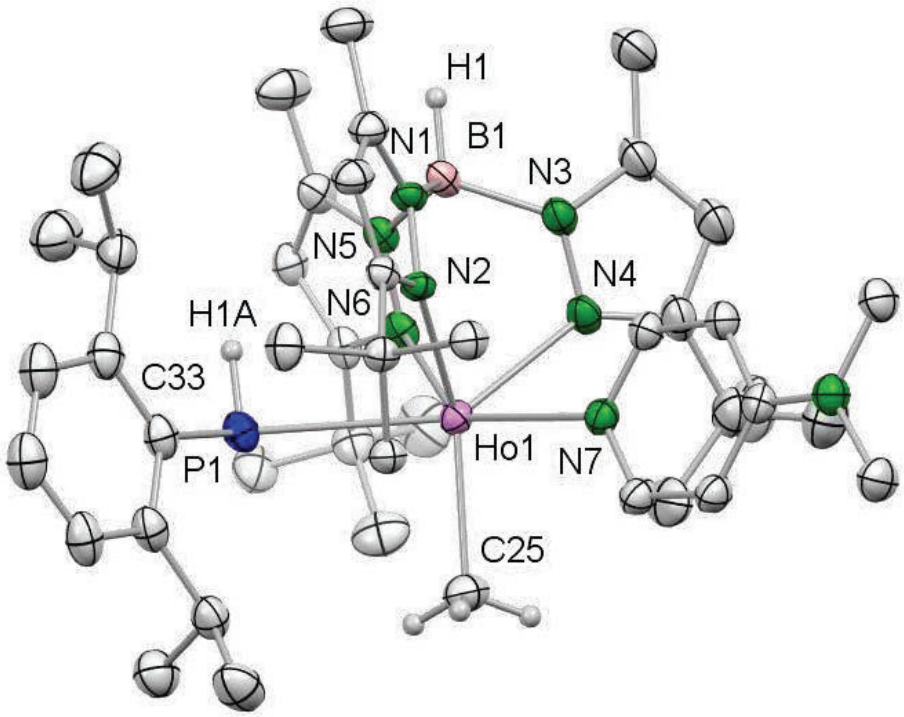

Figure S9. Crystal structure of **5-Ho**. Hydrogen atoms except for the BH, PH and CH_3, one toluene molecule, and the disorder in the whole molecule are omitted for clarity. Atomic displacement ellipsoids were set at 50% probability. Selected interatomic distances [Å] and angles [°]: Ho1–N2 2.368(8), Ho–N4 2.437(5), Ho1–N6 2.451(10), Ho1–N7 2.566(3), Ho1–P1 2.9414(8), Ho1–C25 2.402(3); N2–Ho1–N4 88.2(2), N2–Ho1–N6 94.8(3), N2–Ho1–N7 76.4(2), N2–Ho1–P1 83.3(2), N2–Ho1–C25 133.97(16), N4–Ho1–N6 67.0(2), N4–Ho1–N7 72.84(15), N4–Ho1–P1 135.66(14), N4–Ho1–C25 124.71(16), N6–Ho1–N7 138.88(18), N6–Ho1–P1 70.4(2), N6–Ho1–C25 125.5(2), N7–Ho1–P1 144.79(6), N7–Ho1–C25 84.04(11), P1–Ho1–C25 89.91(10), Ho1–P1–C33 121.7(3).

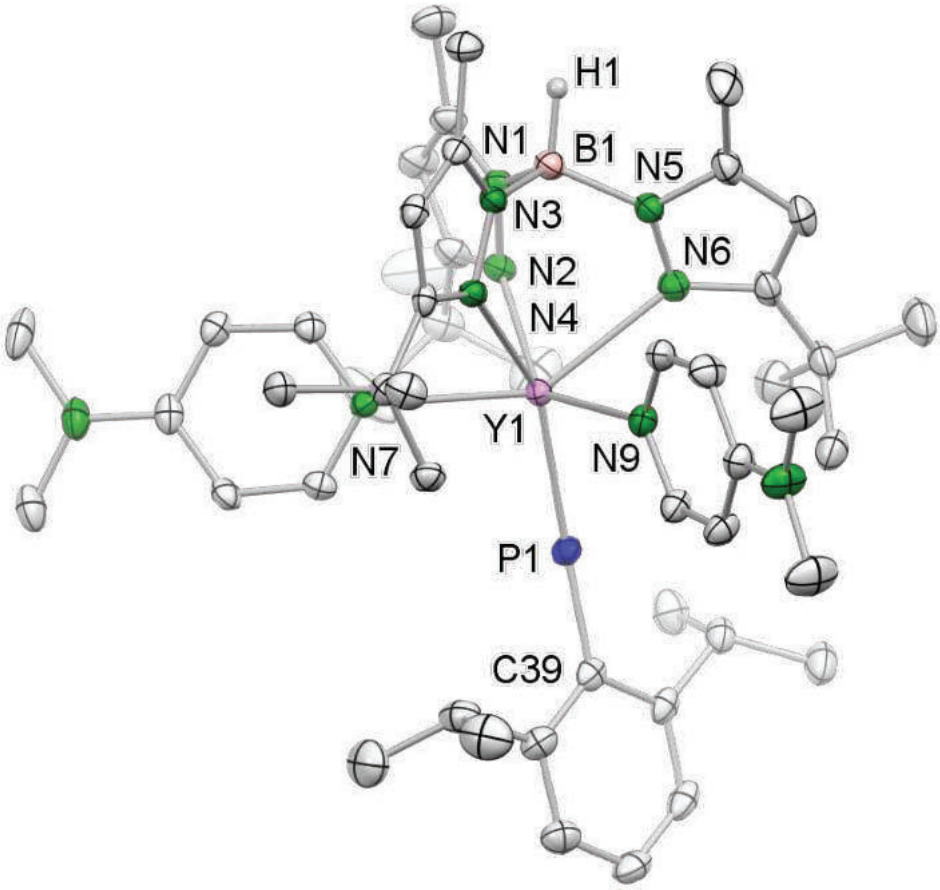

Figure S10. Crystal structure of **6-Y**. Hydrogen atoms except for the BH, and five additional toluene molecules are omitted for clarity. Atomic displacement ellipsoids were set at 50% probability. Selected interatomic distances [Å] and angles [°]: Y1–N2 2.487(2), Y1–N4 2.472(2), Y1–N6 2.498(2), Y1–N7 2.526(2), Y1–N9 2.532(2), Y1–P1 2.4855(7); N2–Y1–N4 88.92(7), N2–Y1–N6 68.81(7), N2–Y1–N7 75.56(7), N2–Y1–N9 140.48(7), N2–Y1–P1 116.86(5), N4–Y1–N6 93.02(7), N4–Y1–N7 74.86(6), N4–Y1–N9 75.29(7), N4–Y1–P1 148.41(5), N6–Y1–N7 142.57(7), N6–Y1–N9 75.99(7), N6–Y1–P1 112.56(5), N7–Y1–N9 131.47(7), N7–Y1–P1 93.28(5), N9–Y1–P1 92.64(5), Y1–P1–C39 163.40(9).

X-ray Crystallography and Crystal Structure Determinations. Single crystals of **1-Y**, **1-Dy**, **3-Y^{Al}**, **4-Y**, **4-Ho**, **5-Y**, **5-Dy**, **5-Ho**, and **6-Y** were grown by standard techniques from saturated solutions using toluene. Suitable crystals for X-ray structure analyses were selected in a glovebox and coated with Parabar 10312 (previously known as Paratone N, Hampton Research) and fixed on a nylon loop/glass fiber.

X-ray data for above mentioned compounds were collected on a Bruker APEX III DUO (all remaining; instruments equipped with an IμS microfocus sealed tube and QUAZAR optics for MoK_α (λ = 0.71073 Å) and CuK_α (λ = 1.54184 Å) radiation. The data collection strategy was determined using COSMO[1] employing ω-scans (APEX III). Raw data were processed using APEX[2] and SAINT,[3] corrections for absorption effects were applied using SADABS.[4] The structures were solved by direct methods and refined against all data by full-matrix least-squares methods on F^2 using ShelXtl[5] and ShelXle.[6] All structures, except **1-Y** and **4-Ho**, showed disorder in the solvent molecules and/or part of the ligands. Disorder models were calculated using DSR, a program for refining disordered structures in ShelXL.[7] For **5-Dy** we found no reliable model, only a connectivity is given. For **5-Y** we only found reflection up to 0.8 Å. All graphics were produced employing ORTEP-3[8] and POV-Ray.[9] Further details of the refinement and crystallographic data are listed in Table S1-S4, and in the CIF files. CCDC depositions 2256661-2256670 contain all the supplementary crystallographic data for this paper. These data can be obtained free of charge from The Cambridge Crystallographic Data Centre via www.ccdc.cam.ac.uk/structures/.

Table S1. Crystallographic data for compounds **1-Y**, **1-Dy**, **2-Dy**, and **3-Y^{Al}**

	1-Y	**1-Dy**	**2-Dy^{Ga}**	**3-Y^{Al}**
formula	$C_{26}H_{46}BN_6Y \cdot 1/2C_7H_8$	$C_{26}H_{46}BN_6Dy \cdot 1/2C_7H_8$	$C_{29}H_{55}BN_6DyGa$	$C_{39}H_{66}AlBN_6PY \cdot 3C_7H_8$
CCDC	2256663	2256664	2256665	2256666
M_r [g mol^{-1}]	588.47	662.06	730.82	1053.04
color	colorless	colorless	colorless	light yellow
crystal dimensions [mm^3]	0.255 x 0.254 x 0.171	0.239 x 0.184 x 0.141	0.103 x 0.086 x 0.068	0.344 x 0.135 x 0.108
cryst syst	monoclinic	monoclinic	monoclinic	triclinic
space group	*C2/c*	*C2/c*	*P2$_1$/n*	$P\bar{1}$
a [Å]	21.1750(18)	21.133(4)	13.5199(12)	12.4454(6)
b [Å]	12.9934(11)	12.985(2)	16.8702(15)	13.6594(6)
c [Å]	24.458(2)	24.413(5)	15.0948(13)	18.9266(9)
α [°]	90	90	90	94.284(2)
β [°]	107.250(2)	107.332(4)	91.183(2)	96.642(2)
γ [°]	90	90	90	109.735(2)
V [Å^3]	6426.5(9)	6395(2)	3442.1(5)	2985.8(2)
Z	8	8	4	2
T [K]	100(2)	100(2)	100(2)	100(2)
ρ_{calcd} [g cm^{-3}]	1.216	1.375	1.410	1.171
μ [mm^{-1}]	1.842	2.364	2.962	1.059
F (000)	2504	2720	1492	1128
θ range [°]	1.744/28.343	1.748/30.556	2.002/29.575	1.596/26.455
Reflns measured	50076	69279	59063	70612
independent reflns	8024	9796	9658	12226
R[b]1/*w*R2 (I>2σ)[c]	0.0423/0.0938	0.0210/0.0468	0.0235/0.0536	0.0432/0.0904
R1[b]/*w*R2 (all data)[c]	0.0644/0.1033	0.0267/0.0493	0.0299/0.0565	0.0652/0.0987
GOF[a]	1.021	1.047	1.038	1.019

[a]GOF = $[\Sigma w(F_0^2 - F_c^2)^2 / (n_0 - n_p)]^{1/2}$. [b]$R_1 = \Sigma(||F_0| - |F_c||) / \Sigma|F_0|$, $F_0 > 4\sigma(F_0)$. [c]$wR_2 = \{\Sigma[w(F_0^2 - F_c^2)^2 / \Sigma[w(F_0^2)^2]\}^{1/2}$.

Table S2. Crystallographic data for compounds **4-Y**, **4-Ho**, and **5-Y**

	4-Y	**4-Ho**	**5-Y***
formula	$C_{37}H_{61}BN_6Y$	$C_{37}H_{61}BN_6PHo$	$C_{44}H_{71}BN_8PY \cdot C_7H_8$
CCDC	2256661	2256662	2256669
M_r [g mol^{-1}]	720.60	796.62	934.91
color	yellow	orange	colorless
crystal dimensions [mm^3]	0.256 x 0.088 x 0.029	0.196 x 0.162 x 0.074	0.130 x 0.093 x 0.092
cryst syst	monoclinic	monoclinic	monoclinic
space group	$P2_1/n$	$P2_1/n$	$P2_1/n$
a [Å]	13.924(2)	13.9290(16)	25.121(4)
b [Å]	18.207(3)	18.188(2)	21.109(3)
c [Å]	16.610(3)	16.6131(19)	20.433(3)
α [°]	90	90	90
β [°]	104.588(3)	104.784(2)	105.490(3)
γ [°]	90	90	90
V [Å^3]	4075.3(11)	4069.6(8)	10442(3)
Z	4	4	8
T [K]	100(2)	100(2)	100(2)
ρ_{calcd} [g cm^{-3}]	1.174	1.300	1.189
μ [mm^{-1}]	1.502	2.015	1.188
F (000)	1536	1648	4000
θ range [°]	1.690/26.493	1.691/23869	1.280/26.372
Reflns measured	27958	41837	142167
independent reflns	8415	6262	21362
R[b]1/wR2 (I>2σ)[c]	0.0635/0.1106	0.0319/0.0658	0.0940/0.1739
R1[b]/wR2 (all data)[c]	0.1572/0.1449	0.0526/0.0755	0.1992/0.1982
GOF[a]	0.963	1.062	1.371

[a]GOF = $[\Sigma w(F_0^2 - F_c^2)^2 / (n_0 - n_p)]^{1/2}$. [b]$R_1 = \Sigma(||F_0| - |F_c||) / \Sigma|F_0|$, $F_0 > 4\sigma(F_0)$. [c]$wR_2 = \{\Sigma[w(F_0^2 - F_c^2)^2 / \Sigma[w(F_0^2)^2]\}^{1/2}$.

* Connectivity only.

Table S3. Crystallographic data for compounds **5-Dy**, **5-Ho**, and **6-Y**

	5-Dy*	**5-Ho**	**6-Y**
formula	$C_{44}H_{71}BN_8PDy \cdot C_7H_8$	$C_{44}H_{71}BN_8PHo \cdot C_7H_8$	$C_{50}H_{77}BN_{10}PY \cdot 4{,}5\ C_7H_8$
CCDC	2256668	2256670	2256667
M_r [g mol^{-1}]	1008.50	1010.93	1363.50
color	yellow	yellow	orange
crystal dimensions [mm^3]	0.231 x 0.175 x 0.080	0.357 x 0.222 x 0.211	0.414 x 0.173 x 0.141
cryst syst	monoclinic	monoclinic	monoclinic
space group	$P2_1/c$	$P2_1/c$	$C2/c$
a [Å]	12.589(2)	12.649(5)	33.4693(15)
b [Å]	21.110(4)	21.053(8)	12.7327(6)
c [Å]	20.444(4)	20.527(10)	36.4322(17)
α [°]	90	90	90
β [°]	105.947(3)	106.463(17)	92.5460(10)
γ [°]	90	90	90
V [Å^3]	5224.0(17)	5242(4)	15510.4(12)
Z	4	4	8
T [K]	100(2)	100(2)	100(2)
ρ_{calcd} [g cm^{-3}]	1.282	1.281	1.168
μ [mm^{-1}]	1.501	1.580	0.821
F (000)	2108	2112	5848
θ range [°]	1.929/28.850	1.935/28.699	1.218/25.260
Reflns measured	103847	124614	86012
independent reflns	13614	13524	14078
R1/wR2 (I>2σ)[a]	0.0972/0.2045	0.0390/0.0885	0.0443/0.0931
R1/wR2 (all data)[a]	0.1218/0.2131	0.0438/0.0910	0.0741/0.1052
GOF[a]	1.294	1.118	1.0218

[a]GOF = $[\Sigma w(F_0^2 - F_c^2)^2 / (n_0 - n_p)]^{1/2}$. [b]$R_1 = \Sigma(||F_0| - |F_c||) / \Sigma|F_0|$, $F_0 > 4\sigma(F_0)$. [c]$wR_2 = \{\Sigma[w(F_0^2 - F_c^2)^2 / \Sigma[w(F_0^2)^2]\}^{1/2}$.

* Connectivity only.

NMR spectroscopy

Notes on NMR spectroscopic characterizations.

Due to the paramagnetic nature of Dy(III) and Ho(III) any conclusive interpretation of the recorded NMR spectra was not possible. In general, solvent peaks are marked with an asterisk (*).

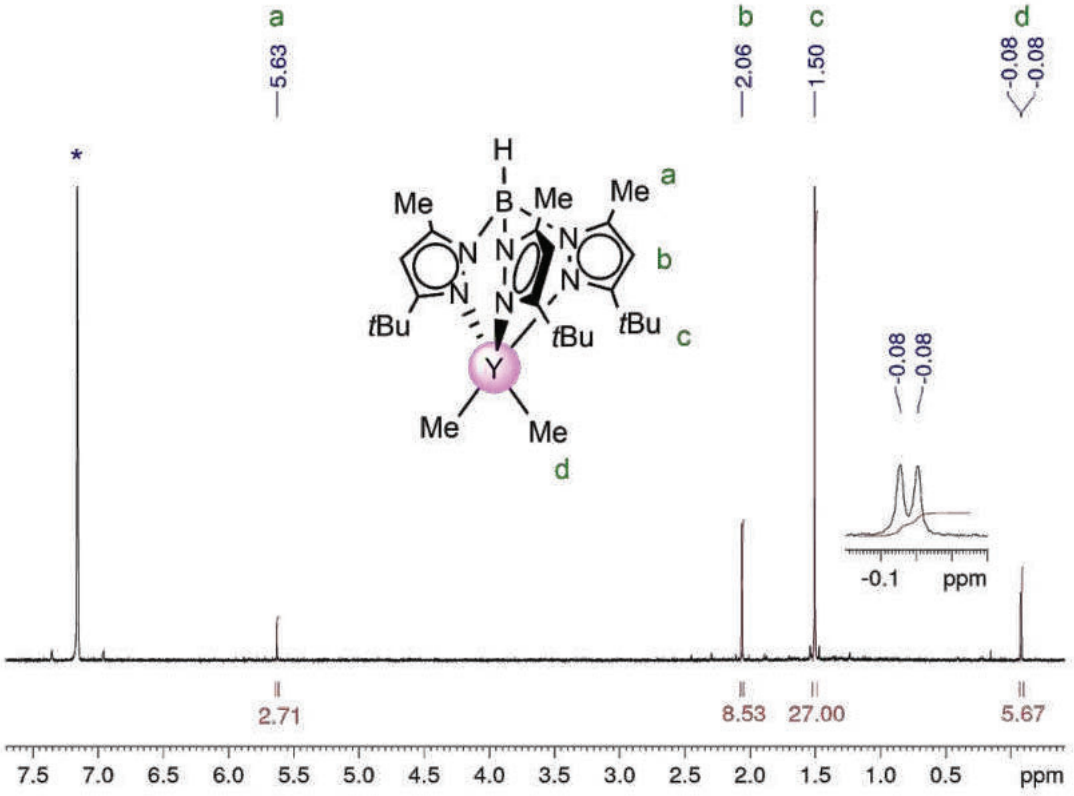

Figure S11. ^{1}H-NMR spectrum (400 MHz) of Tp^{tBu,Me}YMe$_2$ (**1-Y**) in C_6D_6 at 26 °C.

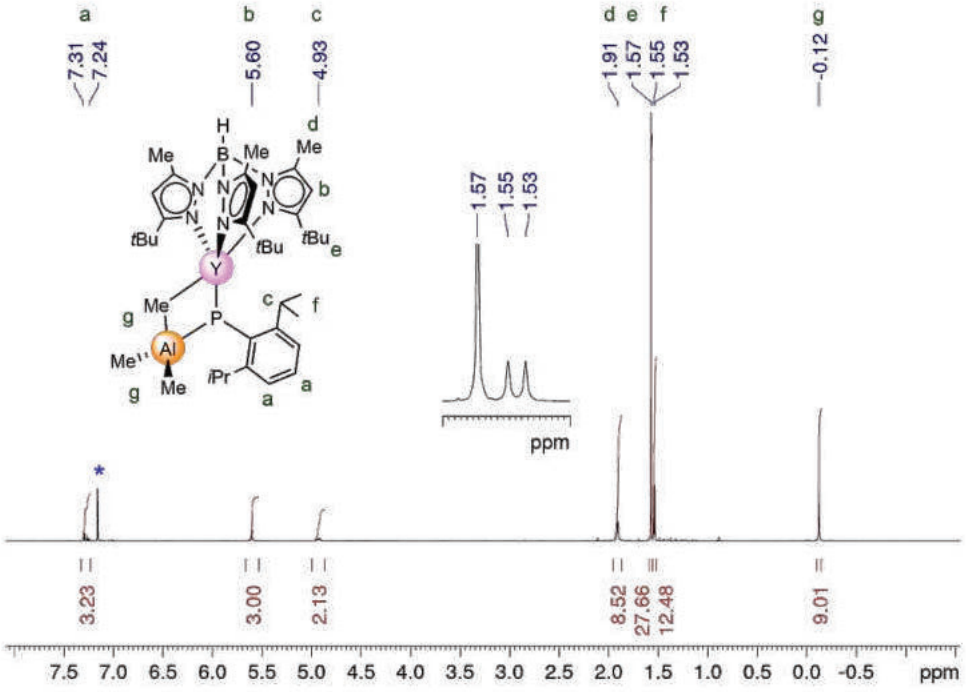

Figure S12. ^{1}H-NMR spectrum (500 MHz) of Tp$^{t\mathrm{Bu,Me}}$YMe[(μ_2-PC$_6$H$_3$*i*Pr$_2$-2,6)(μ_2-Me)AlMe$_2$] (**3-Y$^{\mathbf{Al}}$**) in C$_6$D$_6$ at 26 °C.

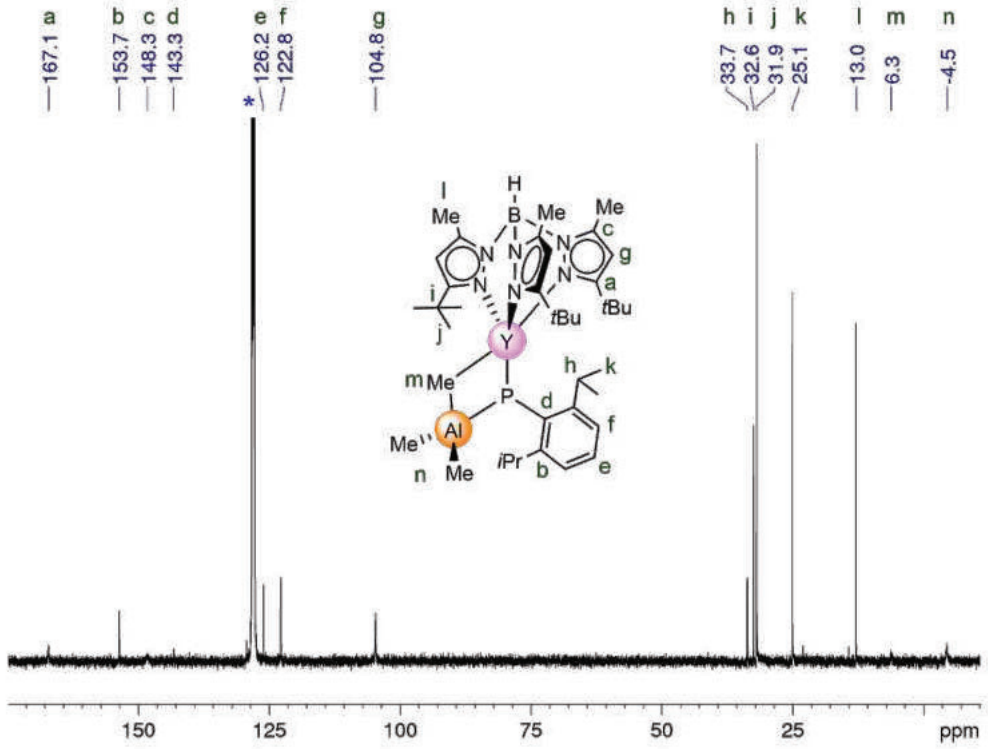

Figure S13. ^{13}C{^{1}H}-NMR spectrum (126 MHz) of Tp$^{t\mathrm{Bu,Me}}$YMe[(μ_2-PC$_6$H$_3$*i*Pr$_2$-2,6)(μ_2-Me)AlMe$_2$] (**3-Y$^{\mathbf{Al}}$**) in C$_6$D$_6$ at 26 °C.

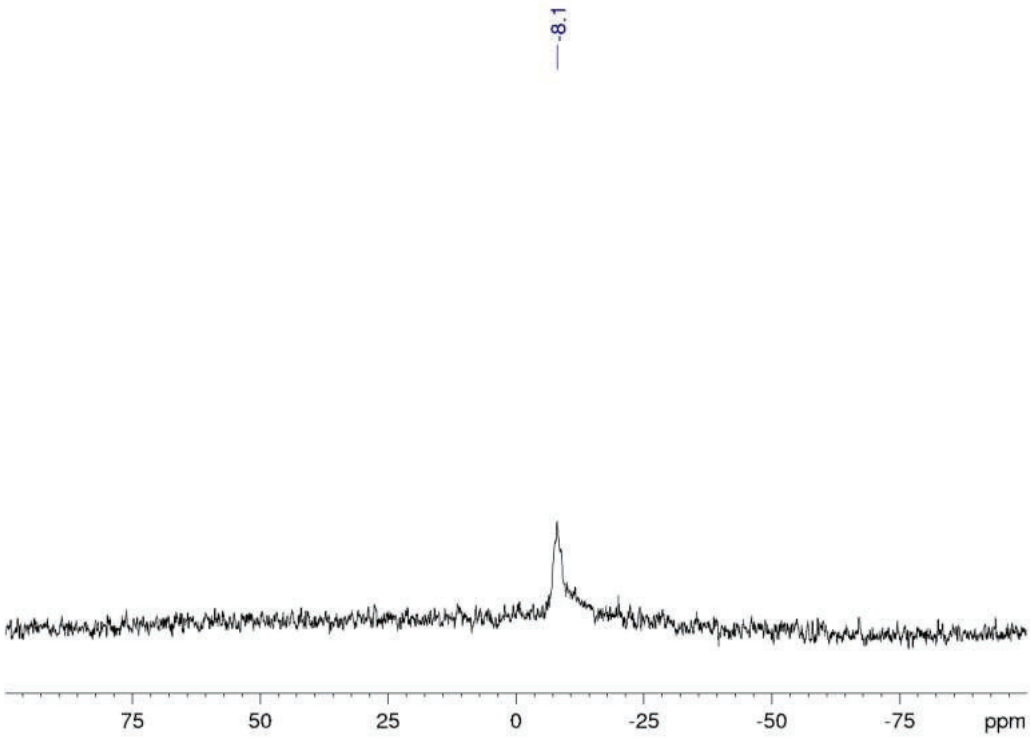

Figure S14. $^{11}B\{^{1}H\}$-NMR spectrum (160 MHz) of $Tp^{tBu,Me}YMe[(\mu_2\text{-}PC_6H_3iPr_2\text{-}2,6)(\mu_2\text{-}Me)AlMe_2]$ (**3-Y^{Al}**) in C_6D_6 at 26 °C.

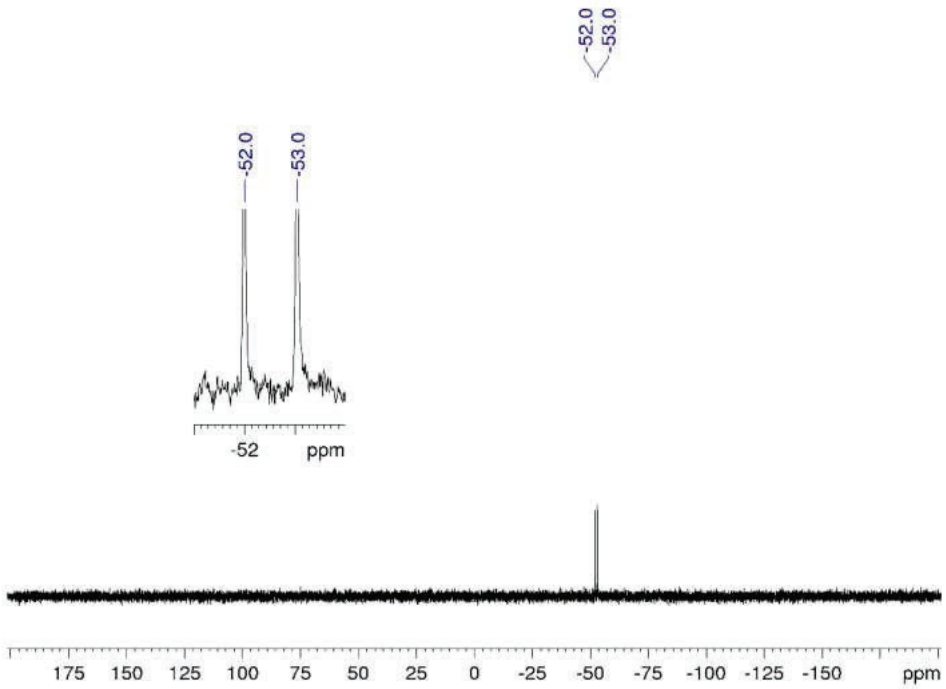

Figure S15. $^{31}P\{^{1}H\}$-NMR spectrum (202 MHz) $Tp^{tBu,Me}YMe[(\mu_2\text{-}PC_6H_3iPr_2\text{-}2,6)(\mu_2\text{-}Me)AlMe_2]$ (**3-Y^{Al}**) in C_6D_6 at 26 °C.

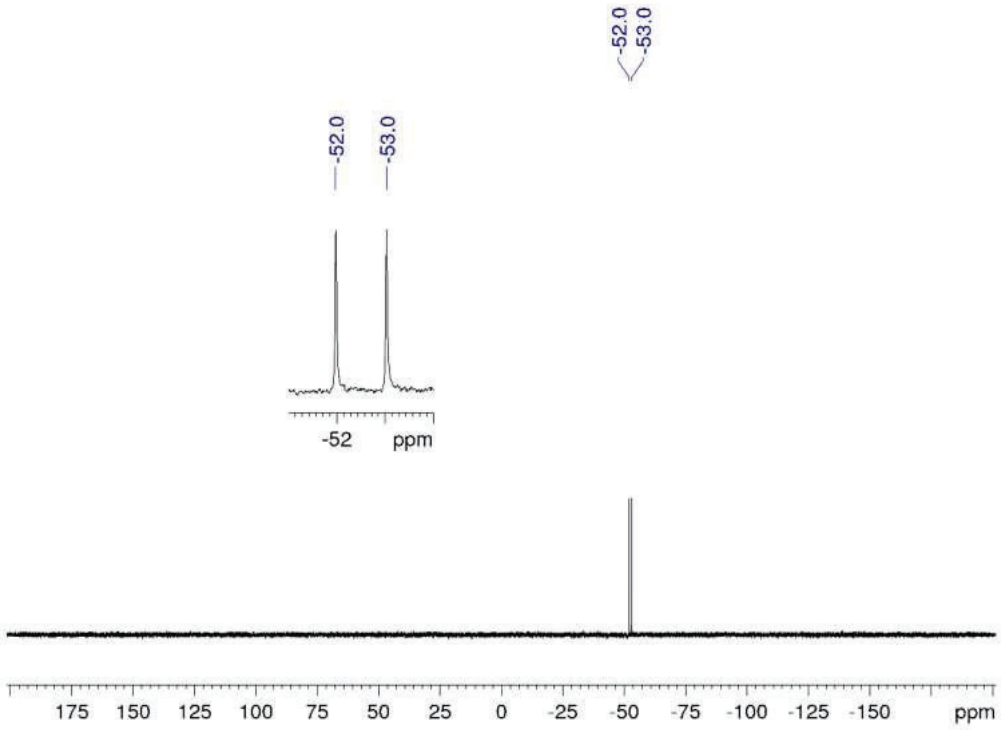

Figure S16. ^{31}P-NMR spectrum (202 MHz) of Tp^{tBu,Me}YMe[(μ_2-PC$_6$H$_3$*i*Pr$_2$-2,6)(μ_2-Me)AlMe$_2$] (**3-Y^{Al}**) in C$_6$D$_6$ at 26 °C.

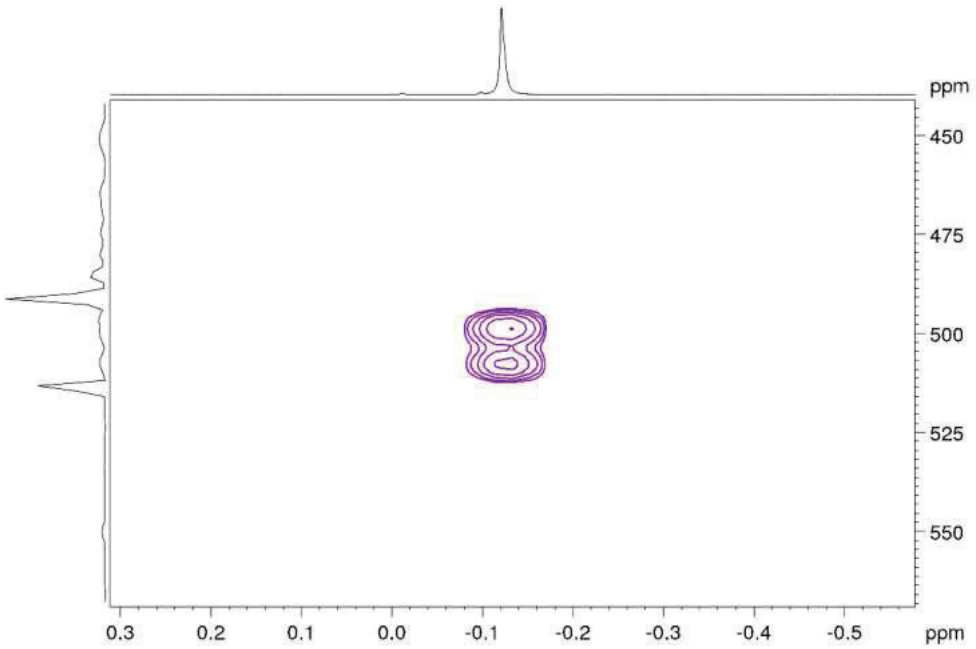

Figure S17. ^{1}H^{89}Y-HSQC NMR spectrum (500/25 MHz) of Tp^{tBu,Me}YMe[(μ_2-PC$_6$H$_3$*i*Pr$_2$-2,6)(μ_2-Me)AlMe$_2$] (**3-Y^{Al}**) in C$_6$D$_6$ at 26 °C.

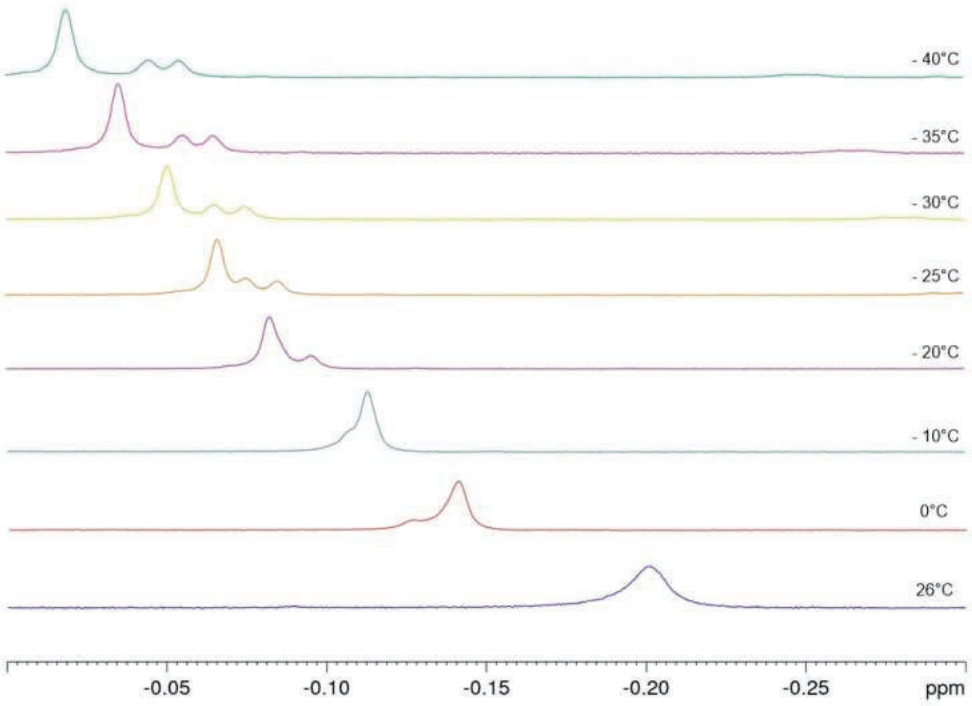

Figure S18. ^{1}H VT NMR spectra (500 MHz) of $Tp^{tBu,Me}YMe[(\mu_2\text{-}PC_6H_3iPr_2\text{-}2,6)(\mu_2\text{-}Me)AlMe_2]$ (**3-Y^{Al}**) in toluene-d_8.

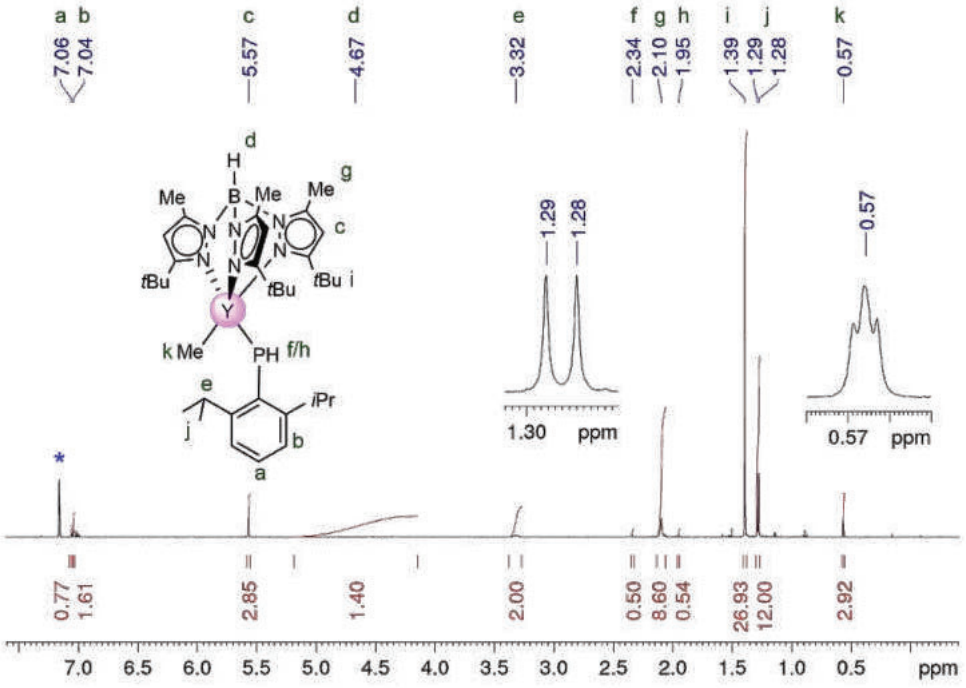

Figure S19. ^{1}H-NMR spectrum (500 MHz) of Tp$^{t\mathrm{Bu,Me}}$YMe[P(H)C$_6$H$_3$*i*Pr$_2$-2,6] (**4-Y**) in C$_6$D$_6$ at 26 °C.

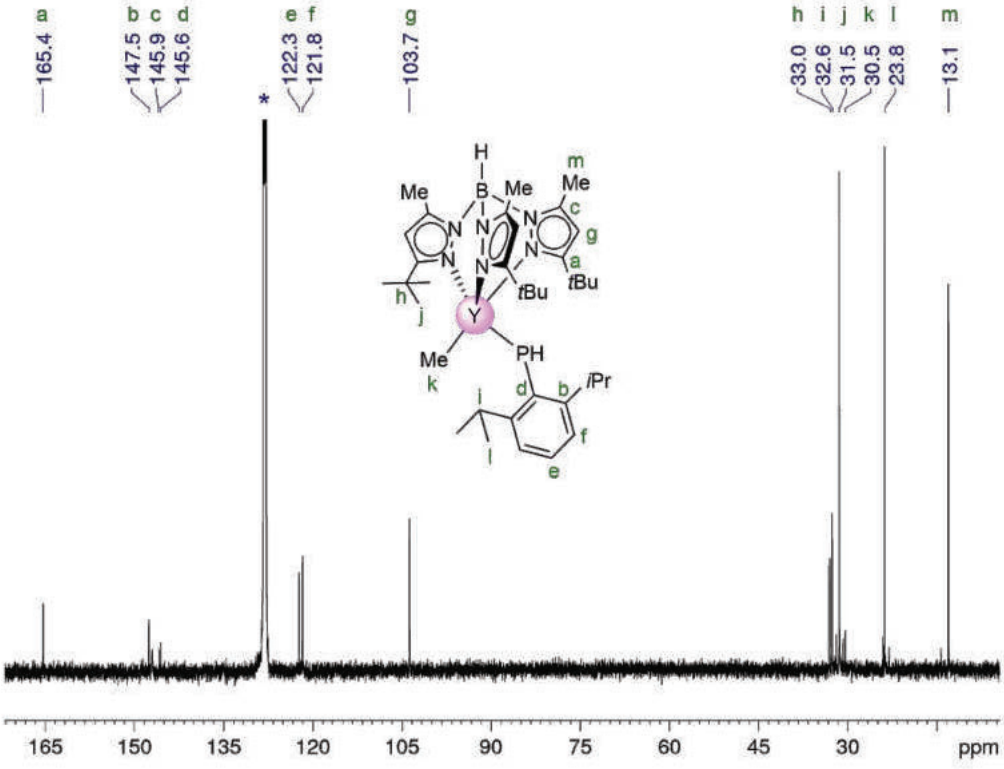

Figure S20. ^{13}C{^{1}H}-NMR spectrum (126 MHz) of Tp$^{t\mathrm{Bu,Me}}$YMe[P(H)C$_6$H$_3$*i*Pr$_2$-2,6] (**4-Y**) in C$_6$D$_6$ at 26 °C.

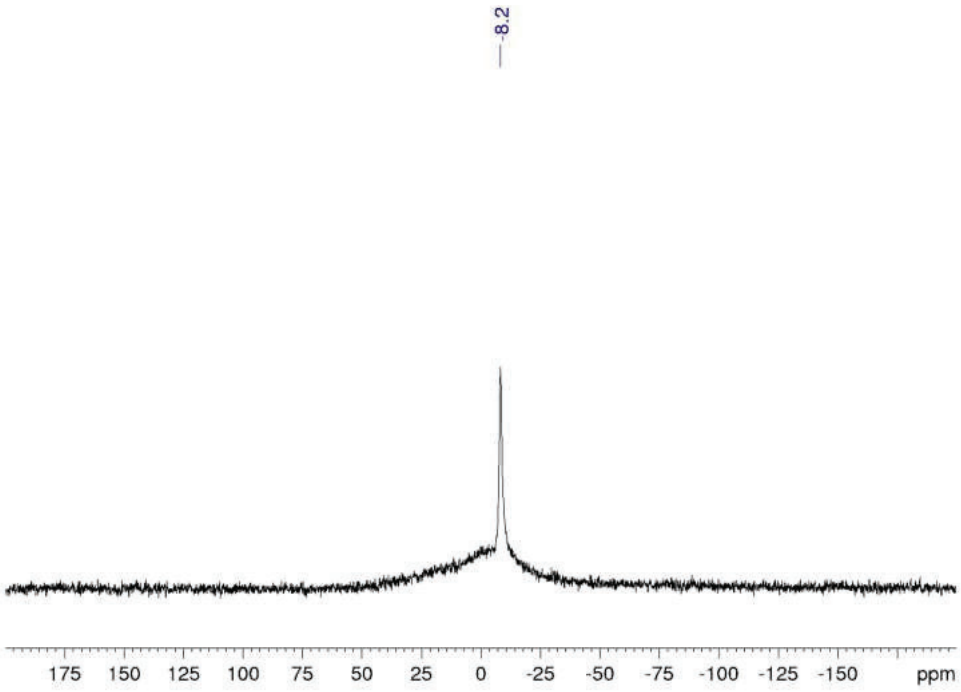

Figure S21. $^{11}B\{^{1}H\}$-NMR spectrum (160 MHz) of Tp^{tBu,Me}YMe[P(H)C$_6$H$_3$*i*Pr$_2$-2,6] (**4-Y**) in C_6D_6 at 26 °C.

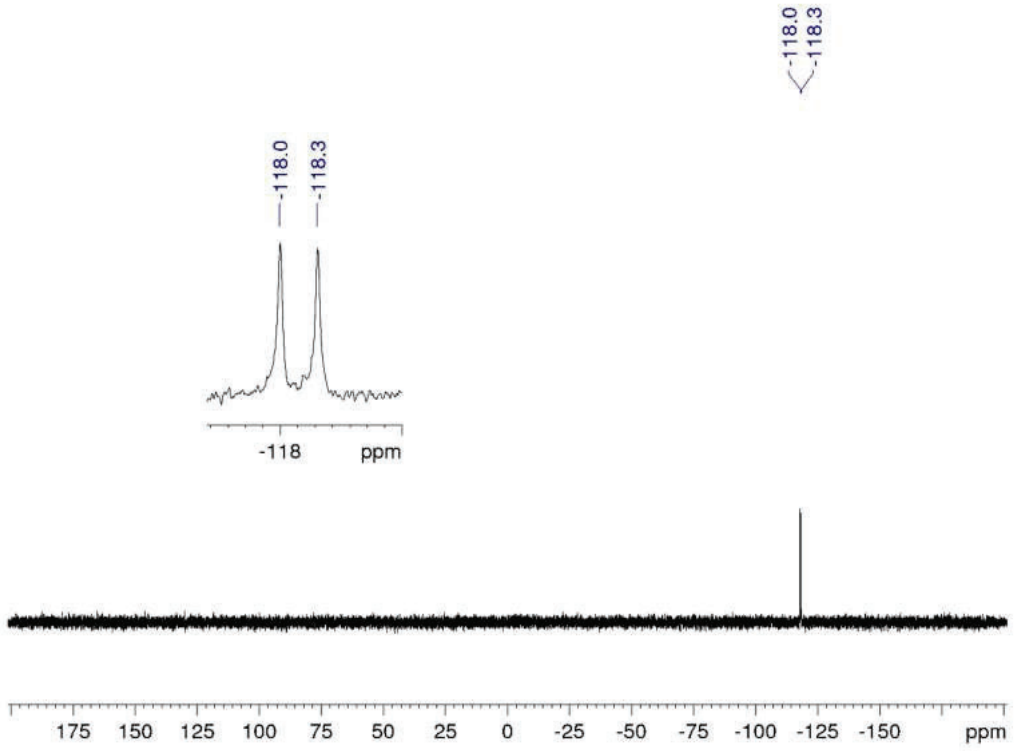

Figure S22. $^{31}P\{^{1}H\}$-NMR spectrum (202 MHz) of Tp^{tBu,Me}YMe[P(H)C$_6$H$_3$*i*Pr$_2$-2,6] (**4-Y**) in C_6D_6 at 26 °C.

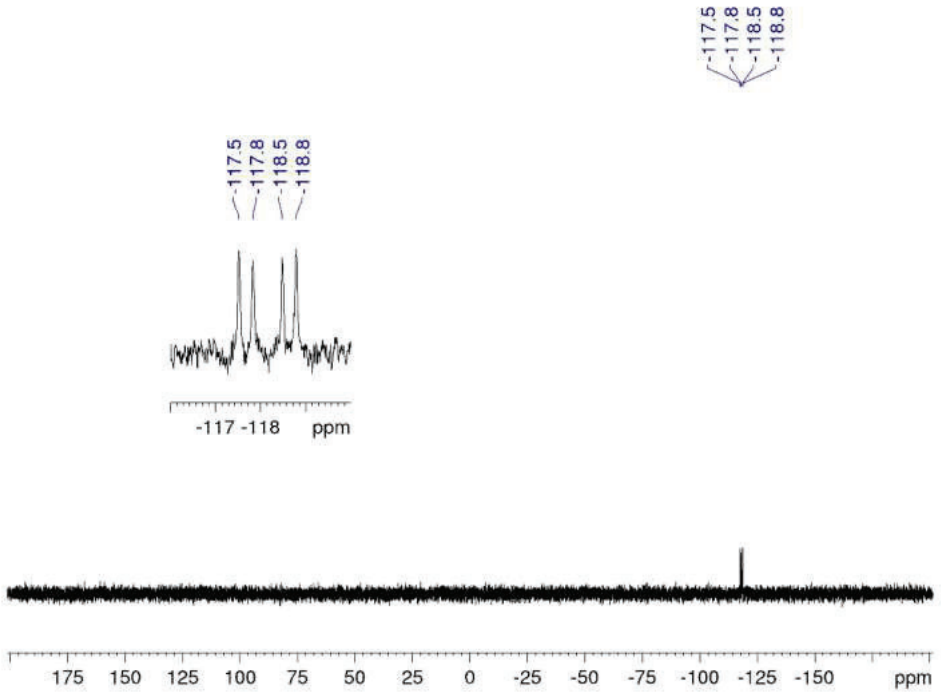

Figure S23. ^{31}P-NMR spectrum (202 MHz) of Tp$^{t\text{Bu,Me}}$YMe[P(H)C$_6$H$_3$*i*Pr$_2$-2,6] (**4-Y**) in C$_6$D$_6$ at 26 °C.

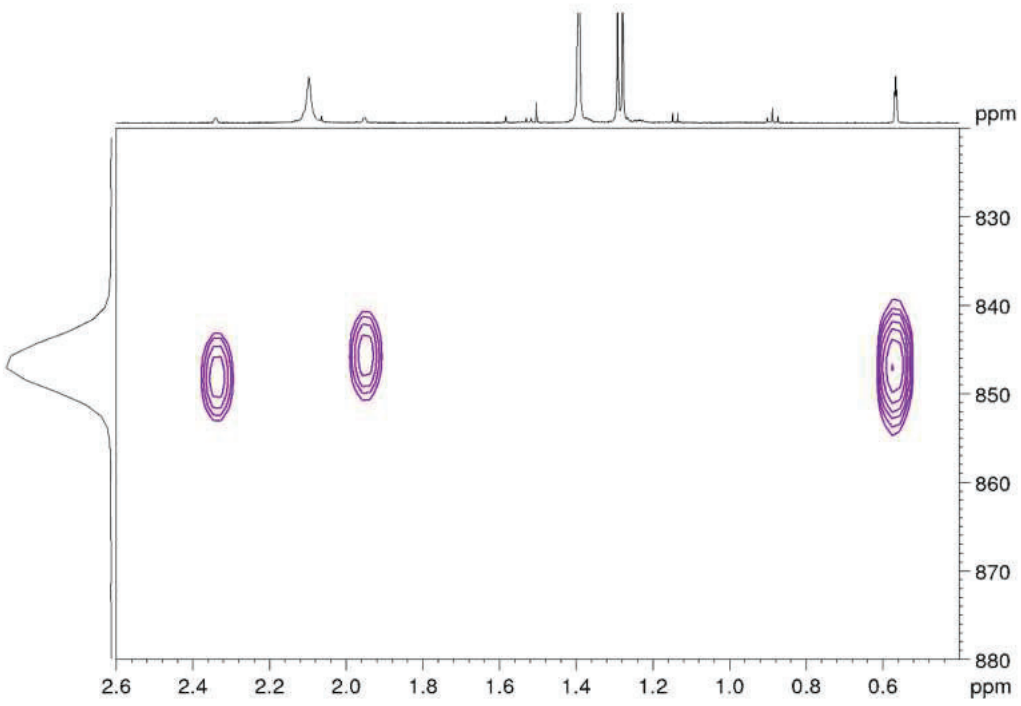

Figure S24. ^{1}H^{89}Y-HSQC NMR spectrum (500/25 MHz) Tp$^{t\text{Bu,Me}}$YMe[P(H)C$_6$H$_3$*i*Pr$_2$-2,6] (**4-Y**) in C$_6$D$_6$ at 26 °C.

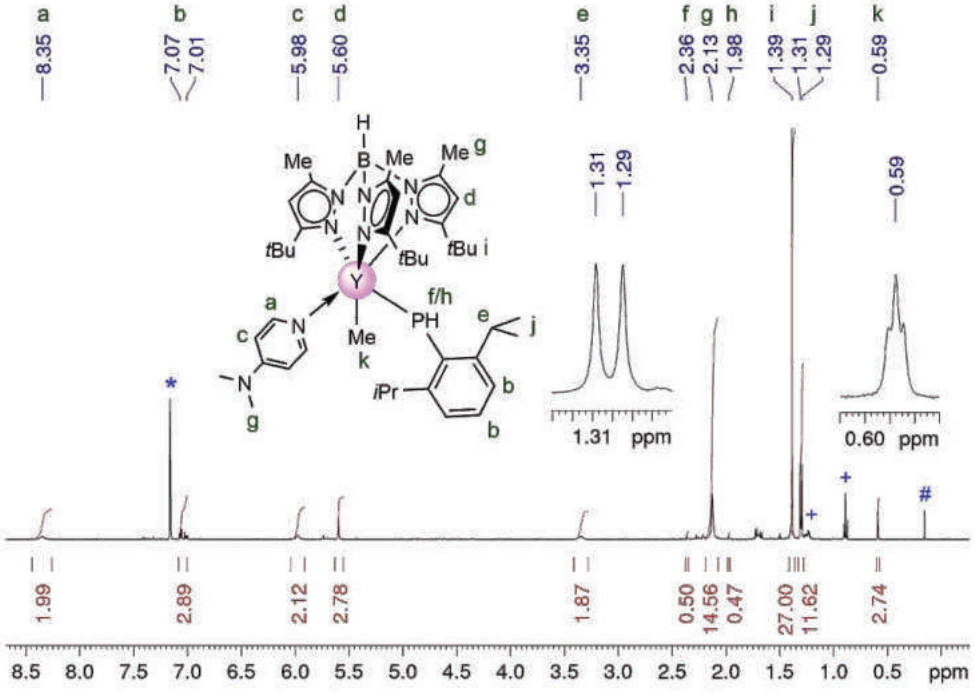

Figure S25. ^{1}H-NMR spectrum (500 MHz) of Tp$^{t\mathrm{Bu,Me}}$YMe[P(H)C$_6$H$_3$*i*Pr$_2$-2,6](DMAP) (**5-Y**) in C_6D_6 at 26 °C (+ denotes *n*-hexane, # denotes methane).

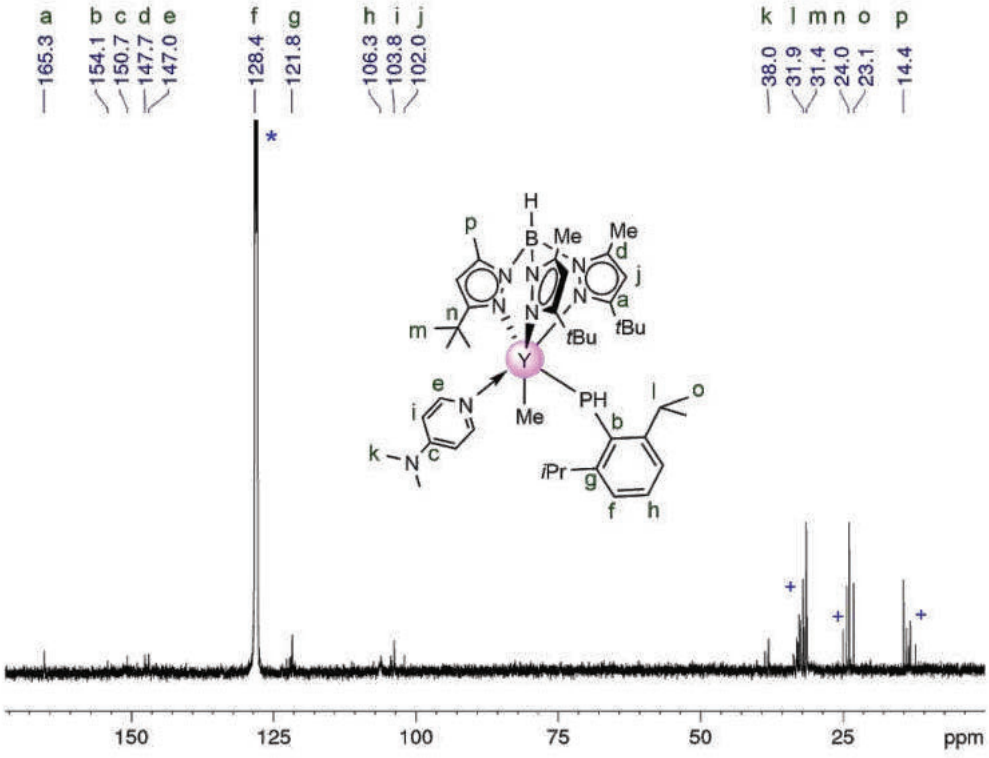

Figure S26. ^{13}C{^{1}H}-NMR spectrum (126 MHz) of Tp$^{t\mathrm{Bu,Me}}$YMe[P(H)C$_6$H$_3$*i*Pr$_2$-2,6](DMAP) (**5-Y**) in C_6D_6 at 26 °C (+ denotes minor impurities).

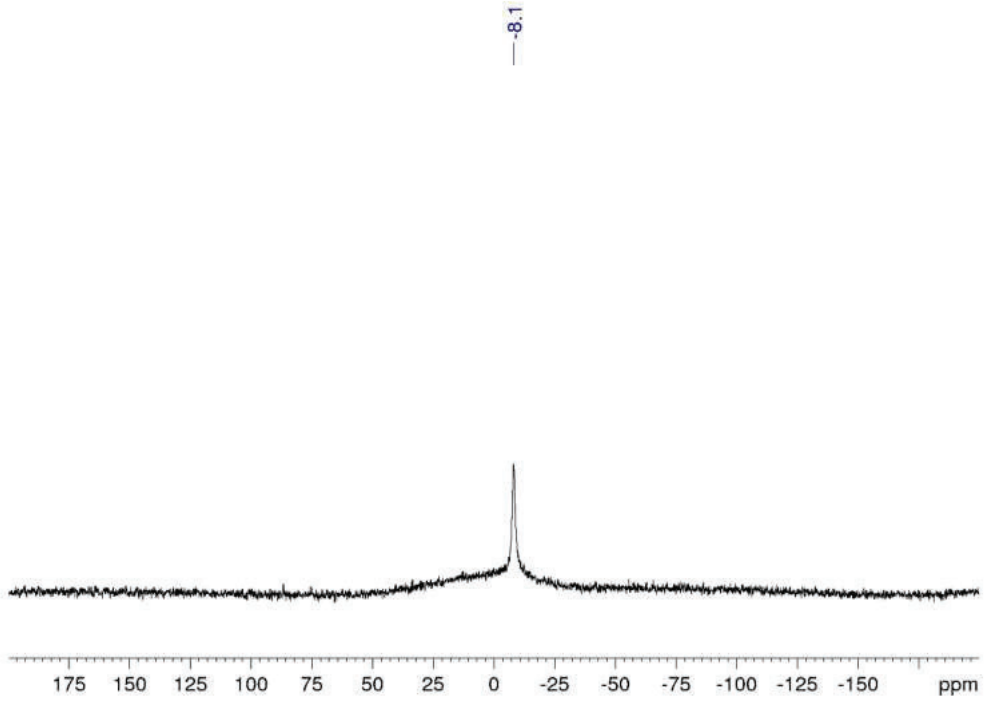

Figure S27. $^{11}B\{^{1}H\}$-NMR spectrum (160 MHz) of $Tp^{tBu,Me}YMe[P(H)C_6H_3iPr_2\text{-}2,6](DMAP)$ (**5-Y**) in C_6D_6 at 26 °C.

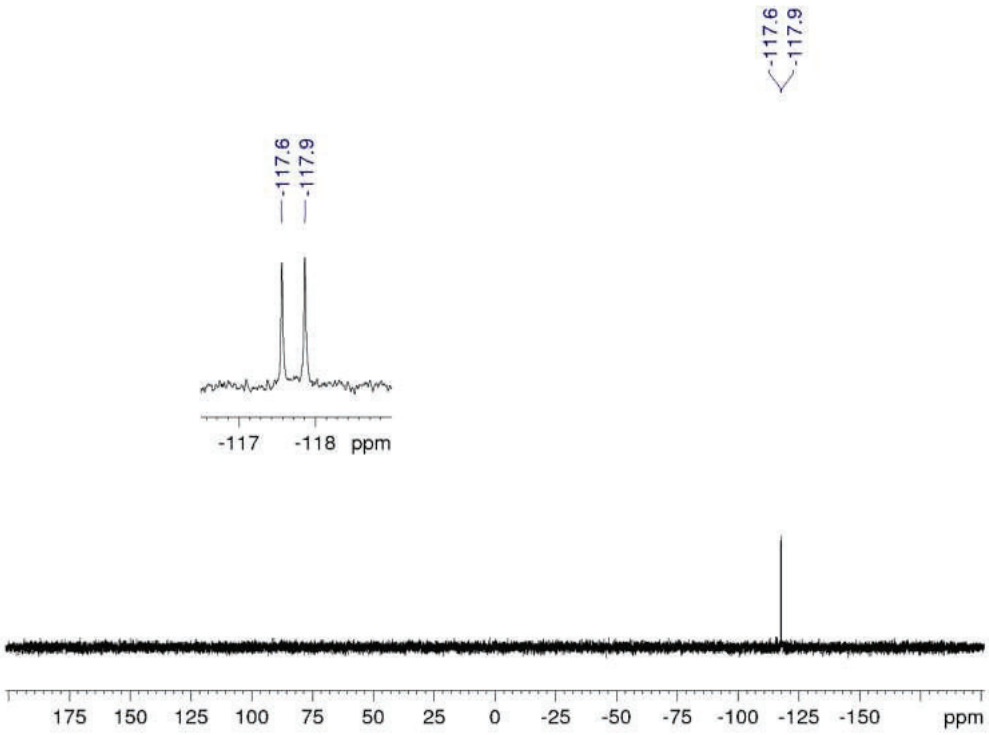

Figure S28. $^{31}P\{^{1}H\}$-NMR spectrum (202 MHz) of $Tp^{tBu,Me}YMe[P(H)C_6H_3iPr_2\text{-}2,6](DMAP)$ (**5-Y**) in C_6D_6 at 26 °C.

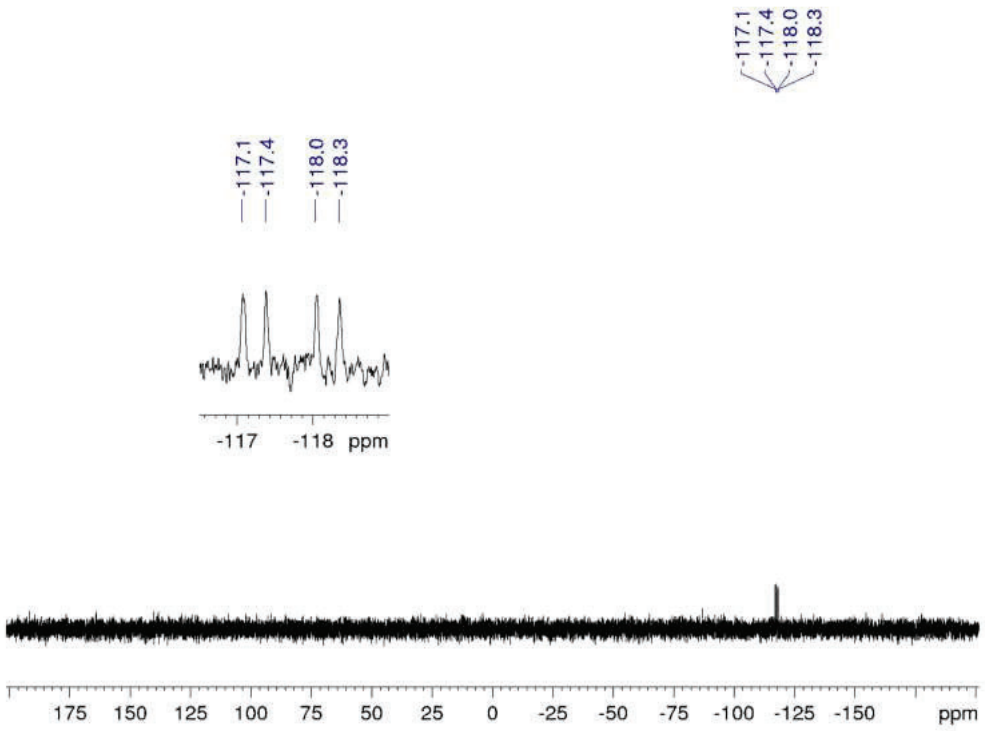

Figure S29. ^{31}P-NMR spectrum (202 MHz) of Tp$^{t\text{Bu,Me}}$YMe[P(H)C$_6$H$_3$*i*Pr$_2$-2,6](DMAP) (**5-Y**) in C_6D_6 at 26 °C.

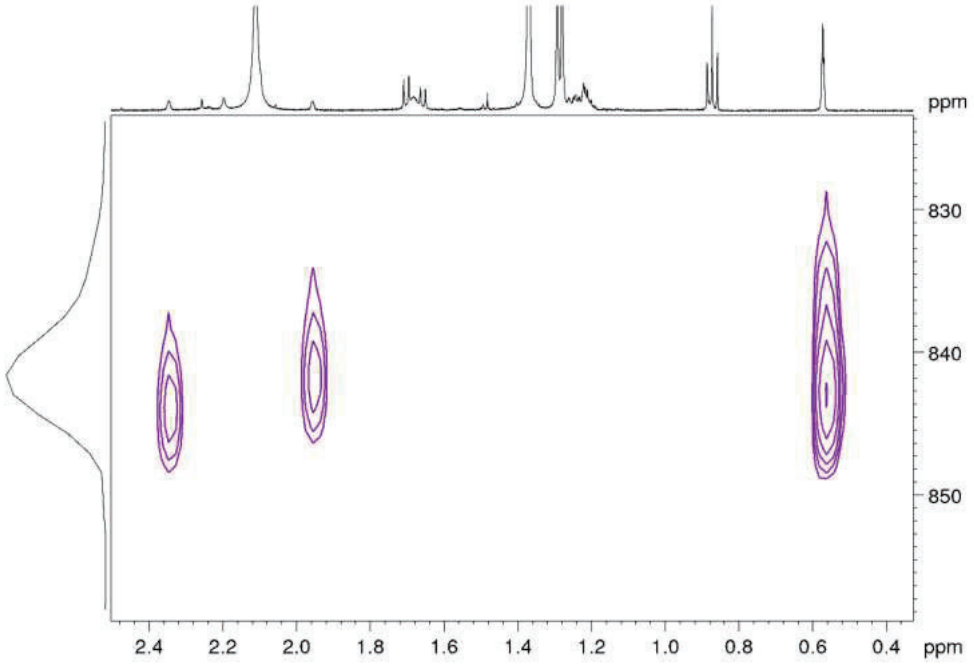

Figure S30. ^{1}H^{89}Y-HSQC NMR spectrum (500/25 MHz) of Tp$^{t\text{Bu,Me}}$YMe[P(H)C$_6$H$_3$*i*Pr$_2$-2,6](DMAP) (**5-Y**) in C_6D_6 at 26 °C.

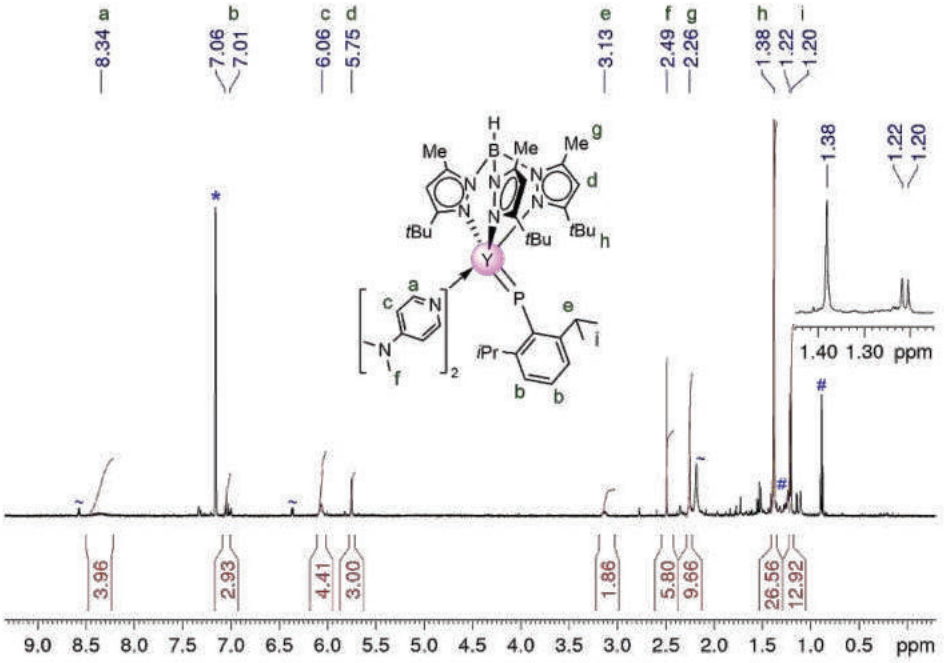

Figure S31. ^{1}H-NMR spectrum (400 MHz) of Tp^{tBu,Me}Y(=PC$_6$H$_3$*i*Pr$_2$-2,6)(DMAP) (**6-Y**) in C_6D_6 at 26 °C (~ denotes minor impurities, # denotes residual solvent).

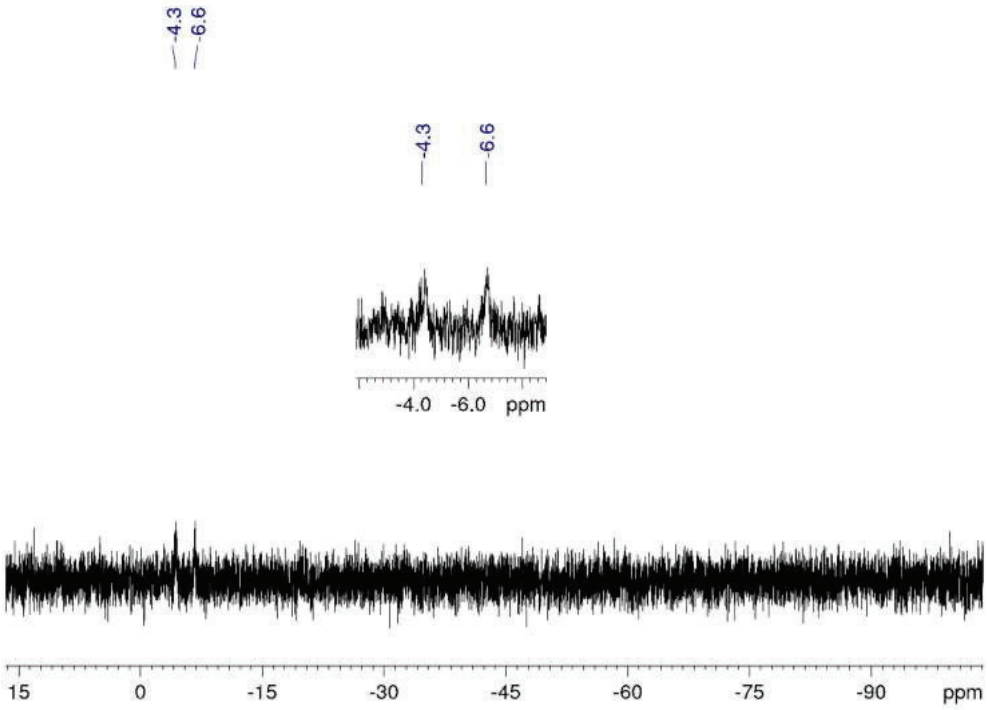

Figure S32. ^{31}P{^{1}H}-NMR spectrum (121 MHz) of Tp^{tBu,Me}Y(=PC$_6$H$_3$*i*Pr$_2$-2,6)(DMAP) (**6-Y**) in C_6D_6 at 26 °C.

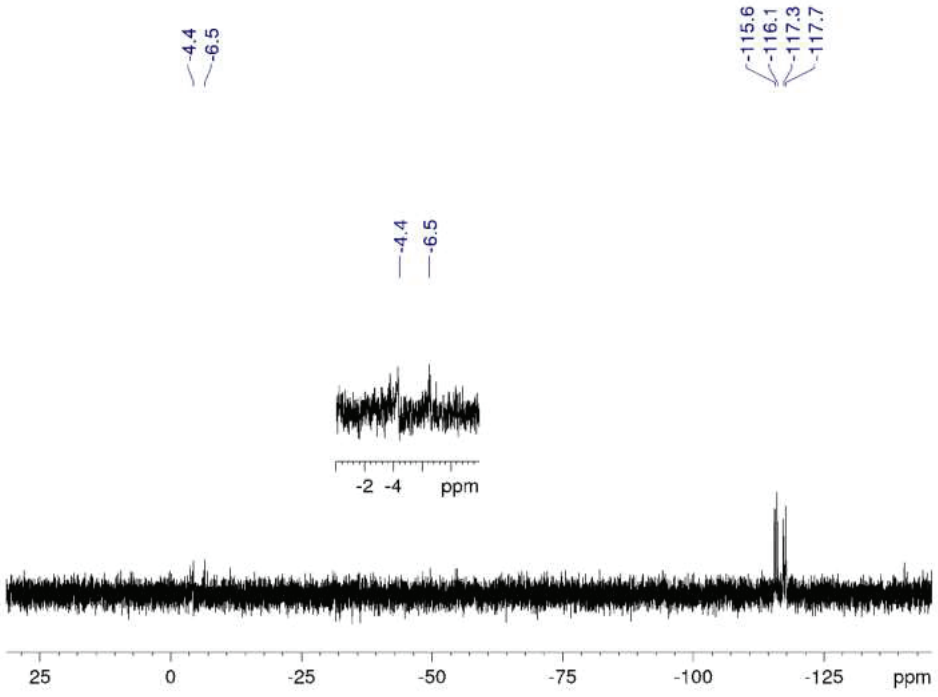

Figure S33. ^{31}P-NMR spectrum (121 MHz) of Tp$^{t\mathrm{Bu,Me}}$Y(=PC$_6$H$_3$*i*Pr$_2$-2,6)(DMAP) (**6-Y**) in C_6D_6 at 26 °C (remaining reactant **5-Y** is still observable).

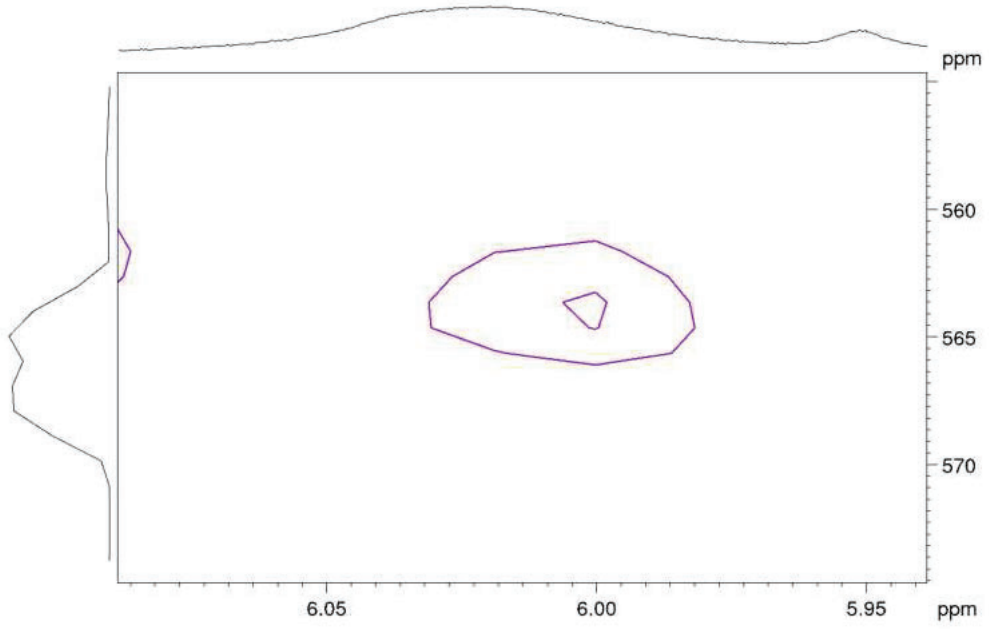

Figure S34. ^{1}H^{89}Y-HSQC NMR spectrum (500/25 MHz) of Tp$^{t\mathrm{Bu,Me}}$Y(=PC$_6$H$_3$*i*Pr$_2$-2,6)(DMAP) (**6-Y**) in C_6D_6 at 8 °C.

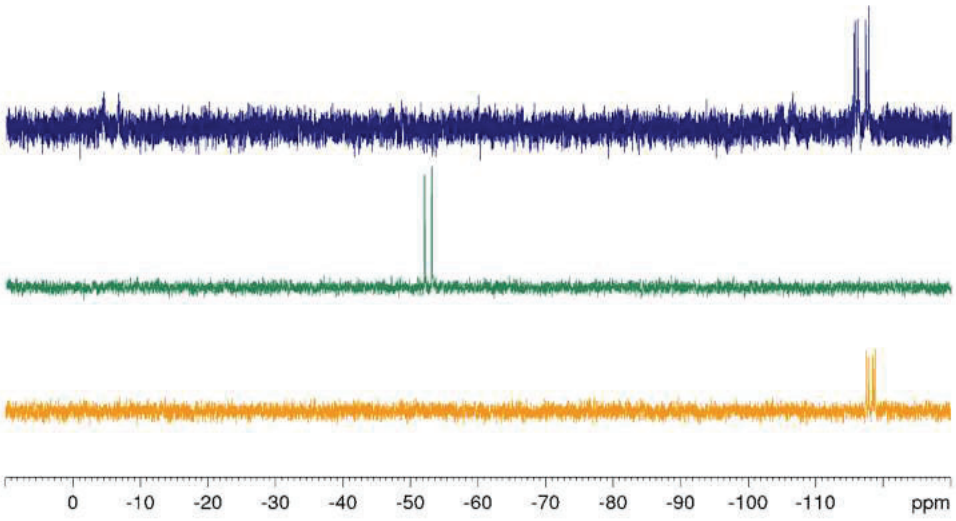

Figure S35. Stacked ^{31}P-NMR spectra (162 MHz) of Tp^{tBu,Me}Y(=PC$_6$H$_3$*i*Pr$_2$-2,6)(DMAP) (**6-Y**) (blue), Tp^{tBu,Me}YMe[(μ_2-PC$_6$H$_3$*i*Pr$_2$-2,6)(μ_2-Me)AlMe$_2$] (**3-Y^{Al}**) (green), and Tp^{tBu,Me}YMe[P(H)C$_6$H$_3$*i*Pr$_2$-2,6] (**4-Y**) (orange) in C$_6$D$_6$ at 26 °C.

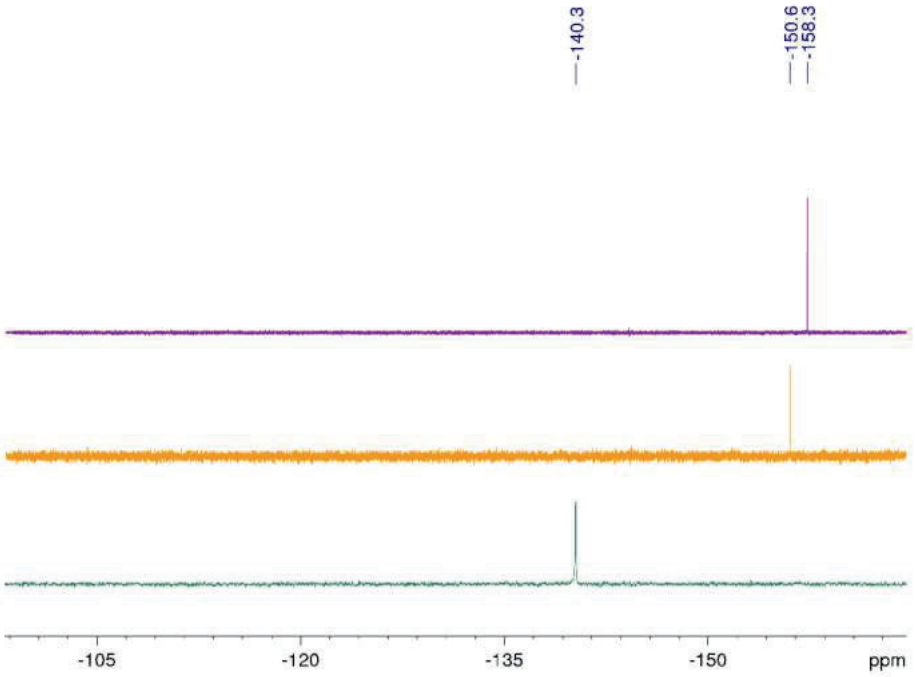

Figure S36. Stacked ^{31}P{^{1}H}-NMR spectra (162 MHz) of H$_2$PC$_6$H$_3$*i*Pr$_2$-2,6 (violet), [Me$_3$GaPH$_2$Ar^{iPr}] (orange), and [Me$_3$AlPH$_2$Ar^{iPr}] (green) in C$_6$D$_6$ at 26 °C.

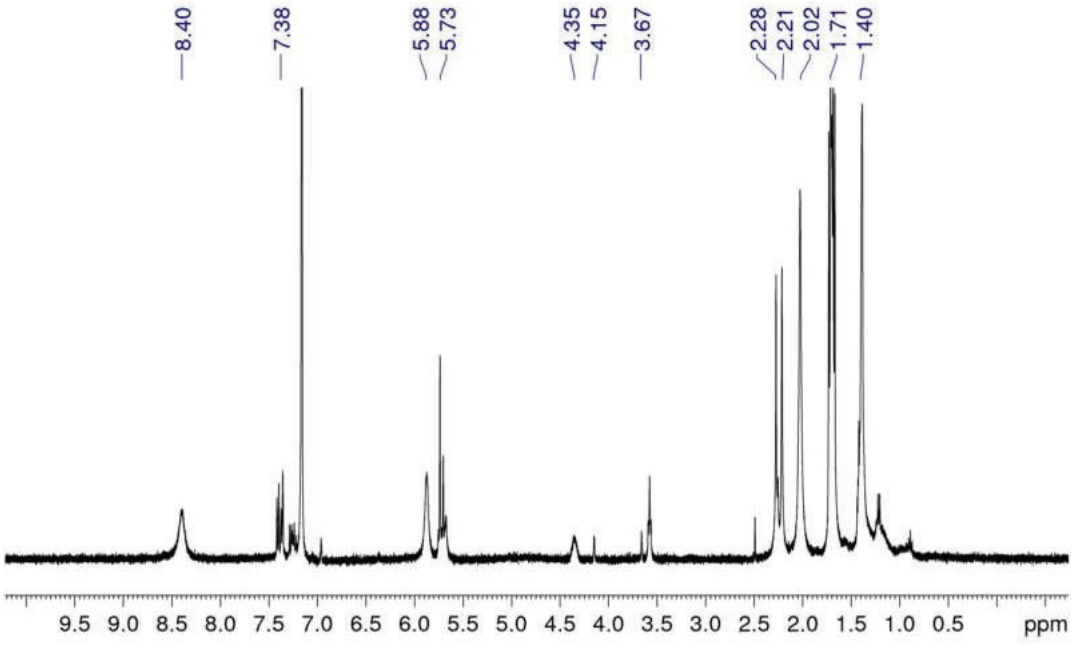

Figure S37. ^{1}H-NMR spectrum (400 MHz) of the unidentified decomposition product(s) of Tp$^{t\mathrm{Bu,Me}}$Y(=PC$_6$H$_3$*i*Pr$_2$-2,6)(DMAP) (**6-Y**) in C$_6$D$_6$ at 26 °C.

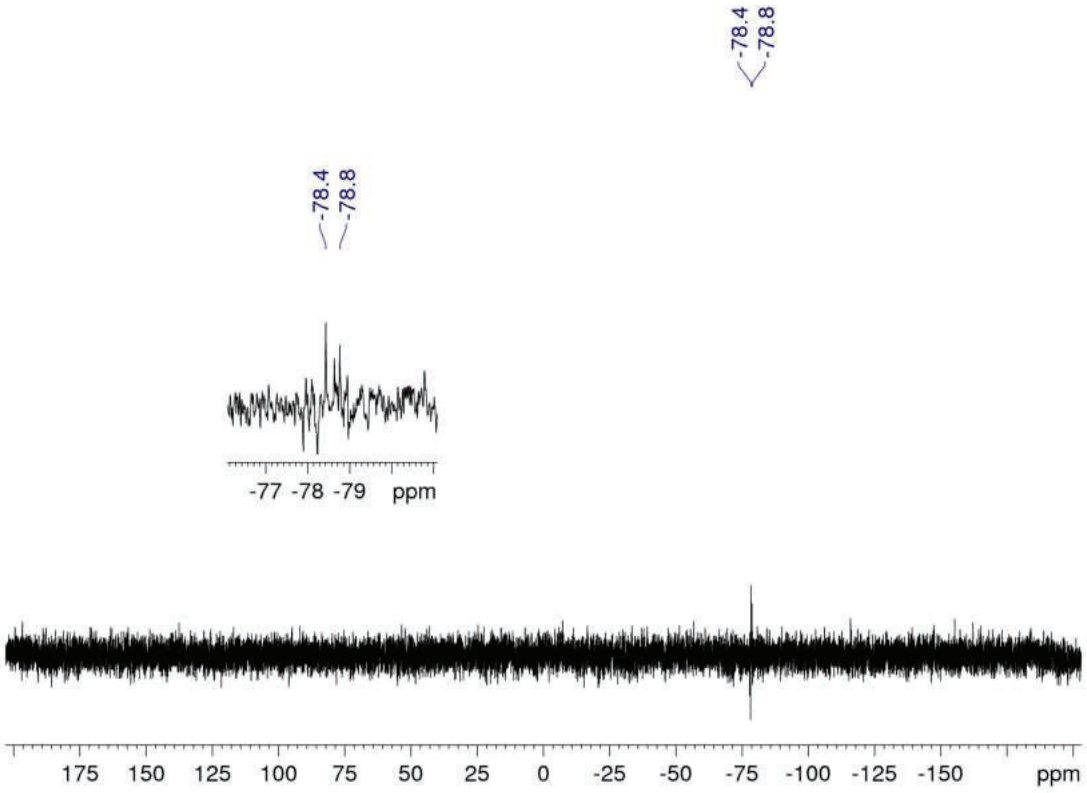

Figure S38. ^{31}P{^{1}H}-NMR spectrum (121 MHz) of the unidentified decomposition product(s) of Tp$^{t\mathrm{Bu,Me}}$Y(=PC$_6$H$_3$*i*Pr$_2$-2,6)(DMAP) (**6-Y**) in C$_6$D$_6$ at 26 °C.

NMR-scale Reactions

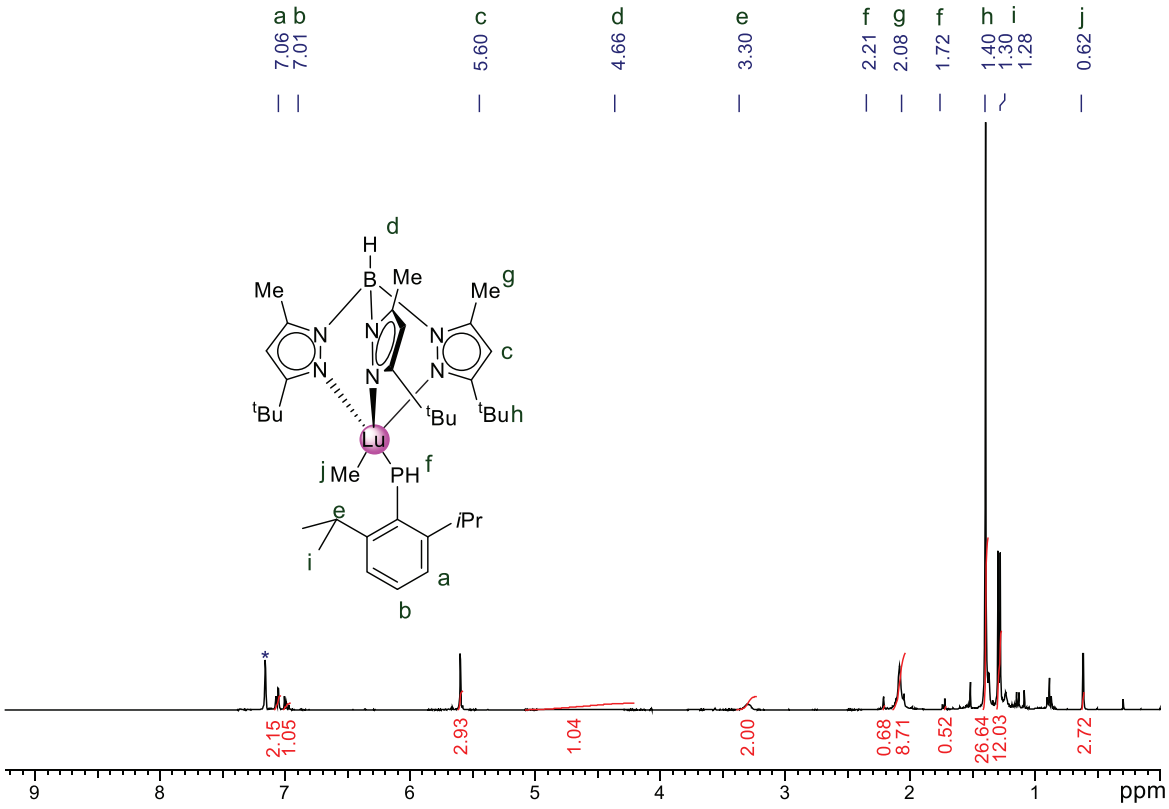

Figure S39. ^{1}H-NMR spectrum (400 MHz) of Tp$^{t\mathrm{Bu,Me}}$YMe[P(H)C$_6$H$_3$*i*Pr$_2$-2,6] (**4-Lu**) in C_6D_6 at 26 °C.

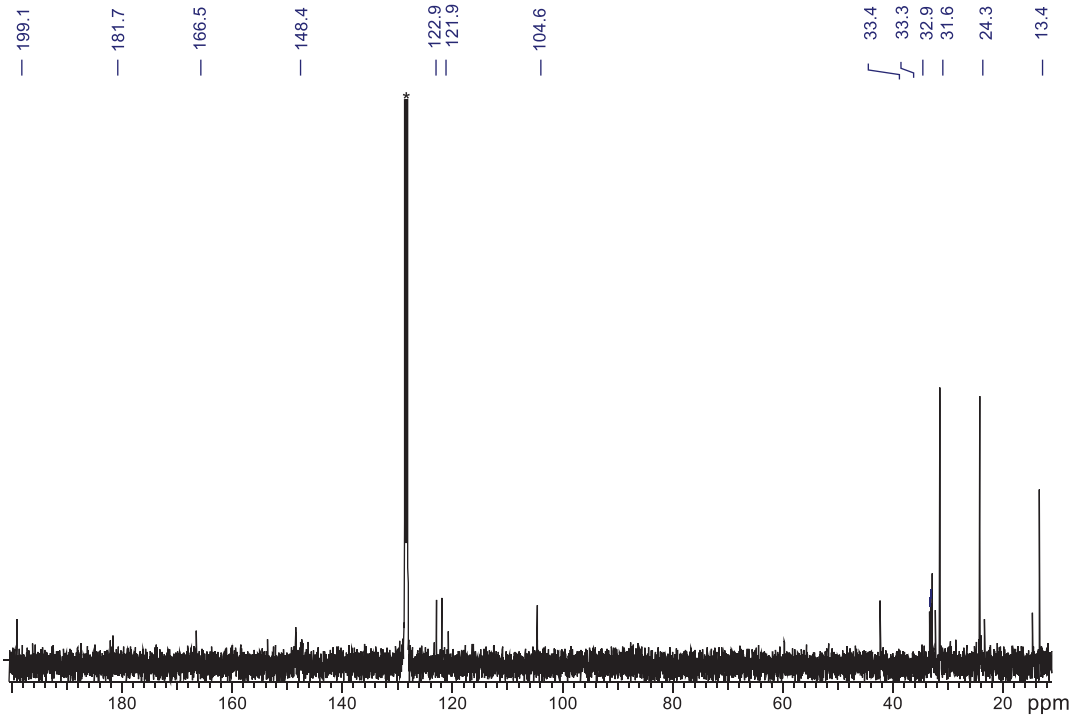

Figure S40. ^{13}C{^{1}H}-NMR spectrum (100 MHz) of Tp$^{t\mathrm{Bu,Me}}$LuMe[P(H)C$_6$H$_3$*i*Pr$_2$-2,6] (**4-Lu**) in C_6D_6 at 26 °C.

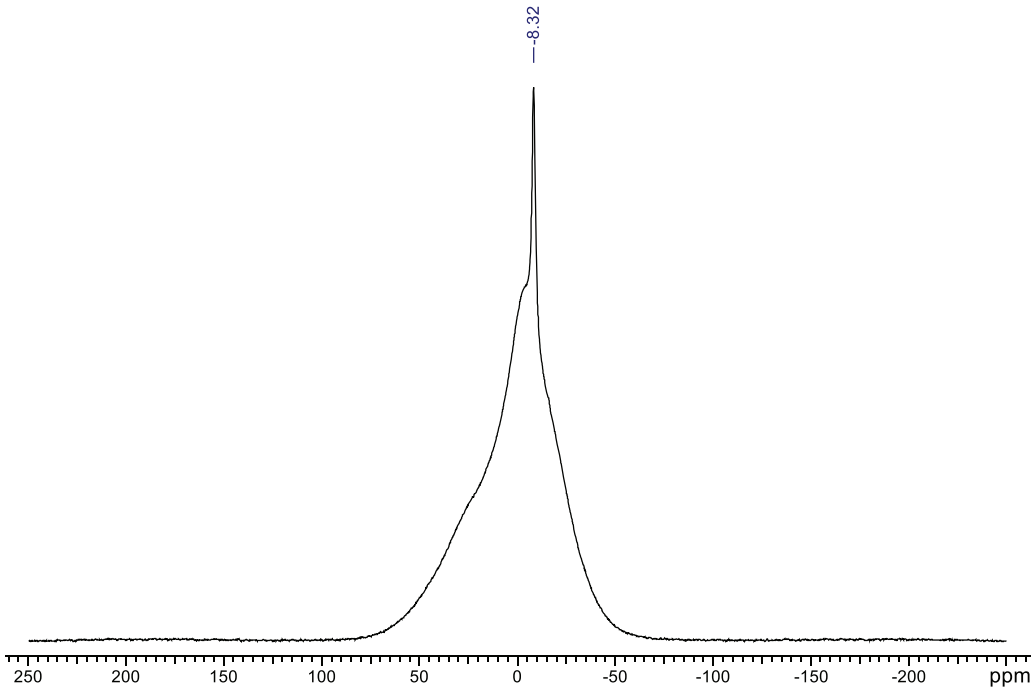

Figure S41. $^{11}B\{^{1}H\}$-NMR spectrum (128 MHz) of $Tp^{tBu,Me}YMe[P(H)C_6H_3iPr_2\text{-}2,6]$ (**4-Lu**) in C_6D_6 at 26 °C.

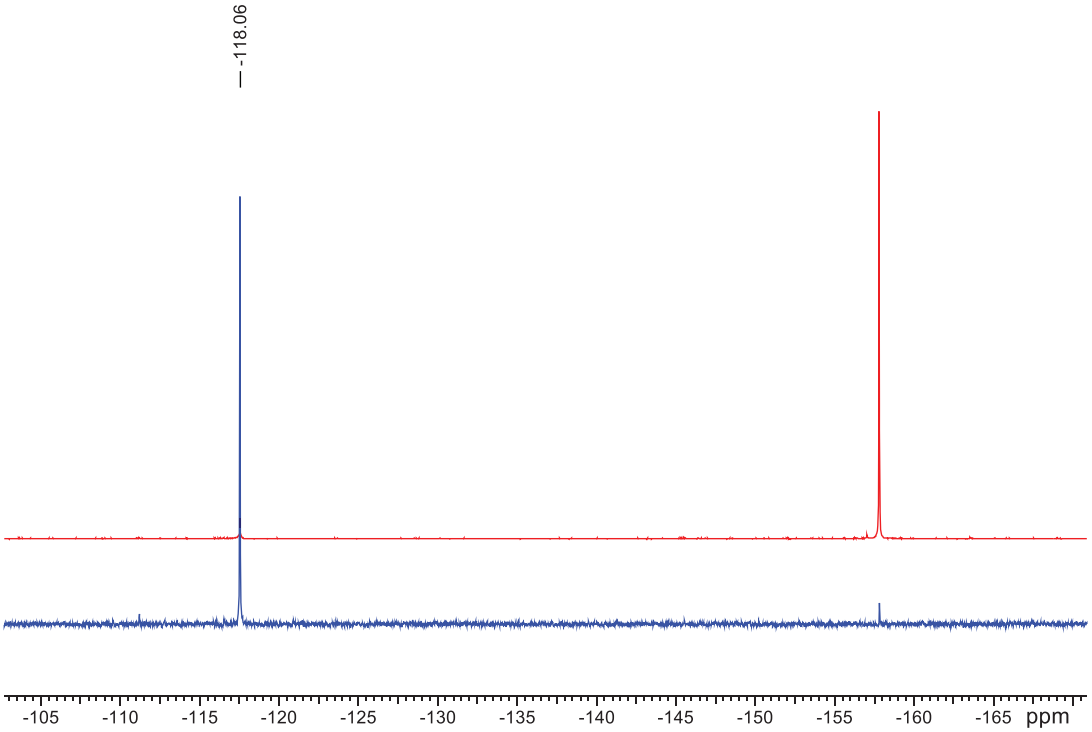

Figure S42. Stacked $^{31}P\{^{1}H\}$-NMR spectra (162 MHz) of $Tp^{tBu,Me}LuMe[P(H)C_6H_3iPr_2\text{-}2,6]$ (**4-Lu**) in C_6D_6 at 26 °C, recorded after 4 h (red) and 24 h (blue).

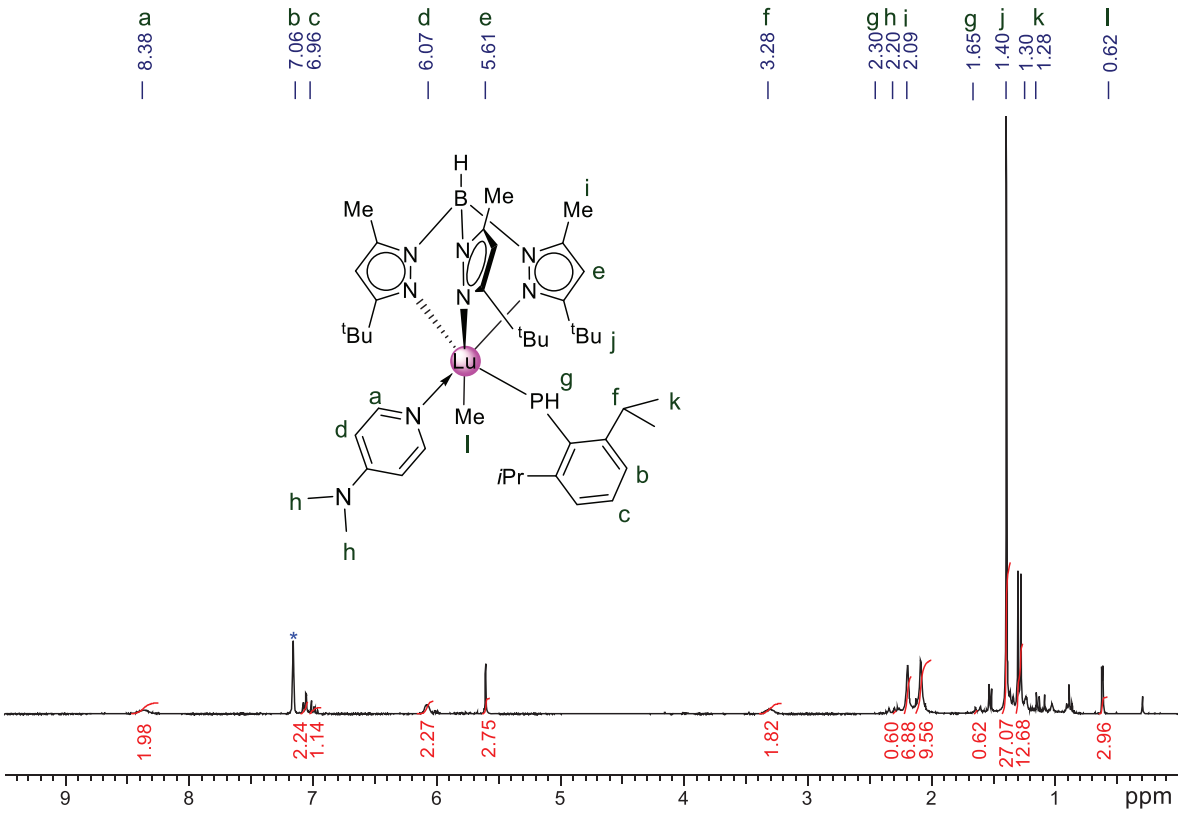

Figure S43. ^{1}H-NMR spectrum (400 MHz) of Tp^{tBu,Me}LuMe[P(H)C$_6$H$_3$*i*Pr$_2$-2,6](DMAP) (**5-Lu**) in C$_6$D$_6$ at 26 °C.

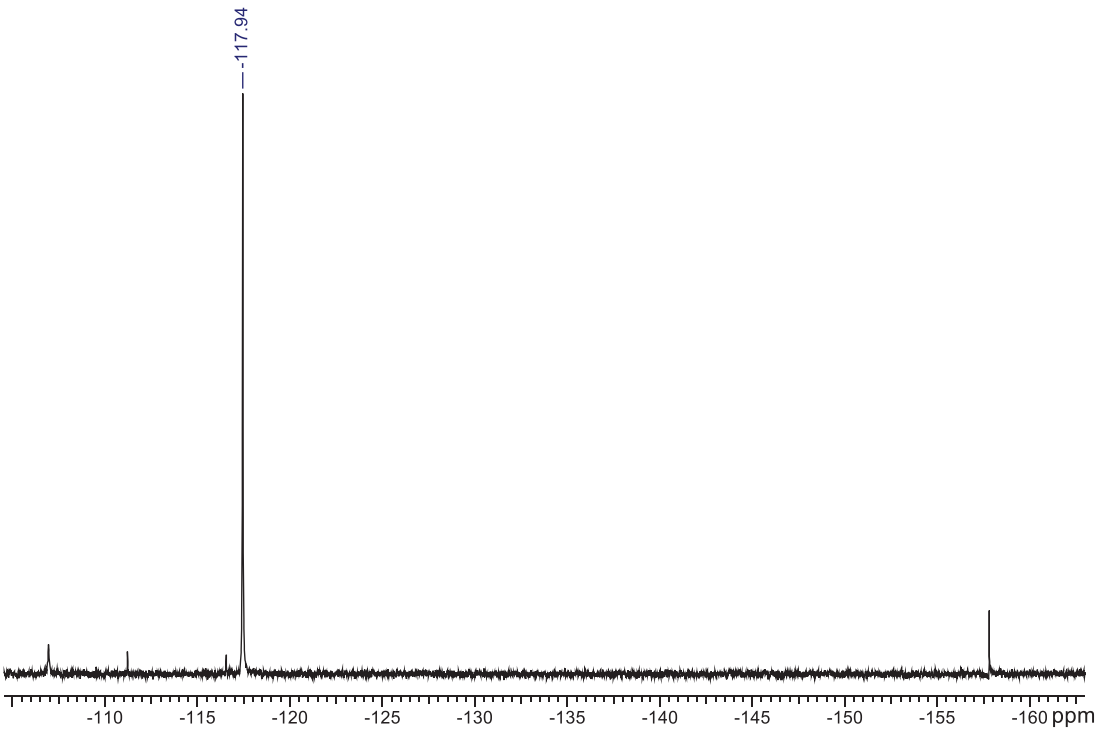

Figure S44. ^{31}P{^{1}H}-NMR spectrum (122 MHz) of Tp^{tBu,Me}LuMe[P(H)C$_6$H$_3$*i*Pr$_2$-2,6](DMAP) **(5-Lu)** in C$_6$D$_6$ at 26 °C.

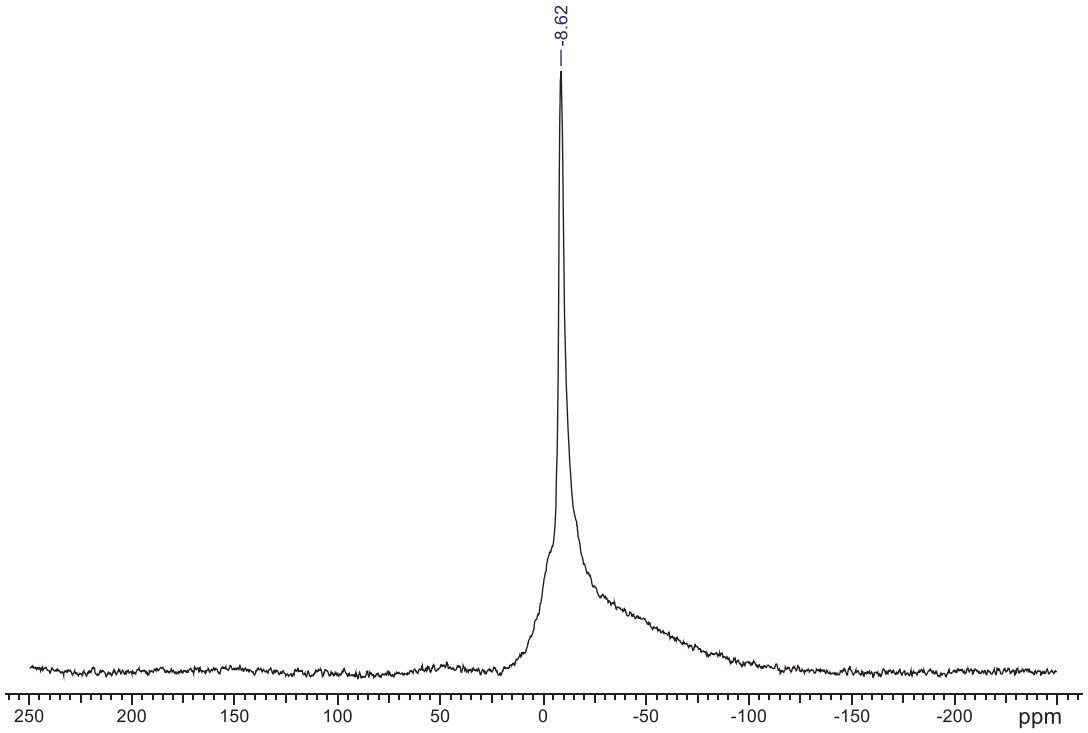

Figure S45. $^{11}B\{^{1}H\}$-NMR spectrum (96 MHz) of $Tp^{tBu,Me}LuMe[P(H)C_6H_3iPr_2\text{-}2,6](DMAP)$ (**5-Lu**) in C_6D_6 at 26 °C.

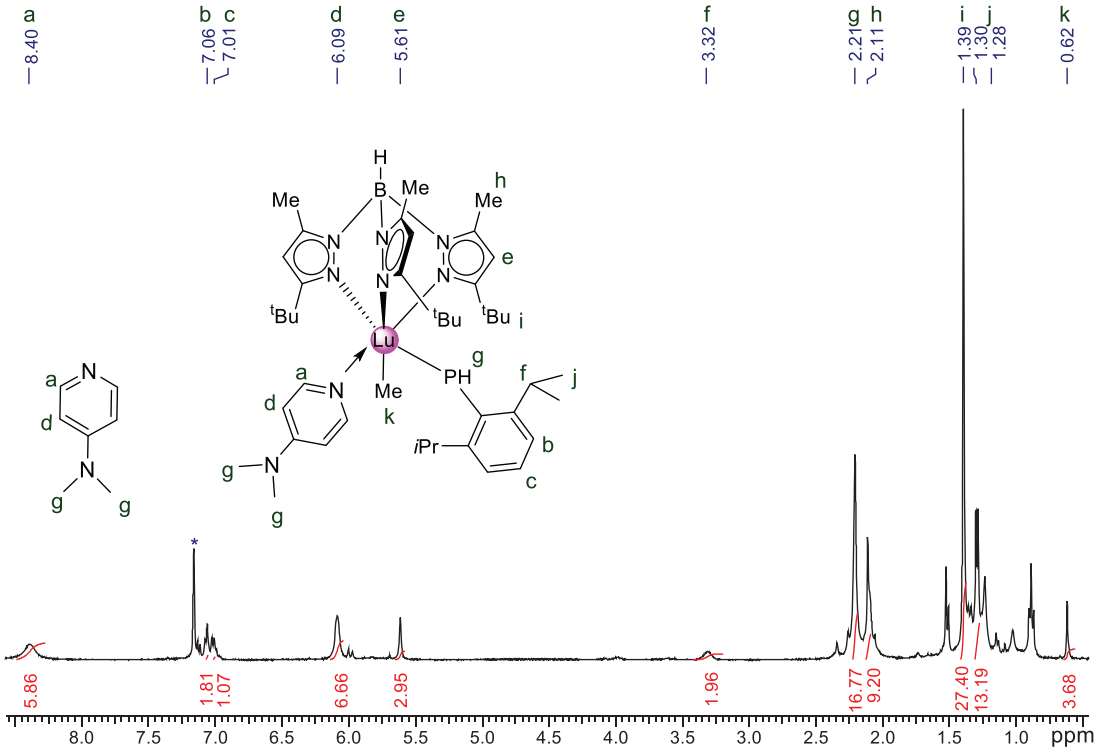

Figure S46. ^{1}H-NMR spectrum (400 MHz) of $Tp^{tBu,Me}LuMe[P(H)C_6H_3iPr_2\text{-}2,6](DMAP)$ (**5-Lu**) +DMAP in C_6D_6 at 26 °C.

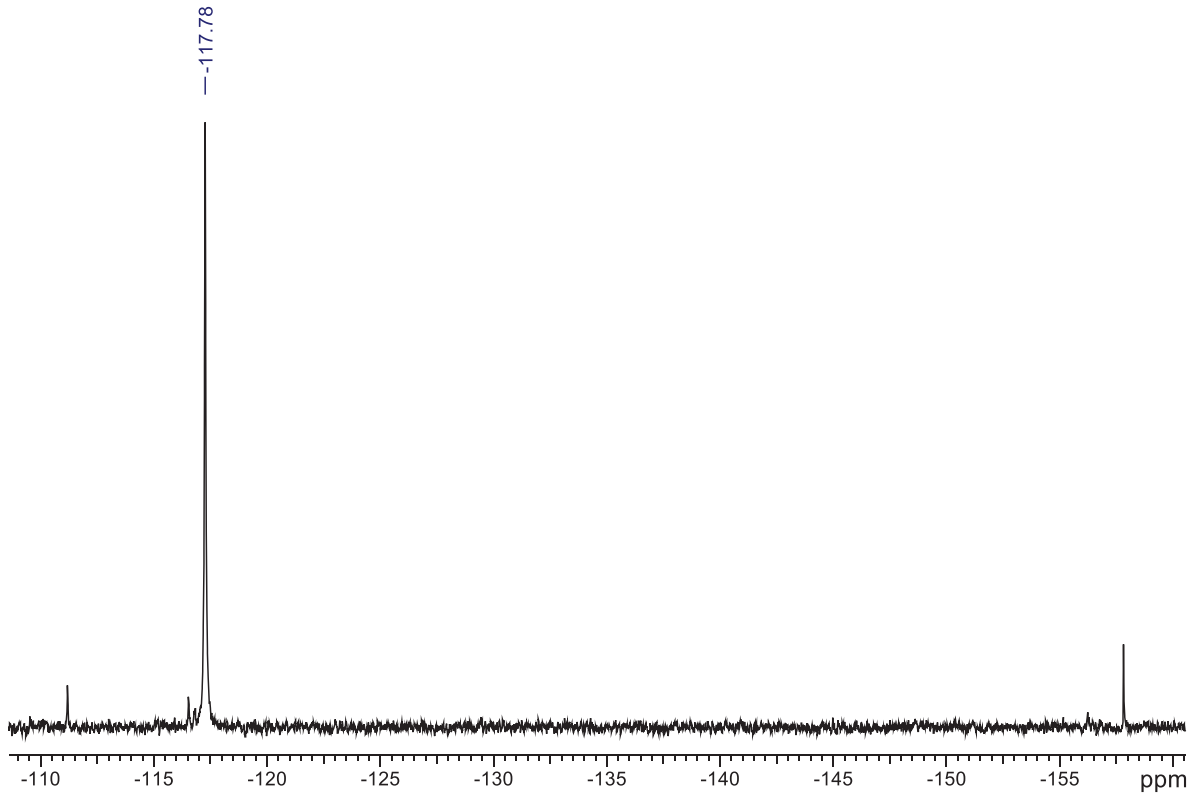

Figure S47. $^{31}P\{^{1}H\}$-NMR spectrum (122 MHz) of $Tp^{tBu,Me}LuMe[P(H)C_6H_3iPr_2$-2,6](DMAP) (**5-Lu**) +DMAP in C_6D_6 at 26 °C.

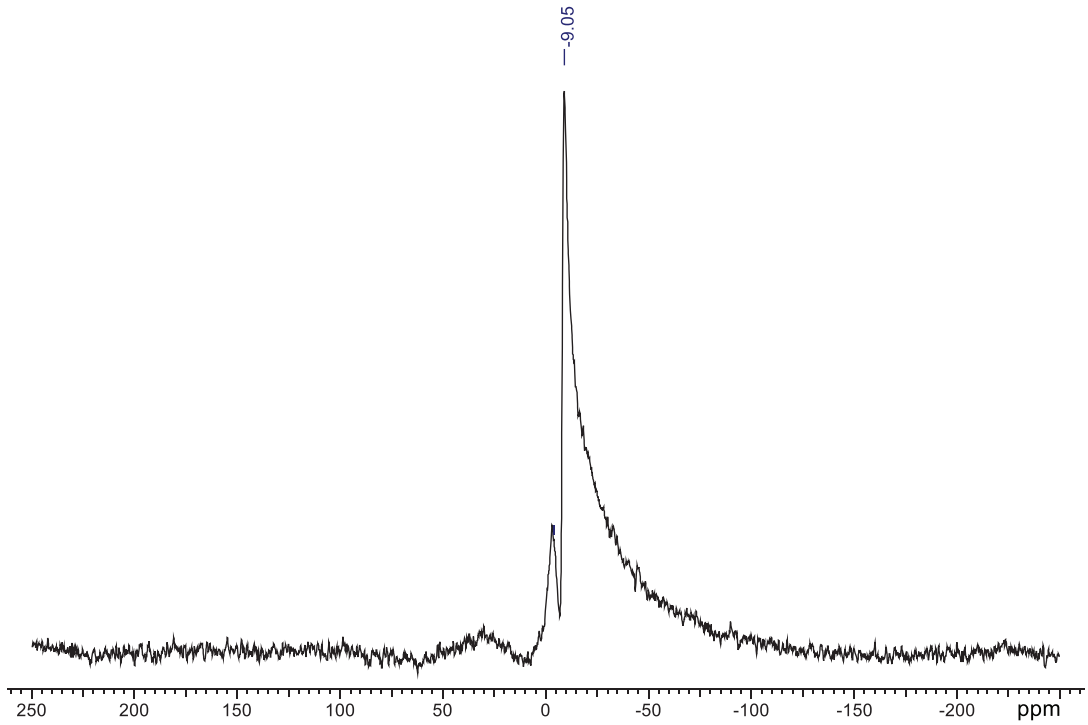

Figure S48. $^{11}B\{^{1}H\}$-NMR spectrum (128 MHz) of $Tp^{tBu,Me}LuMe[P(H)C_6H_3iPr_2$-2,6](DMAP) **(5-Lu**) +DMAP in C_6D_6 at 26 °C.

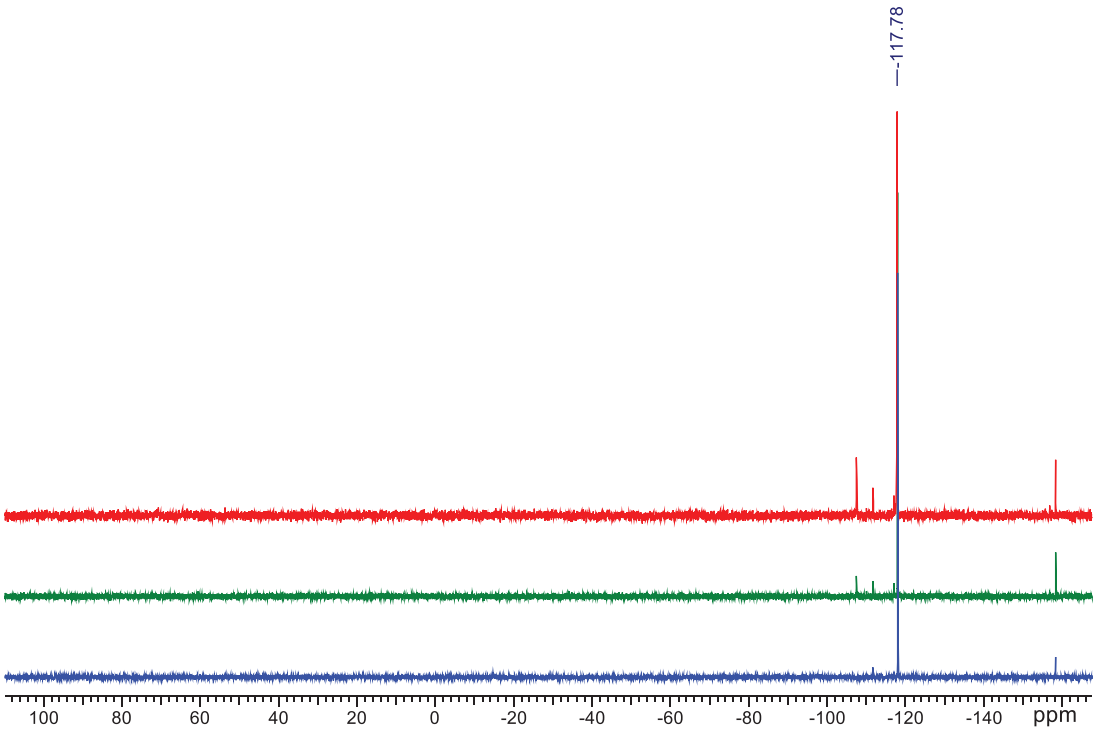

Figure 49. $^{31}P\{^{1}H\}$-NMR spectra (162 MHz) of Tp^{tBu,Me}LuMe[P(H)C$_6$H$_3$*i*Pr$_2$-2,6] (**4-Lu**) (blue), Tp^{tBu,Me}LuMe[P(H)C$_6$H$_3$*i*Pr$_2$-2,6](DMAP) (**5-Lu**) (green), and Tp^{tBu,Me}LuMe[P(H)C$_6$H$_3$*i*Pr$_2$-2,6](DMAP) (**5-Lu**) +DMAP (red), in C$_6$D$_6$ at 26 °C.

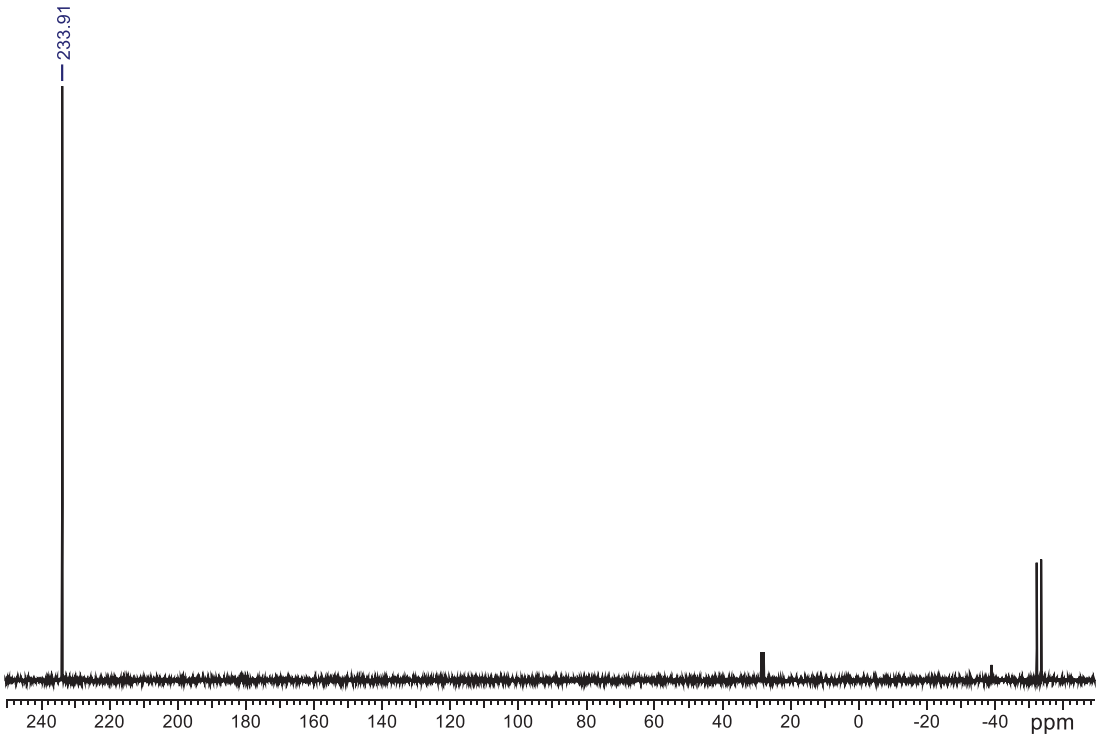

Figure S50. $^{31}P\{^{1}H\}$-NMR spectrum (162 MHz) of the reaction of [Tp^{tBu,Me}Y(PC$_6$H$_3$*i*Pr-2,6)(AlMe$_3$)] (**3-Y^{Al}**) with benzophenone in C$_6$D$_6$ at 26 °C.

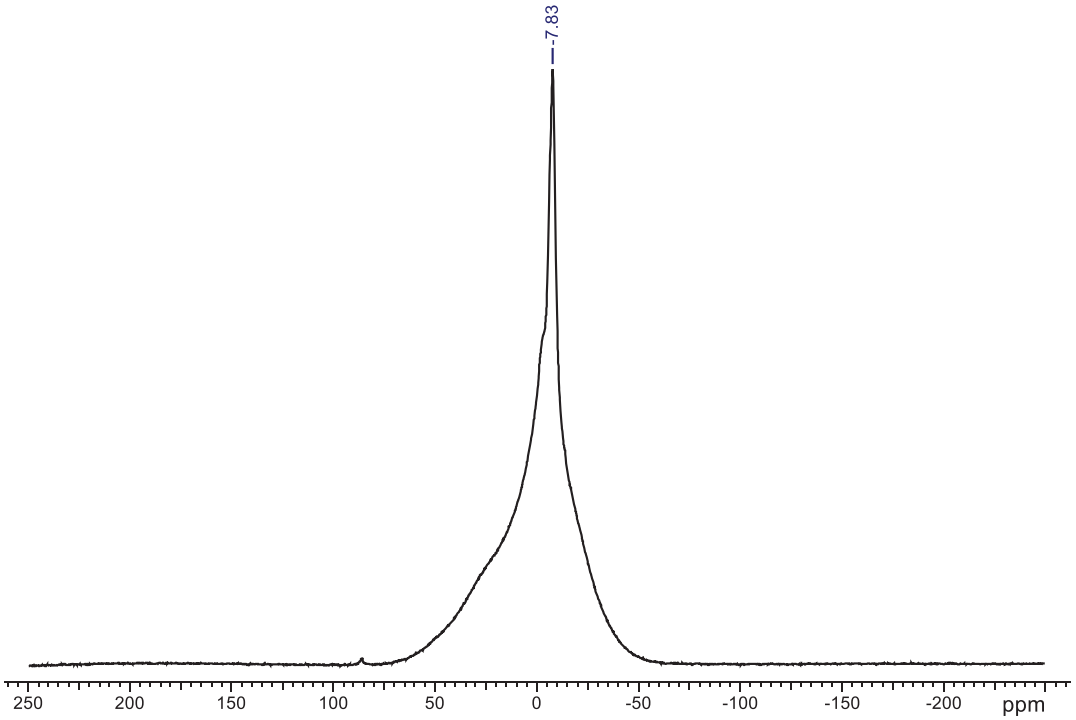

Figure S51. $^{11}B\{^1H\}$-NMR spectrum (128 MHz) of the reaction of [Tp^{tBu,Me}Y(PC$_6$H$_3$*i*Pr-2,6)(AlMe$_3$)] (**3-Y^{Al}**) with benzophenone in C_6D_6 at 26 °C.

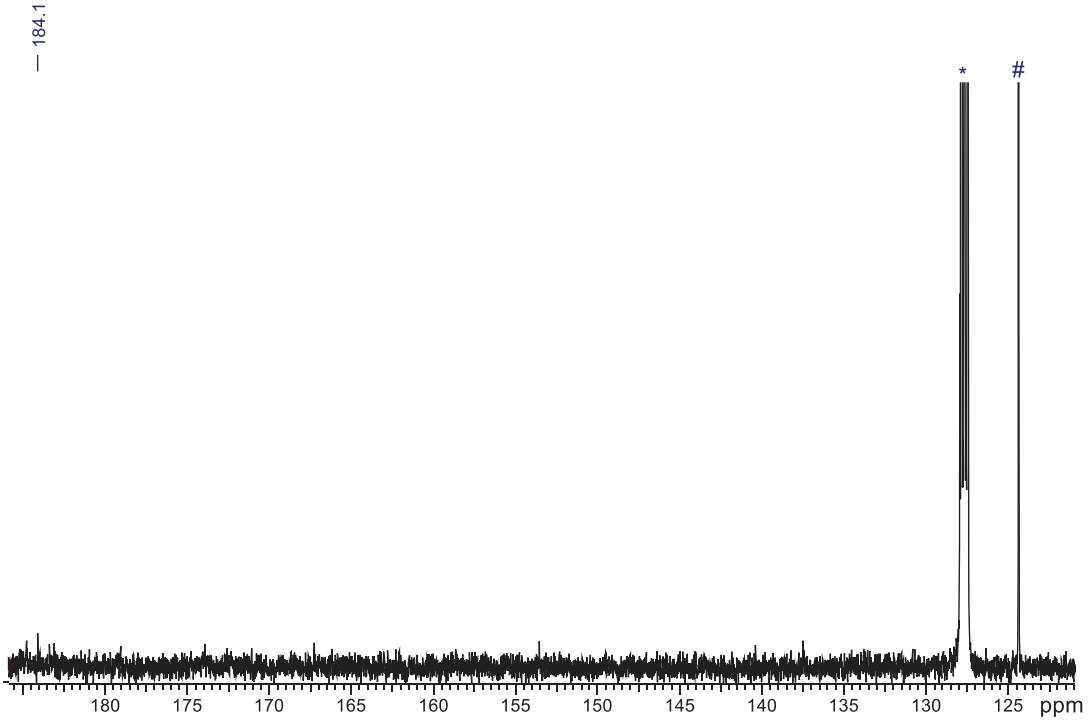

Figure S52. $^{13}C\{^1H\}$-NMR spectrum (126 MHz) of the reaction of [Tp^{tBu,Me}Y(PC$_6$H$_3$*i*Pr-2,6)(AlMe$_3$)] (**3-Y^{Al}**) with $^{13}CO_2$ in C_6D_6 at 26 °C (# denotes $^{13}CO_2$).

DFT calculations

DFT model systems

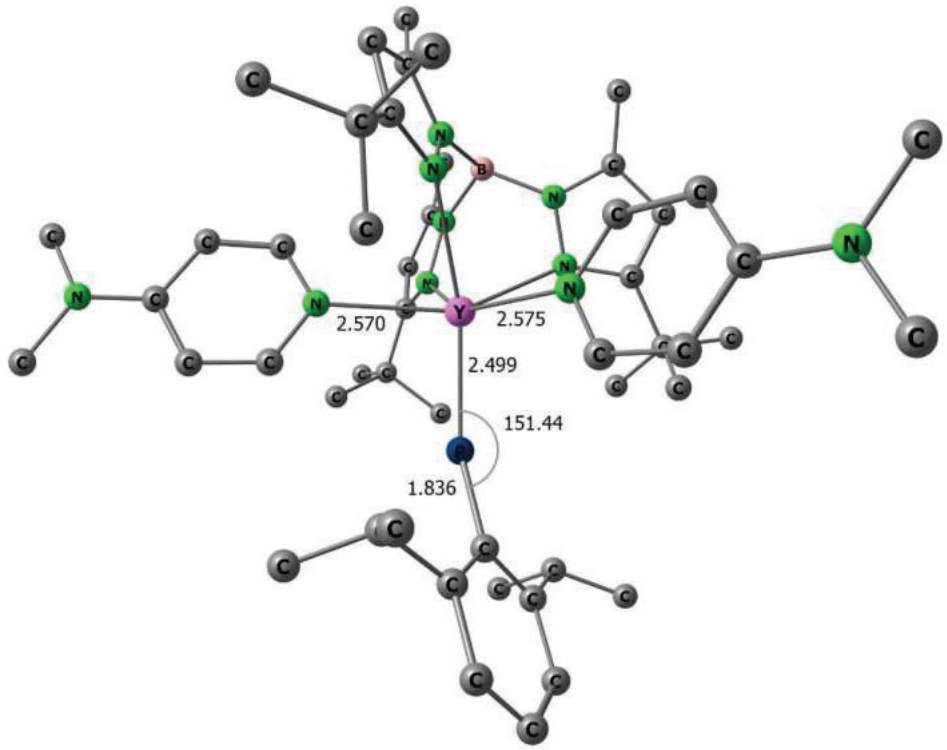

Figure S53. Optimized geometry and selected interatomic distances (Å) and angles (°) of Tp$^{t\mathrm{Bu,Me}}$Y(=PC$_6$H$_3$*i*Pr$_2$-2,6)(DMAP) (**6-Y**); all hydrogen atoms are omitted for clarity.

Table S4. Coordinates of **6-Y**

6	2.665824000	0.260652000	2.981556000
6	3.449934000	1.285254000	3.538796000
1	4.122750000	1.218225000	4.379483000
6	3.182598000	2.423179000	2.803261000
6	2.569362000	-1.159457000	3.522650000
6	1.195420000	-1.363619000	4.188406000
1	1.155473000	-2.351488000	4.661603000
1	0.390845000	-1.322499000	3.448058000
1	1.015549000	-0.606516000	4.959414000
6	2.759747000	-2.211232000	2.420962000
1	3.694370000	-2.050879000	1.872639000
1	1.922395000	-2.207356000	1.718703000
1	2.793871000	-3.209736000	2.872359000
6	3.661171000	-1.370198000	4.585713000
1	3.605786000	-2.396752000	4.961867000
1	3.533471000	-0.700000000	5.442489000
1	4.664923000	-1.217198000	4.173420000
6	3.734276000	3.794418000	3.021743000
1	4.456981000	3.760416000	3.840784000
1	2.951962000	4.510405000	3.293230000
1	4.245098000	4.188505000	2.138283000
6	1.652884000	1.954614000	-2.634943000
6	2.612335000	2.978272000	-2.713371000
1	3.145347000	3.319533000	-3.588530000
6	2.738932000	3.485261000	-1.432974000

6	1.137790000	1.157875000	-3.822894000
6	2.321381000	0.793371000	-4.738801000
1	3.064733000	0.196145000	-4.201291000
1	2.821447000	1.680657000	-5.139585000
1	1.962786000	0.205563000	-5.590975000
6	0.428096000	-0.136022000	-3.417823000
1	1.107945000	-0.824301000	-2.911499000
1	0.046534000	-0.641675000	-4.311440000
1	-0.427900000	0.056546000	-2.767619000
6	0.154454000	2.050031000	-4.609423000
1	0.633220000	2.981356000	-4.929940000
1	-0.715961000	2.306842000	-3.998201000
1	-0.200473000	1.524075000	-5.503434000
6	3.633925000	4.587722000	-0.970202000
1	4.357115000	4.241396000	-0.225166000
1	3.073755000	5.413473000	-0.521476000
1	4.193306000	4.979238000	-1.823376000
6	-1.785630000	2.591140000	2.109293000
6	-1.780253000	3.994683000	2.010832000
1	-2.540130000	4.682805000	2.348701000
6	-0.575622000	4.334530000	1.422880000
6	-2.835738000	1.739370000	2.805589000
6	-2.145681000	0.840897000	3.846199000
1	-1.580529000	1.437725000	4.570498000
1	-1.460634000	0.140628000	3.361955000
1	-2.895802000	0.257432000	4.391550000
6	-3.612149000	0.862429000	1.810885000
1	-2.958893000	0.112946000	1.352986000
1	-4.069060000	1.468613000	1.021245000
1	-4.412345000	0.329820000	2.337546000
6	-3.833529000	2.657426000	3.530087000
1	-4.563292000	2.046598000	4.071283000
1	-4.388906000	3.288613000	2.827226000
1	-3.334517000	3.307071000	4.257448000
6	-0.041975000	5.694310000	1.112749000
1	0.807078000	5.956559000	1.753211000
1	-0.826385000	6.438064000	1.272918000
1	0.295403000	5.774573000	0.074555000
6	3.482673000	-0.375626000	-0.822141000
1	3.473643000	0.680239000	-0.569225000
6	4.664641000	-0.965122000	-1.233549000
1	5.557548000	-0.354912000	-1.290586000
6	4.684119000	-2.341002000	-1.561513000
6	3.453572000	-3.023346000	-1.426319000
1	3.364220000	-4.081914000	-1.635962000
6	2.330640000	-2.341032000	-0.996814000
1	1.381941000	-2.852020000	-0.848494000
6	7.072360000	-2.242990000	-2.039328000
1	7.380960000	-1.870450000	-1.052991000
1	7.007066000	-1.387717000	-2.723661000
1	7.855381000	-2.905501000	-2.409370000
6	5.801137000	-4.395171000	-2.249283000
1	6.787482000	-4.708687000	-2.592539000
1	5.078073000	-4.643480000	-3.035825000
1	5.549709000	-4.980754000	-1.354821000
6	-2.060852000	2.203886000	-1.417622000
1	-1.258741000	2.887093000	-1.154377000
6	-3.199143000	2.689674000	-2.036323000
1	-3.270071000	3.751889000	-2.235442000
6	-4.239818000	1.797923000	-2.386620000
6	-4.026958000	0.441247000	-2.051085000
1	-4.769715000	-0.319356000	-2.256825000
6	-2.855725000	0.060878000	-1.422836000
1	-2.691700000	-0.972165000	-1.126814000
6	-5.576586000	3.630533000	-3.278393000
1	-5.597647000	4.229478000	-2.357636000
1	-6.529107000	3.767668000	-3.791111000
1	-4.786751000	4.028559000	-3.927994000
6	-6.439833000	1.274996000	-3.296208000
1	-6.089117000	0.468869000	-3.952191000
1	-7.251895000	1.792237000	-3.808095000
1	-6.847158000	0.821034000	-2.383024000
6	-2.217607000	-3.308772000	0.401831000
6	-2.381297000	-3.946638000	-0.865406000
6	-3.402934000	-4.882887000	-1.052733000
1	-3.509303000	-5.364444000	-2.022771000
6	-4.276800000	-5.223807000	-0.028433000
1	-5.065668000	-5.953857000	-0.192681000

6	-4.115384000	-4.623375000	1.216305000
1	-4.786592000	-4.898599000	2.026046000
6	-3.110510000	-3.683757000	1.453550000
6	-1.419827000	-3.696713000	-2.016744000
1	-0.868754000	-2.782012000	-1.759537000
6	-2.108098000	-3.470787000	-3.367373000
1	-1.367823000	-3.212351000	-4.134146000
1	-2.836099000	-2.654586000	-3.313310000
1	-2.637027000	-4.363610000	-3.720928000
6	-0.400399000	-4.841485000	-2.111193000
1	0.116465000	-4.976366000	-1.155117000
1	0.348832000	-4.644525000	-2.889148000
1	-0.896118000	-5.788923000	-2.354848000
6	-2.943663000	-3.120874000	2.855703000
1	-2.447942000	-2.148491000	2.737785000
6	-1.995839000	-4.011389000	3.673001000
1	-2.416642000	-5.016639000	3.798331000
1	-1.821738000	-3.589382000	4.670557000
1	-1.029874000	-4.102609000	3.167327000
6	-4.259578000	-2.897920000	3.606833000
1	-4.751972000	-3.839653000	3.877937000
1	-4.968004000	-2.310590000	3.012986000
1	-4.071122000	-2.359550000	4.542951000
7	2.288802000	2.083331000	1.840169000
7	1.964010000	0.754878000	1.942689000
7	1.890731000	2.788607000	-0.633881000
7	1.220987000	1.845891000	-1.365020000
7	0.095435000	3.180125000	1.177337000
7	-0.651564000	2.104066000	1.575406000
7	2.312934000	-1.026710000	-0.698030000
7	5.820813000	-2.970721000	-1.978711000
7	-1.858963000	0.911768000	-1.104601000
7	-5.379836000	2.221245000	-3.006001000
15	-0.904271000	-2.062225000	0.707843000
39	0.205063000	0.123142000	0.218256000
5	1.610771000	3.077031000	0.870323000
1	2.092200000	4.150852000	1.087041000

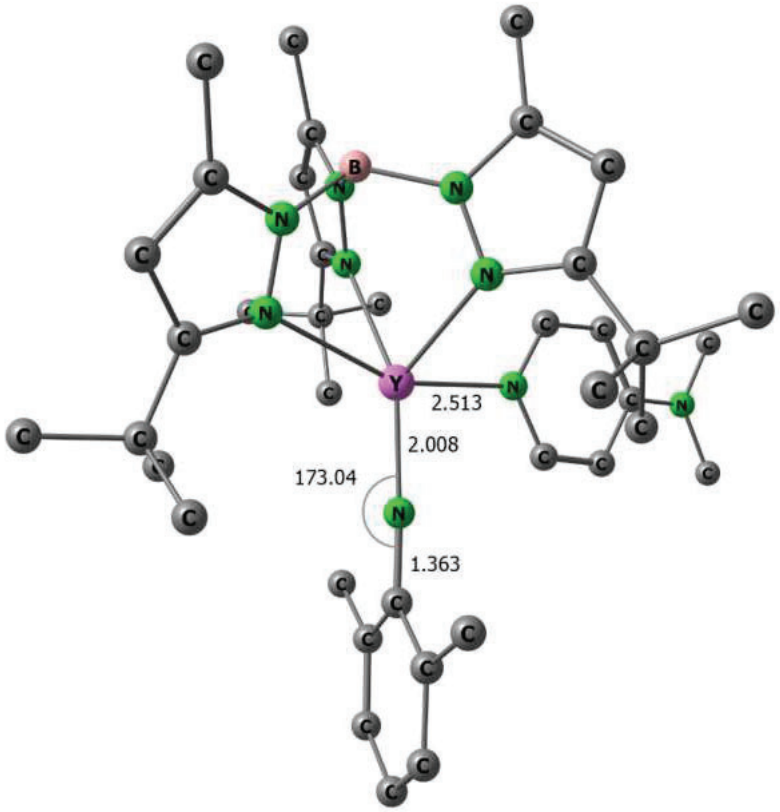

Figure S54. Optimized geometry and selected interatomic distances (Å) and angles (°) of ($Tp^{tBu,Me}$)Y[=$NC_6H_3(CH_3)_2$-2,6](DMAP) (**XXIV**); all hydrogen atoms are omitted for clarity.

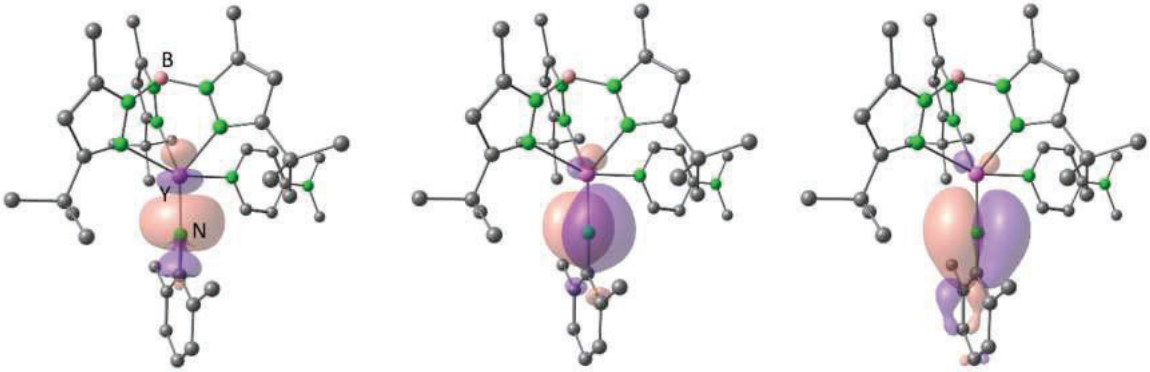

Figure S55. NLMOs representing one σ- and two π-type Y–N bonding interactions in **XXIV**; all hydrogen atoms are omitted for clarity.

Table S5. Coordinates of **XXIV**

39	0.253615000	0.364529000	-0.101040000
7	1.137047000	-2.089079000	1.698676000
7	0.520253000	-0.907611000	2.017956000
7	3.133400000	-0.963242000	0.538937000
7	2.726675000	0.203574000	-0.046839000
7	1.671340000	-2.564534000	-0.796196000
7	0.839322000	-1.727192000	-1.483057000
7	-0.304562000	2.293283000	-0.090469000
7	-2.117072000	-0.460426000	-0.218673000
7	-6.169437000	-1.566526000	-0.201030000
6	2.012885000	-3.623958000	-1.573667000
6	-3.102050000	0.460628000	-0.269741000
6	4.899906000	0.363198000	0.473076000
6	0.832000000	-3.033612000	2.621896000
6	-1.583618000	6.294802000	-0.568493000
6	-1.191329000	4.081119000	-1.503265000
6	3.767387000	2.400878000	-0.720914000
6	-4.447305000	0.145783000	-0.269020000
6	-4.855385000	-1.207816000	-0.204175000
6	-3.815685000	-2.167653000	-0.140949000
6	4.445384000	-0.882976000	0.870751000
6	-0.716722000	3.583451000	-0.244217000
6	-2.498823000	-1.748449000	-0.153470000
6	0.008452000	-2.445789000	3.568385000
6	0.662024000	-2.262664000	-2.699888000
6	-0.698879000	4.516819000	0.845292000
6	1.377346000	-3.467811000	-2.793277000
6	-1.122465000	5.832204000	0.662654000
6	-0.152825000	-1.111806000	3.165541000
6	-1.611527000	5.403900000	-1.638621000
6	3.797489000	1.013226000	-0.105645000
6	-0.175229000	-1.623204000	-3.788422000
6	-0.863664000	-0.003746000	3.921346000
5	2.242768000	-2.222080000	0.604320000
1	-4.025649000	-3.228439000	-0.083644000
1	-1.697061000	-2.481416000	-0.111643000
1	-5.166693000	0.953841000	-0.312391000
1	-2.763828000	1.493734000	-0.302736000
1	-1.964647000	5.742249000	-2.612704000
1	-1.909961000	7.324137000	-0.690804000
1	-1.089376000	6.511861000	1.513946000
1	-0.400551000	-2.926808000	4.443857000
1	1.444003000	-4.136664000	-3.638977000
1	5.906147000	0.738113000	0.582758000
6	5.212047000	-1.973943000	1.543205000
1	5.294506000	-2.867909000	0.916564000
1	6.222765000	-1.622259000	1.763073000
1	4.746007000	-2.275832000	2.486247000
6	2.875872000	2.420738000	-1.972912000
1	1.822039000	2.280918000	-1.704557000
1	2.947091000	3.397819000	-2.463233000
1	3.178499000	1.651719000	-2.692237000
6	5.195044000	2.808001000	-1.120358000
1	5.175142000	3.792037000	-1.599944000
1	5.854711000	2.883104000	-0.249473000
1	5.636731000	2.094950000	-1.825078000
6	3.219977000	3.413273000	0.302560000
1	3.813576000	3.402058000	1.223382000
1	3.253753000	4.425960000	-0.114568000
1	2.177772000	3.185055000	0.543533000
6	-1.229488000	3.169606000	-2.694897000
1	-1.619868000	3.689058000	-3.576926000
1	-0.230932000	2.787945000	-2.941550000
1	-1.856871000	2.287168000	-2.515685000
6	-0.234215000	4.073958000	2.202275000
1	0.737728000	3.571355000	2.153935000
1	-0.150513000	4.925393000	2.886484000
1	-0.927061000	3.351617000	2.648515000
6	2.940070000	-4.719348000	-1.158818000
1	3.955942000	-4.348174000	-0.989933000
1	2.616341000	-5.213669000	-0.238529000
1	2.985092000	-5.471641000	-1.949976000
6	-0.529492000	-0.178036000	-3.436246000
1	0.369501000	0.426578000	-3.273314000

1	-1.087474000	0.290043000	-4.253436000
1	-1.170732000	-0.124187000	-2.550172000
6	0.625927000	-1.628129000	-5.104002000
1	0.038528000	-1.163001000	-5.903433000
1	1.560857000	-1.068736000	-4.997760000
1	0.875645000	-2.644638000	-5.423264000
6	-1.469552000	-2.437025000	-3.982961000
1	-2.072479000	-2.440588000	-3.069413000
1	-2.074219000	-2.004594000	-4.788479000
1	-1.247010000	-3.476119000	-4.246751000
6	1.331433000	-4.439857000	2.583005000
1	1.057823000	-4.943089000	1.650126000
1	2.421115000	-4.489942000	2.675195000
1	0.894150000	-5.003320000	3.410623000
6	-1.940645000	0.666528000	3.055450000
1	-2.459991000	1.435945000	3.638524000
1	-1.512935000	1.162554000	2.176911000
1	-2.684475000	-0.063423000	2.719705000
6	-1.535966000	-0.582250000	5.175564000
1	-0.806636000	-1.040565000	5.851870000
1	-2.039218000	0.219630000	5.725328000
1	-2.289160000	-1.335434000	4.918891000
6	0.185172000	1.037935000	4.356556000
1	0.685295000	1.478311000	3.490911000
1	-0.293457000	1.846012000	4.920719000
1	0.946902000	0.578292000	4.995761000
6	-6.541071000	-2.965829000	-0.121118000
1	-6.180292000	-3.430831000	0.805611000
1	-7.627801000	-3.049925000	-0.137107000
1	-6.146806000	-3.538661000	-0.970269000
6	-7.200413000	-0.546733000	-0.256483000
1	-7.150630000	0.128773000	0.607010000
1	-7.123859000	0.055955000	-1.170071000
1	-8.179343000	-1.026320000	-0.252262000
1	2.935855000	-3.142471000	0.928682000

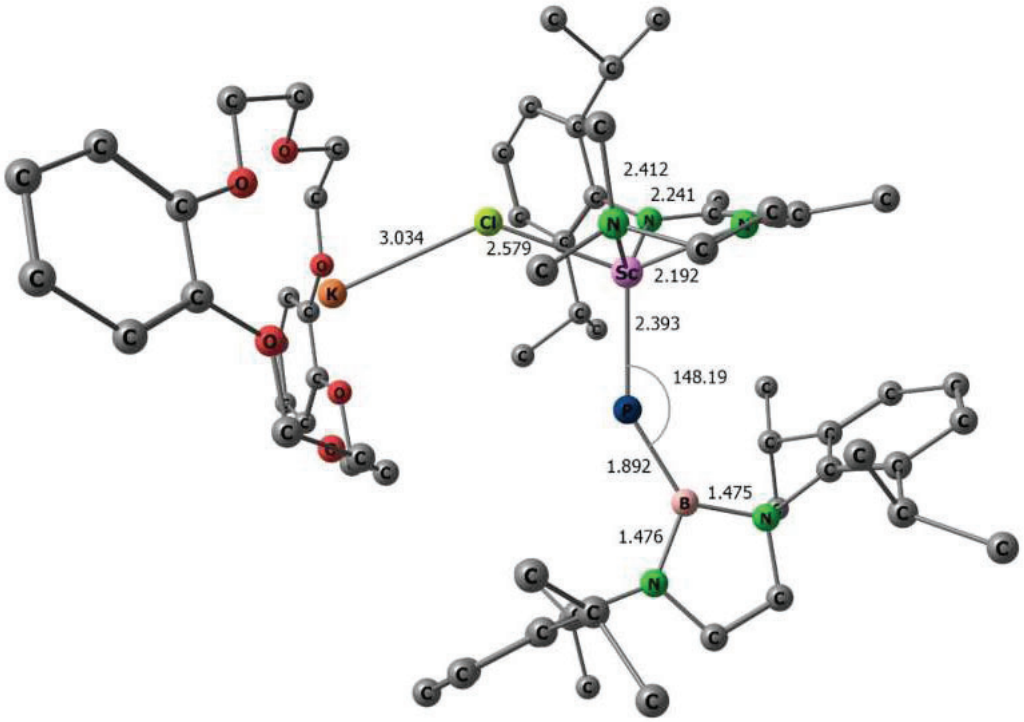

Figure S56. Optimized geometry and selected interatomic distances (Å) and angles (°) of {$N_2C_3HAr^{iPr}$-1-Me_2-2,4-($C_2H_4NMe_2$)-5}Sc[=PB($N_2Ar^{iPr}_2$-2,5-C_2H_2)](μ_2-Cl)K(dibenzo-18-crown-6) (**IX**); all hydrogen atoms are omitted for clarity.

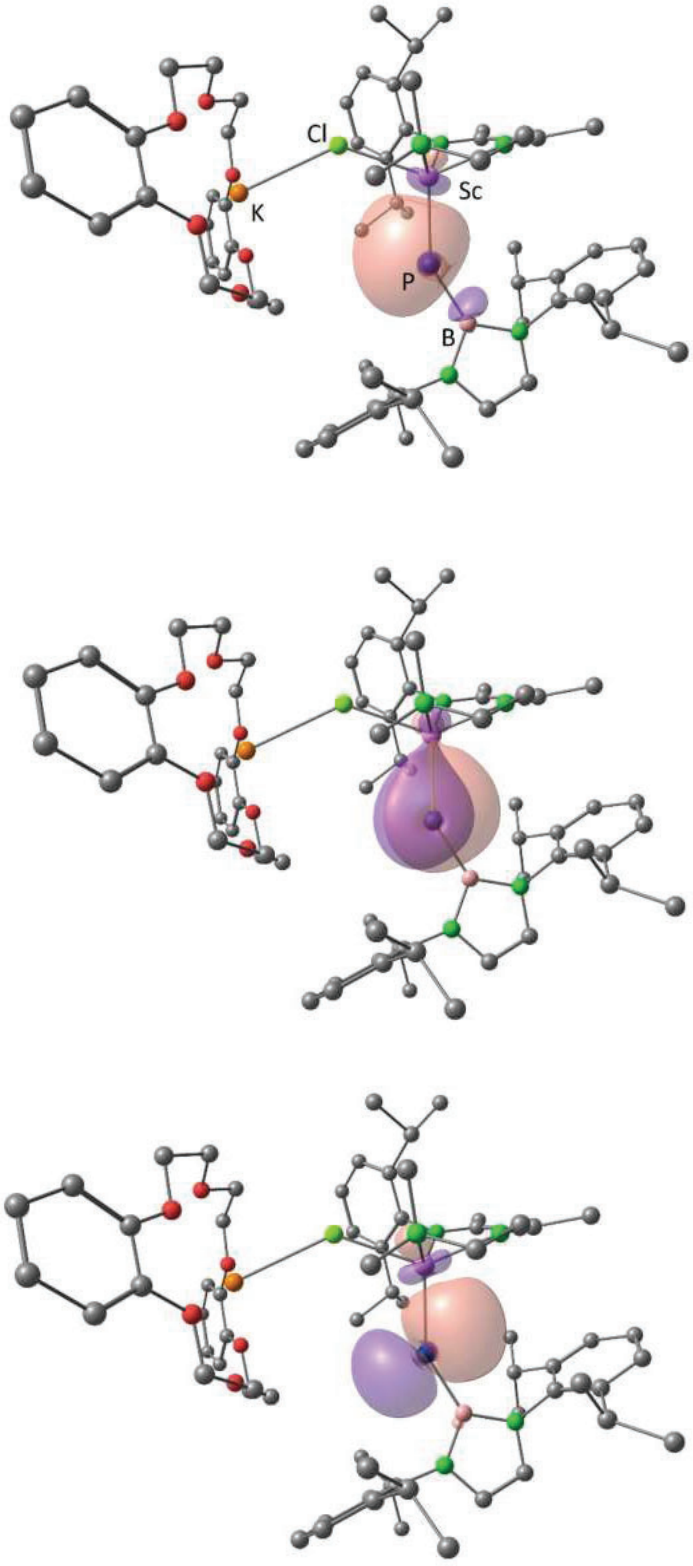

Figure S57. NLMOs representing one σ- and two π-type Y–N bonding interactions in **IX**; all hydrogen atoms are omitted for clarity.

Table S6. Coordinates of **IX**

21	-0.935412000	1.467997000	-1.069873000
19	3.751919000	-0.589816000	-0.125176000
17	1.641132000	1.362027000	-1.095903000
15	-1.831265000	-0.546221000	-0.139697000
8	2.623187000	-3.007323000	0.530044000
8	3.578612000	-2.600912000	-2.100579000
8	5.073103000	-0.534405000	-2.639429000
8	5.649523000	1.433161000	-0.681045000
8	4.916370000	0.843313000	1.979035000
8	3.525827000	-1.280982000	2.564331000
7	-0.853472000	3.395657000	0.070430000
7	-2.502912000	2.480261000	-2.220150000
7	-0.607758000	0.807844000	-3.366522000
7	-4.776162000	-1.154212000	0.563110000
7	-3.366607000	-2.922180000	0.880994000
6	-1.913457000	5.264096000	1.300448000
1	-1.786798000	4.816354000	2.290839000
1	-2.845513000	5.831716000	1.294611000
1	-1.080428000	5.958974000	1.164942000
6	-1.924648000	4.189918000	0.231062000
6	-3.085115000	4.127629000	-0.549503000
1	-3.875593000	4.809781000	-0.260936000
6	-3.315351000	3.418076000	-1.744432000
6	-4.560247000	3.806148000	-2.511127000
1	-4.316666000	4.125740000	-3.530719000
1	-5.084138000	4.624210000	-2.015850000
1	-5.251879000	2.959458000	-2.582314000
6	-2.796268000	1.951591000	-3.546640000
1	-2.567651000	2.702775000	-4.320482000
1	-3.857490000	1.702139000	-3.665800000
6	-2.007019000	0.679470000	-3.801854000
1	-2.437447000	-0.134244000	-3.210842000
1	-2.060122000	0.410987000	-4.871871000
6	0.061154000	-0.492818000	-3.508690000
1	1.090231000	-0.405978000	-3.155951000
1	0.059931000	-0.820752000	-4.562024000
1	-0.463754000	-1.221553000	-2.885906000
6	0.111460000	1.820194000	-4.149324000
1	-0.342295000	2.803694000	-4.007099000
1	0.100313000	1.574741000	-5.224091000
1	1.143064000	1.866542000	-3.796943000
6	0.355237000	3.852640000	0.693077000
6	0.726388000	3.417783000	1.984821000
6	1.904316000	3.918744000	2.551112000
1	2.189443000	3.593268000	3.548657000
6	2.701938000	4.837054000	1.878990000
1	3.594366000	5.240929000	2.352163000
6	2.335589000	5.248955000	0.601482000
1	2.956406000	5.968679000	0.072267000
6	1.178082000	4.765658000	-0.013422000
6	0.835677000	5.242570000	-1.418883000
1	-0.028114000	4.661320000	-1.756614000
6	1.983745000	4.978409000	-2.402966000
1	2.869496000	5.578233000	-2.162258000
1	1.680980000	5.243175000	-3.423035000
1	2.267772000	3.922792000	-2.384831000
6	0.439431000	6.726411000	-1.444945000
1	-0.430745000	6.925231000	-0.813070000
1	0.188688000	7.039746000	-2.465009000
1	1.260344000	7.362829000	-1.094055000
6	-0.106153000	2.424395000	2.780113000
1	-1.036516000	2.248737000	2.229488000
6	-0.466424000	2.945922000	4.178714000
1	0.421931000	3.061986000	4.810232000
1	-1.133111000	2.239033000	4.684231000
1	-0.970978000	3.916683000	4.140903000
6	0.613674000	1.074267000	2.888307000
1	0.798758000	0.657262000	1.895243000
1	-0.006095000	0.359466000	3.439554000
1	1.570619000	1.178205000	3.413550000
6	-5.498048000	-2.251071000	1.044334000
1	-6.563143000	-2.189585000	1.220259000
6	-4.666143000	-3.296217000	1.234543000
1	-4.890504000	-4.287781000	1.601744000

6	-5.513505000	0.021141000	0.235312000
6	-6.354468000	0.007392000	-0.901061000
6	-7.149442000	1.130070000	-1.155193000
1	-7.810082000	1.135358000	-2.017434000
6	-7.120187000	2.235459000	-0.312216000
1	-7.750728000	3.096546000	-0.520408000
6	-6.290787000	2.232367000	0.803579000
1	-6.282540000	3.096662000	1.460049000
6	-5.483738000	1.130892000	1.106229000
6	-4.645333000	1.098815000	2.374903000
1	-3.709906000	0.585281000	2.121326000
6	-4.278476000	2.488830000	2.897756000
1	-3.826802000	3.101671000	2.112833000
1	-3.560094000	2.397944000	3.718704000
1	-5.149881000	3.024125000	3.294787000
6	-5.354066000	0.297604000	3.479783000
1	-6.308521000	0.767516000	3.746863000
1	-4.733839000	0.262857000	4.383328000
1	-5.555087000	-0.731068000	3.169804000
6	-6.385311000	-1.189044000	-1.843088000
1	-6.161815000	-2.080315000	-1.247968000
6	-7.747373000	-1.420159000	-2.505280000
1	-8.555212000	-1.462056000	-1.767286000
1	-7.739337000	-2.369304000	-3.052071000
1	-7.994930000	-0.636597000	-3.230728000
6	-5.277412000	-1.070320000	-2.897984000
1	-5.451687000	-0.201764000	-3.545114000
1	-5.247421000	-1.962869000	-3.534370000
1	-4.303561000	-0.953964000	-2.412713000
6	-2.336292000	-3.889449000	1.030743000
6	-1.835854000	-4.170407000	2.319906000
6	-0.920722000	-5.219804000	2.471420000
1	-0.543929000	-5.459138000	3.463486000
6	-0.505825000	-5.974874000	1.380219000
1	0.190931000	-6.798373000	1.517431000
6	-0.999616000	-5.680047000	0.111420000
1	-0.686842000	-6.286580000	-0.734685000
6	-1.915058000	-4.641499000	-0.088859000
6	-2.510730000	-4.386116000	-1.463881000
1	-2.852511000	-3.346425000	-1.470763000
6	-1.501526000	-4.538673000	-2.605276000
1	-0.628988000	-3.897265000	-2.447113000
1	-1.964150000	-4.244846000	-3.553643000
1	-1.155368000	-5.572257000	-2.725300000
6	-3.729079000	-5.293723000	-1.697075000
1	-3.440900000	-6.351664000	-1.673280000
1	-4.181483000	-5.089217000	-2.674280000
1	-4.493563000	-5.132185000	-0.932030000
6	-2.293802000	-3.387102000	3.540007000
1	-2.955591000	-2.593152000	3.183454000
6	-1.120417000	-2.712284000	4.260711000
1	-0.405553000	-3.446607000	4.652204000
1	-1.482035000	-2.122606000	5.110445000
1	-0.591957000	-2.035686000	3.582913000
6	-3.094095000	-4.271104000	4.507184000
1	-3.962920000	-4.715794000	4.012881000
1	-3.455712000	-3.681405000	5.356882000
1	-2.481456000	-5.088597000	4.905353000
6	1.841763000	-3.308292000	-0.617443000
1	1.220551000	-2.445387000	-0.904057000
1	1.157330000	-4.142556000	-0.408836000
6	2.766188000	-3.715981000	-1.738540000
1	3.404324000	-4.549456000	-1.415641000
1	2.165742000	-4.040696000	-2.598507000
6	4.497256000	-2.773896000	-3.094551000
6	4.672403000	-3.951901000	-3.814234000
1	4.054645000	-4.816210000	-3.600404000
6	5.642180000	-4.032106000	-4.818979000
1	5.762820000	-4.960088000	-5.369284000
6	6.438724000	-2.934638000	-5.104548000
1	7.195092000	-2.987668000	-5.881451000
6	6.272437000	-1.744729000	-4.388104000
1	6.902404000	-0.893068000	-4.617582000
6	5.309953000	-1.653182000	-3.388140000
6	5.839473000	0.630042000	-2.916997000
1	5.713948000	0.926451000	-3.967335000
1	6.904339000	0.435936000	-2.729247000
6	5.350589000	1.750790000	-2.029206000

1	5.862640000	2.679045000	-2.330220000
1	4.268098000	1.896211000	-2.160806000
6	5.210911000	2.432725000	0.228245000
1	4.122012000	2.571060000	0.164636000
1	5.688390000	3.398308000	-0.001912000
6	5.615397000	2.030003000	1.626795000
1	6.699124000	1.855079000	1.670511000
1	5.354851000	2.842792000	2.316817000
6	5.106752000	0.332706000	3.232237000
6	5.969808000	0.870513000	4.181161000
1	6.547831000	1.757908000	3.950467000
6	6.099112000	0.273909000	5.439801000
1	6.777009000	0.708019000	6.168187000
6	5.365583000	-0.861027000	5.747292000
1	5.459209000	-1.331957000	6.720960000
6	4.493837000	-1.409845000	4.801144000
1	3.923703000	-2.296448000	5.052765000
6	4.354035000	-0.823623000	3.547103000
6	2.721726000	-2.425942000	2.840052000
1	2.100398000	-2.246601000	3.726232000
1	3.367464000	-3.295035000	3.025828000
6	1.818923000	-2.688396000	1.659336000
1	1.155427000	-3.528362000	1.908522000
1	1.176131000	-1.820275000	1.447177000
5	-3.352306000	-1.515303000	0.433371000

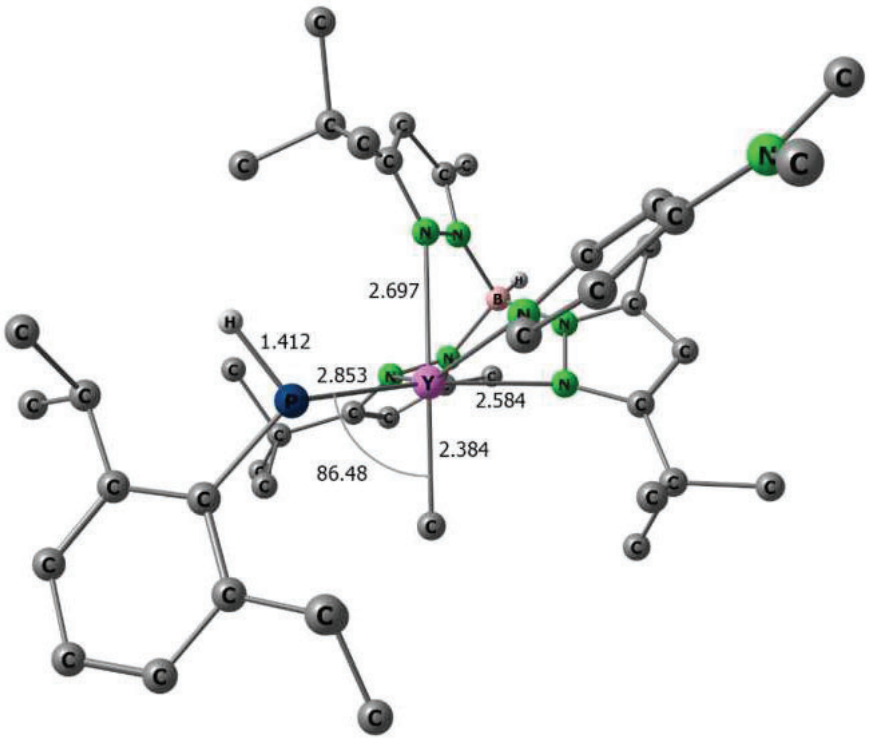

Figure S58. Optimized geometry and selected interatomic distances (Å) and angles (°) of $Tp^{tBu,Me}YMe(HPC_6H_3iPr_2\text{-}2,6)(DMAP)$ (**5-Y**); all hydrogen atoms attached to carbon atoms are omitted for clarity.

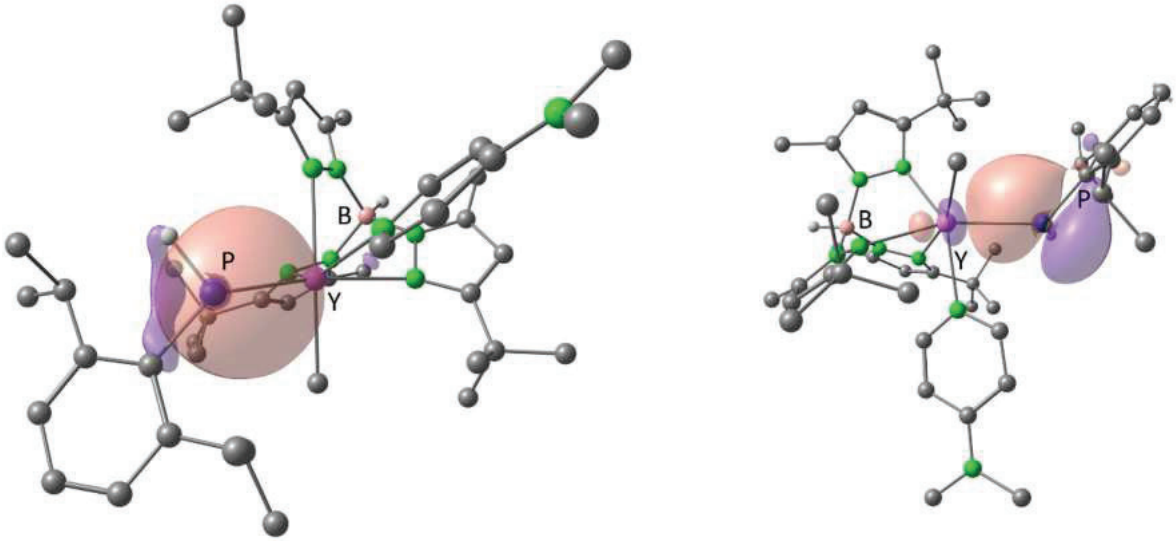

Figure S59. NLMOs representing two σ-type Y–P bonding interactions in **5-Y**; all hydrogen atoms attached to carbon atoms are omitted for clarity.

Table S7. Composition (in %) of the Natural Localized Molecular Orbitals (NLMOs) shown in Figure S43 for **5-Y**

σ(Y−P) (*left*)		σ(Y−P) (*right*)		
Y	P	Y	P	C
90.6	6.8	85.2	9.5	1.9

Table S8. Natural Atomic Charges of the Key Atoms in the Yttrium Phosphido Moiety in **5-Y**

Atom	Charge
Y	+1.85
P	−0.32
C (P−C)	−0.27
C (Y−CH_3)	−1.43
H (P−H)	+0.02

Table S9. Wiberg Bond Indices (WBIs) for the Key Atoms in the Yttrium Phosphido Moiety in **5-Y**

Bond	WBI
Y−P	0.55
P−C	1.00
Y−C	0.41
P−H	0.96

Table S10. Coordinates of **5-Y**

6	-0.922260000	-1.502063000	3.090306000
6	-1.531699000	-2.681393000	3.550621000
1	-1.618988000	-3.027705000	4.569086000
6	-2.007768000	-3.329822000	2.426329000
6	-0.181847000	-0.499805000	3.959062000
6	1.322287000	-0.834156000	3.925336000
1	1.880824000	-0.146179000	4.570407000
1	1.723588000	-0.744284000	2.911863000
1	1.501802000	-1.855864000	4.276256000
6	-0.408600000	0.941469000	3.491810000
1	-1.471857000	1.201414000	3.513818000
1	-0.043146000	1.110638000	2.477452000
1	0.128852000	1.634925000	4.147806000
6	-0.672978000	-0.613584000	5.412727000
1	-0.167498000	0.136030000	6.030607000
1	-0.450921000	-1.594567000	5.844443000
1	-1.752227000	-0.442370000	5.486695000
6	-2.714829000	-4.643755000	2.352068000
1	-2.844592000	-5.039151000	3.362404000
1	-2.145828000	-5.378257000	1.773384000
1	-3.703714000	-4.560222000	1.891155000
6	-3.161884000	-0.168897000	-2.288456000
6	-4.401338000	-0.730341000	-1.940388000
1	-5.375792000	-0.469236000	-2.323941000
6	-4.127851000	-1.728090000	-1.020726000
6	-2.929833000	0.865022000	-3.380373000
6	-4.280778000	1.310573000	-3.963860000
1	-4.916471000	1.779135000	-3.204397000
1	-4.829768000	0.472080000	-4.404966000
1	-4.110242000	2.046844000	-4.755988000
6	-2.207467000	2.114331000	-2.856201000
1	-2.789955000	2.607016000	-2.071479000
1	-2.065757000	2.829113000	-3.675119000
1	-1.221130000	1.871004000	-2.458259000
6	-2.106913000	0.210148000	-4.506923000
1	-2.638559000	-0.653899000	-4.920554000
1	-1.135349000	-0.126411000	-4.142165000
1	-1.941707000	0.928034000	-5.318785000
6	-5.078824000	-2.659923000	-0.345784000
1	-4.972092000	-2.632674000	0.743193000
1	-4.925462000	-3.696740000	-0.663421000
1	-6.104792000	-2.377673000	-0.593840000
6	1.462410000	-3.422186000	-1.127004000
6	0.862351000	-4.496532000	-1.800740000
1	1.351335000	-5.292389000	-2.341149000
6	-0.502807000	-4.351441000	-1.617794000
6	2.947151000	-3.224442000	-0.874432000
6	3.202257000	-3.422932000	0.633304000
1	2.873468000	-4.415312000	0.961020000
1	2.663938000	-2.676159000	1.223523000
1	4.271283000	-3.326437000	0.851537000
6	3.433309000	-1.834683000	-1.299761000
1	2.966622000	-1.033241000	-0.716783000

1	3.230904000	-1.647401000	-2.357466000
1	4.513406000	-1.752463000	-1.139532000
6	3.747627000	-4.279914000	-1.653119000
1	4.816755000	-4.142412000	-1.462495000
1	3.587062000	-4.189447000	-2.732719000
1	3.484625000	-5.298366000	-1.347952000
6	-1.606543000	-5.227099000	-2.110560000
1	-2.103544000	-5.758230000	-1.291734000
1	-1.200284000	-5.971099000	-2.799640000
1	-2.371352000	-4.652543000	-2.641533000
6	-2.774946000	1.342612000	0.753275000
1	-3.048100000	0.292300000	0.731686000
6	-3.706110000	2.279742000	1.156737000
1	-4.694787000	1.940026000	1.438683000
6	-3.353457000	3.649896000	1.193860000
6	-2.026721000	3.954230000	0.810532000
1	-1.652389000	4.970229000	0.817373000
6	-1.169185000	2.940715000	0.429075000
1	-0.134783000	3.160646000	0.175032000
6	-5.578225000	4.249285000	1.987320000
1	-5.572435000	3.590089000	2.865272000
1	-6.122997000	3.742955000	1.180319000
1	-6.131306000	5.151604000	2.248801000
6	-3.820637000	6.003641000	1.617071000
1	-4.662283000	6.620694000	1.932265000
1	-3.496646000	6.354991000	0.629508000
1	-2.998434000	6.163908000	2.326406000
6	3.731873000	1.786279000	-0.102491000
6	3.854954000	2.598934000	-1.263906000
6	5.115942000	2.817191000	-1.824764000
1	5.203804000	3.436079000	-2.713043000
6	6.263700000	2.273598000	-1.261882000
1	7.237298000	2.457029000	-1.709328000
6	6.151400000	1.499184000	-0.115143000
1	7.050540000	1.081767000	0.329050000
6	4.910534000	1.235843000	0.475172000
6	2.656832000	3.327293000	-1.864014000
1	1.761912000	2.741104000	-1.630184000
6	2.703544000	3.470707000	-3.388472000
1	1.754525000	3.880538000	-3.752256000
1	2.862765000	2.504755000	-3.876259000
1	3.492582000	4.156389000	-3.718103000
6	2.499119000	4.701060000	-1.194050000
1	2.391771000	4.590625000	-0.110264000
1	1.616894000	5.227365000	-1.580096000
1	3.376823000	5.328417000	-1.388207000
6	4.876212000	0.406031000	1.750173000
1	3.904911000	-0.103680000	1.771604000
6	4.964588000	1.312995000	2.989200000
1	5.933652000	1.824952000	3.014861000
1	4.866163000	0.730079000	3.912905000
1	4.185596000	2.080941000	2.983846000
6	5.956855000	-0.678894000	1.827597000
1	6.958215000	-0.257809000	1.972211000
1	5.979818000	-1.293444000	0.922543000
1	5.763265000	-1.337505000	2.681566000
7	-1.700371000	-2.556311000	1.356611000
7	-1.027627000	-1.433236000	1.748531000
7	-2.786229000	-1.745654000	-0.831295000
7	-2.182404000	-0.778738000	-1.587653000
7	-0.697658000	-3.239712000	-0.870221000
7	0.503449000	-2.643144000	-0.587989000
7	-1.513581000	1.637533000	0.384890000
7	-4.235753000	4.614026000	1.578472000
15	2.046539000	1.551257000	0.616298000
39	0.038857000	-0.201228000	-0.401105000
5	-2.000931000	-2.881728000	-0.116196000
1	-2.705102000	-3.851556000	-0.132180000
1	2.361051000	1.314237000	1.971836000
6	0.974545000	0.214917000	-2.553642000
1	0.586912000	1.037717000	-3.168934000
1	2.053952000	0.398712000	-2.457987000
1	0.871784000	-0.699797000	-3.161989000

References

1. COSMO, v. 1.61; Bruker AXS Inc.: Madison, WI, **2012**.
2. APEX 3, V. 2019.11-0, Bruker AXS Inc., Madison, WI, **2019**.
3. SAINT, v. 8.40B; Bruker AXS Inc., Madison, WI, **2019**.
4. Krause, L.; Herbst-Irmer, R.; Sheldrick, G. M.; Stalke, D., SADABS – Comparison of silver and molybdenum microfocus X-ray sources for single-crystal structure determination. *J. Appl. Cryst.* **2015**, *48*, 3-10.
5. Sheldrick, G. M., SHELXTL – Integrated space-group and crystal-structure determination. *Acta Cryst.* **2015**, *A71*, 3–8.
6. Hübschle, C. B.; Sheldrick, G. M.; Dittrich, B., ShelXle: a Qt graphical user interface for ShelXle. *J. Appl. Cryst.* **2011**, *44*, 1281-1284.
7. Kratzert, D.; Holstein, J. J.; Krossing, I., DSR: enhanced modelling and refinement of disordered structures with SHELXL. *J. Appl. Cryst.* **2015**, *48*, 933-938.
8. Farrugia, L. J., ORTEP-3 for Windows – a version of ORTEP-III with a Graphical User Interface (GUI). *J. Appl. Cryst.* **1997**, *30*, 565-566.
9. POV-Ray v. 3.6; Persistence of Vision Pty. Ltd.: Williamstown, Victoria, Australia, **2004**. http://www.povray.org/.

Paper III

Terminal Dysprosium and Holmium Organoimides

https://doi.org/10.1039/D3SC06584G
reprinted with permission from
Chem. Sci., **2024**

Chemical Science

ROYAL SOCIETY OF CHEMISTRY

EDGE ARTICLE

View Article Online
View Journal

Cite this: DOI: 10.1039/d3sc06584g

All publication charges for this article have been paid for by the Royal Society of Chemistry

Received 7th December 2023
Accepted 18th January 2024

DOI: 10.1039/d3sc06584g

rsc.li/chemical-science

Terminal dysprosium and holmium organoimides†

Theresa E. Rieser, Dorothea Schädle, Cäcilia Maichle-Mössmer and Reiner Anwander *

Terminal rare-earth-metal imide complexes $Tp^{tBu,Me}Ln(NC_6H_3iPr_2\text{-}2,6)(dmap)$ of the mid-late rare-earth elements dysprosium and holmium were synthesized *via* double methane elimination of Lewis acid stabilized dialkyl precursors $Tp^{tBu,Me}LnMe(GaMe_4)$ with primary aniline derivative $H_2NC_6H_3iPr_2\text{-}2,6$ (H_2NAr^{iPr}). Exploiting the weaker Ln–CH_3···[$GaMe_3$] interaction compared to the aluminium congener, addition of the aniline derivative leads to the mixed methyl/anilido species $Tp^{tBu,Me}LnMe(HNAr^{iPr})$ which readily eliminate methane after being exposed to the Lewis base DMAP (=*N*,*N*-dimethyl-4-aminopyridine). Under the same conditions, [$AlMe_3$]-stabilized dimethyl rare-earth-metal complexes transform immediately to Lewis acid bridged imides $Tp^{tBu,Me}Ln(\mu_2\text{-}NC_6H_3Me_2\text{-}2,6)(\mu_2\text{-}Me)AlMe_2$ (Ln = Dy, Ho). DMAP/THF donor exchange is accomplished by treatment of $Tp^{tBu,Me}Ln(NC_6H_3iPr_2\text{-}2,6)(dmap)$ with 9-BBN in THF while the terminal imides readily insert carbon dioxide to afford carbamate complexes.

Introduction

Recent years have witnessed major progress in the field of rare-earth-metal (Ln) complexes with multiply bonded (dianionic) main-group ligands, most notably (organo)imide chemistry.[1–3] Upon closer inspection this is not all that surprising, since [Ln=NR] moieties display a favourable Pearson hard/hard match and enhanced steric/electronic variability through the imido substituent R,[4] compared to other fragments such as [Ln=O],[5] [Ln=PR],[6] or [Ln=CR_2].[7] Of particular interest have been the synthesis of terminal rare-earth-metal imides[8–15] and a fundamental understanding of the Ln–imido bonding as well as reactivity,[16] and in particular small-molecule-activation scenarios.[17] Closely based on Chen's synthesis protocol of the first terminal scandium imide complex $L^1Sc(NAr^{iPr})(dmap)$ (Ar^{iPr} = $C_6H_3iPr_2\text{-}2,6$; L^1 = [$Ar^{iPr}NC(Me)CHC(Me)N(CH_2)_2NMe_2$]),[8] a donor-promoted intramolecular methane/tetramethylsilane elimination from mixed methyl(neosilyl)/primary amido precursors emerged as the most efficient approach for accessing terminal Ln(III) imides (Scheme 1/A).[8–13] Meanwhile, another three strategies have been successfully pursued for the early larger rare-earth metals. While anionic terminal ceric imides could be obtained by the deprotonation of a neutral primary amide complex with alkali-metal silylamides (Scheme 1/B),[14] a [Ln=$CH_2(GaMe_3)_2$] → [Ln=$NR(thf)_2$] transformation proved feasible for generating the open-shell terminal imides $Tp^{tBu,Me}Ln(NAr^{iPr})(thf)_2$ (Ln = Ce, Nd, Sm) (Scheme 1/C).[15] More recently, an anionic cerium(IV) terminal imide was accessed by a two-electron oxidation of a "Ce(II)" complex supported by a tripodal tris(amido)arene ligand using azide $N_3Ar^{CF_3}$ (Ar^{CF_3} = $C_6H_3(CF_3)_2\text{-}3,5$) (Scheme 1/D).[18] Less surprising, terminal imides of the extremely large divalent rare-earth-metal centres have remained elusive.[19]

Common features of all terminal rare-earth-metal imides, reported so far, are that the imido ligand is derived from a substituted aniline, H_2NAr^R (R = iPr, Me, CF_3), and an

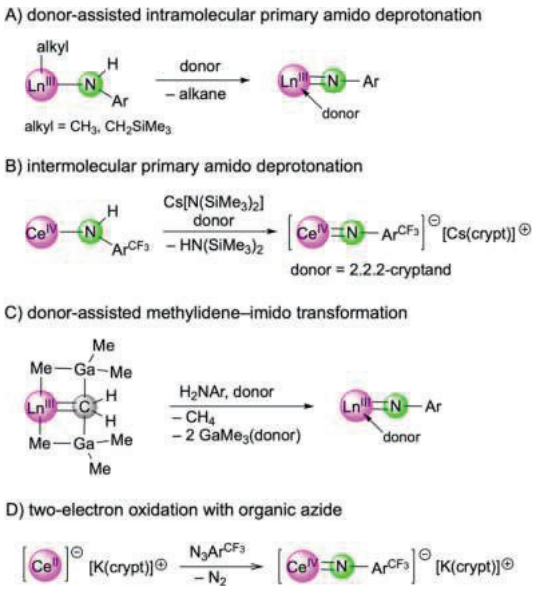

Scheme 1 Synthesis strategies for terminal rare-earth-metal imides.

Institut für Anorganische Chemie, Eberhard Karls Universität Tübingen, Auf der Morgenstelle 18, 72076 Tübingen, Germany. E-mail: reiner.anwander@uni-tuebingen.de

† Electronic supplementary information (ESI) available. CCDC 2312212–2312226. For ESI and crystallographic data in CIF or other electronic format see DOI: https://doi.org/10.1039/d3sc06584g

indispensable kinetic stabilization by use of sterically demanding ancillary co-ligands. Aliphatic amines, benzylic amines, and silylamines engage in imido ligand formation as well but have been detected only as metal-bridging and Lewis acid stabilized versions.[3] Successfully applied ancillaries include β-diketiminato (nacnac),[8,9,11] phosphazene,[10] TriNox,[14] and multidentate pyrazolato ligands.[12,13,15] We found that especially the bulky monoanionic scorpionato ligand hydrotris(3-*tert*-butyl-5-methylpyrazolyl)borato ($Tp^{tBu,Me}$) provides a useful scaffold for stabilizing terminal imides as well as phosphinidenes.[6c,12,15] However, like for all terminal Ln(III) imides, stabilization of the highly polarized Ln=N bond, which predominantly consists of non-directional ionic interactions, is still challenging as it readily reacts with solvent molecules or the ancillary ligand of the aspired complexes.[2,3] DFT calculations performed on the yttrium compound $Tp^{tBu,Me}Y(NC_6H_3Me_2$-2,6)(dmap) confirmed a large ionic character of the Y–N(imido) bond but also a significant covalent bonding pattern with one σ-type and two π-type interactions.[6c]

Given the feasibility of terminal imides of the early open-shell cations Ce(III) (f^1), Nd(III) (f^3), and Sm(III) (f^5),[15] we herein envisaged the synthesis of those of the mid-late open-shell cations Dy(III) (f^9) and Ho(III) (f^{10}). These metal centres exhibit ionic radii similar to Y(III) but would (if at all) contribute to a distinct covalent bonding. On the other hand, their much higher molar mass might promote the crystallization behaviour and hence, the single-crystal X-ray structure diffraction (SCXRD) analysis of the targeted complexes. We also examined the reactivity of the first terminal, trivalent dysprosium and holmium imide complexes.

Results and discussion

Selection of precursors

Our original approach toward the terminal yttrium imide $Tp^{tBu,Me}Y(NC_6H_3Me_2$-2,6)(dmap) involved the mixed methyl/tetramethylgallato complex $Tp^{tBu,Me}YMe(GaMe_4)$ as a suitable precursor.[12] There, the ease of $GaMe_3$ displacement proved to be crucial for the successful synthesis. Consequently, we chose the trimethylgallium-stabilized dialkyl complexes $Tp^{tBu,Me}LnMe(GaMe_4)$ (**1-Ln^{Ga}**; Ln = Y,[12] Dy,[6c] Ho) as precursors for the present study. Like their aluminium congeners,[20] complexes **1-Ln^{Ga}** are available in moderate yield *via* protonolysis of the homoleptic gallates $Ln(GaMe_4)_3$ (ref. 21) with H[$Tp^{tBu,Me}$] (ref. 22) and precipitation from toluene or *n*-hexane solution (Scheme 2; for detailed metrics of $Ln(GaMe_4)_3$ (Dy, Ho) and **1-Ho^{Ga}**; see the ESI, Fig. S1–S3†). The solid-state structure of the bimetallic compounds $Tp^{tBu,Me}LnMe(\mu_2$-$MeEMe_3)$ (**1-Ln^{E}**, E = Al, Ga), depicting one terminal methyl group and an almost linear Ln–Me–E linkage, is not reflected in the solution NMR spectra, which reveal highly fluxional methyl groups at ambient temperature, an even higher mobility in case of the gallium derivatives. The isostructural **1-Ln^{Ga}** show Ln–C(Me) (Dy: 2.389(3) Å,[6c] Y: 2.385(3) Å,[12] Ho: 2.356(5) Å) and Ln–C(Me_{Ga}) distances (Dy: 2.736(2) Å,[6c] Y: 2.688(2) Å,[12] Ho: 2.652(4) Å) in accordance with the distinct Ln(III) radii.[23] Unexpectedly, the solid-state structures of the formally five-coordinate **1-Ln^{Ga}** of

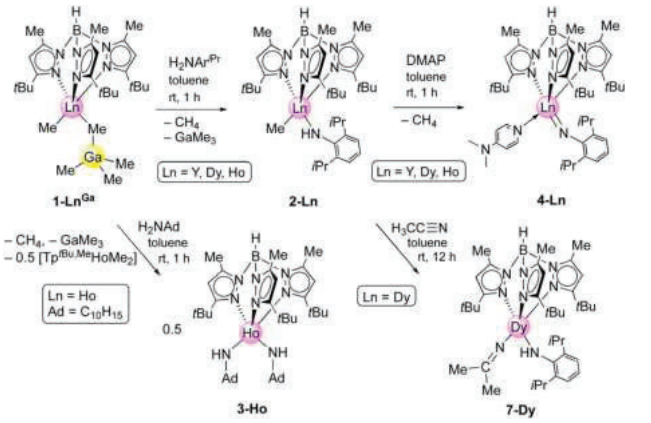

Scheme 2 Formation of $Tp^{tBu,Me}Ln(NAr^{iPr})$(dmap) (**4-Ln**: Ln = Y, Dy, Ho) *via* reaction of $Tp^{tBu,Me}LnMe(GaMe_4)$] (**1-Ln^{Ga}**) with primary aniline H_2NAr^{iPr} to afford mixed methyl/amido complexes $Tp^{tBu,Me}LnMe(HNAr^{iPr})$ (**2-Ln**), and subsequent addition of DMAP. Use of 1-adamantylamine led to bis(amido) complex [$Tp^{tBu,Me}Ho(HNAd)_2$] (**3-Ho**). Nucleophilic attack of acetonitrile by Dy–CH_3 affords **7-Dy**.

the similar sized yttrium and holmium differ in the hapticity of the $Tp^{tBu,Me}$ ligand and in the Ln1–C26–Ga1 angle, which is more linear for the holmium derivative (174.9(2) *vs.* 163.3(1)°). Packing effects of co-crystallizing toluene in **1-Ho^{Ga}** have presumably a major impact on the coordination of the $GaMe_4$ moiety and might also cause the bending of one pyrazolyl moiety toward the rare-earth metal centre. The pyrazolyl nitrogen atoms exhibit Ho–N interatomic distances ranging from 2.334(3) to 2.376(3) Å with an additional close contact to the tilted pyrazolato ligand (Ho···N5, 2.859(3) Å, see Fig. S3†). The proposed mechanism for the formation of **1-Ln^{Ga}** includes the preformation of [$Tp^{tBu,Me}Ln(GaMe_4)_2$] under release of methane and trimethylgallium, and the elimination of a second molecule $GaMe_3$ sterically induced by the bulky $Tp^{tBu,Me}$ ligand.

The primary aniline H_2NAr^{iPr} ($Ar^{iPr} = C_6H_3iPr_2$-2,6) has proven a privileged imido ligand precursor in rare-earth-metal chemistry.[1–3] The molecule not only features the right balance of adequately acidic protons, but also a sufficient steric protection with bulky substituents in the positions 2 and 6 at the aryl group. The reaction of bis(alkyl) **1-Ln^{Ga}** with H_2NAr^{iPr} to form the mixed methyl/primary amido complexes $Tp^{tBu,Me}LnMe(HNAr^{iPr})$ **2-Ln** (Ln = Y, Dy, Ho) is clearly visible by the elimination of methane and displacement of trimethylgallium (Scheme 2).

Complexes **2-Dy** and **2-Ho** are isostructural but crystallize in different space groups (**2-Dy**: $P2_1/c$; **2-Ho**: $P\bar{1}$; for the crystal structures and detailed metrics, see the ESI, Fig. S4/S5†). Both compounds are insoluble in *n*-hexane, but dissolve in aromatic solvents such as toluene. The ancillary ligand coordinates in a κ^3 fashion (*N*, *N*′, *N*″) with considerably varying Ln–N_{pz} distances (**2-Dy**: 2.3752(17)–2.5163(18) Å; **2-Ho**: 2.369(2)–2.536(2) Å). The Ln–N_{amido} (**2-Dy**: 2.212(2) Å; **2-Ho**: 2.222(2) Å) and the Ln–CH_3 (**2-Dy**: 2.436(2) Å; **2-Ho**: 2.427(3) Å) interatomic distances lie in the range of the similar mixed methyl/amido complexes $Tp^{tBu,Me}LuMe(HNAr^{R})$ ($Ar^{R} = Ar^{Me_2} = C_6H_3Me_2$-2,6: Lu–$N_{amido}$ 2.189(2) Å, Lu–CH_3 2.369(2) Å; $Ar^{R} = Ar^{CF_3} = C_6H_3(CF_3)_2$-3,5: Lu–$N_{amido}$ 2.215(1) Å, Lu–CH_3 2.360(1) Å).[12] The

Ln–N_{amido}–C_{ipso} angle spans a wide range from 142.5(1)° (Ln = Lu, Ar^R = Ar^{CF3}),[12] 153.8(1)° (Ln = Lu, Ar^R = Ar^{Me2})[12] over 155.84(16)° (Ln = Dy, Ar^R = Ar^{iPr}) to 160.28(19)° (Ln = Ho, Ar^R = Ar^{iPr}), dependent on the Ln(III) centre and the substitution pattern of the amido ligand. As the paramagnetic nature of dysprosium and holmium impedes conclusive interpretations of their NMR spectra, the yttrium congener **2-Y** was accessed from **1-Y^{Ga}** and H_2NAr^{iPr}. The ^{1}H NMR spectrum of **2-Y** shows a sharp singlet at 0.46 ppm for the methyl group and a broader singlet at 4.87 ppm for the proton of the amido ligand.

Noteworthy, the reaction of **1-Ho^{Ga}** with 1-adamantylamine in a 0.9 : 1 ratio gave the bis(amido) holmium complex $Tp^{tBu,Me}Ho(HNAd)_2$ (**3-Ho**, Ad = adamantyl), even though the primary amine was added in deficit. Apparently, the single deprotonation is favored over the second deprotonation, as the less Brønsted acidic second proton is less prone to be abstracted than the first proton of a second primary aniline. According to the present synthesis protocol, so far only sufficiently acidic aniline derivatives lead to the successful isolation of terminal rare-earth-metal imides, as other, less bulky and less electronically advantageous amines only form bis(amido) complexes,[3,6c] or in case **1-Ln^{Al}** are employed result in trimethylaluminium-stabilized imide species.[20a] Like its precursors, complex **3-Ho** is insoluble in aliphatic solvents, but readily dissolves in toluene and THF. The crystal structure of **3-Ho** (triclinic $P\bar{1}$ space group) shows the expected κ^3 fashion (*N*, *N*′, *N*″) of the ancillary ligand with Ho–N_{pz} distances in the range of 2.393(3)–2.610(3) Å (Fig. 1).

The Ln–N_{amido} distances (ø 2.171 Å) are longer compared to the Ln–N_{imido} interactions in $Tp^{tBu,Me}Ho(\mu_2\text{-}NAd)AlMe_3$ (2.087(2) Å),[20a] but slightly shorter compared to the mixed methyl/amido complexes **2-Ln** (Ln = Dy, Ho) described beforehand. This reflects a better electron donation of two nitrogen atoms to the metal centre, despite increased steric bulk. However, the angles Ho1–N7–C35 (144.0(3)°) and Ho1–N8–C25 (148.5(3)°) are significantly more bent compared to the methyl/anilido complex **2-Ho** (160.28(19)°).

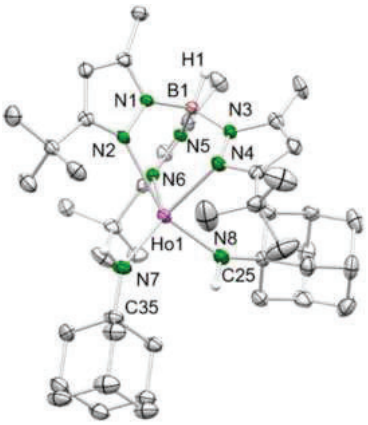

Fig. 1 Crystal structure of **3-Ho**. All atoms are represented by atomic displacement ellipsoids set at 50% probability. Solvent molecules and hydrogen atoms except for those of B–H and N–H are omitted for clarity. Selected interatomic distances (Å) and angles (°): Ho1–N7 2.172(3), Ho1–N8 2.170(3); Ho1–N7–C35 144.0(3), Ho1–N8–C25 148.5(3) (for further metrics, see ESI†).

Ln(III) imide synthesis

Treatment of the mixed methyl/anilido complexes **2-Ln** with the Lewis base DMAP led to the isolation of the targeted terminal lanthanide imide complexes $Tp^{tBu,Me}Ln(NAr^{iPr})(dmap)$ (**4-Ln**: Ln = Y, Dy, Ho). DMAP was used previously for the synthesis of terminal rare-earth-metal imide complexes,[8,10–12] exploiting its strong donor capacity (*versus e.g.*, THF) to induce the elimination of methane *via* inner-sphere deprotonation of the amido species. We assume, that the preceding coordination of DMAP to the metal centre affects the geometry of its coordination sphere in a way that the methyl group and the amido proton come into close proximity and finally evolve methane, being a very potent leaving group. The ^{1}H NMR spectrum of **4-Y** evidences the deprotonation of the amido functionality *via* the methyl ligand since both the N–H and methyl signal disappeared (see Fig. S21†). Complexes **4-Ln** are insoluble in non-polar solvents (*e.g. n*-hexane), but easily dissolve in aromatic or polar solvents like toluene and THF.

While the yttrium complex **4-Y** could not be obtained in very pure form and gave only poor crystal quality (connectivity structure only, see ESI Fig. S7†), the dysprosium and holmium congeners displayed good crystallization and diffraction behaviours (isotypic, monoclinic space group *C*2/*c*, Fig. 2 and S8/9†). The metal centres are pentacoordinate with the ancillary $Tp^{tBu,Me}$ ligand coordinating in the familiar κ^3 fashion (*N*, *N*′, *N*″). The Ln–N_{pz} distances typical of scorpinate ligands show two shorter bonds (**4-Dy**: 2.450(3)/2.452(3) Å, **4-Ho**: 2.426(4)/2.436(3) Å) and one longer (**4-Dy**: 2.517(3) Å, **4-Ho**: 2.492(4) Å). The Ln–N_{imido} distances are in line with those of other terminal imides, considering the changes in the ionic radii (Table 1). Except for the anionic ceric complex [(TriNOx)Ce(NAr^{CF_3})[Cs(2.2.2-cryptand)] (157.3(4)°),[14a] the Ln–N_{imido}–C_{ipso} angles of all trivalent terminal imides are larger than 165° and almost linear (**4-Dy**: 166.0(2)°; **4-Ho**: 166.7(3)°; Table 1). Exchange of the donor ligand dmap for thf seems to entail a shortening of the Ln–N_{imido} bond but doesn't appear to affect the Ln–N_{imido}–C_{ipso} angle.

In contrast, and as pointed out previously, the reaction of the primary aniline $H_2NAr^{Me_2}$ (Ar^{Me_2} = $C_6H_3Me_2$-2,6) with the aluminium congeners $Tp^{tBu,Me}LnMe(AlMe_4)$ (**1-Ln^{Al}**) implies the formation of trimethylaluminium-stabilized imide complexes.[12] These complexes cannot be converted into unsupported terminal rare-earth-metal imide complexes by applying Lewis bases such as 1,4-dioxane, pyridine, DMAP, or TMEDA (*N*,*N*,*N*′,*N*′-tetramethylethylenediamine). Complex **1-Dy^{Al}** is accessible from $Dy(AlMe_4)_3$ (ref. 24) and $H[Tp^{tBu,Me}]$,[22] in analogy to the yttrium and holmium complexes reported previously.[20] In order to probe the effect of the substituents on the aniline, compounds **1-Ln^{Al}** (Ln = Dy, Ho) were reacted with H_2NAr^{iPr}, H_2NAr^{Me2}, and H_2NAr^{Me3} (Ar^{Me3} = $C_6H_2Me_3$-2,4,6) (Scheme 3).

Contrary to the reaction with the weaker coordinated trimethylgallium in complexes **1-Ln^{Ga}**, the **1-Ln^{Al}**/H_2NAr^{iPr}

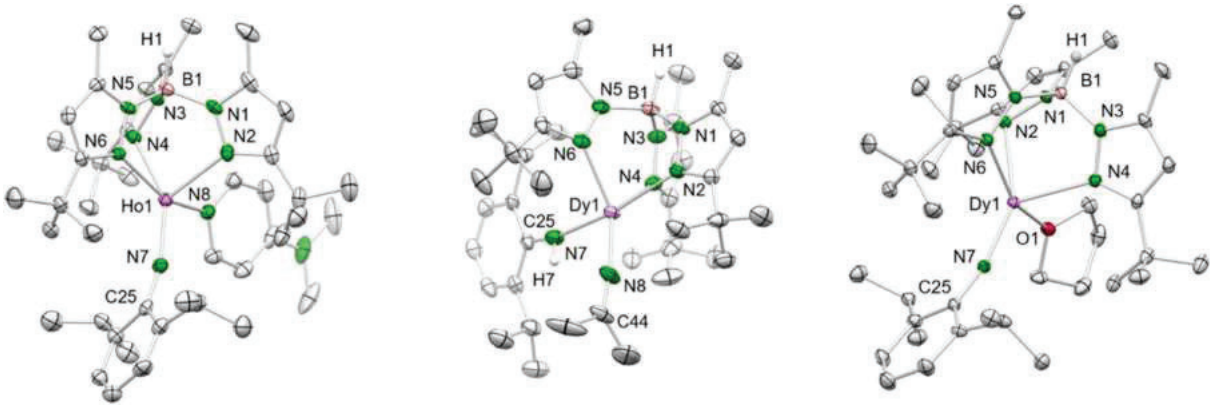

Fig. 2 Left: Crystal structure of **4-Ho**. All atoms are represented by atomic displacement ellipsoids set at 50% probability. Solvent molecules, and hydrogen atoms except for that of B–H are omitted for clarity. For selected interatomic distances and angles, see Table 1 and ESI.† Middle: Crystal structure of **7-Dy**. All atoms are represented by atomic displacement ellipsoids set at 50% probability. Solvent molecules and hydrogen atoms except for those of B–H and N–H are omitted for clarity. Selected interatomic distances (Å) and angles (°): Dy1–N7 2.219(3), Dy1–N8 2.148(3); Dy1–N7–C25 156.3(3), Dy1–N8–C44 165.3(3) (for further metrics, see ESI†). Right: Crystal structure of **8-Dy**. All atoms are represented by atomic displacement ellipsoids set at 50% probability. Only one molecule of the asymmetric unit is shown. Solvent molecules, and hydrogen atoms except for that of B–H are omitted for clarity. For selected interatomic distances and angles, see Table 1 and ESI.†

reaction was inconclusive. Like in the case of yttrium,[12] the sterically less demanding anilines gave the trimethylaluminium-stabilized imides $Tp^{tBu,Me}Ln(\mu_2\text{-}NAr^{Me2})AlMe_3$ (**5-Ln**: Ln = Dy, Ho) and $Tp^{tBu,Me}Ho(\mu_2\text{-}NAr^{Me3})AlMe_3$ (**6-Ln**). The coordinated trimethylaluminium is not removable, neither under vacuum, nor with Lewis bases (*e.g.*, DMAP, THF). Presumably, after the first methane elimination and the coordination of the primary amido functionality to the metal centre, one of the methyl groups at the [μ_2-$MeAlMe_3$] unit abstracts the second amido proton *via* release of another molecule of methane, resulting in **5-Ln**. Compounds **5-Ln** are insoluble in aliphatic solvents, but dissolve in aromatic and polar solvents. The isostructural complexes crystallize in different space groups (**5-Dy**: monoclinic, $P2_1/n$; **5-Ho**: triclinic, $P\bar{1}$; **6-Ho**: monoclinic, *Cc*; Fig. 3, S10 and S11†).

The bulky $Tp^{tBu,Me}$ ligand coordinates again in the κ^3 fashion (*N*, *N*′, *N*″) with interatomic Ln–N distances in the range of 2.423(2)–2.492(2) Å (**5-Dy**), 2.407(4)–2.437(4) Å (**5-Ho**) and 2.394(3)–2.454(3) Å (**6-Ho**). The central metal ion is pentacoordinate and the Ln–N_{imido}–C_{ipso} angle is strongly bent (**5-Dy**: 146.68(17)°; **5-Ho**: 146.7(4)°; **6-Ho**: 151.0(2)°), which is due to the interaction with the Lewis acid trimethylaluminium. Hence, the electronic situation differs considerably compared to the terminal rare-earth-metal imide complexes **4-Ln** (Ln = Dy, Ho) as electron density of the imido nitrogen is shifted to the empty p orbitals of the aluminium ion. This is also reflected in the Ln–N_{imido} bonds of **5-Ln** and **6-Ho** which are elongated by *ca.* 0.1 Å (**5-Dy**: 2.129(2) Å; **5-Ho**: 2.116(4) Å; **6-Ho**: 2.116(4) Å), matching those in $Tp^{tBu,Me}Y(\mu_2\text{-}NAr^{Me})AlHMe_2$ (Y–N_{imido}: 2.133(2) Å; Y–N_{imido}–C_{ipso}: 145.1(2)°).[25] Further structural comparison with

Table 1 Selected metrical parameters of terminal rare-earth-metal imides

Compound	Ln=N_{imido}/Å	Ln–do/Å	Ln–N_{imido}–C_{ipso}/deg	IR[d]/Å (ref. 23)	CN	Ref.
$Tp^{tBu,Me}Lu(NAr^{CF_3})(dmap)$	1.993(5)	2.377(5)	175.8(5)	0.861	5	12
$Tp^{tBu,Me}Y(NAr^{Me_2})(dmap)$	2.024(4)	2.426(4)	173.6(4)	0.900	5	12
$Tp^{tBu,Me}Ho(NAr^{iPr})(dmap)$ (**4-Ho**)	2.012(4)	2.429(4)	166.7(3)	0.901	5	This work
$Tp^{tBu,Me}Dy(NAr^{iPr})(dmap)$ (**4-Dy**)	2.017(3)	2.450(3)	166.0(2)	0.912	5	This work
$Tp^{tBu,Me}Dy(NAr^{iPr})(thf)$ (**8-Dy**)[a]	2.008(3)/2.004(4)	2.397(3)/2.392(3)	166.9(3)/165.3(3)	0.912	5	This work
$Tp^{tBu,Me}Sm(NAr^{iPr})(thf)_2$	2.067(5)	2.527(5)/2.560(4)	169.3(5)	0.958	6	15
$Tp^{tBu,Me}Nd(NAr^{iPr})(thf)_2$	2.076(4)	2.557(4)/2.594(3)	169.2(4)	0.983	6	15
$Tp^{tBu,Me}Nd(NAr^{iPr})(thf)$[a]	2.036(7)/2.047(7)	2.517(6)/2.511(6)	165.8(4)/163.2(6)	0.983	5	15
$Tp^{tBu,Me}Ce(NAr^{iPr})(thf)_2$	2.101(5)	2.599(3)/2.628(3)	171.3(3)	1.01	6	15
$(nacnac^{R1})Sc(NAr^{iPr})(dmap)$[b]	1.881(8)	2.271(5)	169.6(5)	0.745	5	8
$(nacnac^{R1})Sc(NAr^{iPr})(thf)$[b]	1.852(4)	2.251(3)	168.6(3)	0.745	5	11
$(nacnac^{R2})Sc(NAr^{iPr})(dmap)$[c]	1.8591(18)	2.369(2)	167.90(17)	0.745	5	9
$[(PhN=Ph_2P)_2N]Sc(NAr^{iPr})(dmap)_2$	1.853(3)	2.379(3)/2.326(3)	168.8(3)	0.745	6	10
$(BPz_2Py_3)Sc(NAr^{iPr})$	1.877(3)	—	173.1(3)	0.745	6	13
[(TriNOx)Ce(NAr^{CF_3})][Cs(2.2.2-cryptand)]	2.077(3)	—	157.3(4)	0.87	8	14*a*
[(^{Ad}TPBN$_3$)Ce(NAr^{CF_3})][K(2.2.2-cryptand)]	2.0742(4)	—	176.3(4)	<0.87	4	18

[a] Two molecules in the asymmetric unit. [b] $nacnac^{R1}$ = $[Ar^{iPr}NC(Me)CHC(Me)N(CH_2)_2NMe_2]$. [c] $nacnac^{R2}$ = $[Ar^{iPr}NC(Me)CHC(Me)N(CH_2)_2N(CH_2)_2NMe_2]$. [d] Effective ionic radii.

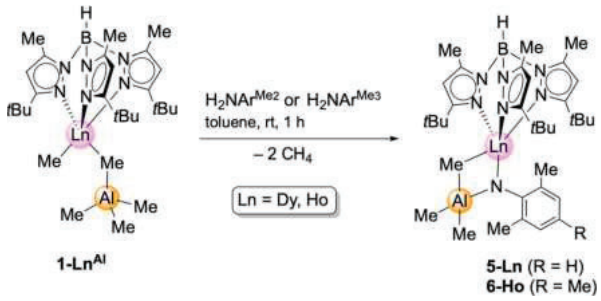

Scheme 3 Synthesis of Lewis acid stabilized, bimetallic imides $Tp^{tBu,Me}Ln(NAr^{Me2})(\mu_2\text{-}MeAlMe_3)$ (**5-Ln**; Ln = Dy, Ho) and $Tp^{tBu,Me}Ho(NAr^{Me3})(\mu_2\text{-}MeAlMe_3)$.

the similar holmium imides $Tp^{tBu,Me}Ho(\mu_2\text{-}NR)AlMe_3$ (R = *t*Bu, adamantyl) clearly indicate a more pronounced $Ln\text{–}N_{imido}$ interaction for the latter ($Ho\text{–}N_{imido}$: 2.083(2), 2.087(2) Å; $Ho\text{–}N_{imido}\text{–}C_{ipso}$: 140.4(2), 140.2(1)°).[20a] Other Lewis acid supported monomeric rare-earth-metal imide complexes include Mindiola's (PNP)Sc(μ_2-NAr^{iPr})(μ_2-Me)$AlMe_2$ [PNP═N(2-P-$(CHMe_2)_2$-4-methylphenyl)$_2$] (ref. 26) or $Tp^{tBu,Me}Ln(NAr^{iPr})(MMe_3)$ (Ln = Ce, Nd, Sm; M = Al, Ga) from our group.[6c]

Probing donors other than DMAP

N,*N*-Dimethyl-4-aminopyridine (DMAP) emerged as a most valuable donor for forcing the elimination of methane *via* inner-sphere deprotonation of the primary amido species in **2-Ln**-type complexes. In order to assess the impact of the donor molecule on the $Ln\text{–}N_{imido}$ bonding, the implementation of other donor ligands was examined. In general, donor ligands might be introduced according to Scheme 1 promoting methane elimination (route A) or *via* post-imide-synthesis exchange (Scheme 4). Since imido ligand formation according to route A could not be achieved with ethereal donors such as OEt_2 or THF, complex **2-Dy** was treated with N-donors TMEDA (tetramethylethylenediamine), TMPDA (tetramethylpropane-1,3-diamine) and acetonitrile. While the potentially bidentate diamines did not undergo any reaction yielding only in the isolation of the starting compounds, acetonitrile formed the insertion complex $Tp^{tBu,Me}Dy[NC(Me)_2](HNAr^{iPr})$ (**7-Dy**, Scheme 2). It was previously shown that acetonitrile does react with rare-earth-metal alkyls either *via* C–H-bond activation/deprotonation or insertion.[27–29] While the product of the deprotonation reaction $(C_5Me_5)_2La[CH(SiMe_3)_2]/CH_3CN$ was structurally characterized as $[(C_5Me_5)_2La(\mu\text{-}CH_2CN)]_2$,[27] the insertion product of the reaction $(C_5Me_5)_2ScCH_3/CH_3CN$ was only spectroscopically analyzed as $(C_5Me_5)_2Sc[NC(Me)_2]$.[28] The SCXRD study of five-coordinate **7-Dy** features distinct bonding behaviour of the primary amido and the dimethyliminato ligand (Dy–N: 2.219(3) *versus* 2.148(3) Å; Dy–N–C: 156.3(3) *versus* 165.3(3)°) (Fig. 2). Thus, the dimethyliminato coordination compares to that of imidazolin-2-iminato complexes like $LY(CH_2SiMe_3)_2(thf)_2$ (L = 1,3-bis(2,6-diisopropylphenyl)imidazoline-2-iminato; Y–N, 2.1255(13) Å, Y–N–C, 176.85(12)° or $LYCl_2(thf)_3$ Y–N, 2.1278(18) Å, Y–N–C, 174.35(16)°) supposedly featuring very short $Ln\text{–}N_{iminato}$ bonds.[30,31]

The post-synthesis exchange approach (route 2, Scheme 4) was probed with **4-Dy** and the strong Lewis acid 9-borabicyclo[3.3.1]nonane (9-BBN) in THF.[11] Accordingly, the equimolar reaction led to the displacement of DMAP and coordination of one THF molecule to the dysprosium centre in $Tp^{tBu,Me}Dy(NAr^{iPr})(thf)$ (**8-Dy**, Scheme 4). Like the dmap adduct, **8-Dy** is soluble in toluene and THF, but insoluble in aliphatic solvents.

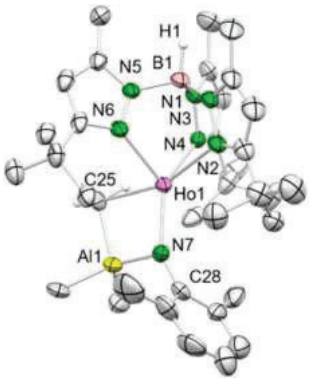

Fig. 3 Crystal structure of **5-Ho**. All atoms are represented by atomic displacement ellipsoids set at 50% probability. Solvent molecules, and hydrogen atoms except for that of B–H are omitted for clarity. Selected interatomic distances (Å) and angles (°): Ho1–N7 2.116(4), Ho1–C25 2.549(5), Al1–C25 2.105(6); Ho1–N7–C28 146.7(4) (for isostructural **5-Dy** and **6-Ho** and further metrics, see ESI†).

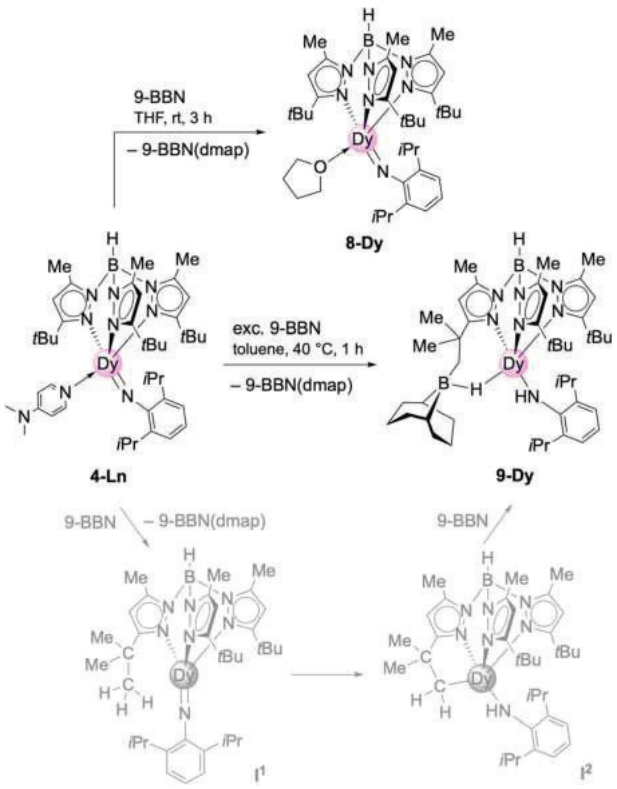

Scheme 4 Reactivity of $Tp^{tBu,Me}Dy(NAr^{iPr})(dmap)$ (**4-Dy**) (Ln = Y, Dy) towards Lewis acid 9-BBN in THF and toluene.

It crystallized in the orthorhombic space group $Pna2_1$ and shows the same κ^3 coordination of the $Tp^{tBu,Me}$ ligand as complex **4-Dy** before (Dy–N_{pz}: 2.465(4)–2.510(4)/2.450(3)–2.539(4) Å) (Fig. 2). As the coordination number did not change, the angle of the imido functionality stayed nearly the same (Dy–N_{imido}–C_{ipso}: 165.2(3)/166.9(3)°) as detected for **4-Dy**. However, the Dy–N_{imido} distance of 2.004(4)/2.008(3) Å) in **8-Dy** appears to be slightly shorter compared to **4-Dy** (Table 1) which can be attributed to the weaker donor properties of the thf ligand.

The 9-BBN-promoted donor exchange was previously introduced by Chen, revealing that prior activation of $L^1Sc(NAr^{iPr})(dmap)$ ($L^1 = [Ar^{iPr}NC(Me)CHC(Me)N(CH_2)_2NMe_2]$) with 9-BBN led to abstraction of the donor molecule DMAP.[11] The emerging donor-free imide intermediate $[L^1Sc(NAr^{iPr})]$ could be trapped with THF to afford $L^1Sc(NAr^{iPr})(thf)$ featuring also a shorter Sc–N_{imido} bond than the DMAP adduct (Table 1: 1.852(4) *versus* 1.881(8) Å). It was also mentioned that the direct synthesis of the THF adduct $L^1Sc(NAr^{iPr})(thf)$ is not possible by thermolysis of the mixed methyl/amido scandium complex in THF, which is the same case for **8-Dy** as well.[2] In contrast, terminal imides $Tp^{tBu,Me}Ln(NAr^{iPr})(thf)_2$ of the larger rare-earth metals can be obtained directly according to the donor(THF)-assisted methylidene → imido transformation (Scheme 1 and Table 1).[6c]

Treatment of **4-Dy** with excess of 9-BBN in toluene gave the mixed primary amido/hydroborato complex **9-Dy** (Scheme 4 and Fig. 4). Again, this is in line with the observation made by Chen with the system $L^2Sc(NAr^{iPr})$/9-BBN ($L^2 = [Ar^{iPr}NC(Me)CHC(Me)N(CH_2)_2N(CH_2)_2NMe_2]$).[32] Correspondingly, it can be hypothesized that initially the strong Lewis acid 9-BBN displaces all of the coordinated DMAP, rendering a highly reactive donor-free terminal imide $[Tp^{tBu,Me}Dy(NAr^{iPr})]$ (Scheme 4, intermediate I^1, lower trace). Subsequent 1,2-addition of a *t*Bu methyl group (C–H-bond activation) across the highly reactive Dy–N_{imido} bond of transient species I^1 reforms the primary amido ligand along with a 5-membered metallacycle in I^2. Then, the highly nucleophilic alkyl attached to the dysprosium attacks a second molecule of 9-BBN to afford the alkylhydroborato moiety. The resulting Dy–N_{amido}–C_{ipso} angle (143.4(2)°) and the Dy–N_{amido} distance (2.237(3) Å) of **9-Dy** are comparable to the dysprosium amide complexes discussed beforehand. The Dy–B distance of 2.703(4) Å is in the range of the Y–B distances in $[(Me_3Si)_2NC(NiPr)_2]Y[\mu\text{-}H(\mu\text{-}Et)_2BEt]_2(thf)_2$ (2.658(4) and 2.671(4) Å)[33] and $(C_5Me_5)_2YH(9\text{-BBN})$ (2.767(6) Å),[34] but longer than those observed in $(tBu_4Carb)Dy(BH_4)_2(thf)$ (2.473(2) and 2.487(2) Å).[35]

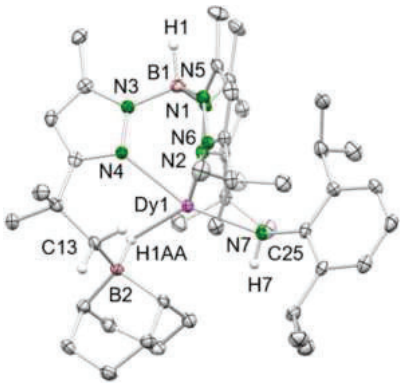

Fig. 4 Crystal structure of **9-Dy**. All atoms are represented by atomic displacement ellipsoids set at 50% probability. Solvent molecules and hydrogen atoms except for those of B–H and N–H are omitted for clarity. Selected bond distances (Å) and angels (°) for **9-Dy**: Dy1–N7 2.237(3), Dy 1–N2 2.452(3), Dy 1–N4 2.405(3), Dy 1–N6 2.461(3), Dy 1–B2 2.703(4); Dy1–H1AA 2.17(3), B2–H1AA 1.23(3); Dy1–N7–C35 143.4(2), N7–Dy1–B2 117.06(11), N7–Dy1–N4 161.07(10), N7–Dy1–N2 93.18(10), N7–Dy1–N6 92.04(10).

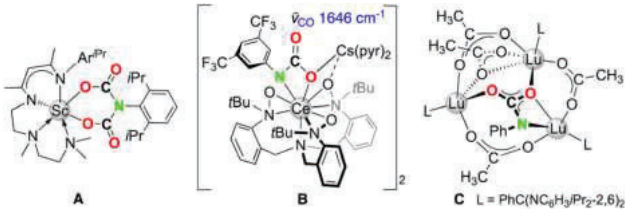

Fig. 5 Structurally authenticated CO_2-insertion products A,[17a] B,[38] and C (ref. 17*d*) emerged from rare-earth-metal imides.

In Chen's system $[L^2Sc(NAr^{iPr})]$/9-BBN the respective C(sp^3)–H bond borylation took place at the $[-CH_2NMe_2]$ side arm of the ancillary nacnac ligand (Sc–$H_{hydrido}$, 2.01(3) Å).[32] Chen also reported on the reaction of $L^1Sc(NAr^{iPr})(dmap)$ with three equivalents of 9-BBN which led to mixed boroamido/hydroborato complex $L^1Sc[NAr^{iPr}(9\text{-BBN–H})](9\text{-BBN} + H)$ (Sc–$H_{hydrido}$, 1.89 Å and 1.20 Å).[11]

Preliminary studies on the reactivity of terminal imide complex **4-Dy** towards carbon dioxide (1 bar) in toluene at ambient temperature clearly indicate CO_2 insertion into the Dy–N_{imido} bond and, hence, carbamate formation in product **10-Dy**. The DRIFT spectrum of **10-Dy** revealed typical carbonyl vibrations at 1701 cm^{-1} and 1641 cm^{-1} assigned to asymmetric and symmetric C=O stretching vibrations (Fig. S17†). Moreover, the B–H vibration of **4-Dy** at 2557 cm^{-1}, typical for the terminal B–H stretch of the $Tp^{tBu,Me}$ ligand when coordinated in a tridentate fashion,[36] changed to 2431 cm^{-1} in **10-Dy**. Such a dramatic change of the position of the B–H band can be ascribed to a $\kappa^3 \rightarrow \kappa^2$ coordination switch of the $Tp^{tBu,Me}$ ligand, likely involving a Dy···H–B interaction.[37] Unfortunately, crystals of **10-Dy** suitable for SCXRD analysis could not be obtained, but **10-Dy** can be tentatively assigned as the dicarboxylate species $[Tp^{tBu,Me}Dy\{(O_2C)_2NAr^{iPr}\}]$ on the basis of the double CO_2-insertion chemistry of the terminal scandium imides $L^2Sc(NAr^{iPr})$ (**A**, Fig. 5)[17a] and $(BPz_2Py_3)Sc(NAr^{iPr})$ ($\tilde{\nu}$ = 1685 and 1632 cm^{-1}).[13] For further comparison, mono insertion of carbon dioxide was observed for the $Lu_3(\mu_3\text{-NPh})$ moiety of the trinuclear cluster $[L^3Lu_3(\mu_2\text{-Me})_3(\mu_3\text{-Me})(\mu_3\text{-NPh})]$ ($L^3 = PhC(NC_6H_3iPr_2\text{-}2,6$; **C**, Fig. 5)[17d] and the alkali-metal stabilized Ce(IV)–N_{imido} bond of $[(TriNOx)Ce(NAr^{CF_3})][Cs(2.2.2\text{-cryptand})]$ (**B**, Fig. 5).[38]

Conclusion

The successful application of the donor-assisted intramolecular primary amido deprotonation protocol towards terminal imides of the rare-earth metals yttrium, dysprosium, and holmium

depends on two crucial factors: first, the kinetic stabilization of the targeted imide *via* appropriate steric shielding of the ancillary ligand, herein supplied by the bulky Tp^{tBuMe} scorpionate ligand; second, sufficient Brønsted acidity and steric demand of the employed primary amine, herein provided by H_2NAr^{iPr} (Ar^{iPr} = $C_6H_3iPr_2$-2,6). With these key factors in mind, it was possible to generate a series of terminal rare-earth-metal imides $Tp^{tBu,Me}Ln(NAr^{iPr})$(dmap) for mid-sized to small rare-earth metals. Their reactivity parallels that of terminal scandium imides, as revealed by treatment with the strong Lewis acid 9-borabicyclo[3.3.1]nonane (9-BBN) and the heteroallene CO_2. These reactions revealed effective DMAP/THF donor exchange and CO_2 insertion into the Ln–N_{imido} bond (carbamate formation). The reactivity studies also include the isolation and structural characterization of the bis(amido) species $Tp^{tBu,Me}Ho(NAd)_2$ (Ad = adamantyl) and dimethyliminate complex $Tp^{tBu,Me}Dy[NC(Me)_2](HNAr^{iPr})$.

Data availability

Experimental, spectroscopic and structural data supporting this article have been uploaded as part of the ESI. Crystallographic data for all compounds have been deposited at the CCDC under 2312212–2312226, and can be obtained from **https://www.ccdc.cam.ac.uk/structures/**.

Author contributions

TR, synthesis and characterization of compounds, writing original draft; DS, synthesis and characterization of compound **1-Ho^{Ga}**, editing original draft; CM-M, crystallography, editing original draft; RA, conceptualization, supervision, writing and project administration, funding acquisition.

Conflicts of interest

There are no conflicts to declare.

Acknowledgements

We are grateful to Felix Kracht for assistance with recording NMR and IR spectra.

Notes and references

1 O. T. Summerscales and J. C. Gordon, Complexes containing multiple bonding interactions between lanthanoid elements and main-group fragments, *RSC Adv.*, 2013, **3**, 66–6692.
2 E. Lu, J. Chu and Y. Chen, Scandium Terminal Imido Chemistry, *Acc. Chem. Res.*, 2018, **51**, 557–566.
3 D. Schädle and R. Anwander, Rare-earth metal and actinide organoimide chemistry, *Chem. Soc. Rev.*, 2019, **48**, 5752–5805.
4 R. Anwander, "Self-Assembly" in Organolanthanide Chemistry: Formation of Rings and Clusters, *Angew. Chem., Int. Ed.*, 1998, **37**, 599–602.
5 (*a*) J. Scott, H. Fan, B. F. Wicker, A. R. Fout, M.-H. Baik and D. J. Mindiola, Lewis Acid Stabilized Methylidene and Oxoscandium Complexes, *J. Am. Chem. Soc.*, 2008, **130**, 14438–14439; (*b*) Y.-M. So, G.-C. Wang, Y. Li, H. H.-Y. Sung, I. D. Williams, Z. Lin and W.-H. Leung, A Tetravalent Cerium Complex Containing a Ce=O Bond, *Angew. Chem., Int. Ed.*, 2014, **53**, 1626–1629; (*c*) P. L. Damon, G. Wu, N. Kaltsoyannis and T. W. Hayton, Formation of a Ce(IV) Oxo Complex via Inner Sphere Nitrate Reduction, *J. Am. Chem. Soc.*, 2016, **138**, 12743–12746; (*d*) M. K. Assefa, G. Wu and T. W. Hayton, Synthesis of a terminal Ce(IV) oxo complex by photolysis of a Ce(III) nitrate complex, *Chem. Sci.*, 2017, **8**, 7873–7878.
6 (*a*) B. F. Wicker, J. Scott, J. G. Andino, X. Gao, H. Park, M. Pink and D. J. Mindiola, Phosphinidene Complexes of Scandium: Powerful PAr Group-Transfer Vehicles to Organic and Inorganic Substrates, *J. Am. Chem. Soc.*, 2010, **132**, 3691–3693; (*b*) B. Feng, L. Xiang, A. Carpentier, L. Maron, X. Leng and Y. Chen, Scandium-Terminal Boronylphosphinidene Complex, *J. Am. Chem. Soc.*, 2021, **143**, 2705–2709; (*c*) T. E. Rieser, P. Wetzel, P. Sirsch, C. Maichle-Mössmer and R. Anwander, A Terminal Yttrium Phosphinidene, *J. Am. Chem. Soc.*, 2023, **145**, 4102–4113.
7 J. Kratsch and P. W. Roesky, Rare-Earth-Metal Methylidene Complexes, *Angew. Chem., Int. Ed.*, 2014, **53**, 376–383.
8 E. Lu, Y. Li and Y. Chen, A scandium terminal imido complex: synthesis, structure and DFT studies, *Chem. Commun.*, 2010, **46**, 4469–4471.
9 E. Lu, J. Chu, Y. Chen, M. V. Borzov and G. Li, Scandium terminal imido complex induced C–H bond selenation and formation of an Sc–Se bond, *Chem. Commun.*, 2011, **47**, 743–745.
10 W. Rong, J. Cheng, Z. Mou, H. Xie and D. Cui, Facile Preparation of a Scandium Terminal Imido Complex Supported by a Phosphazene Ligand, *Organometallics*, 2013, **32**, 5523–5529.
11 J. Chu, X. Han, C. E. Kefalidis, J. Zhou, L. Maron, X. Leng and Y. Chen, Lewis Acid Triggered Reactivity of a Lewis Base Stabilized Scandium-Terminal Imido Complex: C–H Bond Activation, Cycloaddition, and Dehydrofluorination, *J. Am. Chem. Soc.*, 2014, **136**, 10894–10897.
12 D. Schädle, M. Meermann-Zimmermann, C. Schädle, C. Maichle-Mössmer and R. Anwander, Rare-Earth Metal Complexes with Terminal Imido Ligands, *Eur. J. Inorg. Chem.*, 2015, 1334–1339.
13 E. A. Patrick, Y. Yang, W. E. Piers, L. Maron and B. S. Gelfand, A monoanionic pentadentate ligand platform for scandium–pnictogen multiple bonds, *Chem. Commun.*, 2021, **57**, 8640–8643.
14 (*a*) L. A. Solola, A. V. Zabula, W. L. Dorfner, B. C. Manor, P. J. Carroll and E. J. Schelter, Cerium(IV) Imido Complexes: Structural, Computational, and Reactivity Studies, *J. Am. Chem. Soc.*, 2017, **139**, 2435–2442; (*b*) T. Cheisson, L. A. Solola, M. R. Gau, P. J. Carroll and E. J. Schelter, Silyl Transfer Pathway to a Ce(IV) Imido Complex, *Organometallics*, 2018, **37**, 4332–4335.

15 T. E. Rieser, R. Thim-Spöring, D. Schädle, P. Sirsch, R. Litlabø, K. W. Törnroos, C. Maichle-Mössmer and R. Anwander, Open-Shell Early Lanthanide Terminal Imides, *J. Am. Chem. Soc.*, 2022, **144**, 4102–4113.

16 (*a*) J. C. Gordon, G. R. Giesbrecht, D. L. Clark, P. J. Hay, D. W. Keogh, R. Poli, B. L. Scott and J. G. Watkin, The First Example of a μ_2-Imido Functionality Bound to a Lanthanide Metal Center: X-ray Crystal Structure and DFT Study of $[(\mu\text{-ArN})\text{Sm}(\mu\text{-NHAr})(\mu\text{-Me})\text{AlMe}_2]_2$ (Ar = 2,6-$i\text{Pr}_2\text{C}_6\text{H}_3$), *Organometallics*, 2002, **21**, 4726–4734; (*b*) T. Cheisson, K. D. Kersey, N. Mahieu, A. McSkimming, M. R. Gau, P. J. Carroll and E. J. Schelter, Multiple Bonding in Lanthanides and Actinides: Direct Comparison of Covalency in Thorium(IV)- and Cerium(IV)-Imido Complexes, *J. Am. Chem. Soc.*, 2019, **141**, 9185–9190.

17 (*a*) J. Chu, E. Lu, Z. Liu, Y. Chen, X. Leng and H. Song, Reactivity of a Scandium Terminal Imido Complex towards Unsaturated Substrates, *Angew. Chem., Int. Ed.*, 2011, **50**, 7677–7680; (*b*) Z. Jian, W. Rong, Z. Mou, Y. Pan, H. Xie and D. Cui, Intramolecular C–H bond activation induced by a scandium terminal imido complex, *Chem. Commun.*, 2012, **48**, 7515–7518; (*c*) J. Chu, E. Lu, Y. Chen and X. Leng, Reversible Addition of the Si-H Bond of Phenylsilane to the Sc=N Bond of a Scandium terminal Imido Complex, *Organometallics*, 2013, **32**, 1137–1140; (*d*) J. Hong, L. Zhang, K. Wang, Y. Zhang, L. Weng and X. Zhou, Methylidene Rare-Earth-Metal Complexes Mediated Transformations of C=N, N=N and N–H Bonds: New Routes to Imido Rare-Earth-Metal Clusters, *Chem.–Eur. J.*, 2013, **19**, 7865–7873.

18 Y. Wang, J. Liang, C. Deng, R. Sun, P.-X. Fu, B. W- Wang, S. Gao and W. Huang, Two-Electron Oxidations at a Single Cerium Center, *J. Am. Chem. Soc.*, 2023, **145**, 22466–22474.

19 M. Katzenmayer, F. Kracht, C. Maichle-Mössmer and R. Anwander, Potential precursors for terminal ytterbium(II) imide complexes bearing the tris(3-*tert*-butyl-5-methylpyrazolyl)hydroborato ligand, *Dalton Trans.*, 2023, **72**, 6273–6283.

20 (*a*) D. Schädle, C. Maichle-Mössmer, C. Schädle and R. Anwander, Rare-Earth-Metal Methyl, Amide, and Imide Complexes Supported by a Superbulky Scorpionate Ligand, *Chem.–Eur. J.*, 2015, **21**, 662–670; (*b*) R. Litlabø, M. Zimmermann, K. Saliu, J. Takats, K. W. Törnroos and R. Anwander, A Rare-Earth Metal Variant of the Tebbe Reagent, *Angew. Chem., Int. Ed.*, 2008, **47**, 9560–9564; (*c*) M. Zimmermann, J. Takats, G. Kiel, K. W. Törnroos and R. Anwander, Ln(III) methyl and methylidene complexes stabilized by a bulky hydrotris(pyrazolyl)borate ligand, *Chem. Commun.*, 2008, 612–614.

21 (*a*) W. J. Evans, R. Anwander, R. J. Doedens and J. W. Ziller, The Use of Heterometallic Bridging Moieties To Generate Tractable Lanthanide Complexes of Small Ligands, *Angew. Chem. Int. Ed. Engl.*, 1994, **33**, 1641–1644; (*b*) H. M. Dietrich, G. Raudaschl-Sieber and R. Anwander, Trimethylyttrium and Trimethyllutetium, *Angew. Chem., Int. Ed.*, 2005, **44**, 5303–5306.

22 K. O. Saliu, J. Chen, R. McDonald and J. Takats, Acid form of Trofimenko's scorpionates, $\text{H}(\text{Tp}^{\text{R,R'}})$; comments on the synthesis and solid-state structure of $\text{H}(\text{Tp}^{t\text{Bu,Me}})$, *Aust. J. Chem.*, 2022, **75**, 566–570.

23 R. D. Shannon, Revised effective ionic radii and systematic studies of interatomic distances in halides and chalcogenides, *Acta Crystallogr., Sect. A*, 1976, **32**, 751–767.

24 S. N. König, N. F. Chilton, C. Maichle-Mössmer, E. M. Pineda, T. Pugh, R. Anwander and R. A. Layfield, Fast magnetic relaxation in an octahedral dysprosium tetramethyl-aluminate complex, *Dalton Trans.*, 2014, **43**, 3035–3038.

25 C. Schädle, D. Schädle, K. Eichele and R. Anwander, Methylaluminum-Supported Rare-Earth-Metal Dihydrides, *Angew. Chem., Int. Ed.*, 2013, **52**, 13238–13242.

26 J. Scott, F. Basuli, A. R. Fout, J. C. Huffman and D. J. Mindiola, Evidence for the Existence of a Terminal Imidoscandium Compound: Intramolecular C–H Activation and Complexation Reactions with the Transient Sc=NAr Species, *Angew. Chem., Int. Ed.*, 2008, **47**, 8502–8505.

27 (*a*) H. J. Heeres, A. Meetsma and J. H. Teuben, CH Activation of Acetonitrile by Alkyl Compounds of the Early Lanthanoids: Dimeric Cyanomethyl-Lanthanoid Complexes with CH_2CN Bridges, *Angew. Chem., Int. Ed.*, 1990, **29**, 420–422; (*b*) R. Duchateau, C. T. van Wee and J. H. Teuben, Insertion and C–H Bond Activation of Unsaturated Substrates by Bis(benzamidinato)yttrium Alkyl, $[\text{PhC}(\text{NSiMe}_3)_2]_2\text{YR}$ (R = CH_2Ph THF, $\text{CH}(\text{SiMe}_3)_2$, and Hydrido, $\{[\text{PhC}(\text{NSiMe}_3)_2]_2\text{Y}(\mu\text{-H})\}_2$, Compounds, *Organometallics*, 1996, **15**, 2291–2302.

28 J. E. Bercaw, D. L. Davies and P. T. Wolczanski, Reactions of Alkyl and Hydride Derivatives of Permethylscandocene and -zirconocene with Nitriles and Amines. Catalytic Hydrogenation of *tert*-Butyl Cyanide with Permethylscandocene Hydride, *Organometallics*, 1985, **5**, 443–450.

29 W.-Y. Yeh, C.-S. Ting, S.-M. Peng and G.-H. Lee, Reduction of Acetonitrile Ligand on $\text{W}(\text{PhCCPh})_3(\text{NCMe})$ and $\text{W}(\eta^4\text{-}\text{C}_4\text{Ph}_4)(\text{PhCCPH})_2(\text{NCMe})$: Crystal Structure of $\text{W}(\text{PCCPh})_3(\text{NH=C(Me)}_2)$, *Organometallics*, 1995, **14**, 1417–1422.

30 A. G. Trambitas, T. K. Panda, J. Jenter, P. W. Roesky, C. Daniluic, C. G. Hrib, P. Jones and M. Tamm, Rare-Earth Metal Alkyl, Amido, and Cyclopentadienyl Complexes Supported by Imidazolin-2-iminato Ligands: Synthesis, Structural Characterization, and Catalytic Application, *Inorg. Chem.*, 2010, **49**, 2435–2446.

31 T. K. Panda, S. Randoll, C. G. Hrib, P. Jones, T. Bannenberg and M. Tamm, Syntheses and structures of mononuclear lutetium imido complexes with very short Lu–N bonds, *Chem. Commun.*, 2007, 5007–5009.

32 J. Chu, C. Wang, L. Xiang, X. Leng and Y. Chen, Reactivity of Scandium terminal Imido Complex toward Boranes: $\text{C}(\text{sp}^3)$–H Bond Borylation and B–O Bond Cleavage, *Organometallics*, 2017, **36**, 4620–4625.

33 D. M. Lyubov, G. K. Fukin and A. A. Trifonov, N,N'-Diisopropyl-N``-bis(trimethylsilyl)guanidinate Ligand as

a Supporting Coordination Environment in Yttrium Chemistry. Synthesis, Structure, and Properties of Complexes $[(Me_3Si)_2NC(N\textit{i}\text{-}Pr)_2]YCl_2(THF)_2$, $[(Me_3Si)_2NC(N\textit{i}\text{-}Pr)_2]Y(CH_2SiMe_3)_2(THF)_2$, and $[(Me_3Si)_2NC(N\textit{i}\text{-}Pr)_2]Y[\mu\text{-}H](\mu\text{-}Et)_2BEt]_2(THF)_2$, *Inorg. Chem.*, 2007, **46**, 11450–11456.

34 W. J. Evans, S. E. Lorenz and J. W. Ziller, Yttrium metallocene borane chemistry: isolation of 9-BBN substitution and coordination complexes in a single crystal, $\{(C_5Me_5)_2Y[\eta^3\text{-}C_3H_4(BC_8H_{14})]\}$ and $\{(C_5Me_5)_2Y(\mu\text{-}H)_2(BC_8H_{14})\}$, *Chem. Commun.*, 2007, 4662–4664.

35 J. Long, A. N. Selikhov, N. Y. Radkova, A. V. Cherkasov, Y. Guari, J. Larionova and A. A. Trifonov, Synthesis, Structures and Magnetic Properties of two Heteroleptic Dy^{3+} Borohydride Complexes, *Eur. J. Inorg. Chem.*, 2021, 3008–3012.

36 X. W. Zhang, G. H. Maunder, S. Gießmann, R. MacDonald, M. J. Ferguson, A. H. Bond, R. D. Rogers, A. Sella and J. Takats, Stable heteroleptic complexes of divalent lanthanides with bulky pyrazolylborate ligands – iodides, hydrocarbyls and triethylborohydrides, *Dalton Trans.*, 2011, **40**, 195–210.

37 (*a*) D. L. Reger, J. A. Lindemann and L. Lebioda, Synthesis, X-ray Crystal Structure, and Multinuclear NMR Study of the Dynamic Behavior of Tris[dihydridobis(1-pyrazolyl)borato] yttrium(III): A Molecule with Three Three-Center, Two-Electron Bonds, *Inorg. Chem.*, 1988, **27**, 1890–1896; (*b*) M. Akita, K. Ohta, Y. Takahashi, S. Hikichi and Y. Morooka, Synthesis and Structure Determination of Rh–diene Complexes with the Hydridotris(3,5-diisopropylpyrazolyl) borate ligand, $Tp^{iPr}Rh$(diene) (diene = cod, nbd): Dependence of the ν(B–H) Values on the Hapticity of the Tp^{iPr} Ligand (κ^2 vs. κ^3), *Organometallics*, 1997, **16**, 4121–4128; (*c*) X. Zhang, R. MacDonald and J. Takats, Synthesis and structure of the first bis-hydridotris(3-^{t}Bu-5-Mepyrazolyl)borate complexes, $Ln(Tp^{tBu,Me})_2$ (Ln = Sm, Yb): fluxionality, bonding mode exchange and B-H-Ln bridge bonding, *New J. Chem.*, 1995, **19**, 573–585.

38 E. N. Lapsheva, T. Cheisson, C. Álvarez Lamsfus, P. J. Carroll, M. R. Gau, L. Maron and E. J. Schelter, Reactvity of Ce(IV) imido compounds with heteroallenes, *Chem. Commun.*, 2020, **56**, 4781–4784.

Electronic Supplementary Material (ESI) for Chemical Science.

Supporting Information

Terminal Dysprosium and Holmium Organoimides

Theresa E. Rieser, Dorothea Schädle, Cäcilia Maichle-Mössmer, and Reiner Anwander*

Institut für Anorganische Chemie, Eberhard Karls Universität Tübingen, Auf der Morgenstelle 18, 72076 Tübingen, Germany

*E-mail for R.A.: reiner.anwander@uni-tuebingen.de.

Table of Contents

Experimental Section

General Considerations. All manipulations were performed under rigorous exclusion of air and moisture, using standard Schlenk, high-vacuum, and glovebox techniques (MB Braun MB200B; < 0.1 ppm O_2, < 0.1 ppm H_2O, argon atmosphere). The solvents *n*-hexane, *n*-pentane, diethyl ether, toluene and tetrahydrofuran (THF) were purified using Grubbs columns (MBraun SPS, solvent purification system). Tetrahydrofuran was stored over freshly activated molecular sieves (3 Å). 2,6-Di*iso*propylaniline (H_2NAr^{iPr}, 97%, Sigma-Aldrich), 2,6-dimethylaniline (H_2NAr^{Me}, 99%, Sigma-Aldrich), and 2,4,6-trimethylaniline (H_2NAr^{Mes}, 98%, Sigma-Aldrich) were dried over CaH_2 and purified by distillation. 1-Adamantylamine (H_2NAd, 97%, Sigma-Aldrich) was used without further purification. All solvents and reagents were stored inside a glovebox. C_6D_6 and toluene-d_8 were obtained from *Aldrich* or *eurisotop*, degassed, dried over Na for 24 h and filtered. $HTp^{tBu,Me}$ and $KTp^{tBu,Me}$ ($Tp^{tBu,Me}$ = hydrotris(3-tert-butyl-5-methylpyrazol)borate) were synthesized by a modification of the published procedure of $HTp^{tBu,Ph}$.[1] $Ln(AlMe_4)_3$ and $Ln(GaMe_4)_3$ (Ln = Y, Dy, Ho) were synthesized according to literature procedures.[2,3] The NMR spectra of air and moisture sensitive compounds were recorded by using *J. Young*-valved NMR tubes on a *Bruker AVII+400* spectrometer (^{1}H: 400.13 MHz) and AV500 or *Bruker* AVII+500 (5 mm BBO, ^{1}H: 500.13 Hz; ^{13}C: 125.77 MHz). ^{1}H NMR resonances are referenced to solvent residual resonances and reported in *parts per million*, relative to tetramethylsilane (TMS). Coupling constants are given in Hertz. IR spectra were recorded on a *NICOLET 6700 FTIR* spectrometer with a DRIFT cell (KBr window), and the samples were prepared in a glovebox and mixed with KBr powder. Elemental analyses were performed on an *Elementar Vario Micro Cube*.

General procedure for the synthesis of $Tp^{tBu,Me}LnMe(GaMe_4)$ (1-Ln^{Ga}). To a solution of one equivalent $Ln(GaMe_4)_3$ in *n*-pentane (3 mL) a solution of one equivalent $HTp^{tBu.Me}$ in *n*-pentane (3 mL) was slowly added. The mixture was stirred for 15 minutes. After formation of a precipitate, the solution was decanted, and the remaining powder was washed with *n*-pentane (3x 5 mL).

$Tp^{tBu,Me}YMe(GaMe_4)$ (1-Y^{Ga}). Following the procedure described above, $Y(GaMe_4)_3$ (100 mg, 0.210 mmol) and $HTp^{tBu.Me}$ (89.3 mg, 0.210 mmol) yielded **1-Y^{Ga}** as a white precipitate (42 mg, 0.0639 mmol, 30%). ^{1}H NMR (400 MHz, C_6D_6, 26° C): δ 5.60 (s, 3H, pz-*H*), 4.57 (br, 1H, B*H*), 2.01 (s, 9H, pz-CH_3), 1.42 (s, 27H, pz-C(CH_3)$_3$) – 0.09 (s, 15H, Y/Ga(CH_3)) ppm. Elemental analysis (%) calculated for $BN_6C_{29}H_{55}GaY$ (657.24 g/mol): C 53.00, H 8.44, N 12.79; found: C 53.15, H 8.23, N 12.65.

Tp^{tBu,Me}DyMe(GaMe$_4$) (1-Dy^{Ga}). Following the procedure described above, Dy(GaMe$_4$)$_3$ (198 mg, 0.359 mmol) and HTp$^{tBu.Me}$ (152 mg, 0.359 mmol) yielded **1-Dy^{Ga}** as a yellow precipitate (221 mg, 0.302 mmol, 84%). Single crystals suitable for XRD analysis formed from a toluene solution. Elemental analysis (%) calculated for $BN_6C_{29}H_{55}GaDy$ (730.83 g/mol): C 47.66, H 7.59, N 11.50; found: C 47.87, H 7.53, N 11.34.

Tp^{tBu,Me}HoMe(GaMe$_4$) (1-Ho^{Ga}). Following the procedure described above, Ho(GaMe$_4$)$_3$ (111 mg, 0.20 mmol) and HTp$^{tBu.Me}$ (85 mg, 0.20 mmol) yielded **1-Ho^{Ga}** as a pink precipitate (79 mg, 0.108 mmol, 39%). ^{1}H NMR (500 MHz, toluene-d_8, 26 °C): δ 101.83, 50.92, –8.78, –15.58, –152.38, –177.58 ppm. DRIFT (KBr): 2964 s, 2906 s, 2877 m, 2806 ww, 2564 w (B-H), 1539 vs, 1489 w, 1473 m, 1464 m, 1431 vs, 1382 w, 1365 m, 1351 s, 1326 m, 1240 w, 1202 m, 1191 m, 1165 vs, 1141 m, 1065 s, 1027 m, 799 s, 763 s, 731 w, 682 s, 643 m, 584 w, 524 m, 471 w, 411 m cm^{-1}. Elemental analysis calcd (%) for $C_{29}H_{55}BGaHoN_6$: C 47.50, H 7.56, N 11.46; found: C 47.32, H 7.92, N 11.21.

General procedure for the synthesis of Tp^{tBu,Me}LnMe(HNC$_6$H$_3$*i*Pr$_2$-2,6) (2-Ln). To a solution of one equivalent **1-Ln** in toluene (3 mL) a solution of one equivalent $H_2NC_6H_3$*i*Pr$_2$-2,6 in toluene (3 mL) was slowly added. The mixture was stirred for one hour at ambient temperature. After the solvent was removed under vacuum, the powder was washed with *n*-hexane (3x 5 mL).

Tp^{tBu,Me}YMe(HNC$_6$H$_3$*i*Pr$_2$-2,6) (2-Y). Following the procedure described above, **1-Y** (563 mg, 0.857 mmol) and $H_2NC_6H_3$*i*Pr$_2$-2,6 (152 mg, 0.857 mmol) yielded **2-Y** as a white precipitate (467 mg, 0.664 mmol, 77%). ^{1}H NMR (400 MHz, C_6D_6, 26 °C): δ 7.08 (d, 2H, $^3J_{HH}$ 7.52 Hz, *m*-Ar*H*), 6.77 (t, 1H, $^3J_{HH}$ 7.36 Hz, *p*-Ar*H*), 5.56 (s, 3H, pz-*H*), 4.87 (s, 1H, N*H*), 2.87 (br, 2H, *i*Pr-*H*), 2.13 (s. 9H, pz-CH_3), 1.39 (s, 27H, pz-C(CH_3)$_3$), 1.13 (d, 12H, $^3J_{HH}$ 6.43 Hz, *i*Pr-CH_3), 0.46 (d, 3H, $^2J_{YH}$ 1.74 Hz, Y-CH_3) ppm. Elemental analysis (%) calculated for $BN_7C_{37}H_{61}Y$ (703.66 g/mol): C 63.16, H 8.74, N 13.93; found: C 63.35, H 8.58, N 13.72.

Tp^{tBu,Me}DyMe(HNC$_6$H$_3$*i*Pr$_2$-2,6) (2-Dy). Following the procedure described above, **1-Dy** (70 mg, 0.0958 mmol) and $H_2NC_6H_3$*i*Pr$_2$-2,6 (15.3 mg, 0.0862 mmol) yielded **2-Dy** as a yellow precipitate (63 mg, 0.0811 mmol, 85%). Single crystals suitable for XRD analysis formed from a toluene solution. Elemental analysis (%) calculated for $BN_7C_{37}H_{61}Dy$ (777.25 g/mol): C 57.18, H 7.91, N 12.61; found: C 57.30, 7.77, N 12.40.

Tp^{tBu,Me}HoMe(HNC$_6$H$_3$*i*Pr$_2$-2,6) (2-Ho). Following the procedure described above, **1-Ho** (100 mg, 0.136 mmol) and H$_2$NC$_6$H$_3$*i*Pr$_2$-2,6 (21.8 mg, 0.123 mmol) yielded **2-Ho** as a yellow precipitate (87 mg, 0.112 mmol, 82%). Single crystals suitable for XRD analysis formed from a toluene solution. Elemental analysis (%) calculated for $BN_7C_{37}H_{61}Ho$ (779.68 g/mol): C 57.00, H 7.89, N 12.58; found: C 57.28, H 6.87, N 12.44.

Tp^{tBu,Me}Ho(HNC$_{10}$H$_{15}$)$_2$ (3-Ho). To a solution of **1-Ho** (30.0 mg, 0.0409 mmol) in toluene (2 mL) a solution of H$_2$NC$_{10}$H$_{15}$ (5.57 mg, 0.0368 mmol) in toluene (3 mL) was added and stirred for 15 minutes at – 35 °C. After the solvent was removed under vacuum and the powder was washed with *n*-hexane (3x 5 mL), single crystals suitable for XRD analysis formed from a toluene solution. Elemental analysis (%) calculated for $BN_8C_{44}H_{72}Ho$ (888.86 g/mol): C 59.46, H 8.17, N 12.61; found: C 59.28 H 8.09, N 12.54.

General procedure for the synthesis of Tp^{tBu,Me}Ln(NC$_6$H$_3$*i*Pr$_2$-2,6)(dmap) (4-Ln). To a solution of one equivalent **2-Ln** in toluene (3 mL) a solution of one equivalent DMAP in toluene (3 mL) was slowly added. The mixture was stirred for one hour at ambient temperature. After the solvent was removed under vacuum, the powder was washed with *n*-hexane (3x 5 mL).

Tp^{tBu,Me}Y(NC$_6$H$_3$*i*Pr$_2$-2,6)(dmap) (4-Y). Following the procedure described above, **2-Y** (330 mg, 0.469 mmol) and DMAP (57.3 mg, 0.469 mmol) yielded **4-Y** as a beige precipitate (279 mg, 0.345 mmol, 74%). Single crystals suitable for XRD analysis formed from a toluene solution. ^{1}H NMR (400 MHz, C_6D_6, 26 °C): δ 8.47 (d, 1H, $^3J_{HH}$ 6.30 Hz, DMAP, H_{ortho}), 8.01 (s br, 1H, DMAP, H_{ortho}), 7.04 (d, 2H, $^3J_{HH}$ 7.42 Hz, *m*-Ar*H*), 6.71 (t, 1H, $^3J_{HH}$ 7.27 Hz, *p*-Ar*H*), 6.35 (dd, 1H, $^3J_{HH}$ 6.28 Hz, $^4J_{HH}$ 2.71 Hz, DMAP, H_{meta}), 5.72 (s, 3H, pz-*H*), 5.53 (s br, 1 H, DMAP, H_{meta}), 2.79 (br, 2H, *i*Pr-*H*), 2.51 (s, 6H, N(CH_3)$_2$) 2.24 (s. 9H, pz-CH_3), 1.39 (s, 27H, pz-C(CH_3)$_3$), 0.99 (d, 12H, $^3J_{HH}$ 6.93 Hz, *i*Pr-CH_3) ppm. Elemental analysis (%) calculated for $BN_9C_{43}H_{67}Y$ (809.79 g/mol): C 63.78, H 8.34, N 15.57; found: C 64.35, H 8.95, N 14.58.

Tp^{tBu,Me}Dy(NC$_6$H$_3$*i*Pr$_2$-2,6)(dmap) (4-Dy). Following the procedure described above, **2-Dy** (321 mg, 0.413 mmol) and DMAP (50.5 mg, 0.413 mmol) yielded **4-Dy** as a yellow precipitate (109 mg, 0.123 mmol, 30%). Single crystals suitable for XRD analysis formed from a toluene solution. $\tilde{\nu}_{max}$ = 3056 vw, 3023 vw, 2960 vs, 2930 s, 2862 m, 2557 (B-H), 1612 vs, 1582 vs, 1542 vs, 1489 w, 1463 m, 1427 vs, 1399 s, 1351 s, 1329 vs, 1267 s, 1230 m, 1199 m, 1179 s, 1138 w, 1065 s, 1006 s, 990 m, 906 m, 848 w, 802 m, 790 m, 770 m, 739 m, 683 w, 645 m, 541 vw, 515 vw, 441 vw, 415 vw cm^{-1}. Elemental analysis (%) calculated for $BN_9C_{43}H_{67}Dy$ (883.38 g/mol): C 58.47, H 7.65, N 14.27; found: C 60.04, 7.54, N 13.49.

Tp^{tBu,Me}Ho(NC$_6$H$_3$*i*Pr$_2$-2,6)(dmap) (4-Ho). Following the procedure described above, **2-Ho** (177 mg, 0.227 mmol) and DMAP (27.7 mg, 0.227 mmol) yielded **4-Ho** as an orange precipitate (78.3 mg, 0.0884 mmol, 39%). Single crystals suitable for XRD analysis formed from a toluene solution. Elemental analysis (%) calculated for $BN_9C_{43}H_{67}Ho$ (885.81 g/mol): C 58.31, H 7.62, N 14.23; found: C 58.04, H 7.61, N 13.79.

General procedure for the synthesis of Tp^{tBu,Me}Ln(NC$_6$H$_3$*i*Pr$_2$-2,6)(AlMe$_3$) (5-Ln). To a solution of Tp^{tBu,Me}DyMe(AlMe$_4$) (**1-Ln^{Al}**) in toluene (3 mL) a solution of an equimolar amount of $H_2NC_6H_3Me_2$-2,6 in toluene (3 mL) was slowly added. The mixture was stirred for one hour at ambient temperature. After the solvent was removed under vacuum, the powder was washed with *n*-hexane (3x 5 mL).

Tp^{tBu,Me}Dy(NC$_6$H$_3$Me$_2$-2,6)(AlMe$_3$) (5-Dy). Following the procedure described above, Tp^{tBu,Me}DyMe(AlMe$_4$) (**1-Dy^{Al}**, 80.3 mg, 0.0964 mmol) and $H_2NC_6H_3Me_2$-2,6 (11.7 mg, 0.0964 mmol) yielded **5-Dy** as a yellow precipitate (27.8 mg, 0.0358 mmol, 37%). Single crystals suitable for XRD analysis formed from a toluene solution.

Tp^{tBu,Me}Ho(NC$_6$H$_3$Me$_2$-2,6)(AlMe$_3$) (5-Ho). Following the procedure described above, **1-Ho^{Al}** (121 mg, 0.155 mmol) and $H_2NC_6H_3Me_2$-2,6 (18.8 mg, 0.155 mmol) yielded **5-Ho** as a yellow precipitate (37.5 mg, 0.0481 mmol, 31%). Single crystals suitable for XRD analysis formed from a toluene solution. Elemental analysis (%) calculated for $BN_7C_{35}H_{58}HoAl$ (779.62 g/mol): C 53.92, H 7.50, N 12.58; found: C 54.04, H 7.60, N 12.04.

Tp^{tBu,Me}Ho(NC$_6$H$_2$Me$_3$-2,4,6)(AlMe$_3$) (6-Ho). To a solution of Tp^{tBu,Me}HoMe(AlMe$_4$) (**1-Ho^{Al}**) (100 mg, 0.136 mmol) in toluene (4 mL) a solution of $H_2NC_6H_3Me_3$-2,4,6 (16.5 mg, 0.122 mmol) in toluene (3 mL) was added and stirred for 1 h at ambient temperature. After the solvent was removed under vacuum and the powder was washed with *n*-hexane (3x 5 mL), single crystals suitable for XRD analysis formed from a toluene solution.

Tp^{tBu,Me}Dy(HNC$_6$H$_3$*i*Pr$_2$-2,6)(NC(CH$_3$)$_2$) (7-Dy). To a solution of **2-Dy** (200 mg, 0.257 mmol) in toluene (6 mL) acetonitrile (21 mg, 0.512 mmol) was added. The solution was stirred at ambient temperature overnight. After the solvent was removed under vacuum and the yellow powder was washed with *n*-hexane (3x 5 mL), single crystals suitable for XRD analysis formed from a toluene solution.

Tp^{tBu,Me}Dy(NC$_6$H$_3$*i*Pr$_2$-2,6)(thf) (8-Dy). To a solution of **4-Dy** (183 mg, 0.207 mmol) in toluene (3 mL) a solution of 9-BBN (50.6 mg, 0.207 mmol) in THF (3 mL) was added and

stirred for 3 h at ambient temperature. Yellow, single crystals suitable for XRD analysis formed from a toluene solution (36.7 mg, 0.044 mmol, 21%). Elemental analysis (%) calculated for $BN_7C_{40}H_{65}DyO$ (833.32 g/mol): C 57.65, H 7.86, N 11.77; found: C 57.39, H 7.67, N 12.14.

Tp^{tBu,Me}Dy(μ_2-CH$_2$)(μ_2-HBC$_8$H$_{14}$)(HNC$_6$H$_3$*i*Pr$_2$-2,6) (9-Dy). To a solution of **3-Dy** (150 mg, 0.170 mmol) in toluene (10 mL) a solution of 9-BBN (124 mg, 0.510 mmol) in toluene (5 mL) was added. The reaction mixture was stirred for 1 h at 40° C. Single crystals suitable for XRD analysis formed from a toluene solution.

Tp^{tBu,Me}Dy(CO$_2$)$_2$(NC$_6$H$_3$*i*Pr$_2$-2,6) (10-Dy). A solution of **4-Dy** (82.2 mg, 0.0931 mmol) in toluene (2 mL) under 1 bar CO_2 pressure was stirred for 30 minutes. After the color changed from yellow to colorless the solvent was removed under vacuum and the powder was washed with *n*-hexane (3x 5 mL) (44.6 mg, 0.0527 mmol, 57%). Elemental analysis (%) calculated for $BN_7C_{38}H_{57}DyO_4$ (849.23 g/mol): C 53.74, H 6.77, N 11.55; found: C 54.63 H 6.92, N 11.54.

Crystallography

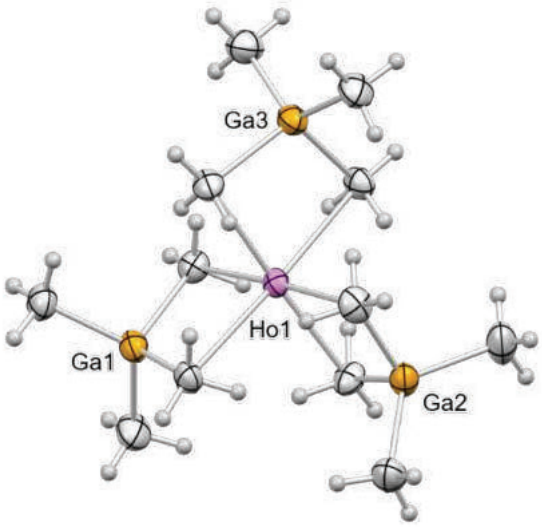

Figure S1. Crystal structure of $Ho(Ga(CH_3)_4)_3$. Atomic displacement ellipsoids were set at 50% probability. Selected interatomic distances [Å] and angles [°]: Ho1–C1 2.508(5), Ho1–C6 2.519(5), Ho1–C5 2.516(5), Ho1–C2 2.521(5), Ho1–C10 2.523(5), Ho1–C9 2.534(5), Ga1–C3 1.978(6), Ga1–C4 1.981(5), Ga1–C2 2.108(5), Ga1–C1 2.108(5); C1–Ho1–C6 90.60(17), C1–Ho1–C5 90.64(17), C1–Ho1–C2 86.84(16), C6–Ho1–C2 91.98(16), C1–Ho1–C10 177.28(17).

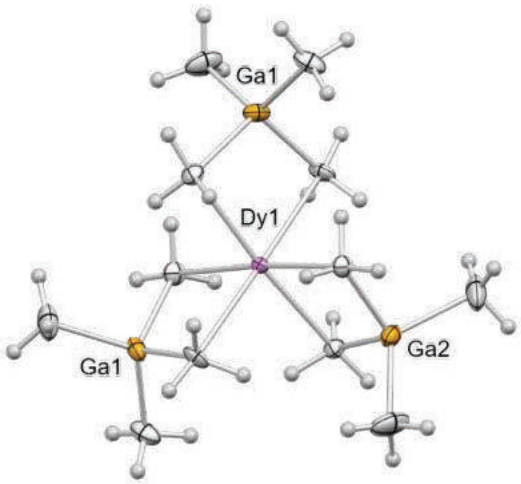

Figure S2. Crystal structure of $Dy(Ga(CH_3)_4)_3$. Atomic displacement ellipsoids were set at 50% probability. Selected interatomic distances [Å] and angles [°]:Ga1–C1 2.113(3), Dy1–C1 2.526(2), Ga1–C2 2.109(3), Dy1–C2 2.521(2), Ga1–C3 1.973(3), Dy1–C5 2.511(2), Ga2–C5 2.118(2), Dy1–C5' 2.511(2), Dy1–C2' 2.521(2), Dy1–C1' 2.527(2); C5–Dy1–C5' 87.06(11), C5–Dy1–C2 91.56(8), C5'–Dy1–C2 89.19(8), C2–Dy1–C2' 178.97(12), C5–Dy1–C1 91.53(9), C5–Dy1–C1' 175.30(8), C2–Dy1–C1 86.36(8), C2'–Dy1–C1 92.91(9), C5–Dy1–C1' 175.30(8), C5'–Dy1–C1' 91.54(9), C2–Dy1–C1' 92.91(9), C2'–Dy1–C1' 86.36(8), C1–Dy1–C1' 90.21(12).

' -x+1, y, -z+1/2

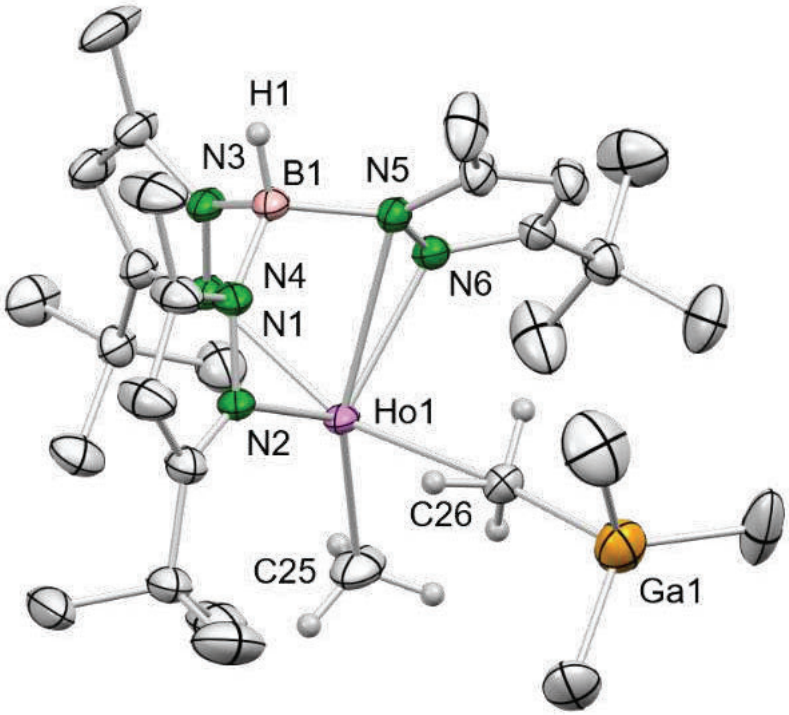

Figure S3. Crystal structure of **1-Ho^{Ga}**. Atomic displacement ellipsoids were set at 50% probability. Hydrogen atoms except for the B–H and H–C25/26, and the disorder of one *tert*-butyl group are omitted for clarity. Selected interatomic distances [Å] and angles [°]: Ho1–N2 2.362(3), Ho1–N4 2.376(3), Ho1–N6 2.334(3), Ho1–C25 2.356(5), Ho1–C26 2.652(4); N2–Ho1–N4 77.82(12), N2– Ho1–N6 102.08(12), N2– Ho1–C25 128.40(19), N2– Ho1–C26 87.39(13), N4– Ho1–N6 75.50(12), N4–Ho1–C25 113.76(17), N4–Ho1–C26 152.60(12), N6–Ho1–C25 129.46(19), N6–Ho1–C26 85.41(13), C25–Ho1–C26 93.53(17), Ho1–C26–Ga1 174.9(2).

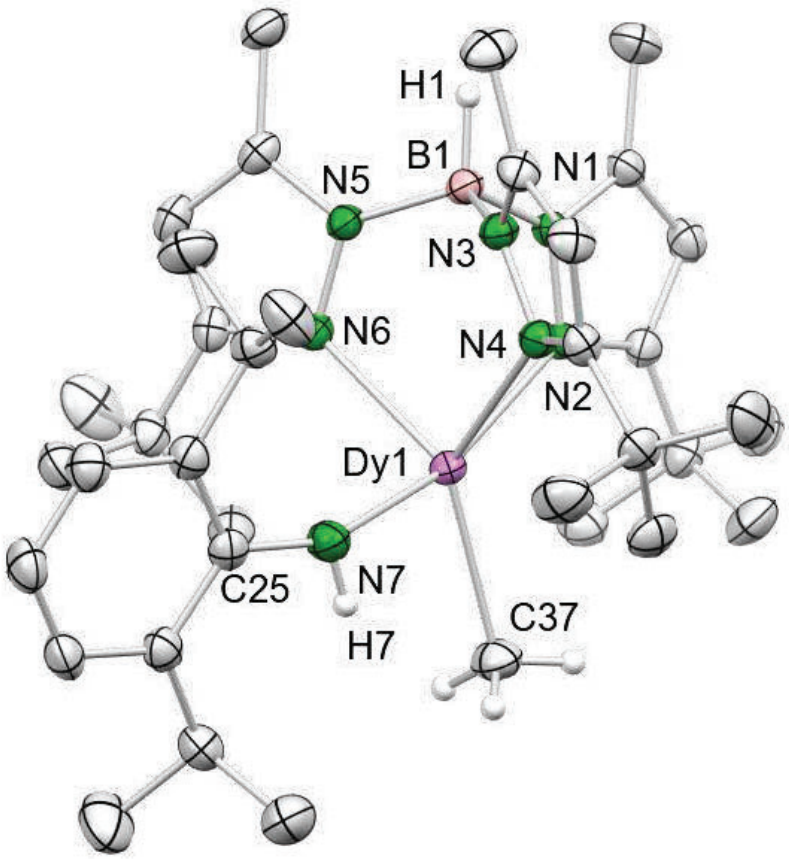

Figure S4. Crystal structure of **2-Dy**. Atomic displacement ellipsoids were set at 50% probability. Hydrogen atoms except for the B–H, the N–H and the H–C37, and the disorder of one *tert*-butyl group are omitted for clarity. Selected interatomic distances [Å] and angles [°]: Dy1–N2 2.5163(18), Dy1–N4 2.3752(17), Dy1–N6 2.4108(17), Dy1–N7 2.212(2), Dy1–C37 2.436(2); N2–Dy1–N4 74.52(6), N2–Dy1–N6 75.11(6), N2–Dy1–N7 166.20(7), N2–Dy1–C37 107.08(7), N4–Dy1–N6 94.33(6), N4–Dy1–N7 98.15(7), N4–Dy1–C37 130.41(8), N6–Dy1–N7 94.13(7), N6–Dy1–C37 134.76(8), N7–Dy1–C37 86.61(8), Dy1–N7–C25 155.84(16).

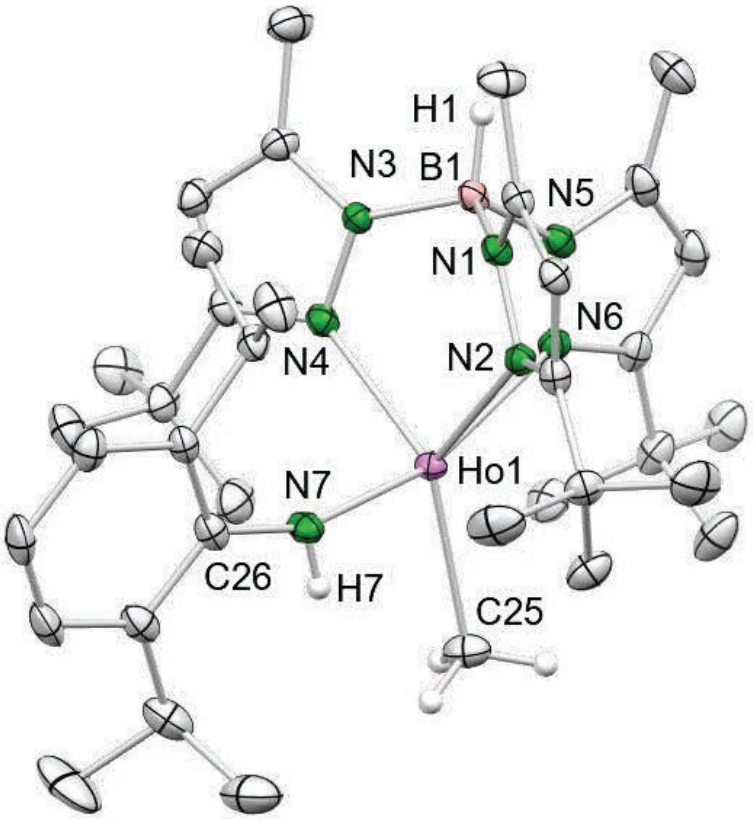

Figure S5. Crystal structure of **2-Ho**. Atomic displacement ellipsoids were set at 50% probability. Hydrogen atoms except for the B–H, the N–H and the H–C37, and one additional toluene molecule are omitted for clarity. Selected interatomic distances [Å] and angles [°]: Ho1–N2 2.373(2), Ho1–N4 2.369(2), Ho1–N6 2.536(2), Ho1–N7 2.222(2), Ho1–C25 2.427(3); N2–Ho1–N4 94.66(8), N2–Ho1–N6 77.23(7), N2–Ho1–N7 94.00(8), N2–Ho1–C25 129.46(9), N4–Ho1–N6 73.22(7), N4–Ho1–N7 94.60(8), N4–Ho1–C25 135.29(9), N6–Ho1–N7 164.08(8), N6–Ho1–C25 106.18(9), N7–Ho1–C25 89.66(9), Ho1–N7–C26 160.28(19).

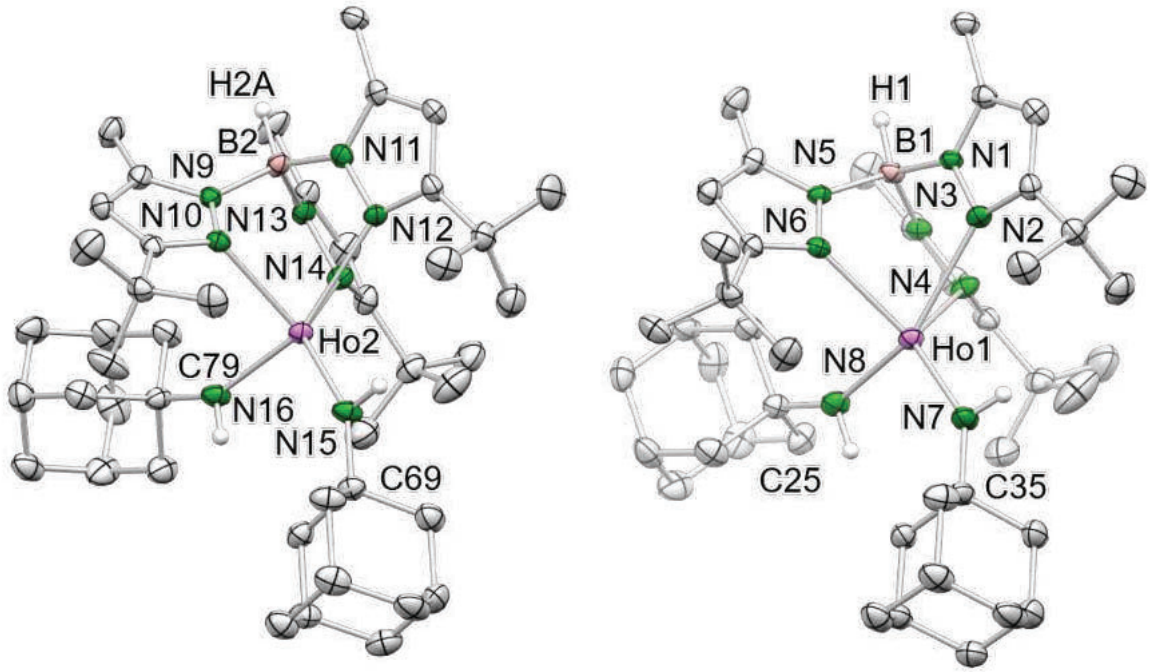

Figure S6. Crystal structure of **3-Ho**. Atomic displacement ellipsoids were set at 50% probability. Hydrogen atoms except for the B–H, the N–H, and lattice solvent (two molecules of THF) are omitted for clarity. The unit cell contains two independent molecules with different parameters. Selected interatomic distances [Å] and angles [°]: Ho1–N2 2.610(3), Ho1–N4 2.406(3), Ho1–N6 2.417(3), Ho1–N7 2.172(3), Ho1–N8 2.170(3), Ho2–N10 2.393(3), Ho2–N12 2.586(3), Ho2–N14 2.410(3), Ho2–N15 2.163(3), Ho2–N16 2.167(3); N2–Ho1–N4 69.77(10), N2–Ho1–N6 72.87(10), N2–Ho1–N7 103.30(12), N2–Ho1–N8 152.73(11), N4–Ho1–N6 100.02(10), N4–Ho1–N7 124.13(13), N4–Ho1–N8 91.54(12), N6–Ho1–N7 131.97(13), N6–Ho1–N8 91.94(12), N7–Ho1–N8 103.66(13), Ho1–N7–C35 144.0(3), Ho1–N8–C25 148.5(3), N10–Ho2–N12 71.81(10), N10–Ho2–N14 101.06(10), N10–Ho2–N15 119.74(12), N10–Ho2–N16 94.22(12), N12–Ho2–N14 70.46(11), N12–Ho2–N15 102.99(12), N12–Ho2–N16 154.81(11), N14–Ho2–N15 134.82(12), N14–Ho2–N16 92.71(12), N15–Ho2–N16 102.15(13), Ho2–N15–C69 146.9(3), Ho2–N16–C79 148.1(3).

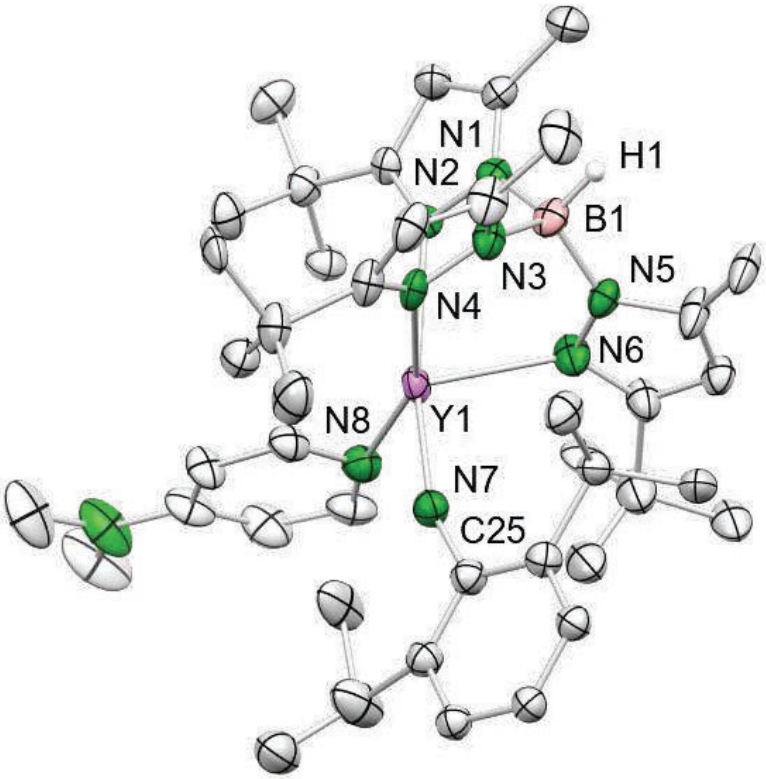

Figure S7. Crystal structure of **4-Y**. Atomic displacement ellipsoids were set at 50% probability. Hydrogen atoms except for the B–H, and three additional THF molecules as well as the disorder in two *tert*-butyl groups, one methyl group, and in the aryl group are omitted for clarity. Selected interatomic distances [Å] and angles [°]: Y1–N2 2.561(13), Y1–N4 2.457(14), Y1–N6 2.425(14), Y1–N7 2.26(3), Y1–N8 2.347(14); N2–Y1–N4 73.4(4), N2–Y1–N6 72.9(5), N2–Y1–N7 161.7(7), N2–Y1–N8 104.1(5), N4–Y1–N6 96.1(5), N4–Y1–N7 92.3(9), N4–Y1–N8 158.7(5), N6–Y1–N7 99.7(9), N6–Y1–N8 103.4(5), N7–Y1–N8 93.9(8), Y1–N7–C25 158(2).

* only connectivity, bond lengths and angles are not reliable

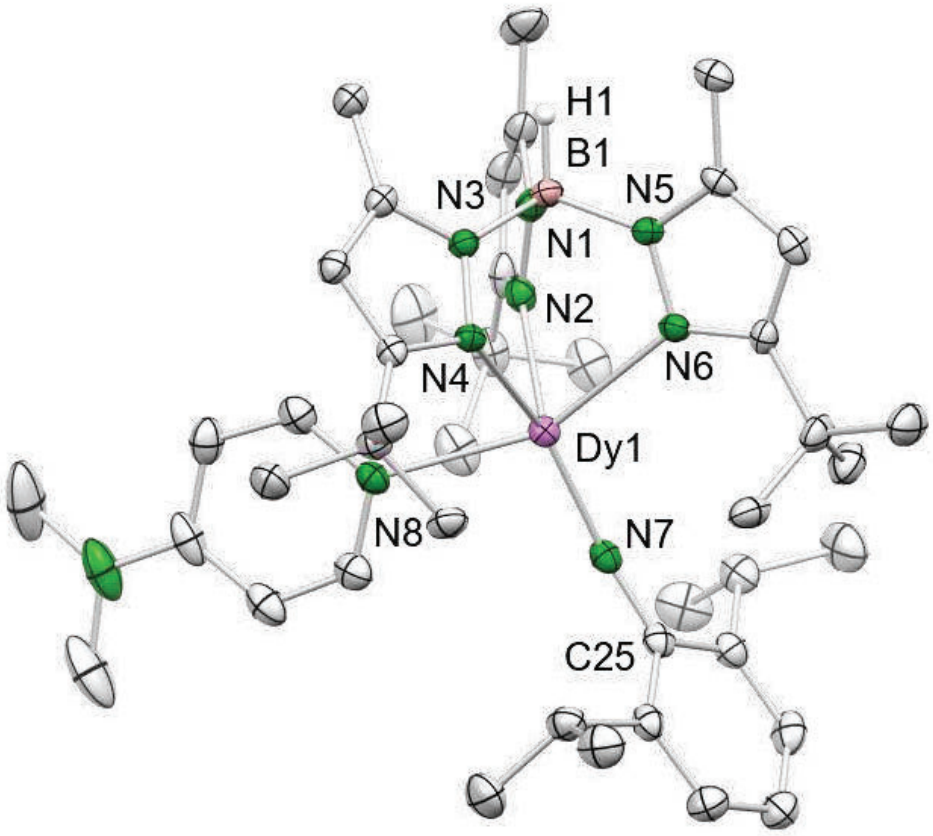

Figure S8. Crystal structure of **4-Dy**. Hydrogen atoms except for the B–H, and one additional toluene molecule are omitted for clarity. Atomic displacement ellipsoids were set at 50% probability. Selected interatomic distances [Å] and angles [°]: Dy1–N2 2.452(3), Dy1–N4 2.517(3), Dy1–N6 2.450(3), Dy1–N7 2.017(3), Dy1–N8 2.450(3); N2–Dy1–N4 92.37(9), N2–Dy1–N6 83.43(9), N2–Dy1–N7 120.04(10), N2–Dy1–N8 90.02(9), N4–Dy1–N6 73.88(9), N4–Dy1–N7 147.59(10), N4–Dy1–N8 80.27(9), N6–Dy1–N7 107.81(10), N6–Dy1–N8 152.99(9), N7–Dy1–N8 98.18(10), Dy1–N7–C25 166.0(2).

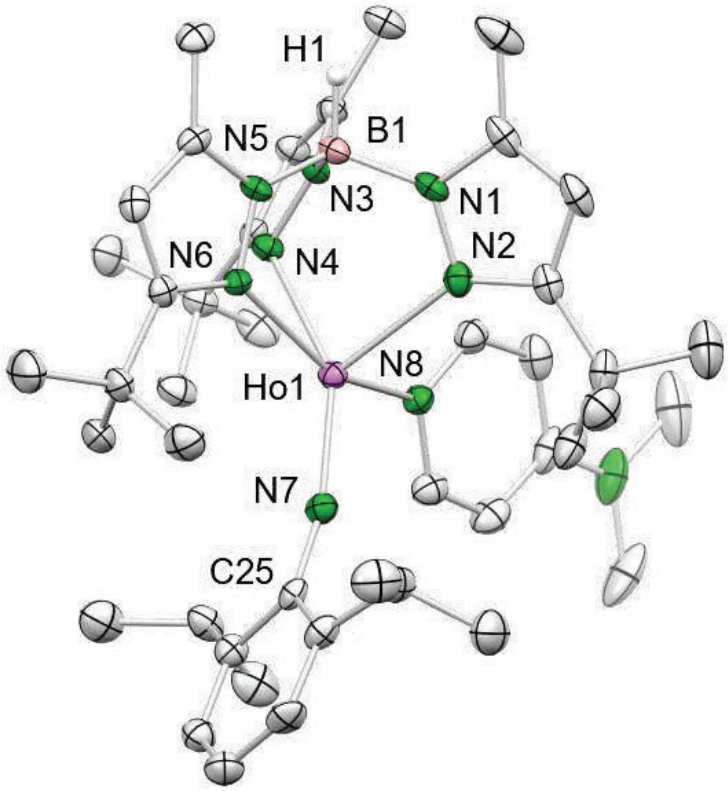

Figure S9. Crystal structure of **4-Ho**. Hydrogen atoms except for the B–H, and one additional toluene molecule are omitted for clarity. Atomic displacement ellipsoids were set at 50% probability. Selected interatomic distances [Å] and angles [°]: Ho1–N2 2.426(4), Ho1–N4 2.492(4), Ho1–N6 2.436(3), Ho1–N7 2.012(4), Ho1–N8 2.429(4); N2–Ho1–N4 93.34(12), N2–Ho1–N6 84.01(12), N2–Ho1–N7 120.38(13), N2–Ho1–N8 89.92(12), N4–Ho1–N6 74.40(12), N4–Ho1–N7 146.25(13), N4–Ho1–N8 79.83(12), N6–Ho1–N7 108.14(13), N6–Ho1–N8 153.09(12), N7–Ho1–N8 97.56(13), Ho1–N7–C25 166.7(3).

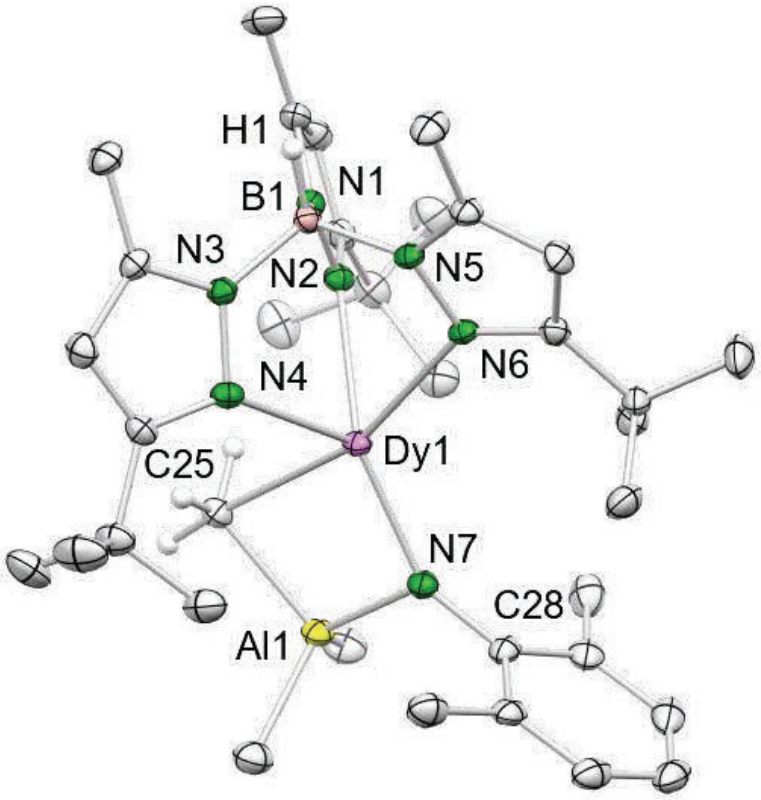

Figure S10. Crystal structure of **5-Dy**. Atomic displacement ellipsoids were set at 50% probability. Hydrogen atoms except for the B–H, and one additional toluene molecule are omitted for clarity. Selected interatomic distances [Å] and angles [°]: Dy1–N2 2.466(2), Dy1–N4 2.492(2), Dy1–N6 2.423(2), Dy1–N7 2.129(2), Dy1–C25 2.549(3), Al1–C25 2.091(3); N2–Dy1–N4 89.39(7), N2–Dy1–N6 74.80(7), N2–Dy1–N7 137.44(7), N2–Dy1–C25 90.18(8), N4–Dy1–N6 83.91(7), N4–Dy1–N7 131.58(7), N4–Dy1–C25 88.06(8), N6–Dy1–N7 114.82(8), N6–Dy1–C25 163.00(8), N7–Dy1–C25 81.61(8), Dy1–N7–C28 146.68(17).

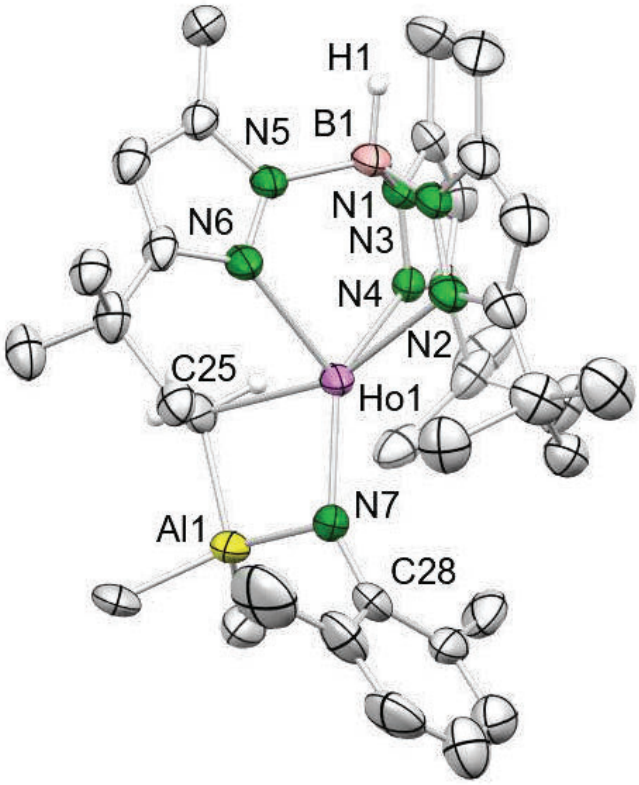

Figure S11. Crystal structure of **5-Ho**. Atomic displacement ellipsoids were set at 50% probability. Hydrogen atoms except for the B–H, the disorder of the *tert*-butyl groups and of the methyl groups of the trimethylaluminum are omitted for clarity. Selected interatomic distances [Å] and angles [°]: Ho1–N2 2.407(4), Ho1–N4 2.437(4), Ho1–N6 2.416(4), Ho1–N7 2.116(4), Ho1–C25 2.549(5), Al1–C25 2.105(6); N2–Ho1–N4 76.98(14), N2–Ho1–N6 77.74(15), N2–Ho1–N7 118.39(17), N2–Ho1–C25 159.64(16), N4–Ho1–N6 98.00(15), N4–Ho1–N7 132.41(16), N4–Ho1–C25 91.63(17), N6–Ho1–N7 128.39(16), N6–Ho1–C25 87.38(17), N7–Ho1–C25 81.76(17), Ho1–N7–C28 146.7(4).

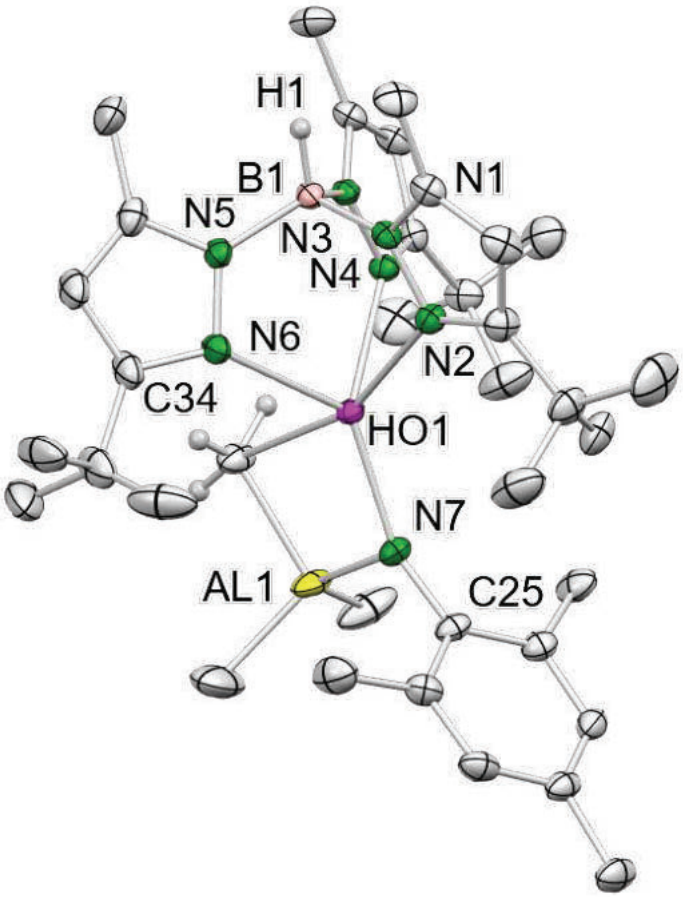

Figure S12. Crystal structure of **6-Ho**. Atomic displacement ellipsoids were set at 50% probability. Hydrogen atoms except for the B–H, and C34–H, one additional toluene molecule, and the disorder of the *tert*-butyl groups are omitted for clarity. Selected interatomic distances [Å] and angles [°]: Ho1–N2 2.394(3), Ho1–N4 2.436(3), Ho1–N6 2.454(3), Ho1–N7 2.116(3), Ho1–C34 2.554(3), Al1–C34 2.106(4); N2–Ho1–N4 76.67(9), N2–Ho1–N6 80.27(9), N2–Ho1–N7 116.96(10), N2–Ho1–C34 160.51(12), N4–Ho1–N6 95.45(9), N4–Ho1–N7 133.51(10), N4–Ho1–C34 89.54(11), N6–Ho1–N7 129.59(11), N6–Ho1–C34 87.52(13), N7–Ho1–C34 82.53(12), Ho1–N7–C25 151.0(2).

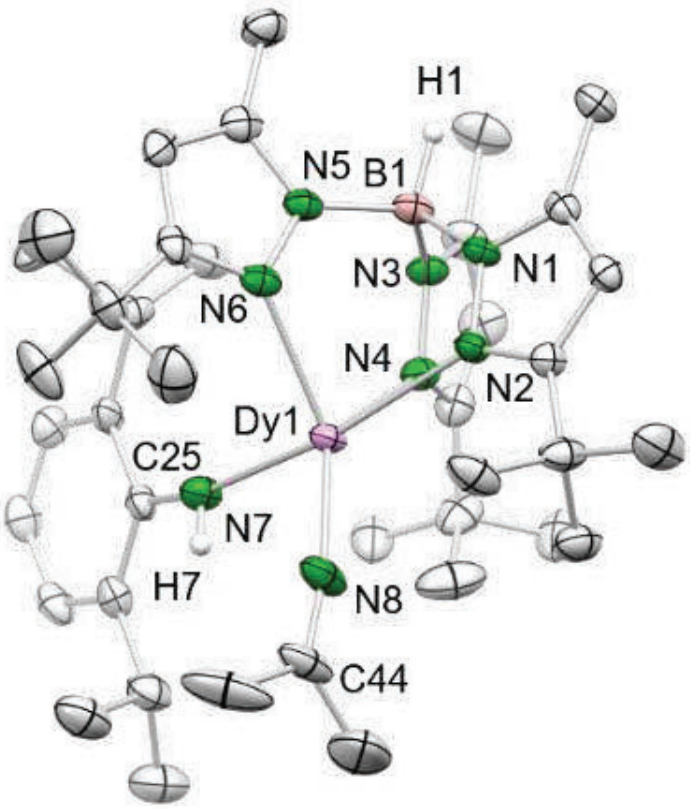

Figure S13. Crystal structure of **7-Dy**. Atomic displacement ellipsoids were set at 50% probability. Hydrogen atoms except for the B–H, and N–H are omitted for clarity. Selected interatomic distances [Å] and angles [°]: Dy1–N2 2.487(3), Dy1–N4 2.414(3), Dy1–N6 2.396(3), Dy1–N7 2.219(3), Dy1–N8 2.148(3); N2–Dy1–N4 75.05(10), N2–Dy1–N6 75.43(10), N2–Dy1–N7 167.88(11), N2–Dy1–N8 103.62(11), N4–Dy1–N6 95.88(10), N4–Dy1–N7 94.91(12), N4–Dy1–N8 136.15(12), N6–Dy1–N7 99.31(12), N6–Dy1–N8 126.77(12), N7–Dy1–N8 88.30(12), Dy1–N7–C25 156.3(3), Dy1–N8–C44 165.3(3).

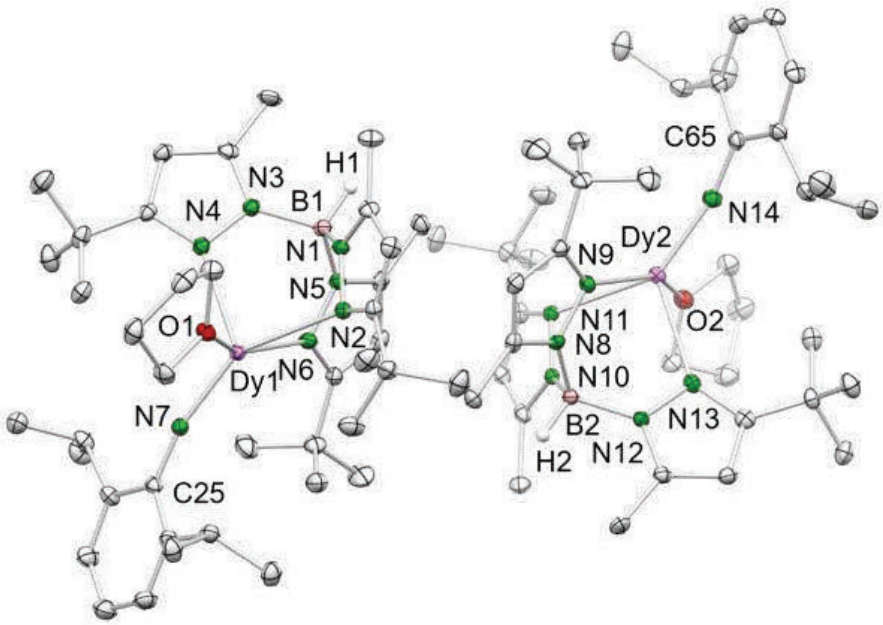

Figure S14. Crystal structure of **8-Dy**. Atomic displacement ellipsoids were set at 50% probability. Hydrogen atoms except for the B–H, and one additional THF molecule are omitted for clarity. The unit cell contains two independent molecules with different parameters. Selected interatomic distances [Å] and angles [°]: Dy1–N2 2.539(4), Dy1–N4 2.450(3), Dy1–N6 2.458(4), Dy1–N7 2.008(3), Dy1–O1 2.397(3), Dy2–N9 2.465(4), Dy2–N11 2.510(4), Dy2–N13 2.472(3), Dy2–N14 2.004(4), Dy2–O2 2.392(3); N2–Dy1–N4 92.82(12), N2–Dy1–N6 72.98(12), N2–Dy1–N7 149.01(13), N2–Dy1–O1 81.63(11), N4–Dy1–N6 82.59(12), N4–Dy1–N7 118.07(13), N4–Dy1–O1 91.16(11), N6–Dy1–N7 106.67(14), N6–Dy1–O1 153.45(11), N7–Dy1–O1 99.07(13), Dy1–N7–C25 166.9(3), N9–Dy2–N11 73.58(12), N9–Dy2–N13 83.99(11), N9–Dy2–N14 106.64(14), N9–Dy2–O2 151.86(11), N11–Dy2–N13 93.37(11), N11–Dy2–N14 144.82(14), N11–Dy2–O2 79.59(10), N13–Dy2–N14 121.80(14), N13–Dy2–O2 89.36(11), N14–Dy2–O2 100.11(13), Dy2–N14–C65 165.3(3).

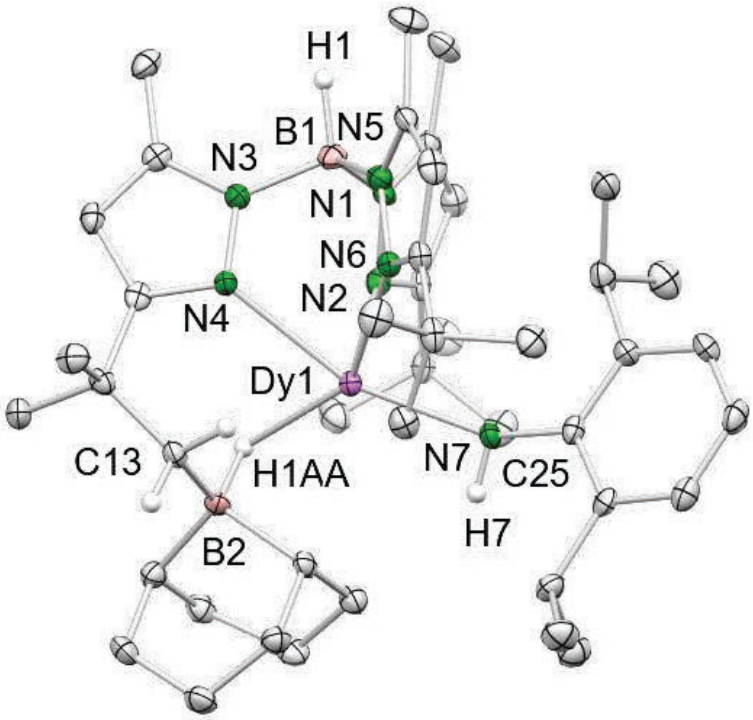

Figure S15. Solid-state structure of **9-Dy**. Atomic displacement ellipsoids were set at 50% probability. Hydrogen atoms except for the B–H, CH_2 and N–H are omitted for clarity. Selected interatomic distances [Å] and angles [°]: Dy1–N2 2.452(3), Dy1–N4 2.405(3), Dy1–N6 2.461(3), Dy1–N7 2.237(3), Dy1–H1AA 2.17(3), B2–C13 1.658(5); N2–Dy1–N4 79.55(9), N2–Dy1–N6 90.63(9), N2–Dy1–N7 93.18(10), N2–Dy1–H1AA 90.3(8), N4–Dy1–N6 70.77(9), N4–Dy1–N7 161.07(10), N4–Dy1–H1AA 75.5(8), N6–Dy1–N7 92.04(10), N6–Dy1–H1AA 145.4(8), N7–Dy1–H1AA 122.4(8), Dy1–N7–C25 143.4(2), Dy1–H1AA–B2 101.98.

Table S1. Crystallographic data for compounds **1-Ho**, **2-Dy**, and **2-Ho**

	1-Ho	**2-Dy**	**2-Ho**
formula	$C_{29}H_{55}GaBN_6Ho \cdot 1.5\ C_7H_8$	$C_{37}H_{61}BN_7Dy$	$C_{37}H_{61}BN_7Ho \cdot C_7H_8$
CCDC	2312222	2312224	2312220
M_r [g mol^{-1}]	871.45	777.23	871.80
color	colorless	colorless	colorless
crystal dimensions [mm^3]	0.557 x 0.340 x 0.082	0.198 x 0.117 x 0.091	0.214 x 0.176 x 0.089
cryst syst	triclinic	monoclinic	triclinic
space group	$P\bar{1}$	$P2_1/c$	$P\bar{1}$
a [Å]	9.8291(10)	11.6084(10)	10.767(5)
b [Å]	13.4472(12)	18.3503(15)	12.621(6)
c [Å]	18.5931(17)	18.8307(15)	17.188(9)
α [°]	96.149(2)	90	77.029(13)
β [°]	100.699(2)	98.396(2)	81.681(16)
γ [°]	110.456(2)	90	88.061(9)
V [Å^3]	2222.7(4)	3968.3(6)	2252.1(19)
Z	2	4	2
T [K]	100(2)	100(2)	173(2)
ρ_{calcd} [g cm^{-3}]	1.302	1.301	1.286
μ [mm^{-1}]	2.404	1.916	1.793
F (000)	898	1612	908
θ range [°]	1.645/30.507	1.558/30.507	1.228/28.699
unique reflns	74018	107390	59343
observed reflns	13452	12124	11646
R_1/wR_2 ($I>2\sigma$)[b]	0.0469/0.1284	0.0279/0.0623	0.0344/0.0907
R_1/wR_2 (all data)[b]	0.0601/0.1370	0.0368/0.0667	0.0371/0.0925
GOF[a]	1.090	1.052	1.057

[a]$GOF = [\Sigma w(F_0^2 - F_c^2)^2 / (n_0 - n_p)]^{1/2}$. [b]$R_1 = \Sigma(||F_0| - |F_c||) / \Sigma|F_0|$, $F_0 > 4\sigma(F_0)$. [c]$wR_2 = \{\Sigma[w(F_0^2 - F_c^2)^2 / \Sigma[w(F_0^2)^2]\}^{1/2}$.

Table S2. Crystallographic data for compounds **4-Y**, **4-Dy**, and **4-Ho**

	4-Y*	**4-Dy**	**4-Ho**
formula	$C_{43}H_{67}BN_9Y \cdot 3\ C_4H_8O$	$C_{43}H_{67}BN_9Dy \cdot 1/2\ C_7H_8$	$C_{43}H_{67}BN_9Ho \cdot 1/2\ C_7H_8$
CCDC	2312214	2312225	2312219
M_r [g mol^{-1}]	1026.08	929.43	931.86
color	colourless	light yellow	yellow
crystal dimensions [mm^3]	0.267 x 0.176 x 0.072	0.145 x 0.081 x 0.056	0.107 x 0.105 x 0.054
cryst syst	monoclinic	monoclinic	monoclinic
space group	*P2₁*	*C2/c*	*C2/c*
a [Å]	11.4785(19)	41.940(3)	41.814(2)
b [Å]	17.511(3)	11.5627(7)	11.5565(6)
c [Å]	14.619(2)	19.9969(12)	20.0524(10)
α [°]	90	90	90
β [°]	105.928(4)	102.8940(10)	102.683(2)
γ [°]	90	90	90
V [Å^3]	2825.5(8)	9452.7(10)	9453.4(8)
Z	2	8	8
T [K]	100(2)	100(2)	100(2)
ρ_{calcd} [g cm^{-3}]	1.206	1.306	1.309
μ [mm^{-1}]	1.081	1.622	1.715
F (000)	1104	3872	3880
θ range [°]	1.449/ 22.520	1.830/28.720	1.832/28.508
unique reflns	34654	75914	68042
observed reflns	7276	12234	11080
R_1/wR_2 (I>2σ)[b]		0.0385/0.0773	0.0519/0.0805
R_1/wR_2 (all data)[b]		0.0629/0.0870	0.1002/0.0939
GOF[a]	1.110	1.022	1.013

[a]GOF = $[\Sigma w(F_0^2 - F_c^2)^2 / (n_0 - n_p)]^{1/2}$. [b]$R_1 = \Sigma(||F_0| - |F_c||) / \Sigma|F_0|$, $F_0 > 4\sigma(F_0)$, $wR_2 = \{\Sigma[w(F_0^2 - F_c^2)^2 / \Sigma[w(F_0^2)^2]\}^{1/2}$.

* Connectivity only.

Table S3. Crystallographic data for compounds **5-Dy**, **5-Ho** and **6-Ho**

	5-Dy	**5-Ho**	**6-Ho**
formula	$C_{35}H_{58}B_2N_7DyAl_{0.86}/Ga_{0.14}$ ·1/2 C_7H_8	$C_{35}H_{58}BN_7HoAl$	$C_{36}H_{60}BN_7HoAl$· C_7H_8
CCDC	2312218	2312216	2312215
M_r [g mol^{-1}]	829.43	779.60	885.76
color	yellow	colorless	yellow
crystal dimensions [mm^3]	0.341 x 0.072 x 0.039	0.315 x 0.067 x 0.028	0.273 x 0.173 x 0.150
cryst syst	monoclinic	triclinic	monoclinic
space group	$P2_1/n$	$P\bar{1}$	Cc
a [Å]	9.5640(11)	11.8446(8)	21.5531(9)
b [Å]	23.328(3)	12.0811(8)	11.2886(5)
c [Å]	18.369(2)	15.8693(11)	19.1515(8)
α [°]	90	81.388(2)	90
β [°]	100.874(2)	80.802(2)	108.0490(10)
γ [°]	90	66.125(2)	90
V [Å^3]	4024.6(8)	2040.7(2)	4430.3(3)
Z	4	2	4
T [K]	173(2)	100(2)	100(2)
ρ_{calcd} [g cm^{-3}]	1.369	1.269	1.328
μ [mm^{-1}]	2.005	1.991	1.843
F (000)	1714	804	1840
θ range [°]	2.079/30.550	1.852/24.850	1.988/28.770
unique reflns	73807	43797	35460
observed reflns	12298	7013	11130
R_1/wR_2 (I>2σ)[b]	0.0334/0.0719	0.0432/0.0908	0.0216/0.0429
R_1/wR_2 (all data)[b]	0.0462/0.0773	0.0656/0.0992	0.0237/0.0438
GOF[a]	1.042	1.046	1.015

[a]GOF = $[\Sigma w(F_0^2 - F_c^2)^2 / (n_0 - n_p)]^{1/2}$. [b]$R_1 = \Sigma(||F_0| - |F_c||) / \Sigma|F_0|$, $F_0 > 4\sigma(F_0)$, $wR_2 = \{\Sigma[w(F_0^2 - F_c^2)^2 / \Sigma[w(F_0^2)^2]\}^{1/2}$.

Table S4. Crystallographic data for compounds **7-Dy**, **9-Dy** and **3-Ho**

	7-Dy	**9-Dy**	**3-Ho**
formula	$C_{42}H_{64}BN_8Dy \cdot 3/2\ C_7H_8$	$C_{44}H_{72}B_2N_7Dy$	$C_{44}H_{72}BN_8Ho \cdot\ C_4H_8O$
CCDC	2312217	2312221	2312223
M_r [g mol^{-1}]	956.49	883.20	960.94
color	yellow	colourless	colorless
crystal dimensions [mm^3]	0.121 x 0.090 x 0.080	0.141 x 0.141 x 0.064	0.184 x 0.128 x 0.064
cryst syst	monoclinic	monoclinic	triclinic
space group	*P2₁/n*	*C2/c*	$P\bar{1}$
a [Å]	12.1758(12)	42.723(6)	10.851(2)
b [Å]	17.8931(17)	10.3005(13)	20.269(4)
c [Å]	23.260(2)	21.324(2)	22.192(5)
α [°]	90	90	96.949(3)
β [°]	96.643(2)	90.449(2)	96.699(3)
γ [°]	90	90	100.067(3)
V [Å^3]	5033.5(8)	9384(2)	4722.7(17)
Z	4	8	4
T [K]	100(2)	100(2)	100(2)
ρ_{calcd} [g cm^{-3}]	1.262	1.250	1.351
μ [mm^{-1}]	1.524	1.628	1.719
F (000)	2000	3688	2016
θ range [°]	1.439/28.700	1.907/ 27.128	1.287/27.157
unique reflns	59881	49937	99190
observed reflns	12905	10376	20871
R_1/wR_2 ($I>2\sigma$)[b]	0.0439/0.0888	0.0376/0.0806	0.0412/0.0832
R_1/wR_2 (all data)[b]	0.0820/0.1048	0.0552/0.0888	0.0703/0.0941
GOF[a]	1.018	1.022	1.010

[a]$GOF = [\Sigma w(F_0^2 - F_c^2)^2 / (n_0 - n_p)]^{1/2}$. [b]$R_1 = \Sigma(||F_0| - |F_c||) / \Sigma|F_0|$, $F_0 > 4\sigma(F_0)$, $wR_2 = \{\Sigma[w(F_0^2 - F_c^2)^2 / \Sigma[w(F_0^2)^2]\}^{1/2}$.

Table S5. Crystallographic data for compounds **8-Dy**, **Ho[Ga(CH$_3$)$_4$]$_3$** and **Dy[Ga(CH$_3$)$_4$]$_3$**

	8-Dy	**Ho[Ga(CH$_3$)$_4$]$_3$**	**Dy[Ga(CH$_3$)$_4$]$_3$**
formula	$C_{40}H_{65}BN_7ODy \cdot 1/2\ C_4H_8O$	$C_{12}H_{36}Ga_3Ho$	$C_{12}H_{36}Ga_3Dy$
CCDC	2312226	2312212	2312213
M_r [g mol^{-1}]	869.35	554.50	552.07
color	yellow	pink	colorless
crystal dimensions [mm^3]	0.241 x 0.137 x 0.107	0.60 x 0.40 x 0.30	0.348 x 0.180 x 0.174
cryst syst	orthorhombic	tetragonal	monoclinic
space group	*Pna2$_1$*	*I4$_1$/a*	*C2/c*
a [Å]	19.7303(9)	17.6111(4)	10.8711(6)
b [Å]	11.5097(5)	17.6111(4)	15.7025(9)
c [Å]	37.3911(18)	26.4443(6)	12.4891(7)
α [°]	90	90	90
β [°]	90	90	102.0700(10)
γ [°]	90	90	90
V [Å^3]	8491.1(7)	8201.7(4)	2084.8(2)
Z	8	16	4
T [K]	100(2)	173(2)	100(2)
ρ_{calcd} [g cm^{-3}]	1.360	1.796	1.759
μ [mm^{-1}]	1.801	7.698	7.360
F (000)	3624	4288	1068
θ range [°]	1.089/30.487	4.834/ 29.234	3.078/ 29.144
unique reflns	219882	76662	16607
observed reflns	25876	5511	2800
R_1/wR_2 (I>2σ)[b]	0.0316/0.0645	0.0404/0.0773	0.0189/0.0479
R_1/wR_2 (all data)[b]	0.0371/0.0669	0.0434/0.0782	0.0196/0.0483
GOF[a]	1.040	1.395	1.065

[a]GOF = $[\Sigma w(F_0^2 - F_c^2)^2 / (n_0 - n_p)]^{1/2}$. [b]$R_1 = \Sigma(||F_0| - |F_c||) / \Sigma|F_0|$, $F_0 > 4\sigma(F_0)$, $wR_2 = \{\Sigma[w(F_0^2 - F_c^2)^2 / \Sigma[w(F_0^2)^2]\}^{1/2}$.

X-ray Crystallography and Crystal Structure Determinations. Single crystals of the reported compounds **1-Ln** – **9-Ln** were grown by standard techniques from saturated solutions using toluene. Suitable crystals for X-ray structure analyses were selected in a glovebox and coated with Parabar 10312 (previously known as Paratone N, Hampton Research) and fixed on a nylon loop/glass fiber.

X-ray data for above mentioned compounds, except for **1-Ho^{Ga}** and $Ho(Ga(CH_3)_4)_3$, were collected on a Bruker APEX II DUO (all remaining; instruments equipped with an IμS microfocus sealed tube and QUAZAR optics for MoKα (λ = 0.71073 Å) and CuKα (λ = 1.54184 Å) radiation. **1-Ho^{Ga}** was measured on a Bruker SMART APEX II instrument equipped with a fine focus sealed tube and TRIUMPH monochromator using MoK_α radiation (λ = 0.71073 Å). The data collection strategy was determined using COSMO[4] employing ω-scans. Raw data were processed using APEX II/III[5] and SAINT,[6] corrections for absorption effects were applied using SADABS.[7] Data for $Ho(Ga(CH_3)_4)_3$ were collected at 173(2) K on a STOE IPDS II system, equipped with a fine focus sealed tube and graphite monochromator using MoK_α radiation (λ = 0.71073 Å) performing ϕ-scans. Raw data were collected and integrated using Stoe's X-Area[8] software package. Absorption correction has been done using X-Red[9] and X-Shape[10]. The structures were solved by direct methods and refined against all data by full-matrix least-squares methods on F^2 using ShelXl[11] and ShelXle.[12] All graphics were produced employing ORTEP-3[13] and POV-Ray.[14] Further details of the refinement and crystallographic data are listed in Table S1-S5, and in the CIF files. CCDC depositions 2312212-2312226 contain all the supplementary crystallographic data for this paper. These data can be obtained free of charge from The Cambridge Crystallographic Data Centre via www.ccdc.cam.ac.uk/structures/.

DRIFT Spectroscopy

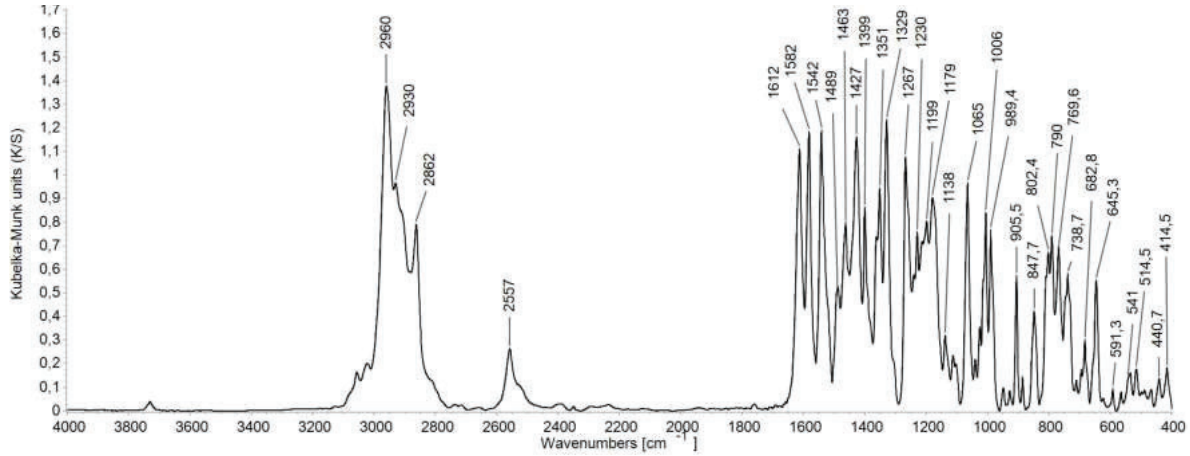

Figure S16. DRIFT spectrum (KBr) of compound **4-Dy** at 26 °C.

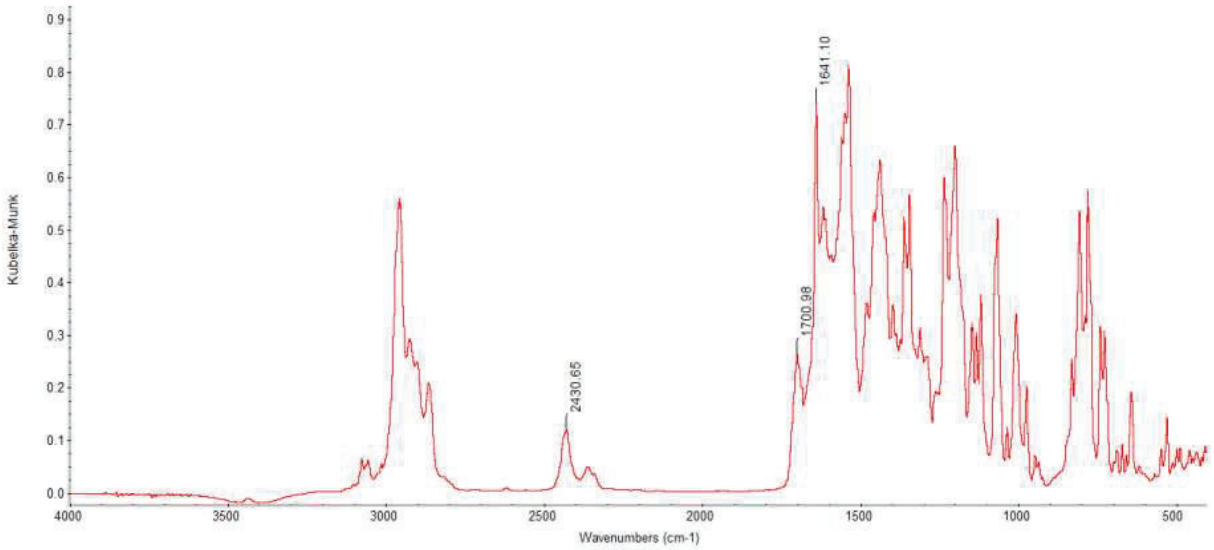

Figure S17. DRIFT spectrum (KBr) of compound **10-Dy** at 26 °C.

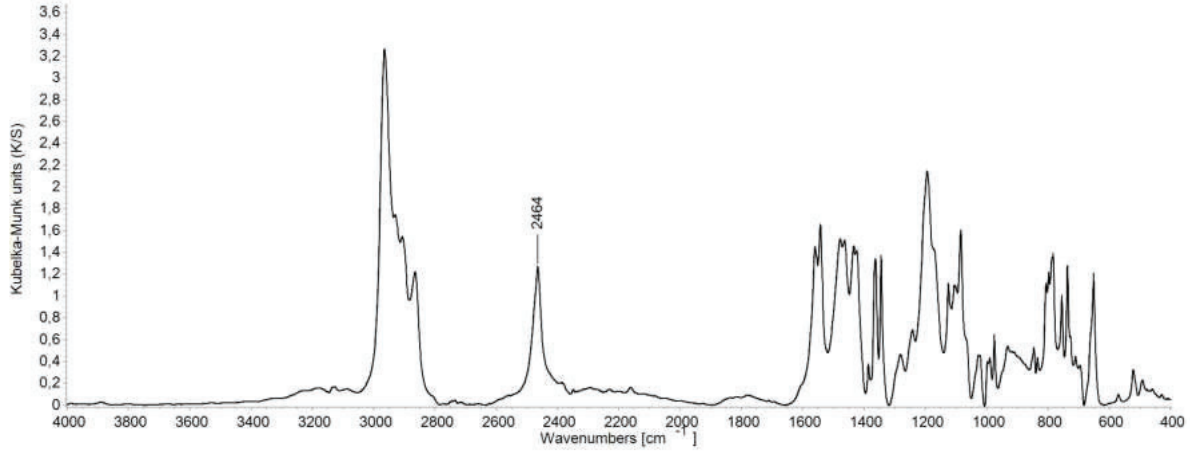

Figure S18. DRIFT spectrum (KBr) of compound of HTp^{tBu,Me} at 25 °C.

NMR spectroscopy

Notes on NMR spectroscopic characterizations.

Due to the paramagnetic nature of Dy(III) and Ho(III) any conclusive interpretation of the recorded NMR spectra was not possible. In general, solvent peaks are marked with an asterisk (*).

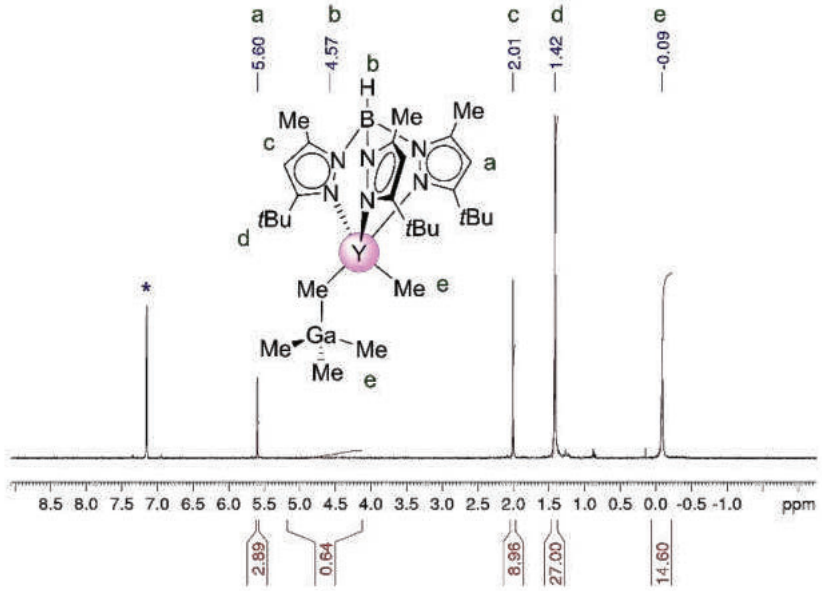

Figure S19. ^{1}H NMR spectrum (400 MHz) of compound **1-Y^{Ga}** in C_6D_6 at 26 °C.

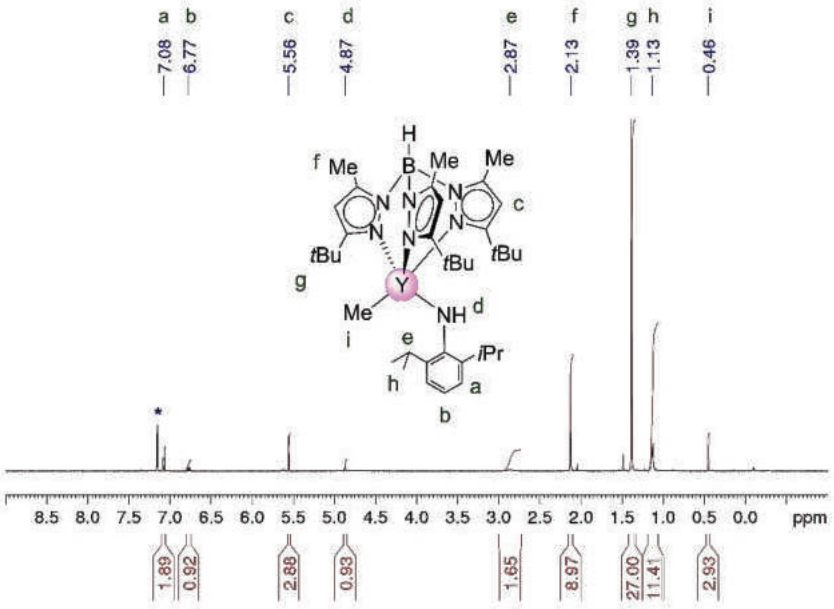

Figure S20. ^{1}H NMR spectrum (400 MHz) of compound **2-Y** in C_6D_6 at 26 °C.

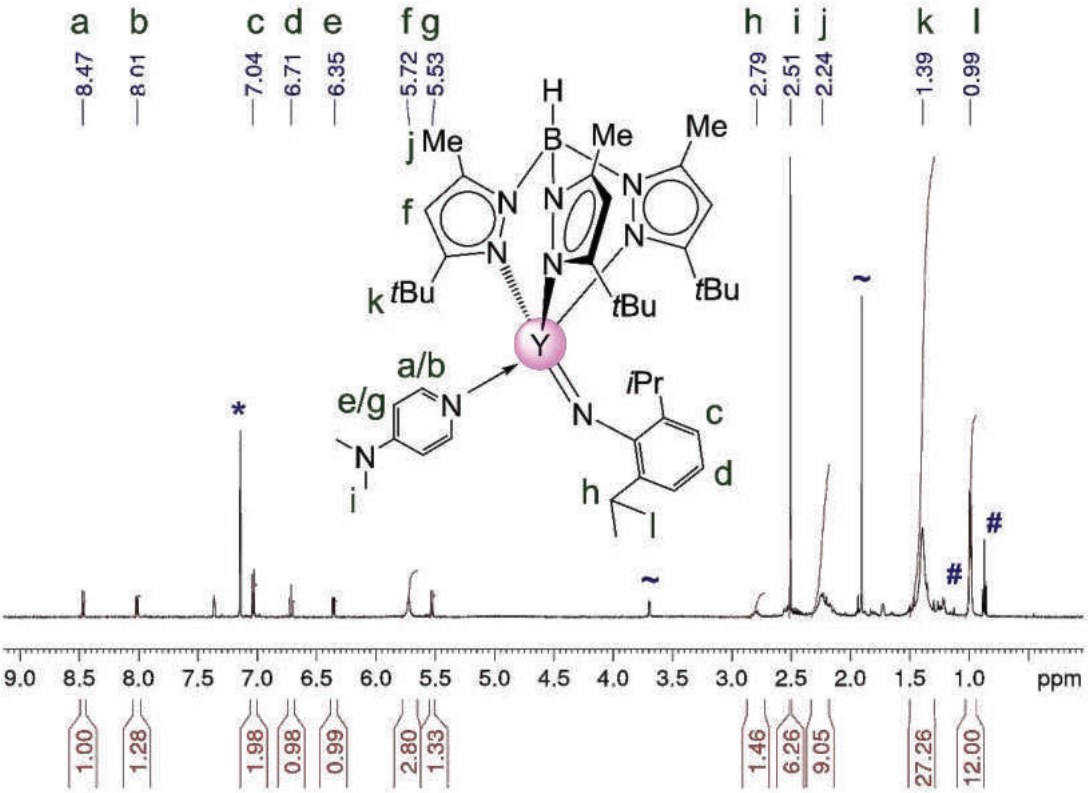

Figure S21. ^{1}H NMR spectrum (500 MHz) of compound **4-Y** in C_6D_6 at 26 °C.

References

[1] J. L. Kisko, T. Hascall, C. Kimblin and G. Parkin, *J. Chem. Soc., Dalton Trans.,* 1999, 1929-1936.

[2] M. Zimmermann, N. Å. Frøystein, A. Fischbach,. P. Sirsch, H. M. Dietrich, K. W. Törnroos, E. Herdtweck and R. Anwander, *Chem. Eur. J.*, 2007, **13**, 8784-8800.

[3] W. J. Evans, R. Anwander, R. J. Doedens and J. W. Ziller, *Angew. Chem. Int. Ed. Engl.*, 1994, **33**, 1641-1644.

[4] COSMO, v. 1.61; Bruker AXS Inc.: Madison, WI, 2012.

[5] APEX 3 V. 2019.11-0, Bruker AXS Inc., Madison, WI, 2019.
APEX *2 V. 2012.10_0*, Bruker AXS Inc., Madison, WI, 2012.

[6] *SAINT V. 8.38A*, Bruker AXS Inc., Madison, WI, 2017.
SAINT V. 8.40B, Bruker Nano, Inc., Madison, WI, 2019.

[7] SADABS: L. Krause, R. Herbst-Irmer, G. M. Sheldrick and D. Stalke, *J. Appl. Crystallogr.* 2015, **48**, 3.

[8] *X-Area v. 1.55*, Stoe & Cie GmbH, Darmstadt, Germany, 2009.

[9] *X-Red 32 v. 1.53*, Stoe & Cie GmbH, Darmstad, Germany, 2009.

[10] *X-Shape v.2.12.2*, Stoe & Cie GmbH, Darmstadt, Germany, 2009.

[11] ShelXL: Sheldrick, G. M., Crystal structure refinement with SHELXL, *Acta Cryst.* **2015***,* C71, 3-8

[12] ShelXle: C. B. Hübschle, G. M. Sheldrick and B. Dittrich, *J. Appl. Crystallogr.* 2011, **44**, 1281-1284.

[13] L. J. Farrugia, *J. Appl. Crystallogr.* 1997, **30**, 565-566.

[14] POV-Ray v. 3.6; Persistence of Vision Pty. Ltd.: Williamstown, Victoria, Australia, 2004. http://www.povray.org/ .

F

Appendix

Appendix

Analytical data of compounds not included in the main results or manuscripts

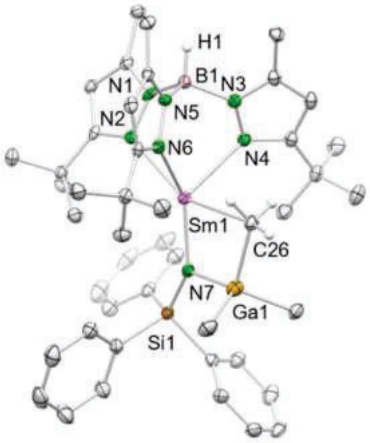

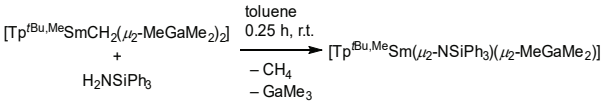

$[Tp^{tBu,Me}Sm(\mu_2\text{-}NSiPh_3)(\mu_2\text{-}MeGaMe_2)]$ TR136

R_1[I>sigma(I)] 4.07%, wR_2(all data) 10.70%

a = 12.0526(7) Å, α = 79.486(2)°

b = 12.8860(7) Å, β = 81.093(2)°

c = 18.3379(10) Å, γ = 88.459(2)°

Structurally characterized complexes

On the following pages all X-ray structurally characterized compounds are listed as *ChemDraw* sketches.

Rare-Earth-Metal Methylidene, and Bis(alkyl) Complexes

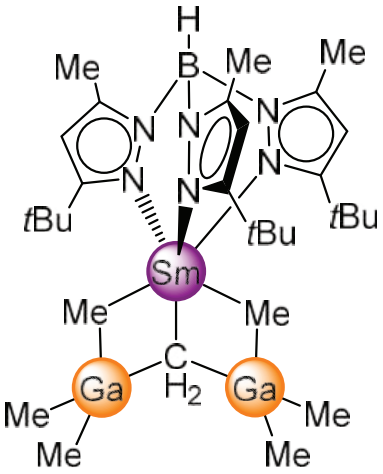

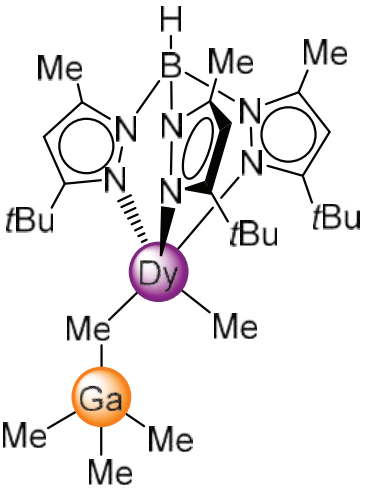

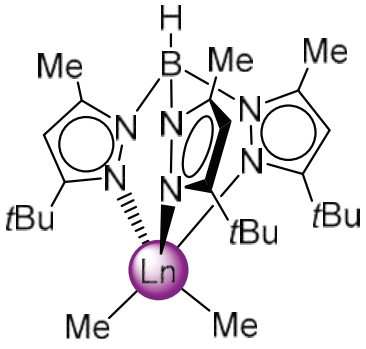

Ln = Y, Dy

Rare-Earth-Metal Amide Complexes

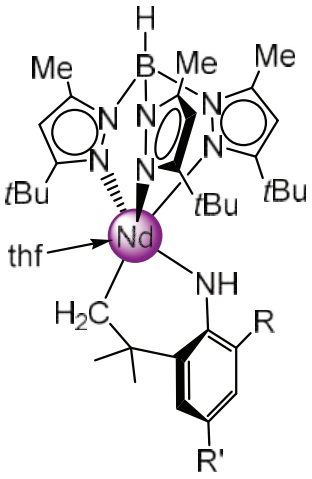

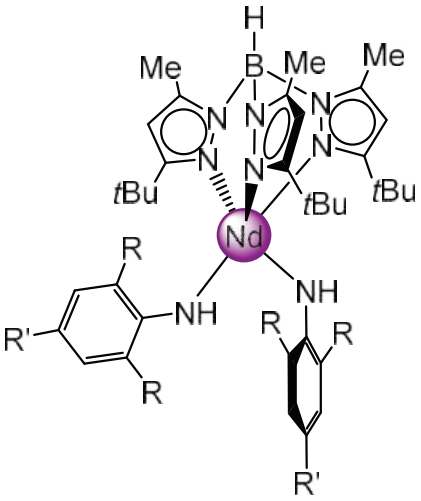

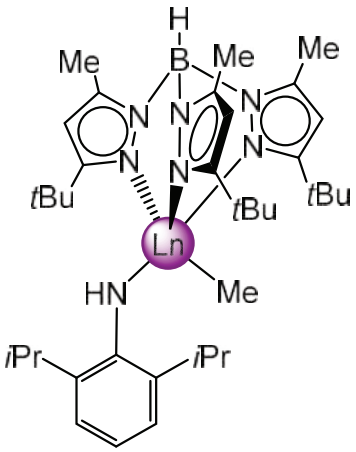

Ln = Y, Dy, Ho

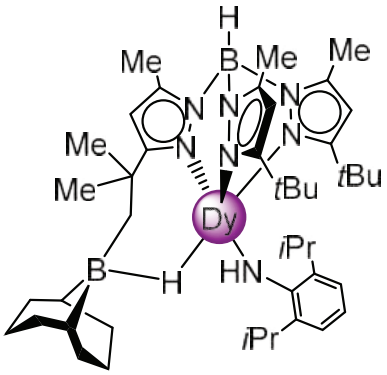

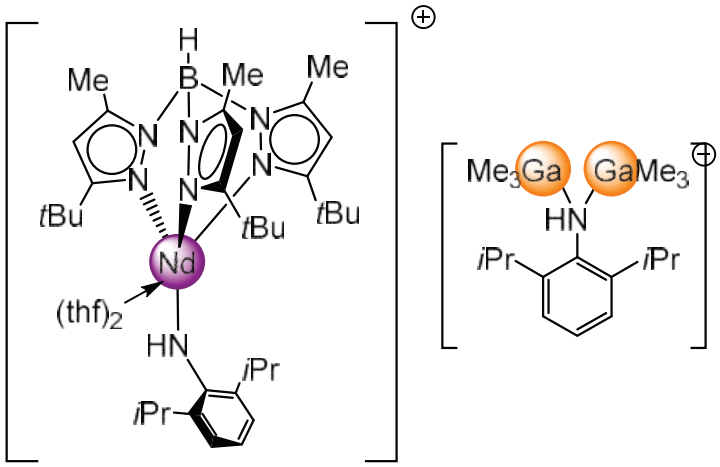

Rare-Earth-Metal Imide Complexes

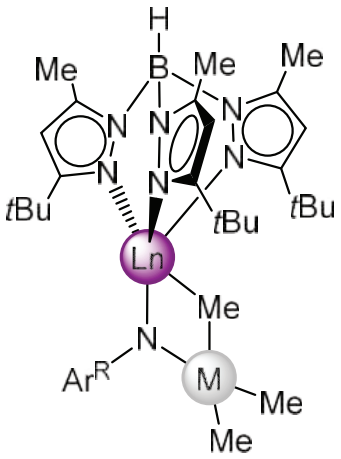

Ln = Nd, Sm, Dy, Ho
M = Al, Ga
R = *i*Pr, Me

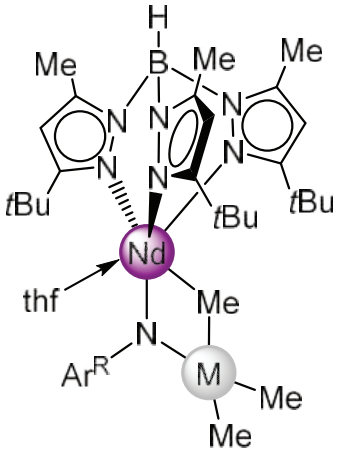

Ar^{Mes} = $C_6H_2Me_3$-2,4,6

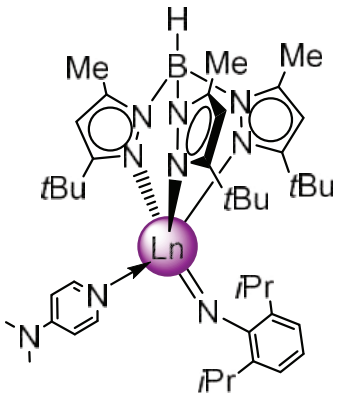

Ln = Y, Dy, Ho

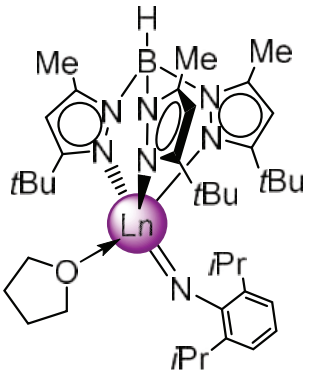

Ln = Nd, Dy

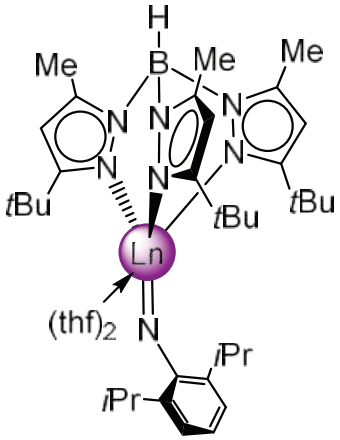

Ln = Nd, Sm
Ar^{iPr} = $C_6H_3iPr_2$-2,6

Rare-Earth-Metal Phosphide and Phosphinidene Complexes

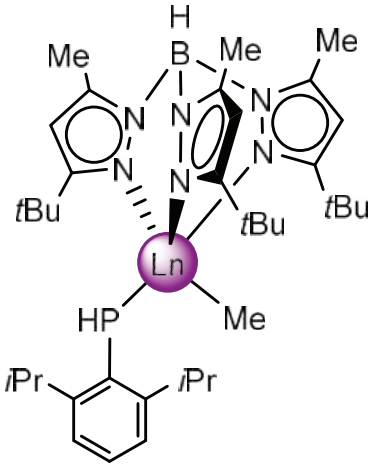

Ln = Y, Ho

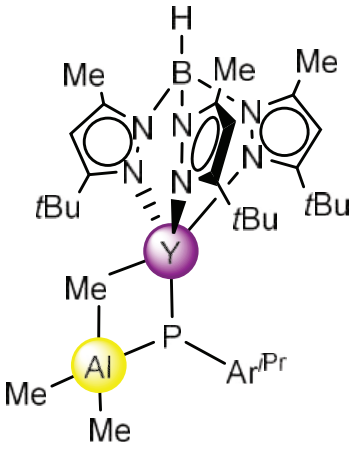

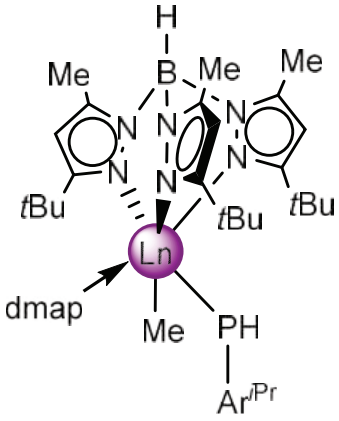

Ln = Y, Ho

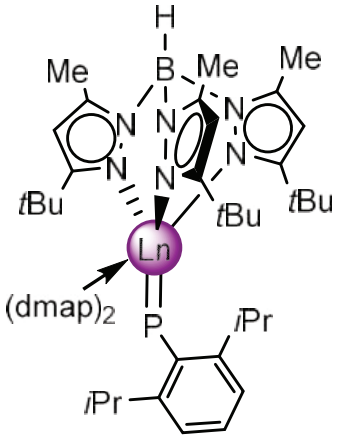

Ln = Y

Terminal Rare-Earth-Metal Methyl Complexes and *n*-Hexane Activation

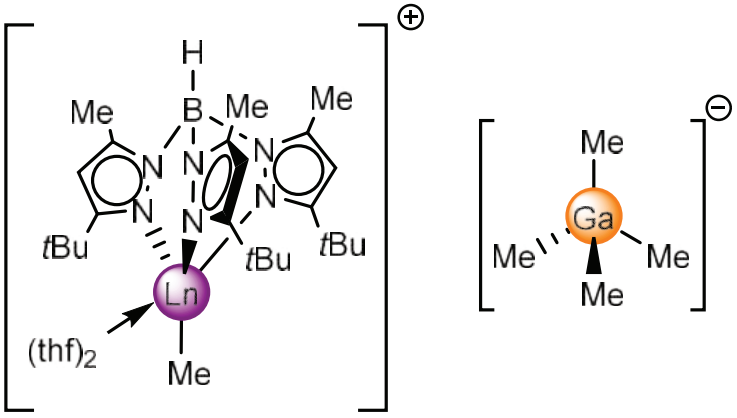

Ln = Sm, Dy, Ho